Department of Civil Engineering
University of Alberta
Edmonton

Structural Engineering Report No. 138

FINITE ELEMENT PREDICTION OF REINFORCED CONCRETE BEHAVIOR

by

S. BALAKRISHNAN

D. W. MURRAY

July, 1986

RECENT STRUCTURAL ENGINEERING REPORTS

Department of Civil Engineering

University of Alberta

133. *Behaviour of Fillet Welds as a Function of the Angle of Loading* by G.S. Miazga and D.J.L. Kennedy, March 1986.

134. *Inelastic Seismic Response of Precast Concrete Large Panel Coupled Shear Wall Systems* by M.R. Kianoush and A. Scanlon, March 1986.

135. *Finite Element Prediction of Bin Loads* by A.H. Askari and A.E. Elwi, June 1986.

136. *Shear Behavior of Large Diameter Fabricated Steel Cylinders* by J. Mok and A.E. Elwi, June 1986.

137. *Local Buckling Rules for Structural Steel Members* by S. Bild and G.L. Kulak, May 1986.

138. *Finite Element Prediction of Reinforced Concrete Behavior* by S. Balakrishnan and D.W. Murray, July 1986.

139. *Behavior and Strength of Masonry Wall/Slab Joints* by T.M. Olatunji and J. Warwaruk, July 1986.

140. *Bayesian Analysis of In-Situ Test Data for Estimating the Compressive Strength of Concrete in Existing Structures* by G.J. Kriviak and A. Scanlon, July 1986.

141. *Shear-Moment Transfer in Slab-Column Connections* by S.D.B. Alexander and S.H. Simmonds, July 1986.

142. *Minimum Thickness Requirements for Deflection Control of Two-Way Slab Systems* by D.P. Thompson and A. Scanlon, November 1986.

143. *Shrinkage and Flexural Tests of Two Full-Scale Composite Trusses* by A. Brattland and D.J.L. Kennedy, December 1986.

144. *Combined Flexure and Torsion of I-Shaped Steel Beams* by R.G. Driver and D.J.L. Kennedy, March 1987.

145. *Cyclic and Static Behaviour of Thin Panel Steel Plate Shear Walls* by E.W. Tromposch and G.L. Kulak, April 1987.

146. *Postbuckling Behavior of Thin Steel Cylinders Under Transverse Shear* by V.G. Roman and A.E. Elwi, May 1987.

147. *Incipient Flow in Silos - A Numerical Approach* by R.A. Link and A.E. Elwi, May 1987.

148. *Design of Web-Flange Beam or Girder Splices* by D. Green and G.L. Kulak, May 1987.

149. *Spreadsheet Solution of Elastic Plate Bending Problems* by G.E. Small and S.H. Simmonds, July 1987.

150. *Behaviour of Transversely Loaded Continuous Steel-Concrete Composite Plates* by S.J. Kennedy and J.J. Cheng, July 1987.

151. *Behaviour and Ultimate Strength of Partial Joint Penetration Groove Welds* by D.P. Gagnon and D.J.L. Kennedy, July 1987.

152. *KBES for Design of Reinforced Concrete Columns* by A. Bezzina and S.H. Simmonds, July 1987.

153. *Compressive Behavior of Gusset Plate Connections* by S.Z. Hu and J.J. Cheng, July 1987.

154. *Development of Structural Steel Design Standards* by P.J. Marek and D.J.L. Kennedy, October 1987.

155. *Behaviour of Bolted Joints of Corrugated Steel Plates* by R.W.S. Lee and D.J.L. Kennedy, January 1988.

156. *Masonry Veneer Wall Systems* by W.M. McGinley, J. Warwaruk, J. Longworth and M. Hatzinikolas, January 1988.

157. *Stability of Concrete Plates* by A.O. Aghayere and J.G. MacGregor, February 1988.

158. *The Flexural Creep Behaviour of OSB Stressed Skin Panels* by P.C.K. Wong, L. Bach and J.J. Cheng, April 1988.

159. *Ultimate Strength of Eccentrically Loaded Fillet Welded Connections* by D.F. Lesik and D.J.L. Kennedy, May 1988.

160. *Fatigue Strength of Coped Steel Beams* by M.C.H. Yam and J.J. Cheng, June 1988.

161. *Analysis of Concrete Panels* by B. Massicotte, A.E. Elwi and J.G. MacGregor, July 1988.

162. *Behavior and Design of Reinforced Concrete Ice-Resisting Walls* by R.M. Ellis and J.G. MacGregor, November 1988.

163. *An Analysis of the Performance of Welded Wide Flange Columns* by D.E. Chernenko and D.J.L. Kennedy, December 1988.

164. *Nonlinear Dynamic Analysis of Caisson-Type Offshore Structures* by I.R. Soudy and T.M. Hrudey, March 1989.

165. *NORCO - A Program for Nonlinear Finite Element Analysis of Reinforced Concrete Structures - Users' Manual* by S. Balakrishnan, A.E. Elwi and D.W. Murray, April 1989.

The University of Alberta

Finite Element Prediction of Reinforced Concrete Behavior

by

S. Balakrishnan

D.W. Murray

Structural Engineering Report No. 138

Department of Civil Engineering

University of Alberta

Edmonton, Alberta, Canada, T6G 2G7

July 1986

ABSTRACT

In order for practicing engineers to have confidence in the finite element method (FEM), there is a need for verification that the method gives results which consistently agree with experimental data on structures exhibiting a wide range of failure modes. Also, in order for the practicing engineer to use the nonlinear FEM, the cost and time constraints must not be exceeded.

In this study a simple concrete constitutive relationship, oriented in the principal strain directions, has been developed, which has been found to be adequate, when incorporated into a finite element program, to closely predict the behavior and failure mechanisms of beams and panels.

Predicted behavior of orthogonally reinforced panels in which failure modes vary from ductile steel yielding, to one layer of steel yielding, to brittle failure of concrete is compared to the behavior observed in tests on panels exhibiting these various failure modes. It is shown that the ultimate strength of shear panels failing by at least one layer of steel yielding, can be closely predicted using equilibrium considerations alone, if the post-cracking compressive strength criterion developed herein is adopted.

Predicted behavior of beams, which exhibit different failure mechanisms as the shear span to depth ratio is varied, is compared to the behavior observed in the laboratory for specimens in which the failure modes vary from ductile flexural failures, to shear-compression failures, to diagonal tension failures, to arch and bearing failures. The effects, on the analysis, of tension softening of concrete at

cracks, tension stiffening of concrete segments between the cracks, secondary cracking, compressive strain softening, concrete confinement, shear stiffness of cracked concrete and bond-slip at concrete/steel interfaces are examined. The influence of modeling parameters such as the order of the element, order of numerical integration and mesh size is discussed. Recommendations on the parametric values of concrete characteristic properties, which produce reliable predictions of behavior for practical applications, are made. Insights gained during the analysis into the behavior of shear critical beams are discussed.

It is shown that, for reliable predictions, the descending branch of the tensile stress-strain curve must be modelled and the variation of the shear modulus of cracked concrete with crack strain must be represented.

ACKNOWLEDGEMENTS

This report is based upon the research carried out by the first author in partial fulfillment of the requirements for the degree of Ph.D. in Civil Engineering at the University of Alberta.

The author wishes to express his deep appreciation and gratitude to Professor David W. Murray whose supervision and guidance have been invaluable. The author wishes to thank Dr. Alaa E. Elwi for his support and advice and Professor James G. MacGregor for a number of valuable discussions. The author thanks Ms. Nola Shaw for careful typing of the manuscript.

The author deeply appreciates the support and patience of his wife throughout the course of this study.

TABLE OF CONTENTS

LIST OF TABLES

LIST OF FIGURES

LIST OF SYMBOLS

Vectors and Matrices

$\mathbf{B}$	Matrix differential operator associated with strain-displacement equations
$\mathbf{D}$	Symmetric elastic constitutive matrix
$\mathbf{D}_{ep}$	Elastic-plastic constitutive matrix
$\mathbf{D}^{co}$	Uncracked concrete constitutive matrix
$\mathbf{D}^{cr}$	Crack interface stress-strain relationship
$\mathbf{D}_t$	Tangent constitutive matrix
$\mathbf{E}$	Nonlinear function of strains
$\mathbf{e}^{cr}$	Crack strains in local axes
$\mathbf{F}$	Concentrated forces
$\mathbf{f}^S$	Surface tractions
$\mathbf{f}^b$	Body forces
$\mathbf{G}$	$\mathbf{B}^t\mathbf{D}_t\mathbf{B}$ det J
$\mathbf{J}$	Jacobian operator
det J	Determinant of J
$\mathbf{K}_t$	Tangent structure stiffness matrix
$^L\mathbf{K}$	Tangent structure stiffness matrix corresponding to any equilibrium configuration L
$^o\mathbf{K}$	Initial structure stiffness matrix
$\mathbf{K}_{s_t}$	Stiffness matrix of reinforcing element
$\mathbf{K}^s_{ss}\mathbf{K}^s_{ss}\mathbf{K}^s_{sb}\mathbf{K}^s_{bb}$	Submatrices obtained by partitioning $\mathbf{K}_{s_t}$
$\mathbf{K}_{s+b_t}$	Stiffness matrix of combined reinforcing and bond element
$\mathbf{N}$	Displacement interpolation matrix in Chapter 2
	Strain transformation matrix in Chapter 3

$\mathbf{Q}$	Set of forces equilibrating the internal stresses
$\mathbf{R}$	External forces applied to the structure
$\mathbf{S}^{cr}$	Crack interface stresses
$\mathbf{u}$	Displacement at any point
$\mathbf{U}$	Vector of nodal displacmenets
$\overline{\mathbf{U}}$	Vector of nodal displacments including slip degrees of freedom
$\mathbf{U}^*$	Correct nodal displacements
$\boldsymbol{\varepsilon}$	Strain tensor
$\boldsymbol{\varepsilon}_e$	Elastic strains
$\boldsymbol{\varepsilon}_p$	Plastic strains
$\boldsymbol{\sigma}$	Stress tensor
$\boldsymbol{\sigma}_o$	Initial stress tensor
$\boldsymbol{\Psi}$	Unbalanced nodal forces

Scalars

A_s	Cross sectional area of reinforcement
A_p	Circumferential area of reinforcement
A_c	Area of concrete
A_v	Area of web reinforcement
a	Shear span
B	Indicates failure by concrete crushing without steel yielding
b	Width of reinforced concrete beam cross-section
C	Concrete cover (Chapter 3) Compressive force resultant (Chapter 5)
C_d	Diagonal compression in the truss model

c	Distance from the extreme compression fibre to the neutral axis
D	Indicates failure by steel yielding
D_b	Local bond modulus
D_{bt}	Tangent bond modulus
DB	Indicates failure by concrete crushing after steel yielding in one direction
d	Effective depth, i.e., the distance from the extreme compression fibre to the reinforcement
dr	differential length of reinforcement
E_1	Tangent modulus determined from equivalent uniaxial stress-strain curve in the major principal stress direction
E_2	Tangent modulus determined from equivalent uniaxial stress-strain curve in the minor principal stress direction
E_c	Tangent modulus of concrete. In cracked concrete, tangent modulus parallel to the crack direction.
E_{cr}	Tangent modulus of cracked concrete in tension
E_i	Current tangent modulus in the ith direction used in relation to the equivalent uniaxial stress-strain curve
E_s	Modulus of steel reinforcement
E_{s_t}	Tangent modulus of steel
E_t	Tensile strain softening modulus
F	Yield function
f_c	Stress in concrete

	Effective compressive strength of concrete in connection with plasticity based models
f_{c_1}	Stress in concrete in the major principal strain direction
f_{c_2}	Stress in concrete in the minor principal strain direction
f'_c	Uniaxial compressive strength
f_{cd}	Diagonal compression stress in concrete
f_{cu}	Compressive strength of concrete
f_{c_x}	Stress in concrete in the x direction
f_{c_y}	Stress in concrete in the y direction
$f_{c_{xy}}$	Shear stress in concrete referred to x-y axes
f_{c_ξ}	Major principal stress in concrete
f_{c_η}	Minor principal stress in concrete
f_r	Modulus of rupture of concrete
f_s	Stress in steel
$f_s^{(1)}$	Stress in steel at the onset of primary cracking
f_{s_x}	Stress in steel in the x direction
f_{s_y}	Stress in steel in the y direction
$\overline{f}_{s_x}$	Yield strength of steel in the x direction
$\overline{f}_{s_y}$	Yield strength of steel in the y direction
f_t	Tensile stress in concrete
f_{tu}	Tensile strength of concrete
f'_t	Uniaxial tensile strength of concrete
$f^{(ts)}$	Tension stiffening stress in concrete
$f_{t_{sf}}$	Tension softening stress in concrete
f_v	Stress in stirrups
f_x	Applied stress in the x direction
f_y	Applied stress in the y direction

f_{y_w}	Yield strength of web reinforcement
G	Shear modulus of uncracked concrete
G_{cr}	Shear modulus of cracked concrete
G_F	Fracture energy release rate
H_j	Shape function corresponding to slip d.o.f. j
H'	Plastic strain hardening modulus
h	Assumed width of the fracture zone
h_c	Width of the fracture zone
h_{cr}	Height of crack
J_s	Jacobian for steel element
jd	Distance between the compressive and tensile force resultants, i.e., 'lever arm'
K_1, K_2	Constants used to determine average crack spacing
K_{IST}	Interface shear stiffness of a crack
K_N	Stiffness normal to crack
k	A factor to account for the distribution of bond stress (Chapter 3)
	Hardening parameter in the plasticity theory (Chapter 3)
k_1	A constant (Chapter 3)
	Ratio of the volume of compression stress block to the rectangular stress block (Chapter 5)
k_2c	Location of the resultant compressive force from the extreme compression fibre
k_3	Ratio of the compressive stress at the extreme compression fibre to the cylinder compressive strength of concrete
M	Bending moment at a concrete section
M_u	Usable moment capacity of a beam cross-section

$M_{f\ell}$	Flexural capacity of a beam cross-section
N_i	Displacement interpolation function corresponding to node i
p	Number of slip d.o.f. in an element
Q	Plastic potential
q	Number of element nodes (Chapter 2)
	'Shear flow' (Chapter 5)
S	Crack spacing (Chapter 3)
	Stirrup spacing (Chapter 5)
S_o	'Bond length' used in slip theory
S_b	Area of contact between concrete and reinforcement
S_m	Average crack spacing
T	Tensile force in steel reinforcement
U_{b_j}	Displacement corresponding to bond slip d.o.f. j
u	Displacement at any point in the x direction
u_i	Displacement at node i in the x direction
V	Shear force
V_{arch}	Shear resistance due to 'arch action'
V_{beam}	Shear resistance due to 'beam action'
V_I	Shear force at inclined cracking
V_s	Shear resistance provided by stirrups
V_u	Shear capacity of a beam cross-section
V_{uc}	'Concrete contribution' to the shear capacity
v	Volume
	Displacement at any point in the y direction
v_i	Displacement at node i in the y direction
v_s	Nominal shear stress 'resisted' by web reinforcement

w	Crack displacement
w_o	Initial crack width
w_c	Displacement of concrete
w_b	Bond slip
w_s	Displacement of steel
x,y	Coordinates at any point
x_i,y_i	Nodal coordinates
α	σ_1/σ_2 - Ratio of minor to major principal stress (Chapter 3)
	Effectiveness factor (Chapter 4)
	Crack inclination in the truss model (Chapter 5)
α_o	Angle of the asperity from the average crack orientation
α_{ij}	Weighting factors corresponding to Gauss points ξ_i,η_j
β	Factor to account for the apparent degradation of compression strength due to normal crack strain
γ_{12}	Shear strain referred to 1-2 axes
γ_{xy}	Shear strain referred to x-y axes
δ	'Variation in'
δ_g	Slip due to deformation of asperities of a crack
δ_n	Relative displacement of the crack faces normal to the average orientation of the crack
δ_s	'Free slip' of a crack (movement before contact of the asperities)
δ_t	Relative displacement of the crack faces tangent to the average orientation of the crack
ε	Normal strain

ε_1	Major principal strain. Also, strain normal to crack.
ε_2	Minor principal strain
ε_{cr}	Cracking strain of concrete (corresponding to f_t')
ε_c'	Uniaxial strain corresponding to f_c' in cylinder test
ε_{iu}	Equivalent uniaxial strain in the ith direction
ε_s	Strain in steel
$\bar{\varepsilon}_s$	Yield strain of steel
ε_{up}	Plastic strain in the uniaxial test
ε_{ut}	Threshold strain at which tensile stress has reduced to zero
ε_{gt}	Threshold strain at which shear modulus of cracked concrete is reduced to the minimum value
ε_x	Strain in the x direction
ε_y	Strain in the y direction
σ_1	Major principal stress
σ_{1c}	Compressive strength in the major principal stress direction under biaxial compression
σ_{1t}	Tensile strength under biaxial stresses
σ_2	Minor principal stress
σ_{2c}	Compressive strength in the minor principal stress direction under biaxial compression
σ_b	Bond stress
σ_i	Principal stress in the ith direction
σ_s	Stress in steel
σ_y	Uniaxial stress
η	Local coordinate direction
η_i	Local coordinate corresponding to the ith node or Gauss

	point
θ	Orientation of reinforcement (Chapter 2)
	Orientation of principal stress axes (Chapter 4)
θ'	Orientation of principal strain axes
λ	Proportionality constant used in the plasticity theory
λ_U	Displacement tolerance
λ_R	Tolerance on unbalanced nodal forces
ν	Poisson's ratio
ξ	Local coordinate direction
ξ_i	Local coordinate corresponding to the ith node or Gauss point
ρ	Reinforcement ratio
ρ_x	Steel reinforcement ratio in the x direction
ρ_y	Steel reinforcement ratio in the y direction
τ	Applied shear stress
τ_b	Bond stress
τ_{12}	Shear stress referred to 1-2 axes
ϕ	Diameter of reinforcing bar
Δ	Increment in
Σ	Sum

Notation for Superscripts

(m)	Element m
s	Surface
(j),(j-1)	Iteration number
t	Transpose
$\ell, \ell+\Delta\ell$	Load steps

cr	Cracked concrete
co	Uncracked concrete
(0),(-1),(-2),(1),(2),(ℓ),(k)	Damage regions

CHAPTER 1

INTRODUCTION

1.1 Finite Element Analysis of Reinforced Concrete

The design of simple reinforced concrete structures is usually performed following approximate or empirical procedures prescribed in codes of recommended practice to satisfy safety and serviceability requirements. The design of complex structures, such as offshore oil platforms, nuclear containment structures, high rise buildings and long span bridges, requires the prediction of the behavior of these structures under load from a knowledge of the basic properties of the constituent materials. Predicting the response of structures to loads and imposed deformations involves two interrelated tasks: (1) modelling the structure as a system of discrete structural elements interconnected at joints or nodal points to determine how the load is shared among the different elements, usually called 'global analysis'; and, (2) predicting the response of each individual structural element under its share of the applied load, usually called 'member analysis'. Depending upon whether the objective is a global analysis or member analysis, the finite element chosen may be large, such as beam, column or panel type elements; or small, such as plane stress, plate bending or three-dimensional solid elements representing portions of an assumed continuum.

The vast majority of global structural analyses in engineering offices follow traditional patterns - linearized, simplified models in which the reinforced concrete system is assumed to be uncracked, homogeneous and isotropic. The internal forces and moments calculated

from these models are then used to design the members based on ultimate strength using the code provisions which in turn have been based on simplified models and synthesis of experimental data. Special and complex structural problems are often solved using intuitive judgement and/or tests on small scale models. The FEM (i.e. finite element method), because of its ability to take into account the conditions of equilibrium, compatibility and nonlinear material behavior, is a valuable analytical tool which can be used to: (1) directly predict the structural response in the entire load range up to failure; (2) gain greater understanding of the behavior so that simpler but realistic models can be developed; and, (3) study the effects of important parameters on member behavior thus providing a firmer basis for code provisions.

However, in order for practicing engineers to have confidence in the FEM, there is a need for verification that the method gives results which consistently agree with experimental data for a wide range of geometric and material parameters. Also, in order for the practicing engineer to use the nonlinear FEM, the cost and time constraints must not be exceeded. The cost and time involved in the application of the nonlinear FEM must be competitive with other possible approaches, such as a testing program, or perhaps just using a larger factor of safety in design. Thus there is a need to determine the influence of various parameters used in the numerical analysis in predicting the behavior so that individual analyses can be tuned to the desired accuracy.

1.2 Objectives of this Study

The objectives of this study are:

1. To formulate finite elements and to develop simple constitutive models which are adequate, when incorporated into a finite element program, to closely predict the behavior of beams and panels in which failure modes vary from ductile flexural failures, to shear compression failures, to diagonal tension failures, to arch action and bearing failures.

2. To verify the applicability of the models by comparing the predicted behavior to the behavior observed in the laboratory for specimens which exhibit these various types of failure modes.

3. To study the effects (on the analysis) of bond slip, tensile strain softening, tension stiffening, compression softening, secondary cracking, multiaxial stress conditions and the shear stiffness of the cracked concrete, and their importance relative to the various failure modes.

4. To determine the parametric values of concrete properties and solution techniques which produce reliable predictions of beam and panel behavior for practical applications.

1.3 Scope of this Study

This study is concerned with the application of the FEM to predict the behavior of reinforced concrete (hereafter denoted as R/C) structures and structural members when subjected to in-plane static loads. The results of this study may, therefore, be used to predict the behavior of two-dimensional planar continuum structures which can be discretized into interconnected elements subjected to in-plane forces, and to predict the behavior of individual structural members such as beams, as shown in Fig. 1.1. Displacements are considered small. High

temperature and creep effects are outside the scope of this work.

1.4 Organization of the Thesis

In Chapter 2, fundamentals of the FEM are briefly described. Specific formulations are developed for concrete, reinforcement and bond elements based on the principle of virtual work. A numerical analysis procedure is described.

In Chapter 3, the salient features of the various constitutive models for concrete and concrete/steel interface behavior that are available in the literature are discussed. The constitutive models used in this study are described and the rationale for their adoption is explained.

In Chapter 4, the behavior of net reinforced concrete elements is discussed. Simple expressions are developed to estimate the post cracking compressive strength of concrete. The constitutive models developed are used to predict the behavior of shear panels and deep beams for which experimental results are available.

In Chapter 5, the behavior of R/C beams exhibiting various failure modes is discussed. The computer program incorporating the simple constitutive model is used to predict the behavior of some laboratory specimens exhibiting a wide range of behavior. Required attributes for the close prediction of behavior are examined. Insights gained from the analysis into the behavior of beams are described.

In Chapter 6, conclusions derived from the study are given. Recommendations are made for the material parameters which produce reliable predictions for practical applications. Recommended areas of future study are given.

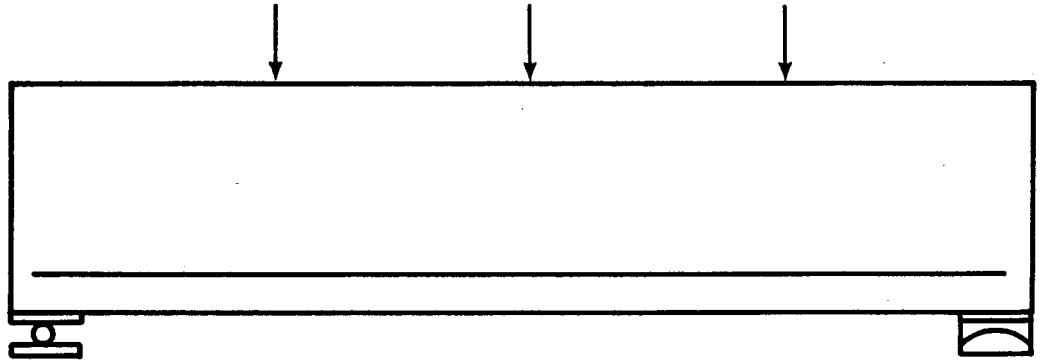

(a) Shallow Beam

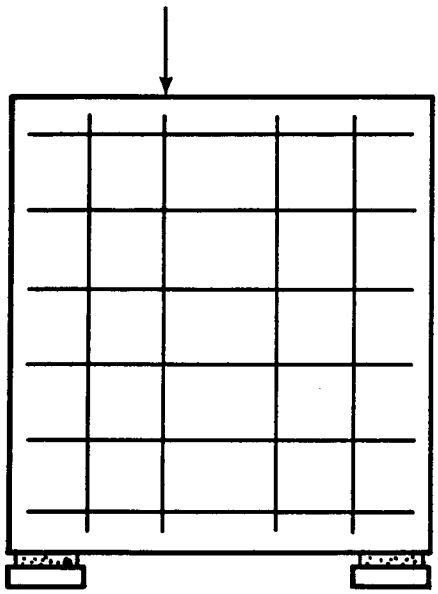

(b) Deep Beam or Large Panel

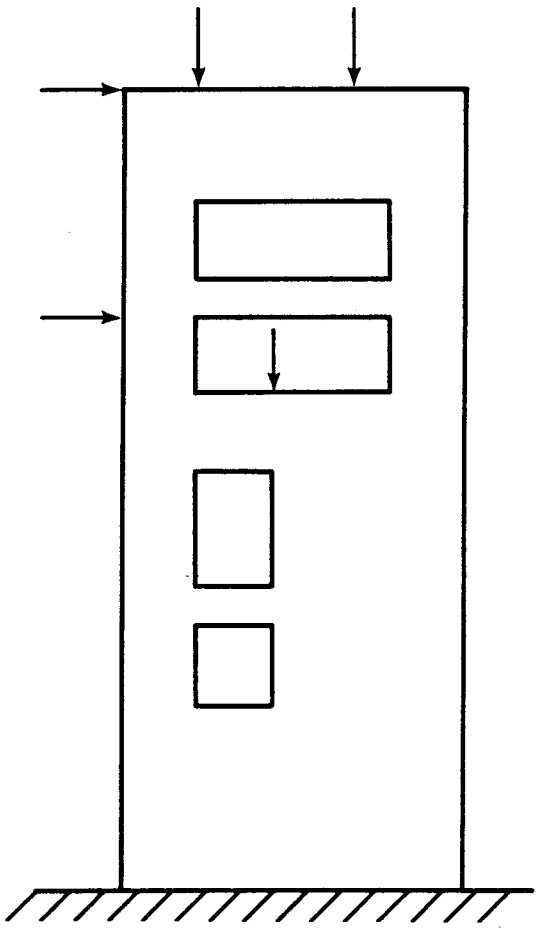

(c) Shear Wall

FIG. 1.1. Some Structural Types for which This Study is Applicable

CHAPTER 2

FINITE ELEMENT FORMULATIONS

2.1 Introduction

In this chapter, fundamentals of the finite element method (FEM) are briefly described. Specific formulations are then developed for concrete, reinforcement and bond elements based on the principle of virtual work. Where appropriate, finite element models developed herein are compared to others currently available (ASCE, 1982). Numerical analysis procedures are described and convergence criteria are discussed.

2.2 Funadmental Variational Formulation

The principle of virtual work (Dym and Shames, 1973) states that the necessary and sufficient condition for equilibrium is that for any kinematically compatible displacement field, the external virtual work of the body forces and surface tractions must equal the internal virtual work. The following derivation follows closely that by Bathe (1982).

Consider a general structure, such as in Fig. 2.1. The external forces acting on the structure are surface tractions $\mathbf{f}^s$, body forces $\mathbf{f}^b$, and concentrated forces $\mathbf{F}$. These forces include all externally applied forces and reactions. The displacements of the structure from the unloaded configuration are denoted by $\mathbf{u}$ and the corresponding kinematically compatible internal strains are denoted by $\boldsymbol{\varepsilon}$. Let virtual displacements $\delta\mathbf{u}$ (where δ denotes 'variation in') produce strains $\delta\boldsymbol{\varepsilon}$. According to the principle of virtual work, equilibrium exists if

$$\int_v \delta\boldsymbol{\varepsilon}^t \boldsymbol{\sigma} dv = \int_v \delta\mathbf{u}^t \mathbf{f}^b dv + \int_s \delta\mathbf{u}^{s\,t} \mathbf{f}^s ds + \delta\mathbf{u}^t \mathbf{F} \tag{2.1}$$

in which the superscript t denotes a transpose.

The internal virtual work is given by the left hand side of Eq. 2.1 and is equal to the internal stresses σ going through the virtual strains $\delta\boldsymbol{\varepsilon}$ that are kinematically compatible with the imposed virtual displacements $\delta\mathbf{u}$. The external virtual work is given on the right side of Eq. 2.1 and is equal to the external forces $\mathbf{f}^b$, $\mathbf{f}^s$ and $\mathbf{F}$ going through virtual displacements $\delta\mathbf{u}$. All bold faced symbols represent vectors or matrices.

Since the displacement field is assumed to be kinematically compatible,

$$\boldsymbol{\varepsilon} = \mathbf{B}\mathbf{u} \tag{2.2}$$

where $\mathbf{B}$ is the matrix differential operator associated with the strain-displacement equations.

In the finite element analysis, we approximate the body in Fig. 2.1 as an assemblage of discrete finite elements with the elements being interconnected at nodal points on the element boundaries. The displacements at any point within a typical element, $\mathbf{u}$, are assumed to be a function of the n discrete nodal displacements, contained in vector $\mathbf{U}$ (n is the total number of degrees of freedom in the structure).

$$\mathbf{u}^{(m)} = \mathbf{N}^{(m)}\mathbf{U} \tag{2.3}$$

where $\mathbf{N}^{(m)}$ are the displacement interpolation functions, called shape functions and superscript (m) denotes element m.

Although all nodal point displacements are listed in $\mathbf{U}$, only the displacements at the nodes of an element affect the displacements and strains within that element. Thus, using Eq. 2.2 and Eq. 2.3,

$$\boldsymbol{\varepsilon}^{(m)} = \mathbf{B}^{(m)}\mathbf{U} \tag{2.4}$$

where $\mathbf{B}^{(m)}$ is obtained by appropriately differentiating $\mathbf{N}^{(m)}$.

Using the assumption on the displacements within each finite element, as expressed in Eq. 2.3, we can now derive equilibrium equations that correspond to the nodal point displacements of the assemblage of finite elements. Equation 2.1 can be rewritten as a sum of integrations over the volume and areas of all finite elements; i.e.,

$$\sum_m \int_{v^{(m)}} \delta\boldsymbol{\varepsilon}^{(m)t}\boldsymbol{\sigma}^{(m)}\,dv^{(m)} = \sum_m \int_{v^{(m)}} \delta\mathbf{u}^{(m)t}\mathbf{f}^{b(m)}\,dv^{(m)} + \sum_m \int_{S^{(m)}} \delta\mathbf{u}^{S(m)^t}\mathbf{f}^{S(m)}\,dS^{(m)} + \delta\mathbf{U}^t\mathbf{F} \tag{2.5}$$

where m = 1, 2, ... k, with k = total number of elements.

Substituting for $\delta\varepsilon^t$ in Eq. 2.5 by using Eq. 2.4 and for $\delta u^{(m)}$ by using Eq. 2.3, we obtain,

$$\delta\mathbf{U}^t\left[\sum_m \int_{v^{(m)}} \mathbf{B}^{(m)t}\boldsymbol{\sigma}^{(m)}\,dv^{(m)}\right] =$$

$$\delta\mathbf{U}^t\left[\sum_m \int_{v^{(m)}} \mathbf{N}^{(m)^t}\mathbf{f}^{b(m)}\,dV^{(m)} + \sum_m \int_{S^{(m)}} \mathbf{N}^{S(m)^t}\mathbf{f}^{S(m)}\,dS^{(m)} + \mathbf{F}\right] \tag{2.6}$$

where the surface displacement interpolation matrices $\mathbf{N}^{S(m)}$ are obtained from volume displacement interpolation matrices $\mathbf{N}^{(m)}$ in Eq. 2.3 by specializing to the element surface coordinates and $\mathbf{F}$ is the vector of nodal loads.

Using the notation,

$$\mathbf{Q} = \sum_m \int_{v^{(m)}} \mathbf{B}^{(m)^t} \sigma^{(m)} dv^{(m)} \tag{2.7}$$

and

$$\mathbf{R} = \sum_m \int_{v^{(m)}} \mathbf{N}^{(m)^t} \mathbf{f}^{b(m)} dv^{(m)} + \sum_m \int_{S^{(m)}} \mathbf{N}^{S(m)^t} \mathbf{f}^{S(m)} dS^{(m)} + \mathbf{F} \tag{2.8}$$

Eq. 2.6 becomes,

$$\delta \mathbf{U}^t \left[\mathbf{Q} - \mathbf{R} \right] \equiv 0 \tag{2.9}$$

Since the virtual displacements $\delta \mathbf{U}$ are arbitrary, Eq. 2.9 can be satisfied if and only if,

$$\Psi(\mathbf{U}) \equiv \mathbf{0} \tag{2.10a}$$

where

$$\Psi(\mathbf{U}) = \mathbf{Q} - \mathbf{R} \tag{2.10b}$$

Ψ is a function of **U** because **Q** is a function of U. Equations 2.10, which are n simultaneous equations, represent the requirement for equilibrium for each of the n degrees of freedom. **R** is the vector of forces applied externally to the structure. **Q** is the set of forces equilibrating the internal stresses (i.e. the forces of resistance of the structure). In the event that Eqs. 2.10 are not satisfied, it is useful to interpret the residual vector as an unbalanced force vector. This provides a convenient physical measure of the error by which the equations are not satisfied.

If the stress-strain relationship of the material is nonlinear, the vector of nodal point forces that equilibrate the element stresses depends nonlinearly on **U** and Eqs. 2.10 will be nonlinear. Then, it is necessary to iterate in the solution of Eqs. 2.10.

An incremental step-by-step solution procedure is used in this study to solve the non-linear equations. The basic approach in this procedure is to assume that the solution for the load step ℓ is known and that solution for the load step $\ell + \Delta\ell$ is required, where $\Delta\ell$ is the load increment. Denoting by **U*** the correct displacements at load step $\ell + \Delta\ell$, Eqs. 2.10 become,

$$\Psi(\mathbf{U}^*) \equiv \mathbf{0} \equiv {}^{\ell+\Delta\ell}\mathbf{Q}(\mathbf{U}^*) - {}^{\ell+\Delta\ell}\mathbf{R} \tag{2.11}$$

where the left superscript denotes "at load step $\ell + \Delta\ell$".

Assume that the $(j-1)^{st}$ iteration has yielded an approximation for **U*** as $\mathbf{U}^{(j-1)}$. Then a Taylor series expansion gives,

$$\Psi(\mathbf{U}^*) \doteq \Psi(\mathbf{U}^{(j-1)}) + \frac{\partial \Psi}{\partial \mathbf{U}}\bigg|_{\mathbf{U}^{(j-1)}} (\mathbf{U}^* - \mathbf{U}^{(j-1)}) \tag{2.12}$$

Equations 2.12 are approximate because higher order terms are neglected. Differentiating Eqs. 2.11,

$$\frac{\partial \Psi}{\partial \mathbf{U}} = \frac{\partial \mathbf{Q}}{\partial \mathbf{U}} \quad , \tag{2.13}$$

if the external load vector ${}^{\ell+\Delta\ell}\mathbf{R}$ is assumed to be independent of $\mathbf{U}$.

Differentiating Eq. 2.7 with respect to displacements, we obtain

$$\frac{\partial \mathbf{Q}}{\partial \mathbf{U}} = \sum_{m} \int_{V^{(m)}} \mathbf{B}^{(m)^t} \frac{\partial \sigma^{(m)}}{\partial \mathbf{U}} \, dv^{(m)} \tag{2.14}$$

The stresses in the finite element are expressed as a function of strains using

$$\sigma^{(m)} = \mathbf{E}(\varepsilon)^{(m)} + \sigma_o^{(m)} \tag{2.15}$$

where $\mathbf{E}(\varepsilon)^{(m)}$ is in general a nonlinear function of strains and $\sigma_o^{(m)}$ are the initial stresses in the undeformed element.

From Eq. 2.15, the expression for incremental stresses, $\Delta\sigma^{(m)}$, is obtained as

$$\Delta\sigma^{(m)} = \frac{\partial \mathbf{E}^{(m)}}{\partial \boldsymbol{\varepsilon}} \Delta\boldsymbol{\varepsilon} \tag{2.16a}$$

$$= \mathbf{D}_t^{(m)} \Delta\varepsilon \tag{2.16b}$$

where $\mathbf{D}_t^{(m)}$ is the tangent constitutive matrix for material of element m. Using Eq. 2.4 to substitute for $\Delta\varepsilon$ in Eq. 2.16b in terms of

displacements, we obtain

$$\Delta\sigma^{(m)} = \mathbf{D}_t^{(m)}\,\mathbf{B}^{(m)}\Delta\mathbf{U} \tag{2.16c}$$

which yields, at the limit,

$$\frac{\partial\sigma^{(m)}}{\partial\mathbf{U}} = \mathbf{D}_t^{(m)}\mathbf{B}^{(m)} \tag{2.16d}$$

Substituting for $\left(\frac{\partial\sigma}{\partial\mathbf{U}}\right)^{(m)}$ from Eq. 2.16d into Eq. 2.14, we obtain,

$$\frac{\partial\mathbf{Q}}{\partial\mathbf{U}} = \sum_m \int_{v^{(m)}} \mathbf{B}^{(m)^t}\mathbf{D}_t^{(m)}\mathbf{B}^{(m)}dv^{(m)} = \mathbf{K}_t \tag{2.17}$$

where $\mathbf{K}_t$ denotes the tangent stiffness matrix. Denoting

$$\mathbf{U}^* - \mathbf{U}^{(j-1)} = \Delta\mathbf{U}^{(j)} \tag{2.18}$$

and using Eqs. 2.13 and 2.18, Eqs. 2.12 become,

$$\mathbf{\Psi}(\mathbf{U}^*) \equiv 0 \doteq \mathbf{\Psi}\left(\mathbf{U}^{(j-1)}\right) + \left.\frac{\partial\mathbf{Q}}{\partial\mathbf{U}}\right|_{\mathbf{U}^{(j-1)}}\Delta\mathbf{U}^{(j)} \tag{2.19}$$

Substituting for $\mathbf{\Psi}\left(\mathbf{U}^{(j-1)}\right)$ from Eq. 2.10 and for $\frac{\partial\mathbf{Q}}{\partial\mathbf{U}}$ from Eqs. 2.17

$$\left({}^{\ell+\Delta\ell}\mathbf{Q}^{(j-1)} - {}^{\ell+\Delta\ell}\mathbf{R}\right) + {}^{\ell+\Delta\ell}\mathbf{K}_t^{(j-1)}\Delta\mathbf{U}^{(j)} \equiv 0 \tag{2.20}$$

which yield the recurrence relation,

$${}^{\ell+\Delta\ell}\mathbf{K}_t^{(j-1)}\,\Delta\mathbf{U}^{(j)} = {}^{\ell+\Delta\ell}\mathbf{R} - {}^{\ell+\Delta\ell}\mathbf{Q}^{(j-1)} \tag{2.21}$$

Since Eqs. 2.12 represent only a Taylor series approximation, the displacement increment correction $\Delta \mathbf{U}^{(j)}$ is used to obtain the next displacement approximation,

$$\mathbf{U}^{(j)} = \mathbf{U}^{(j-1)} + \Delta \mathbf{U}^{(j)} \tag{2.22}$$

The relations in Eqs. 2.21 and 2.22 constitute the Newton-Raphson solution of Eqs. 2.11.

A modification of the above approach, called 'modified Newton-Raphson iteration', can be employed wherein the Eqs. 2.21 will use ${}^{L}\mathbf{K}$ in place of ${}^{\ell+\Delta\ell}\mathbf{K}^{(j-1)}$, ${}^{L}\mathbf{K}$ being the tangent stiffness matrix corresponding to any one of the equilibrium configurations. That is, Eq. 2.21 is approximated as

$${}^{L}\mathbf{K}\,\Delta \mathbf{U}^{(j)} = {}^{\ell+\Delta\ell}\mathbf{R} - {}^{\ell+\Delta\ell}\mathbf{Q}^{(j-1)} \tag{2.23}$$

In the 'inital stiffness method', this will become

$${}^{o}\mathbf{K}\,\Delta \mathbf{U}^{(j)} = {}^{\ell+\Delta\ell}\mathbf{R} - {}^{\ell+\Delta\ell}\mathbf{Q}^{(j-1)} \tag{2.24}$$

where ${}^{o}\mathbf{K}$ is the initial stiffness matrix.

Since an incremental analysis is performed with load steps, the initial conditions for the first iteration in each load step are ${}^{\ell+\Delta\ell}\mathbf{Q}^{(o)} = {}^{\ell}\mathbf{Q}$ and ${}^{\ell+\Delta\ell}\mathbf{U}^{(o)} = {}^{\ell}\mathbf{U}$. The iteration is continued until the convergence criteria are satisfied.

If the stress-strain relationship is linear, Eqs. 2.10 are linear

and we obtain

$$\mathbf{Q} \equiv \mathbf{R} \tag{2.25a}$$

where

$$\mathbf{Q} = \sum_m \left[\int_{V^{(m)}} \mathbf{B}^{(m)^t} \mathbf{D}^{(m)} \mathbf{B}^{(m)} dv^{(m)}\right] \mathbf{U}^* + \sum_m \int \mathbf{B}^{(m)^t} \sigma_o dv^{(m)} \tag{2.25b}$$

with $\mathbf{D}^{(m)}$ being independent of displacements.

One dimensional representations of the three iterative schemes of Eqs. 2.21, 2.23 and 2.24 are shown in Fig. 2.3a, b and c respectively. The computer implementation of a typical material nonlinear finite element analysis procedure is described in Fig. 2.4 as a flow diagram.

The test for convergence of the iterative scheme is carried out on both the displacements and the equilibrating loads

$$\frac{||\Delta \mathbf{U}^{(j)}||}{||\mathbf{U}^{(j-1)}||} \leq \lambda_U \tag{2.26a}$$

$$\frac{||\mathbf{R} - \mathbf{Q}^{(j-1)}||}{||\mathbf{R}||} \leq \lambda_R \tag{2.26b}$$

where the symbol $||\ ||$ denotes the Euclidean vector norm; λ_U, the user specified tolerance on displacements and λ_R, the user specified tolerance on unbalanced forces.

2.3 Isoparametric Element Formulation

The basic procedure in the isoparametric finite element formulation is to express the element displacements and the element coordinates by

the same interpolation functions using the natural coordinate system of the element (Zienkiewicz, 1977).

Considering a two dimensional element, as in Fig. 2.2, the coordinate interpolations are

$$x = \sum_{i=1}^{q} N_i x_i \tag{2.27a}$$

$$y = \sum_{i=1}^{q} N_i y_i \tag{2.27b}$$

where x and y are the coordinates at any point of the element and x_i, y_i, i = 1, 2, ... q are the coordinates of the q element nodes. The interpolation functions N_i are defined in the natural coordinate system of the element ξ and η, each of which varies from -1 to +1 as they span the element. The fundamental property of the interpolation function N_i is that its value in the natural coordinate system is unity at node i and is zero at all other nodes. The interpolation functions can be constructed for an element with a variable number of nodes by constructing first the interpolations correspoding to a basic linear element. The addition of another node then results in an additional interpolation function and a correction to be applied to the already existing interpolation functions. The process is further explained in Appendix A.1 where shape functions for linear, quadratic and cubic elements of the Serendipity and Lagrangian families are constructed using the above procedure.

In the isoparametric formulation (Zienkiewicz et al., 1970) the element displacements are interpolated in the same way as the geometry.

$$u^m = \sum_{i=1}^{q} N_i u_i \tag{2.28a}$$

$$v^m = \sum_{i=1}^{q} N_i v_i \tag{2.28b}$$

where u^m and v^m are the displacements at any point of the element and u_i, v_i, $i = 1 \ldots q$ are the corresponding element displacements at its nodes.

The evaluation of the strain-displacement transformation matrix $\mathbf{B}^{(m)}$ in Eq. 2.4 is performed by relating the derivatives in the natural coordinates to those in global coordinates by the Jacobian operator, J,

$$\frac{\partial}{\partial \boldsymbol{\xi}} = \mathbf{J} \frac{\partial}{\partial \mathbf{x}} \tag{2.29}$$

where

$$\mathbf{J} = \begin{bmatrix} \frac{\partial x}{\partial \xi} & \frac{\partial y}{\partial \xi} \\ \frac{\partial x}{\partial \eta} & \frac{\partial y}{\partial \eta} \end{bmatrix} \tag{2.30a}$$

$$\frac{\partial}{\partial \boldsymbol{\xi}} = \begin{Bmatrix} \frac{\partial}{\partial \xi} \\ \frac{\partial}{\partial \eta} \end{Bmatrix} \tag{2.30b}$$

$$\frac{\partial}{\partial \mathbf{x}} = \begin{Bmatrix} \frac{\partial}{\partial x} \\ \frac{\partial}{\partial y} \end{Bmatrix} \tag{2.30c}$$

for a plane element.

From Eqs. 2.29, $\frac{\partial}{\partial \mathbf{x}}$ is obtained as

$$\frac{\partial}{\partial x} = J^{-1} \frac{\partial}{\partial \xi} \tag{2.31}$$

The inverse of the Jacobian operator exists if there is a unique correspondence between the natural and global coordinates of the element.

Using Eqs. 2.29 and 2.31, the volume differential $dv^{(m)}$ in the intergrands of Eqs. 2.5 to 2.8 is written as

$$dv = \det J \, d\xi \, d\eta \tag{2.32}$$

where det J is the determinant of the Jacobian operator (Zienkiewicz et al., 1970).

Numerical integration is used to evaluate the integrals in Eqs. 2.5 to 2.8. For example, the expression for $\mathbf{K}_t^{(m)}$ in Eq. 2.17 can be written as

$$\mathbf{K}_t^{(m)} = \int_v \mathbf{G}^{(m)} d\xi \, d\eta \tag{2.33a}$$

where

$$\mathbf{G}^{(m)} = \mathbf{B}^{(m)^t} \mathbf{D}_t^{(m)} \mathbf{B}^{(m)} \det J \tag{2.33b}$$

Since $\mathbf{B}^{(m)}$ is in natural coordinates, the integration is performed in natural coordinates. Using numerical integration, the element stiffness matrix is now evaluated as

$$\mathbf{K}^{(m)} = \sum_{i,j} \alpha_{ij} \mathbf{G}_{ij} \tag{2.34}$$

where G_{ij} is the matrix **G** evaluated at the integration points located at ξ_i and η_j, and α_{ij} are the corresponding weighting factors.

2.4 Formulations of Reinforcing Element and Bond Element

2.4.1 Alternatives for Representations of the Reinforcement

Reinforcement can be represented: (a) as being built into the solid element, called an embedded formulation; or, (b) as being uniformly distributed over the concrete element, in which case a composite concrete-reinforcement constitutive relation may be used; or, (c) as discrete one dimensional truss or beam elements (ASCE, 1982). Perfect bond between steel and concrete is usually assumed when using distributed and embedded representations of reinforcement (ASCE, 1982). The bond slip phenomenon may be represented in conjunction with the discrete reinforcement element as: (a) link elements, which consists of discrete orthogonal springs with no physical dimension and which connect and transmit shear and normal forces at the nodes of the reinforcement (Ngo and Scordelis, 1967); (b) interface bond elements which are continuous elements of zero thickness, with the constitutive relation formulated in terms of the relative displacements of the nodes (Ngo, 1975); or as, (c) bond zone elements of finite dimension (the thickness being approximately equal to the radius of the reinforcing bar) wherein the contact surface between the steel and concrete as well as the concrete in the bond zone are considered to have separate constitutive relationships (de Groot et al., 1981). Since all the above bond elements are associated with discrete representations of reinforcement, the finite element mesh layout is controlled by the

reinforcement locations.

2.4.2 Formulation of Reinforcing Element

To the author's knowledge, all embedded and distributed representations for reinforcement that are currently availalbe in literature assume perfect bond between steel and concrete. An embedded reinforcement formulation including bond-slip is developed herein.

The virtual work of a reinforcing element to be included in Eq. 2.5 is given by

$$\sum_{m} \int \delta\varepsilon_s \sigma_s A_s dr$$

where A_s is the cross-sectional area of reinforcement; dr is the differential length; ε_s is the strain in reinforcement and σ_s is the stress in reinforcement. Considering the reinforcing element, as in Fig. 2.5, the displacement w_s at any point of the element in a direction tangential to the reinforcing bar is written as

$$w_s = w_c + w_b \tag{2.35}$$

where w_c is the displacement of the concrete at that point as interpolated from nodal displacements using Eqs. 2.28 and w_b is the bond slip (i.e. the relative displacement between the steel and the concrete).

From Fig. 2.5,

$$w_c = u \cos\theta + v \sin\theta \tag{2.36}$$

Let U_{b_1}, U_{b_2} ... U_{b_p} be p slip degrees of freedom of p nodes located on the reinforcing element. Then,

$$w_b = \sum_{j=1}^{p} H_j \, U_{b_j} \tag{2.37}$$

where H_j are the shape functions used to interpolate the bond slip at any point. The strain in the reinforcing steel at any point is

$$\varepsilon_s = \frac{dw_s}{dr} \tag{2.38}$$

where dr is the differential length of the reinforcing element. From Eqs. 2.31, 2.32 and 2.34, and assuming that θ does not vary along the element,

$$\varepsilon_s = \frac{du}{dr} \cos\theta + \frac{dv}{dr} \sin\theta + \frac{dw_b}{dr} \tag{2.39}$$

Considering for simplicity that the reinforcing element is placed parallel to a natural coordinate axis, say the ξ axis, the relationships

$$du = \frac{\partial u}{\partial \xi} d\xi + \frac{\partial u}{\partial \eta} d\eta \tag{2.40a}$$

$$dv = \frac{\partial v}{\partial \xi} d\xi + \frac{\partial v}{\partial \eta} d\eta \tag{2.40b}$$

will reduce to

$$du = \frac{\partial u}{\partial \xi} d\xi \tag{2.41a}$$

$$dv = \frac{\partial v}{\partial \xi} d\xi \tag{2.41b}$$

since $d\eta = 0$ when η = a constant (Elwi and Murray, 1980).

From Fig. 2.5,

$$\cos \theta = \frac{dx}{dr} \tag{2.42a}$$

$$\sin \theta = \frac{dy}{dr} \tag{2.42b}$$

and

$$dr = \sqrt{dx^2 + dy^2} \tag{2.42c}$$

Also, since the element is isoparametric,

$$dx = \frac{dx}{d\xi} d\xi \tag{2.43a}$$

$$dy = \frac{dy}{d\xi} d\xi \tag{2.43b}$$

Substituting Eqs. 2.43a and b into Eq. 2.42c

$$dr = \sqrt{\left(\frac{dx}{d\xi}\right)^2 + \left(\frac{\partial y}{\partial \xi}\right)^2}\, d\xi \tag{2.44a}$$

That is,

$$dr = J_s \cdot d\xi \tag{2.44b}$$

where the Jacobian for steel element is

$$J_s = \sqrt{\left(\frac{\partial x}{\partial \xi}\right)^2 + \left(\frac{\partial y}{\partial \xi}\right)^2} \tag{2.44c}$$

Substituting from Eq. 2.44c into Eqs. 2.42a and b,

$$\cos\theta = \frac{1}{J_s}\frac{\partial x}{\partial \xi} \tag{2.45a}$$

$$\sin\theta = \frac{1}{J_s}\frac{dy}{d\xi} \tag{2.45b}$$

Substituting Eqs. 2.41a and b into Eq. 2.39, and using Eq. 2.44b

$$\varepsilon_s = \frac{1}{J_s}\left(\frac{\partial u}{\partial \xi}\cos\theta + \frac{\partial v}{\partial \xi}\sin\theta + \frac{dw_b}{d\xi}\right) \tag{2.46}$$

Using Eqs. 2.27a, b and Eq. 2.37

$$\varepsilon_s = \frac{1}{J_s} < \cos\theta \quad \sin\theta > \begin{bmatrix} \langle \frac{\partial N_i}{\partial \xi} \rangle & \langle 0 \rangle \\ \langle 0 \rangle & \langle \frac{\partial N_i}{\partial \xi} \rangle \end{bmatrix} \begin{Bmatrix} u_i \\ v_i \end{Bmatrix} + \frac{1}{J_s} \langle \frac{dH_j}{d\xi} \rangle \{U_{b_j}\} \tag{2.47}$$

wherein i = 1, 2, ... q and j = 1, 2 ... p.

Or,

$$\varepsilon_s = \mathbf{B}_s^{\,t}\,\overline{\mathbf{U}} \tag{2.48a}$$

where

$$\mathbf{B}_s = \frac{1}{J_s} \langle\langle \cos\theta \ \sin\theta \rangle \begin{bmatrix} \langle \frac{\partial N_i}{\partial \xi} \rangle & \langle 0 \rangle \\ \langle 0 \rangle & \langle \frac{\partial N_i}{\partial \xi} \rangle \end{bmatrix} \langle \frac{dH_j}{d\xi} \rangle \rangle \tag{2.48b}$$

and

$$\overline{\mathbf{U}} = \begin{Bmatrix} u_i \\ v_i \\ U_{b_j} \end{Bmatrix} \tag{2.48c}$$

If the tangent modulus of reinforcing steel is denoted as $E_s t$, then the contribution of the reinforcing element to the tangent-stiffness matrix ${}^{\ell+\Delta\ell}K^{(j-1)}$ in Eq. 2.17 is obtained, by referring to Eqs. 2.7, as

$$\mathbf{K}_{s_t} = \sum_m \int_{-1}^{1} \mathbf{B}_s{}^{(m)t} E_{s_t}^{(m)} \mathbf{B}_s{}^{(m)} A_s J_s d\xi \tag{2.49}$$

which is partitioned as,

$$\mathbf{K}_{s_t} = \begin{bmatrix} \mathbf{k}^s_{ss} & \mathbf{k}^s_{sb} \\ k^s_{bs} & \mathbf{k}^s_{bb} \end{bmatrix} \tag{2.50a}$$

where,

$$\mathbf{k}^s_{ss} = \sum_m \int_{-1}^{1} \begin{bmatrix} \{\frac{\partial N_i}{\partial \xi}\} & \{0\} \\ \{0\} & \{\frac{\partial N_i}{\partial \xi}\} \end{bmatrix} \begin{Bmatrix} \cos\theta \\ \sin\theta \end{Bmatrix}$$

(2.50b)

$$E_{s_t} \langle \cos\theta \ \sin\theta \rangle \begin{bmatrix} \langle \frac{\partial N_i}{\partial \xi} \rangle & \langle 0 \rangle \\ \langle 0 \rangle & \langle \frac{\partial N_i}{\partial \xi} \rangle \end{bmatrix} \frac{A_s}{J_s} d\xi$$

$$k^s_{sb} = \sum_m \int_{-1}^{1} \begin{bmatrix} \{\frac{\partial N_i}{\partial \xi}\} & \{0\} \\ \{0\} & \{\frac{\partial N_i}{\partial \xi}\} \end{bmatrix} \begin{Bmatrix} \cos\theta \\ \sin\theta \end{Bmatrix} E_{s_t} \langle \frac{\partial H_j}{\partial \xi} \rangle \frac{A_s}{J_s} d\xi \qquad (2.50c)$$

$$k^s_{bs} = \sum_m \int_{-1}^{1} \{\frac{\partial H_j}{\partial \xi}\} E_{s_t} \langle \cos\theta \ \sin\theta \rangle \begin{bmatrix} \langle \frac{\partial N_i}{\partial \xi} \rangle & \langle 0 \rangle \\ \langle 0 \rangle & \langle \frac{\partial N_i}{\partial \xi} \rangle \end{bmatrix} \frac{A_s}{J_s} d\xi \qquad (2.50d)$$

$$k^s_{bb} = \sum_m \int_{-1}^{1} \{\frac{\partial H_j}{\partial \xi}\} E_{s_t} \langle \frac{\partial H_j}{\partial \xi} \rangle \frac{A_s}{J_s} d\xi \qquad (2.50e)$$

For reinforcing elements placed along the η coordinate axis, derivatives with respect to ξ are replaced by derivatives with respect to η in Eqs. 2.50a through e, and Eqs. 2.45a and b.

2.4.3 Formulation of Bond Element

The virtual work of the bond element to be included in Eqs. 2.5 is given by

$$\sum_m \int_{S_b} \delta w_b \sigma_b dS_b \qquad (2.51)$$

where S_b is the area of contact between concrete and reinforcement and σ_b is the bond stress.

The differential length dr of reinforcing steel is related to differential contact area dS_b by

$$dS_b = A_p dr \tag{2.52}$$

where A_p is the contact area per unit length of reinforcing steel. The bond stress σ_b is related to the bond slip w_b by

$$\sigma_b = D_b w_b \tag{2.53}$$

where D_b is the local bond modulus.

Substituting from Eq. 2.44b for dr, Eq. 2.53 for σ_b and Eq. 2.37 for w_b, into the expression in Eq. 2.51, the virtual work of bond slip ($V.W._{bond}$) is obtained as

$$V.W._{bond} = \delta \langle U_{b_j} \rangle \left[\sum_m \int_{-1}^{1} \{H_j\} D_b \langle H_j \rangle A_p J_s d\xi \right] \{U_{b_j}\} \tag{2.54}$$

where $\{U_{b_j}\}$ is the vector of element-slip degrees of freedom.

The contribution of the bond elements to the tangent stiffness matrix in Eq. 2.17 is obtained as

$$k^b_{bb} = \sum_m \int_{-1}^{1} \{H_j\} D_{bt} \langle H_j \rangle A_p J_s d\xi \tag{2.55}$$

where D_{bt} is the tangent bond modulus.

Thus the combined contribution of reinforcing and bond elements to the structure tangent stiffness matrix is obtained by modifying Eq. 2.50a to become

$$\mathbf{k}_{(s+b)_t} = \begin{bmatrix} \mathbf{k}^s_{ss} & \mathbf{k}^s_{sb} \\ \mathbf{k}^s_{bs} & \mathbf{k}^s_{bb} + \mathbf{k}^b_{bb} \end{bmatrix} \tag{2.56}$$

2.5 Implementation of Finite Element Formulation

The finite element formulations discussed in this Chapter have been incorporated into the finite element code FEPARCS5 (Elwi and Murray, 1980a, 1980b). The primary modification required to the coding of this program for this study were:

(a) the generalization of the element library to include both Lagrangian and variable node elements (See Appendix A1); and incompatible elements (See Appendix A3);

(b) Eigenvalue analysis capability for a single element or entire structure (See Appendix A3);

(c) the inclusion of the bond element as formulated in Sect. 2.4 (Note that this required the introduction of an ID array);

(d) the inclusion of the nonlinear concrete constitutive relationships which will be developed in Chapter 3; and,

(e) provision for the use of the fixed crack procedure (Chapter 5) and the rotating crack procedure (Chapter 4) in the iterative nonlinear solution.

A typical finite element model for one-half of a beam structure with quadratic serendipity concrete elements, embedded primary reinforcing steel, and embedded stirrups is shown in Fig. 2.6. Bond elements may be included or excluded with each layer of reinforcing steel. Where they are included, nodal points along the reinforcement layer, each with a single slip degree of freedom, must be added. In Fig. 26 the x's represent such nodal points for quadratic bond elements on the primary reinforcement in the outer quarter span of the model.

Based on some fundamental studies on cracked reinforced elements (not included herein but related to the convergence studies of Appendix

A3), a modelling technique in which steel layers are located through the concrete element integration points (i.e. Gauss points) has been adapted. Thus the stirrups in Fig. 2.6 are lumped on the vertical lines passing through the Gauss points. The primary reinforcement passes through the Gauss points in the horizontal direction and the areas of these layers are proportioned such that their accumulated area equals that of the primary reinforcement and their centroid coincides with the centroid of the primary reinforcement.

The suitability, or lack of suitability, of this modelling technique will become evident in the numerical studies undertaken in Chapters 4 and 5.

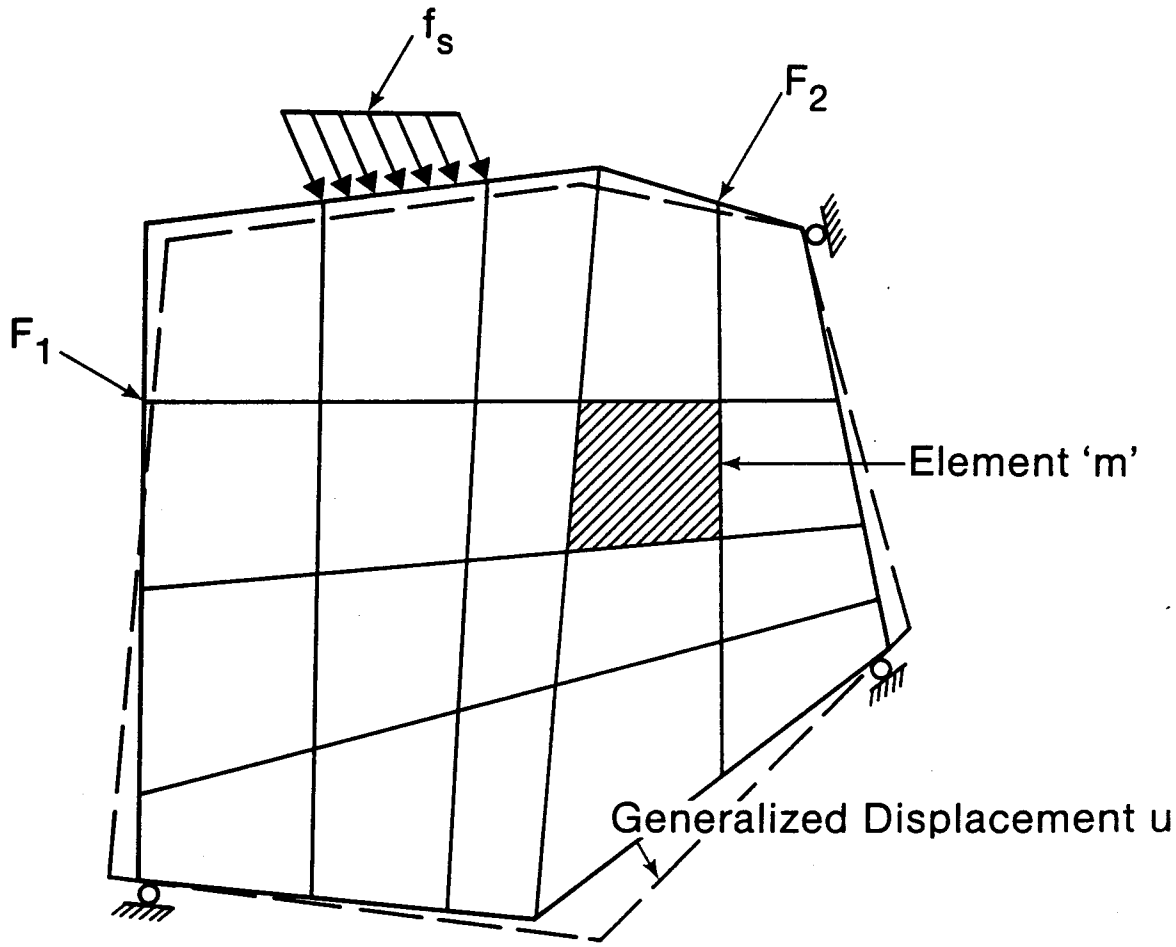

FIG. 2.1. General Structure

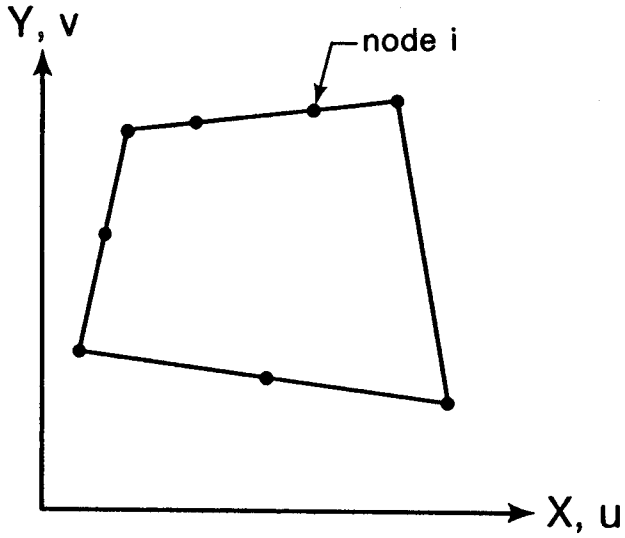

Element 'm' in Global Coordinates

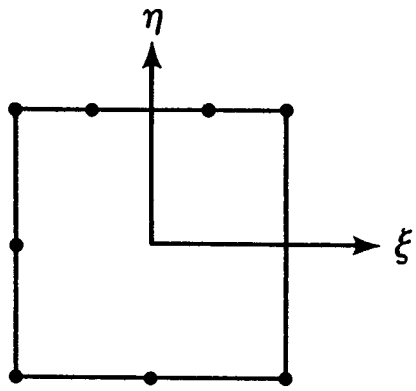

Element 'm' in Natural Coordinates
('Parent Element')

FIG. 2.2. Isoparametric Elements

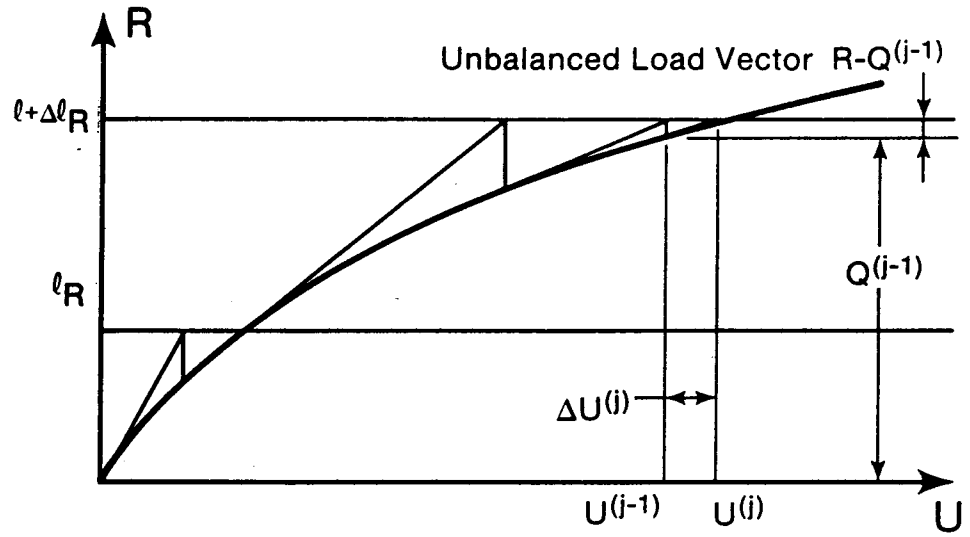

(a) Newton-Raphson Iteration Scheme

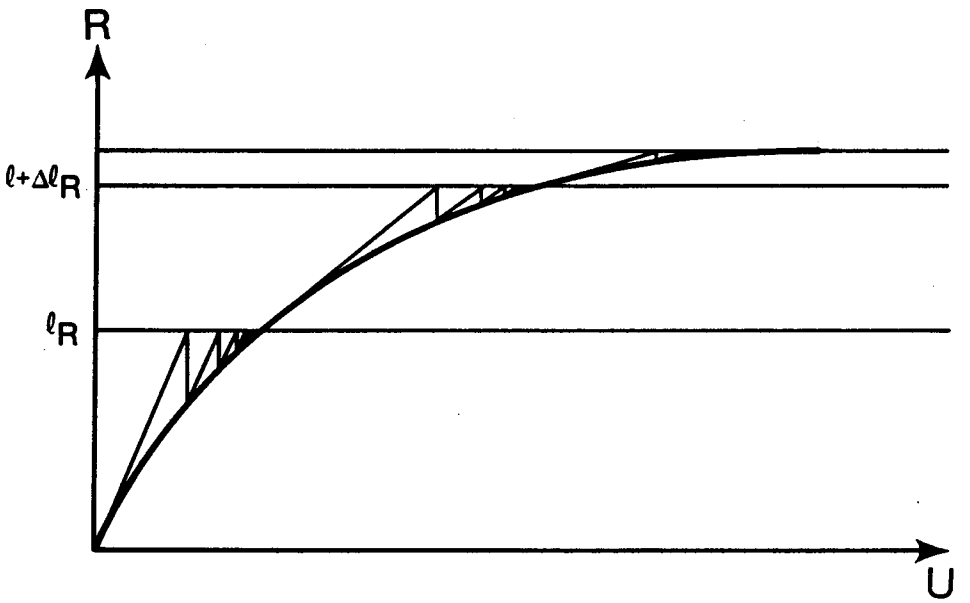

(b) Modified Newton-Raphson Method

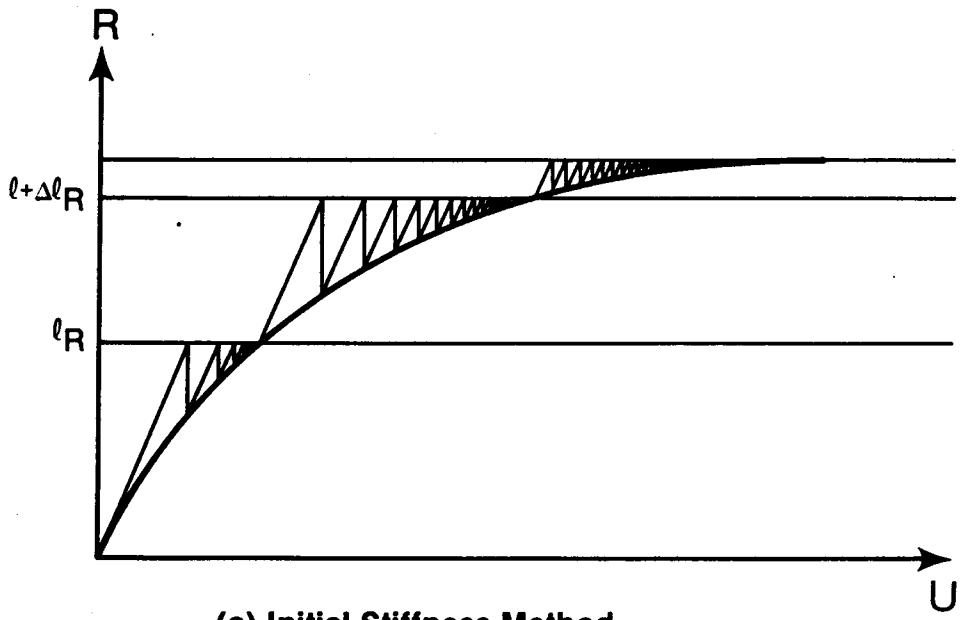

(c) Initial Stiffness Method

FIG. 2.3. Iterative Schemes

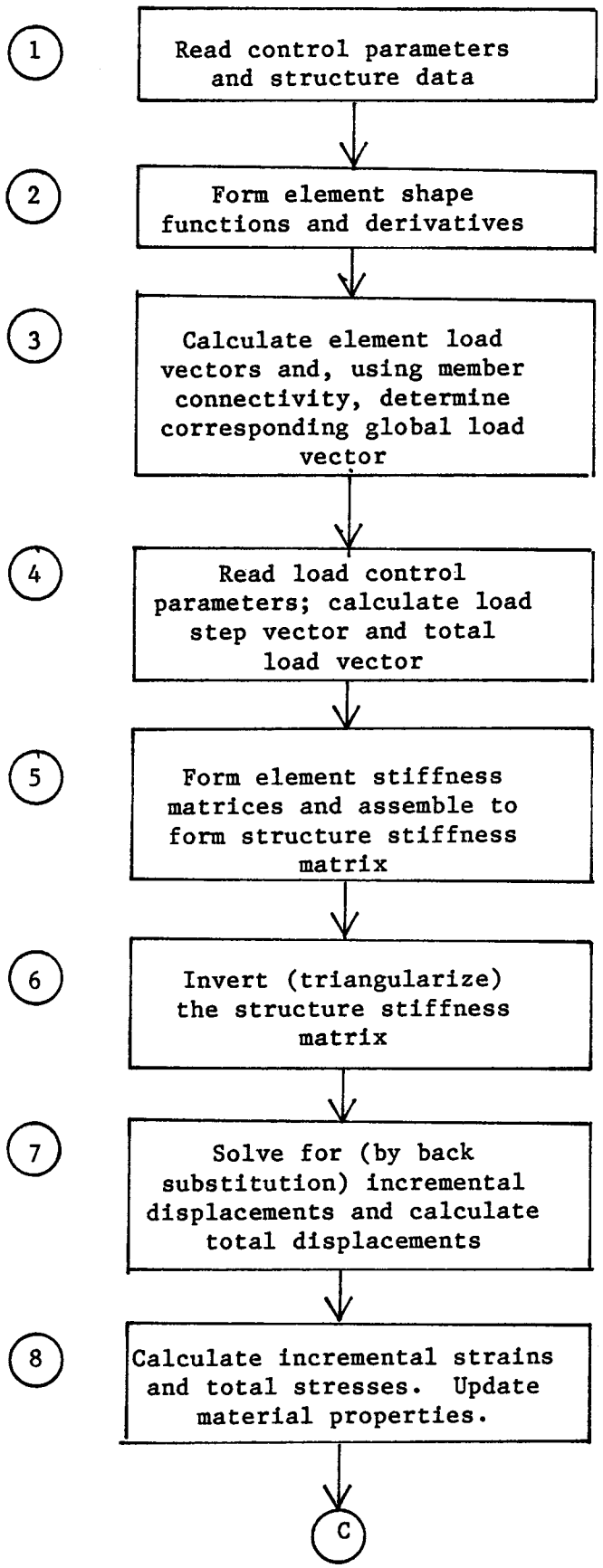
1
Read control parameters and structure data
2
Form element shape functions and derivatives
3
Calculate element load vectors and, using member connectivity, determine corresponding global load vector
4
Read load control parameters; calculate load step vector and total load vector
5
Form element stiffness matrices and assemble to form structure stiffness matrix
6
Invert (triangularize) the structure stiffness matrix
7
Solve for (by back substitution) incremental displacements and calculate total displacements
8
Calculate incremental strains and total stresses. Update material properties.
C

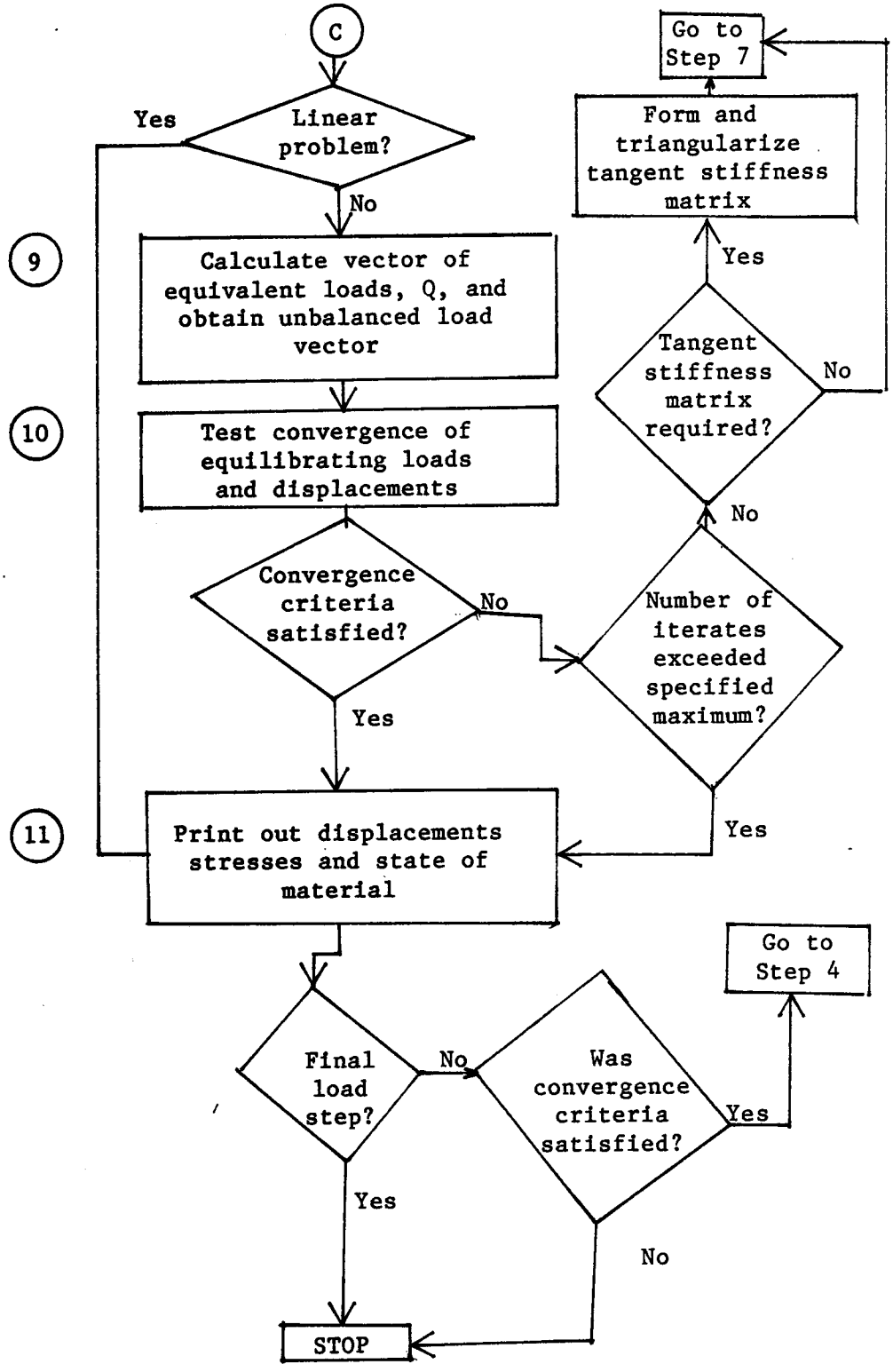

FIG. 2.4 __ Nonlinear FE Program Flow Diagram

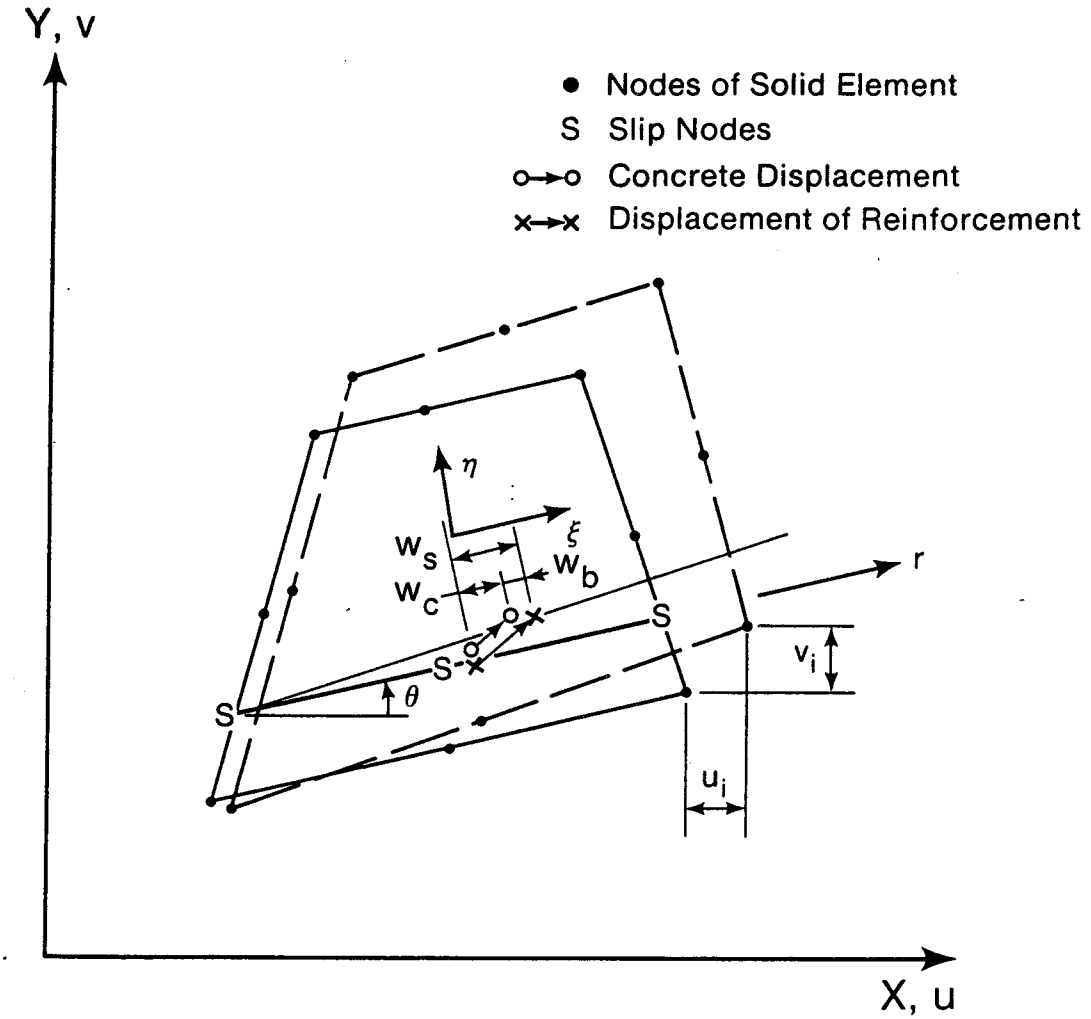

FIG. 2.5. Reinforcing Element and Bond Element

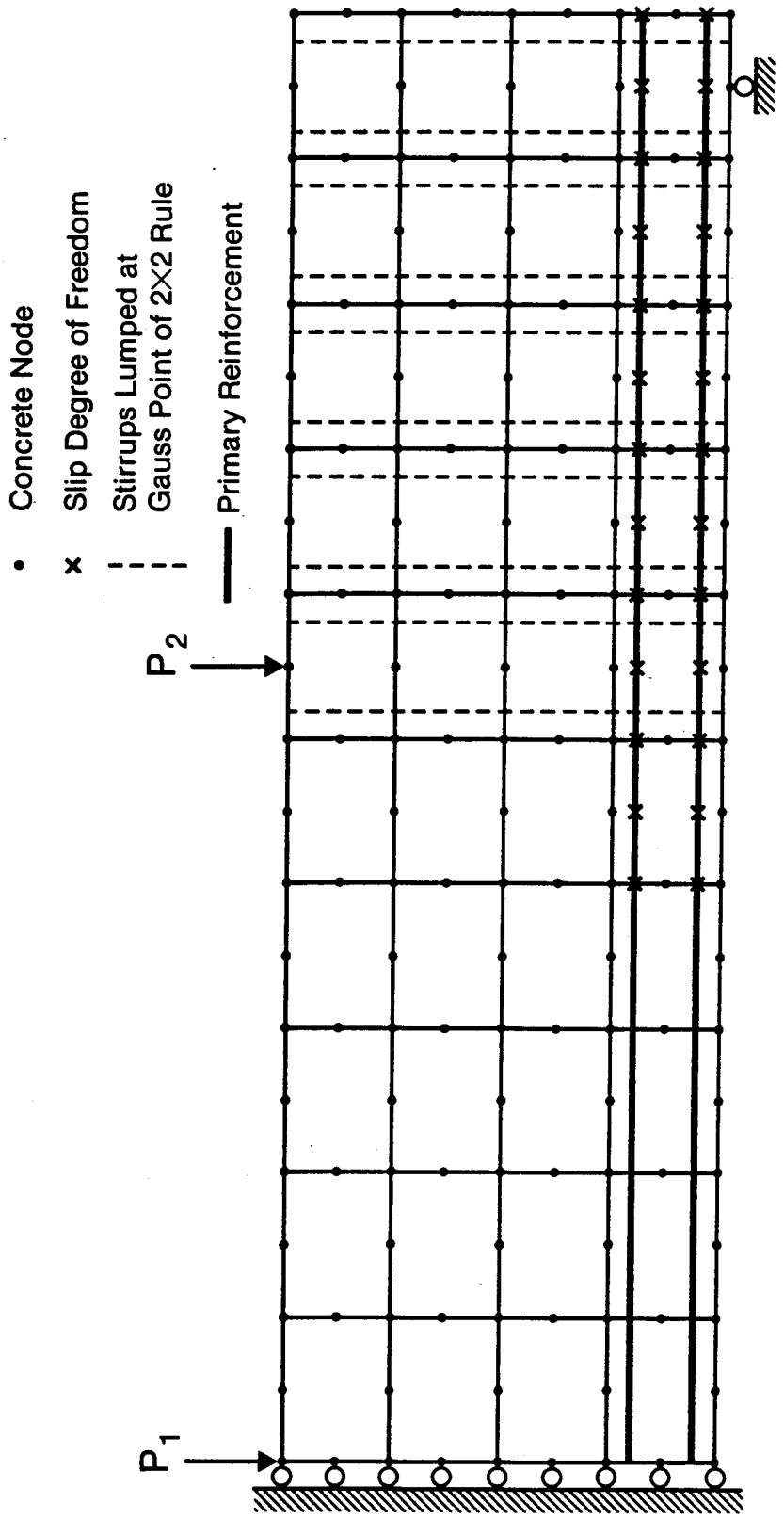

FIG. 2.6. Typical Finite Element Model of a Reinforced Concrete Beam

CHAPTER 3

CONSTITUTIVE MODELS FOR CONCRETE

3.1 Introduction

In reinforced concrete members where the failure mode is ductile as a result of steel yielding, the constitutive model adopted for concrete has only a small influence on the prediction of failure load (Bathe and Meyer, 1982) whereas in the case of brittle failure (such as the shear failure of beams) the concrete material model has a predominant effect (Ingraffea and Saouma, 1985). Therefore, in order to be able to predict the behavior of reinforced concrete beams with different physical characteristics, proper modelling of the material behavior is important. However, a number of factors have so far prevented the evolution of a constitutive model for concrete that is universally acceptable. The major factors are:

1. Concrete stress-strain behavior is inherently complex due to its dependence on a large number of variables such as the water-cement ratio, aggregate characteristics, workmanship, curing conditions, specimen size, temperature, moisture conditions, loading rate and age.

2. Test results show considerable scatter, and for a number of important conditions, are either unavailable or incomplete. For example, only limited test results are available for concrete under multiaxial loading conditions. No test results are available to determine the post cracking compressive strength of concrete and few are available for concrete subjected to nonproportional loading.

In this chapter, various constitutive models that are available in the literature for concrete and concrete/steel interface behavior are

briefly described. Constitutive models used in the present study and the rationale for their adoption are explained at the appropriate places in this review.

3.2 Stress-Strain Relationship for Concrete in Uniaxial Tension

3.2.1 Uniaxial Tension Test

Let us consider the behavior of a plain concrete specimen in a uniaxial tension test, which is displacement controlled and therefore stable (Fig. 3.1a). By measuring the total elongation of the specimen, a curve of the type shown in Fig. 3.1b is obtained (Hillerborg, 1985). Initially, in the prepeak region, microcracking is fairly uniformly distributed throughout the specimen. When the peak stress is reached a fracture zone will form somewhere along the specimen, as in Fig. 3.1a. The increasing damage within the fracture zone, when the deformation is further increased, causes a decrease in resistance within that zone and thus a decreasing stress in the specimen. This is referred to as 'tensile strain softening'. As the stress decreases the parts outside the fracture zone are unloaded. Thus the fracture zone does not spread along the specimen, but is limited to the position where it first started leading to 'strain localization' (Bazant, 1976). The stress-strain history in the fracture zone and the remainder of the specimen is illustrated in Fig. 3.1c. In a completely homogeneous material the width of the fracture process zone, h_c, should theoretically approach zero, but for concrete this width should be several times the inhomogeneities, that is, several times the aggregate size (Bazant, 1985).

Because of the strain localization, an objective post-peak tensile

stress-strain relationship cannot be directly deduced from the stress-elongation curve since such a relationship will depend on the gage length used. However, the stress versus crack displacement curve is independent of the gage length and is considered an invariant property of concrete (Hillerborg, 1985).

The area under the stress versus crack displacement (i.e., the displacement across the fracture process zone) curve is the fracture energy, G_F, which is defined as the amount of energy consumed by crack formation per unit area of the crack plane. That is,

$$G_F = \int^{w_{max}} \sigma dw \tag{3.1}$$

where dw is the elongation in the fracture zone, σ is the corresponding stress and w_{max} is the threshold crack displacement at which the stress has dropped to zero.

In order to aid further discussion on Eq. 3.1 and on concrete cracking, the fundamental aspects of fracture mechanics are reviewed in Sect. 3.2.2 (Broek, 1982).

3.2.2 Some Fundamental Concepts in Fracture Mechanics

One of the basic equations of fracture mechanics was developed by Griffith (1921). The Griffith criterion states that crack propagation occurs if the energy released upon crack growth is sufficient to provide all the energy required for crack growth. The condition for crack growth is

$$\frac{dU}{da} = \frac{dW}{da} \tag{3.2}$$

where $\frac{dU}{da}$ is the elastic energy released by change in stress due to an increment in crack length of da and $\frac{dW}{da}$ is the energy required for the formation of increment da of the crack length.

This is illustrated in Figs. 3.2a and b for the case when the ends of the specimen are fixed against displacement after stressing to a level σ. The elastic energy contained in the specimen before crack extension is given by area OAB of Fig. 3.2b. If the crack extends over a length da, the stiffness of the specimen will drop to line OCE thus relieving the average stress to a level $\sigma^{(1)}$. The elastic energy content in the specimen now drops to a magnitude given by area OCB. Thus crack propagation from a to a+da will result in an elastic energy release equal in magnitude to area OAC and is equal to the term $\frac{dU}{da}$ in Eq. 3.2.

The term $\frac{dU}{da}$ in Eq. 3.2 can be looked upon as the crack driving force, G, and the term $\frac{dW}{da}$ as crack resistance, R. If R is a constant, then G must exceed a certain critical value, the critical energy release rate, for crack propagation to occur. Griffith derived his equation for glass, which is a very brittle material. Therefore, he assumed that R consisted of surface energy only. In ductile materials, such as mild steel, plastic deformation occurs at the crack tip. Much work is required in producing a new plastic zone at the tip of the advancing crack. Since this plastic zone must be produced upon crack growth the energy for its formation can be considered as energy required for crack propagation. This means that for metals R is mainly plastic energy, as the surface energy is so small that it can be neglected.

3.2.3 Fracture Mechanics Application to Concrete

For concrete, no well defined crack tip exists and micro cracks (and hence 'Griffith flaws') are randomly distributed throughout the specimen (Willam, 1984). However, somewhat analogous to the plastic zone in metals, it can be argued that the fracture energy in concrete, G_F, consists mainly of the energy in the fracture process zone, i.e. the area under the crack displacement curve obtained from a tension test such as that shown in Fig. 3.1a. Thus, in concrete, G_F is the critical energy release rate, given by Eq. 3.1.

The energy criterion is a necessary criterion for crack extension and may not be a sufficient criterion. Even if sufficient energy for crack propagation can be provided, the crack will not propagate unless the material at the crack tip is stressed to its capacity. Hence for crack propagation to occur, the stress criterion and the energy criterion have to be fulfilled simultaneously (Broek, 1982).

With the crack band approach proposed by Bazant and Oh (1983a), the deformation w of the fracture zone is looked upon as being caused by strains ε within the fracture zone. That is,

$$w = \int_0^{h_c} \varepsilon d\ell \tag{3.3}$$

The width of the fracture zone, h_c, has a very limited influence upon the behavior of a specimen as long as this width is small compared to the specimen size. The exact distribution of ε within the fracture zone is also then not important. Considering ε to be uniformly distributed along the width of the fracture zone, we obtain

$$G_F = h \int_0^{\varepsilon_{ut}} \sigma \, d\varepsilon \tag{3.4}$$

where h is the assumed width of the fracture zone (i.e. crack band) and $\varepsilon_{ut} = w_{max}/h$.

If the stress-displacement relation is idealized with linear ascending and descending branches as in Fig. 3.3, we obtain

$$G_F = h \frac{1}{2} f_t' \varepsilon_{ut} \tag{3.5a}$$

from which ε_{ut} can be determined for a given h, G_F and f_t'. The descending branch of the stress-strain curve representing the reduction of stress in the fracture process zone is termed 'tension-softening' in this study. The tension-softening stress, $f_{t_{sf}}$, is given by

$$f_{t_{sf}} = f_t' \left(\frac{\varepsilon_{ut} - \varepsilon}{\varepsilon_{ut} - \varepsilon_{cr}}\right) \quad \text{for } \varepsilon_{cr} < \varepsilon < \varepsilon_{ut} \tag{3.5b}$$

$$f_{t_{sf}} = 0 \qquad \text{for } \varepsilon > \varepsilon_{ut} \tag{3.5c}$$

It is incorporated into the material representation adapted for the study as described in Sect. 3.3.3 and Sect. 3.7.2.2.

3.2.4 Representation of Cracking in Finite Element Analysis

The crack band approach is used in conjunction with 'smeared crack' models wherein the cracking is accounted for by changing the isotropic elastic matrix to an orthotropic one, reducing the material stiffness in the direction normal to the cracks in the band (ASCE, 1982). In

contrast, the 'discrete crack' models (Hillerborg, 1985 and Ingraffea et al., 1984) assume that the fracture zone consists of only a 'tied' crack, i.e. a crack of varying width w with the ability to transfer stresses σ according to the σ-w curve.

The smeared crack approach offers a number of advantages over the discrete crack approach in the finite element analysis. These are

1. Redefinition of the topology of the structure is not required.
2. Multiaxial stress conditions can be easily included.
3. Rotation of the principal stress axes during strain softening can be treated.

Although the discrete crack approach also offers some advantages, such as the ability to model more realistically the interface shear transfer and distribution of concrete and steel stresses, the smeared crack approach is used in this investigation because of its numerical efficiency.

3.3 Tension Stiffening

3.3.1 Introduction

In contrast to Sect. 3.2 wherein the behavior of a plain concrete tension pull specimen was considered, the behavior of a tension member containing reinforcement is considered in this section. When a reinforced concrete member is subjected to tension, the phenomenon of tension stiffening becomes significant. Tension stiffening refers to the effect that the intact concrete between the cracks has on reducing the elongation of the reinforcement by virtue of its being bonded to the steel. The term bond-slip refers to the relative displacement between the steel reinforcement and concrete in the tangential direction at the

steel-concrete interface.

The effects of bond-slip which should be included in a realistic finite element analysis can be classified into two major categories (Bergan and Holand, 1978): (1) Anchorage bond; and, (2) Tension-stiffening bond (see Fig. 3.4a and b).

Anchorage bond (Fig. 3.4a) is bond stress which is required to balance the change in steel stress required by statics rather than compatibility. This situation arises when the reinforced concrete member is subjected to shear forces and at anchorage zones of reinforcing bars. In this case, the concrete may be considered to be held in place while the unbalanced force in the steel bar tends to pull it out of the concrete.

In the case of tension stiffening bond, both the concrete and steel are subjected to tension so that primary cracks form. Figure 3.4b shows the concrete between two such primary cracks. Intact concrete segments between the cracks carry some tension which is transferred by bond from steel and the average stress in steel is less than that at the crack locations. Hence the stiffness of the steel/cracked concrete system is greater than that due to steel alone. This tension stiffening effect has been found to be significant in beams, slabs and shell structures (Scanlon and Murray, 1972; Floegl and Mang, 1982).

In a smeared representation of cracking, tension stiffening bond cannot be accounted for by the bond elements described in Chapter 2, but its effects may be included indirectly by using a shallower softening branch in the tensile stress-strain curve of concrete (Scanlon and Murray, 1972) or by using an increased stiffness for reinforcement (Gilbert and Warner, 1978). Anchorage bond is accounted for by using

bond elements as described in Chapter 2, for which the constitutive relation is discussed in Section 3.4 (i.e. the local bond stress-bond slip relationship).

The role of bond-slip in tension stiffening can be clarified by considering the tension pull specimen shown in Fig. 3.5 wherein the characteristic tensile strength is denoted as f'_t. Two basically opposing theories have been advanced to determine the stable crack pattern: 1. slip theory, 2. no slip theory (Beeby (1979); Base (1982)).

3.3.2 Theories to Predict Crack Spacing

3.3.2.1. Slip theory

Consider the situation when the first crack forms in the member, say at 1 in Fig. 3.5. Since the variation in the tensile strength is randomly distributed along the specimen, the location of this crack cannot be determined. Assuming for the present discussion that a tension cut-off condition prevails, the stresses in concrete will be reduced to zero at the crack (Fig. 3.5b). However the bond between steel and concrete counteracts the unloading of the concrete between the cracks. The distance from the crack at which the stress distribution remains unaffected by the crack is called the bond length, S_o (Fig. 3.5b). Since the crack has reduced the average concrete stresses to below the tensile strength within a distance S_o from the crack, the next crack must form outside the region. The minimum distance between cracks is thus S_o. If two cracks form at a distance greater than $2S_o$ apart, there will be an area between the cracks where the stress is not affected by either of the cracks and so another crack can form between them (Figs. 3.5c and 3.5d). Whereas, if cracks form at a lesser spacing

than $2S_o$, the concrete stresses will be reduced over the entire length between the two cracks and another crack will not form. When all the cracks have developed, the maximum possible spacing is thus $2S_o$, and the final crack pattern will consist of cracks having some distribution of spacings within the range $S_o \leq S \leq 2S_o$.

The bond length, S_o, can be related to the bond stress as follows.

$$S_o \tau_{max} k \pi \phi = f_t' A_c \tag{3.6}$$

where τ_{max} is the maximum bond stress; k is a factor to account for the distribution of bond stresss; ϕ is the diameter of reinforcement; and A_c is the area of concrete tributary to a reinforcing bar. Solving for S_o yields,

$$S_o = k_1 \frac{\phi}{\rho} \frac{f_t'}{\tau_{max}} \tag{3.7a}$$

where

$$\rho = \frac{A_s}{A_c} = \frac{\pi\phi^2}{4} / A_c \tag{3.7b}$$

and

$$k_1 = \frac{4}{k} , \tag{3.7c}$$

a constant.

3.3.2.2. No Slip Theory (Base, 1982)

This theory is opposite to the slip theory. It contends that there is no slip between steel and concrete at the time the cracks are developed and the distance S_o between the crack and the point where the stresses remain undisturbed by the cracks is roughly equal to the concrete cover. (This is approximately what would be obtained by the application of St. Venant's principle!) Hence, according to this theory, the minimum crack spacing, S_o, is given by

$$S_o = C \tag{3.8}$$

where C is the cover distance.

3.3.2.3 Beeby's Theory of Crack Spacing

Beeby (1979) attempted to reconcile the slip and no slip theories and suggested the following stages in the development of a stable crack pattern:

(a) The primary cracks form at locations depending on the tensile strength distribution.

(b) Further loading causes loss of adhesion adjacent to the primary cracks, transferring load to the ribs of the bar.

(c) Internal cracks form close to the primary cracks.

(d) Further loading causes more internal cracks to form at successively greater distances from the main crack.

At stage (a), the bond length S_o is approximately equal to the cover. The effect of developments (b), (c) and (d) is to increase the bond-length with increase in load.

Based on the above argument, Beeby offered the following expression for the average crack spacing, S_m, for a stabilized crack pattern.

$$S_m = K_1 C + K_2 \frac{\phi}{\rho} \tag{3.9}$$

where K_1 and K_2 are constants.

Equation 3.9 could be used to determine the average crack spacing in a reinforced concrete tension member. It has commonly been assumed that the conditions in the tension zone of a R/C beam are identical to those in a tension pull specimen. But this is not the case, since the cracking in a R/C beam is 'curvature controlled', and the primary crack spacing, S, is given by (Beeby, 1979)

$$h_{cr} < S < 2h_{cr} \tag{3.10}$$

where h_{cr} is the crack height, which is approximately equal to the distance from the tension face to the neutral axis of the beam.

If the ratio of concrete cover to crack height, C/h_{cr}, is high (as in slabs and panels) secondary cracks do not form since the primary crack spacing will be less than that given by Eq. 3.9. On the other hand, if C/h_{cr} approaches zero, second and higher order cracks will form as for a tension pull specimen. Thus, for beams Eq. 3.9 can only be used with K_2 dependent on C/h_{cr}. Table 3.1 gives values of K_1 and K_2 for use with Eq. 3.9 (Beeby, 1979) for beams. This equation gives the stabilized spacing of cracks at a load level that is only slightly greater than that at which primary cracks form. Equation 3.9 has been used to determine the tension stiffening effect in beams (Chapter 5).

3.3.3 Tension Stiffening Relationships

3.3.3.1 Introduction

Once the crack pattern has been stabilized, the tension stiffening contribution of concrete depends on the bond-slip characteristics of the steel-concrete interface and the stabilized crack spacing. In this study, the tension softening of concrete at the cracks and the tension stiffening contribution of concrete segments between the cracks, have been combined together and represented by the descending branch of the tensile stress-strain curve adopted for concrete. Figures 3.6a and b illustrate schematically the stress distribution in concrete. Initially the reduction in tension stiffening occurs due to the increase in the bond length. Once this bond length has extended to one half the crack spacing, further reduction in tension stiffening occurs due to the reduction in the stiffness of the bond-slip layer.

Similar to the slip theory and the no slip theory, discussed in Sect. 3.3.2, the tension stiffening contribution of concrete may be estimated by assuming in turn (1) a zero bond length; and (2) a bond length equal to one half the stabilized crack spacing.

3.3.3.2 Tension Stiffening Assuming Zero Initial Bond Length

First the tension stiffening contribution is calculated as follows, assuming: (1) a tension cut-off condition at the crack; and, (2) the bond length S_o is negligible at the onset of cracking (i.e. 'no slip' theory). At the onset of cracking, assuming no bond slip, the average stress in concrete representing tension stiffening, $f^{(ts)}$, is given by Eq. 3.12.

$$f^{(ts)} = f'_t \quad \text{at } \varepsilon = \varepsilon_{cr} \tag{3.12}$$

With increase in loading, the stress and strain in steel increases. This increases the incompatibility of strains in the steel and concrete and produces internal cracks in concrete surrounding the reinforcement. The greater the steel stress, the larger is the distance along the reinforcement over which internal cracks are produced. That is, the 'bond length' increases with loading thus decreasing the tension stiffening contribution of concrete. It is assumed that this can be represented by

$$f^{(ts)} = f'_t \left(\frac{f_s^{(cr)}}{f_s}\right) \tag{3.13}$$

where

$f_s^{(cr)}$ = stress in steel at the onset of primary cracking, assuming no stress in concrete

f_s = stress in steel at the current load level, again assuming no stress in concrete.

Equilibrium at the onset of primary cracking requires that

$$\rho f_s^{cr} = f'_t (1 + n\rho) \tag{3.14}$$

where n is the ratio of Young's modulus of steel to that of concrete.

Substituting for f_s^{cr} from Eq. 3.14 into Eq. 3.13,

$$f^{(ts)} = \frac{f_t'^2 (1 + n\rho)}{\rho f_s} \tag{3.15}$$

The relationship between the average tensile strain, ε, and the tensile stiffening stress, $f^{(ts)}$, is obtained as follows.

$$\varepsilon = \frac{f_s A_s - f^{(ts)} A_c}{A_s E_s} = \frac{\left(f_s - \frac{f^{(ts)}}{\rho}\right)}{E_s} \tag{3.16}$$

Substiting for f_s from Eq. 3.15 into Eq. 3.16 and simplifying,

$$\varepsilon = \frac{f^{(ts)}}{\rho E_s} \left[\left(\frac{f'_t}{f^{(ts)}}\right)^2 (1 + n\rho) - 1\right] \tag{3.17}$$

The total tensile stress in concrete, f_t, is obtained as the sum of the tensile stiffening contribution, $f^{(ts)}$, between the cracks and tensile softening stress, $f_{t_{sf}}$, at the cracks. That is,

$$f_t = f^{(ts)} + f_{t_{sf}} \quad \text{for } \varepsilon > \varepsilon_{cr} \tag{3.18a}$$

subject to

$$f_t \leq f'_t \tag{3.18b}$$

At the onset of plastic yielding in steel at the crack faces, the tension stiffening contribution disappears because the tensile capacity of steel at the crack faces cannot increase any further. This leads to the constraint given by Eqs. 3.19

$$f_t = 0 \quad \text{for } \frac{f_s}{E_s} \geq \bar{\varepsilon}_s \tag{3.19a}$$

where $\bar{\varepsilon}_s$ is the average strain at which steel yields at the crack. The value of $\bar{\varepsilon}_s$ is obtained by substituting the yield strength of steel, $\bar{f}_s$, for f_s in Eqs. 3.15 and 3.16. From Eq. 3.16,

$$\bar{\varepsilon}_s = \frac{\bar{f}_s}{E_s} - \frac{f_t'^2}{\rho^2} \frac{(1 + n\rho)}{\bar{f}_s E_s} \tag{3.19b}$$

The effective area of concrete contributing to the tension stiffening effect depends on the cover, the spacing and diameter of the reinforcement, the orientation of the reinforcement, confining reinforcement if any etc. The CEB/FIP model code recommends the tributary areas shown in Fig. 3.7b and is used in this study.

For very small steel percentages, $f_s^{(cr)}$ might exceed $\bar{f}_s$, the yield strength of steel. For this condition, no tension stiffening exists and the tension softening relationship of Fig. 3.3 is used (See Fig. 3.7a).

3.3.3.3 Tension Stiffening Assuming Bond Length as One Half the Crack Spacing

Assuming: (1) linear variation of concrete stress along the bond transfer length; and, (2) the crack spacing is stabilized at twice the transfer length we can solve for f_t as

$$f_t = \frac{f_t' + f_{t_{sf}}}{2} \quad \text{for } \varepsilon \leq \varepsilon_{ut} \tag{3.20a}$$

$$f_t = \frac{f_t'}{2} \quad \text{for } \varepsilon > \varepsilon_{ut} \tag{3.20b}$$

Substituting for $f_{t_{sf}}$ from Eq. 3.5b into Eq. 3.20a,

$$f_t = \frac{f'_t}{2} + \frac{f'_t}{2}\left(\frac{\varepsilon_{ut} - \varepsilon}{\varepsilon_{ut} - \varepsilon_{cr}}\right) \quad \text{for } \varepsilon_{cr} < \varepsilon < \varepsilon_{ut} \tag{3.21a}$$

The value of $\bar{\varepsilon}_s$ in this case is again obtained using Eq. 3.16

$$\bar{\varepsilon}_s = \left(\frac{\bar{f}_s}{E_s} - \frac{f_t}{\rho E_s}\right) \tag{3.21b}$$

Substituting for f_t from Eq. 3.21a into Eq. 3.21b,

$$\bar{\varepsilon}_s = \frac{\bar{f}_s}{E_s} - \frac{f'_t}{2\rho E_s}\left[1 + \frac{\varepsilon_{ut} - \bar{\varepsilon}_s}{\varepsilon_{ut} - \varepsilon_{cr}}\right] \tag{3.21c}$$

Simplifying,

$$\bar{\varepsilon}_s = \frac{\bar{f}_s \frac{2\rho}{f'_t} - 1 - \left(\frac{\varepsilon_{ut}}{\varepsilon_{ut} - \varepsilon_{cr}}\right)}{E_s \frac{2\rho}{f'_t} - \left(\frac{1}{\varepsilon_{ut} - \varepsilon_{cr}}\right)} \tag{3.21d}$$

Equations 3.20 are applicable if the stiffness of the bond slip layer remains constant.

Figure 3.7a shows schematically the tensile stress-average tensile strain relationships for concrete for different transfer lengths and crack spacing. The tension stiffening adopted in this study depends on the estimated crack spacing (the larger the crack spacing, the greater is the tension stiffening contribution) and the bond characteristics of the reinforcement.

Figures 3.8a and b show the relationship of the anchorage bond and tension stiffening bond in a cracked R/C beam subjected to moment gradient. It can be seen that the average bond stress is the anchorage

bond stress and the tension stiffening bond stress augments the anchorage bond stress to produce a local bond stress which exceeds the anchorage bond stress. However, this local variation has not been accounted for, because of the smeared crack approach used in this study.

3.4 Local Bond Stress-Slip Relationship

3.4.1 Mechanism of Bond-Slip Resistance

The bond stress-slip relationship depends on the mechanism of slip resistance which arises from different sources based on the magnitude of slip (Gambrova et al., 1982). With reference to a deformed bar embedded in concrete, for very small values of the average bond stress, τ_b, the only mechanism of bond resistance is chemical adhesion which allows negligible slip. At increasing values of the average bond stress, the chemical adhesion is destroyed as a consequence of the wedging action of the ribs which separate the concrete and steel in between the ribs and transverse cracks from close to the steel ribs as shown in Fig. 3.9a. The next mechanism which is developed is due to the interaction between the steel ribs and the concrete 'teeth' between the ribs. This interaction induces large bearing pressures at the sloping rib surfaces and tensile 'hoop' stresses in the annular concrete teeth between the ribs (Tepfers, 1979). With increasing average bond stress, the transverse crack size increases, crushed concrete wedges form in front of the sloping ribs and the increase in hoop stresses induces localized splitting cracks (longitudinal cracks lying in planes passing through the bar axis). If no external confinement is provided, the annular concrete teeth fail in hoop tension resulting in continuous splitting cracks as shown in Fig. 3.9b which indicate the limit of the bond

capacity. If adequate confinement is provided, say, by web reinforcement, the transverse and longitudinal cracks divide the concrete into blocks which behave like struts and resist further bond slip. After the failure of these struts, the confinement action provides a limited bond resistance and is similar to frictional behavior. The ranges of different mechanisms of slip resistance are shown in the bond stress-slip curve of Fig. 3.10.

3.4.2 Parameters Affecting the Bond Slip Behavior

Tests conducted to determine the local bond stress-slip relationship show results with considerable scatter (CEB, 1982b). General agreement is lacking among researchers on the relative influence of various parameters affecting the bond stress-slip relationship. Consistent with the description of slip resistance (Section 3.4.1), the following factors are considered significant (CEB, 1982b).

1. The tensile strength of concrete is of major importance if the bond failure is caused by splitting. Tensile splitting forces are generated or by the 'hoop tension' described in Section 3.4.1.

2. The compressive strength of concrete at the steel concrete interface is a major factor since the reinforcement ribs bear against the concrete "teeth" after chemical adhesion is overcome. If the resistance of the concrete cover is sufficient to prevent splitting failure, bar slip can occur only due to cracking and concrete crushing in front of the ribs, thus leading to a situation conducive to a pull-out failure. For this failure mechanism the compressive strength is important.

3. Pressure in the transverse direction affects the bond behavior

due to its effect on the splitting and compressive strength of concrete around the reinforcing bars. If the transverse pressure confines the concrete, it counteracts the splitting forces thus increasing the slip resistance. It also increases the pull-out resistance by creating a triaxial compressive stress field in the concrete in front of the reinforcement ribs. If the transverse pressure is tensile, it reduces the splitting resistance.

4. The deformations on the surface of reinforcement significantly influence not only the mode of bond failure but also the bond strength and stiffness. With increase in the relative rib area (which is measured by the ratio of volume of steel ribs to the volume of the bar), the bond strength and stiffness increase as long as the failure mode is by bar pull out. The higher the relative rib area the more likely it is that a splitting failure mode occurs. The inclination of the rib faces, within an interval of 45° to 90° relative to the longitudinal axis of the bar, has no significant influence on the bond behavior. In North America, deformed reinforcing bars meeting the ASTM specifications have the same relative rib area.

5. Position of the bars during casting of concrete significantly influences the bond behavior. Bars cast in a horizontal position show lower bond strength than bars cast in a vertical position. This can be explained by an accumulation of porous mortar at the lower half of the bar and settling of fresh concrete which reduces the effective depth of corbels of concrete between ribs.

6. Proximity to a crack seems to influence the local bond slip behavior significantly (Nilson, 1972; Jiang, Shah and Andonian, 1984) although tests by Mirza and Houde (1979) contradict this claim.

Other parameters such as concrete cover, aggregate size, bar spacing, and bar diameter may affect the bond-slip behavior by influencing any of the factors mentioned above.

3.4.3 Determination of Local Bond Stress-Slip Relationship

Local bond stress-slip relationships obtained by several investigators based on tests show considerable scatter. Figure 3.11 shows the local bond stress-slip relationships for unconfined concrete (f'_c approximately 35 MPa) obtained by various investigators. Houde and Mirza (1979) and Shah et al. (1981) used tension-pull specimens whereas Giuriani (1981) and Eligehausen et al. (1982) used pull-out type specimens with short bond lengths. The trilinear relationship adopted in this study is also shown in Fig. 3.11. It is consistent with the description of the mechanism of bond resistance described in Sect. 3.4.1 and offers the advantage that parameters can be easily varied as more test data become available. In the presence of confining reinforcement, the transition stresses τ_a and τ_b may be increased by up to 250%, as indicated by Eligehausen et al. (1982) (Fig. 3.12).

3.5 Behavior of Concrete in Compression

3.5.1 Basic Mechanism of Concrete Under Uniaxial Compressive Stress

Concrete exhibits varying deformation characteristics under different loading conditions and load levels. A typical stress-strain curve for concrete under compression is shown in Fig. 3.13. The stress-strain relation is closely related to the development of microcracking in concrete. Three distinct stages are observed namely linear, nonlinear and post-failure. Even before any loads are applied, micro-

cracks at the interface between coarse aggregate and mortar (called 'bond cracks') exist (see, for example, Mindess et al., 1981). These cracks do not apparently extend until the applied load reaches about 30% of peak value, which is the limit of the linear elastic stage. Above this stress level, bond cracks begin to increase in length, width and number resulting in nonlinear response. At about 70% to 90% of the peak load, cracks through the mortar increase noticeably and start bridging between bond cracks to form continuous crack patterns. The development of continuous crack patterns does not lead to the immediate loss of load carrying capacity because concrete at this stage behaves as a highly redundant structure (Chen, 1985). As successive load paths become inoperative through bond cracking, alternate load paths are mobilized to carry the additional load. As the number of load paths decreases, the intensity of stress on the remaining load paths increases at a faster rate than the external load. When the number of load paths has been reduced considerably the stress-strain relation enters the descending branch.

The above explanation implies that compressive strain softening is not an inherent material property but is rather a structural property wherein the proliferation of cracking leads to a reduction in the effective cross sectional area. This conclusion is evidenced by experimental findings (Chen, 1985) of splitting tensile modes of failure under uniaxial compression wherein steeper softening branches are exhibited with increasing specimen heights, as discussed in Appendix A4.

3.5.2 Basic Mechanism of Concrete Behavior Under Multiaxial Stresses

Compared to the uniaxial compression case, the crack propagation

process in concrete under multiaxial conditions has not been well-studied. Qualitatively, the major difference arises in the post peak (post-failure) behavior. Under multiaxial stress conditions, the possible failure modes include the tensile splitting mode and shear failure mode which results from the stepwise joining of the areas of high crack densities. Splitting modes exhibit strain localization. The shear failure mode under low to moderate confinement has also been shown to exhibit strain localization (Chen, 1985). Under high confinement (for which the octahedral normal stress, σ_{oct}, is large) strain localization does not occur, strain softening has not been observed, and concrete behaves in a ductile manner.

3.6 Brief Review of Constitutive Models

There are three aspects to the constitutive modelling of concrete under multiaxial stress conditions:

(1) Failure envelope

(2) Pre-peak stress-strain relationship

(3) Post-peak behavior.

These three aspects of behavior are discussed in the following subsections. Since this study deals primarily with beams under in-plane loading, plane stress conditions are assumed and the following discussion is restricted to these conditions unless indicated otherwise.

3.6.1 Failure Envelope

A widely accepted representation of the biaxial failure envelope for concrete is that developed by Kupfer et al. (1969, 1973) shown in Fig. 3.14. The failure surface is expressed individually for the

regions of biaxial tension, tension-compression, and biaxial compression (Kupfer and Gerstle, 1973):

Biaxial tension: $$\sigma_{it} = f'_t \quad ; \; i = 1, 2 \tag{3.22}$$

Tension-compression: $$\sigma_{1t} = \left(1 + 0.8 \frac{\sigma_2}{f'_c}\right) f'_t \tag{3.23}$$

Biaxial compression: $$\sigma_{2c} = \frac{1 + 3.65\alpha}{(1 + \alpha)^2} f'_c \tag{3.24a}$$

$$\sigma_{1c} = \alpha\sigma_{2c} \tag{3.24b}$$

where $\alpha = \sigma_1/\sigma_2$; σ_{it} and σ_{ic} $(i = 1,2)$ are the peak principal stresses in tension and compression, respectively; and tensile stresses are taken to be positive with $\sigma_1 \geq \sigma_2$.

The above failure envelope was developed based on experiments on concrete plates subjected to monotonically increasing proportional loading. The failure modes (whether tensile splitting or shear) and their range of applicability are not well delineated. Nevertheless, Eqs. 3.22, 3.24 and a modified form of Eq. 3.23 are used in the material description adopted, herein, as will be discussed in Section 3.7.3.

3.6.2 Pre-peak Stress-Strain Relationship

3.6.2.1 Introduction

Almost all the constitutive models assume concrete to be homogeneous in the macroscopic sense such that a continuum mechanics approach is justified. The stress-strain relationship of a concrete element, in general, is nonlinear. However, most of the finite element

analyses to date (ASCE, 1982) use a linear elasticity approach for modelling material response in the pre-peak stress range. Perhaps this is due to the difficulties encountered in assessing various parameters involved with complex material models and in their computer implementation (Buyukozturk and Shareef, 1985). Significant improvement in behavior prediction can be obtained when nonlinearities in the material stress-strain relationship are taken into account.

Most of the available constitutive models can be included in one of the following groups:

1. Elasticity based models
2. Plasticity based models
3. Plastic-fracturing type models
4. Endochronic models

3.6.2.2 Elasticity Based Models

Elasticity based models are either of the hyperelastic (Kupfer and Gerstle, 1973) or of the hypoelastic type (Darwin and Pecknold, 1974; Elwi and Murray, 1979). Hyperelastic formulations characterize the total stress-strain relationship in variable secant modulus form whereas in the hypoelastic formulation incremental stress-strain relationships are characterized using variable tangent moduli. Hyperelastic formulations approximate a path independent reversible process with no memory, the material response at any instant being a function only of the current state of stress or strain and not of load history. The hypoelastic formulation approximates a path dependent, irreversible process with limited memory (Buyukozturk and Shareef, 1985), the material response at any instant being a function of the current state

of strain and the stress path followed to reach that strain.

Kupfer and Gerstle (1973) devised a hyperelastic isotropic total stress-strain relation, based on variable secant bulk and shear moduli, expressions for which were derived from tests on concrete specimens under various combinations of biaxial stresses. They obtained a good match with experimental data at low values of stress, but a poor match at high values of stress and in the tension compression stress field.

Another isotropic total stress-strain model for concrete under biaxial loading was developed by Romstad, Taylor and Herrmann (1974). Rather than utilizing continuous curves to represent the degradation of concrete, their model uses a number of damage regions, in which the material properties are altered to match the decrease in stiffness at higher stresses, as shown in Figs. 3.15a. Within each region, the modulus of elasticity and Poisson's ratio are held constant.

An orthotropic constitutive model based on total strains was proposed by Liu, Nilson and Slate (1972) assuming that principal stress and principal strain axes coincide at all loading stages. The model expresses the principal stress, σ_i, as closed form functions of the principal strains, the ratio of principal stress, $\alpha = \sigma_1/\sigma_2$, and Poisson's ratio, ν.

An incrementally isotropic hypoelastic model has been developed by Gerstle (1981) wherein the constitutive relations are expressed in terms of tangential bulk and shear moduli which are assumed to vary linearly as functions of the octahedral normal and shear stresses, respectively. This formulation was based on decoupling of the hydrostatic and deviatoric components of the response which contradicts the material response at high stress levels.

The hypoelastic model proposed by Darwin and Pecknold (1974) is incrementally orthotropic and is based on the concept of 'equivalent uniaxial strain'. This concept provides a method for separating the Poisson effect from the cumulative strain. With this model, the tangent moduli of elasticity are established separately in the current principal stress directions, as functions of the state of stress and strain in each of the current principal stress directions, which form the axes of orthotropy. For an incremental change in principal stress, $\Delta\sigma_i$, the change in equivalent uniaxial strain, $\Delta\varepsilon_{iu}$, is given by

$$\Delta\varepsilon_{iu} = \frac{\Delta\sigma_i}{E_i} \tag{3.25}$$

where E_i are the current tangent moduli. The term $\Delta\varepsilon_{iu}$ may be thought of as the strain increment that would exist in one direction for zero stress in the other direction. The total equivalent uniaxial strains accumulated in principal stress directions are given by integration over the loading path:

$$\varepsilon_{iu} = \sum_{\substack{\text{all} \\ \text{load} \\ \text{increments}}} \frac{\Delta\sigma_i}{E_i} \tag{3.26}$$

Material properties and stress corrections are based on the equivalent uniaxial stress-strain curves. From these curves, the stress at any strain is given as a function of the total accumulated equivalent uniaxial strain, the principal stress ratio, and load history. The equivalent uniaxial stress-strain curves are determined using the peak stress, the strain corresponding to the peak stress, and the initial

tangent modulus, all of which are derived from test results. The form of equivalent uniaxial stress-strain curve used by Darwin et al. (1974) is shown in Fig. 3.16.

Referring to the material axes as the current principal stress axes, the incremental constitutive relation is given as (Darwin and Pecknold, 1974)

$$\begin{Bmatrix} d\sigma_1 \\ d\sigma_2 \\ d\tau_{12} \end{Bmatrix} = \frac{1}{1-\nu^2} \begin{bmatrix} E_1 & \nu\sqrt{E_1E_2} & 0 \\ \nu\sqrt{E_1E_2} & E_2 & 0 \\ 0 & 0 & \frac{1}{4}(E_1+E_2-2\nu\sqrt{E_1E_2}) \end{bmatrix} \begin{Bmatrix} d\varepsilon_1 \\ d\varepsilon_2 \\ d\gamma_{12} \end{Bmatrix} \quad (3.27)$$

The tangent moduli E_1 and E_2 are determined from the equivalent uniaxial curves. The shear modulus term is determined such that it is invariant with respect to coordinate transformation. It is interesting to note that this incremental constitutive relation is isotropic under proportional loading if the shape of the uniaxial stress-strain curve is not altered between regions. That is, with the equivalent uniaxial stress-strain curve for compression shown in Fig. 3.16, the incremental stress-strain relationship is isotropic in the biaxial compression region whereas in the tension-compression region it is orthotropic because a linear stress-strain relation is used in tension.

3.6.2.3 Plasticity Based Models

Plasticity based models which include work-hardening are essentially equivalent to hypoelastic models for the loading process but they differ in defining the unloading paths (Buyukozturk, 1985). The plasticity based models can accurately predict inelastic dilatancy and

hydrostatic pressure sensitivity but damage accumulation and degradation in stiffness exhibited by concrete under stress reversals may not be represented satisfactorily. However, this degradation is not crucial in the prepeak region while it is significant in the post peak region (Chen, 1985). The basic plasticity model is briefly described in the following.

The central notion with work-hardening plasticity models is the existance of a yield function of the form

$$F(\sigma, k) = 0 \tag{3.28}$$

where k is a 'hardening' parameter (Zienkiewicz, 1977), and a flow rule relating the increments of plastic strain $d\varepsilon_p$ to the plastic potential $Q(\sigma,k)$ as

$$d\varepsilon_p = \frac{\partial Q}{\partial \sigma} \lambda \tag{3.29}$$

where λ is a proportionality constant. If the hardening parameter, k, is not a constant, the function F becomes the loading function. Prager's consistency condition (Chen, 1982) requires that

$$dF = \frac{\partial F}{\partial \sigma_1} d\sigma_1 + \frac{\partial F}{\partial \sigma_2} + \ldots + \frac{\partial F}{\partial k} dk = 0 \tag{3.30}$$

With a 'work hardening' material, k is taken to be represented by the amount of plastic work done during plastic deformation. Thus,

$$dk = \sigma^t d\varepsilon_p \tag{3.31}$$

During an infinitesimal increment of stress, changes of strain are assumed to be divisible into elastic and plastic parts.

$$d\boldsymbol{\varepsilon} = d\boldsymbol{\varepsilon}_e + d\boldsymbol{\varepsilon}_p \tag{3.32}$$

The elastic strain increments are related to the stress increments by a symmetric elastic constitutive matrix **D**. After substituting from Eq. 3.29, Eq. (3.32) becomes

$$d\boldsymbol{\sigma} = \mathbf{D}\left[d\boldsymbol{\varepsilon} - \frac{\partial Q}{\partial \boldsymbol{\sigma}}\lambda\right] \tag{3.33}$$

Substituting from Eq. 3.31 into Eq. 3.30,

$$dF = \left(\frac{\partial F}{\partial \boldsymbol{\sigma}}\right)^t d\boldsymbol{\sigma} + \frac{\partial F}{\partial k}\boldsymbol{\sigma}^t d\boldsymbol{\varepsilon}_p = 0 \tag{3.34}$$

Substituting from Eq. 3.29 for $d\boldsymbol{\varepsilon}_p$,

$$dF = \left(\frac{\partial F}{\partial \boldsymbol{\sigma}}\right)^t d\boldsymbol{\sigma} + \frac{\partial F}{\partial k}\lambda\ \boldsymbol{\sigma}^t \frac{\partial Q}{\partial \boldsymbol{\sigma}} = 0 \tag{3.35}$$

Substituting for $d\boldsymbol{\sigma}$ from Eq. 3.33,

$$dF = \left(\frac{\partial F}{\partial \boldsymbol{\sigma}}\right)^t \mathbf{D}\, d\boldsymbol{\varepsilon} - \lambda\left(\frac{\partial F}{\partial \boldsymbol{\sigma}}\right)^t \mathbf{D}\frac{\partial Q}{\partial \boldsymbol{\sigma}} + \lambda\frac{\partial F}{\partial k}\boldsymbol{\sigma}^t\frac{\partial Q}{\partial \boldsymbol{\sigma}} = 0 \tag{3.36}$$

Solving for λ,

$$\lambda = \frac{\left(\frac{\partial F}{\partial \boldsymbol{\sigma}}\right)^t \mathbf{D}\, d\boldsymbol{\varepsilon}}{\left(\frac{\partial F}{\partial \boldsymbol{\sigma}}\right)^t \mathbf{D}\frac{\partial Q}{\partial \boldsymbol{\sigma}} - \frac{\partial F}{\partial k}\boldsymbol{\sigma}^t\frac{\partial Q}{\partial \boldsymbol{\sigma}}} \tag{3.37}$$

Substituting for λ from Eq. 3.37 into Eq. 3.33,

$$d\sigma = \left[\mathbf{D} - \frac{\mathbf{D} \frac{\partial Q}{\partial \sigma} \left(\frac{\partial F}{\partial \sigma}\right)^t \mathbf{D}}{\left(\frac{\partial F}{\partial \sigma}\right)^t \mathbf{D} \frac{\partial Q}{\partial \sigma} - \frac{\partial F}{\partial k} \sigma^t \frac{\partial Q}{\partial \sigma}} \right] d\varepsilon \tag{3.38a}$$

$$= \mathbf{D}_{ep} d\varepsilon \tag{3.38b}$$

The term inside the square brackets is the incremental elastic plastic constitutive matrix, denoted as $\mathbf{D}_{ep}$ in Eq. 3.38b.

In case F = Q, called associated plasticity, the elastic-plastic constitutive matrix $\mathbf{D}_{ep}$ is symmetric. If incremental plastic work, dk, is determined from a uniaxial test, then

$$dk = \sigma_y \, d\varepsilon_{up} \tag{3.39}$$

where $d\varepsilon_{up}$ is the incremental plastic strain and σ_y is the uniaxial stress. Noting that for a uniaxial test,

$$F(\sigma_y, k) = 0 = \sigma_y + k \tag{3.40}$$

the consistency condition (Eq. 3.30) yields,

$$- \frac{\partial F}{\partial k} = \frac{\partial \sigma_y}{\partial k} = \frac{\partial \sigma_y}{\partial \varepsilon_{up} \cdot \sigma_y} = \frac{\left(\frac{\partial \sigma_y}{\partial \varepsilon_{up}}\right)}{\sigma_y} \tag{3.41}$$

Thus, the term $- \frac{\partial F}{\partial k} \sigma^t \frac{\partial Q}{\partial \sigma}$ in the denominator of Eq. 3.38a can be

obtained using associated plasticity as simply $\left(\frac{\partial \sigma_y}{\partial \varepsilon_{up}}\right)$ which is the slope of the uniaxial stress versus plastic strain curve. Denoting $\frac{\partial \sigma_y}{\partial \varepsilon_{up}}$ by H', we obtain the incremental elastic plastic stress-strain relation for associated plasticity as,

$$\mathbf{D}^*_{ep} = \mathbf{D} - \frac{\mathbf{D}\left(\frac{\partial F}{\partial \boldsymbol{\sigma}}\right)\left(\frac{\partial F}{\partial \boldsymbol{\sigma}}\right)^t \mathbf{D}}{H' + \left(\frac{\partial F}{\partial \boldsymbol{\sigma}}\right)^t \mathbf{D}\left(\frac{\partial F}{\partial \boldsymbol{\sigma}}\right)} \tag{3.42}$$

With elastic-perfectly plastic models, H' = 0.

In the above derivation, isotropic hardening has been assumed. Plasticity based models using nonuniform loading surfaces have also been developed (Chen, 1985).

Murray et al. (1979) have developed a constitutive relationship based on a three parameter elastic-plastic strain hardening theory for biaxial stress conditions, in terms of equivalent plastic strains in tension and compression.

3.6.2.4 Other Constitutive Models

In the plastic-fracturing theory the inelastic behavior is attributed to microcracking in addition to plastic slip (Bazant and Kim, 1979). The plastic strain increments are obtained using conventional plastic loading surfaces whereas the fracturing stress decrements are given by a potential function in the strain space. This theory accounts for pressure sensitivity, inelastic dilatancy due to microcracking, strain softening, degradation of elastic moduli due to microcracking and hydrostatic nonlinearity (ASCE, 1982). The resulting constitutive relation is incrementally linear but the tangential moduli are

nonsymmetric.

In the endochronic theory (Bazant, 1976) the basic concept is that of intrinsic time as a non-decreasing scalar variable representing the evolution of irreversible damage. This theory is even more comprehensive than the plastic fracturing theory. Increased realism obtained by plastic fracturing and endochronic theories are associated with greater complexities and increased number of material parameters. Both these theories treat the prepeak strain hardening and post-peak strain softening as material properties. This is in conflict with the experimental evidence (Chen, 1985) wherein the post-peak behavior is found to be dependent on the specimen size.

3.6.3 Post-Peak Behavior in Compression and Combined Stresses

As discussed in Sect. 3.5, the post-peak behavior under compressive and multiaxial loading depends on the failure mode. It was stated that the tensile cracking failure mode and the localized shear failure mode exhibit strain softening that is not a material property but a structural property. Thus in these cases the strain softening moduli are mesh dependent. Hence the load displacement curve should be traced in tests rather than the stress-strain relationship. Willam et al. (1985) developed a Composite Damage Model (CDM) based on a series model of an intact elastic zone and a localized damage zone as shown in Fig. 3.17. In one extreme, the CDM recovers the fracture mechanics postulate of an invariant fracture energy release rate which introduces a characteristic size effect responsible for the non-local (i.e. mesh dependent) format of the constitutive model for the equivalent continuum. In the other extreme, the CDM reduces to the traditional

strain-softening approach in which the local fracture energy density is considered a proper property for describing distributed fracture occuring in concrete under high confinement. At the present stage of development of this model, these two types of failure are distinguished according to the triaxial failure criterion of Mohr-Coulomb for distributed shear slip and the major principal stress condition for localized cleavage. Clearly there is a need for a continuous transition between these two extreme positions. The Mohr-Coulomb failure criterion may predict the shear slip type of failure under the biaxial loading of tension and compression as long as the maximum tensile strength is not reached (Chen, 1985). This is contrary to the experimental evidence which indicates that both the tensile failure and uniaxial compression failure exhibit strain localization.

3.6.4 Post-Peak Behavior in Tension

The post cracking stress-strain relationship in tension originally proposed by Litton (Riggs, 1981) and recently used by Rots et al. (1985), is analogous to the plasticity based models. The fundamental concept of this approach is the separation of strain into uncracked concrete strains and crack strains. The incremental strains, $\Delta\varepsilon$, are resolved into solid concrete strains, $\Delta\varepsilon^{co}$, and crack strain increments, $\Delta\varepsilon^{cr}$.

$$\Delta\varepsilon = \Delta\varepsilon^{co} + \Delta\varepsilon^{cr} \tag{3.43}$$

Equation 3.43 is analogous to Eq. 3.32. The stresses are based on the uncracked concrete strains through the uncracked constitutive

relations. The number and orientation of the cracks are not defined *a priori*, but rather a crack forms perpendicular to the maximum principal tensile stress when the tensile strength is reached. The formulation is briefly described as follows:

The global crack strains, ε^{cr}, are obtained by transformation of local smeared crack strains (in crack axes), $\mathbf{e}^{cr}$, into the global coordinate system using the strain transformation matrix $\mathbb{N}$.

$$\varepsilon^{cr} = \mathbb{N}\, \mathbf{e}^{cr} \tag{3.44}$$

Then, the vector of crack interface stresses, $\mathbf{S}^{cr}$, is obtained by transforming the global stress vector, σ, as

$$\mathbf{S}^{cr} = \mathbf{N}^{t}\, \sigma \tag{3.45}$$

The incremental stresses in global areas, $\Delta\sigma$, are related to the incremental solid concrete strains, $\Delta\varepsilon^{co}$, through the uncracked concrete constitutive matrix $\mathbf{D}^{co}$.

$$\Delta\sigma = \mathbf{D}^{co}\, \Delta\varepsilon^{co} \tag{3.46}$$

The incremental crack interface stresses, $\Delta\mathbf{S}^{cr}$, are related to the incremental local crack strains, $\Delta\mathbf{e}^{cr}$, through the matrix of crack interface stress-strain relationship, $\mathbf{D}^{cr}$.

$$\Delta\mathbf{S}^{cr} = \mathbf{D}^{cr}\, \Delta\mathbf{e}^{cr} \tag{3.47}$$

Substituting for $\Delta\varepsilon^{co}$ from Eq. 3.43 and ε^{cr} from Eq. 3.44 into Eq. 3.46,

$$\Delta\sigma = \mathbf{D}^{co} \left(\Delta\varepsilon - \mathbf{N}\Delta\mathbf{e}^{cr}\right) \tag{3.48}$$

Substituting for $\Delta\sigma$ from Eq. 3.48 into Eq. 3.45

$$\Delta\mathbf{S}^{cr} = \mathbf{N}^{t}\, \mathbf{D}^{co} \left(\Delta\varepsilon - \mathbf{N}\Delta\mathbf{e}^{cr}\right) \tag{3.49}$$

Substituting for $\Delta\mathbf{S}^{cr}$ from Eq. 3.47 into Eq. 3.49,

$$\mathbf{D}^{cr}\, \Delta\mathbf{e}^{cr} = \mathbf{N}^{t}\, \mathbf{D}^{co} \left(\Delta\varepsilon - \mathbf{N}\Delta\mathbf{e}^{cr}\right) \tag{3.50}$$

Solving for $\Delta\mathbf{e}^{cr}$,

$$\Delta\mathbf{e}^{cr} = \frac{\mathbf{N}^{t}\, \mathbf{D}^{co}}{\mathbf{D}^{cr} + \mathbf{N}^{t}\mathbf{D}^{co}\mathbf{N}}\, \Delta\varepsilon \tag{3.51}$$

Substituting for $\Delta\mathbf{e}^{cr}$ from Eq. 3.51 into Eq. 3.48,

$$\Delta\sigma = \left[\mathbf{D}^{co} - \frac{\mathbf{D}^{co}\, \mathbf{N}\, \mathbf{N}^{t}\, \mathbf{D}^{co}}{\mathbf{D}^{cr} + \mathbf{N}^{t}\, \mathbf{D}^{co}\, \mathbf{N}}\right] \Delta\varepsilon \tag{3.52}$$

It can be shown that (Rots et al., 1985) for a single crack orientation, the above formulation will yield the same results as the formulation in Sect. 3.2.

3.6.5 Interface Shear Transfer

3.6.5.1 Introduction

Cracking in concrete alters the load-carrying mechanisms of the structure significantly. Shear, which is transmitted by the concrete continuum before cracking, is either redistributed or carried across crack interfaces after cracking. Resistance to the relative displacement of crack faces parallel to each other, called 'shear slip', arises from the roughness of the crack faces (termed 'interface shear transfer', abbreviated herein as IST), and the resistance of the reinforcement to deformation perpendicular to its longitudinal axis (termed 'dowel action'). Also, if the reinforcement is not perpendicular to the crack, axial stiffness of the reinforcement contributes directly to shear resistance, in addition to the indirect resistance it provides by decreasing the crack opening displacement which contributes to IST. Experimental results (ASCE, 1982 and Park and Paulay, 1974) and analytical studies (Ottosen, 1978) have shown that IST resists far more shear than dowel action, because large amounts of slip are usually required to develop significant dowel action.

3.6.5.2 Physical Behavior at Crack Interface

The basic shear carrying mechanism of a single crack can be described using Fig. 3.18a and b (Riggs, 1981), where the crack has been idealized by a sawtooth representation. Application of a minimal shear stress will cause a free slip, δ_s, after which the asperities come into contact. The kinematics of deformation for a rigid sawtooth crack when the crack surfaces are in contact, is given by

$$\delta_t = \frac{\delta_n}{\tan \alpha_o} \tag{3.53a}$$

in which δ_t is the relative displacement of the crack faces tangent to the average orientation of the crack, α_o is the angle of the asperity from the average orientation, and δ_n is the relative displacement between the two faces normal to the average orientation (See Fig. 3.18a). However the crack surfaces (asperities) are not rigid and surface deformation of the faces occurs. This additional displacement due to deformation and shearing off of individual asperities is denoted by δ_g. Thus the total δ_t is

$$\delta_t = \delta_s + \delta_n \cot \alpha_o + \delta_g \tag{3.53b}$$

which is illustrated schematically in Fig. 3.18b.

For small crack openings, when the asperities are enmeshed, the IST is mainly by the bearing mode (represented by δ_g in Eq. 3.53b). When the shearing stresses are high enough, the bearing mode of resistance is overcome and the frictional mode of resistance (represented by $\delta_n \cot \alpha_o$) is the major component of IST. The level of resistance due to friction depends on the compressive force across the crack. Because of the irregular surface, as slip occurs the crack must also dilate. The dilation is restrained by the axial stiffness of the reinforcement crossing the crack. Tensile forces in the reinforcement created by the dilation must be balanced by 'compressive stresses across the crack which in turn increase the frictional shear capacity.

A number of experiments have been conducted to determine the influence of various parameters on IST (for a summary, see ASCE, 1982)

and they indicate that: (1) the initial crack width is the most important parameter influencing the shear stiffness, (2) rougher crack surfaces lead to stiffer response and roughness of the crack surface is somewhat insensitive to the aggregate size; (3) IST increases with increase in concrete strength until the reinforcement yields. Figure 3.19 (ASCE, 1982) shows the variation of interface shear stiffness, K_{IST}, with the initial crack width obtained by several experimental investigators (Paulay and Loeber, 1974; Fenwick and Paulay, 1968; Houde and Mirza, 1972; Jiminez et al., 1978). Jiminez et al. (1978) developed an expression for the interface shear stiffness as a function of the normal stiffness, in which the coefficients were determined by a regression analysis of the test results of the references cited above, which is given by Eq. 3.54a.

$$K_{IST} = \left[3.9(w_o - 0.002) - 1.09 \times 10^{-7} \frac{K_N}{w_o} + 0.0367\right]^{-1} \qquad (3.54a)$$

in which w_o is the initial crack width in inches, K_N is the normal stiffness in ksi/in. and K_{IST}, given in ksi/in., is the interface shear stiffness (i.e., the slope of shear stress-shear slip curve which is approximately linear). For the case of $K_N = \infty$, this is claimed to reduce to Eq. 3.54b.

$$K_{IST} = \left[3.9(w_o - 0.002)\right]^{-1} \qquad (3.54b)$$

The normal stiffness, K_N, which is the stiffness of the reinforcement perpendicular to the crack may include the tension-stiffening effect.

3.6.5.3 Analytical Models

A number of analytical models are available to represent IST in finite element analysis. Fardis and Buyukozturk (1979) developed a model based on a fundamental analysis of the crack behavior. They modelled the crack surface 'general roughness' by piecewise parabolic segments and accounted for the normal stresses that develop as the transverse reinforcement restrained the dilation. They obtained the following incremental rigidity relationship for a crack in one direction:

$$d\tau_{ij} = \frac{1}{\frac{1}{G_{ij}} + \frac{1}{\alpha_i}} \left(d\gamma_{ij} - \frac{c_1}{1 + \beta_i} d\varepsilon_{ii} \right) \tag{3.55}$$

where G_{ij} is the uncracked shear modulus; $\alpha_i = (\bar{A}_N + c_2\bar{A}_D)h/c_2$ in which $\bar{A}_N$, $\bar{A}_D$ are extensional and dowel stiffnesses per unit area of the crack, and h is the crack spacing; $\beta_i = c_2\bar{A}_D/\bar{A}_N$; c_1 and c_2 are constants to be determined from experiments and are dependent on crack geometry; $d\gamma_{ij}$ is the incremental shear strain; $d\varepsilon_{ii}$ is the incremental normal strain; $d\tau_{ij}$ is the incremental shear stress.

The model did not allow for degradation of materials, that is, the shape of the crack was assumed to remain constant. Thus its applicability to general structures is limited. Buyukozturk et al. (1979) also developed a more simplified model based on the stiffness of the reinforcement, of the form (ASCE, 1982)

$$G_{cr} = \left[\frac{1}{h_1\left(\frac{K_{N_1}}{\beta_1} + K_{D_1}\right)} + \frac{1}{h_2\left(\frac{K_{N_2}}{\beta_2} + K_{D_2}\right)} + \frac{1}{G} \right]^{-1} \tag{3.56}$$

for orthogonally cracked reinforced concrete elements. In Eq. 3.56, subscripts 1 and 2 refer to the orthogonal crack directions, h is the crack spacing, K_N and K_D are the transverse and dowel stiffnesses of the reinforcing, G is the shear modulus of the uncracked concrete, and β is K_N/K_{IST}, which is assumed to be a function of the initial crack width.

Bazant and Tsubaki (1980) developed a model for the interface behavior based on the linearized representations of contact friction and dilatancy:

$$|\sigma_{nt}^{cr}| = -k\,\sigma_{nn}^{cr} + c \qquad (\sigma_{nn} \leq 0) \tag{3.57a}$$

$$\delta_n = \alpha_d\,|\delta_t| + e \qquad (\sigma_n \geq 0) \tag{3.57b}$$

where $|\sigma_{nt}^{cr}|$ is the absolute value of the shear stress; σ_{nn}^{cr} is the normal compressive stress; c is the 'cohesion'; k, the friction coefficient; α_d, the dilatancy ratio, and e is the initial crack width. In this formulation, damage to the crack surface has not been modelled.

Walraven (1981) investigated analytically the fundamental nature of the aggregate interlock in concrete. Using a statistical analysis to determine the size and distribution of aggregates protruding from the crack surfaces, and assuming a crushing strength for the matrix and a friction coefficient for the matrix and aggregate, the forces acting across the crack were computed. This model is well suited for specific studies on aggregate interlock but not easily amenable for computer analysis using the finite element method.

3.6.5.4 Shear Modulus of Cracked Concrete to be used in Smeared Crack Model

In spite of the availability of the various analytical models described above, the most common approach in finite element analysis is to use a post-cracking shear stiffness as a function or fraction of the uncracked concrete shear stiffness. This is mainly due to the lack of experimental data on parameters to be used in the models described above and their complexity. Since the most important parameter influencing the interface shear stiffness is the crack width (which in a smeared crack approach is distributed along a tributary length as crack strain), the cracked shear modulus, G_{cr}, is assumed in this study to decrease linearly with normal crack strain (Fig. 3.20).

3.7 Representation of Material Behavior in this Study

3.7.1 Requirements of the Constitutive Model

This study is concerned with reliable predictions of the behavior of reinforced concrete beams and panels under static loads. Inaccuracies in predictions may result from: (1) the inaccurate characterizations of the material behavior; and, (2) the errors involved in the analytical procedure. The desired accuracy of predictions must be balanced against the scatter of the test results and the costs involved in the analysis.

The behavior of concrete is inherently complex. Hence, constitutive models to describe its full range of behavior tend also to be complex. A number of constitutive models have been reviewed in Sect. 3.6. Such models become mathematically complex in an attempt to establish consistency and objectivity from a continuum mechanics

viewpoint. Yet experience has shown that the classical mathematical theories have been only partially successful in describing concrete behavior over its full range. Further, many complex material models have yielded results which do not properly reproduce failure loads or failure modes in routine structures (see, for example, Collins et al., 1985) for which designers require reliable answers and for which empirical design rules give better results.

The approach taken in this study is to attempt to find the simplest constitutive relationship possible that can capture those essential characteristics of concrete behavior which are necessary in order that the model properly reproduce all observed failure modes, with reasonable accuracy of failure loads, for a limited class of structures, namely, net reinforced panels and reinforced concrete beams. Reliability of the model to achieve the above objectives at reasonable cost is the paramount consideration.

Since a simple and reliable material characterization for concrete, which covers its entire range of behavior, has proved to be an elusive goal, the available procedure is to incorporate appropriate experimental data directly into the analysis (Bathe and Ramaswamy, 1979; Romstad et al., 1974). Thus the following requirements may be identified for the material representation in this study:

1. It must be amenable to easy incorporation of standard data obtained from test specimens.

2. It must cover the entire range of the material behavior for monotonic time independent deformations.

3. It must capture the major features of the nonlinear behavior.

4. It must be simple, yet be able to predict the behavior of beams

and panels, exhibiting a wide range of failure modes, with an accuracy within the scatter of experimental results.

3.7.2 Adoption of Material Representation

In order to determine the major factors influencing the predicted behavior of concrete beams and panels, numerical analyses were performed on a number of sample structures for which test results were available.

Some of these 'numerical experiments' are described in Chapters 4 and 5 and more details about parametric variations are contained in Appendix A3. From these analyses the following were identified as being important factors which must be incorporated into the material characterisation in order to obtain reliable predictions of behavior.

1. Tensile cracking
2. Tension softening and tension stiffening
3. Variation of shear modulus with tensile strain after cracking
4. Strain hardening at high compressive stresses
5. Post-peak strain softening in compression

A description of the resulting material model is contained in the following subsections.

3.7.2.1 The Uniaxial Stress-Strain Relationship

The piecewise linear uniaxial stress-strain relationships adopted in this study are shown in Fig. 3.20a to d. The basic idea for the use of a multilinear relation was put forth by Romstad et al. (1974) (see Fig. 3.15). Such a relationship satisfies all the requirements mentioned in Sect. 3.7.1 and includes consideration of all factors

listed above. The concrete is assumed to be strained monotonically and at any given time to be in one of 5 damage regions identified by the integers -2 to 2 (Fig. 3.20).

Material properties to be determined from standard test specimens for input into the computer program are: (1) f_c', the cylinder compressive strength; (2) $E_c^{(o)}$, the initial elastic modulus; (3) $E_c^{(-1)}$, the compressive strain hardening modulus; (4) $E_c^{(-2)}$, the compressive strain softening modulus (which depends on the compressive strength, confinement by reinforcement etc.); (5) f_t', the uniaxial direct tensile strength; (6) ν, the Poisson's ratio; (7) G, the shear modulus of uncracked concrete; (8) ε_{ut}, the strain at which the tension softening stress is reduced to zero and (9) ε_{gt}, the tensile strain at which the shear modulus of cracked concrete, G_{cr}, has reduced to the minimum value (of 0.05G), if different from ε_{ut}.

Among the various characteristic properties listed above, only f_c', the uniaxial compressive strength, is readily available. The procedure for estimating the other remaining properties, in the absence of test data, is described in Appendix A4. The values of f_{cu} and f_{tu}, shown in Fig. 3.20 as the peak compressive and tensile stresses, respectively, are calculated in the stress computation subroutine using the biaxial failure envelope to be discussed in Sect. 3.7.3. The tension softening at crack interfaces, the tension stiffening effect of intact concrete between the cracks and the shear modulus of the cracked concrete are all influenced by the same set of physical characteristics such as crack spacing, concrete/steel interface behavior, area and location of reinforcement and crack interface behavior. Hence, the values selected for ε_{ut} and ε_{gt} must be consistent with each other and with the expected

physical behavior of the structural system.

3.7.2.2 The Tension Softening Relationship

The tension softening (Sect. 3.2.3) and tension stiffening (Sect. 3.4) effects of concrete are combined and represented by the descending branch of the tensile stress strain curve of Fig. 3.20, as discussed in Appendix A4. The tension softening is given by Eq. 3.5.

$$G_F = \frac{1}{2} f_{tu} \varepsilon_{ut} h \qquad (3.5)$$

where G_F is the fracture energy expended in the formation of a crack; f_{tu} is the tensile strength; h is the width of the crack band; and, ε_{ut} is the strain at the completion of the fracture process.

Equation 3.5 relates to the formation of a single crack and its application will lead to a mesh independent load-deflection response of a specimen containing that crack. However, in R/C beams a number of cracks form at different spacings in the tension zone based on parameters such as the depth of tension zone, reinforcement ratio, bond characteristics of the reinforcement and the statistical scatter in the tensile strength of concrete. If, in the analysis, these individual cracks can be reproduced (i.e., if 'strain localization' occurs) then in Eq. 3.5, h may be taken as the length that is tributary to a Gauss point.

Although attempts have been made to do so (for example by Rots et al., 1985), localization has not been obtained in the context of smeared cracking. Bazant (1985) reports that for very fine mesh layout the cracking zone localizes into narrow, separate crack bands of single

element width at their tips only if the loading steps are taken to be so small that no more than one element cracks during the first iteration of each loading step. However, the significance of strain localization for reliable prediction of beam behavior has not been established. Hence, to obtain objective results independent of mesh refinement (i.e., to obtain the same load-displacement response in the tension zone independent of mesh size) in a R/C beam, it is appropriate to use in Eq. 3.5 the crack spacing in place of the characteristics length, h. For beams the crack spacing may be calculated using Eq. 3.9 and the results of Beeby (1979) in Table 3.1.

3.7.2.3 The Tension Stiffening Relationship

The tension stiffening effect has been incorporated by modifying the descending branch of the tensile stress-strain curve. The influence of tension stiffening decreases with increasing distance from the reinforcement. As shown in Fig. 3.20, a bilinear descending branch is used for elements containing reinforcement. For elements not containing reinforcement and outside the effective concrete area (i.e. the area of concrete contributing to the tension stiffening effect which may be determined using Fig. 3.7b) a linear descending branch is used with ε_{ut} calculated using Eq. 3.5 in which the estimated crack spacing is substituted for h. For elements inside the effective concrete area but not containing the reinforcement, the value of ε_{ut} is increased as described in Appendix A4. In all cases, the tension stiffening is reduced to zero if the strain in steel at the crack exceeds the yield strain.

3.7.2.4 Shear Modulus Relationship

Since the variation of the shear modulus of the cracked concrete is dependent on the crack width, which in a smeared crack representation depends on the crack strain, the value of ε_{gt} is chosen such that the crack shear stiffness is consistent with the physical behavior described in Sect. 3.6.5.2. As discussed in Sect. 3.6.5, the shear modulus of cracked concrete, G_{cr}, is calculated as a function of the normal tensile strain and the shear modulus of the uncracked concrete and is given by Eq. 3.58a subject to the constraint given by Eq. 3.58b.

$$G_{cr} = \left(\frac{\varepsilon_{gt} - \varepsilon_1}{\varepsilon_{gt} - \varepsilon_{cr}}\right) G \qquad (3.58a)$$

$$G_{cr} > 0.05G \qquad (3.58b)$$

where

$$G = \frac{E_c^{(o)}}{2(1 + \nu)} , \qquad (3.58c)$$

is the shear modulus of uncracked concrete in the elastic region; ε_{cr} is the tensile strain at which cracking occurs; and, ε_1 is the current total normal tensile strain perpendicular to the crack. This relation is shown in Fig. 3.20.

As discussed in Sect. 3.6.5.2, for small crack openings (i.e. up to about 0.25 mm (0.01"), as estimated by Laible (quoted by Riggs, 1981)), the IST is mainly by the bearing mode. When the shearing stresses are high enough, the bearing mode of resistance is overcome and the frictional mode of resistance is the major component of IST. The

variation of crack shear stiffness shown in Fig. 3.19 is based on Eq. 3.54b and is applicable for crack widths exceeding 0.125 mm (0.005") where frictional mode of resistance is dominant. This corresponds to a uniform strain of 0.001 for a crack spacing of 125 mm (5"). For this crack spacing and with f_{tu} as 2.0 MPa (290 psi) and G_F as 125 N/m (0.714 lb/in.), the value of ε_{ut} computed from Eq. 3.5 is 0.001. This indicates that the bearing mode of resistance is dominant until the tension softening stress is reduced to zero.

In shallow reinforced concrete beams without web reinforcement (or with only a small amount of web reinforcement) the crack width is significantly greater at increasing distance from the reinforcement. Thus the crack shear stiffness due to frictional mode of resistance is very small. (This can be deduced from Eq. 3.54a. With increasing distance from the reinforcement, the normal stiffness provided by the reinforcement, K_N, reduces with the consequent reduction in crack shear stiffness). Therefore, for shallow reinforced concrete beams ε_{ut} is assumed to coincide with ε_{gt}.

For net-reinforced panels and deep beams, the crack spacing is smaller and the crack width is also smaller and more uniform. Furthermore, the dominant mechanism of shear resistance in these structures is through the development of compression struts or compression fields and IST is not as important as for beams in which diagonal tension mode of shear failure occurs. Based on numerical studies of test panels (discussed in Chapter 4), ε_{gt} may be taken as 0.01 for net-reinforced panels and deep beams.

3.7.2.5 Comment on Uniaxial Material Model

The multilinear representation of Fig. 3.20 encompasses the entire range of material behavior. It delineates the different stages of behavior discussed in Sect. 3.5 for uniaxial compression, namely, region '0' where the behavior is linear and elastic, region '-1' where strain hardening occurs and region '-2' where compressive strain softening occurs. It also distinguishes the post cracking stage, namely the development of the fracture process zone, region '1', and the fully cracked stage, region '2'.

3.7.3 Multilinear Representation of Biaxial Behavior

For uncracked concrete (i.e., damage regions 0, -1 and -2), the damage level is assumed to be constant and the material properties to be linear isotropic constants. For concrete cracked in tension (i.e., damage regions 1 and 2 in one or both directions) the material is considered to be orthotropic, with the axes of orthotropy parallel and perpendicular to the crack.

The assumption that material response may be referenced to orthotropic local axes parallel and perpendicular to the crack has a number of advantages.

(a) It recognizes that cracking is the dominant factor in redistribution of stresses in reinforced concrete beams and panels and hence makes it easier to capture an essential aspect of the physical behavior.

(b) It permits an adequate description of material response which can be described simply, by imposing minor modifications arising from biaxial test results onto observed uniaxial behavior. That is, f_{cu}

and f_{tu} may be adjusted to fit a biaxial failure envelope.

(c) It eliminates the complications which arise when attempting to describe complex material behavior relative to invariant reference frames. Indeed, if the simple locally oriented description is adequate to reliably predict behavior of the class of problems under consideration, which, to the author's knowledge, has not been accomplished to date, the fact that the description may be nonobjective or lacking in mathematical consistency for tortuous load paths become irrelevant.

For uncracked concrete, the incremental stress-strain relation is given by

$$\begin{Bmatrix} d\sigma_1 \\ d\sigma_2 \\ d\tau_{12} \end{Bmatrix} = \frac{E_c^{(k)}}{1 - \nu^2} \begin{bmatrix} 1 & \nu & \\ \nu & 1 & \\ & & \frac{(1 - \nu)}{2} \end{bmatrix} \begin{Bmatrix} d\varepsilon_1 \\ d\varepsilon_2 \\ d\gamma_{12} \end{Bmatrix} \tag{3.59}$$

where $E_c^{(k)}$ is the current tangent modulus (i.e. the modulus depending on the damage region k, k =0, -1 or -2); ν is the Poisson's ratio, assumed constant; $d\varepsilon_1$, and $d\varepsilon_2$ are the principal strain increments and $d\sigma_1$ and $d\sigma_2$ are the corresponding principal stress increments. The incremental stresses are accumulated on the principal axes to obtain the total stresses.

The total principal stresses σ_1 and σ_2 are checked against the biaxial failure envelope given by Eq. 3.22 in biaxial tension and Eqs. 3.24a and b in biaxial compression. In the tension-compression stress field, the biaxial strength envelope is given by

$$f_{tu} = \frac{2f'_c}{\left(\frac{\sigma_2}{\sigma_1} + \frac{2f'_c}{f'_t}\right)} \tag{3.60}$$

The failure envelope is shown in Fig. 3.21. Once the major principal stress, σ_1, has reached a value of f_{tu}, concrete is assumed to have cracked perpendicular to the principal strain direction and is subsequently treated as orthotropic with the local material axes (i.e., the axes of orthotropy), parallel and perpendicular to the crack orientation. The Poisson's ratio is then set to zero. The post-cracking incremental stress-strain relation in local axes is given by

$$\begin{Bmatrix} d\sigma_1 \\ d\sigma_2 \\ d\tau_{12} \end{Bmatrix} = \begin{bmatrix} E_t^{(\ell)} & & 0 \\ 0 & E_c^{(k)} & 0 \\ 0 & 0 & G_{cr} \end{bmatrix} \begin{Bmatrix} d\varepsilon_1 \\ d\varepsilon_2 \\ d\gamma_{12} \end{Bmatrix} \tag{3.61}$$

where $E_t^{(\ell)}$ is the tensile strain softening modulus in damage region ℓ, ℓ = 1 or 2 (Fig. 3.20); and G_{cr} is the shear modulus of the cracked concrete. All subsequent stress computations are performed by transforming strain increments to the 1-2 material directions and then applying Eq. 3.61. The resultant stress increments are added to the previous total stresses in the 1-2 system.

In the so called 'fixed crack model', once tensile cracking occurs crack orientation is assumed fixed for all subsequent loading and hence the orientation of 1-2 material axes are assumed fixed. Whereas, in the so-called 'rotating crack model' (Akbar and Gupta, 1985; Milford and Schnobrich, 1984) the axes of orthotropy are reoriented in the principal strain directions at the beginning of each iteration, i.e., the 1-2 axes are aligned with respect to the most recent 'average crack direction'

(Milford and Schnobrich, 1984). In anistropically reinforced panels it has been shown analytically (Akbar and Gupta, 1985) and experimentally (Vecchio and Collins, 1982) that crack directions do change, whereas in unreinforced concrete or concrete reinforced in one direction only, no definite shift in the crack orientation has been observed. Thus, in this study the rotating crack model has been employed for net reinforced panels and deep beams (Chapter 4) and the fixed crack models for shallow beams (Chapter 5).

Once tensile cracking occurs, the Poisson's ratio is set to zero (Eq. 3.61), i.e. axes 1 and 2 are decoupled. However, at the instant of crack formation, the stress σ_2 contains the stresses due to the Poisson effect amounting to $(\nu E_c \varepsilon_1)/(1 - \nu^2)$. Setting the Poisson's ratio to zero at the instant of cracking lets the stress σ_2 'rebound' by this amount. (If σ_2 is compressive it increases in magnitude and if σ_2 is tensile, it decreases in magnitude). This rebound is included by considering that, at the instant of cracking, the stresses become

$$\sigma_1 = f_{tu} \tag{3.62a}$$

$$\sigma_2 = E_c^{(k)} \varepsilon_2 \tag{3.62b}$$

The ability of this simple multilinear model to reliably predict the behavior of beams and panels is demonstrated in Chapters 4 and 5.

Table 3.1 Constants K_1 and K_2 for use in Eq. 3.9 (From Beeby (1979)

Probability of exceedance	K_1	K_2					
		Value of c/h_{cr}					
		0	0.1	0.15	0.2	0.25	0.3
Mean	1.33	0.08	0.04	0.03	0.02	0.01	0.01
20%	1.59	0.12	0.07	0.05	0.04	0.03	0.02
5%	1.86	0.20	0.12	0.09	0.07	0.06	0.04
2%	1.94	0.28	0.17	0.13	0.10	0.08	0.06

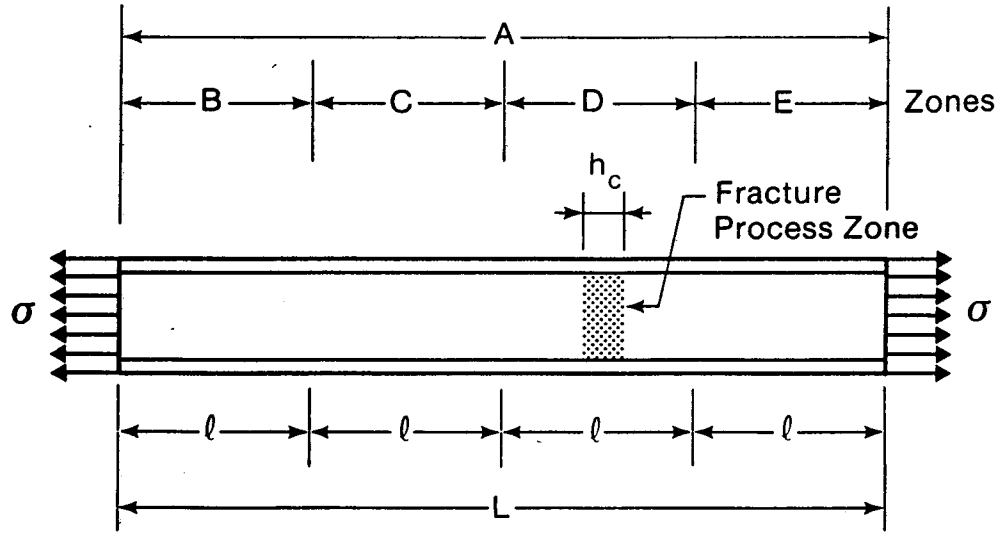

(a) Tension Specimen

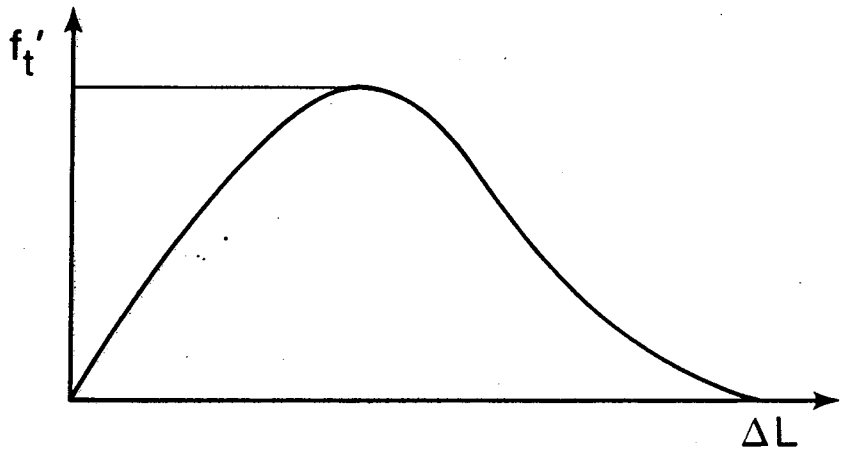

(b) Stress-Displacement Response in Gage Length L

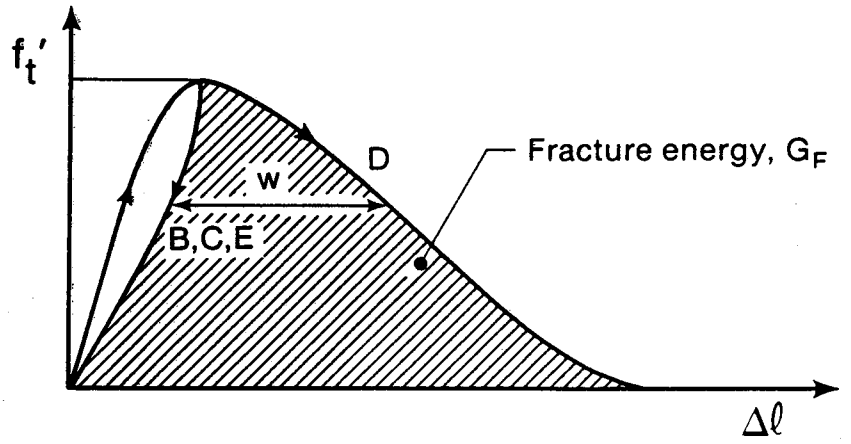

(c) Stress-Displacement Response For Gage Length ℓ

FIG. 3.1. Uniaxial Tension Test (Adapted from Hillerborg, 1985)

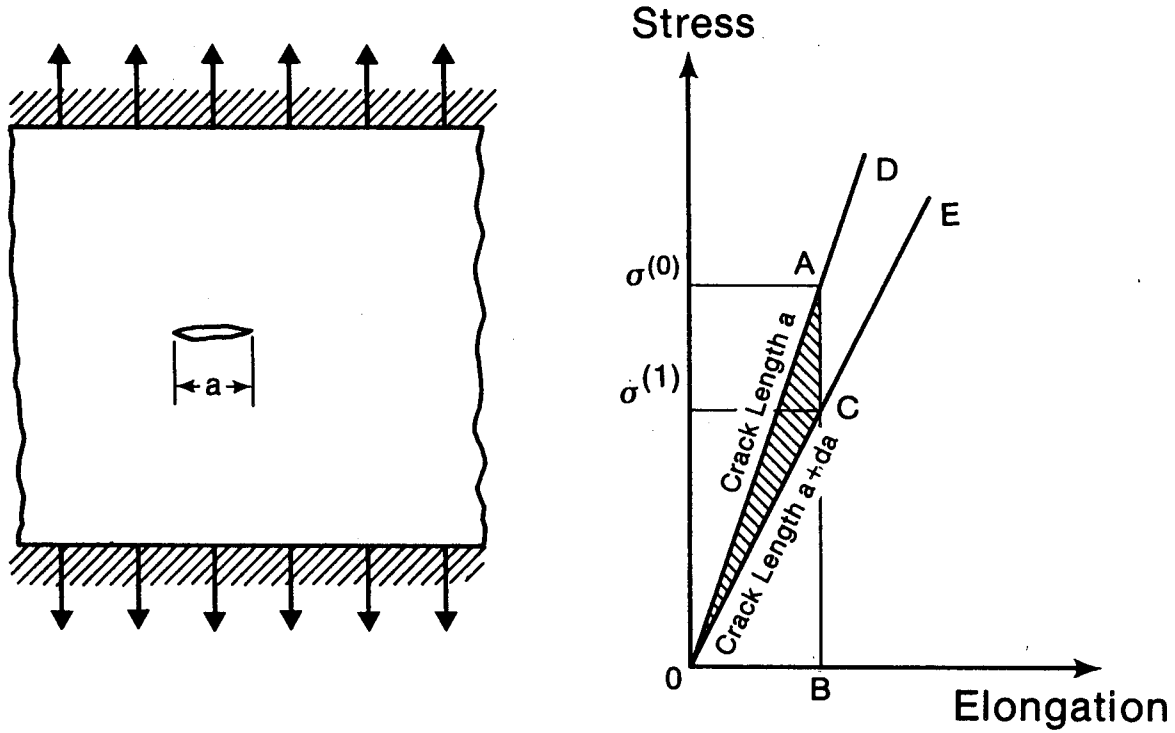

(a) Cracked Plate With Fixed Ends

(b) Elastic Energy

FIG. 3.2. The Griffith Criterion for Fixed Grips (Adapted from Broek, 1982)

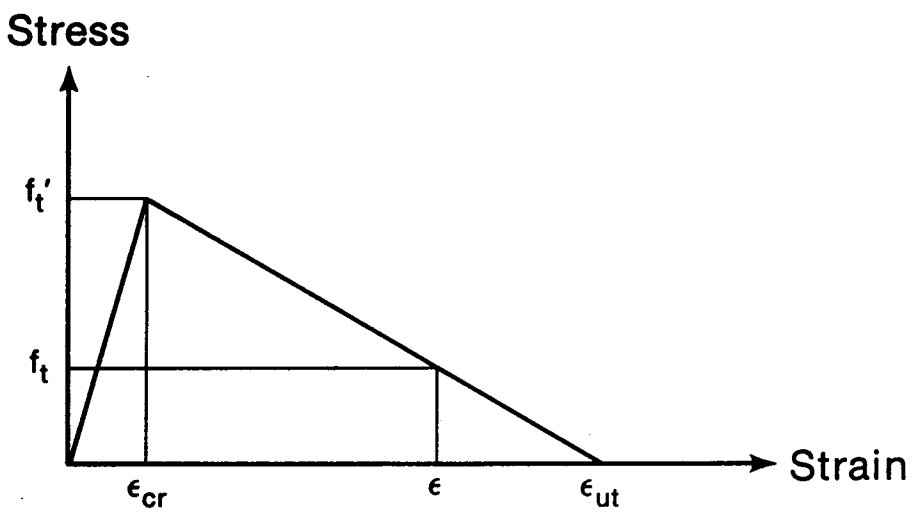

FIG. 3.3. Concrete Stress-Strain Curve in Tension

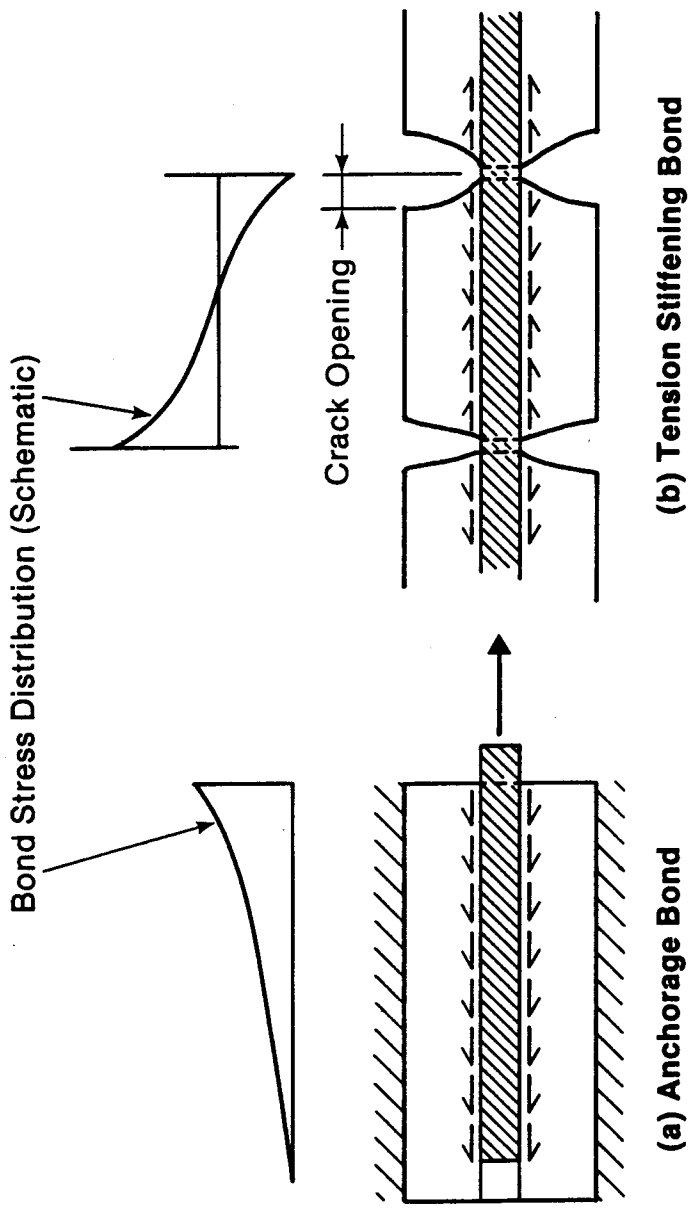

FIG. 3.4. Classification of Bond

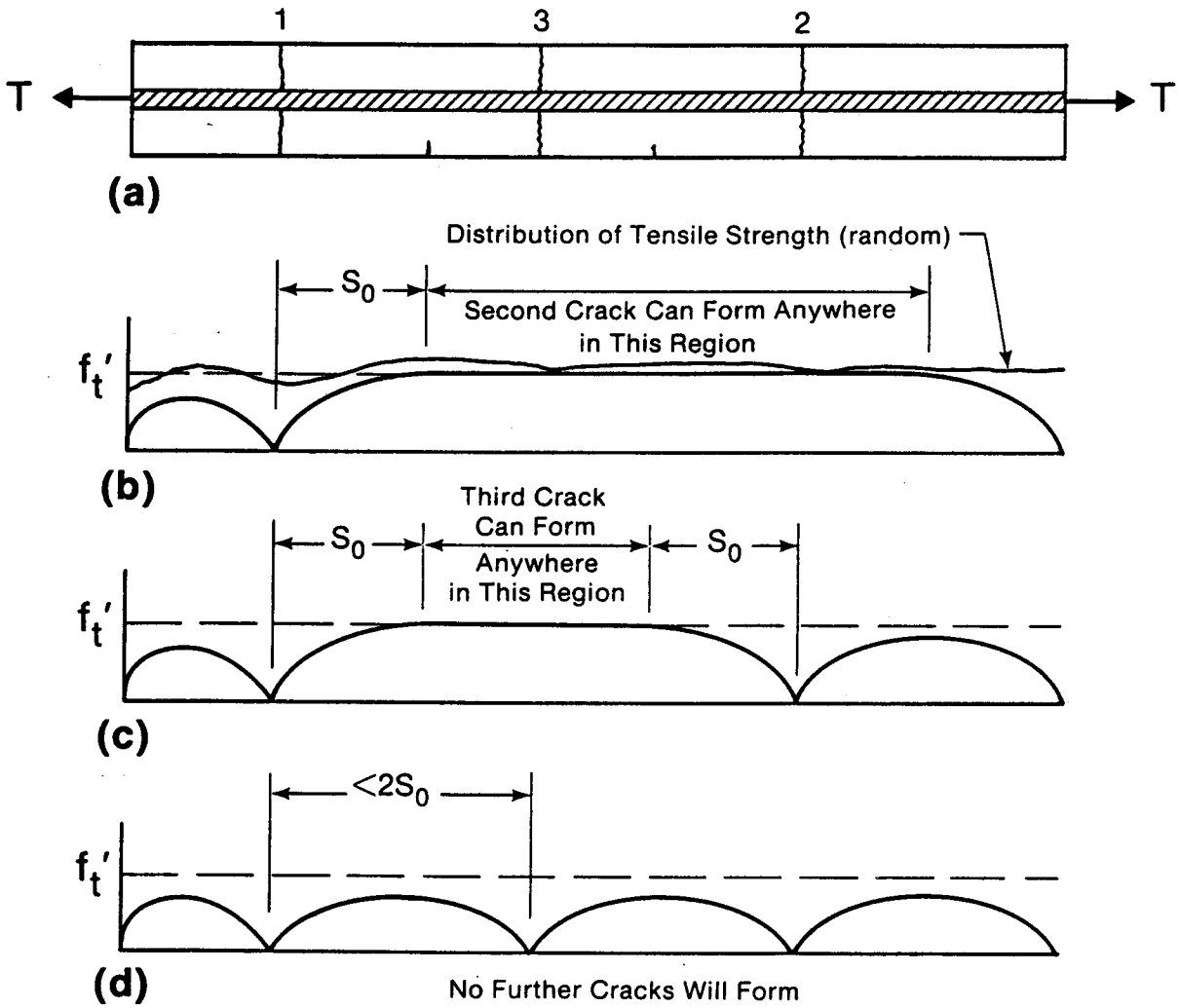

FIG. 3.5. Cracking of a Reinforced Concrete Tension Member

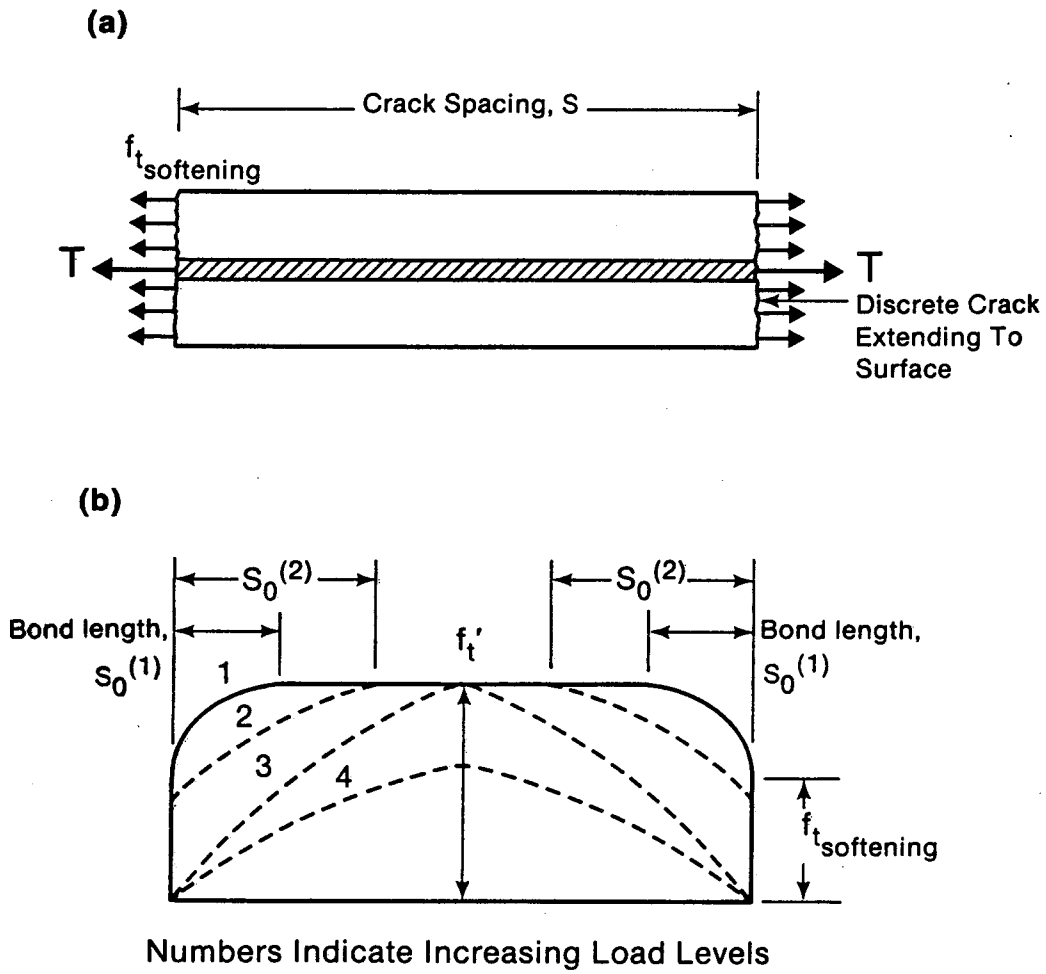

FIG. 3.6. Stress Distribution in a Concrete Segment with Increasing Load
(a) Concrete Segment Between Cracks
(b) Stress Distribution

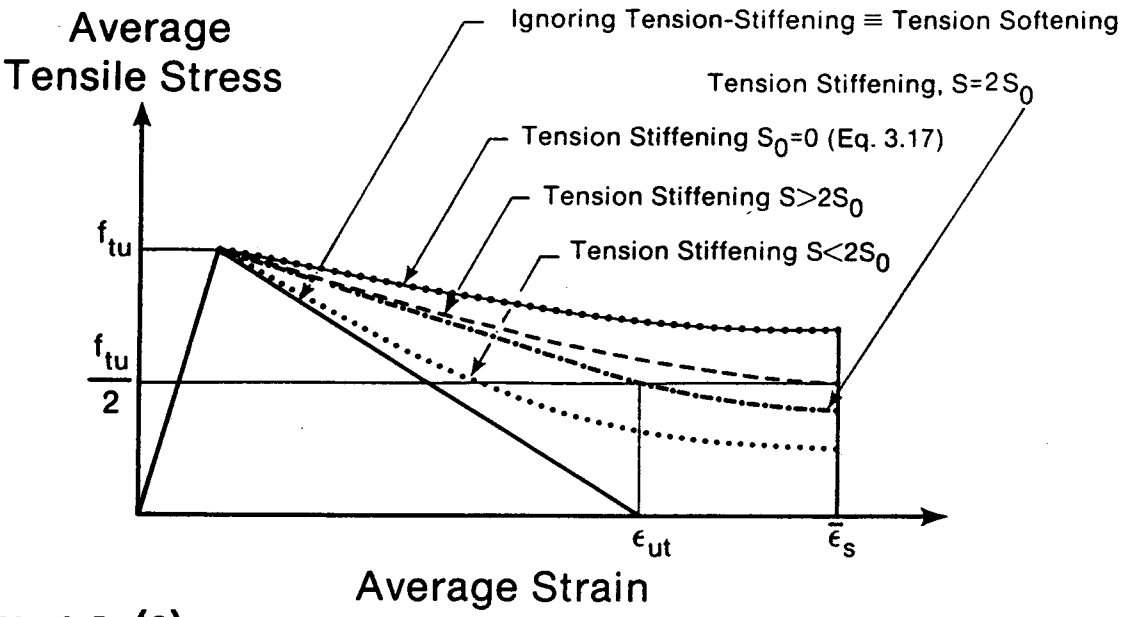

FIG. 3.7. **(a)** Tensile Stress-Strain Diagram for Concrete Element Containing Reinforcement

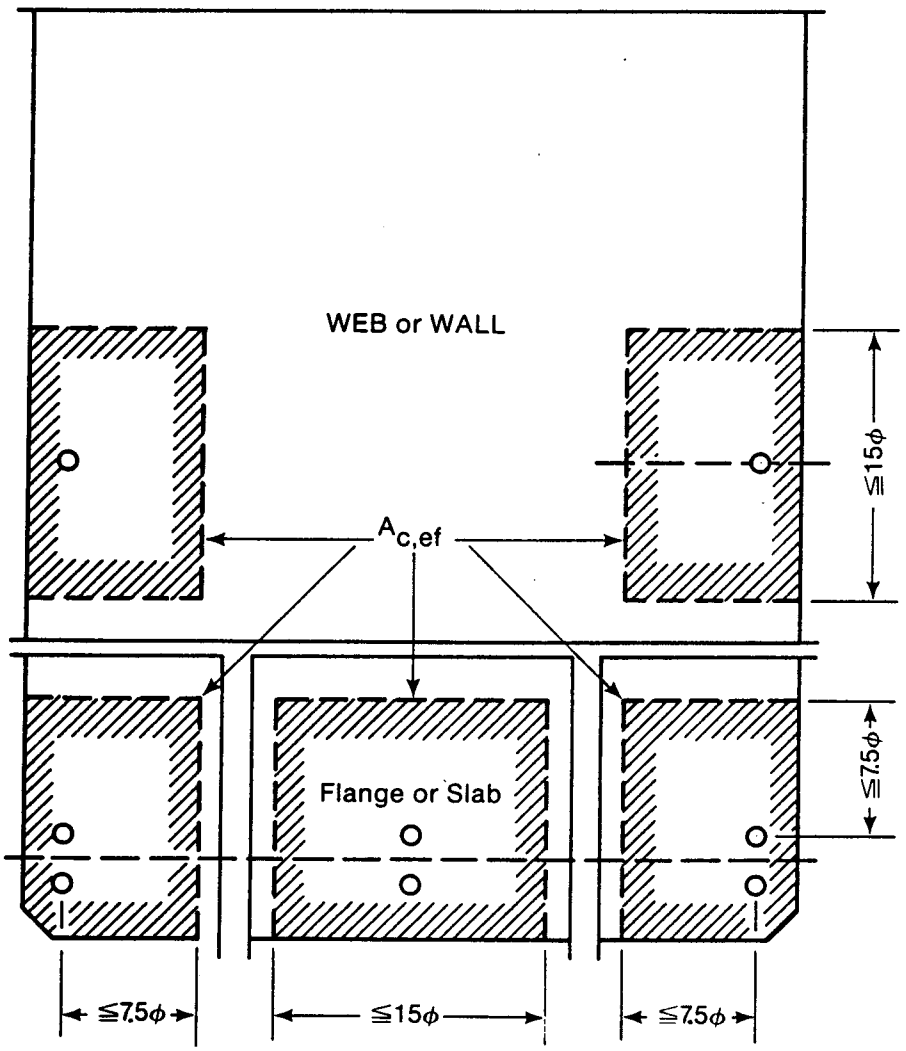

FIG. 3.7. **(b)** Effective Concrete Embedment Section Recommended by CEB (Adapted from CEB, 1978)

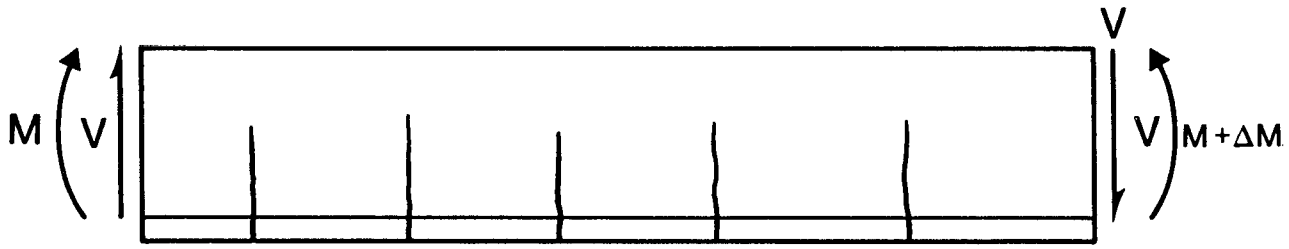

(a) R/C Beam With Moment Gradient

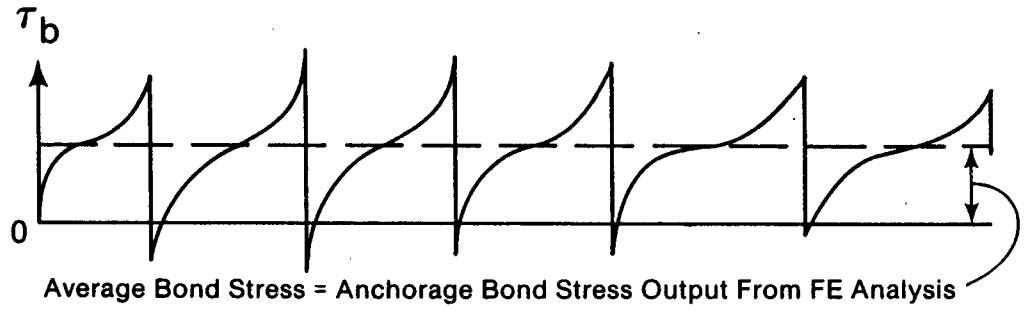

(b) Variation of Local Bond Stress

FIG. 3.8. Local and Average Bond Stresses

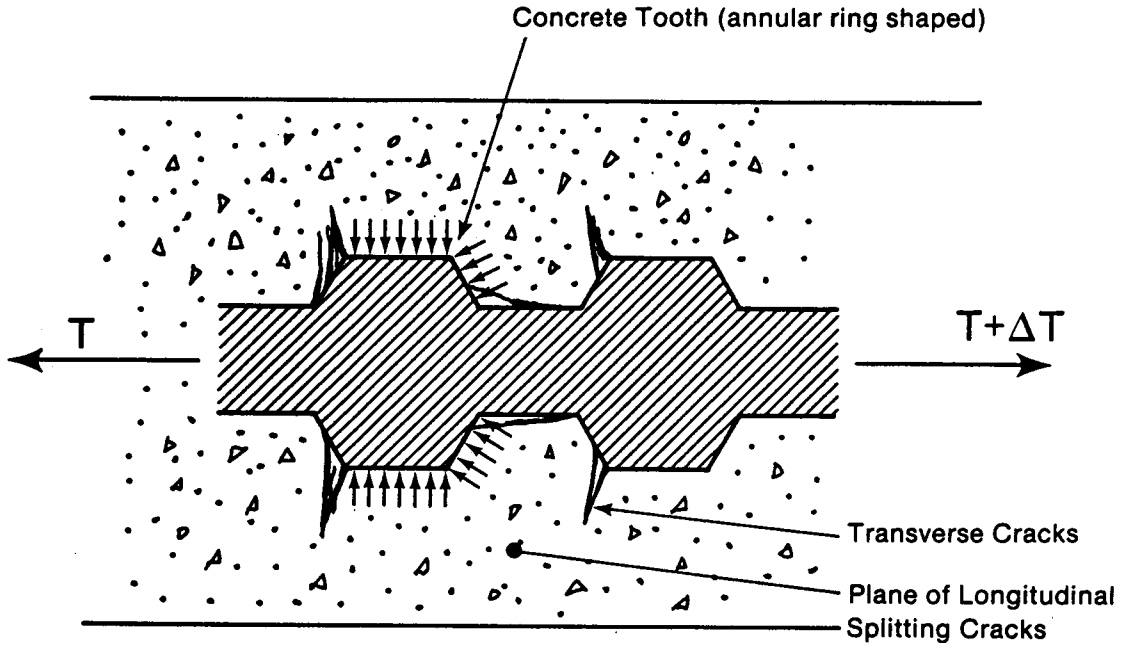

(a) Radial Section Through Reinforced Concrete Tension Spectron.

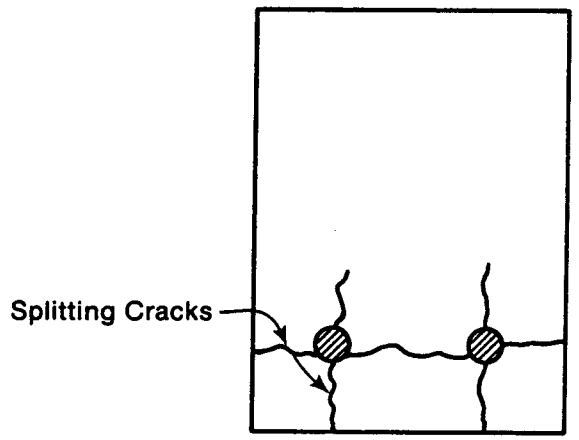

(b) Cross Section of a Rectangular Concrete Beams Showing Possible Locations of Splitting Cracks.

FIG. 3.9. Mechanism of Interface Bond

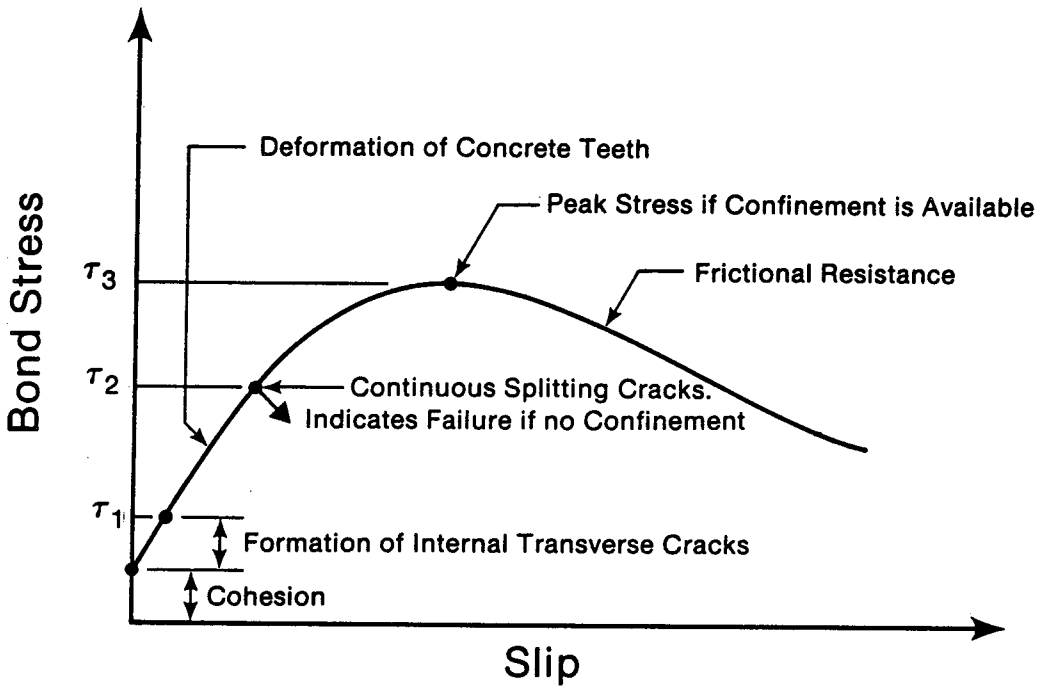

FIG. 3.10. Schematic Bond Stress-Slip Relationship (Adapted from Gambrova, 1982)

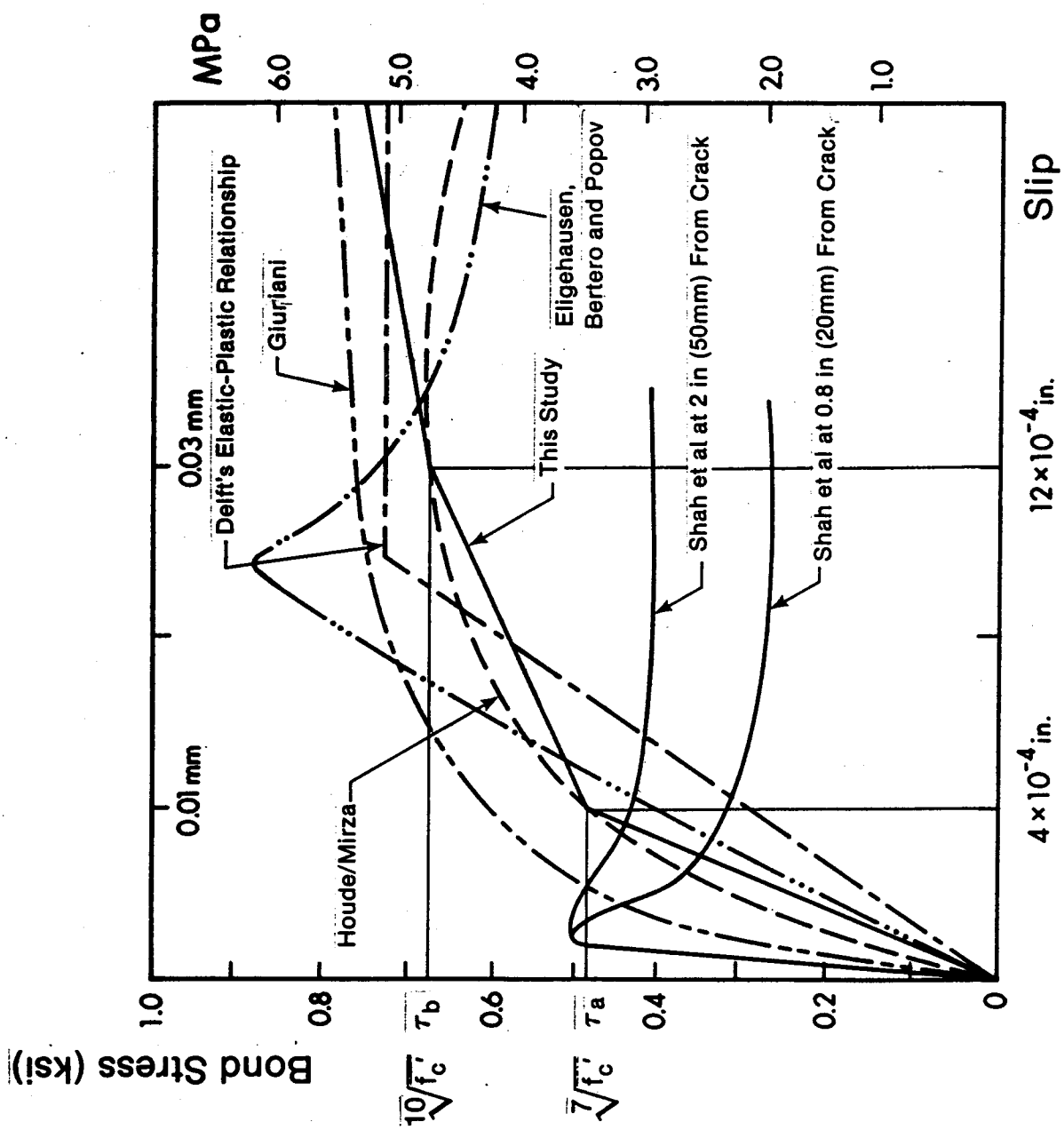

FIG. 3.11. Local Bond Stress-Slip Relationships

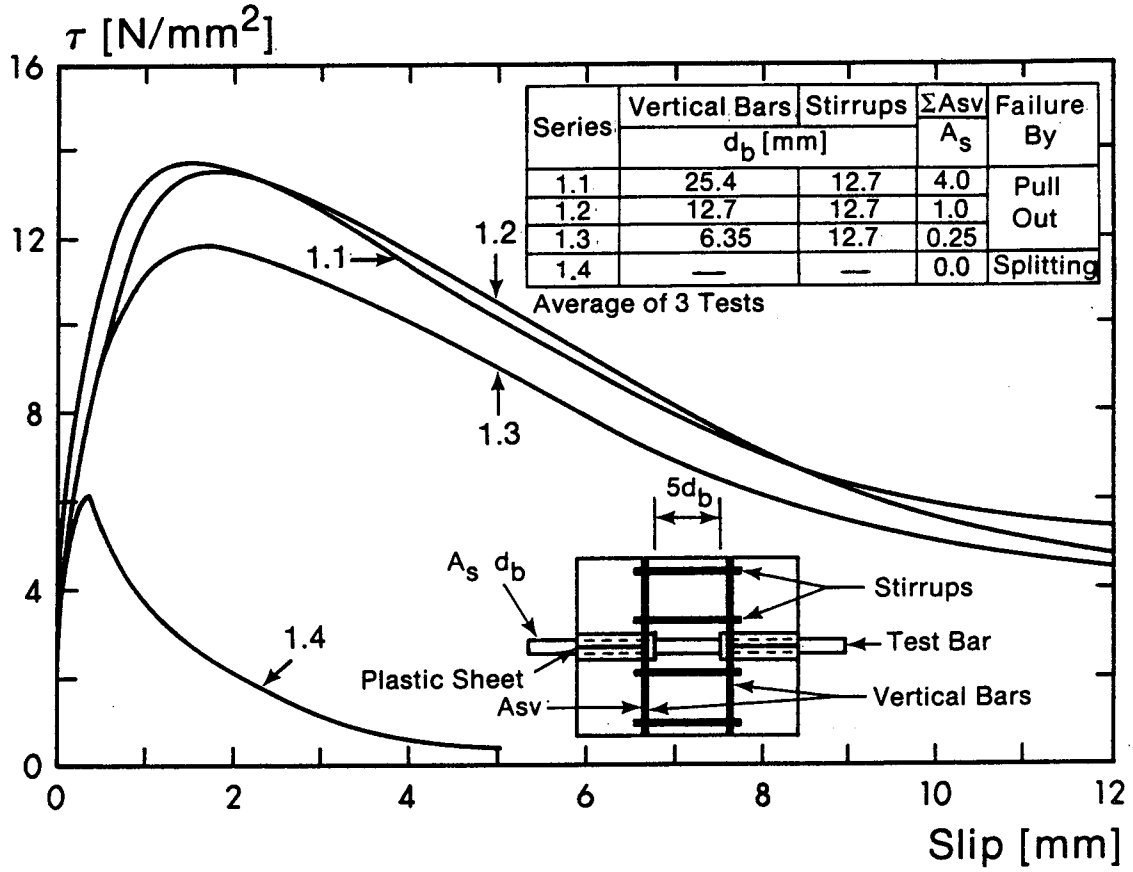

Series	Vertical Bars d_b [mm]	Stirrups d_b [mm]	ΣAsv / A_s	Failure By
1.1	25.4	12.7	4.0	Pull Out
1.2	12.7	12.7	1.0	
1.3	6.35	12.7	0.25	
1.4	—	—	0.0	Splitting

FIG. 3.12. Influence of Confining Reinforcement on the Local Bond Stress-Slip Relationship (Adapted from Eligehausen, Bertero and Popov, 1982)

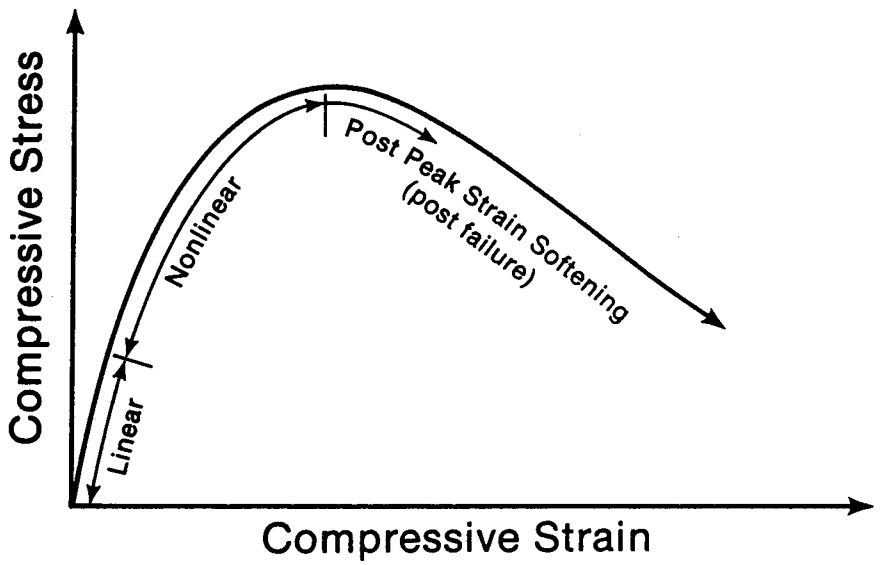

FIG. 3.13. Typical Uniaxial Stress-Strain Curve for Concrete in Compression

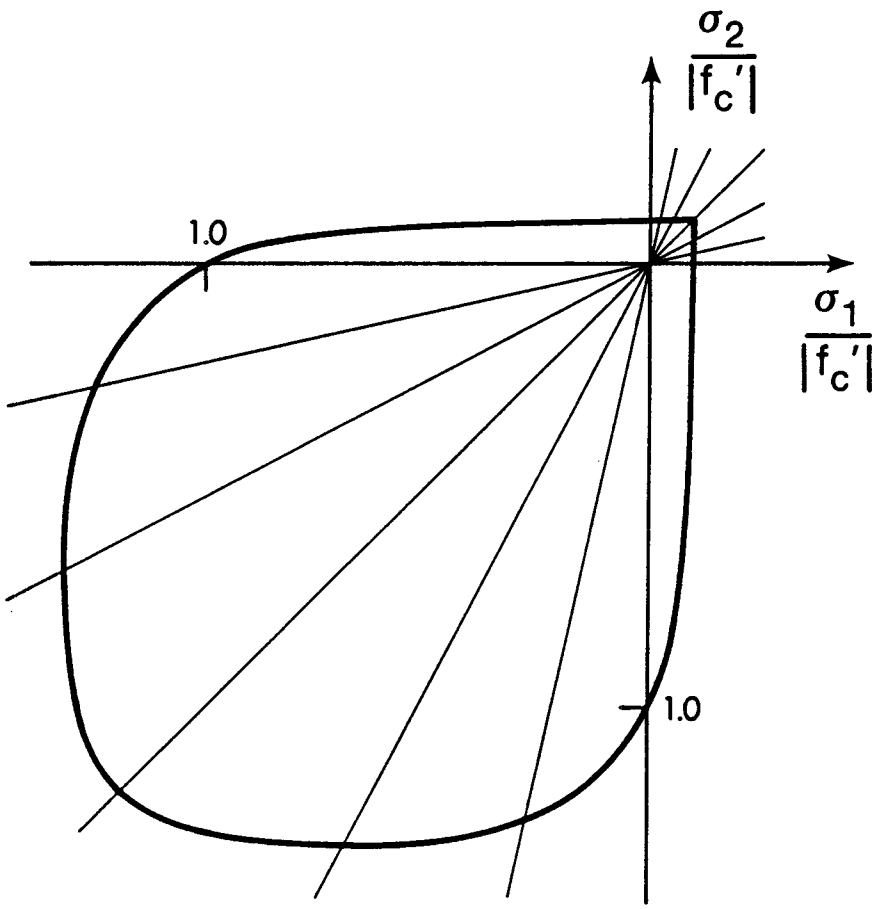

FIG. 3.14. Biaxial Strength Envelope (Adapted from Kupfer et al., 1969)

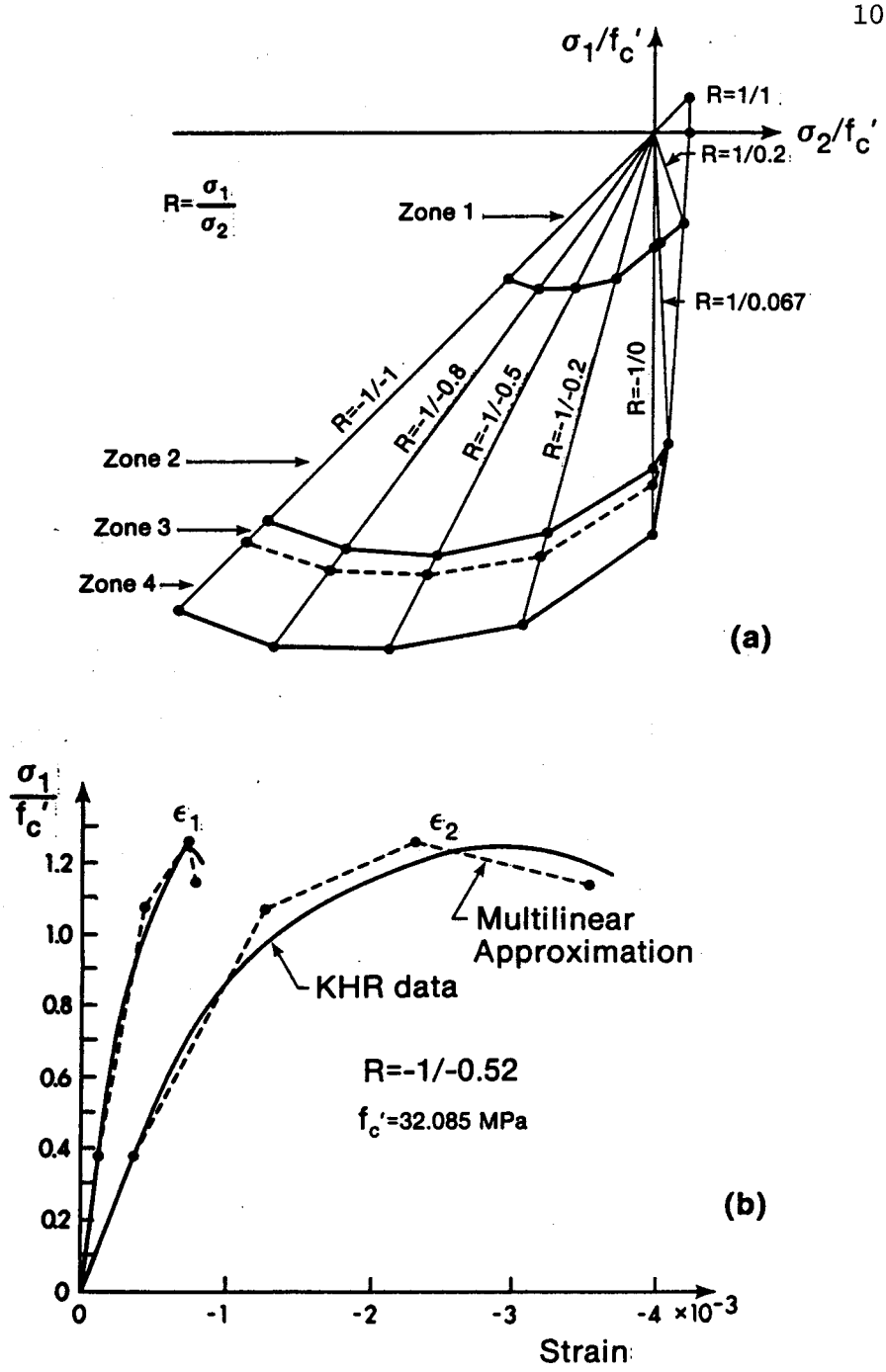

FIG. 3.15. Multilinear Approximation
(a) Damage Zones in Biaxial Stress Space;
(b) 'Linearized' Biaxial Stress-Strain Relationships
(Adapted from Romstad, et al., 1975)

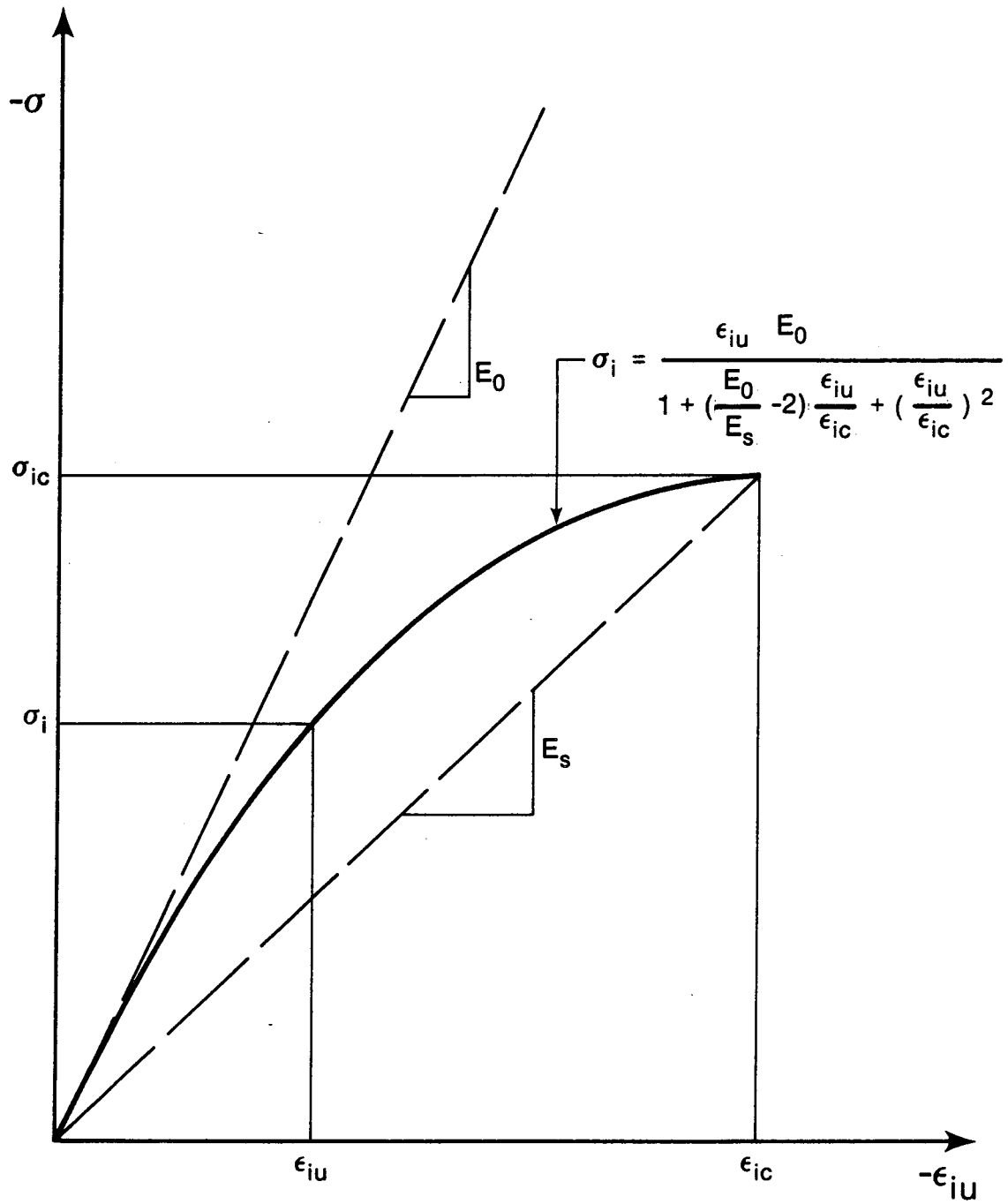

FIG. 3.16. Equivalent Uniaxial Stress-Strain Curve in Compression (Adapted from Darwin and Pecknold, 1974)

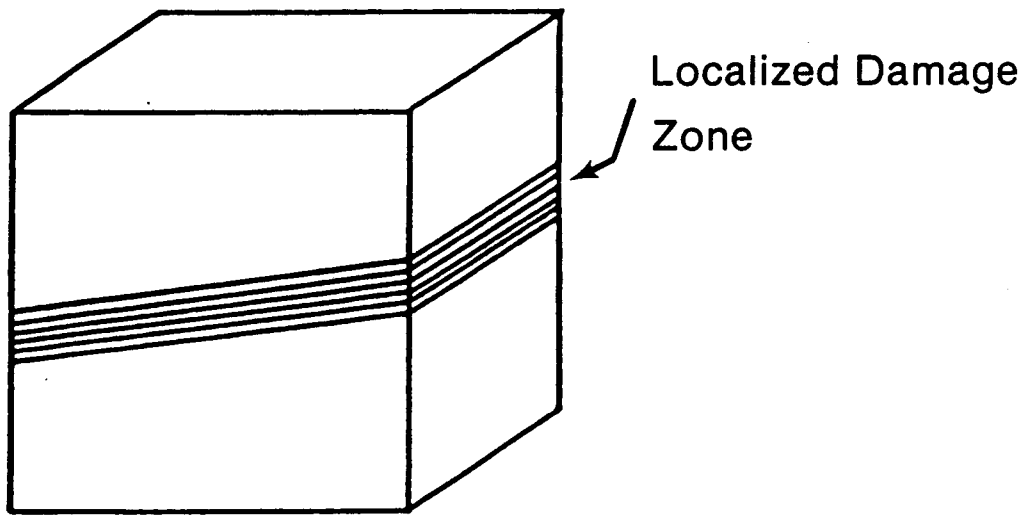

FIG. 3.17. Composite Damage Model (Adapted from Willam et al., 1984)

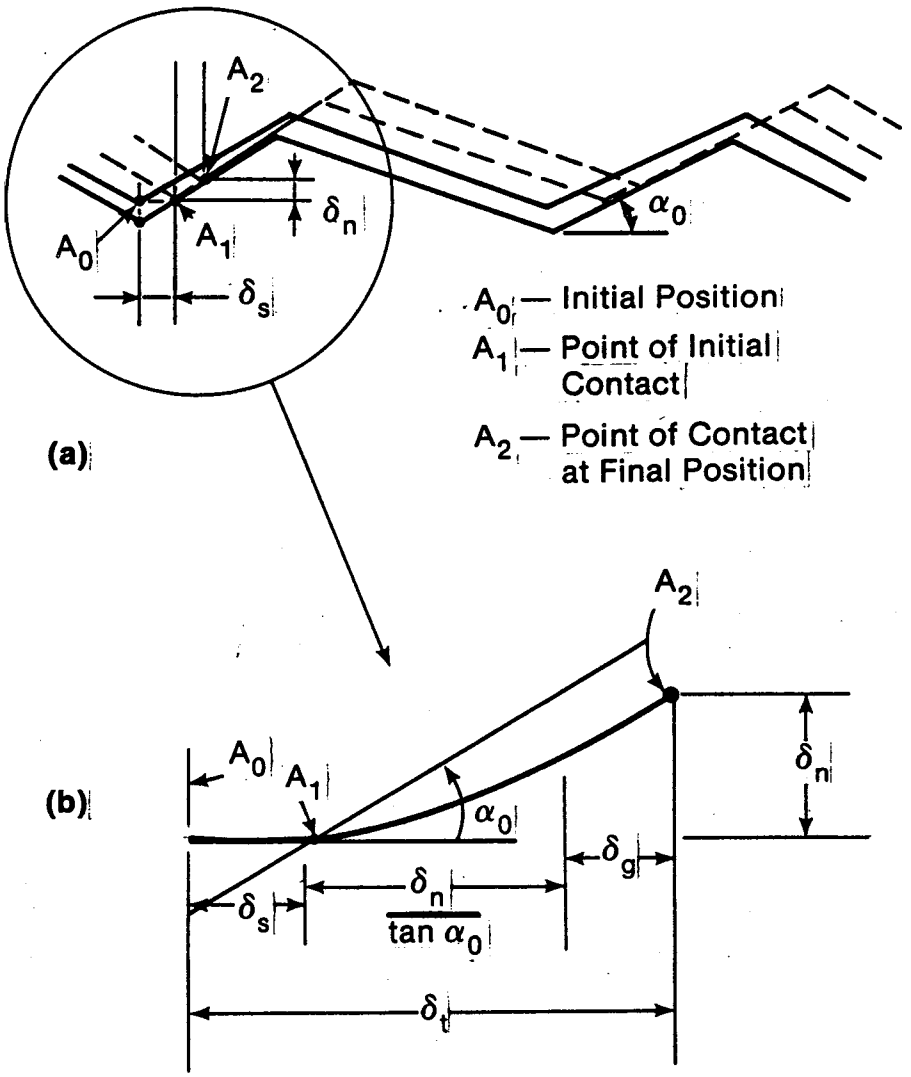

FIG. 3.18. Components of Shear Slip at a Discrete Crack

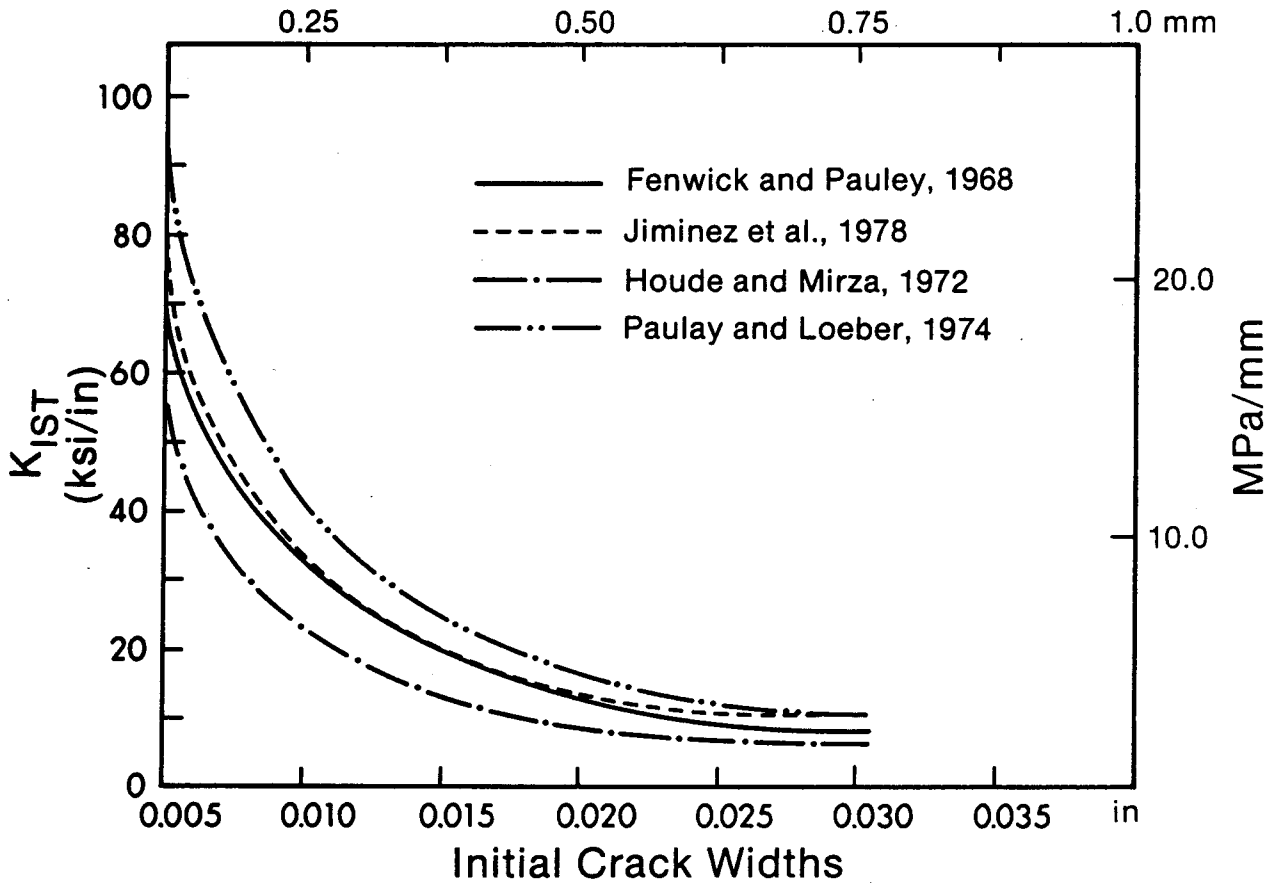

FIG. 3.19. Comparison of Shear Stiffness Expressions (Adapted from ASCE, 1982)

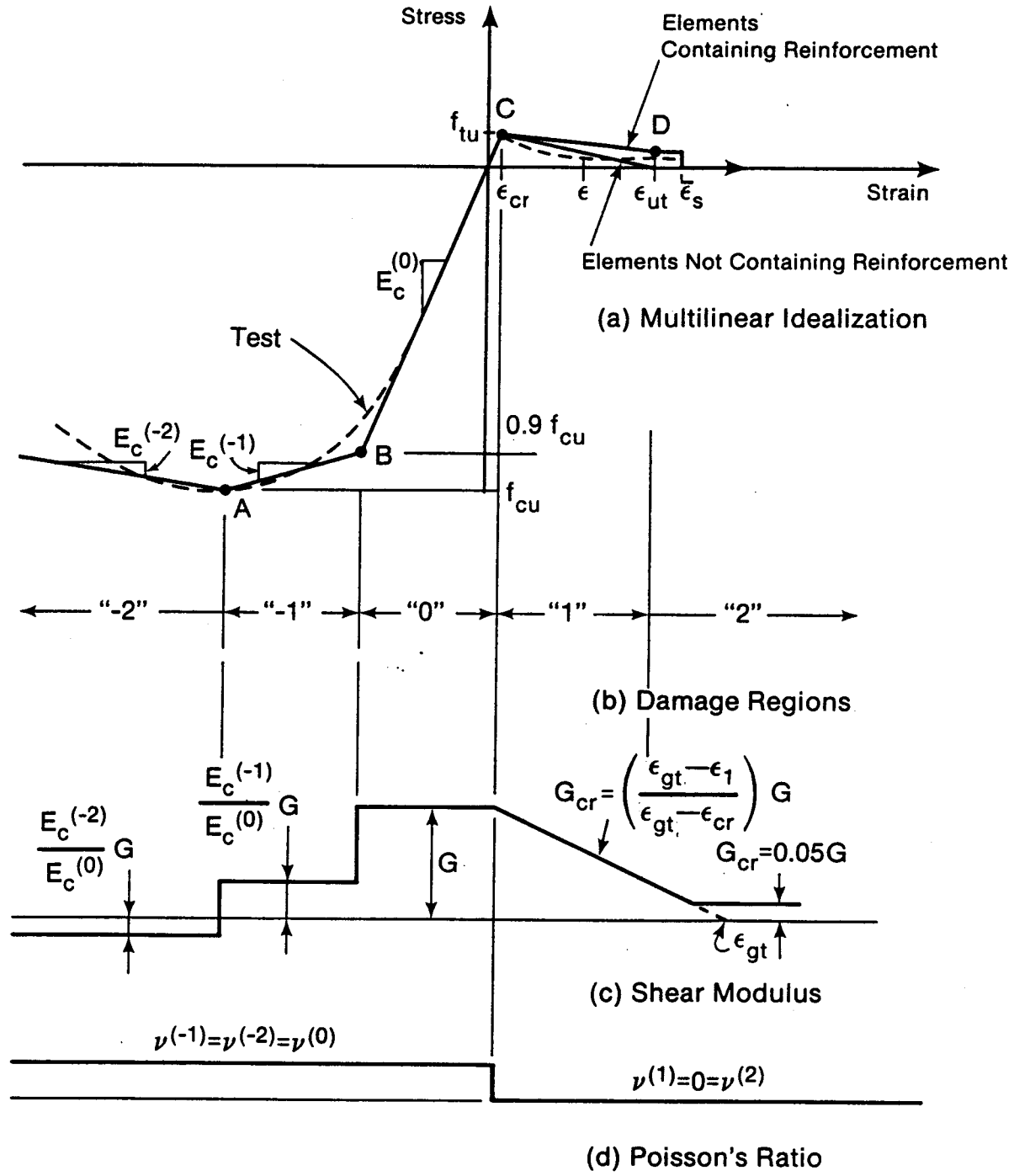

Note: superscripts in parentheses denote damage regions.

FIG. 3.20. Representation of Concrete Stress-Strain Relationship

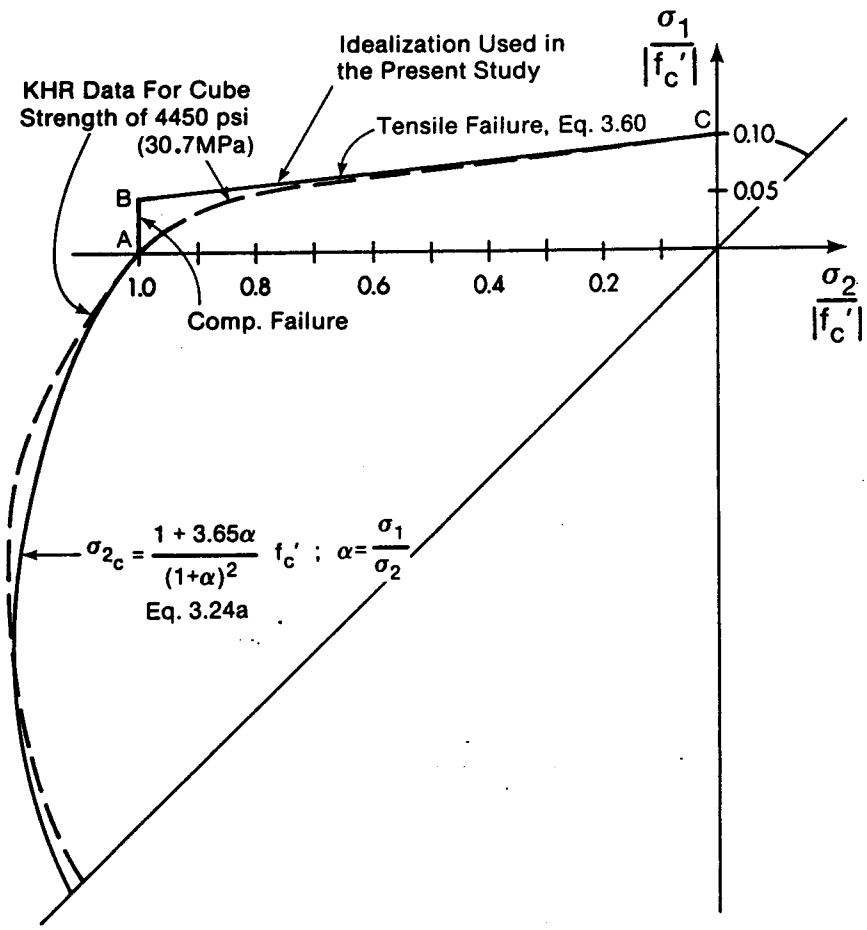

FIG. 3.21. Biaxial Failure Envelope

CHAPTER 4

APPLICATION TO REINFORCED CONCRETE SHEAR PANELS AND DEEP BEAMS

4.1 Introduction

Reinforced concrete shear panels and deep beams are, in practice, usually designed on the basis of equilibrium considerations alone (Nielsen, 1984; ACI 318-83; CEB-FIP Model Code, 1978), although design theories considering the associated compatibility conditions (Vecchio and Collins, 1982) have been incorporated into the Canadian Code (CSA A23.3-M84). In this chapter, the physical behavior of concrete elements reinforced in two orthogonal directions (i.e. net reinforced elements) under in-plane loads is described.

A hypothesis is presented for estimating the post-cracking compressive strength of these elements based on the biaxial stress conditions prior to cracking. Ultimate strength predictions, obtained using this hypothesis in conjunction with equilibrium considerations alone, are compared to the test data and are found to be sufficiently accurate for engineering purposes.

Finite element analyses incorporating the simple constitutive relationships described in Chapter 3 are described. The finite element predictions are compared to the behavior observed in tests for shear panels exhibiting various failure modes. The applicability of the finite element method, and the constitutive relationships developed herein, to shear panels having been thus verified, the behavior of a net reinforced deep beam (which is comprised of net reinforced concrete elements) is then predicted using these constitutive relationships and compared to the behavior observed in the test.

4.2 Behavior of Net-Reinforced Concrete Elements

4.2.1 Equilibrium of Net-Reinforced Concrete Elements

Consider an orthogonally reinforced R/C panel as shown in Fig. 4.1a subjected to biaxial stresses in plane x-y. Let ρ_x and ρ_y be the cross-sectional areas of the reinforcement per unit cross sectional area of the panel, in the x and y directions respectively. In all the ensuing discussion in this chapter, the subscript notation adopted is as follows: subscripts x and y are used to denote the coordinate directions; subscripts c and s are used to denote concrete and steel respectively; subscripts ξ and η are used to denote the major and minor principal stress directions respectively; subscripts 1 and 2 are used to denote the major and minor principal strains, respectively. For example, f_{c_x} denotes the stress in concrete in the x direction; ε_{c_1} the major principal strain in concrete. Tensile stresses and strains are assumed positive and the major axis refers to the direction of the greatest algebraic value.

Considering an element which has unit cross-sectional areas normal to the x and y axes, equilibrium in the x direction requires that, referring to Fig. 4.1b,

$$f_x = (1 - \rho_x)\, f_{c_x} + \rho_x\, f_{s_x} \tag{4.1}$$

Approximating $1.0 - \rho_x \simeq 1.0$,

$$f_x = f_{c_x} + \rho_x\, f_{s_x} \tag{4.2}$$

Similarly, considering equilibrium in the y direction, we obtain

$$f_y = f_{c_y} + \rho_y f_{s_y} \tag{4.2b}$$

Neglecting the shear stress in reinforcement, moment equilibrium requires that,

$$\tau = f_{c_{xy}} \tag{4.2c}$$

where $f_{c_{xy}}$ is the shear stress in concrete.

First the case of pure shear is considered.

In order to aid further discussion on the ultimate strength of panels, expressions for principal stresses are derived. This can most easily be illustrated using Mohr's circle construction, shown in Fig. 4.2a for the case of applied pure shear. The free body diagrams are shown in Fig. 4.2b and 4.2c indicating the state of stress in the panel. The Culmann Diagram is shown in Fig. 4.2d.

Considering equilibrium along the x direction for unit area in the y direction, we obtain from the free body diagram of Fig. 4.2b,

$$\rho_x f_{s_x} = \tau \cot \theta - f_{c_\xi} \tag{4.3a}$$

Similarly, considering equilibrium along the y direction of the panel with unit area in the x direction,

$$\rho_y f_{s_y} = \tau \tan \theta - f_{c_\xi} \tag{4.3b}$$

Similarly, using the free body diagram in Fig. 4.2.c,

$$\rho_x f_{s_x} = -\tau \tan\theta - f_{c_\eta} \tag{4.3c}$$

$$\rho_y f_{s_y} = -\tau \cot\theta - f_{c_\eta} \tag{4.3d}$$

Substituting for $\rho_x f_{s_x}$ from Eq. 4.3c into Eq. 4.3a, we obtain,

$$f_{c_\eta} = f_{c_\xi} - \tau (\cot\theta + \tan\theta) \tag{4.4}$$

Substituting for $\tau \tan\theta$ and $\tau \cot\theta$ from Eqs. 4.3a and 4.3b into Eq. 4.3c, we obtain,

$$f_{c_\eta} + f_{c_\xi} = -(\rho_x f_{s_x} + \rho_y f_{s_y}) \tag{4.5}$$

The geometric representation of Eqs. 4.3 to 4.5 can be seen on the Mohr's circle of Fig. 4.2a. The total stress state is represented by the Mohr's circle on the right. The stress state in the concrete (only) is represented by the Mohr's circle on the left. When the tensile stress contributions of steel on the x and y planes are added to the concrete stress state the total stress state is recovered.

4.2.2 Ultimate Strength of Net-Reinforced Concrete Elements in Pure Shear

Expressions based solely on equilibrium considerations can now be derived for the ultimate strength of orthogonally reinforced elements. In order to simplify the derivation at this point, a tension cut-off criterion is used for concrete. That is, that cracking occurs on the ξ

plane and that $f_{c_\xi} \equiv 0$ after cracking. In this case, the post-cracking form of Eq. 4.5 becomes,

$$f_{c_\eta} = -\left(\rho_x f_{s_x} + \rho_y f_{s_y}\right) \tag{4.6}$$

Dividing Eq. 4.3a by Eq. 4.3b, yields the post-cracking condition,

$$\tan^2\theta = \frac{\rho_y f_{s_y}}{\rho_x f_{s_x}} \tag{4.7a}$$

and Eq. 4.4 gives,

$$\tau = - f_{c_\eta} \sin\theta \cos\theta \tag{4.7b}$$

Interpreting Eq. 4.7a geometrically as shown in Fig. 4.3, and substituting for $\sin\theta$ and $\cos\theta$ in Eq. 4.7b yields

$$\tau = - f_{c_\eta} \left(\frac{\sqrt{\rho_x f_{s_x}}}{\sqrt{\rho_x f_{s_x} + \rho_y f_{s_y}}} \cdot \frac{\sqrt{\rho_y f_{s_y}}}{\sqrt{\rho_x f_{s_x} + \rho_y f_{s_y}}}\right) \tag{4.8}$$

Noting from Eq. 4.6 that the denominator of Eq. 4.8 is $- f_{c_\eta}$, Eq. 4.8 becomes,

$$\tau = \sqrt{\rho_x f_{s_x} \, \rho_y f_{s_y}} \tag{4.9}$$

Let $\rho_y \leq \rho_x$. Substituting for $\rho_x f_{s_x}$ from Eq. 4.6,

$$\tau = \sqrt{\rho_y f_{s_y} \left(- f_{c_\eta} - \rho_y f_{s_y}\right)} \qquad (4.10)$$

Three post-cracking failure conditions can now be identified by referring to Eq. 4.6.

(1) If neither the steel along the x direction nor the steel along the y direction yields, a compression failure of concrete will occur. Denoting the compressive strength of concrete as f_c (a negative number), and assuming that the stiffness contribution of reinforcement before concrete cracking is neglible, θ will be at 45°, and we obtain from Eq. 4.7b,

$$\tau_{max} = - \frac{f_{c_\eta}}{2} = - \frac{f_c}{2} \qquad (4.11)$$

This type of failure can be characterised as being 'brittle' and is identified as the 'B' failure mode in subsequent discussion.

(2) If concrete failure occurs prior to yielding of the steel in the x direction, so that only the y direction reinforcement yields, maximum shear stress at failure will be given by Eq. 4.10, with $\overline{f}_{s_y}$, the yield strength of steel in y direction, substituted for f_{s_y} and f_c for f_{c_η}. That is,

$$\tau_{max} = \sqrt{\rho_y \overline{f}_{s_y} \left(-f_c - \rho_y \overline{f}_{s_y}\right)} \qquad (4.12)$$

From Eq. 4.6

$$\rho_s f_{s_x} = - f_{c_\eta} - \rho_y f_{s_y}$$

Hence, if the steel in the x direction has not yielded at failure it follows that

$$\rho_x \bar{f}_{s_x} > - f_c - \rho_y \bar{f}_{s_y}$$

Although final failure is by crushing of the concrete the yielding of steel in the y direction provides more ductility than the 'brittle' mode described above. Hence, this mode of failure is identified as a 'DB' failure mode in subsequent discussion.

(3) If both x direction and y direction reinforcement yield, then, from Eq. 4.9,

$$\tau_{max} = \sqrt{\rho_x \bar{f}_{s_x} \rho_y \bar{f}_{s_y}} \qquad (4.13)$$

in which case failure is due to steel yielding and hence the behavior is characterized as 'ductile' and designated as the 'D' failure mode in subsequent discussion.

4.2.3 Prediction of Failure Mode for Pure Shear

Given the values of ρ_y, ρ_x, $\bar{f}_{s_y}$, $\bar{f}_{s_x}$ and f_c, the failure load and failure mode can be predicted as follows. Referring to Eq. 4.6, it is seen that if f_{s_x} and f_{s_y} reach the corresponding yield strengths before f_{c_η} reaches f_c, a ductile failure results, i.e. the condition for yielding of both layers of reinforcement at failure is given by the

relationship,

$$\frac{\rho_y \bar{f}_{s_y}}{|f_c|} + \frac{\rho_x \bar{f}_{s_x}}{|f_c|} \leq 1.0 \qquad (4.14)$$

Hence, if Eq. 4.14 is satisfied failure will be by mode D.

If Eq. 4.14 is violated it follows from Eq. 4.6 that failure involves concrete crushing and steel yields in neither direction or only in one direction. For the case under consideration (pure shear) cracking will occur at 45° (assuming the steel is not activated in any substantial way until after cracking) and it follows from Eq. 4.7a that

$$\rho_y f_{s_y} = \rho_s f_{s_x}$$

Hence, Eq. 4.14 implies that if both fractions exceed 0.5 a compressive failure will occur without steel yield in either direction. That is, failure mode B will occur if

$$\frac{\rho_y \bar{f}_{s_y}}{|f_c|} \geq 0.5 \quad \text{and} \quad \frac{\rho_x \bar{f}_{s_x}}{|f_c|} \geq 0.5$$

Failure mode DB will occur if Eq. 4.14 is violated and either $\rho_y \bar{f}_{s_y}$ or $\rho_x \bar{f}_{s_x}$ is less than $0.5|f_c|$.

4.2.4 General Stress Conditions

If biaxial normal stresses, f_x and f_y are applied in addition to the shear stresses, these will be subtracted from $\rho_x f_{s_x}$ and $\rho_y f_{s_y}$ respectively in the above derivations. This follows from equilibrium considerations represented by Eqs. 4.2. In this case Eq. 4.12 becomes

$$\tau_{max} = \sqrt{(\rho_y \bar{f}_{s_y} - f_y)(|f_c| - (\rho_y \bar{f}_{s_y} - f_y))} \qquad (4.15)$$

when only y-direction steel yields, and Eq. 4.13 becomes

$$\tau_{max} = \sqrt{(\rho_y \bar{f}_{s_y} - f_y)\ (\rho_x \bar{f}_{s_x} - f_x)} \qquad (4.16)$$

when both steel layers yield. When neither layer yields, the load capacity is reached when the principal compressive stress reaches the compressive strength of concrete. For cracked reinforced panels this load is given by Eq. 4.11 if f_x and f_y are equal.

4.2.3 Plasticity Theory of Net Reinforced Elements

Equations 4.11 through 4.16 represent the basis of plasticity based methods (Nielsen, 1984) wherein elastic deformations and tensile strength of concrete are neglected and concrete is assumed to be perfectly plastic. In order to match the experimental results, the plasticity based methods assume an "effective" concrete strength, f_c, (to be used in Eqs. 4.11 to 4.15 for calculating the ultimate strength) as a fraction of the cylinder compressive strength. That is

$$f_c = \alpha\ f'_c \qquad (4.17)$$

where α is the "effectiveness factor".

The effectiveness factor, α, is presumed to account for compressive strain softening, geometrical effects, size effects, loading conditions, distribution and orientation of cracks and loading history. The

necessity to use an effeciveness factor is the principal limitation of the plasticity based methods. Other significant limitations are: (1) the neglect of tensile strain softening and tension stiffening which might lead to inaccurate predictions of failure load and failure mode; (2) the assumption that the crack shear resistance of concrete is adequate for the yield condition to be attained (the implication of this assumption is discussed in the following subsection); and, (3) the assumption of perfect plasticity in concrete.

4.2.4 Modified Compression Field Theory

The so-called Modified Compression Field Theory developed by Vecchio and Collins (1982) overcomes most of the limitations identified in Sect. 4.2.3. In this theory, the cracked concrete is treated as a new material with its own stress-strain characteristics. Considerations of equilibrium, compatibility and average stress-average strain behavior are included at all loading stages up to failure.

In order to aid further discussion on the average stress-average strain relationship, expressions for strain transformations are derived in the following by constructing Mohr's circles of strain. In this derivation compatibility between steel and concrete is assumed, i.e. bond slip is ignored. Therefore, only the subscripts denoting the directions are required for strains. The principal stress and the principal strain axes do not necessarily coincide and subscripts 1 and 2 indicate major and minor principal strains, respectively. Denoting the orientation of principal strain axes by θ', the relationships represented by the following Eqs. 4.18 are deduced from the Mohr's circle construction as described in Appendix A2.

$$\tan \theta' = \frac{\varepsilon_x - \varepsilon_2}{(\frac{\gamma_{xy}}{2})} \tag{4.18a}$$

$$\tan^2 \theta' = \frac{\varepsilon_1 - \varepsilon_y}{\varepsilon_1 - \varepsilon_x} \tag{4.18b}$$

$$\varepsilon_x + \varepsilon_y = \varepsilon_1 + \varepsilon_2 \tag{4.18c}$$

In the Modified Compression Field Theory, the equilibrium requirements are represented by Eqs. 4.3 and the compatibility requirements are represented by Eqs. 4.18. Complete stress and strain states in the panel could thus be calculated for any combinations of applied in-plane stresses, if the relationship between the principal stresses and principal strains were known. In order to determine this relationship, Vecchio and Collins (1982) tested thirty reinforced concrete panels under uniform stresses. Based on these test results and assuming cracked concrete as a new material with its own stress-strain characteristics, they developed expressions relating the principal stresses and principal strains given by Eqs. 4.19.

$$\beta = \frac{1}{0.85 - 0.27 \frac{\varepsilon_1}{\varepsilon_2}} \tag{4.19a}$$

$$f_{c_{\eta_{max}}} = \beta f'_c \tag{4.19b}$$

$$f_{c_\eta} = f_{c_{\eta_{max}}} \left[2 \left(\frac{\varepsilon_2}{\varepsilon'_c}\right) - \beta \left(\frac{\varepsilon_2}{\varepsilon'_c}\right)^2 \right] \tag{4.19c}$$

$$f_{c_\xi} = \frac{f'_t}{1 + \sqrt{\frac{\varepsilon_1}{0.005}}} \qquad (4.19d)$$

In the above equations, f'_c is the uniaxial cylinder compressive strength, ε'_c is the uniaxial strain corresponding to f'_c in cylinder test and, f'_t is the uniaxial tensile strength.

The factor β was introduced by Vecchio and Collins to account for the apparent degrading effect of the normal crack strain on the compressive strength of the cracked concrete. The expression for β, given by Eq. 4.19a, was derived by Vecchio and Collins from a plot of the maximum value of the principal compressive stress calculated for each test panel, <u>including those test panels where the failure was due to steel yielding</u>, versus the corresponding strain ratio $(\frac{\varepsilon_1}{\varepsilon_2})$, as shown in Fig. 4.4.

Other major assumptions in the modified compression field theory are

(1) the principal stress axes and the principal strain axes coincide, i.e.

$$\theta = \theta' \qquad (4.20)$$

(2) the multiaxial stress conditions before cracking do not significantly influence the ultimate strength of the panel

(3) the average stress-average strain relation in steel can be represented by the bilinear elastic-plastic relationships given by Eqs. 4.21.

$$f_{s_x} = E_s \varepsilon_x \tag{4.21a}$$

$$\text{but} \quad f_{s_x} \leq \overline{f}_{s_x} \tag{4.21b}$$

$$f_{s_y} = E_s \varepsilon_y \tag{4.21c}$$

$$\text{but} \quad f_{s_y} \leq \overline{f}_{s_y} \tag{4.21d}$$

where E_s is the modulus of elasticity of steel reinforcement.

The effect of the stress in concrete between the cracks (the tension stiffening effect) is represented by Eq. 4.19d. The tensile stress in concrete, $f_{c\xi}$ is set to zero if both the x and y direction reinforcement have yielded. As shown in Fig. 4.5, which contains points covering the full range of loading, the test points exhibit considerable scatter.

4.3 Finite Element Prediction of Panel Behavior

4.3.1 Finite Element Modeling

The behavior of net reinforced concrete elements has been investigated in this study using the Finite Element Method (FEM). In order to investigate a wide range of behavior, nine test panels were selected for this study from about thirty panels tested by Vecchio and Collins (1982).

The material parameters of the selected panels and the observed failure modes are tabulated in Table 4.1. All the test panels were 70 mm thick x 890 mm x 890 mm. They were reinforced with two layers of welded wire mesh, with the reinforcement parallel to the edges of the

panel. The welded wire mesh was made of heat treated smooth wires at 50 mm grid spacing. Brass targets were fixed on the reinforcement at 200 mm grid spacing and the average strains were measured using mechanical strain gages.

The finite element modelling of the test panel is shown in Fig. 4.6. The panel was modelled by a four noded square serendipity element with the reinforcement concentrated at Gauss sampling points. For quadratic serendipity elements with the embedded formulation of reinforcement, lumping steel into equivalent bars through the Gauss points is required in order for the cracked element to respond with uniform strains.) Modeling the panel by only one element is adequate because the average stress-average strain relationship is of interest rather than the local stress-strain relationships at different points in the panel. Bond slip between the reinforcement and concrete is ignored (i.e. perfect bond assumed). The constitutive relation used for the steel reinforcement is shown in Fig. 4.7. A strain hardening modulus of 2.0 per cent of the elastic modulus is adopted to stabilize the numerical procedure after steel yielding. The constitutive relation used for concrete is that described in Chapter 3. To the author's knowledge, no test results are available wherein the post-cracking compressive strength of concrete was determined directly. A hypothesis for estimating the post cracking compressive strength of concrete is presented in Sect. 4.3.2. The tensile stress-strain relation adopted for these panels is discussed in Sect. 4.3.3. The stress computation subroutine is described in Sect. 4.3.4.

4.3.2 Post-Cracking Compressive Strength of Concrete

The biaxial peak strength envelope for concrete in the tension-compression stress field is shown in Fig. 4.8 where the data from tests conducted by Kupfer et al. (1969) are compared to the cracking and post-cracking strength envelopes proposed herein.

As discussed in Sect. 3.7.3, the peak strengths f_{cu} and f_{tu} of Fig. 3.20 can be obtained from the biaxial strength envelope illustrated in Fig. 3.21. In this figure line AB represents compressive 'failure' and line BC represents tensile 'failure'. However, in the tension-compression zone it has been found that in order to obtain results more consistent with experimental behavior it is beneficial to introduce a post-cracking peak compressive strength envelope in addition to the peak tensile strnegth envelope (i.e. - the cracking envelope). The assumed peak strength relationships are given below in equation form and are represented graphically in Fig. 4.8.

A compressive failure is assumed to occur for the condition

$$|f_{c_\eta}| = |f'_c| = f_{cu} \tag{4.22a}$$

providing the biaxial stress path intersects the envelope in the region

$$|\frac{f_{c_\eta}}{f_{c_\xi}}| > |\frac{f'_c}{0.5f'_t}| \ . \tag{4.22b}$$

This is represented by line AB in Fig. 4.8.

Cracking is assumed to occur when

$$f_{c_\xi} > f_{t_u} \tag{4.23a}$$

where f_{tu} is given by,

$$f_{tu} = \frac{2f'_c}{\frac{f_{c_\eta}}{f_{c_\xi}} + \frac{2f'_c}{f'_t}} \qquad (4.23b)$$

(line BC of Fig. 4.8) providing that the biaxial stress path intersects the envelope in the region

$$\left|\frac{f_{c_\eta}}{f_{c_\xi}}\right| < \left|\frac{f'_c}{0.5f'_t}\right| \cdot \qquad (4.23c)$$

The proposed post-cracking compressive strength envelope is given by,

$$f_{cu} = \left(1.5 - \frac{f_{tu}}{f'_t}\right) f'_c \qquad (4.23d)$$

That is, the line BD of Fig. 4.8 defines the post-cracking compressive strength f_{cu} if the stress path intersects the cracking envelope BC which establishes the value of f_{tu}. The compressive strength f_{cu} of Fig. 3.20 is thus modified for any particular Gauss point at the instant of cracking if cracking occurs in the tension-compression stress field. For the stress path OE of Fig. 4.8, the abcissa of F becomes the value of f_{cu}.

Equations 4.22 and 4.23 are consistent with the following hypothesis.

As discussed in Chapter 3, Sect. 3.5, internal microcracks (called bond cracks) exist in concrete at the cement-aggregate interface even before any loads are applied. If concrete is subjected to uniaxial

compression, the stress-strain behavior is linear elastic at low load levels (up to about 30 per cent of ultimate) because the bond cracks do not propagate. With increase in load the bond cracks increase in length, width and number (Mindess and Young, 1981). The effect of the tensile stress in the biaxial tension-compression stress field is to accentuate this damage by increasing strains normal to the compressive stress direction, thus reducing the compressive strength. With low ratios of compressive to tensile stress, macrocracking occurs at low load levels when the behavior is still essentially elastic. Thus, when macrocracking occurs the direct tensile strain in concrete between the macrocracks, caused by the tensile stress, is mostly recovered in plain concrete because the tensile stress drops. In reinforced concrete, however, significant direct tensile strain is still present because of the presence of the reinforcement which prevents the complete recovery. With continued tensile loading after the formation of macrocracks the stresses in the reinforcement increase and the stresses in concrete decrease in the vicinity of the macrocracks. The maximum local tensile strain in concrete between the cracks cannot, in any case, exceed the cracking strain. Hence no increase in the direct tensile strain causing reduction in the compression strength occurs for tensile straining subsequent to the intersection of the stress path with the cracking envelope. This is implied in Eq. 4.23d wherein it has been assumed that the maximum damage in concrete with respect to the compressive strength occurs at the onset of tensile macrocracking.

The major difference between the expressions for compressive strength in Eqs. 4.19, proposed by Vecchio and Collins (1982), and in Eqs. 4.23, proposed in this study, is that Eqs. 4.23 are based on the

multiaxial stress conditions at incipient tensile macrocracking while Eqs. 4.19 are based on average tensile strains after cracking.

4.3.3 Tensile Stress-Strain Relation

The tension softening and tension stiffening aspects of cracked concrete have been discussed in Chapter 3, Sects. 3.2 and 3.3. The tension softening of concrete at macrocracks and the tension stiffening effect of concrete segments between the macro-cracks are combined and represented by the descending branch of the concrete stress-strain curve in tension. The tension softening contribution is calculated using the fracture energy release rate and the estimated crack spacing in Eq. 3.5. The tension-stiffening contribution is estimated as follows.

The welded wire mesh used in the test panels is well anchored because of the cross-welds. Thus, after the onset of cracking, decrease in tensile stresses in concrete between the cracks due to bond slip is less for the welded wire mesh reinforcement and the tensile stress strain relationship will approach the 'no slip' curve, that shown for $S_o = 0$ in Fig. 3.7. Another factor considered when determining the tension stiffening is that higher strength was used in the perimeter zone of the test panels in order to avoid edge failures. This increases the tension stiffening effect, at least at lower load levels.

When the yield strength of the reinforcement is reached its stiffness becomes negligible. Thus, the tension-stiffening contribution is set to zero when at least one layer of reinforcement yields at the crack locations. The adopted average tensile stress-average strain relationship, given by the following Eqs. 4.24, is plotted in Fig. 4.5a and in Fig. 4.5b wherein it is compared to the Vecchio/Collins test data

and their recommended relationship.

$$f_{c_1} = \left(\frac{.01 - \varepsilon_1}{.01 - \varepsilon_{cr}}\right) f_{tu} \qquad (4.24a)$$

subject to the constraints,

$$f_{c_1} = 0 \ , \quad \text{if} \quad f_{c_1} + \rho_y f_{s_y} > \rho_y \overline{f}_{s_y} \qquad (4.24b)$$

$$f_{c_1} = 0 \ , \quad \text{if} \quad f_{c_1} + \rho_x f_{s_x} > \rho_x \overline{f}_{s_x} \qquad (4.24c)$$

In Eq. 4.24a, ε_{cr} is the tensile strain at which cracking occurs. Eq. 4.24 can be derived directly from the Mohr's circles of Fig. 4.2a and the condition that f_{c_1} shall vanish when at least one layer of steel yields.

For percentages and yield strengths of reinforcement used in Vecchio/Collins shear panels, the constraints of Eqs. 4.24b and c provide the cut-off for tensile stiffening at $\overline{\varepsilon}_s$ of Fig. 4.5.

4.3.4 Computation of Stresses in Concrete

The stress computation procedure is shown as a flow diagram in Fig. 4.9. The principal strain axes are taken to be the axes of orthotropy and constitute the local material axes. The stresses and strains are computed with respect to the local axes. The stresses and strains with respect to the global axes are obtained using coordinate transformation. The directions of orthotropy are not, in general, constant and 'rotate' based on the relative stiffnesses of concrete and steel after concrete cracking. This implies that the crack direction

changes, at least in the average sense. That the crack direction can change has been confirmed in tests conducted by Vecchio and Collins (1982) and others, and has been recognized by a number of investigators (for example, Akbar and Gupta, 1985; Milford and Schnobrich, 1984). Herein, an explanation of this behavior is given with the aid of Mohr's circle construction.

Consider a reinforced concrete panel containing different amounts of reinforcement in two orthogonal directions as shown in Fig. 4.6 but being loaded in pure shear. Based on equilibrium considerations, Mohr's circles of stress in concrete and the applied stress condition, similar to those shown in Fig. 4.2a, can be constructed. As the applied stress is increased, let it be assumed that the steel layer along the y direction yields, say at load step 'ℓ'. The Mohr's circles corresponding to this load step can be drawn as shown in Fig. 4.10. With increase in the applied stress at load step $\ell + \Delta\ell$, the stress in y direction steel cannot increase because it has already yielded. In order to maintain equilibrium, the compressive stresses in concrete and the stresses in the steel layer not yielded must increase as can be deduced from Eqs. 4.4 and 4.5. The Mohr's circle of stresses for load step $\ell + \Delta\ell$ therefore shows an increase in stresses in concrete and x direction steel and a decrease in the tensile stress (the concrete having already cracked), whereas the stresses in the y direction steel remains the same as in load step ℓ. This necessitates a change in the principal axes' orientation, as shown in Fig. 4.10. The shear stress transferred across 'old' cracks (at load step 'ℓ') by aggregate interlock makes the rotation of principal axes possible.

The shear modulus, G_{cr}, referenced to the local coordinates, makes

the rotation of principal axes possible by developing shear stresses across cracks. As described in Chapter 3, Sect. 3.7.2.4, the shear modulus of cracked concrete is assumed to be given by,

$$G_{cr} = \left(\frac{0.01 - \varepsilon_1}{0.01 - \varepsilon_{cr}}\right) G \quad ; \; 0.05G \leq G_{cr} \leq G \tag{4.25}$$

where G is the shear modulus of the uncracked concrete.

The axes of orthotropy at any iteration, j, are assumed to coincide with the principal (total) strain axes in the previous iterate (j-1). The constitutive matrix relating incremental strains and stresses after concrete cracking is given by Eq. 4.26

$$\begin{Bmatrix} \Delta f_{c_1} \\ \Delta f_{c_2} \\ \Delta f_{c_{12}} \end{Bmatrix} = \begin{bmatrix} E_{cr} & 0 & 0 \\ 0 & E_c & 0 \\ 0 & 0 & G_{cr} \end{bmatrix} \begin{Bmatrix} \Delta\varepsilon_1 \\ \Delta\varepsilon_2 \\ \Delta\gamma_{12} \end{Bmatrix} \tag{4.26}$$

where: E_{cr} is the tangent modulus of cracked concrete in tension, obtained from Eqs. 4.24; E_c is the tangent modulus of uncracked concrete; and, G_{cr} is the tangent shear modulus of cracked concrete given by Eq. 4.25.

The uniaxial stress-strain relationship is summarized in Fig. 4.11. Since only one element has been used to model the panel, the compressive strain softening has been ignored and a small positive modulus is used in order to stabilize the numerical procedure at concrete compressive failure.

4.3.5 Numerical Solution Procedure

The standard Newton-Raphson iterative solution procedure has been adopted. In calculating the tangent stiffness matrix for the computation of deflections using the Standard Newton-Raphson procedure, the actual material tangent moduli are used, except that after concrete cracking, the material modulus perpendicular to the crack direction is taken to be zero (i.e. Eq. 4.26 with $E_{cr} = 0$ is used for the structure stiffness calculations but not for stress increment calculations). Numerical integration with 2x2 Gauss quadrature has been used. The size of the load step is varied. The first load step is such that concrete cracking does not occur. Subsequent to concrete cracking, 5 to 10 load steps are applied until failure is reached. Failure is assumed to be reached when in 50 iterations the convergence tolerance of 0.001 on the incremental displacement norm and the unbalanced load vector norm is not satisfied. Unconverged results are output and analysed to determine whether the steel has yielded ($f_s > \bar{f}_s$) and/or the concrete has crushed ($|f_{c_\eta}| > |f_{cu}|$) and thereby to determine the mode of failure.

Thirty net reinforced concrete panels were tested by Vecchio and Collins (1982), the majority of them in pure shear. Of the thirty panels tested, only 18 failed in 'proper' failure modes. The remainder failed at the edges, or the welded wire mesh ruptured at the cross welds, or the concrete contained voids. Of the 18 exhibiting proper failure modes, one was tested in uniaxial compression, and one was reinforced in one direction only; four of the panels failed by steel yielding in both directions from which two were selected for this study (Panel PV4 which was isotropically reinforced and Panel PV11 which was orthotropically reinforced); five panels failed by concrete crushing

subsequent to one layer of steel yielding, from which three were selected for this study (Panels PV19, PV21 and PV10); six panels failed by concrete crushing without steel yielding from which three were selected (Panels PV27, PV25 and PV23); one panel, PV29, was subjected to nonproportional loading and has been selected for this study. Panels PV19, PV27, PV25 and PV29 were the subject of an international competition (Collins et al., 1985).

4.3.6 Analytical Results

4.3.6.1 Panel PV4 (Failure by Steel Yielding in Both Directions)

This panel is reinforced with equal amounts of steel in the x and y directions and was loaded in pure shear. It failed due to both layers of steel yielding simultaneously. The behavior of this panel was first analysed in this study using the tension cut off criterion (wherein concrete is assumed to carry no stresses perpendicular to the crack). Another analysis was performed incorporating the tensile stress-strain relation given by Eqs. 4.24. The results of the analyses are plotted in Figs. 4.12a to c.

The tension cut off analysis is illustrative of the panel behavior at the onset of cracking. Figures 4.12 show that the panel 'expands' after concrete cracking in order to activate the reinforcement to supply the tensile stresses required for equilibrium. It can also be seen that tension stiffening must be taken into account in order to closely predict the behavior prior to steel yielding. The strains obtained from the computer analyses were used to construct the Mohr's circles shown in Fig. 4.13. The sudden large increase in tensile strain when the tension cut off criterion is used is apparent.

The predicted failure load is compared with the experimental load for this panel (and all subsequent panels) in Table 4.2.

Figure 4.14 shows the Mohr's circles of stress immediately prior to steel yielding. In order to predict the failure load correctly, the importance of reducing the tensile stress in concrete to zero when steel yields is apparent from Figs. 4.12.

4.3.6.2 Panel PV19 and Panel PV21 (Failure by Concrete Crushing after Steel Yielding)

These panels, tested in pure shear, were nonisotropically reinforced and are reported to have failed by crushing of concrete after one layer of reinforcement yielded. For Panel PV19, the applied shear stress versus shear strain relationship predicted by the FEM is compared to the observed behavior in Fig. 4.15a where the relation predicted by Vecchio/Collins procedure is also shown. The applied shear stress versus strains in the x and y directions (directions of reinforcement) are plotted in Fig. 4.15b and 4.15c respectively. The experimental failure load is given as 3.95 MPa. The finite element prediction is 4.45 MPa. The concrete crushing failure mode has been correctly predicted in this analysis, the reinforcement yielded in the y direction and the x direction reinforcement stresses were below the yield strength. The failure load predicted by Eq. 4.12 is 4.22 MPa if f_c, the post cracking compressive strength, is calculated using Eqs. 4.23 (i.e, f_{cu} given by Eq. 4.23d is taken as f_c in Eq. 4.12). The Mohr's circles of stress and strain obtained from the FE analysis are shown in Figs. 4.16 where the rotation of principal axes is seen.

Panel PV21 is similar to panel PV19, except for more reinforcement

in the y direction. The finite element prediction is compared to the experimental behavior in Fig. 4.17. The predicted failure load of 5.2 MPa using the FEM compares favorably with the experimental failure load of 5.03 MPa. Again, using f_c given by Eq. 4.23, a failure load of 5.16 MPa is obtained from Eq. 4.12.

4.3.6.3 Panel PV25 and Panel PV23 (Failure by Concrete Crushing Without Steel Yielding)

These panels were subjected to combined biaxial compression and shear stresses. Both panels were isotropically reinforced and are reported to have failed by concrete crushing before steel yielding. The shear stress versus shear strain relation for Panel PV25 predicted by the FEM is compared to the experimental behavior in Fig. 4.18a and the shear stress versus strain in x and y directions are compared in Fig. 4.18b and Fig. 4.18c. The predicted failure load of 7.7 MPa for panel PV25 is lower than the experimental failure load of 9.1 MPa although a softening trend is seen at 8.3 MPa when the hydraulic system (used for loading) failed during the experiment. The influence of biaxial compressive stresses on the shear capacity of Panel PV25 can be estimated by comparing the higher failure load of Panel PV25 to that of Panel PV27 (described in Sect. 4.3.6.4). Panel PV27 contained the same amount of reinforcement as Panel PV25, but was loaded in pure shear. The application of Eqs. 4.23 to estimate the post-cracking compressive strength leads to the correct prediction of increase in shear capacity with the applied biaxial compressive stress.

The predictive failure loads of Panels PV25 and PV23 are very sensitive to the tension stiffening used. This was found to be true for

all panels investigated in this study which failed by concrete crushing without steel yielding. The failure load predicted by the limit Eq. 4.11 using the tension cut off criterion and the post cracking compressive strength given by Eqs. 4.23, is 6.51 MPa for Panel PV25 and 6.15 MPa for Panel PV23. Thus the tension stiffening contribution to the load capacity of these panels, predicted by this study, is in the order of 18 to 24%.

The applied shear stress versus shear strain relation for Panel PV23 is shown in Fig. 4.19. Although panel PV23 was subjected to a biaxial compressive stress of only 39 percent of shear stress (compared to 69 per cent of shear stress for panel PV25) the increase in load capacity in both panels (compared to panel PV27 of Sect. 4.3.6.4) is approximately the same, indicating that an increase in biaxial compressive stresses does not yield a proportional increase in shear capacity.

4.3.6.4 Panel PV27 (Failure by Concrete Crushing Without Steel Yielding)

This isotropically reinforced panel had high reinforcement content and was loaded in pure shear. Failure of the panel occurred by concrete crushing before steel yielding. The predicted behavior is compared to the experimentally observed response in Figs. 4.20a and b. The predicted response agrees well with the observed behavior. The stress in the reinforcement obtained from this analysis was 276 MPa at failure, which is well below the yield strength of 442 MPa. Using the tension cut off criterion, and the post cracking compressive strength calculated using Eqs. 4.23, the load capacity is obtained as 5.64 MPa compared to the finite element prediction of 6.25 MPa. Thus, the tension stiffening

contribution to the load capacity is approximately 12.5 per cent for this panel.

4.3.6.5 Panel PV29 (Nonproportional Loading)

This panel was subjected to non-proportional loading. The panel was initially loaded in pure shear up to a stress of 3.9 MPa (which is approximately 80% of calculated ultimate strength in pure shear). The y direction reinforcement yielded at this load level. Further increments in shear stress were accompanied by biaxial compressive stresses of equal magnitude. Thus, the validity of the post-cracking compressive strength relations of Eqs. 4.23 may be evaluated by comparing the finite element prediction with the observed behavior, as shown in Figs. 4.21a to c. The ultimate strength has been correctly predicted as 5.9 MPa. The load at which the y direction reinforcement yields has also been correctly predicted as 3.9 MPa. The failure mode has also been correctly predicted as being that of concrete crushing. The deviation in the predicted stress-strain behavior subsequent to the application of compressive stresses is attributable to the assumed reduction of tension stiffening to zero even if one steel layer yields and to the nonzero strain hardening modulus used for steel.

4.3.6.6 Panel PV11 (Failure by Yielding of Reinforcement)

Panel PV11 is similar to panel PV4 except that the amounts of reinforcement in the x and y directions are not the same. Panel PV11 is reported to have failed in a ductile manner after yielding of both x and y direction reinforcement. The finite element prediction of 3.6 MPa is very close to 3.56 MPa observed in the experiment. The load deformation

relationship is shown in Fig. 4.22.

4.3.6.7 Panel PV10 (Failure by Concrete Crushing after One Layer of Steel Yielding)

Panel PV10 is reported to have failed by concrete crushing after yielding of one steel layer. The predicted failure load of 4.0 MPa agrees with the observed load of 3.97 MPa. The load-deformation relationship is shown in Fig. 4.23.

4.3.7 Predicting Panel Behavior

The failure loads predicted by the finite element anaysis of this study are compared to the experimental values in Table 4.2. The ratio of predicted versus test values has a mean of 1.04 and a coefficient of variation of 8.55%.

The predictions are accurate within 11% for panels PV4 and PV11 which failed in a 'ductile' manner due to steel yielding and for panels PV10, PV19 and PV21 which also failed in a ductile manner but with only y direction reinforcement (lesser steel percentage) yielding.

The predicted failure loads for panels PV23 and PV25 which failed in a 'brittle' manner by concrete crushing (and no steel yielding) are lower than the observed failure loads, mainly due to the fact that Eqs. 4.24 underestimate the tension stiffening contribution for panels that fail without steel yielding. The Vecchio/Collins model given by Eqs. 4.19 also underestimate the failure loads of these panels for the same reason (Vecchio and Collins, 1982). Both of these panels were subjected to biaxial compression in addition to shear and their predicted failure loads are very sensitive to the compressive strength of concrete. The

fact that the failure load of panel PV29 has been predicted accurately lends support to the post cracking compressive strength estimate given by Eqs. 4.23.

Simple ultimate load predictions using hand computations from the equilibrium equations, the post cracking compressive strength from Eq. 4.23, and neglecting tension stiffening, are shown in Table 4.3. It is seen that the predictions are reasonably accurate for ductile failures (in which at least one steel layer yields). The failure loads of panels failing in a brittle manner by concrete crushing are underestimated by these equations because tension-stiffening has been neglected. The failure mode has been correctly predicted in most cases by these equations. Even in cases where the predicted failure modes are incorrect, the difference in the predicted failure loads is small.

The failure loads predicted by these equations are compared in Fig. 4.24 to the experimentally observed failure loads for panels subjected to pure shear. It can be concluded that the ultimate strength of panels failing in a ductile manner is accurately predicted by the equilibrium Eqs. 4.12 and 4.13, and a lower bound is given by Eq. 4.11 for panels failing in a brittle manner.

It can also be concluded that the material model used for the finite element analysis in this study predicts with reasonable accuracy the behavior of the panels exhibiting a wide range of stress-strain response.

4.3.8 Factors Influencing the Strength of Shear Panels

The influence of various material parameters on the ultimate shear strength of panels may be deduced from Eqs. 4.11 to 4.13. The influence

of the reinforcement percentage on the ultimate shear strength is shown in Fig. 4.25. With 1.0% reinforcement in the x direction, ductile failure by both layers of steel yielding is obtained for y steel reinforcement up to 2.67%. Increasing the x direction steel to 2.0% increases the ultimate shear strength significantly. With further increase in x direction steel content, the marginal increase in ultimate shear strength reduces. There is nothing to be gained by increasing the x-direction steel content from 3.0 to 4.0%. It is also seen that with x direction steel at 2.0%, there is no significant increase in strength if y direction steel exceeds 1.83% (which corresponds to the transition from DB to B type failure).

The influence of the cylinder compressive strength, as predicted by Eqs. 4.11 to 4.13, on the shear capacity of panels is shown in Fig. 4.26. With small percentages of reinforcement (say, less than 1.5%) ductile failure by steel yielding occurs for concrete widely used in practice (i.e., with $f'_c > 20$ MPa) and hence concrete cylinder compressive strength does not influence the shear strength. With increasing reinforcement percentages, brittle failure by concrete crushing becomes the failure mode and hence the shear capacity is determined by the compressive strength of concrete.

The interface shear transfer stiffness of cracked concrete (i.e. shear transfer by aggregate interlock and dowel action) does not have a significant influence on the ultimate strength of the shear panels investigated in this study. As discussed in Section 4.3.4, the sliding shear capacity of crack interface is of significance only in panels where the average crack direction (i.e. principal strain axes) changes. The influence of the crack shear stiffness on the ultimate

strength was investigated by analysing panel PV11 with: (1) the crack shear stiffness same as that of uncracked concrete; and, (2) the crack shear stiffness equal to 5.0% of the uncracked concrete shear stiffness. The predicted ultimate strength in both cases was the same. For panel PV19 (where the difference between the amounts of x and y direction reinforcement is greater than in panel PV11), the increase in ultimate strength was approximately 5.0% when crack shear stiffness was increased from 5.0 percent to that given by Eq. 4.25. However, the crack shear stiffness has greater influence on the stress strain response of the panel as shown in Fig. 4.27 for Panel PV19.

4.4 Prediction of Deep Beam Behavior

4.4.1 Finite Element Modelling

The analysis of beams will be addressed in Chapter 5. However, net reinforced deep beams are similar to shear panels and one of the reinforced concrete deep beams tested by Leonhardt and Walther (1966) was investigated in this study with the same stress computation and numerical procedure used for investigating Vecchio/Collins shear panels. The deep beam selected, WT3, has been studied by a number of investigators (Al-Mahaidi, 1979; Floegl and Mang, 1982; Buyukozturk, 1977). The 100 mm (3.9 in.) thick beam had a simple span of 1600 mm (63 in.) and a total depth of 1600 mm (63 in.). It was subjected to a uniform load along its top edge. The dimensions and reinforcement arrangements are shown in Fig. 4.28. The deep beam was supported by rigid steel plates on top of steel rollers. The main longitudinal reinforcement consisted of four layers of two 8 mm diameter (0.315 in.) bars each securely anchored by hooks lying in a horizontal plane with

steel wires of 2 mm (.08 in.) diameter helically wrapped around each pair of horizontal hooks at both ends. The stress-strain relation for concrete and steel are shown in Fig. 4.29.

The finite element mesh layout is shown in Fig. 4.30. Taking advantage of the symmetry, only one-half of the deep beam is modelled. Bilinear rectangular serendipity elements are used with reinforcement embedded inside the elements. Material parameters input into the program are listed in Table 4.4. The tensile strength of concrete, f'_t, was calculated as 60 per cent of the modulus of rupture as discussed in Appendix A4. The compressive strength of concrete is taken to be approximately 88 per cent of the cube compressive strength given by Leonhardt and Walther (1966). The compressive strength of concrete for elements 41 and 46 which are directly above the support was assumed to be 40 MPa to account for the increase in strength provided by the spiral reinforcement confining the concrete and the hooks of the main reinforcement. The implications of this assumption are discussed in the following subsection. The tension softening and tension stiffening were calculated as discussed in Chapter 3 and the curves are shown in Fig. 4.31. Because of the low percentage of horizontal and vertical web reinforcement in elements 1 to 40, tension stiffening has been neglected, whereas in elements 41 to 50 containing the main reinforcement, tension stiffening has been included, which is consistent with the procedure described in Chapter 3. The tension stiffening contribution is neglected after steel yielding at cracks, as discussed in Chatper 3.

The post-cracking compressive strength and other aspects of the material model are same as those used for the Vecchio/Collins shear

panels.

4.4.2 Predicted Versus Experimental Behavior

The load-midspan deflection relationship is shown in Fig. 4.32. The left support failed during the experiment at a load of 1000 kN due to insufficient compaction of concrete at this location (Leonhardt and Walther, 1966). The damaged support was repaired by connecting steel plates to the sides of the beam at this support location and the experiment was continued. However, no further deflection readings were taken. The final failure was due to concrete crushing at the right support at a total load of 1290 kN. This corresponds to a bearing pressure of 40.0 MPa at the support. In order to investigate the influence of concrete strength at the support location, the deep beam was analysed with no increase in strength for elements 41 and 46 (i.e., with f'_c = 30 MPa throughout). This analysis gave a failure prediction of 960 kN, again due to concrete crushing at the support location. Thus the finite element prediction of the failure mode is correct.

An analysis of the stresses output (with f'_c = 40 MPa in elements 41 and 46) indicates that element 36 immediately above the support elements 41 and 46 has entered into region -1 (Fig. 4.11) at failure, thus indicating that any further increase in the strength of the support elements 41 and 46 would not have resulted in a significant increase in the load capacity of the beam. The failure mode is further confirmed by the predicted deflected positions of the beam at two successive load steps near failure, shown in Figs. 4.33a and 4.33b. It can be seen that the crushing at the support produced an essentially uniform settlement of the beam.

The progress of cracking with increase in load is shown in Figs. 4.34a to e and compares favorably with the experimentally observed crack patern shown in Fig. 4.35.

The principal stress trajectories at load levels of 47.3% and 100% of ultimate load are shown in Fig. 4.36a and b, respectively. The 'truss action' is apparent even at the lower load.

The distribution, at the failure load level, of normal longitudinal and vertical stresses and shear stresses across the depth of a vertical section near midspan, predicted by the finite element analysis is shown in Fig. 4.37. The stress distribution is compared to that obtained using a linear elastic analysis performed on the uncracked beam. It is seen that a linear analysis underestimates the maximum longitudinal compressive stress, and the stress distribution is significantly different. The location of the neutral axis is markedly higher at the failure load than at smaller load levels. The shear stress distribution indicates that most shear is being carried by truss action and the shear carried by aggregate interlock in the cracked region is very small.

The variation of steel stress at midspan with increase in load is shown in Fig. 4.38. The actual strain in steel, of course, depends on the proximity to a crack. It is seen from Fig. 4.38 that the stresses (and strains) are bounded by the curve which includes the effects of tension softening and tension stiffening, and by the curve which ignores the effects of tension softening and tension stiffening. The curve which includes tension softening in concrete at the cracks, but excludes tension stiffening, matches more closely the experimentally observed value because the strains were measured in the test very close to a crack at midspan.

It can be concluded that the finite element method can be used as described herein to predict the behavior of deep beams with an accuracy that is completely acceptable for engineering purposes.

Table 4.1 Test Panels Investigated

Panel	Loading Condition $\tau:f_x:f_y$	Steel Reinforcement				Concrete		Failure Mode (See Note below for description)
		X Direction		Y Direction		ε_c'	f_c'	
		ρ_x	$\overline{f}_{s_x}$ MPa	ρ_y	$\overline{f}_{s_y}$ MPa		MPa	
PV4	1:0:0	.01056	242	.01056	242	.0025	26.6	D
PV10	1:0:0	.01785	266	.00999	276	.0027	14.5	DB
PV11	1:0:0	.01785	235	.01306	235	.0026	15.6	D
PV19	1:0:0	.01785	458	.00713	299	.00215	19.0	DB
PV21	1:0:0	.01785	458	.01296	302	.0018	19.5	DB
PV23	1:-0.39:-.39	.01785	518	.01785	518	.0020	20.5	B
PV25	1:-.69:-.69	.01785	466	.01785	466	.0018	19.2	B
PV27	1:0:0	.01785	442	.01785	442	.0019	20.5	B
PV29	1:0:0 1:-1:-1	.01785	441	.00885	324	.0018	21.7	DB (Non-proportional loading)

D - Both x and y direction reinforcement yielded at failure
DB - Y direction reinforcement yielded; X direction reinforcement not yielded, concrete crushing failure
B - Neither reinforcement layer yielded at failure; concrete crushing failure

Table 4.2 Finite Element Prediction of Panel Failure

Panel	Experimental		Finite Element Prediction[c]		Experimental Failure Load / Finite Element Prediction
	Failure Mode[a,b] (MPa)	Failure Load[b]	Failure Mode (MPa)	Failure Load	
PV4	D	2.89	D	2.60	1.11
PV10	DB	3.97	DB	4.00	0.99
PV11	D	3.56	D	3.60	0.99
PV19	DB	3.95	DB	4.45	0.89
PV21	DB	5.03	DB	5.20	0.97
PV23	B	8.87	B	7.60	1.17
PV25	B	9.12	B	7.70	1.18
PV27	B	6.35	B	6.25	1.02
PV29	B	5.87	DB	5.90	1.0
					Mean = 1.03 Coefficient of Variation = 9.53%

Notes:
a. D = Failure by steel yielding in both directions
   B = Failure by concrete crushing without steel yielding
   DB = Failure by concrete crushing after steel yielding in one direction.
b. Vecchio and Collins (1982)
c. For reinforcement ratio and concrete strengths, see Table 4.3.

Table 4.3 Failure Prediction Using Equilibrium Relationships Only

Panel	$\lvert f'_c \rvert$ (MPa)	$\lvert f_c \rvert$ (MPa)	$\frac{\rho_y \bar{f}_{s_y}}{\lvert f_c \rvert}$	Failure Mode (Experiment)	Experimental[b] Failure Load (MPa)	Prediction Using Equilibrium Relationships			Experimental[b] Failure Load / Least of Equilibrium Predictions	Correct Failure Mode Predicted?
						Eq. 4.13 (Eq. 4.16) D	Eq. 4.12 (Eq. 4.15) DB	Eq. 4.11 B		
PV4	26.6	14.63	0.175	D	2.89	2.56	N.A.[a]	7.32	1.13	Yes
PV6	29.8	16.39	0.290	D	4.75	4.75	N.A.	8.20	1.00	Yes
PV10	14.5	7.98	0.346	DB	3.97	3.69	3.79	3.99	1.08	No
PV11	15.6	8.58	0.359	D	3.56	3.59	4.11	4.29	0.99	Yes
PV12	16.0	8.80	0.138	DB	2.98	3.17	3.02	4.40	0.99	Yes
PV16	21.7	11.94	0.158	D	1.89	1.89	N.A.	5.97	1.00	Yes
PV18	19.5	10.73	0.123	DB	3.28	3.16	3.50	5.36	1.04	No
PV19	19.0	10.45	0.203	DB	3.95	4.17	4.22	5.22	0.95	No
PV20	19.6	10.78	0.245	DB	4.49	4.65	4.63	5.39	0.97	Yes
PV21	19.5	10.73	0.366	DB	5.03	5.66	5.16	5.36	0.98	Yes
PV22	19.6	10.78	0.592	B	6.18	7.23	5.29	5.39	1.17	No
PV23	20.5	12.30	0.752	B	8.87	15.16	N.A.	6.15	1.44	Yes
PV25	19.2	13.02	0.639	B	9.12	26.83	N.A.	6.51	1.40	Yes
PV27	20.5	11.28	0.701	B	6.35	7.89	N.A.	5.64	1.13	Yes

Notes: a. N.A. - Not Applicable since reinforcement is same in both directions.
b. Experimental results from Vecchio and Collins (1982).

Table 4.4 Material Properties for Leonhardt-Walther Deep Beam WT3

Elements	f'_c MPa	E_c MPa	f'_t MPa	f_y MPa	ρ_x	ρ_y	ε_{ut}
1 to 40	30.0	27000	3.0	240	.0017	.0017	0.0019
41, 46	40.0	27000	4.0	428	.0179	.0017	Fig. 4.31b
42 to 45 47 to 50	30.0	27000	3.0	428	.0179	.0017	Fig. 4.31b

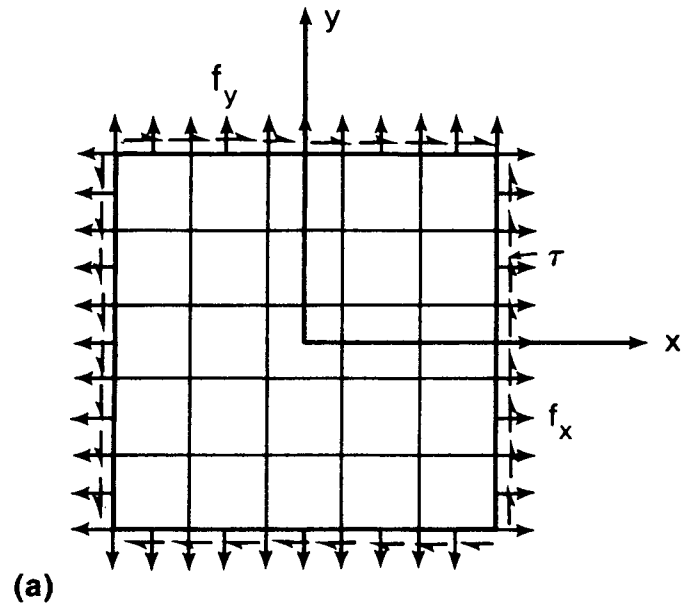

(a)

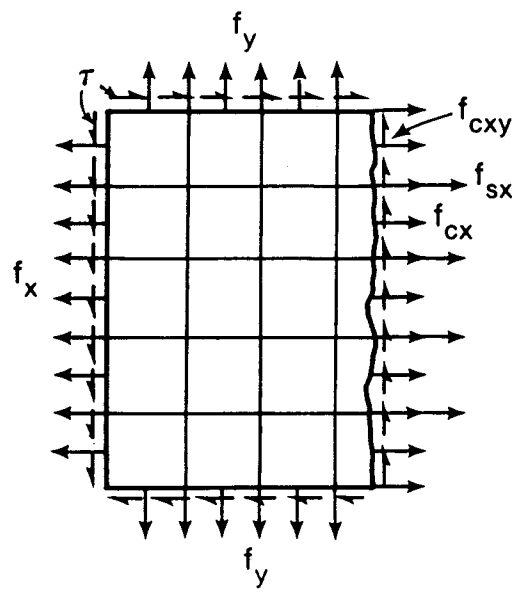

(b)

FIG. 4.1. Orthogonally Reinforced Panel
(a) Subjected to Biaxial Normal and Shear Stress;
(b) Free-body Diagram of a Panel Segment

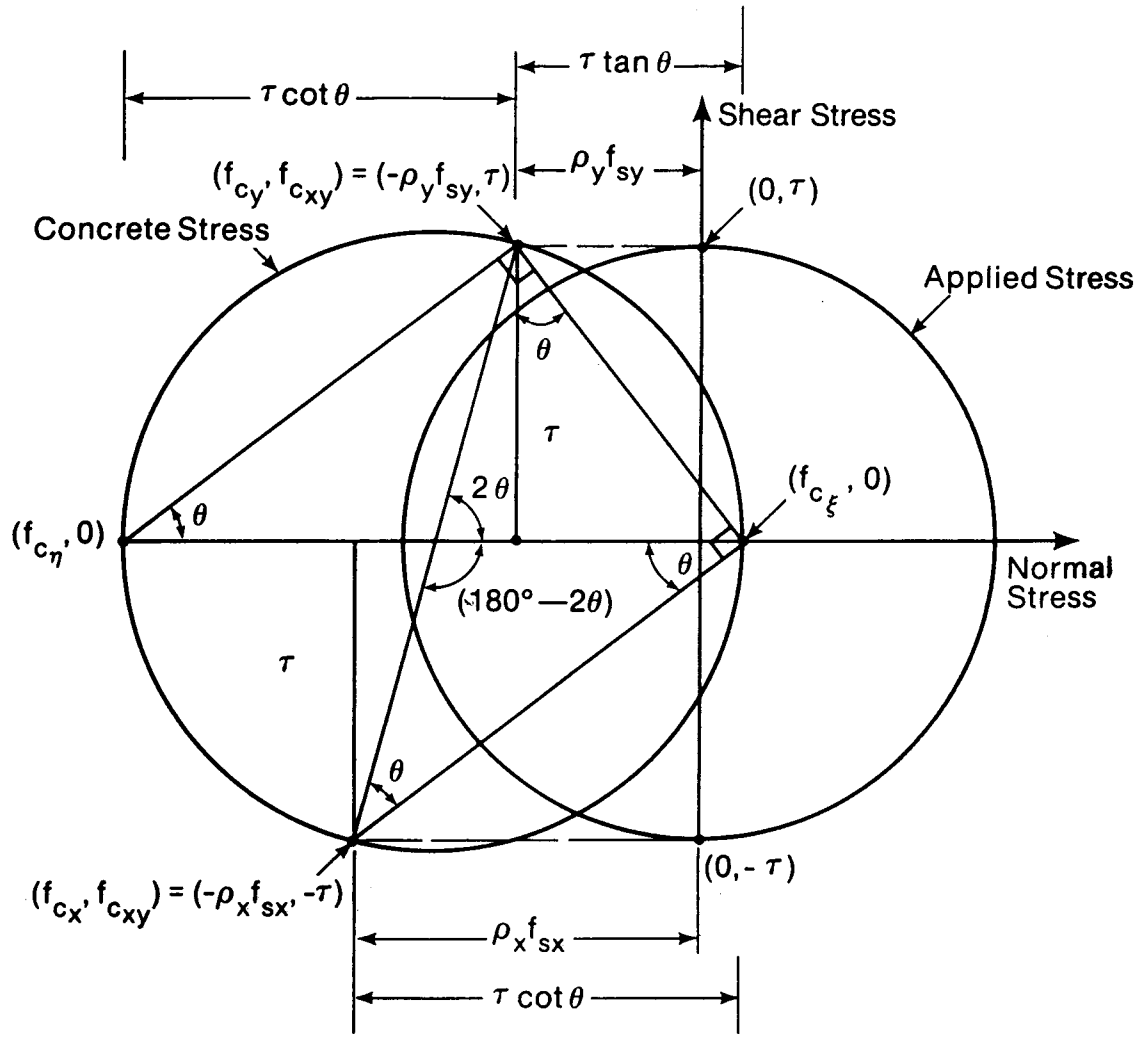

FIG. 4.2. (a) Mohr's Circles of Stress for Orthogonally Reinforced Element Subjected to Pure Shear

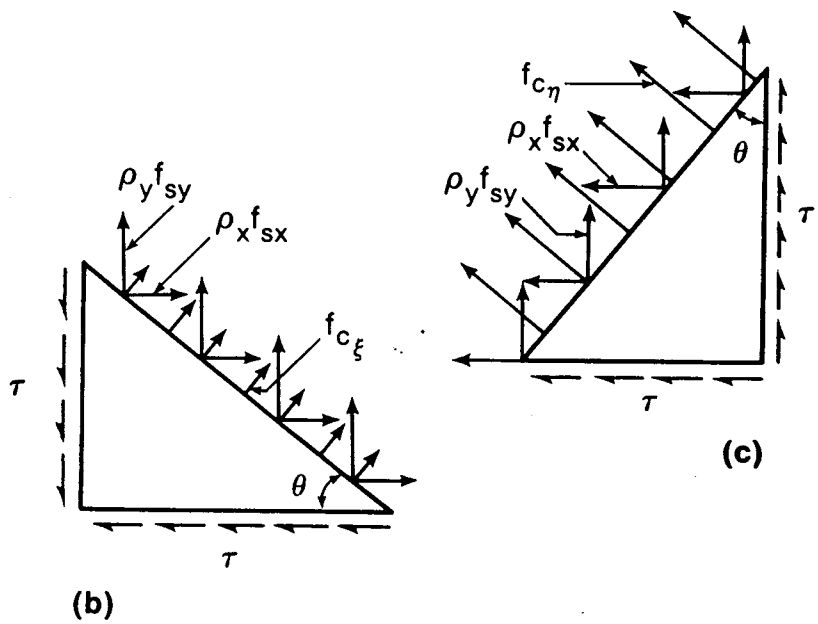

FIG. 4.2. (b) Stresses on Major Plane (c) Stresses on Minor Principal Plane

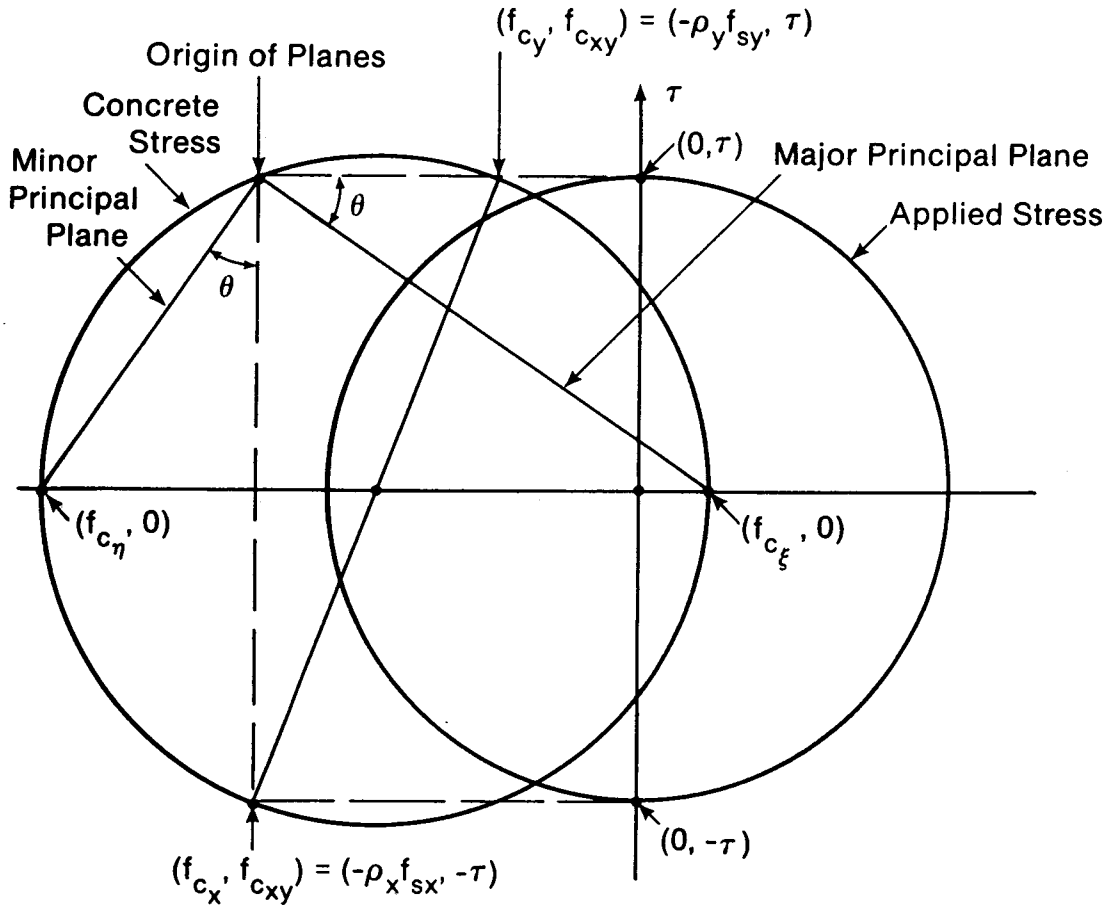

FIG. 4.2. (d) Culmann Diagram for Stress in an Orthogonally Reinforced Element Subjected to Pure Shear

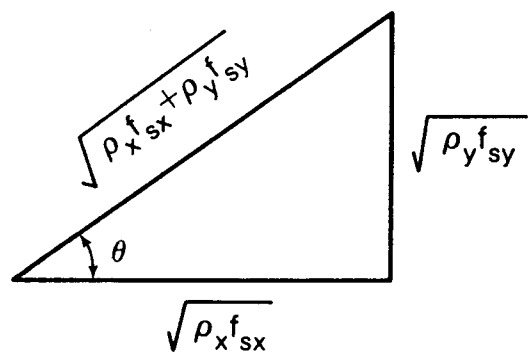

FIG. 4.3. Geometric Interpretation of Equation 4.7a

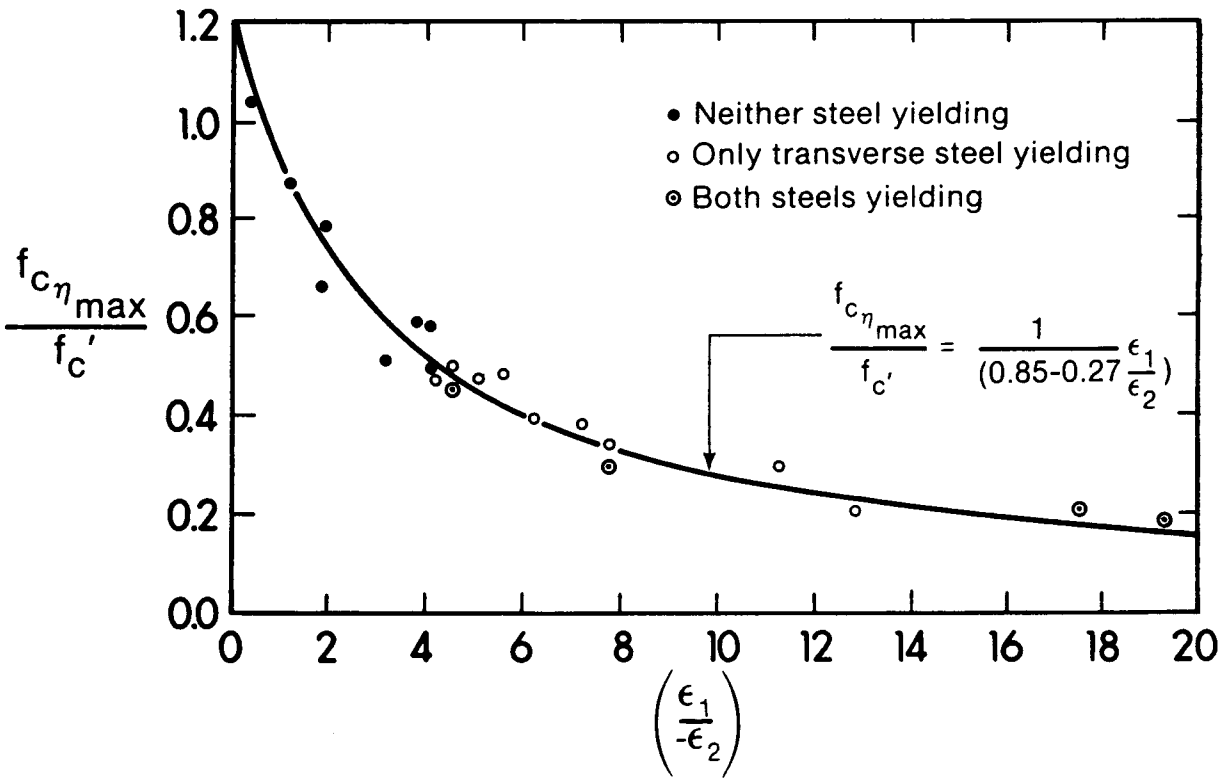

FIG. 4.4. Peak Principal Compressive Stresses Versus the Corresponding Strain Ratios (Adapted from Vecchio and Collins, 1982)

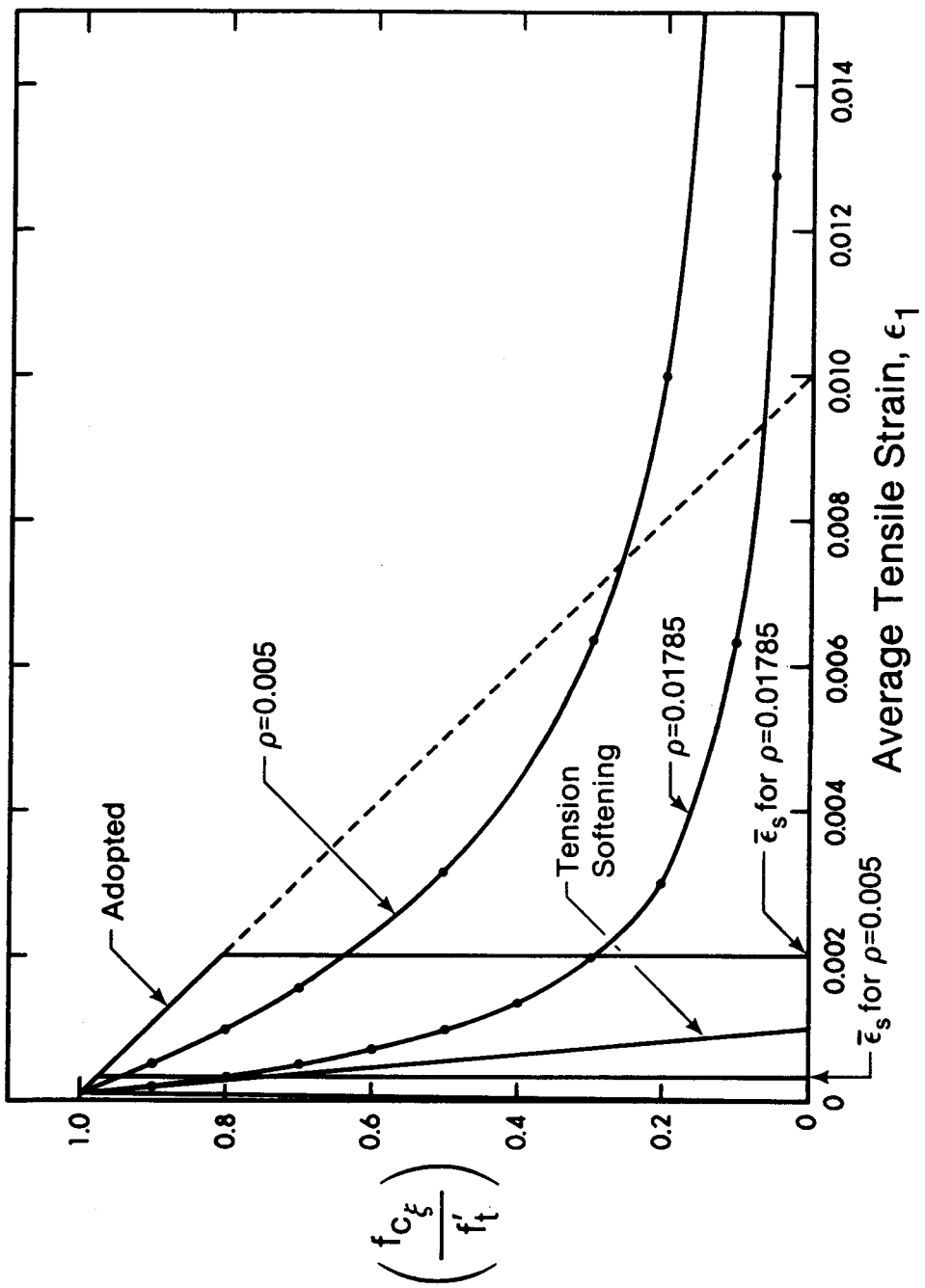

FIG. 4.5. Principal Tensile Stress-Strain Relationships
(a) Tension Stiffening Relationships

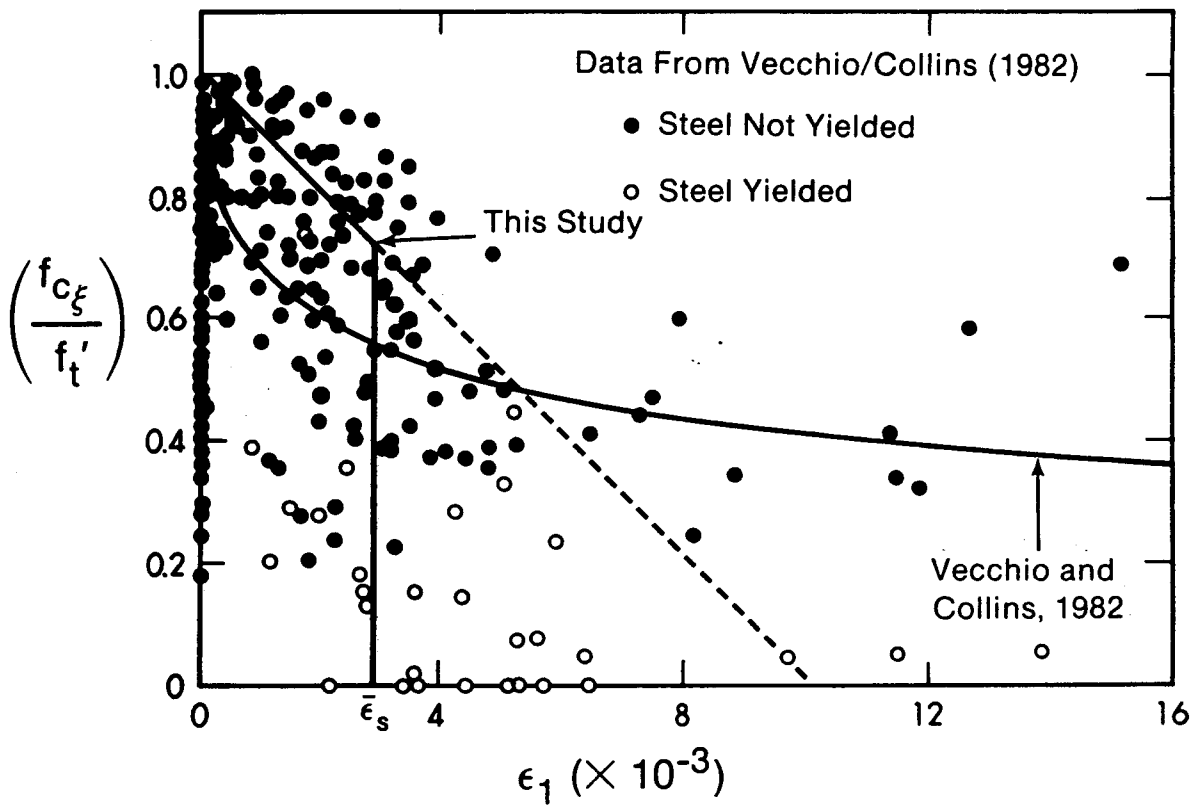

FIG. 4.5. Principal Tensile Stress-Strain Relationship (Contd.)
(b) Comparison with Test Data of Vecchio/Collins (1982)

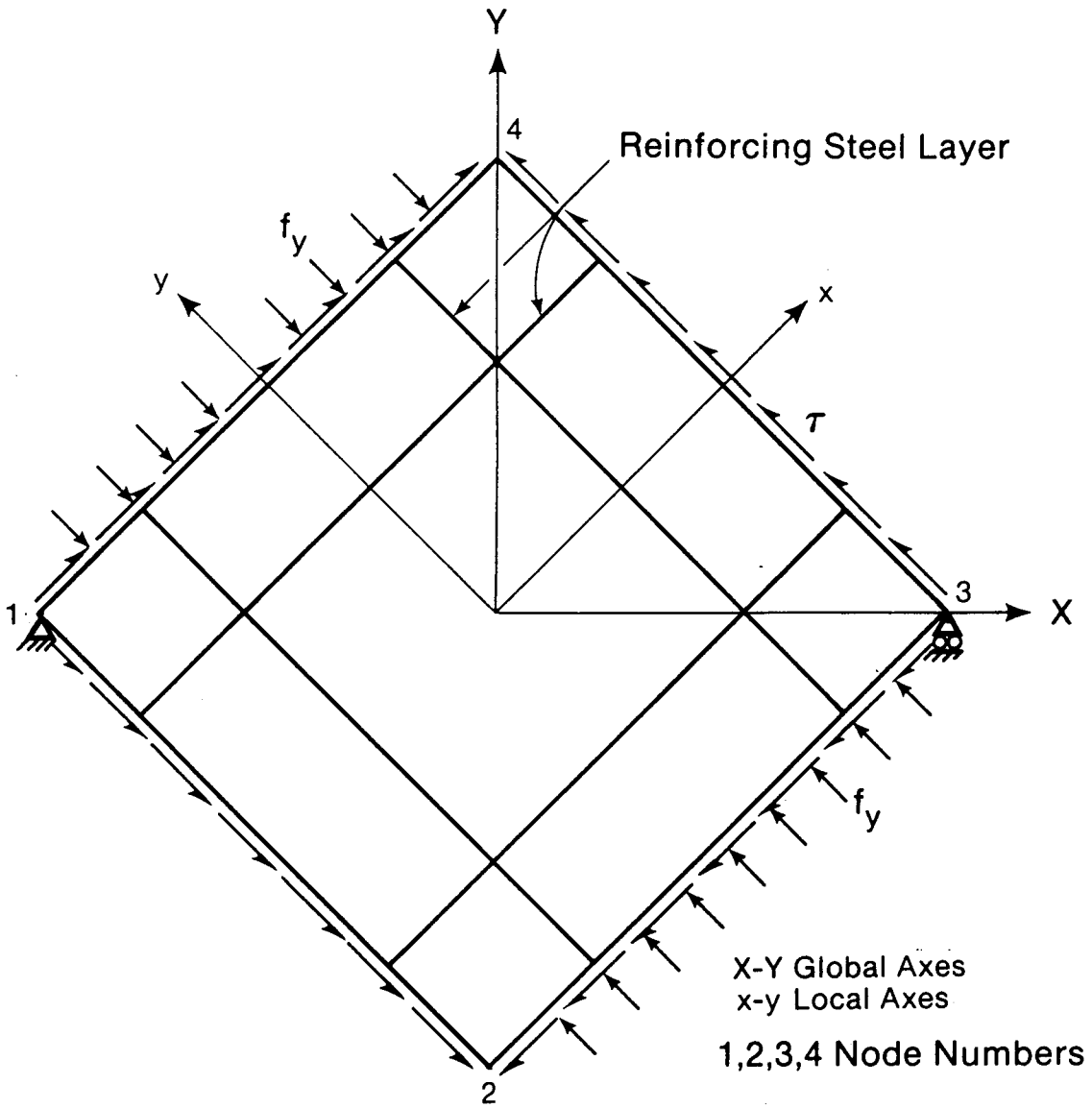

FIG. 4.6. Finite Element Model of an Orthogonally Reinforced Panel

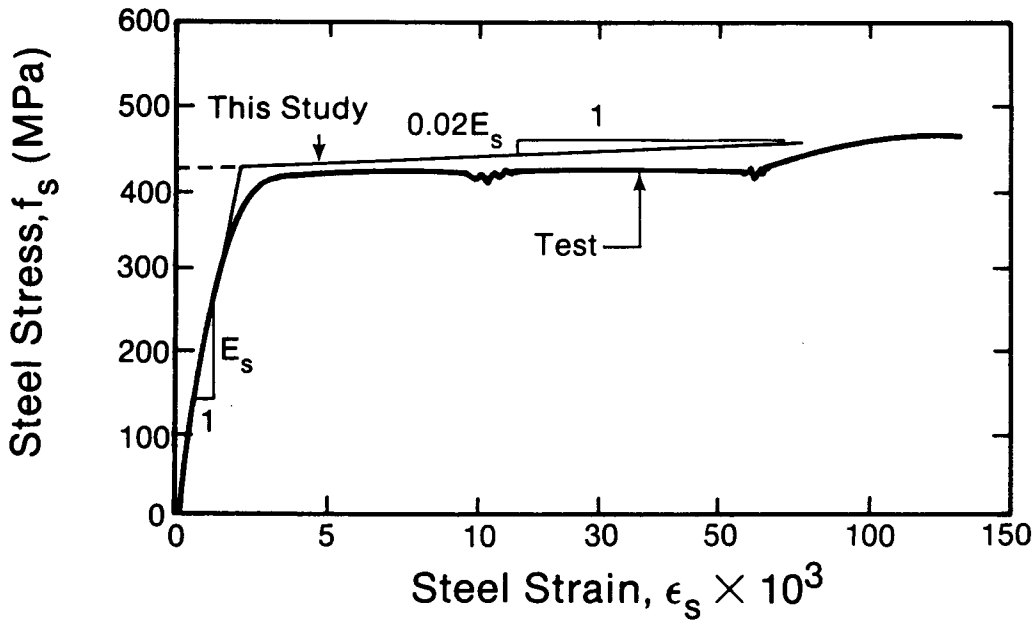

FIG. 4.7. Stress-Strain Relationship for Welded Wire Mesh

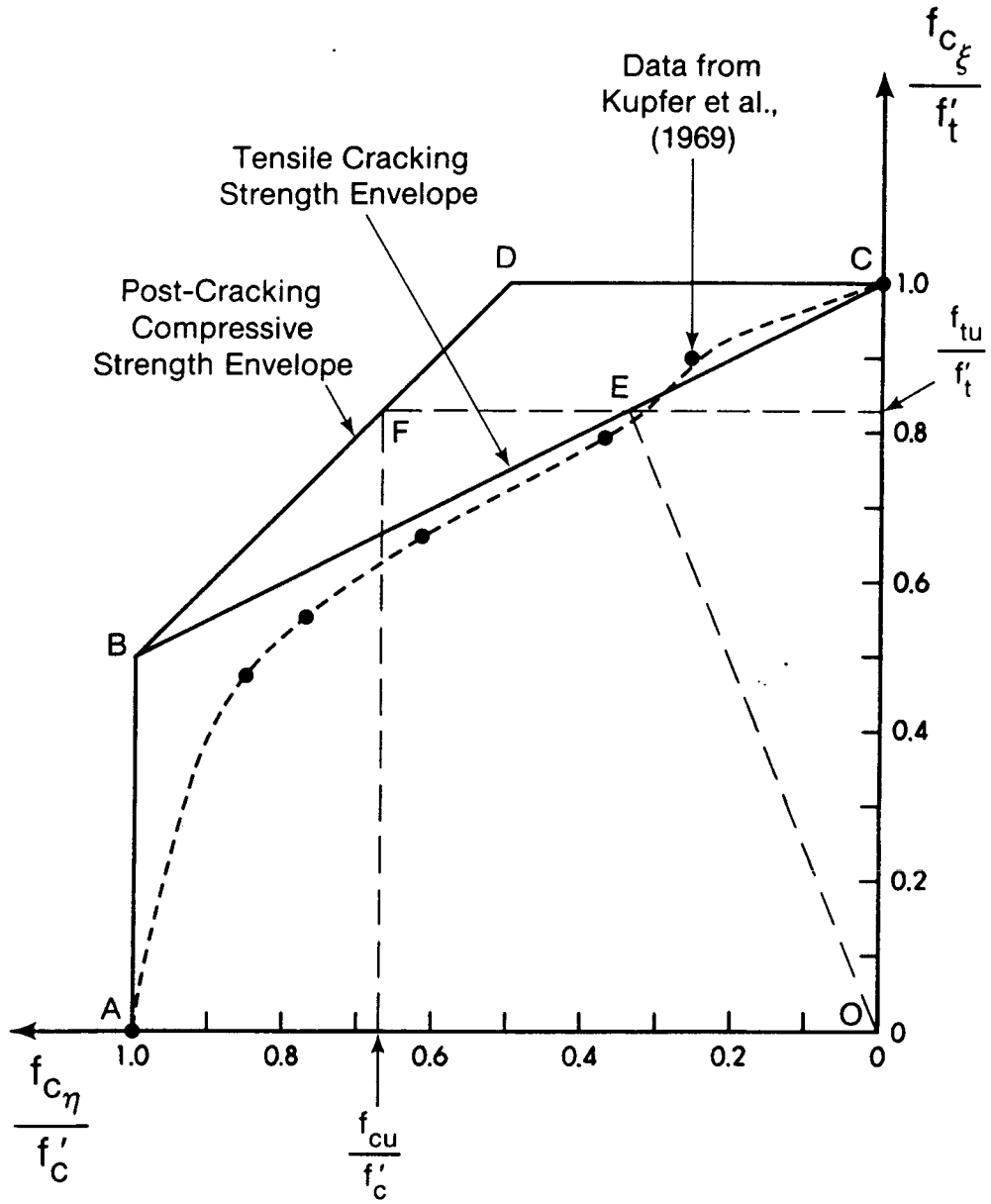

FIG. 4.8. Strength Envelope in the Tension-Compression Region. Used for Orthogonally Reinforced Elements.

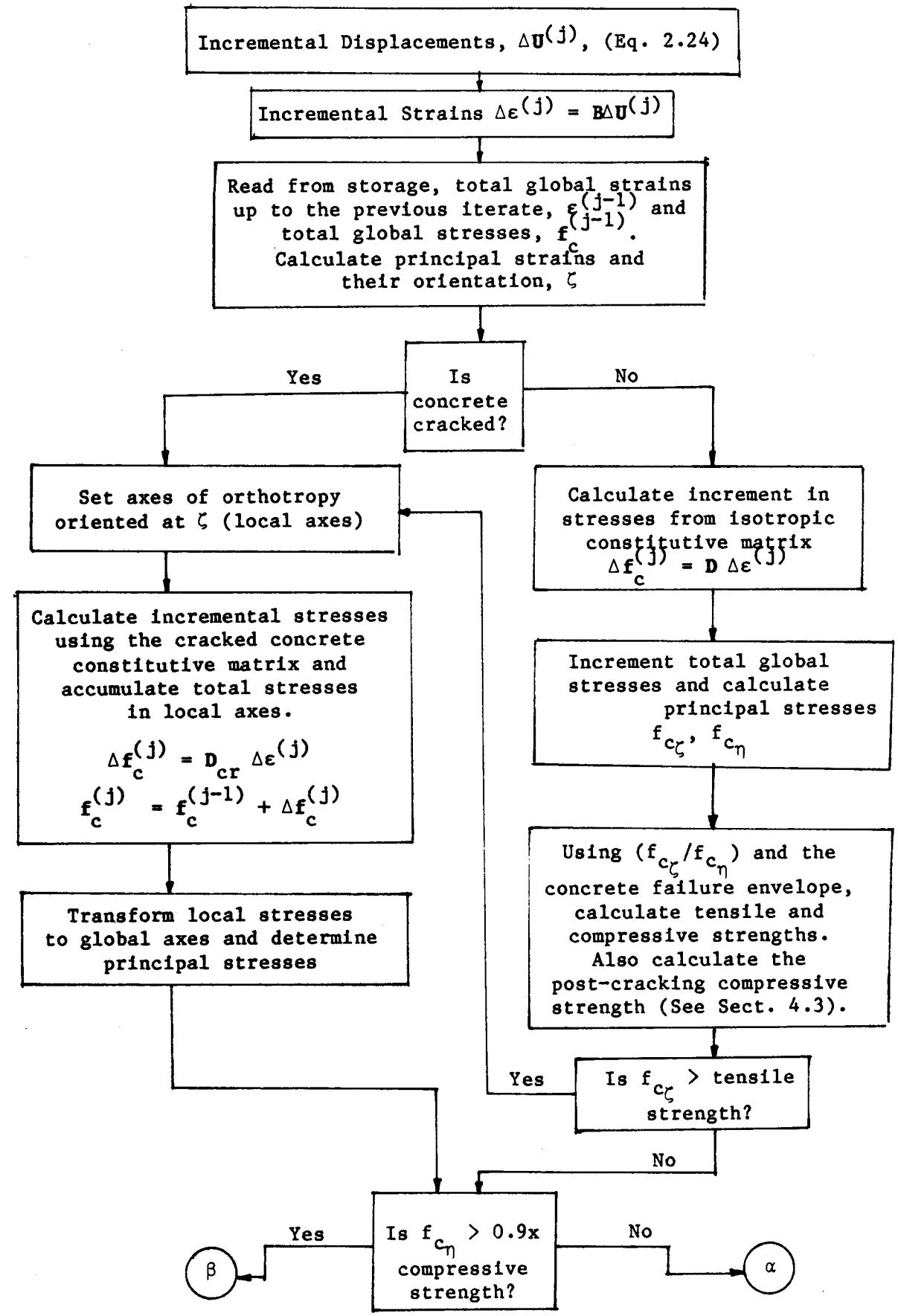
Incremental Displacements, $\Delta U^{(j)}$, (Eq. 2.24)
Incremental Strains $\Delta\varepsilon^{(j)} = B\Delta U^{(j)}$
Read from storage, total global strains up to the previous iterate, $\varepsilon^{(j-1)}$ and total global stresses, $f_c^{(j-1)}$. Calculate principal strains and their orientation, ζ
Is concrete cracked?
Yes
No
Set axes of orthotropy oriented at ζ (local axes)
Calculate incremental stresses using the cracked concrete constitutive matrix and accumulate total stresses in local axes.
$\Delta f_c^{(j)} = D_{cr}\,\Delta\varepsilon^{(j)}$
$f_c^{(j)} = f_c^{(j-1)} + \Delta f_c^{(j)}$
Transform local stresses to global axes and determine principal stresses
Calculate increment in stresses from isotropic constitutive matrix
$\Delta f_c^{(j)} = D\,\Delta\varepsilon^{(j)}$
Increment total global stresses and calculate principal stresses f_{c_ζ}, f_{c_η}
Using (f_{c_ζ}/f_{c_η}) and the concrete failure envelope, calculate tensile and compressive strengths. Also calculate the post-cracking compressive strength (See Sect. 4.3).
Is f_{c_ζ} > tensile strength?
Yes
No
Is f_{c_η} > 0.9x compressive strength?
Yes
No
β
α

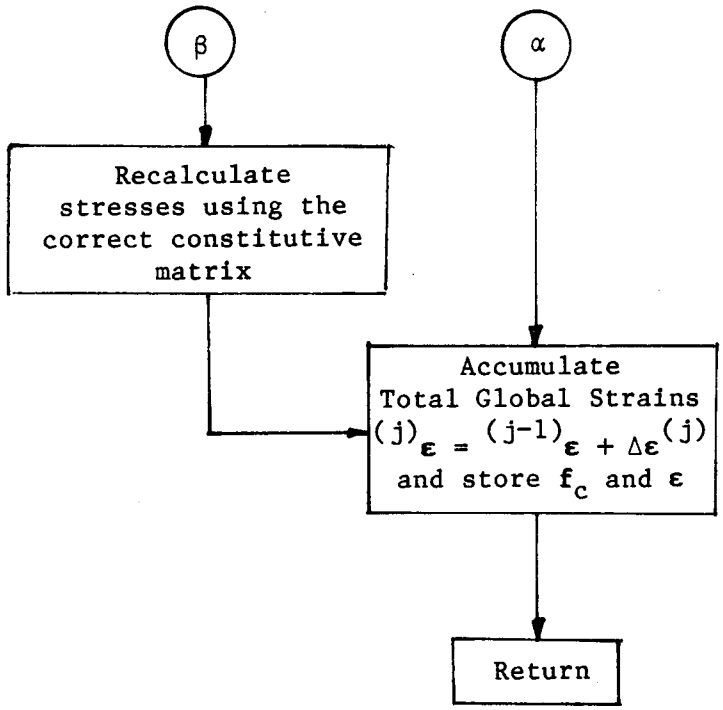

Fig. 4.9 Flow Diagram of Stress Calculation for Rotating Crack Model

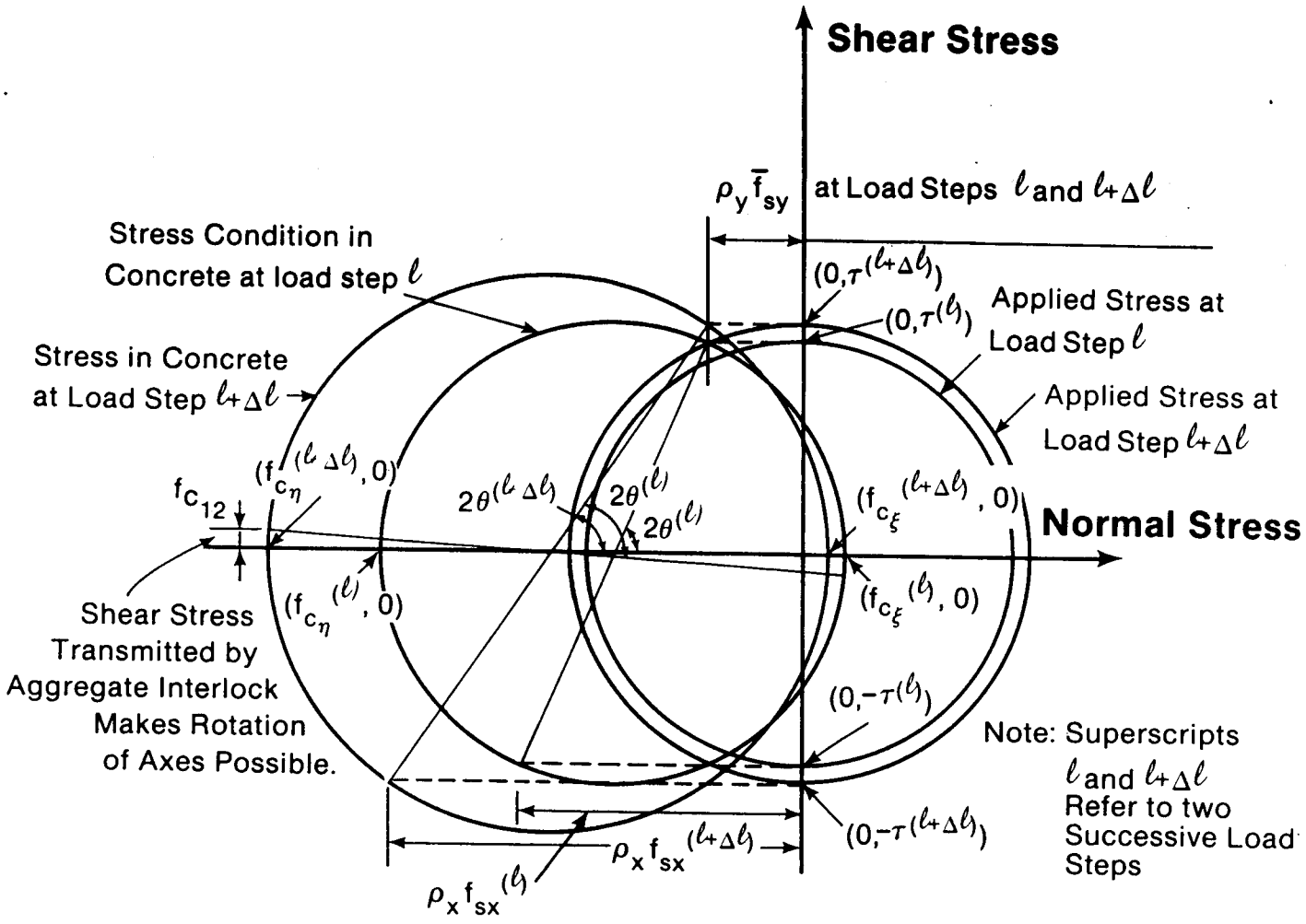

FIG. 4.10. Rotation of Principal Axes ('Rotating Cracks')

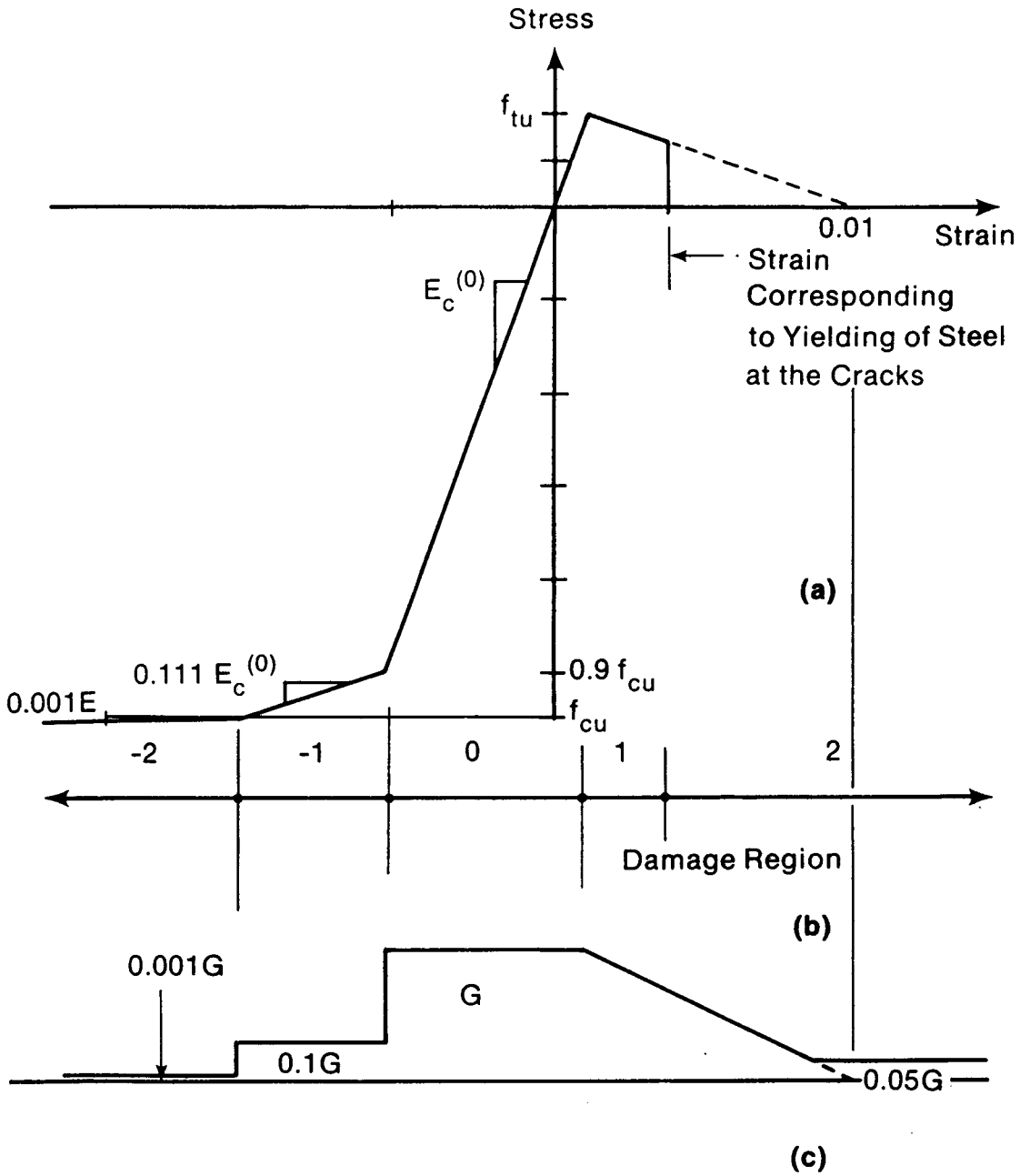

FIG. 4.11. Stress-Strain Curves for the Investigation of Vecchio/Collins Panels; (a) Normal Stress-Strain Curve; (b) Damage Regions and (c) Shear Moduli

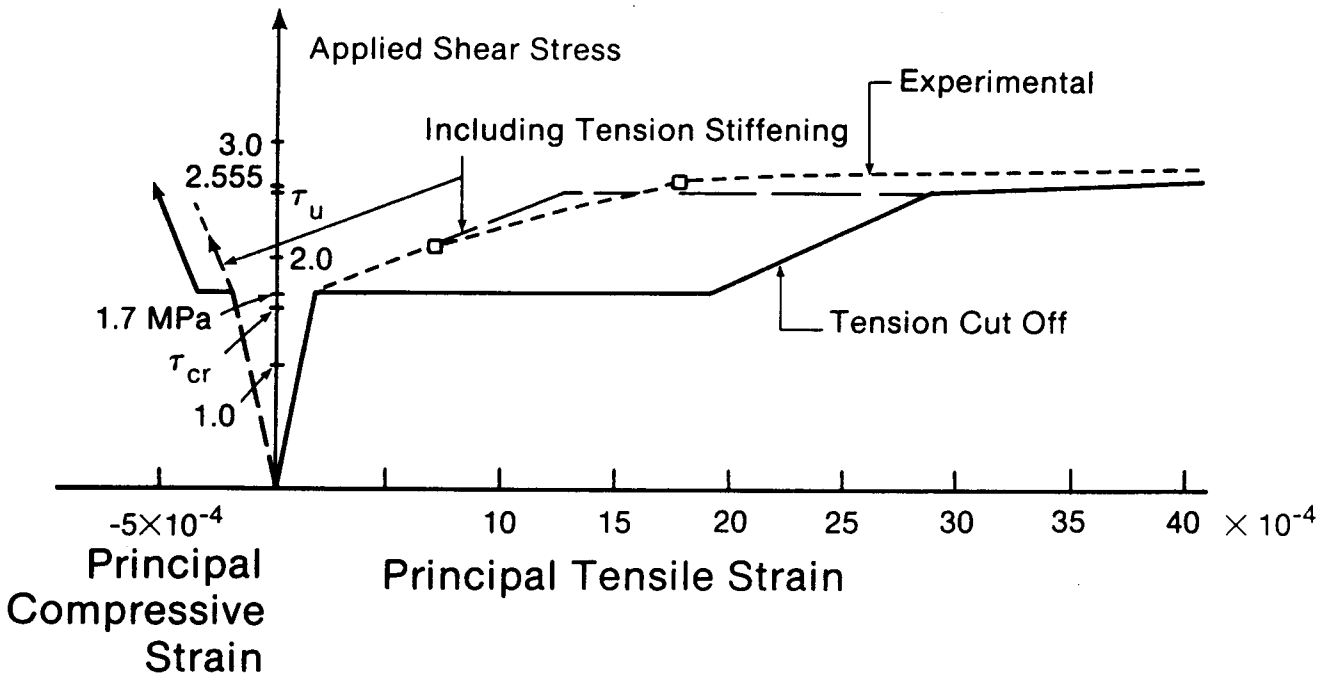

FIG. 4.12. Applied Shear Stress Versus Strain Relationships for Panel PV4; (a) Principal Strains

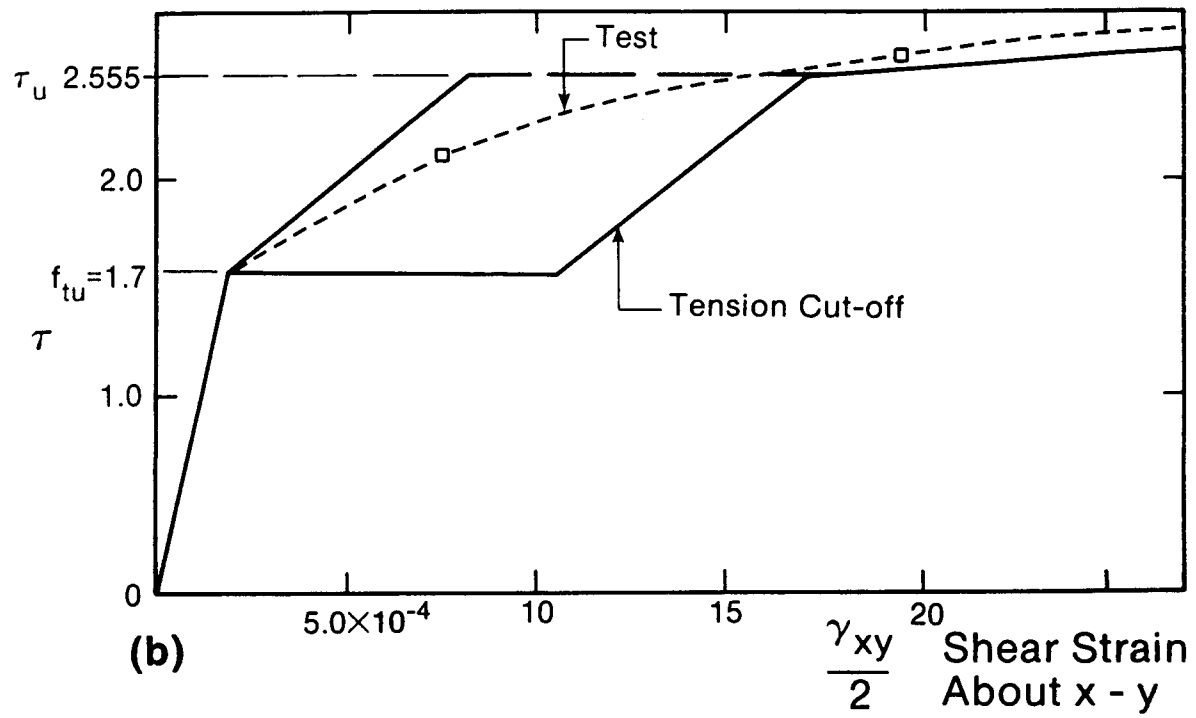

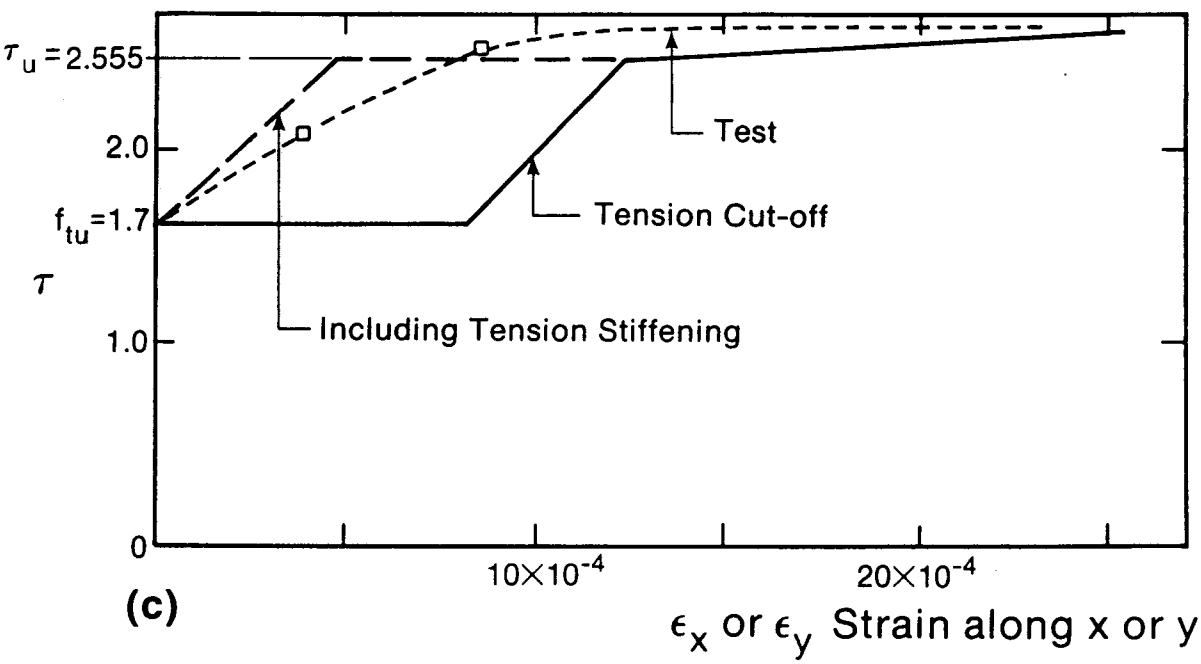

FIG. 4.12. (Continued) (b) Shear Strains; (c) Normal Strains

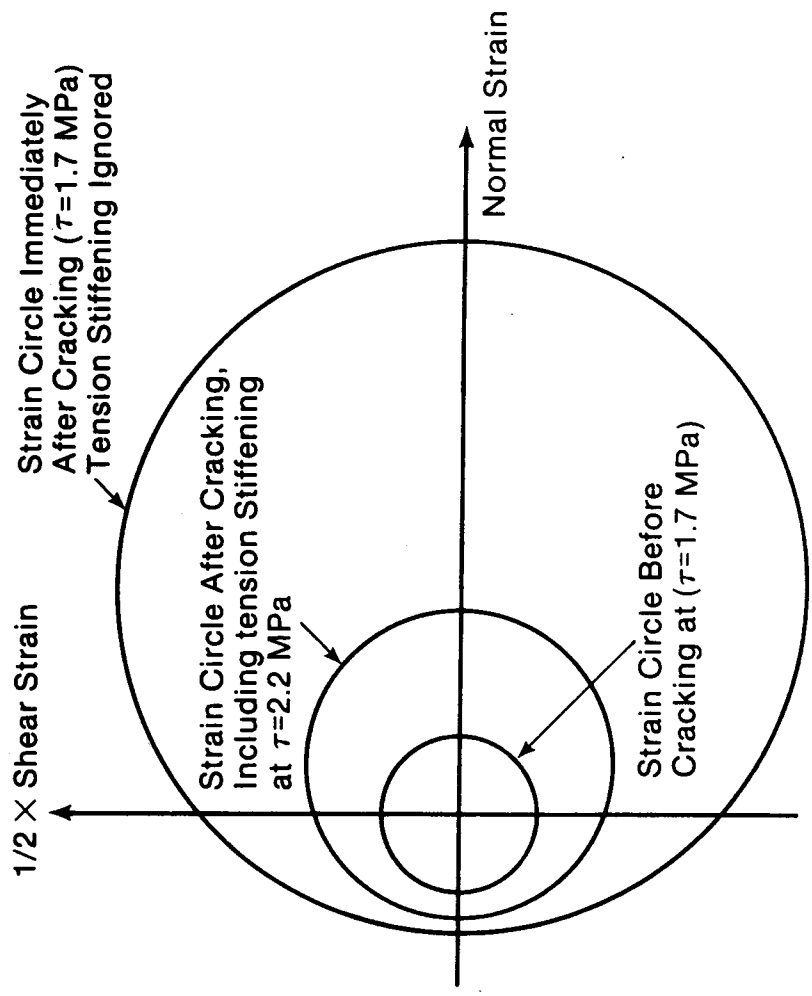

FIG. 4.13. Mohr's Circles of Strain for Panel PV4 Subjected to Pure Shear

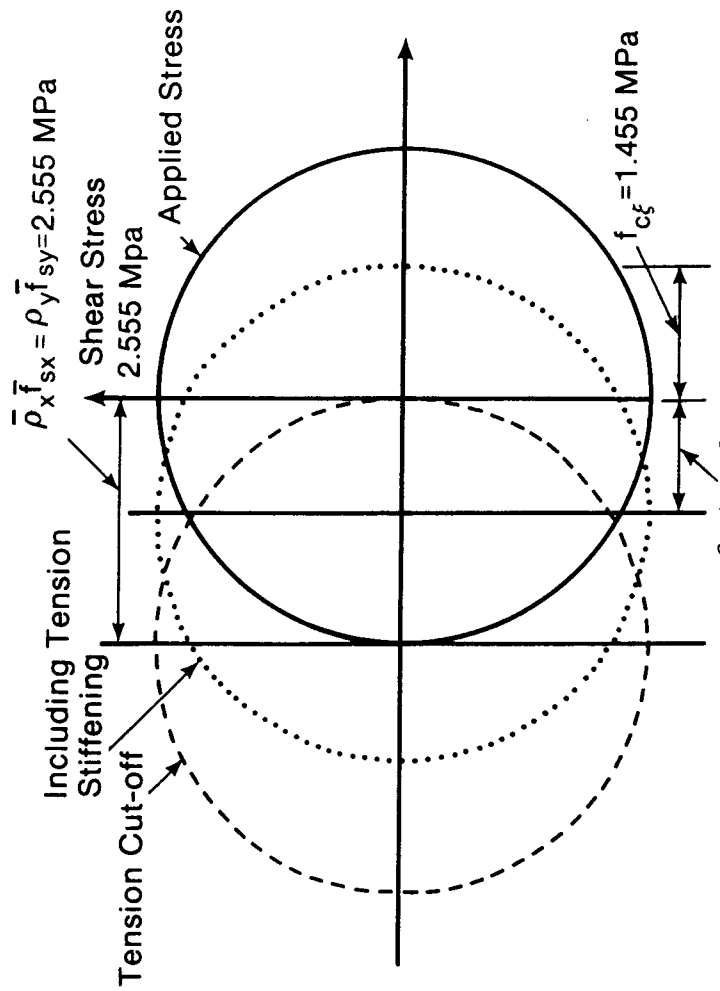

FIG. 4.14. Mohr's Circles of Stress for Panel PV4 Immediately Prior to Steel Yielding

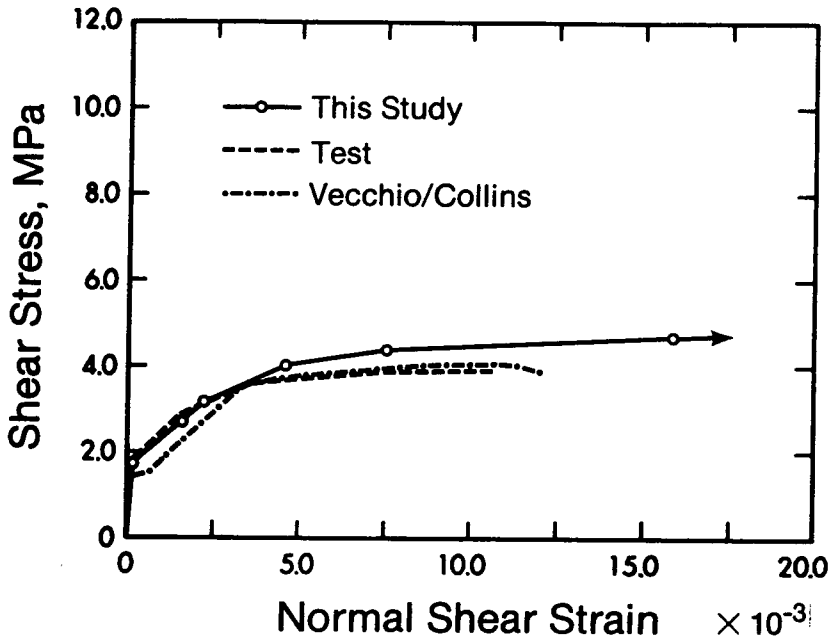

FIG. 4.15. Panel PV19 - Applied Shear Stress vs Strain
(a) Applied Shear Stress vs Shear Strain

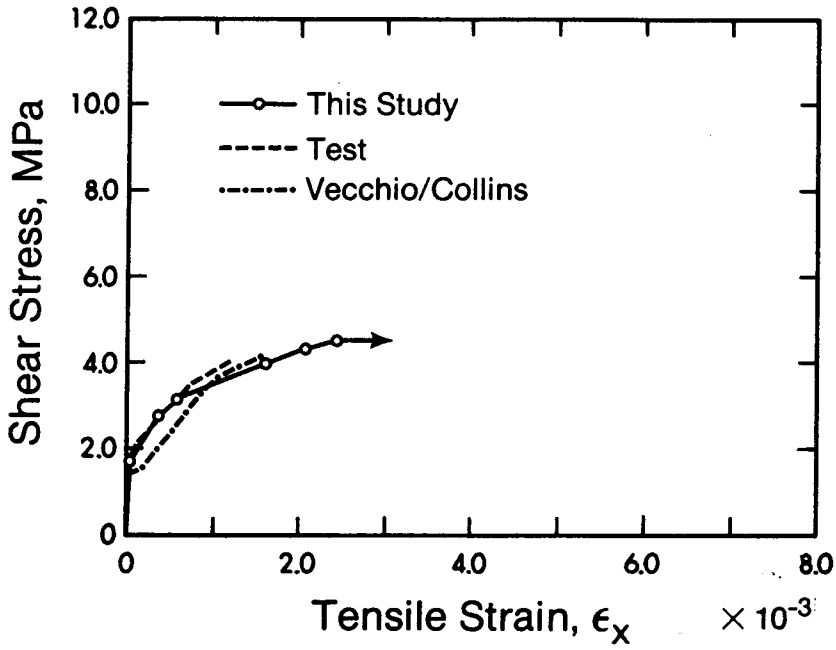

FIG. 4.15. (Continued)
(b) Applied Shear Stress vs Normal Strain ε_x

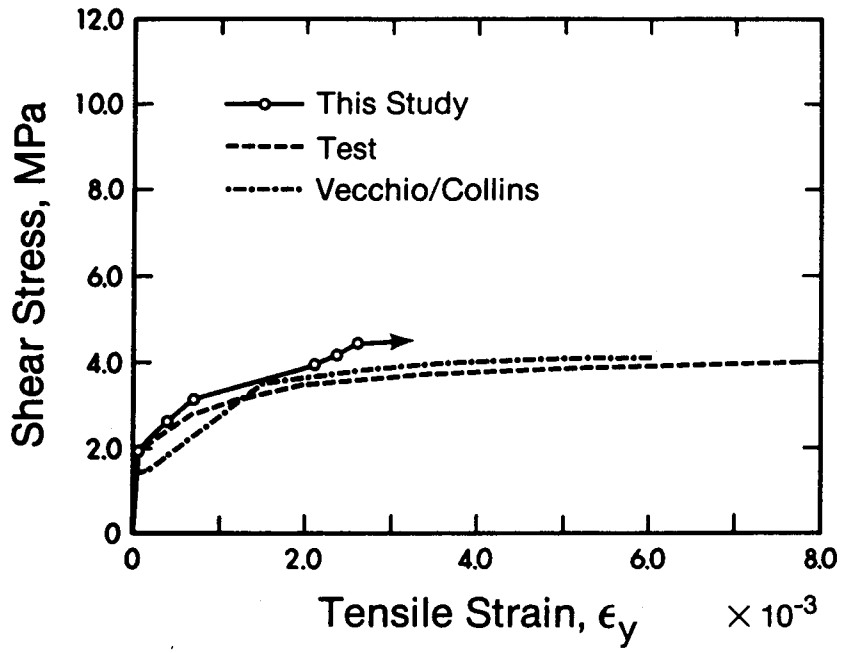

FIG. 4.15. (Continued)
(b) Applied Shear Stress vs Normal Strain ε_y

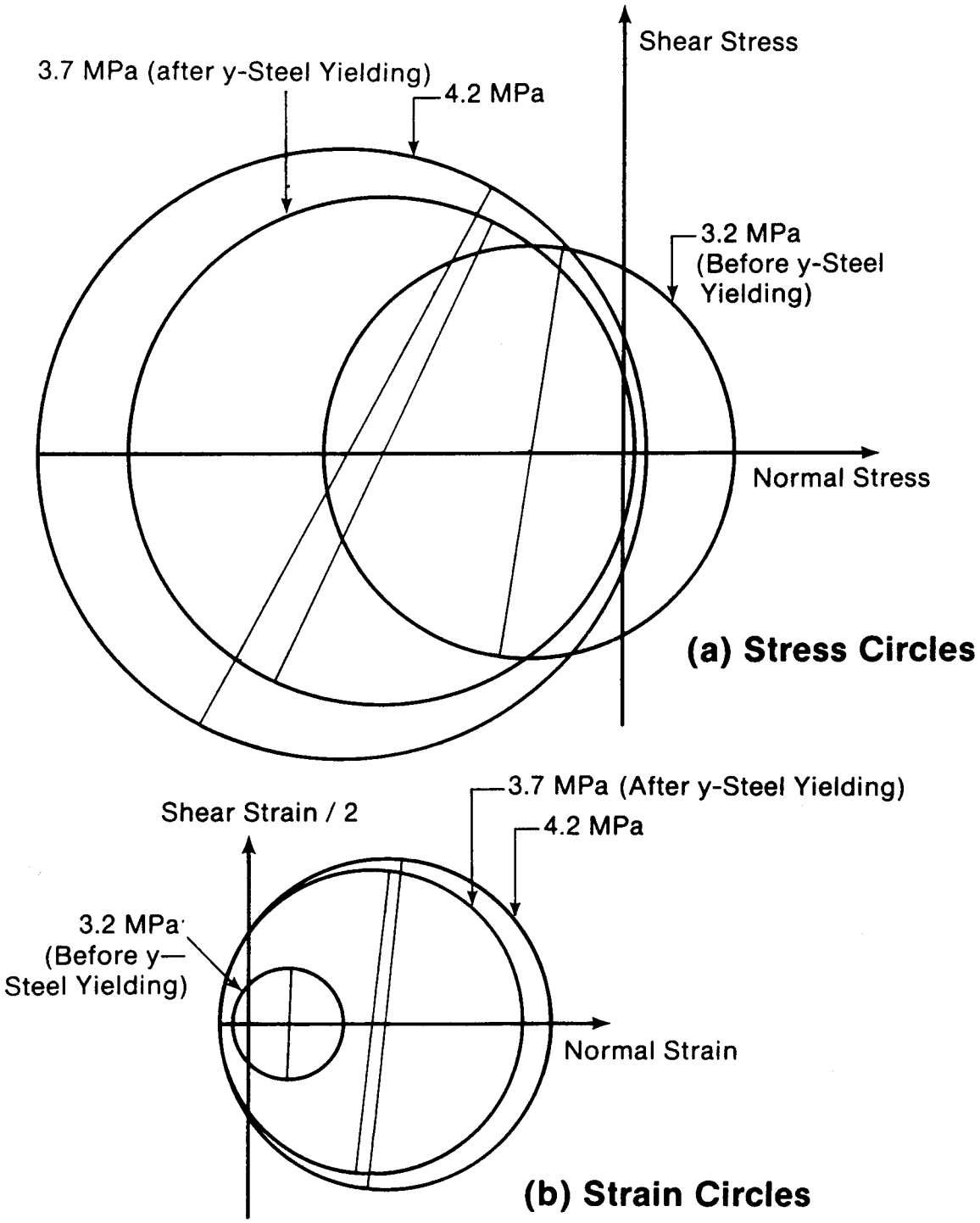

FIG. 4.16. Mohr's Circles of Stress and Strain for Panel PV19

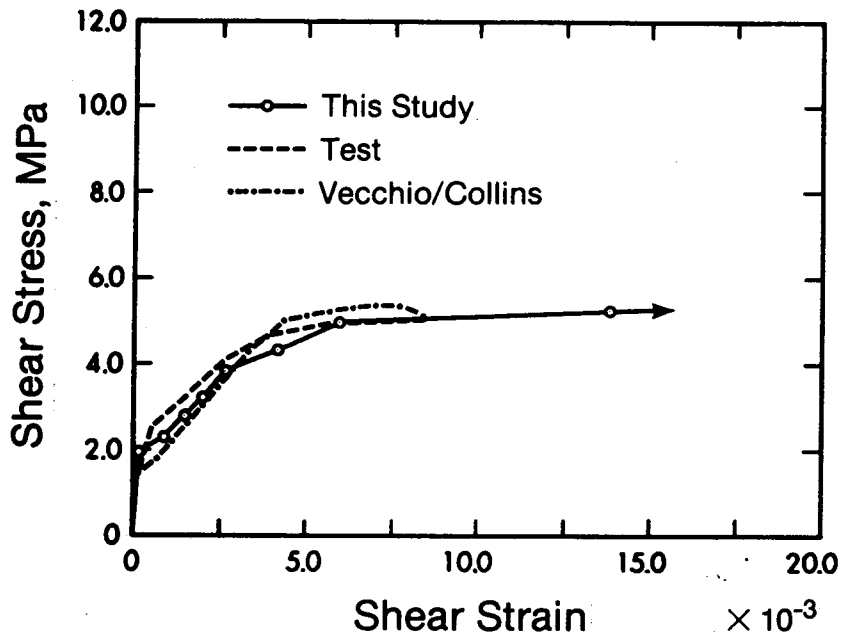

FIG. 4.17. Panel PV21 - Applied Shear Stress vs Shear Strain

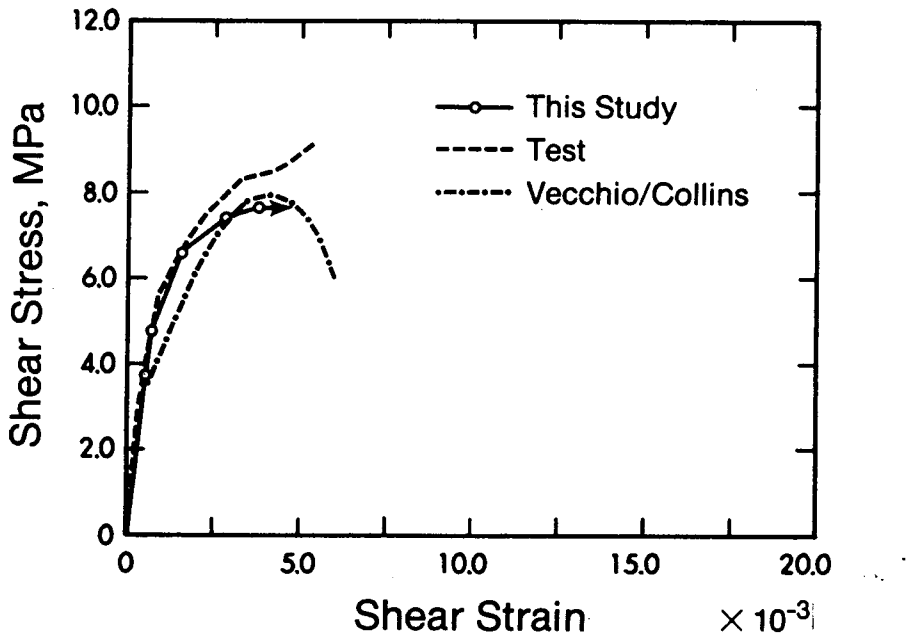

FIG. 4.18. Panel PV25 - Applied Shear Stress vs Strain
(a) Applied Shear Stress vs Shear Strain

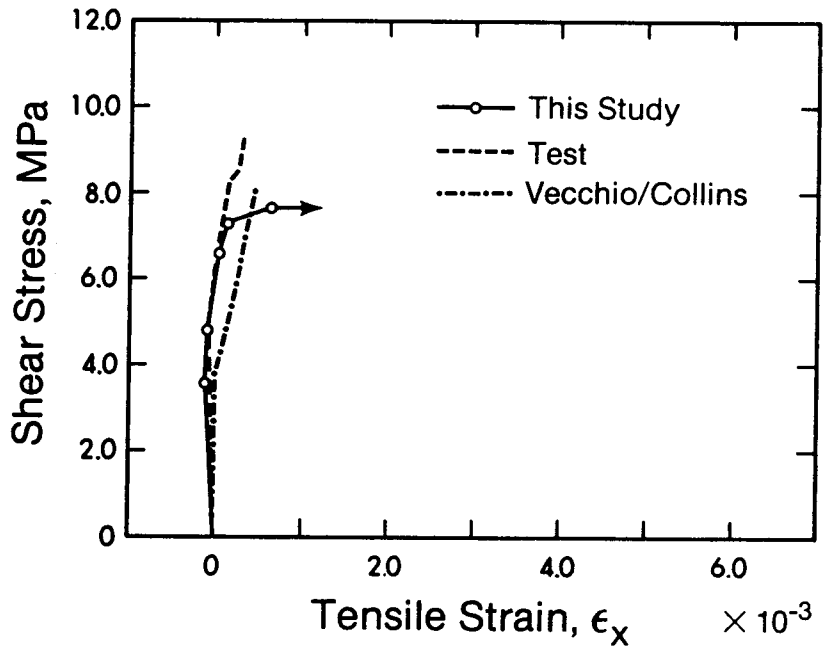

FIG. 4.18. (Continued)
(b) Applied Shear Stress vs Normal Strain ε_x

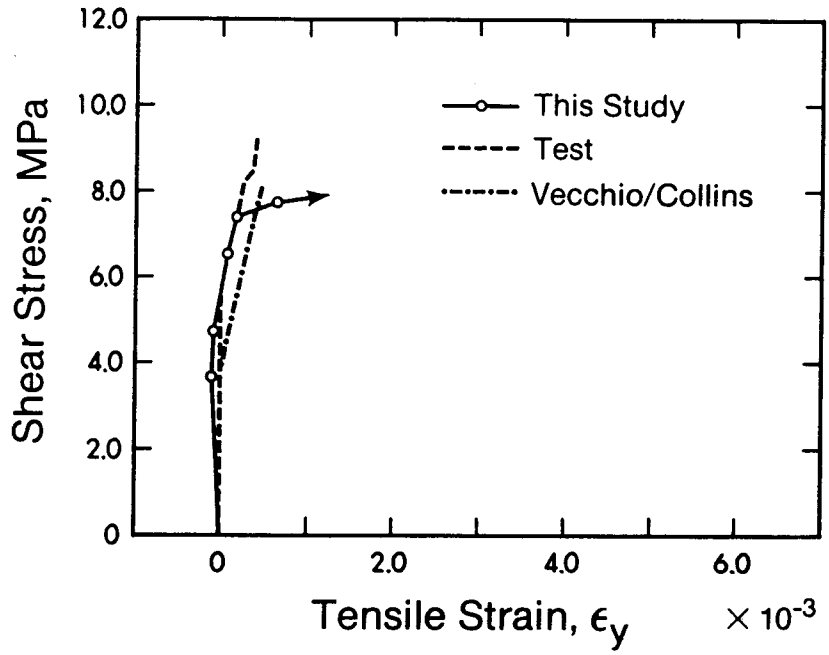

FIG. 4.18. (Continued)
(c) Applied Shear Stress vs Normal Strain ϵ_y

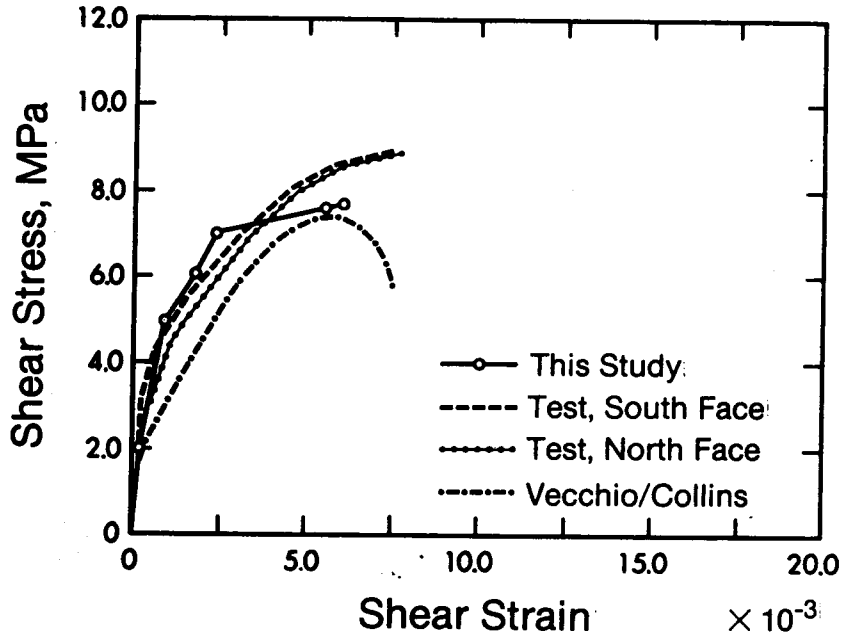

FIG. 4.19. Panel PV23 - Applied Shear Stress vs Shear Strain

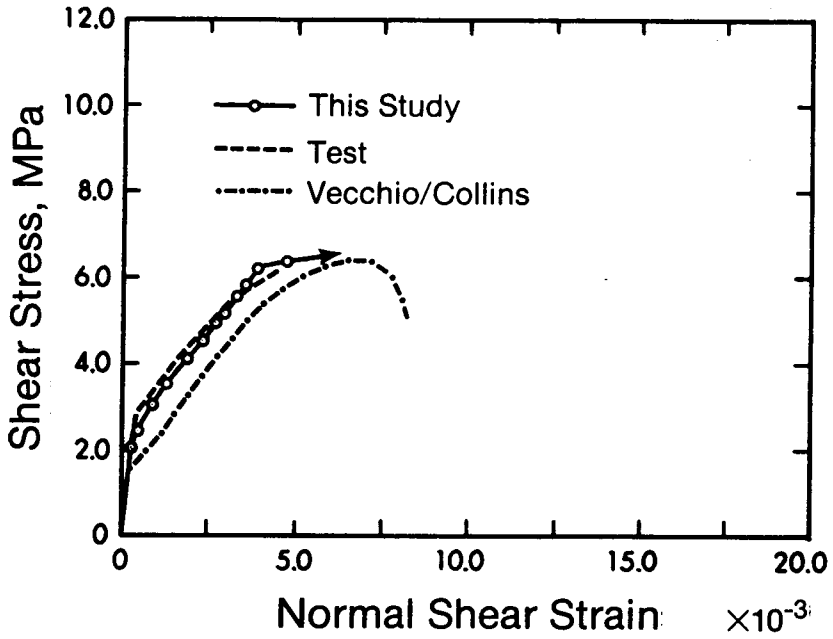

FIG. 4.20. Panel PV27 - Applied Shear Stress vs Strain
(a) Applied Shear Stress vs Shear Strain

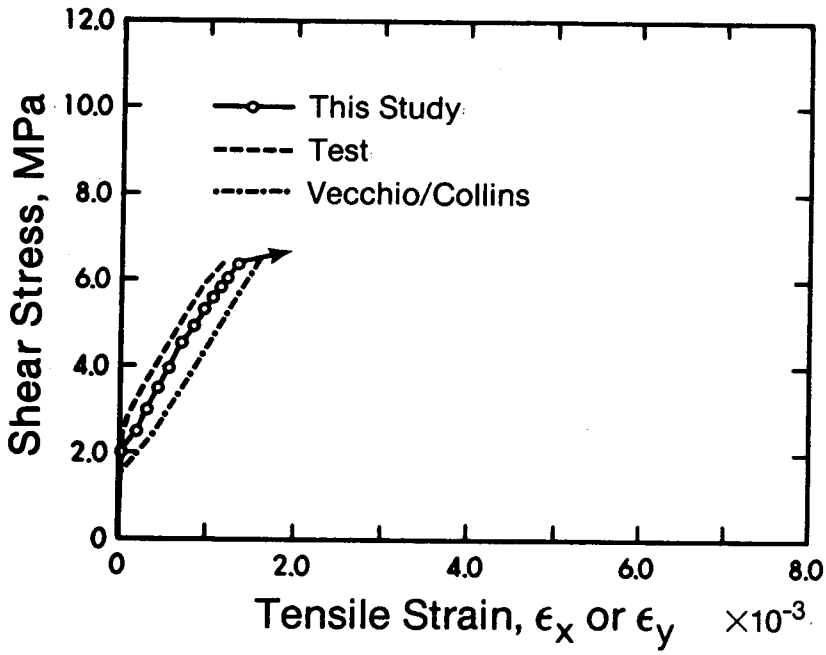

FIG. 4.20. (Continued)
(b) Applied Shear Stress vs Normal Strain ε_x or ε_y

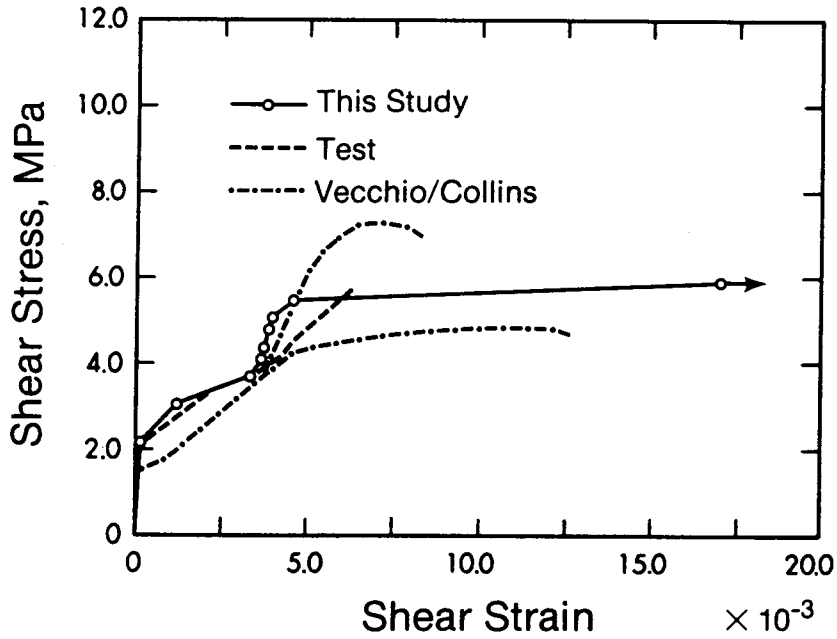

FIG. 4.21. Panel PV29 - Applied Shear Stress vs Strain
(a) Applied Shear Stress vs Shear Strain

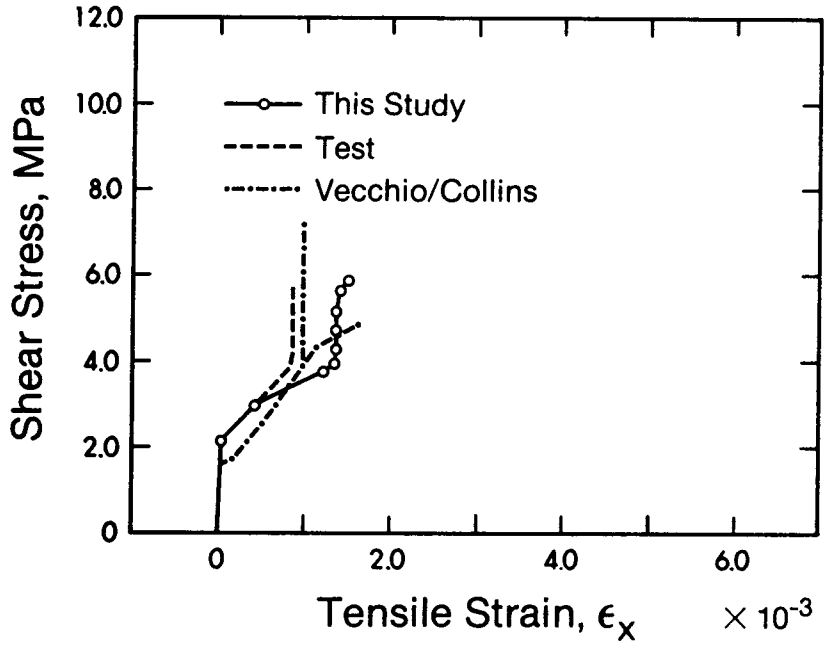

FIG. 4.21. (Continued)
(b) Applied Shear Stress vs Normal Strain ϵ_x

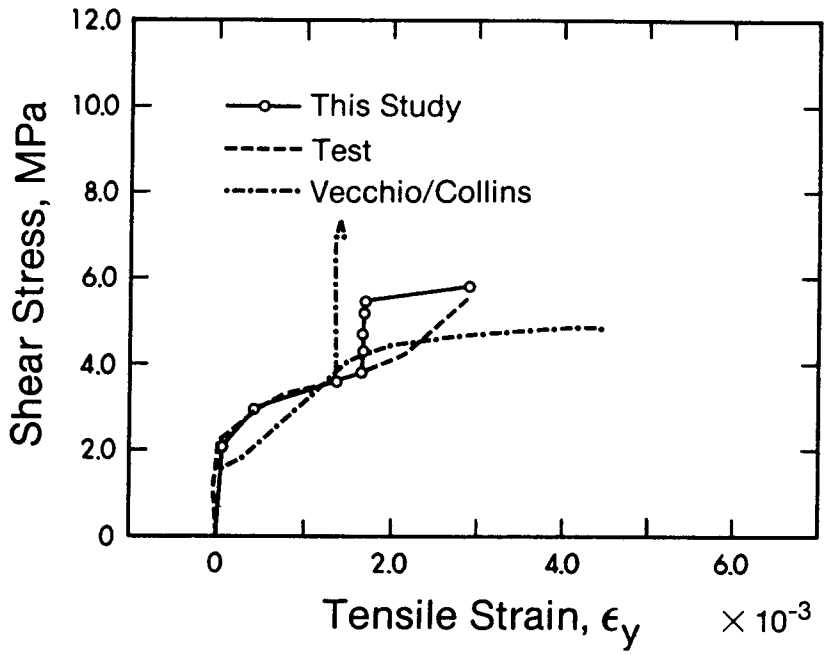

FIG. 4.21. (Continued)
(c) Applied Shear Stress vs Normal Strain ϵ_y

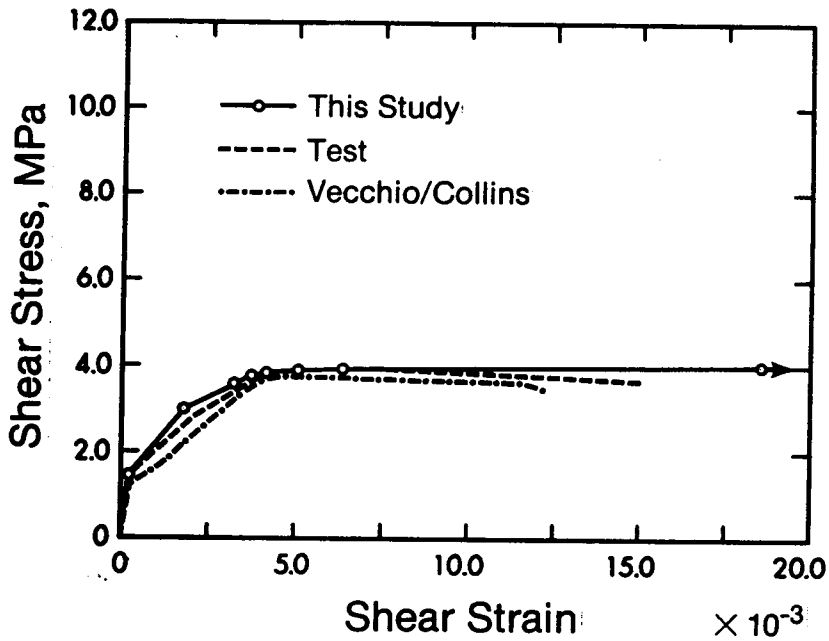

FIG. 4.22. Panel PV10 - Applied Shear Stress vs Shear Strain

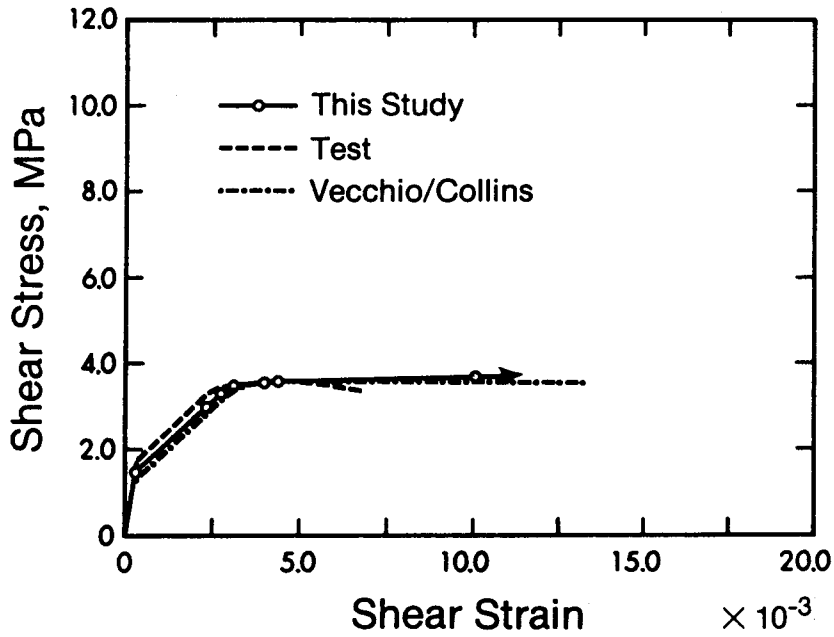

FIG. 4.23. Panel PV11 - Applied Shear Stress vs Shear Strain

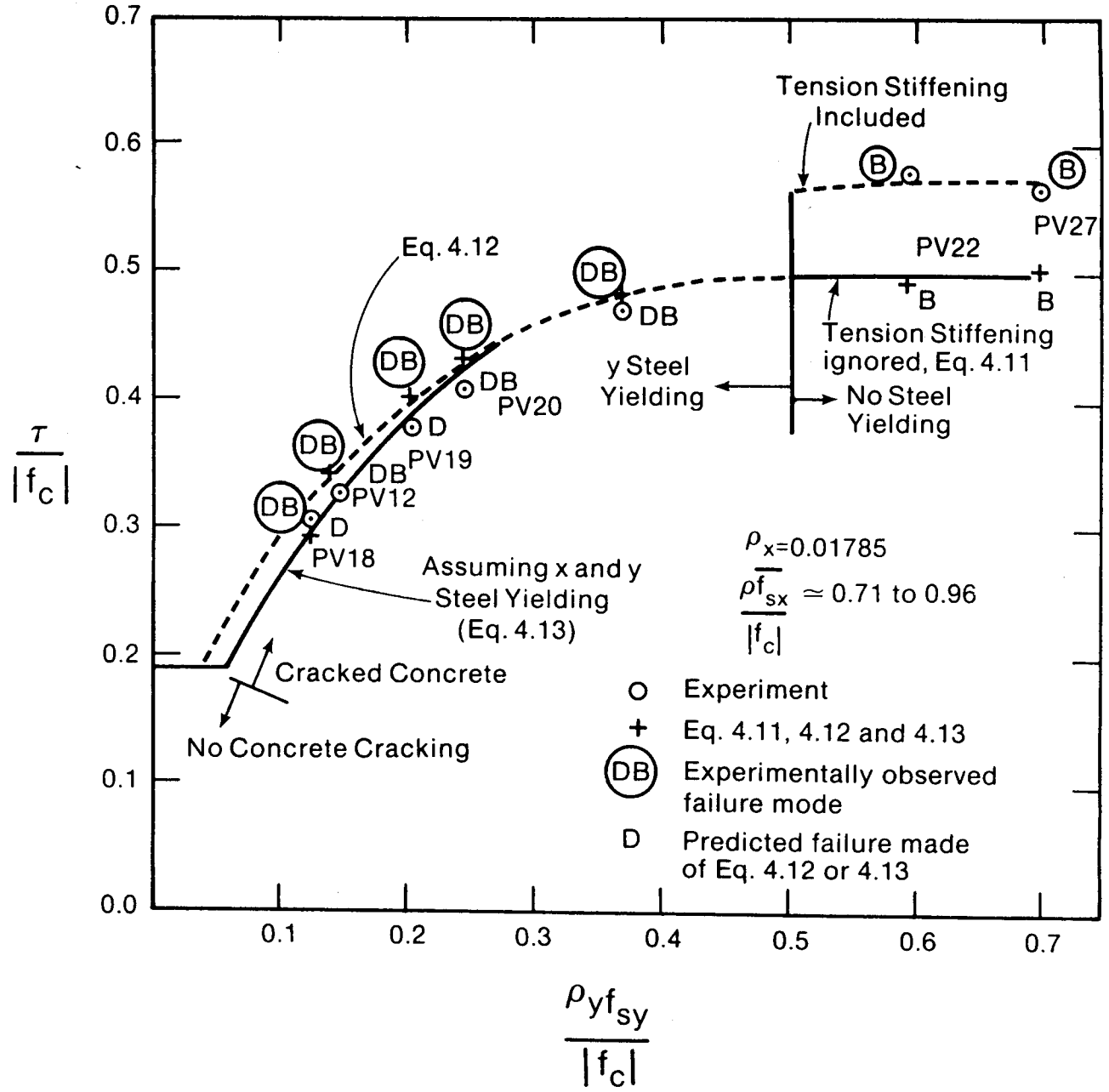

FIG. 4.24. Variation of Shear Strength with y direction Steel Content - x Direction Steel Content Constant

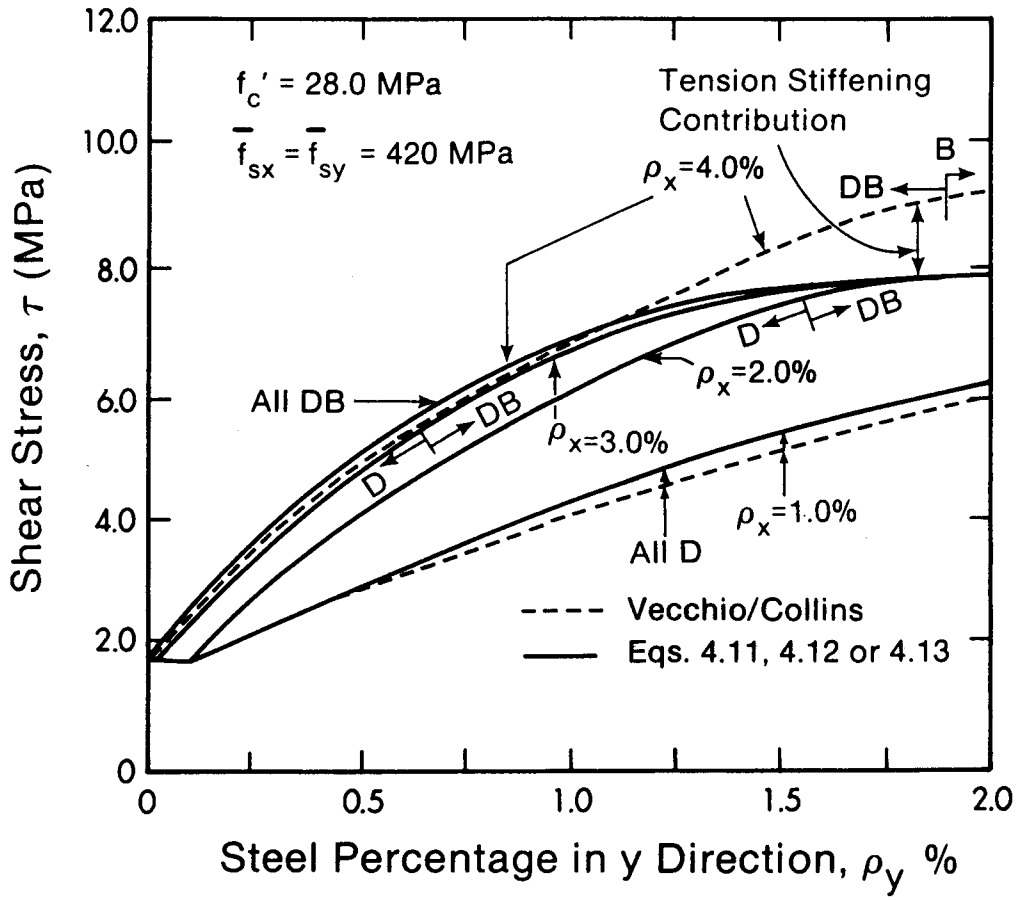

FIG. 4.25. Variation of Shear Strength with Percentage of Reinforcement

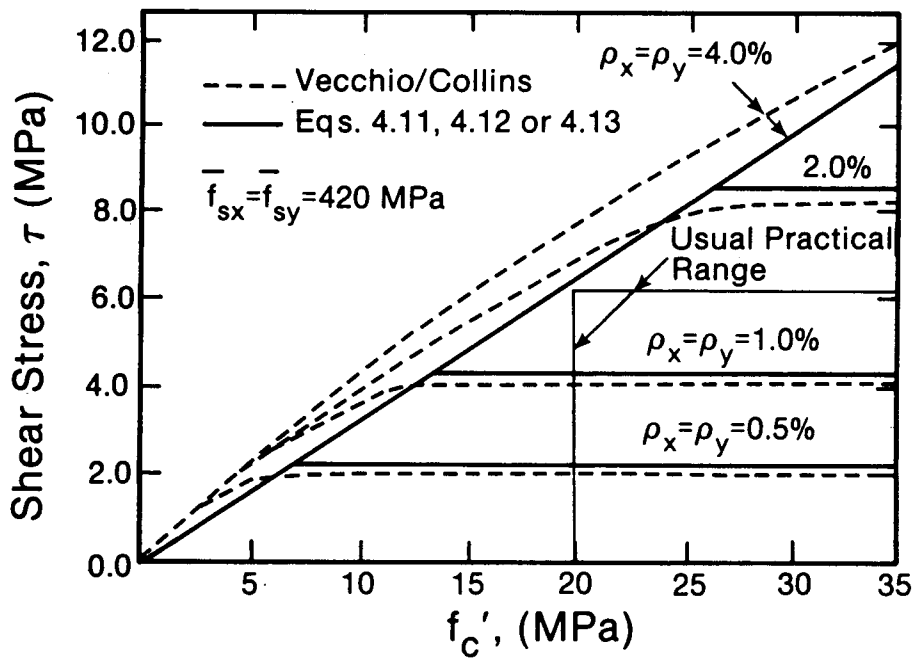

FIG. 4.26. Influence of Concrete Compressive Strength on the Shear Strength of Isotropically Reinforced Panels

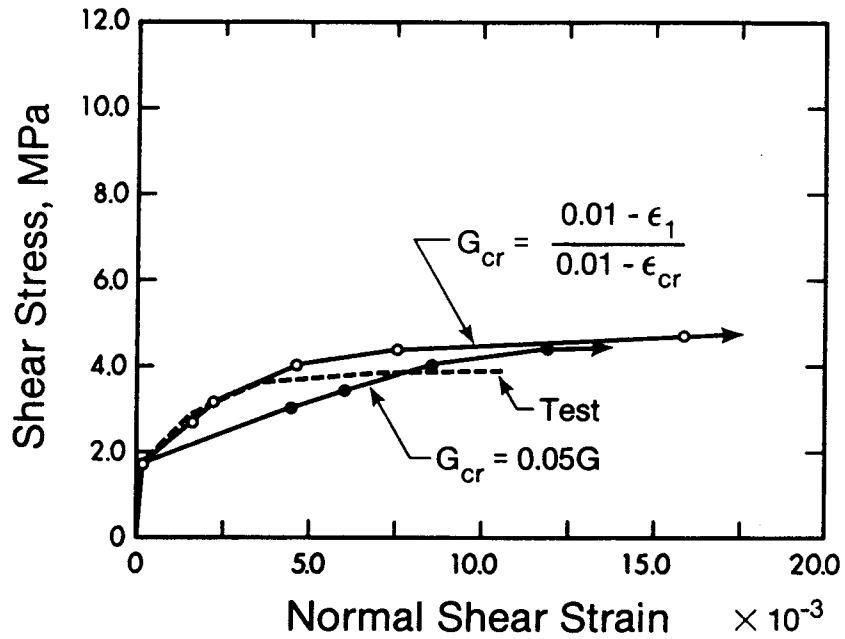

FIG. 4.27. Panel PV19 - Influence of Crack Shear Stiffness

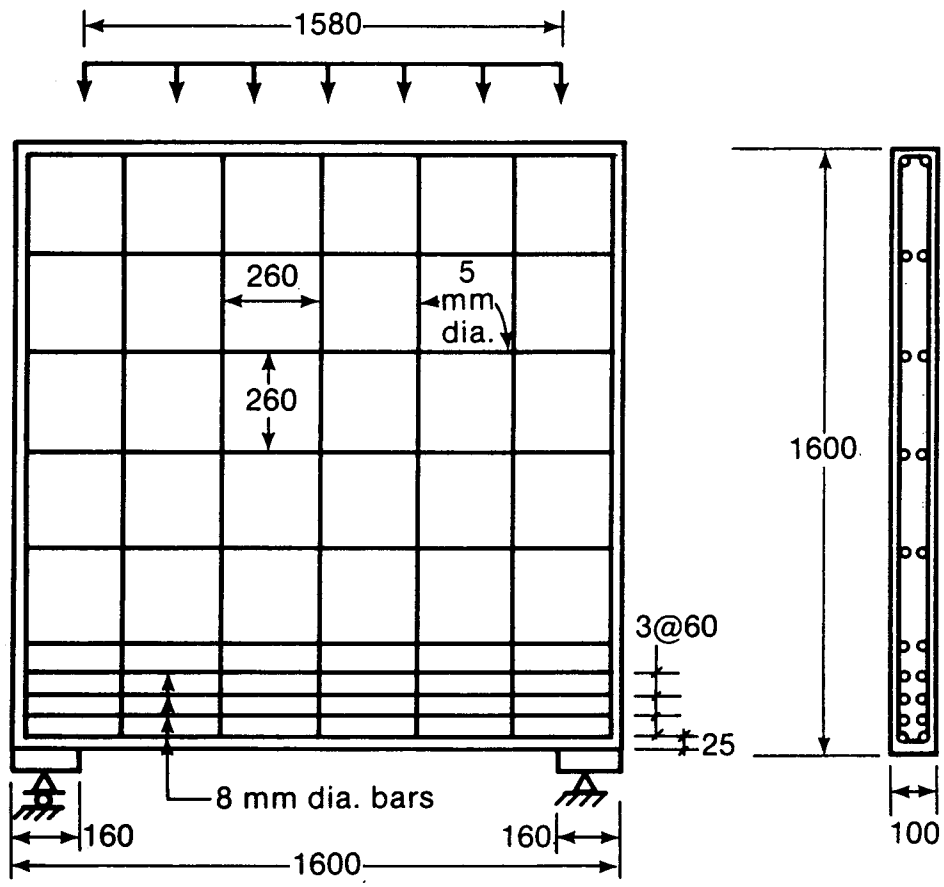

FIG. 4.28. Leonhardt/Walther Deep Beam WT3

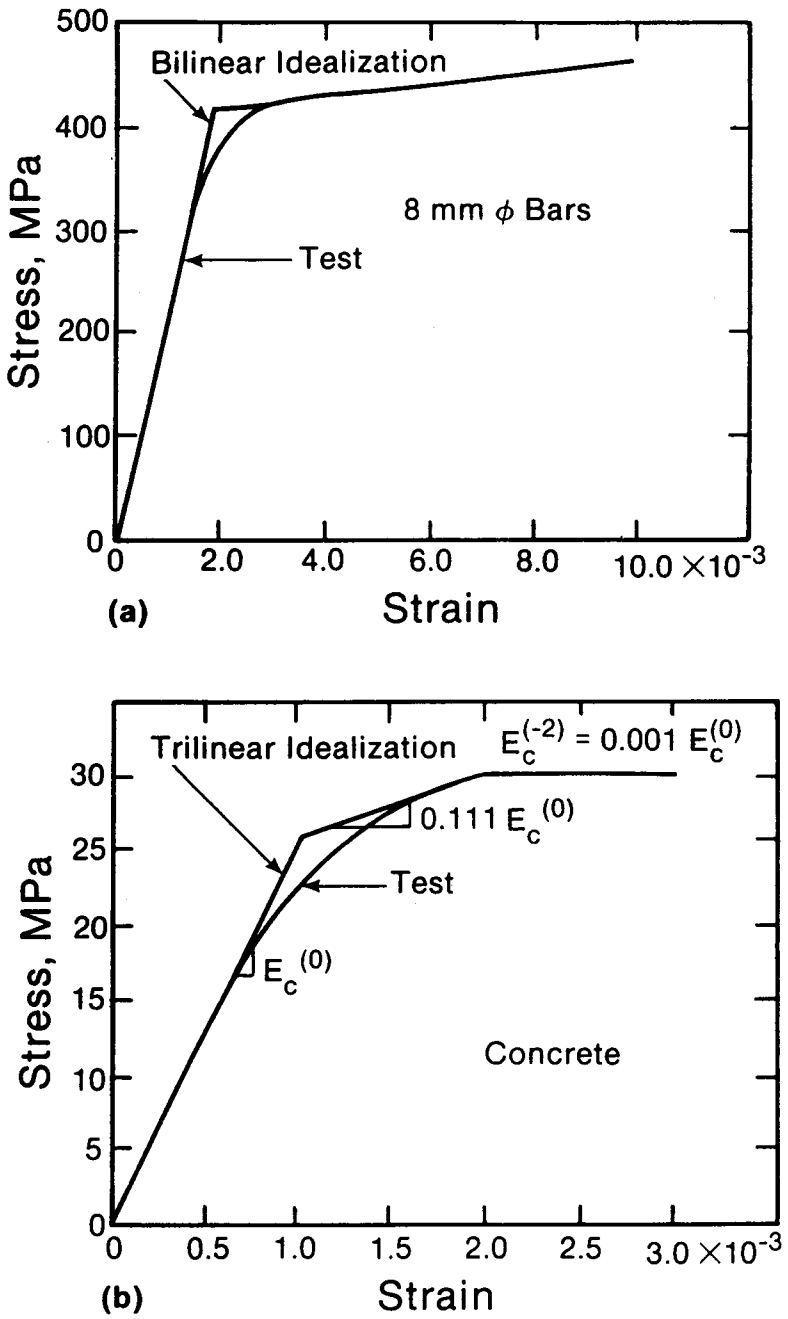

FIG. 4.29. Stress-Strain Diagrams for (a) 8 mm Diameter Steel Bars and (b) Concrete

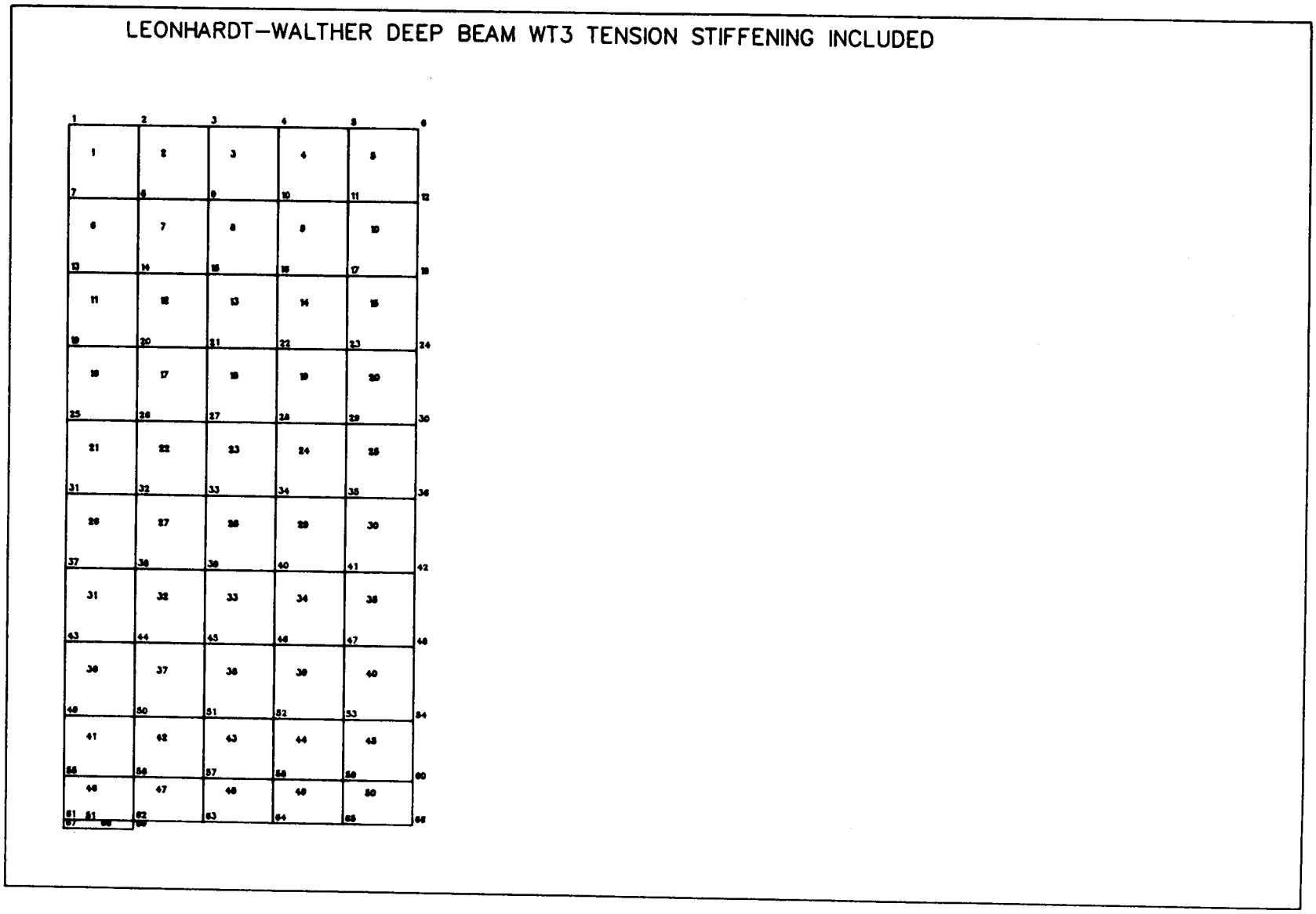

FIG. 4.30. Finite Element Mesh Layout - Leonhardt/Walther Deep Beam WT3

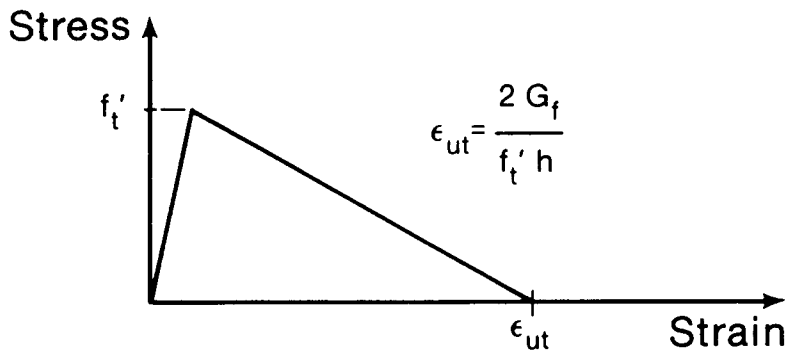

(a) Tension Softening — Elements 1 to 40

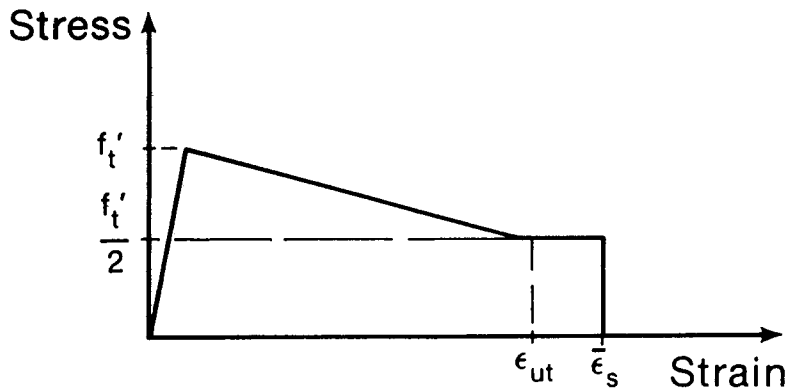

(b) Tension Stiffening - Elements 41 to 50

FIG. 4.31. Tensile Stress-Strain Relationships - Leonhardt/Walther Deep Beam WT3

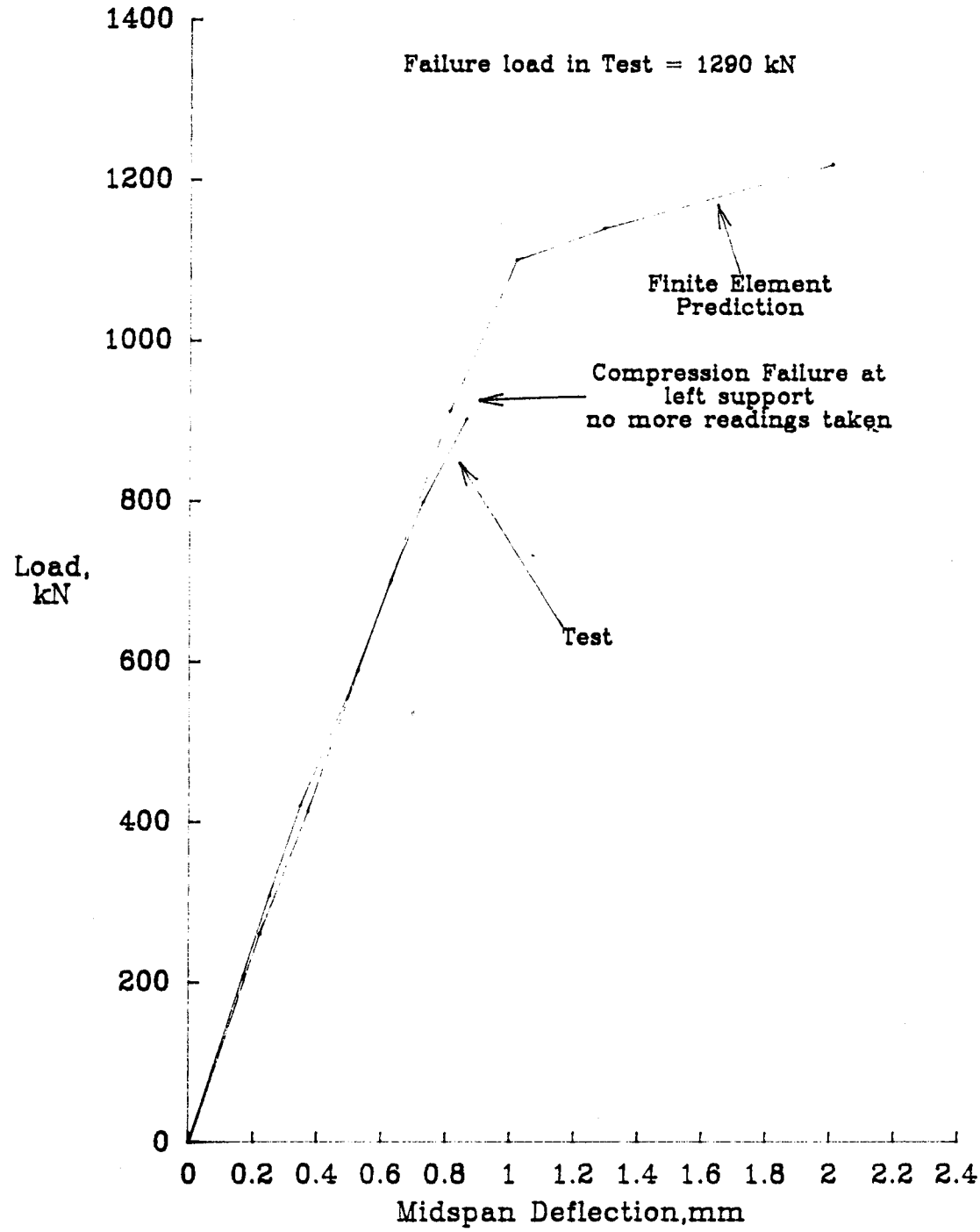

FIG. 4.32 Leonhardt/Walther Deep Beam Load–Deflection Curve

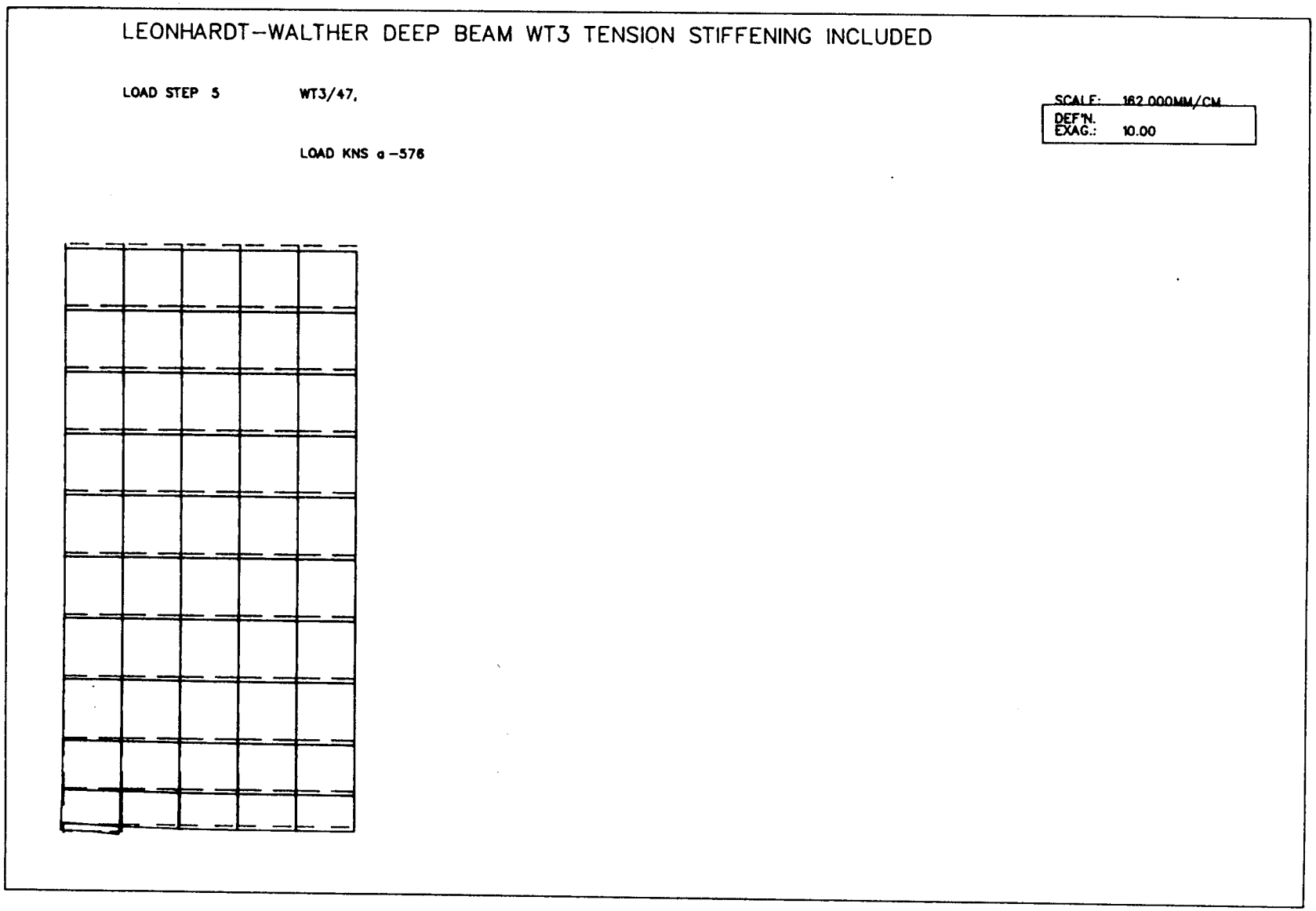

FIG. 4.33. Leonhardt/Walther Deep Beam WT3
(a) Deflected Shape Just Prior to Failure

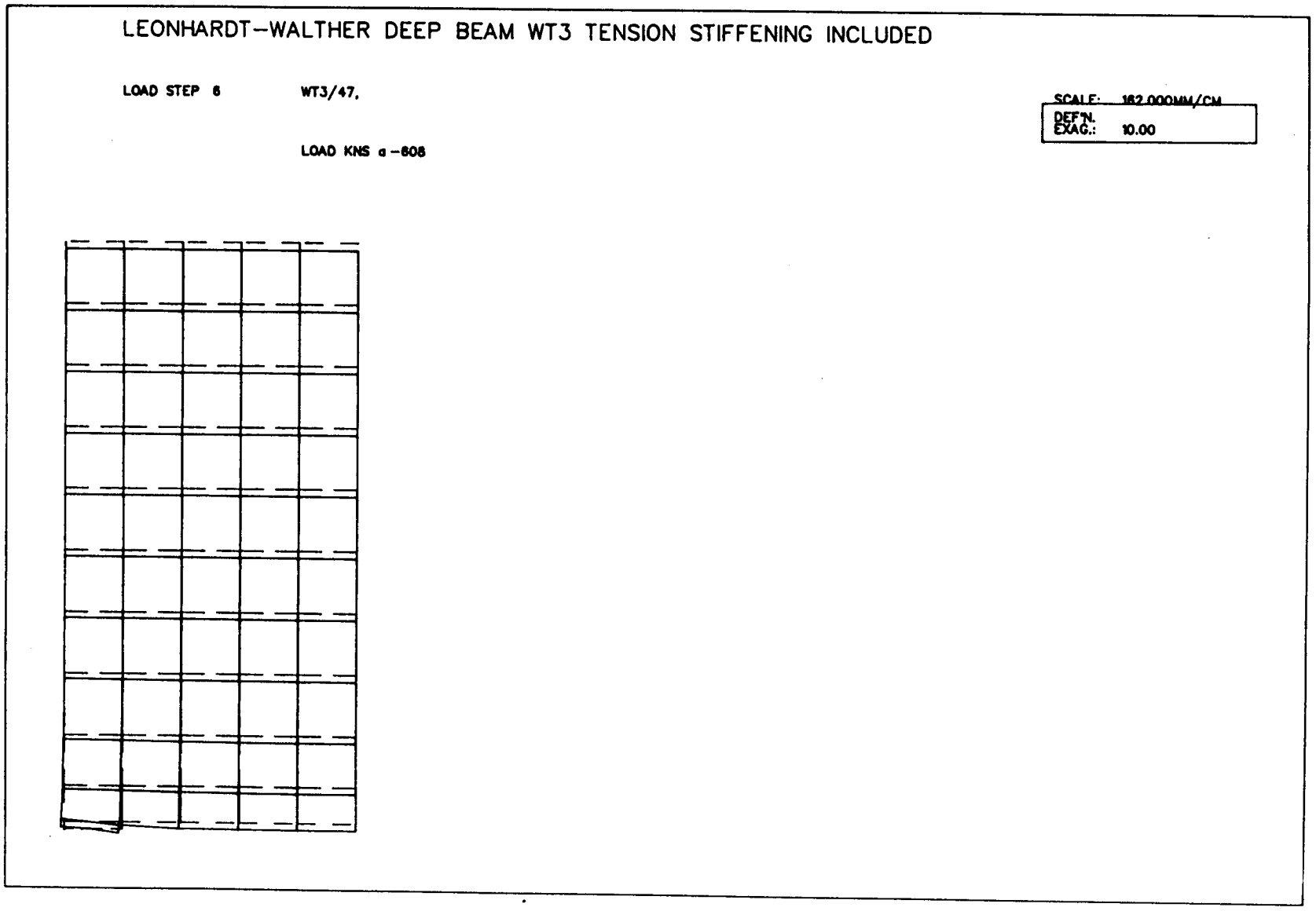

FIG. 4.33. (b) Deflected Shape at Failure

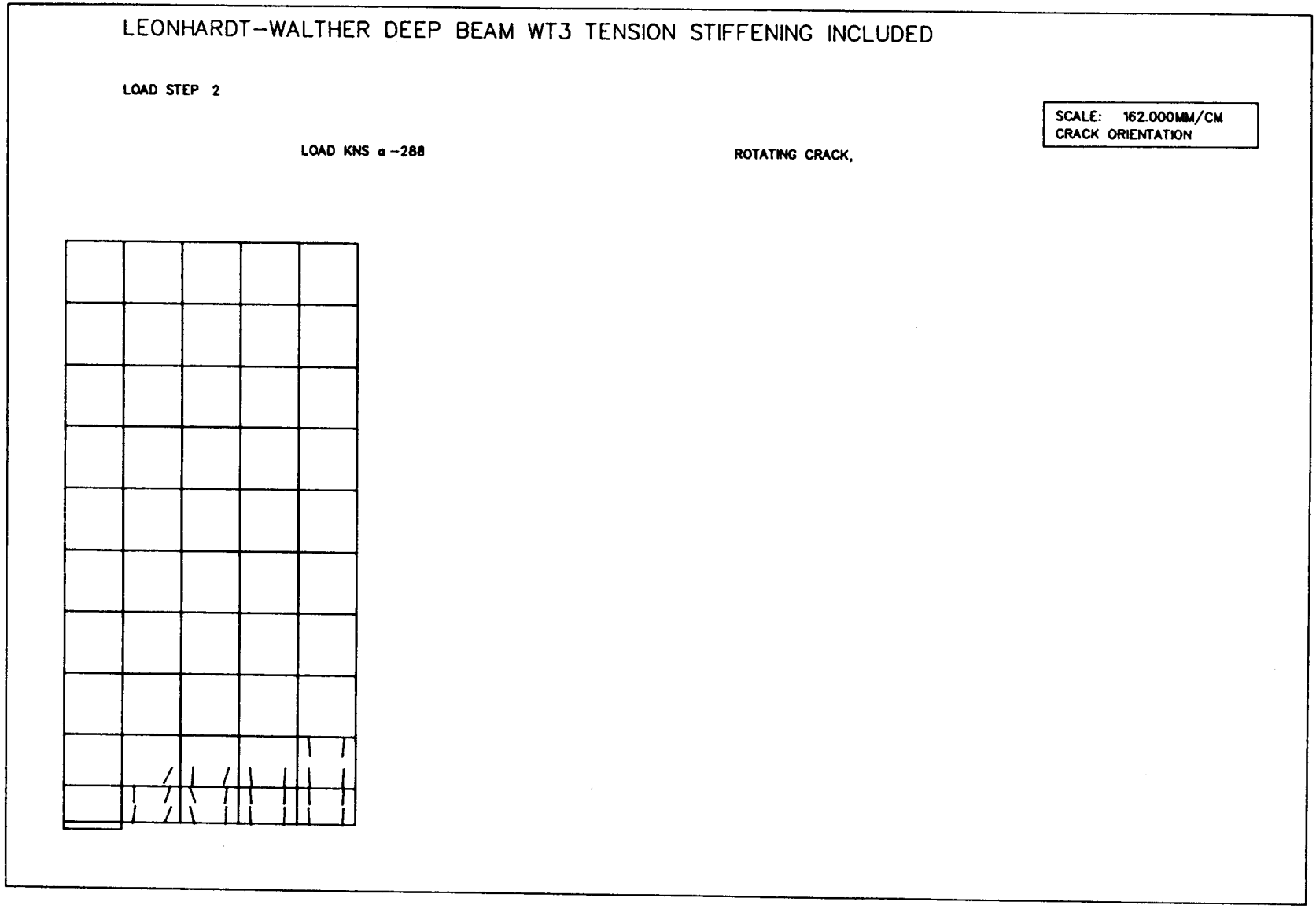

FIG. 4.34. Leonhardt/Walther Deep Beam WT3 - Analytical Crack Patterns
(a) Shear = 288 kN

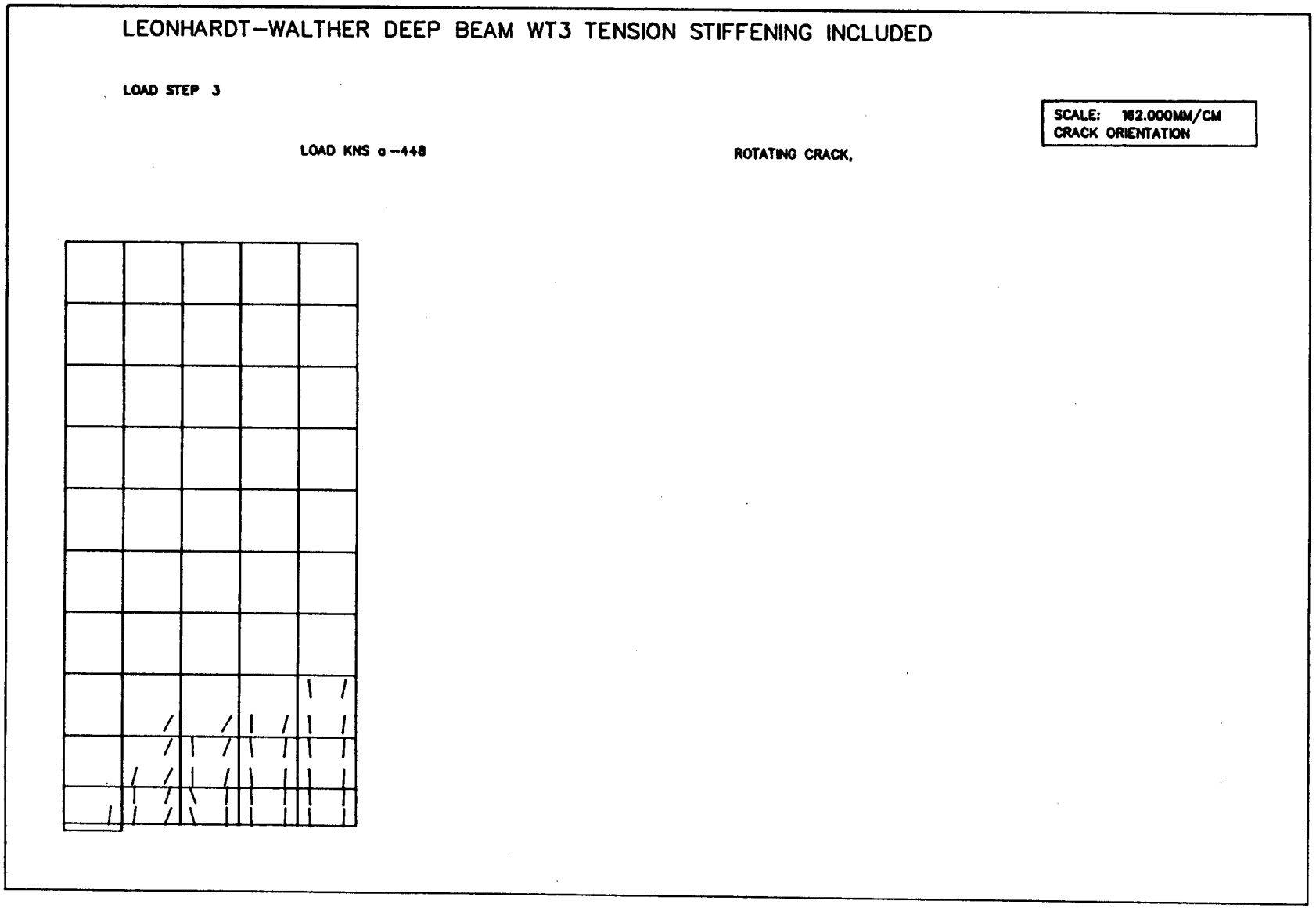

FIG. 4.34. (b) Shear = 448 kN

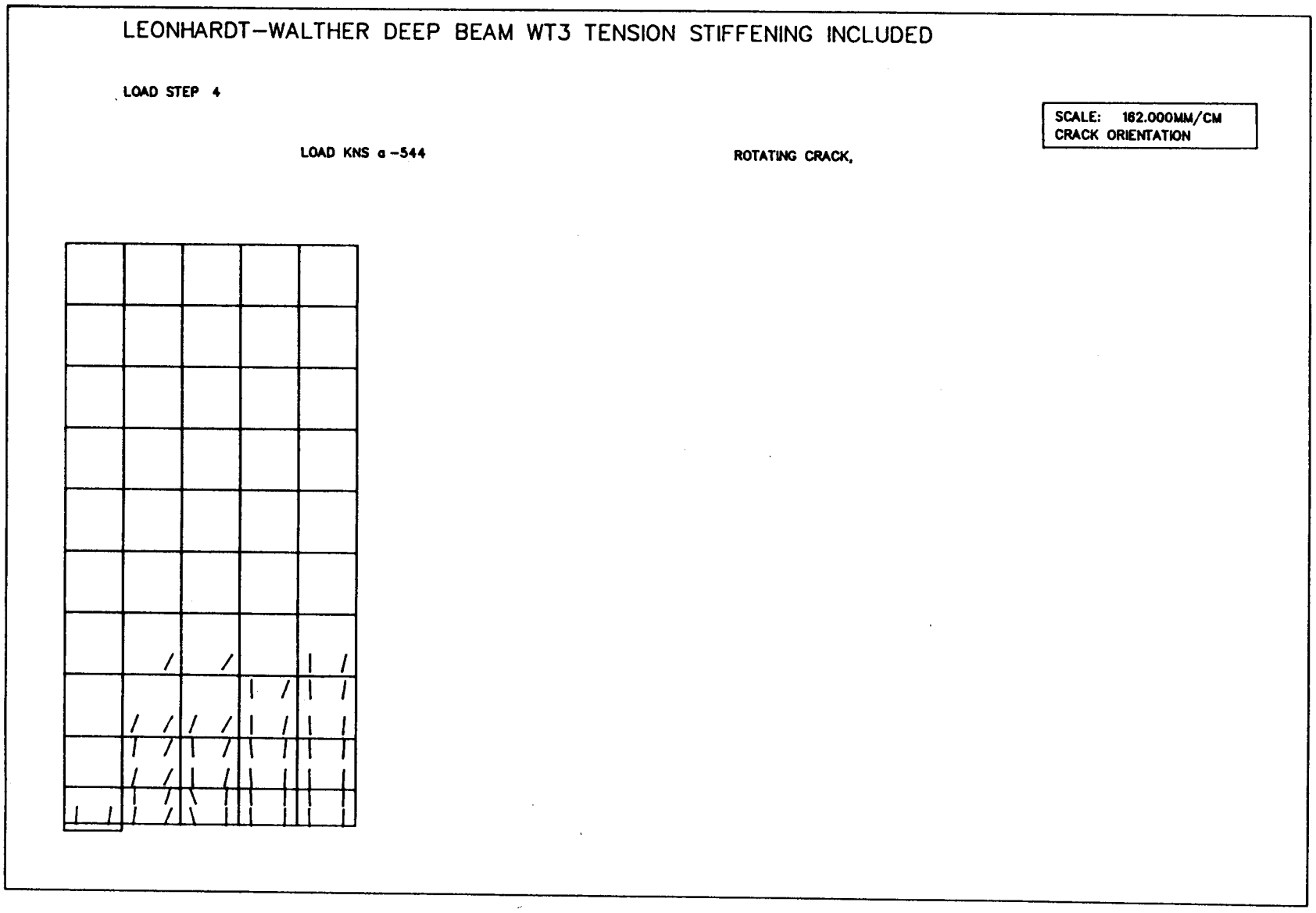

FIG. 4.34. (c) Shear = 544 kN

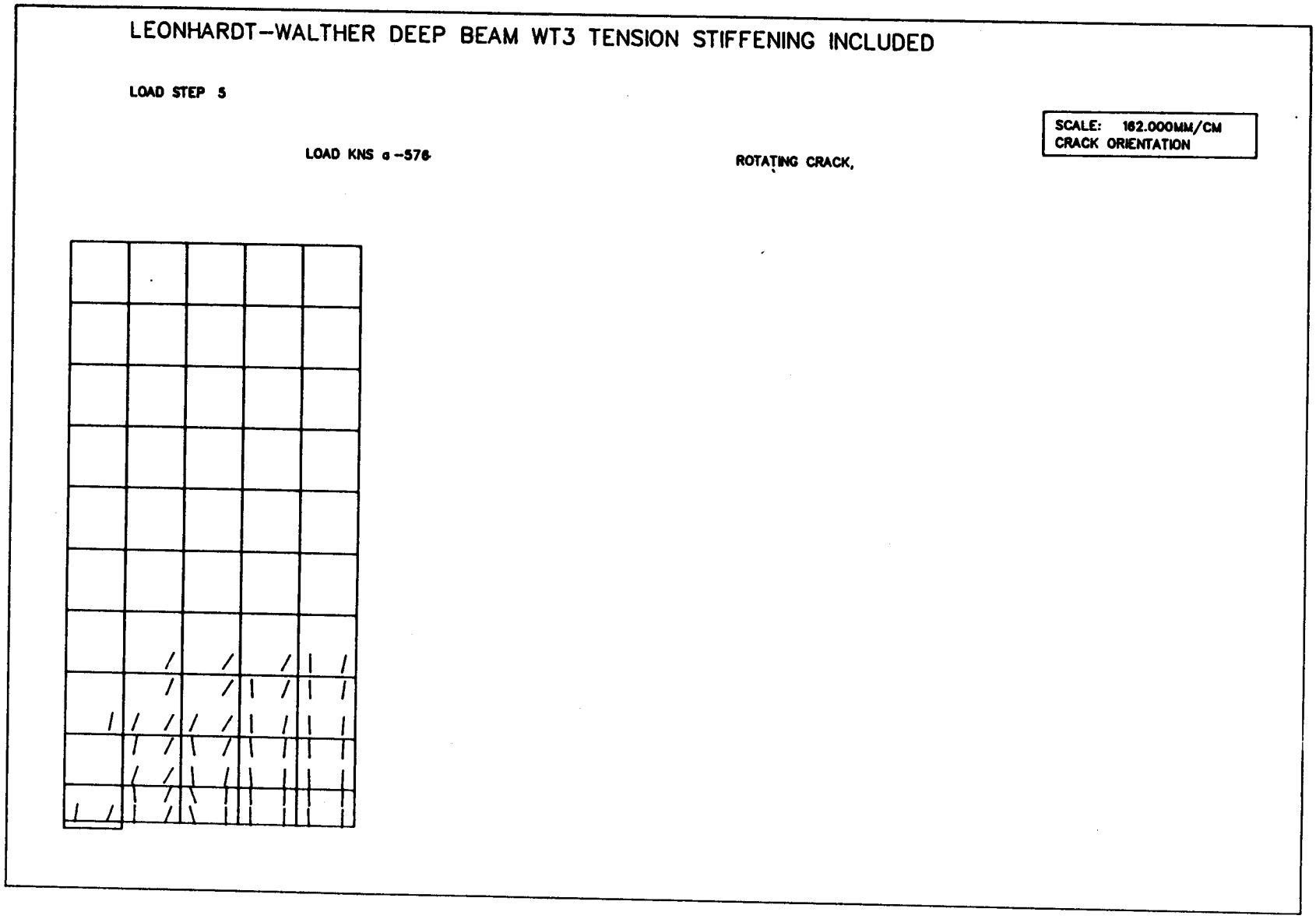

FIG. 4.34. (d) Shear = 576 kN

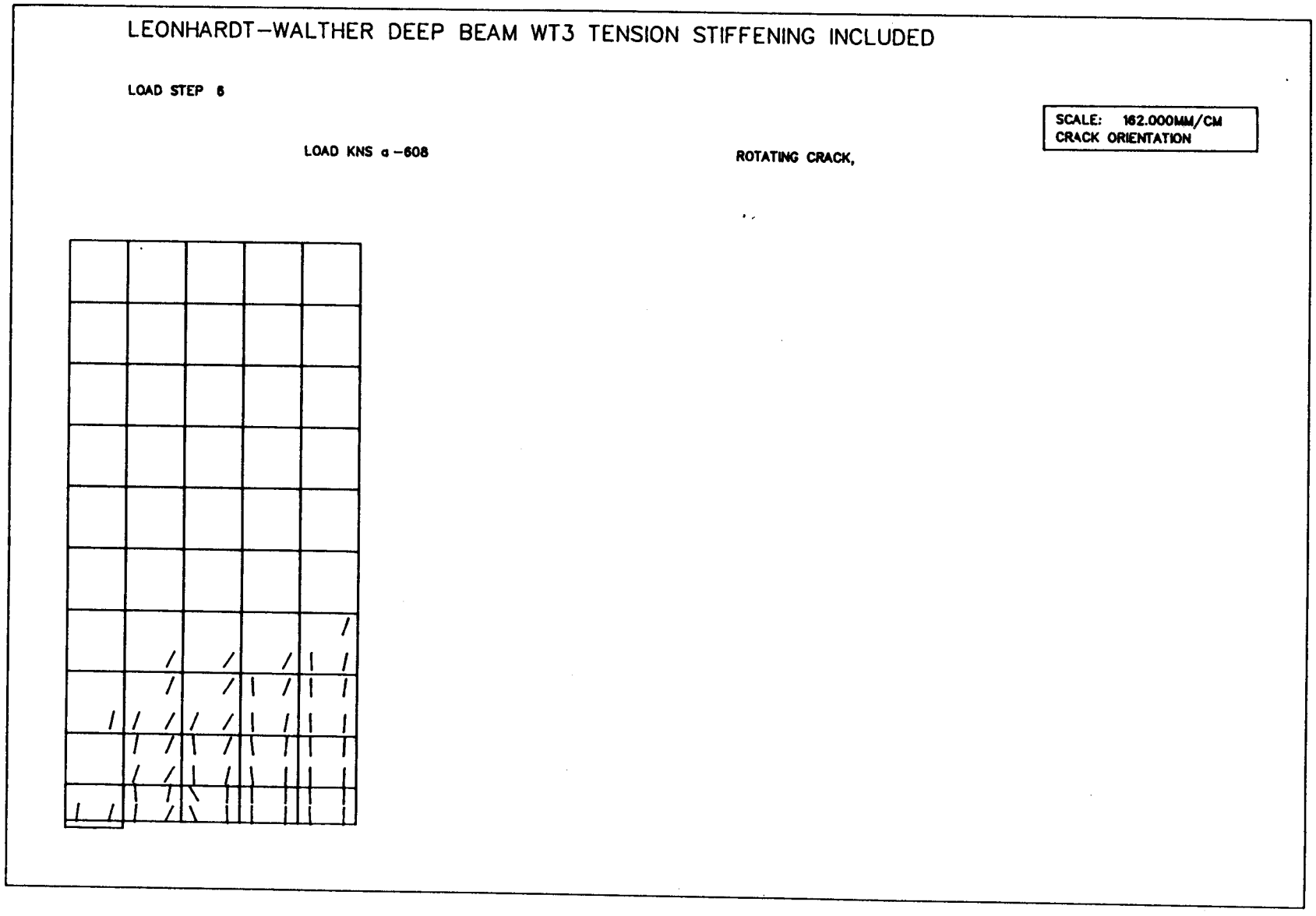

FIG. 4.34. (e) Shear = 608 kN

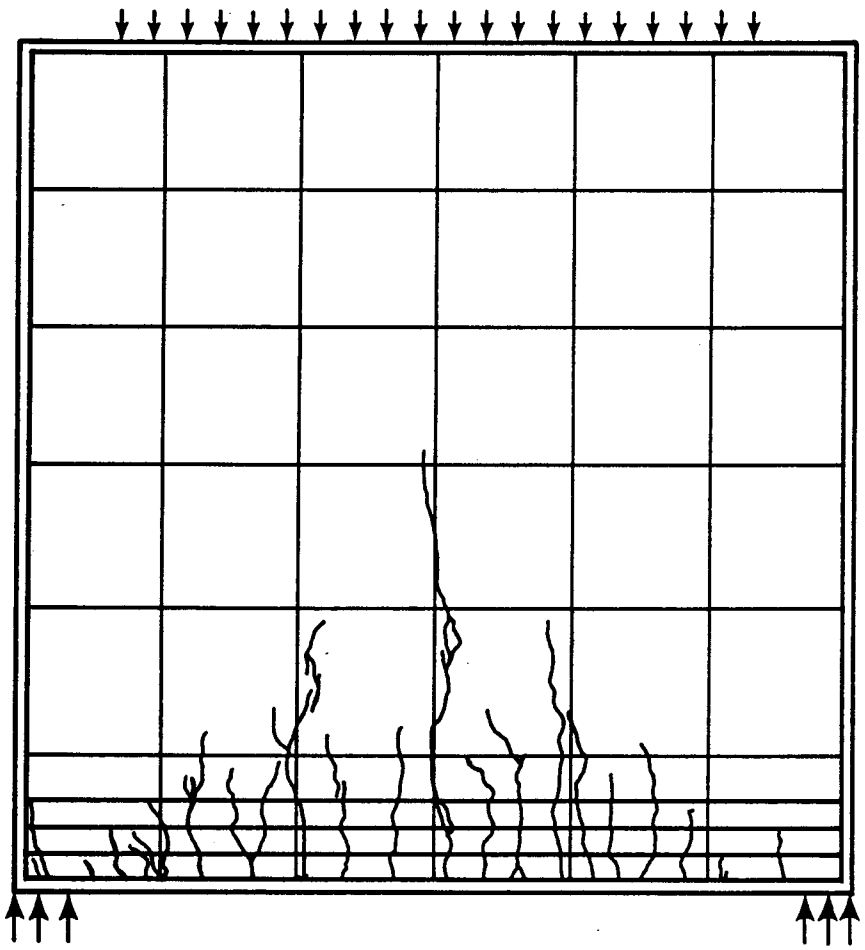

FIG. 4.35. Crack Pattern at Failure Observed in Test, Leonhardt/Walther Deep Beam WT3

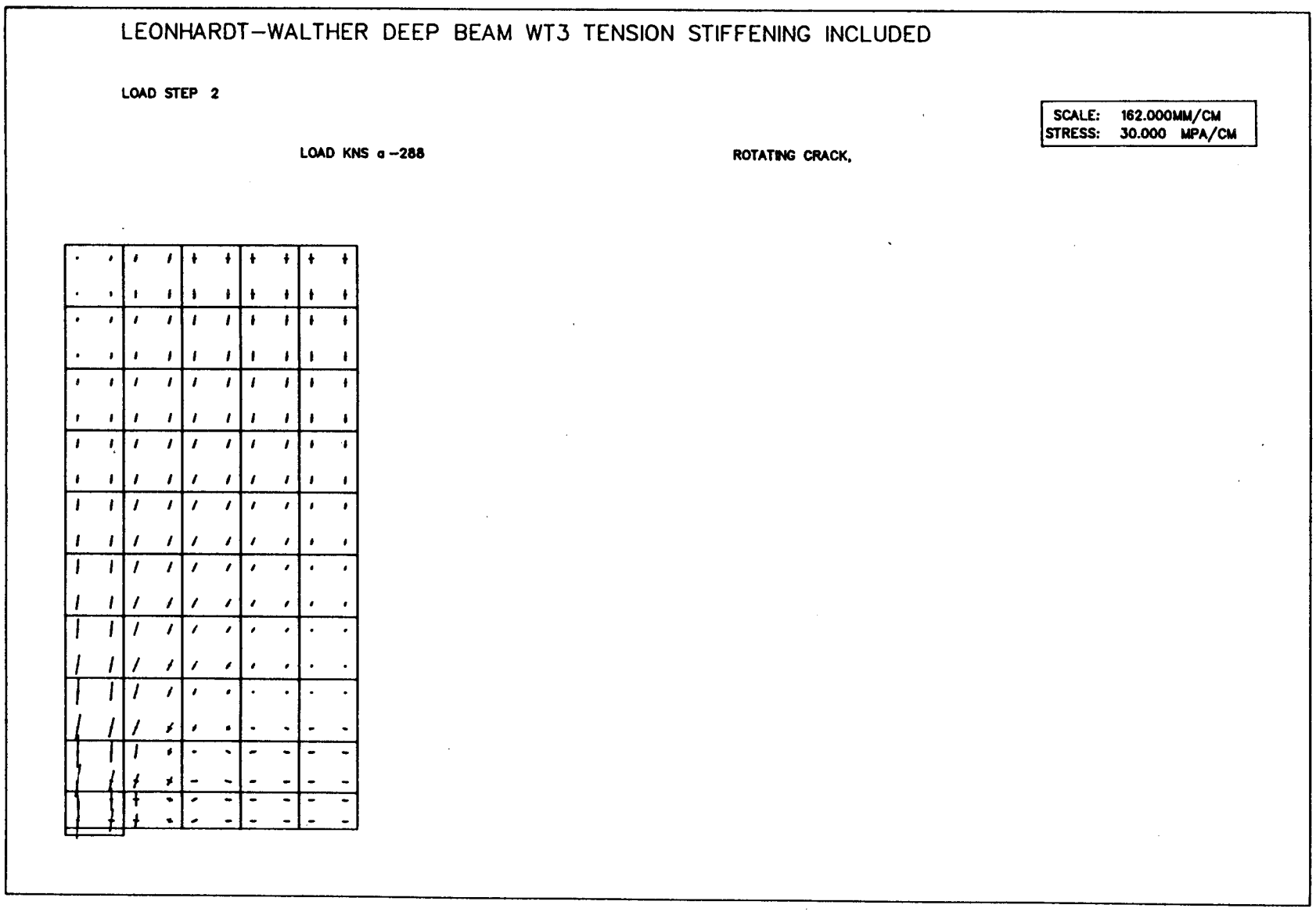

FIG. 4.36. Leonhardt/Walther Deep Beam WT3 - Principal Stress Plots
(a) Shear = 288 kN

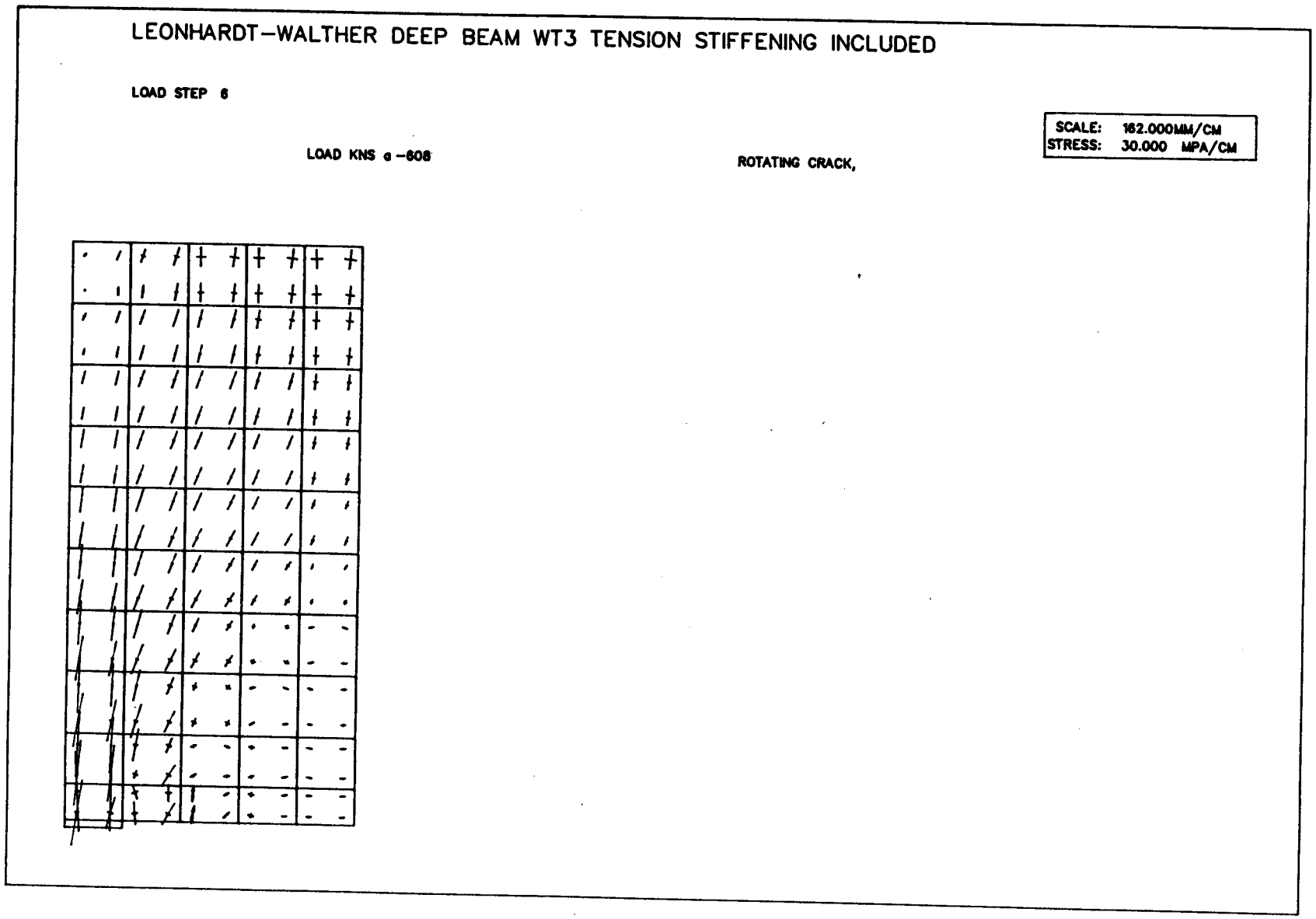

FIG. 4.36. (b) Shear = 608 kN

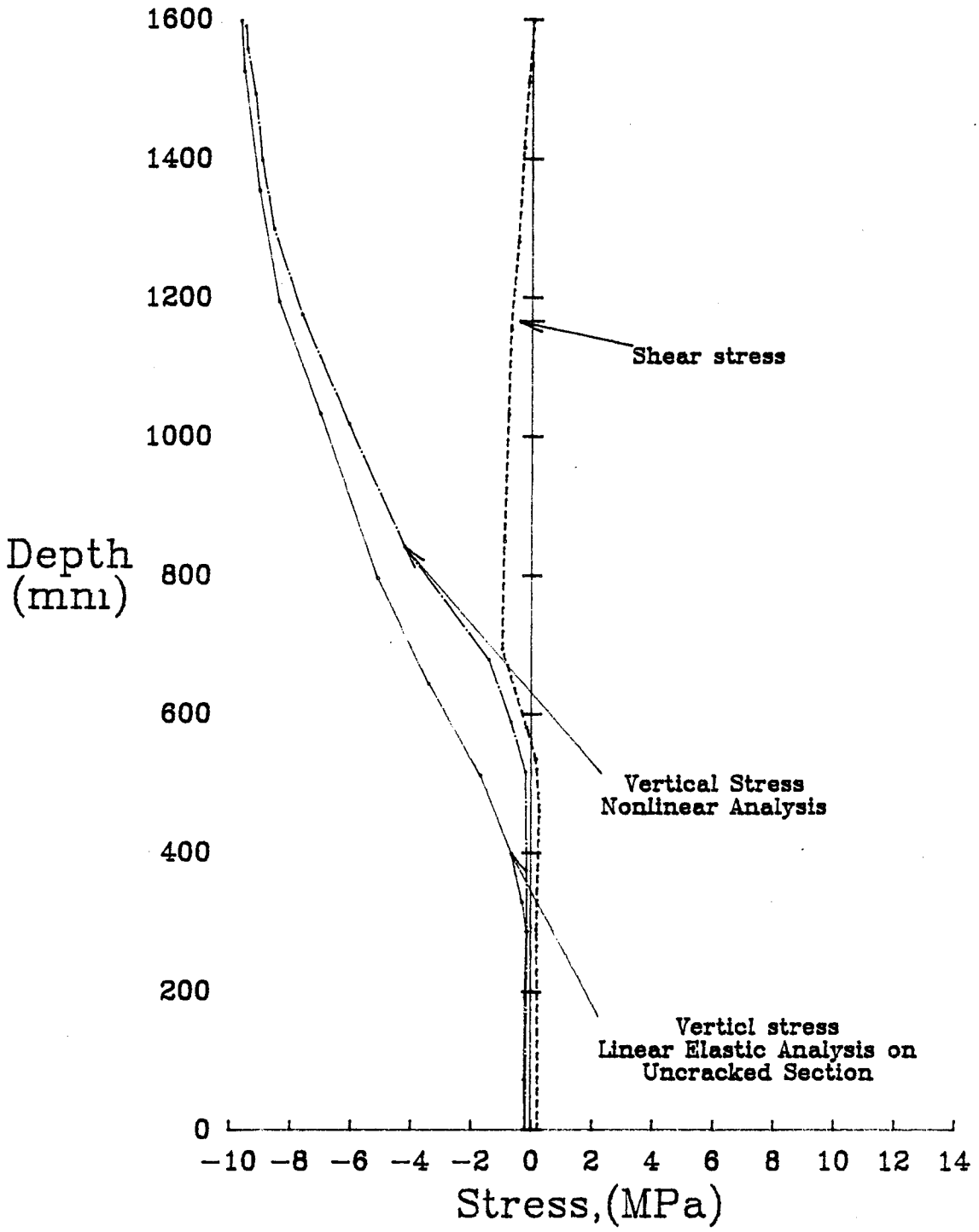

FIG. 4.37 Leonhardt/Walther Deep Beam
(a) Stress Distribution at Midspan

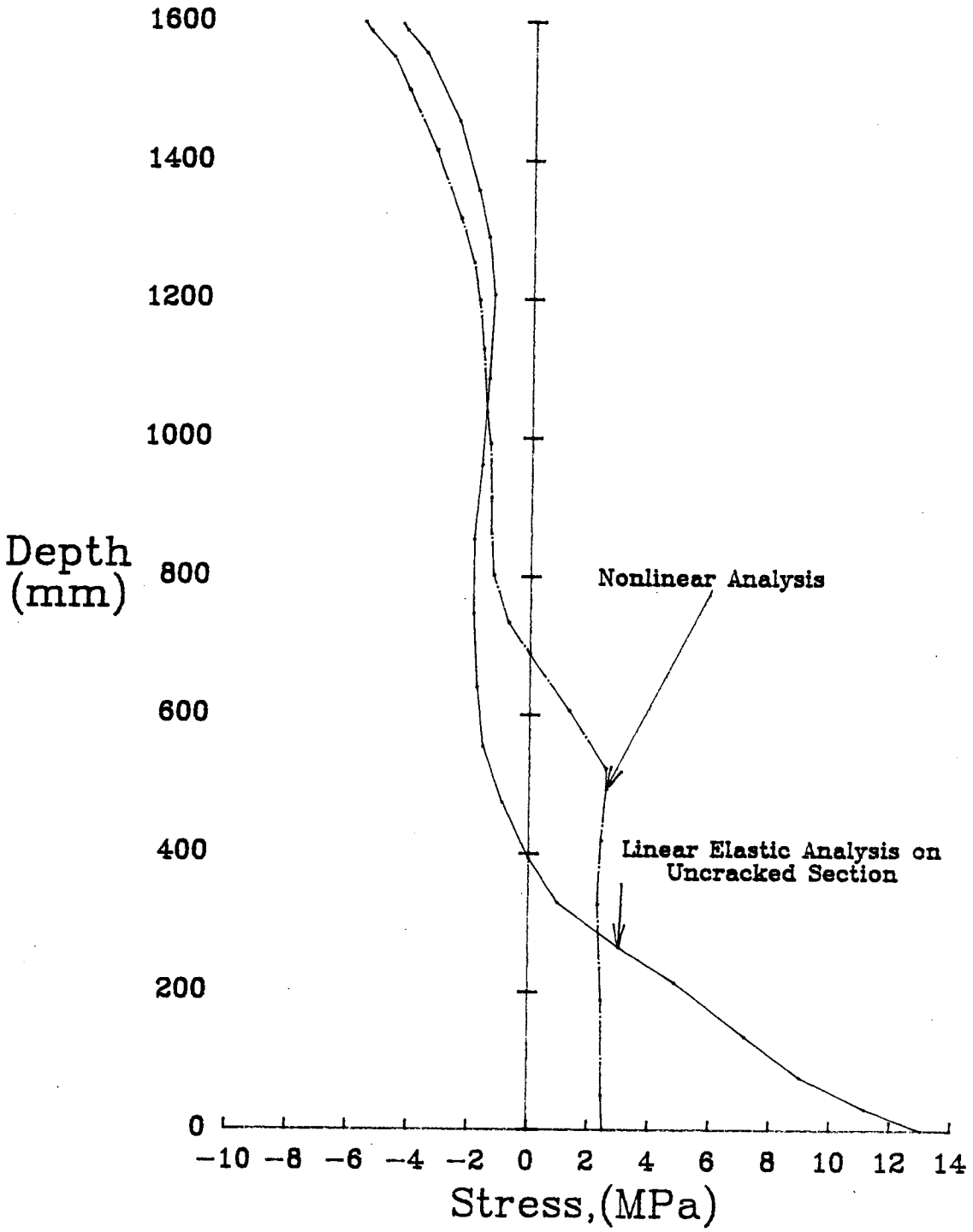

FIG. 4.37(b) Distribution of Longitudinal Stress

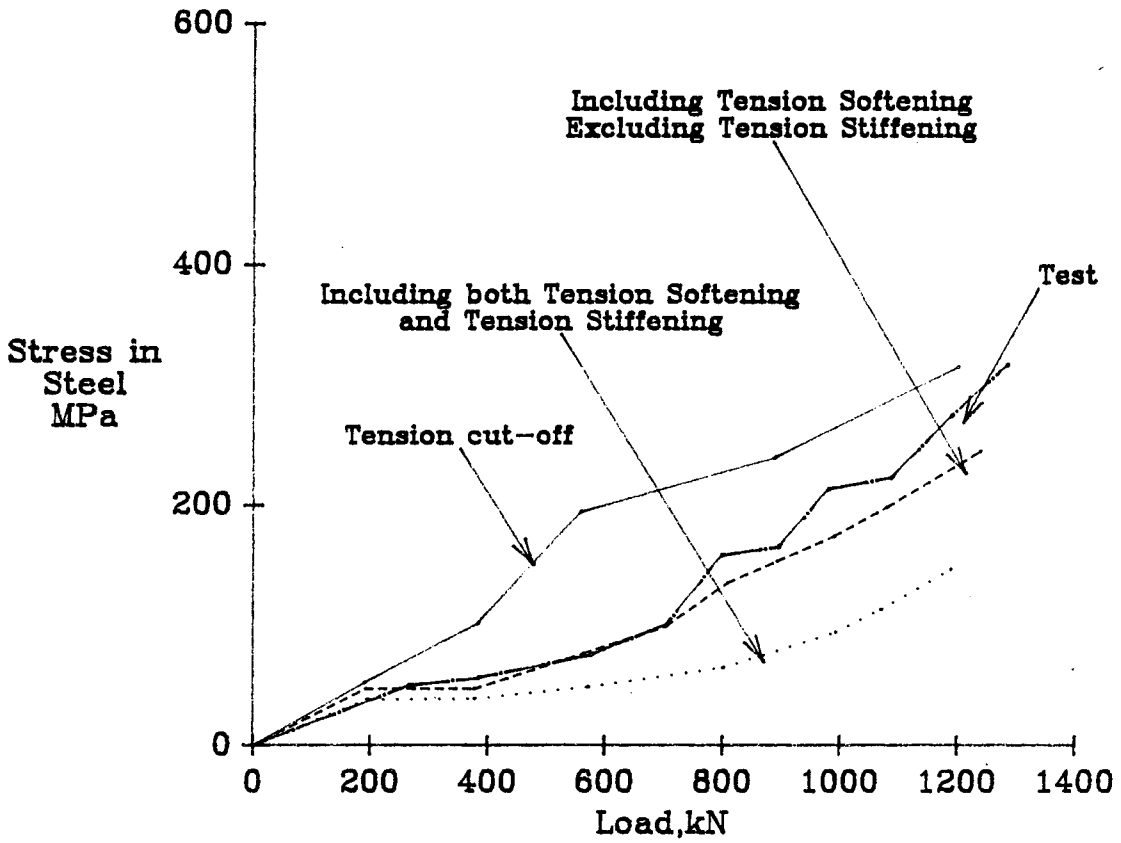

FIG. 4.38 Variation of Stress in Steel with Load

CHAPTER 5

APPLICATION TO REINFORCED CONCRETE BEAMS

5.1 Introduction

In this chapter, the physical behavior of reinforced concrete (R/C) beams under monotonic loading is discussed and application of the finite element method (FEM) to predict the behavior, including beam failure modes, is described. Through the finite element analysis, in which the important parameters were varied conveniently and systematically, new insights were gained which may provide a rational basis for the comparison and evaluation of appropriate code provisions.

5.2 Engineering Theory of the Strength and Ultimate Load Behavior of R/C Beams

5.2.1 Introduction

For reliable predictions of R/C beam behavior using the FEM it is required that: (1) appropriate material parameters are available from test specimens; (2) the material representations capture the salient features of the material behavior; (3) the finite element model and mesh layout, and the numerical analysis procedure, are adequate to detect the significant aspects of the structural response; and, (4) the output from the analysis is displayed and interpreted in an appropriate manner. In order to satisfy the last two requirements, an understanding of the fundamentals of R/C beam behavior is necessary. A brief description of the behavior of beams exhibiting various failure modes, as is commonly understood, follows.

5.2.2 Flexural Failure

5.2.2.1 Assumptions and Basic Equilibrium Relationships

Consider a reinforced concrete beam without web reinforcement, as shown in Fig. 5.1. Typical load-deflection behavior of this beam is schematically shown in Fig. 5.2a and 5.2b. Three basic assumptions used in deriving an engineering theory for the flexural strength of reinforced concrete sections are (Park and Paulay, 1975)

1. Bernoulli's hypothesis holds, i.e., plane sections which are normal to the neutral axis before bending remain plane after bending. This hypothesis implies that perfect bond exists between concrete and reinforcement and shear deformations are negligible.

2. The tensile strength of concrete may be neglected. This, of course, implies that tension stiffening (contribution of intact concrete between cracks) does not influence the ultimate moment capacity.

3. Stress-strain relationships for concrete and steel are known for all strain ranges.

A reinforced concrete section has a stress distribution as illustrated in Fig. 5.3 when the flexural strength is reached.

The resultant internal tensile force is

$$T = A_s f_s \tag{5.1}$$

where A_s is the area of steel and f_s is the steel stress.

The resultant internal compressive force is expressed as

$$C = k_1 k_3 f'_c bc \tag{5.2}$$

where c is the distance from the extreme compression fibre to the neutral axis, $k_3 f'_c$ is the compressive stress at extreme fibre and k_1 is the ratio of the volume of the compressive stress block to the rectangular stress block defined by $k_3 f'_c bc$.

The distance between the resultant internal forces, known as the internal lever arm, is given by

$$jd = d - k_2 c \tag{5.3}$$

where $k_2 c$ is the location of the resultant compression force from the extreme compression fibre.

The moment of resistance is therefore

$$M = Tjd = Cjd \tag{5.4}$$

5.2.2.2 Flexural Tension Failure

If the steel content of the section is small, the steel will reach the yield strength, f_y, before concrete reaches its maximum capacity. Assuming an elastic-perfectly plastic stress-strain relationship for steel, the steel force will remain constant at $A_s f_y$ with further loading. A slight additional load causes large plastic elongation of the steel across the flexural cracks, resulting in wide cracking and a large increase in strain at the extreme compression fibre of the concrete. This increases the mean compressive stress in the concrete stress block and, because equilibrium of the internal forces must be maintained, a reduction in the depth to the neutral axis results. This reduction in the depth of the neutral axis causes an increase in the

lever arm and hence in the moment resistance. The flexural strength of the section is reached when the strain in the extreme compression fibre of concrete reaches a limit after which any further increase in strain will lead to a reduction in the compressive resultant and crushing occurs. These stages are schematically shown in Fig. 5.2a.

5.2.2.3 Flexural Compression Failure

If the steel content is large relative to the concrete strength, concrete may reach its maximum capacity before the steel yields. In such a case the depth to the neutral axis increases as a result of the nonlinear compressive stress-strain response, causing an increase in the compressive force as required. Again the flexural strength of the section is reached when the strain in the extreme compression fibre of concrete is such that any further increase will lead to a reduction in the resultant compressive force. The section then fails suddenly in a brittle fashion. There may be little visible warning of failure since the widths of the flexural cracks in the tension zone of the concrete are small because the tensile steel does not yield. This behavior is schematically illustrated in Fig. 5.2b.

5.2.2.4 Balanced Failure

If the maximum compressive capacity of concrete and maximum tensile capacity of steel are simultaneously reached, a 'balanced failure' is said to occur.

Figure 5.2c (Park and Paulay, 1975) shows the variation of flexural strength of a section with the steel content. Because the flexural compression failure is brittle and sudden, most codes specify a maximum

limit on steel content in order to obtain a ductile failure.

5.2.2.5 Engineering Analysis

For any given moment across a reinforced concrete beam cross-section, the strain distribution (and the corresponding stress distribution) may be calculated using the assumptions described in Sect. 5.2.2.1 and the conditions of equilibrium. Since the depth to the neutral axis is not known in advance, this involves an iterative procedure as follows: (1) a strain in steel and a strain in concrete at the extreme compression fibre are assumed; (2) the depth to the netural axis is easily calculated since the variation of strain across the section has been assumed to be linear; (3) the corresponding stress distributions are obtained from the stress-strain curves of concrete and steel; (4) the condition of equilibrium, C = T, is then checked. If this condition is violated, another set of strains in concrete and steel are assumed and steps (1) through (4) are repeated until C = T; (5) the moment of resistance is then calculated using Eq. 5.4. If this moment is not equal to the applied moment, steps (1) through (5) are repeated.

5.2.3 Shear Failure

5.2.3.1 Definition

A 'shear failure' is said to occur when the R/C beam collapses in a nonductile manner under combined shear force and bending moment before full flexural capacity is reached (MacGregor et al., 1973). Considering the beam in Fig. 5.1, a shear failure would imply that sections within the shear span would fail before flexural failure occurs in the midspan region.

5.2.3.2 Mechanism of Shear Resistance (Park and Paulay, 1975)

In a reinforced concrete member, such as that shown in Fig. 5.1, cracks form when the principal tensile stresses exceed the tensile strength of concrete. In a region of high bending moments (such as the midspan region in Fig. 5.1) these stresses are greatest at the extreme tensile fibre of the member and are responsible for the initiation of the flexural cracks perpendicular to the axis of the member. In the region of high shear force (such as the shear span region in Fig. 5.1), the principal tensile stresses produce cracks (also referred to as diagonal tension cracks) that are oriented at an angle inclined to the axis of the member. Most often, these inclined cracks are extensions of flexural cracks. Either a reinforced concrete member collapses immediately after the formation of diagonal cracks, or an entirely new shear carrying mechanism develops which is capable of sustaining further load in a cracked beam.

The freebody diagram of a segment of a concrete beam, without shear reinforcement, between two adjacent cracks in the shear span is shown in Fig. 5.4. Considering now the equilibrium shear-moment relationship,

$$V = \frac{dM}{dx} \tag{5.5}$$

and substituting for M from Eq. 5.4, we obtain

$$V = \frac{dM}{dx} = \frac{d}{dx}\left(Tjd\right) = \frac{dT}{dx}\,jd + T\,\frac{d(jd)}{dx} \tag{5.6}$$

The term $\frac{dT}{dx}\,jd$ expresses the behavior of a true prismatic flexural

member in which the internal tensile force T changes from section to section to exactly balance the applied moment intensity. The term $\frac{dT}{dx}$, the rate of change of internal tension force, is transmitted by bond between reinforcement and concrete as bond force q to the concrete segment. The concrete segment, in turn, acts as a cantilever fixed at the neutral axis and transfers this bond force q to concrete at the neutral axis to balance the change in the compressive force, as in a perfect beam. Should the internal lever arm remain constant so that $\frac{d(jd)}{dx} = 0$, then the entire shear resistance is derived from the "beam action" as

$$V_{beam} = \frac{dT}{dx} jd = qjd \tag{5.7}$$

When $\frac{d(jd)}{dx} \neq 0$, the external shear is also resisted by inclined internal compression, called "arch action", as

$$V_{arch} = T \frac{d(jd)}{dx} = C \frac{d(jd)}{dx} \tag{5.8}$$

In the normal reinforced concrete beam the two mechanisms, as expressed by Eq. 5.6, offer a combined resistance against shear forces. The extent to which each mechanism contributes to shear resistance at various levels of external load intensity will depend on the compatibility of deformations associated with these actions.

Each of the concrete segments between cracks, such as the one shown in Fig. 5.4, may be considered to act as a cantilever with its base nn at the compression zone. For perfect beam action to take place, these cantilevers must effectively resist the full bond force q. Experiments

(Taylor, 1974) have indicated that, in the tension zone, most of the shear resistance (50 to 70%) is due to aggregate interlock, some (15 to 25%) due to dowel action and only about 20% due to the bending resistance at the 'built in' end of these cantilevers.

The stiffness of these cantilevers reduces with reduction in stiffness of any of these components. This reduction in stiffness of the cantilever and any slip between steel and concrete increases the arch action component of shear resistance. This increase depends on the a/d ratio, as discussed in the next paragraph. Failure of beam action may be initiated by the breakdown of any of the components (i.e., aggregate interlock, bending resistance of the cantilever and dowel action), producing secondary cracking at the 'built-in' ends of the cantilevers in an approximately horizontal direction. These secondary cracks most often occur as extensions of inclined flexure-cracks. After the failure of beam action, the remaining intact concrete above the cracks might not be adequate to resist the applied shear by arch action alone, leading to diagonal tension failure.

Arch action, as signified by Eq. 5.8, requires that the reinforcement be properly anchored. For efficient arch action, the line of thrust (connecting the reaction point to the load point) must be steep. That is, the smaller the shear span to depth ratio, i.e. a/d ratio of Fig. 5.1, the higher the resistance due to arch action. For large a/d ratios, say above 2.5, the line of thrust is so shallow that the resistance capacity due to arch action is less than the load producing diagonal tension failure. Figure 5.5 schematically illustrates this concept.

5.2.3.3 Parameters Influencing Shear Failure

In practice, the important parameter in evaluating the performance of a beam is the ratio of the usable moment capacity, M_u, in the presence of shear to the full flexural moment capacity, $M_{f\ell}$. The important parameters affecting this ratio, $\frac{M_u}{M_{f\ell}}$, in the case of beams without web reinforcement, are the shear span to depth ratio, a/d, and ρ, the tensile reinforcement ratio. Figure 5.6, due to Kani (1979), shows this relationship. The dependence of $\frac{M_u}{M_{f\ell}}$ on ρ is not only due to the fact that calculation of $M_{f\ell}$ involves ρ, but also because: (1) the dowel shear will be smaller if ρ is reduced; and, (2) as ρ is reduced, the flexural cracks extend higher into the beam and are wider, reducing both the shear capacity of the compression zone and interface shear transfer.

Another important parameter influencing the shear strength of beams failing in diagonal tension appears to be beam depth (Kani, 1979). The ultimate shear stress in beams without web reinforcement decreases as the effective depth increases. For beams with web reinforcement, however, the size effect appears to be minor (Park and Paulay, 1975).

The role of web reinforcement is to increase the shear resistance by:

(1) improving the capacity of the concrete "cantilevers" by altering them to act as tied cantilevers. That is, a "truss action" develops whereby the concrete cantilevers act as diagonal compression members of the truss and the stirrups act as vertical tension members,

(2) improving the contribution of the dowel action by supporting the longitudinal reinforcement,

(3) reducing the flexural tensile stresses at the 'built-in' ends

of cantilevers by means of diagonal compression mentioned in (1),

(4) limiting the opening of diagonal cracks within the elastic range, thus enhancing and preserving shear transfer by aggregate interlock, and

(5) providing confinement, thus increasing the compressive strength of concrete so as to increase the capacity of arch action.

The truss mechanism traditionally used to explain the behavior of beams with web reinforcement involves forces C_d in the diagonal compression strut and V_s in stirrups, as shown in Fig. 5.7. In this figure, α denotes the angle of inclination of cracks. V_s being the resultant of all stirrups forces crossing the crack, we obtain

$$V_s = \frac{A_v f_v}{S} jd \cot \alpha \tag{5.9}$$

where A_v is the cross-sectional area of the stirrups, S is the stirrup spacing and f_v is the stress in the stirrups. The diagonal compression force, C_d, arising from a single concrete 'strut' becomes

$$C_d = \frac{V_s}{\sin \alpha} \tag{5.10}$$

and the diagonal compressive stress, f_{cd}, becomes

$$\begin{aligned} f_{cd} &= \frac{C_d}{bjd \cot \alpha \sin \alpha} = \frac{V_s}{bjd \cot \alpha \sin^2 \alpha} \\ &= \frac{V_s}{bjd \sin \alpha \cos \alpha} = \frac{v_s}{\sin \alpha \cos \alpha} \end{aligned} \tag{5.11}$$

where

$$v_s = \frac{V_s}{bjd} \tag{5.12}$$

Substituting for V_s in Eq. 5.11 from Eq. 5.9 yields

$$f_{cd} = \frac{A_v f_v}{bS} \left(\frac{1}{\sin^2 \alpha}\right) \tag{5.13}$$

From Eqs. 5.9 and 5.13, V_s, the shear resistance due to web reinforcement, and f_{cd}, the diagonal compressive stress in concrete, are expected to increase with higher web steel and flatter crack inclinations.

All the "beam action" mechanisms in beams without web reinforcement are empirically assumed to be present in beams with web reinforcement as well and, in practice, it is assumed that (Park and Paulay, 1975),

$$V = V_I + V_s \tag{5.14}$$

where V_I is the shear force at inclined cracking and V_s is the shear resistance provided by web reinforcement assuming $\alpha = 45°$.

5.3 Requirements for Finite Element Prediction of Behavior

In order to inspire confidence in a practicing engineer about the ability of the Finite Element Method to predict the behavior of planar structures reliably, the following requirements may be identified:

1. The material properties required as input must be readily available or easily derivable from standard tests.

2. The failure load and failure mode must be predicted with

reasonable accuracy for structures such as beams with a wide range of variation of geometric and material parameters (such as shear span to depth ratios, reinforcement percentages and concrete strengths).

3. The load deflection behavior and crack patterns must be predicted with reasonable accuracy.

4. Computational cost (including manhour costs) should not be excessive.

From the earliest days of the application of the finite element method to the analysis of reinforced concrete, the prediction of R/C beam behavior has been attempted. Ngo and Scordelis (1967) performed a linear elastic analysis on a R/C beam with a predefined diagonal tension crack. Nilson (1968), Scordelis et al. (1974) and Houde and Mirza (1974) used the discrete crack approach while Franklin (1970), Valliappan and Doolan (1972), Colville and Abbasi (1974), Nam and Salmon (1974), Cedolin and Dei Poli (1977), Buyukozturk (1977), Bergan and Holand (1978), Ottosen (1982), Taniguchi (1984) and Rots et al. (1985) used the smeared crack approach to predict the behavior of R/C beams. However, to the best of the author's knowledge, none of the published work meets all the requirements cited above, especially the second requirement. This study endeavours to fulfill this need. In order to cover a wide range of beam behavior, the following beams were selected for analysis.

1. One beam tested by Burns and Seiss (1966), shown in Fig. 5.8, which failed in the ductile flexural mode (i.e., it failed in compression subsequent to the yielding of longitudinal reinforcement).
2. Three beams with different shear span to depth ratios, tested by Bresler and Scordelis (1961), all of which failed in shear in the

diagonal tension mode (i.e., failure of 'beam action'). These are designated as beams 0A1, 0A2 and 0A3 in Figs. 5.9 and have shear span to depth ratios of approximately 4.0, 5.0 and 7.0 respectively.

3. Two beams without web reinforcement tested by Kani (1979) and shown in Fig. 5.10, with shear span to depth ratios of approximately 2.0 and 2.5.
4. Three beams with web reinforcement designated as A1, A2 and A3 in Figs. 5.9, with geometric and material properties very similar to 0A1, 0A2 and 0A3 respectively except for the web reinforcement.

The geometric and material properties of these beams are summarized in Table 5.1.

5.4 Nonlinear Finite Element Analysis of R/C Beams

5.4.1 Introduction

The element formulations described in Chapter 2 and the consitutive modelling described in Chapter 3 have been coded in the form of computer subroutines suitable for incorporation into a general purpose nonlinear finite element analysis code as discussed in Chapter 1. In this study, these subroutines have been incorporated into the finite element code FEPARCS5 (Elwi and Murray, 1980b). Figure 5.11 illustrates the values of concrete properties at various stress/damage regions. All results in this chapter are obtained using the material properties shown in Fig. 5.11 unless otherwise noted. Concrete material properties to be input into the program were derived from the properties obtained from specimen tests, as described in Appendix A4 and summarized in Table 5.2. Reinforcing steel has been modeled as elastic-strain hardening plastic material. The stress-strain curves for steel obtained from specimen

tests are input into he program as piecewise linear curves.

The method of stress computation, the finite element modelling and solution procedure, comparison of experimental results with the finite element prediction, relative influence of parameters on the predictive failure loads, internal stress distribution and the load-deflection behavior are dealt with in the following subsections of this chapter.

5.4.2 Stress Computation

The flow chart of the stress computation subroutine is shown in Fig. 5.12. Concrete is assumed to be isotropic unless tensile cracking develops whereafter the axes of orthotropy are set parallel and perpendicular to the primary crack orientation. These axes of orthotropy (local material axes) are assumed fixed for all subsequent loading. Thus the assumption about orientation of the axes of orthotropy differs from the rotating crack model used in Chapter 4. This assumption is appropriate for elements under proportional loading and containing no reinforcement or reinforcement in one direction only.

The use of a positive shear modulus for cracked concrete in conjunction with fixed axes of orthotropy allows the direction of the principal concrete stresses to rotate, and hence there is the potential for subsequent cracking to occur in new directions non-orthogonal to the initial crack direction. However, this secondary cracking is often ignored or inconsistently dealt with in the literature (ASCE, 1982). In several cases the second crack is assumed to occur only if the tensile stress exceeds the tensile strength in the orthogonal direction (Darwin and Pecknold, 1974). But such a limitation may violate the tension

failure criterion within the element (Crisfield, 1984; Milford, 1984) and hence overestimate the failure load.

In this study this problem is dealt with as shown in Fig. 5.12. The second crack is assumed to develop orthogonal to the first crack when the stress at any orientation to the first crack exceeds the tensile strength, and the shear stress is limited to such a value that the tension failure criterion is not violated. The tangent shear modulus is set to zero after the appearance of the second crack.

That such a procedure reasonably represents the actual physical behavior can be seen by considering shear critical beams in which failure of the 'beam action' occurs. The shear stiffness of the elements is a measure of the stiffness of the concrete 'cantilevers' such as that shown in Fig. 5.4. The secondary cracking is expected to be parallel to direction n-n at the 'built-in' ends of these 'cantilevers', approximately perpendicular to the primary crack and the loss of shear stiffness is a manifestion of the attainment of the limit capacity of these 'cantilevers'.

5.4.3 General Considerations for Finite Element Model

The finite element modelling parameters were selected based on detailed studies of their comparative influence, as discussed in Appendix A3. A typical finite element mesh layout for beams investigated in this study is shown in Fig. 5.13. The quadratic serendipity element has been selected instead of four node quadrilaterals because such elements are more flexible and produce reliable crack patterns even for coarse mesh layout (Appendix A3). The aspect ratio of the elements has been selected to be between 1 and 2 in

order to minimize the directional bias with respect to crack formation (Rots et al., 1985; Darwin, 1985). The size of the elements is expected to have a significant influence on the predicted failure loads, especially for shear critical beams when fracture energy considerations are not included (Appendix A3; Darwin, 1985). Even when fracture energy aspects are considered, selection of an appropriate mesh size is important because local failure at a node will result in the failure of the numerical procedure which is then interpreted, herein, as the onset of structural failure. Local failure at a node will be observed only when all the elements connected to this node fail. Thus, the element size should be such that it contains the localized failure region yet not so large as to overestimate the stiffness of the structure. This is discussed in detail in Appendix A3.

Both the flexural and shear failure of reinforced concrete beams involve crushing of concrete in compression at the ultimate load. Thus the size of the element for R/C beams has been chosen such that it approximately equals, at ultimate stage, the distance of the neutral axis from the extreme compression fibre. In the tension region of beams, the retention of a minimum shear modulus of 5 percent of the uncracked concrete modulus (Fig. 5.11) was found to prevent spurious local instabilities from occuring.

The cracking at a sampling point (Gauss point) is assumed to be distributed only in an area of the element that is tributary to that point. The behavior of the element is relatively insensitive towards local cracking because the overall behavior of the element reflects the material response at all contributing integration points within the element. Thus, there is a stabilizing effect on the solution procedure

when numerical integration is used, the effect being more pronounced the higher the order of integration and the greater the strain gradient in relation to the mesh size. The beneficial effects of increasing the number of integration points must be weighed against the cost of analysis which increases considerably. With the quadratic serendipity element the choice of integration rule is essentially limited to 2x2 reduced integration or 3x3 full integration. Reduced integration has been found to produce spurious zero energy deformation modes where a concrete element is cracked and also lead to nonobjective results with mesh refinement (Appendix A3; Darwin, 1985). Thus 3x3 Gauss quadrature has been selected for use in this study.

Some fundamental studies on cracked reinforced elements (not discussed herein, but related to the convergence studies described in Appendix A3) indicated that the embedded formulation of the reinforcement in quadratic elements may not, in general, be able to reproduce a constant strain condition unless the reinforcement is lumped at the Gauss points corresponding to 2x2 integration. Specific studies on beams showed that the main (longitudinal) reinforcement may be located at the actual location whereas the stirrups must be lumped at the natural coordinates of $\pm$ 0.5774 (i.e., Gauss points corresponding to 2x2 integration).

The standard (or 'full') Newton-Raphson interation procedure has been used to solve the nonlinear system of equations until the failure load of the structure is reached. The maximum number of iterations were specified as 25, the norms of incremental displacement and unbalanced force vectors as 0.1% and 1.0% respectively. In calculating the tangent structure stiffness matrix, actual tangent material moduli are used

except in the cracked regions where the material moduli perpendicular to crack directions are set to zero. Failure load is assumed to have been reached when there is failure of convergence of both the displacement and force vector norms in the specified number of iterations or if the structure tangent stiffness matrix contains a zero or negative element in the diagonal.

The corresponding load level is referred to as the collapse load although it might actually be only the numerical procedure that has failed and not the structure. Thus, in order to confirm that failure of the structure has in fact occurred and to determine the mode and causes of failure, it is useful to output the stresses and strains at the unconverged final load step. A modified Newton-Raphson iterative procedure, wherein the structure stiffness matrix of the last converged equilibrium position is used, may be adopted for this purpose. In some instances it might also be illustrative to modify the tangent moduli (for example, reduce the compressive strain softening modulus or increase the crack shear modulus) in order to obtain a solution. The stresses and strains thus output are examined to ascertain the mode and causes of failure.

In the following sections, the results of the application of the FEM to predict the behavior of beams failing in flexure, shear critical beams without web reinforcement and beams with web reinforcement are described. The effects of bond slip (i.e. bond elements) have been included for shear critical beams without web reinforcement because, in these beams, the relative proportion of shear carried by beam action and arch action, as represented by Eq. 5.6, is dependent on the bond between steel and concrete. Whereas in beams with web reinforcement, the change

in the shear carrying mechanism after concrete cracking can be reproduced without bond elements.

5.5 Prediction of Flexural Failure

As an example of ductile flexural failure, a beam (Mark J4) tested by Burns and Siess (1966) has been selected. This beam is reported to have failed in a ductile manner, after yielding of the longitudinal reinforcement. Numerical analyses of this beam by the finite element method have been carried out by a number of investigators using different approaches (Arnesen, 1979; Darwin and Pecknold, 1974; Hand, Pecknold and Schnobrich, 1972; Suidan and Schnobrich, 1973).

The finite element mesh layout used in this study is shown in Fig. 5.13, wherein, due to symmetry, only one half of the span is modelled. The post-yield stress-strain relationship for steel is not available. In order to stabilize the numerical solution after steel yielding, an elastic-strain hardening stress-strain curve has been used in this study, as shown in Fig. 5.14. In order to investigate the effect of the steel strain hardening modulus, analyses were performed with two different values for this modulus, one with $0.1E_s$ and another with $0.005E_s$ (the latter being closer to the test value). Large load steps were used, the size of each load step until steel yield being about 1/5 ultimate load. After steel yielding the size of the load step was reduced. Convergence was obtained in about 20 to 25 iterates. The load deflection relationship is shown in Fig. 5.15.

It is seen that the finite element analysis which takes into account the tension softening in concrete, predicts the load deflection response well. The load corresponding to the yielding of steel has also

been closely predicted. In addition, the deflection corresponding to concrete crushing agrees closely with the test value. The 'rise' of the neutral axis after steel yielding is shown in Fig. 5.16. The crack pattern obtained using the finite element analysis is shown in Fig. 5.17 for two successive load steps, one before steel yielding and the other after steel yielding. The cracking is predominantly vertical (because of the low reinforcing percentage). Secondary cracking has occurred at a number of Gauss points, but not sufficient to produce shear failure.

The longitudinal stress distribution in concrete and steel are shown in Figs. 5.18a and b for a load of 37.5 kips (167 kN). It can be readily seen that a linear elastic analysis seriously underestimates the stresses in concrete. The horizontal 'shift' in the steel stress due to the inclination of cracks has also been predicted by the finite element analysis. This 'shift' is rather small in this case, because the cracks are nearly vertical.

The load-deflection curves obtained by several investigators are compared to that obtained in this study in Fig. 5.19. The simple concrete material model used in this study is thus seen to be adequate for predicting all the salient features of the physical behavior of this beam and, by inference, those of all beams which fail in a ductile flexural mode.

5.6 Prediction of Shear Failure - Beams Without Web Reinforcement

5.6.1 Bresler Scordelis Beam 0A1 - $a/d \simeq 4.0$

The finite element mesh layouts for all the shear critical beams without web reinforcement investigated in this study are shown in Figs. 5.20a through e. The load-deflection curve for the Bresler-Scordelis

beam 0A1 (with shear span to depth ratio of 3.97) predicted by the finite element method is compared to the experimental curve in Fig. 5.21. The curves are essentially identical up to the experimental failure load. The experimental crack pattern is shown in Fig. 5.22a. The analytical crack pattern obtained in this study is shown in Fig. 5.22b and c. Figure 5.22 b corresponds to a load level of 60 kip (167 kN) (the load at which inclined cracking was observed in the test), and Fig. 5.22c to a load level close to the ultimate. Figures 5.22d and 5.22e show the corresponding crack patterns when a tension cut-off criterion is used. The development of horizontal cracking at ultimate load close to the neutral axis is apparent in the analytical crack pattern.

At the analytical failure load level the number of Gauss points in damage region 2 of Fig. 5.11 significantly increased, particularly near the mid span of the beam. In the next load step, divergence occurred regardless of the structural stiffness matrix used for iteration. The reduction in the size of the load step to 1.0 percent of the total load could not produce convergence either. An analysis of the stresses at the failure load level and at the next unconverged load step leads to the conclusion that the numerical failure was connected to the uncontrollable increase in strain at a number of cracked integration points. At the maximum load level (at which convergence occurred) no element exhibited compression softening (although the top four Gauss points nearest to the load entered into region -1 of Fig. 5.11, that is, they entered the compression hardening region). The stress in steel was approximately 42.0 ksi (290 MPa), well below the yield strength of 80.5 ksi (555 MPa). Thus the numerical failure is directly attributable to

the loss of shear stiffness in a number of elements which is the manifestation of the failure mode designated as 'beam action' in Sect. 5.2.2 (that is, the failure of concrete segments between the cracks).

The failure mode can also be verified by comparing the relative vertical displacement between the top and bottom faces of the beam as shown in Fig. 5.23. The marked change in slope at the onset of inclined cracking, which was observed in the test, has been reproduced using the finite element analysis that takes into account the tension softening in concrete. The prediction using the tension cut-off assumption is evidently too soft, as also observed by Ottosen (1982).

The principal stress trajectories can be identified in Fig. 5.24 for a load level very close to the ultimate. The length of line of the 'cross' at each Gauss point is proportional to the magnitude of the stress and the lines are oriented along principal stress axes. The absence of arching action from the load point to the support is apparent, again indicating the failure mode as diagonal tension.

The stress distribution across three sections, first at a section close to the load point, second near quarter span and the third at a section near the support, are shown in Fig. 5.25. The shear stresses were averaged over the element whereas normal stresses were averaged over Gauss points at the same level in the element. This shear stress distribution indicates greater contribution from aggregate interlock than that assumed by MacGregor and Walters (1967). The normal stress distribution is essentially linear. The distribution of shear and normal strains indicates the large increase in shear strains in the cracked region.

The stresses in the reinforcement are compared to those obtained

using the engineering analysis described in Sect. 5.2.2.5 as shown in Fig. 5.26. The finite element analysis using the tension cut-off criterion correctly predicts a 'shift' in the stress level due to the inclination of the cracking. The average stresses obtained when tension softening and tension stiffening are included, can be used to determine the stresses at the crack locations by adding the tension contribution from the concrete to these average stresses. Such computations show the stress level in the steel reinforcement to be approximately same as that obtained using the tension cut-off analysis. It is also apparent that the practice of using elastic linear finite element analysis to determine the tensile stresses in steel and concrete and lumping all tension in steel underestimates the stresses in the reinforcement.

The longitudinal compressive stresses in concrete at the top Gauss points are shown in Fig. 5.27. The linear elastic analysis significantly underestimates the stresses because uncracked section properties were used. The stresses near the load point exceed the uniaxial compressive strength due to the presence of normal compressive stresses in this region (i.e. due to biaxial compression, see Fig. 3.21). The reduction in concrete compressive stresses from the cracked section engineering analysis due to tension softening and tension stiffening is minor. This is in contrast to deep beams where the tension stiffening signficantly reduces the compressive stresses (Chapter 4, Floegl and Mang, 1982).

5.6.2 Kani's Beam No. 65 - ($a/d \simeq 2.5$)

This beam with shear span to depth ratio of 2.46, shown in Fig. 5.10, was tested by Kani (1967) and was reported to have failed in the

diagonal tension mode. The computed load deflection curve is shown in Fig. 5.28. (Except for the experimental failure load, no other data on the results of the experiment are available.) Convergence to the specified tolerance of 1.0 percent on the norm of the unbalanced load vector occurred up to a load of 27.5 kips (122 kN). At the next load step (for a total load of 30.0 kips (133 kN)) the unbalanced load vector fluctuated, the least value of the norm being 1.75 per cent. In the subsequent load step divergence occurred starting from the first iteration and both displacement and force tolerances were exceeded. Displacement and stresses output on this unconverged load level indicated disproportionate increase in strains over the previous load level. The load versus relative vertical displacement between the top and bottom faces of the beam (shown in Fig. 5.29) also indicates an abrupt increase at the unconverged load step signifying diagonal tension failure. Figure 5.29 also shows a marked change in slope at a load level of 20 kip (89 kN) indicating the onset of inclined cracking. Compressive stresses throughout the beam were in region '0', i.e. elastic at failure. Thus, the failure was not initiated by the compression softening near the load point but rather by the uncontrolled increase in strain at a number of cracked integration points. This can also be deduced from the analytical crack pattern shown in Fig. 5.30. It is apparent that the height of cracks is greater in the shear span than in the constant moment region. (Also most of the 'cracked' Gauss points were in damage zone 2 in the shear span whereas they were in damage zone 1 in the constant moment region. The prevalence of secondary cracking (in sections adjacent to the load) in the shear span region can also be seen.

The principal stress trajectories are shown in Fig. 5.31. The length of the line of the 'cross' at each Gauss point is proportional to the magnitude of the stress. The absence of a 'direct' load path between the load and support points (i.e. the absence of arch action) can be seen. (This is even more evident when the crack pattern shown in Fig. 5.36 for Kani's Beam 72, which is discussed subsequently, is compared to that for Beam 65.) Some degree of 'strain localization' can be discerned from the analytical crack pattern.

The longitudinal stress distribution along the length of the beam is shown in Fig. 5.32 and is compared to the linear elastic finite element analysis and to the conventional engineering analysis neglecting concrete in tension. The linear elastic finite element analysis underestimates the concrete stresses in the cracked region. There is also significant increase in concrete stresses at the load point due to stress concentration. The shear stress distribution across a section approximately 6 in. (150 mm) away from the load point in the shear span is shown in Fig. 5.33 and is compared to that assumed by MacGregor and Walters (1967) in their analysis. As for beam OA1, greater contribution from aggregate interlock is predicted by this analysis than they have assumed.

5.6.3 Kani's Beam 72 - $a/d \simeq 2.0$

This beam, also tested by Kani, has been reported to have failed in the 'slow diagonal failure' mode. The experimental load deflection curve is not available. The load-midspan deflection curve obtained using the finite element analysis is shown in Fig. 5.34. Convergence to the specified tolerance of 1.0 percent on the unbalanced force vector

norm was obtained up to a load level of 37.5 kips (166.8 kN). In the next load step (at a total load of 40.0 kips (178 kN)), the best convergence that could be obtained was 1.5 percent. In the subsequent load step, divergence occurred starting from the second iteration. The stresses and strains output on this unconverged load indicated a highly disproportionate increase in displacements and a large increase in the number of cracked integration points. The load versus relative vertical displacement between the top and bottom faces of the beam ('thickening') is shown in Fig. 5.35. In contrast to Beam 65, the thickening is gradual, probably due to the 'arch action'. Some degree of arch action can also be identified from the analytical crack pattern shown Fig. 5.36. The absence of 'strain localization' is significant, especially when compared to the crack pattern for Beam 65.

The shear stress distribution across the depth of the section is shown in Fig. 5.37. The distribution is smoother than for the other beams and approaches that of a solid section. This can be attributed to the strain softening in tension and the smaller reduction in the cracked shear stiffness compared to beams with greater shear span to depth ratios. The principal stress plot shown in Fig. 5.38 also supports the notion that the contribution of arch action to shear resistance is significant in this case.

5.6.4 Bresler-Scordelis Beam 0A2 - $a/d \simeq 5.0$

The load-deflection curve for this beam with a shear span to depth ratio of 4.90 is shown in Fig. 5.39. The deflected shape at two successive load steps near failure load is shown in Figs. 5.40. The finite element prediction is again in good agreement with test

results. The convergence to the specified tolerance of 0.1 per cent on the incremental displacement norm and 1.0 percent on the unbalanced force vector norm, occurred up to a load level of 90 kips (400 kN) although a definite reduction in stiffness occurred at 80 kips (356 kN) load level (i.e. at the experimental failure load). At the next load step divergence occurred starting at the first iteration. The failure mode can be identified by comparing the cracking pattern at failure, Fig. 5.41b, to that of the previous load step, shown in Fig. 5.41a. The horizontal cracking near the load point and the increase in the number of Gauss points with secondary cracking, clearly indicate the failure mode as diagonal tension. The analytical crack pattern compares favorably with that obtained from the experiment, shown in Fig. 5.41c.

There was no 'compression softening' in any of the elements, although a majority of Gauss points in the top two elements adjacent to the load point have entered into the damage region '-1'. Even when this region was extended such that the strain corresponding to the maximum compressive strength was 0.00375 instead of 0.002, the numerical failure occurred at the same load level. This does not support the assertion made by Ottosen (1982) and by Glemberg anbd Samuelsson (1984) that the visible diagonal cracking is a consequence of the crushing and softening in the compression zone. It is interesting to note that a tension cut-off analysis indicates compression softening at some Gauss points near the load, which perhaps might have led to the above assertion. As for beam OA1, the numerical failure, attributable to the uncontrollable increase in tensile strain at a number of Gauss points, indicates a diagonal tension mode of failure.

The failure mode can also be verified by comparing the relative

vertical displacement between top and bottom faces of the beam obtained from the analysis to that measured during the experiment, as shown in Fig. 5.42. The marked increase in the 'thickening' at failure load is apparent. As for beam OA1, the prediction using tension cut-off criterion is too soft. This figure also illustrates the significant loss of stiffness at 80 kips (356 kN) load level, and hence indicates that this may be appropriate as a predicted failure load.

The distribution of shear stress across the depth of the section is shown in Figs. 5.43a and b for two different load levels. The distribution of average shear stress is more even than if tension cut-off and a constant shear reduction factor are assumed. Comparison of the shear stress distribution across section closer to the load point, at two successive load steps near failure, indicates that shear carried by intact concrete at the top increased substantially with increase in load while the shear carried in the cracked portion below the neutral axis did not increase significantly. Failure occurs because of the reduction in shear stiffness of the cracked concrete and its consequent inability to transfer the incremental force in steel without undergoing large strains. This of course confirms the importance of aggregate interlock in shear resistance.

The distribution of shear stress across sections farther from the critical section is more uniform and the increase in stress at two successive load steps is also more uniform. The shear stress distribution assumed by MacGregor and Walters (1967) is also shown in Fig. 5.43. As for Beam OA1 the difference is mainly attributable to the estimated contribution from aggregate interlock. The finite element analysis including tension softening predicts the contribution from

aggregate interlock and dowel action to shear resistance to be approximately 50 percent.

The principal stress plot is shown in Fig. 5.44. The absence of arch action is evident. The distribution of longitudinal stress across the depth of a section approximately 11.75 in. (300 mm) from the load point, is shown in Fig. 5.45. The penetration of the crack well into the compression region at ultimate load (in approximately horizontal direction) is apparent. The change in neutral axis location is insignificant, indicating that flexural failure is far from being imminent.

The longitudinal distribution of maximum compressive stress is shown in Fig. 5.46. As for beam 0A1, linear elastic finite element analysis underestimates the stresses.

5.6.5 Bresler-Scordelis Beam 0A3 - $a/d \simeq 7.0$

This beam with a shear span to depth ratio of 6.94 is reported to have failed in the diagonal tension mode. The load deflection relationship observed during the experiment is compared to the finite element prediction in Fig. 5.47. Again the prediction is good. The numerical failure was initiated by compression softening and crushing near the load point. This is confirmed by the absence of numerical failure until a load of 115 kips (511 kN), instead of 90 kips (400 kN), when the length of the compression damage zone '-1' was increased such that the strain corresponding to the maximum uniaxial compressive stress is 0.00375 (instead of about 0.002 obtained from cylinder tests). The increase in shear capacity of this beam when higher compressive ductility of concrete is assumed can be attributed to the high bending

compressive stresses resisting the penetration of diagonal cracking into the compressive zone above the neutral axis.

The load versus relative vertical displacement between the top and bottom faces of the beam is shown in Fig. 5.48. The onset of diagonal cracking has been predicted well using this analysis. That the failure mode may be characterized as diagonal tension is supported by the large increase in the relative vertical displacement beyond the 90 kip load level.

The crack pattern observed in the experiment, shown in Fig. 5.49a, compares favorably with that predicted by the analysis, shown in Fig. 5.49b.

The distribution of longitudinal and shear stresses across the depth of the section is shown in Fig. 5.50. Compared to beam 0A2, there is less penetration of cracking into the compressive zone due to the larger compressive stresses. The shear stress distribution across the section is fairly even. The shear strain distribution is highly skewed towards the cracked region and the magnitude of the shear strain in the cracked region is in the same order as that of normal strain. Failure occurred because of the loss of shear stiffness above and below the neutral axis. This is in contrast to beams 0A1 and 0A2 which failed due to the loss of shear stiffness in the tensile cracked region only.

The principal stress plot is shown in Fig. 5.51. Vertical compressive stresses are insignificant and arch action is absent.

5.7 Prediction of Behavior of Beams with Web Reinforcement

5.7.1 Bresler-Scordelis Beam A3 - Flexural Failure

The finite element mesh layouts for the beams with web

reinforcement investigated in this study are shown in Figs. 5.52a, b and c. Bresler-Scordelis Beam A3 with web reinforcement had material and geometric properties the same as those of Beam 0A3 and is reported to have failed in flexural compression. Since the longitudinal reinforcement ratio in this beam exceeds the 'balanced' ratio, as calculated using the ACI code, the beam is expected to fail in compression. The increased ductility in concrete due to confinement provided by the steel stirrups has been accounted for by using a shallower compression softening branch as shown in Table 5.2. The post yield stress-strain relationship used for longitudinal steel reinforcement becomes important in this case. The stress-strain curve for steel obtained from test is compared to that used in this study in Fig. 5.53. Since the use of a horizontal 'plateau' in the stress-strain curve for steel will introduce numerical instabilities in the solution procedure, strain hardening is assumed to start at the yield point.

The load deflection relation predicted by the finite element method is compared to that observed in the experiment, in Fig. 5.54. The failure load calculated by Bresler and Scordelis (using a rectangular equivalent compressive stress block and a limiting strain of 0.003 for concrete) as governed by flexure has been given as 96 kips (427 kN). The experimental failure load of 105.3 kips (468 kN) exceeds this value due to the increased ductility in concrete. This is confirmed by calculations using the ACI code assumptions and the finite element analysis which give the load corresponding to the onset of steel yielding as 106 kips (471 kN). The finite element analysis gives converged solutions beyond this level because the horizontal plateau in the steel stress-strain curve has been ignored.

The failure mode is characterized as flexural compression which is inferred from the strain softening in the biaxial compression region near the load point indicated by the finite element analysis. This is also confirmed by the absence of significant deformation in the load-relative vertical displacement relation shown in Fig. 5.55. The stirrups have not yielded and their effect in increasing the load carrying capacity above that of beam 0A3 is due to confinement of concrete in compression. Thus the presence of stirrups in this beam has altered the failure mode from diagonal tension to flexural compression.

The experimental crack pattern shown in Fig. 5.56 compares favorably with the finite element prediction, shown in Fig. 5.57a and 5.57b at two successive load steps just before failure. The increase in the number of Gauss points in the midspan region where secondary cracking has occurred and the number of cracked Gauss points in the end regions is apparent.

5.7.2 Bresler Scordelis Beam A2 - Shear Compression Failure

Except for the provision of web reinforcement, this beam has geometric and material properties the same as for Beam 0A2. This beam is reported to have failed in shear-compression. The increased ductility in concrete due to the confinement provided by the steel stirrups has been accounted for in the input material properties, as shown in Table 5.2. Tension stiffening in the web reinforcement has been neglected because the cross-sectional area of stirrups is very small compared to the area of concrete. The load deflection relation predicted by the finite element method is compared in Fig. 5.58 to that observed in the experiment. Again, the prediction is seen to be good.

Failure (in the analysis) is initiated by the yielding of steel stirrups. The longitudinal steel has not yielded. The compressive stress at most of the Gauss points near the load is in region '-1' but no softening (region '-2') occurred at any of the Gauss points. The numerical failure was manifested as a zero or negative term on the main diagonal of the tangent structure stiffness matrix. That the failure was initiated by the yielding of stirrups is confirmed by the load-relative vertical displacement curve shown in Fig. 5.59, which shows a sudden increase in the 'thickening' of the beam prior to failure. This is further confirmed by the increase in failure load to 112 kips (498 kN) in a finite element analysis in which tension stiffening was assumed in web reinforcement as well. This analysis also exhibited compressive strain softening at some Gauss points near the load. Thus it is seen that, in contrast to Beam A3, an increase in the amount of web reinforcement would change the finite element prediction to a flexural compression failure at about 112 kips (498 kN) load rather the shear compression failure at 100 kips (448 kN).

The distribution of stresses in stirrups at various distances from the center of the beam is shownin Fig. 5.60. It is seen that yielding has occurred in stirrups in the end quarter spans of the beam rather than the mid half span. This could be explained using the crack pattern. The crack pattern observed in the experiment is shown in Fig. 5.61 and that obtained using the finite element analysis is shown in Fig. 5.62. Both crack patterns show the crack inclination to be closer to the horizontal in the end quarter span because of the higher ratio of shear stresses to flexural stresse in this region. It could be deduced that the diagonal tension crack started at the end closer to the support

and propagated towards the load point, the function of the web reinforcement being to delay this propagation. This is also confirmed by the thickening at various distances from the load point, observed during the experiment, shown in Fig. 5.63. The relative vertical displacement is much greater at ends closer to the supports indicating that the stirrups have yielded in this region.

The distribution of shear stresses across the depth of the section is shown in Fig. 5.64. The form of distribution does not differ significantly from that for Beam 0A2.

The finite element model thus correctly predicts that the effect of stirrups is to change the failure mode from diagonal tension failure of Beam 0A2 to the shear compression failure of Beam A2, as observed in tests.

5.7.3 Bresler-Scordelis Beam A1 - Shear Compression Failure

Except for the addition of web reinforcement, this beam has the same material and geometric properties as for beam 0A1. As indicated in Table 5.2, the confinement provided by the web reinforcement increases the strain softening modulus and the ductility and this is taken into account in the selection of the input parameters. The load-deflection behavior predicted by the FEM is compared to that observed in the experiment in Fig. 5.65. Failure of the numerical analysis was initiated by the yielding of stirrups. This is confirmed by the load-relative vertical displacement ('thickening') behavior, shown in Fig. 5.66. At the final load step, there was an abrupt increase in stirrup stresses from the previous load step with stirrups yielding at a number of Gauss points, indicating that failure occurred when the released

stresses from the cracked concrete could not be accommodated by steel stirrups. The crack pattern obtained from the finite element analysis for the last two successive load steps is shown in Fig. 5.67a and 5.67b and compares well with the observed crack pattern shown in Fig. 5.67c. The large increase in the number of cracked Gauss points in elements closer to the support can be seen when Figures 5.67a and 5.67b are compared. The crack inclination is almost horizontal at a number of Gauss points lying just below the neutral axis and are at sections where stirrups have yielded. In contrast to Beam A2, the yielding of stirrups has occurred at a number of points not only in the outer 1/4 span but in the full span. This might again be attributed to the higher ratio of shear to normal stresses inducing cracking closer to horizontal.

The distribution of stresses in stirrups at various locations in the span is shown in Fig. 5.68 for two successive load steps near failure. The abrupt increase in stresses is apparent.

The distribution of stresses in concrete at two successive load steps near failure is shown in Figs. 5.69a and Fig. 5.69b. The increase in the principal compressive stresses due to yielding of stirrups in 'Region A' and due to additional cracking in 'Region B' can be seen. The compressive stresses at a number of Gauss points near the load point have entered into damage region "-1" at failure. Thus the change in failure mode effected by web reinforcement, from that of diagonal tension for Beam 0A1 to shear compression for Beam A1, has been correctly predicted by the finite element analysis.

5.8 Evaluation of Finite Element Prediction

Failure loads predicted by the finite element analysis are compared

to the experimental values in Table 5.3 and in Fig. 5.70. Comparison is also made in Table 5.3 and Fig. 5.71 to Zsutty's (1971) prediction. Zsutty developed the following empirical equations for lower bound based on the statistical analysis of a large number of test results:

For beams without web reinforcement:

$$V_{uc} = 60 \left(f'_c \rho \frac{d}{a}\right)^{1/3} bd \qquad \text{for } a/d > 2.5 \qquad (5.15a)$$

$$V_{uc} = 59 \left(f'_c \rho \frac{d}{a}\right)^{1/3} bd \left(\frac{2.5}{a/d}\right) \qquad \text{for } a/d < 2.5 \qquad (5.15b)$$

For beams with web reinforcement:

$$V_u = V_{uc} + \frac{A_v}{S} f_{y_w} d \qquad (5.15c)$$

where V_{uc} is the concrete contribution given by 5.15a or 5.15b and A_v is the area of stirrups, f_{y_w} is the yield strength, S is the spacing of stirrups, ρ is the main reinforcement ratio, b is the width of cross section, and d is the effective depth.

In Table 5.3, comparison is made as well to the provisions of the ACI code (1983) which are given by Eq. 5.16a for beams without web reinforcement and Eq. 5.16b for beams with web reinforcement

$$V_{uc} = \left(1.9\sqrt{f'_c} + 2500\rho \frac{V_u d}{M_u}\right) bd \qquad (5.16a)$$

$$V_u = V_{uc} + \frac{A_v f_{y_w}}{S} d \qquad (5.16b)$$

where $\frac{M_u}{V_u d} = \frac{a}{d} = \frac{\text{shear span}}{\text{depth}}$

The ratio of the Zsutty's predictions to the finite element predictions varies between 0.82 and 0.96 which is certainly acceptable considering the wide variation in material properties and reinforcement ratios for the test beams of this study.

The correlation in Table 5.3 with the ACI code equations is also good, the ratio of the ACI loads to the predicted loads varying from 0.63 to 0.82. Since the ACI code provision ignores the additional capacity due to arch action for low a/d ratios (a/d < 2.5), it underestimates the shear capacity of beams in this range. The finite element method predicts the 'valley' of diagonal failure of Fig. 5.5 as well, as shown in Fig. 5.72.

The finite element method predicts not only the failure load but also other salient aspects of the physical behavior such as the failure mode, relative vertical displacement between the top and bottom faces of the beam and the load deflection relationship for a wide range of beams, with an accuracy that is completely acceptable for engineering purposes. With the application of the FEM the unifying and differentiating features of each beam can be identified and the qualitative and the quantitative influence of different material parameters can be estimated, as is done in the following paragraphs for beams studied in this investigation.

5.9 Comments on the Behavior of Shear Critical Beams

Considering concrete as a continuum even after cracking, a shear failure criterion can now be identified as follows. Shear failure, either by diagonal tension or shear compression, occurs when the shear modulus of concrete above or below the neutral axis has decreased

sufficiently to produce shear strains of the same order of magnitude as normal strains. Diagonal tension failure occurs when cracked concrete below the neutral axis loses its shear stiffness. Shear-compression failure occurs when concrete above the neutral axis loses its stiffness. The role of the web reinforcement is simply to decrease the rate at which the shear stiffness is reduced; by providing confinement for concrete above the neutral axis and by reducing crack strains below the neutral axis. Arch action reduces the shear to be transferred from below the neutral axis and therefore increases the load at which diagonal tension failure occurs. It is postulated that these failures may be schematically shown by Fig. 5.73.

Although only three beams with web reinforcement were studied, some conclusions may be drawn as to the effectiveness of the web reinforcement. For beams containing web reinforcement which fail due to the yielding of stirrups, such as A1 and A2, the load carrying capacity can be increased by increasing the amount of web reinforcement whereas for beams failing in flexural compression, such as A3, increase in the amount of web reinforcement does not significantly increase the load capacity. Referring to Fig. 5.73, it can be stated that the effect of web reinforcement is to raise curve 'A' towards curve 'B'. Curve 'B' also rises, though by a minor amount, due to the increase in compressive strength resulting from confinement provided by the stirrups.

5.10 Influence of Material Parameters

5.10.1 Tension Softening Modulus

The tension softening modulus influences the numerical solution directly by contributing to the capacity of the shear critical beams at

least at the smaller load levels, and indirectly by its effect on the shear stiffness (due to the assumed relation between the shear stiffness of the cracked concrete and the normal crack strain). The load-deflection relationships obtained from the analyses using the tension cut-off criterion are shown in Fig. 5.74 for Bresler-Scordelis beams 0A1, 0A2 and 0A3 and in Fig. 5.76 for Kani's Beam 72. While failure loads of the Bresler/Scordelis beams have been predicted equally well by both tension softening and tension cut-off analyses it is apparent that tension cut off analysis underestimates the actual stiffness. The tension cut-off analysis considerably underestimates the failure load for Kani's beam 72.

Considering the load versus relative vertical displacement between the top and bottom faces of the beams (i.e., the 'thickening'), it is obvious from Figs. 5.23 and 5.42 that the tension cut-off analysis fails to predict the observed behavior. An advantage of the tension cut-off analysis is that it yields an upper bound on the stresses in the reinforcement. The major disadvantage of the tension cut off analysis is that the predicted failure load in beams where arch action is significant (for shear span to depth ratios less than about 2.5) depends largely on the shear retention factor. This dependence is discussed in more detail in subsection 5.10.5. A more fundamental objection to the tension cut-off analysis is that it does not represent the observed material behavior.

Analyses performed in this study with different strain softening moduli show that the predicted failure load is somewhat sensitive to the softening modulus for shallow beams with short shear spans (for $a/d < 2.5$) such as Beam 72. For Beam 72, as seen from Fig. 5.75, an increase

in the ultimate tensile strain from 0.0014 to 0.0018 (a 22% increase) resulted in an increase in the predicted failure load from 37.5 kips to 40.0 kips (a 6.7% increase). This dependence is not only because of the increase in the residual shear stiffness when a shallower tension softening branch is used but mainly because the development of the fracture process zone in this beam is incomplete at failure.

The load-deflection relationship for a plain concrete beam with a shear span to depth ratio of 2.0 is shown in Fig. A4.6. It is seen that the maximum load carrying capacity of this beam at point 2 in Fig. A4.6 occurs when the fracture process zone is not fully developed i.e. the effective tensile stress has not been reduced to zero at the tip of the crack. Thus an increase in the fracture energy will increase the failure load of this beam. For shallow reinforced concrete beams with short spans, where the fracture process zone is not fully developed, similar dependency exists although to a lesser degree. For Kani's Beam 72 (with shear span to depth ratio of approximately 2), this dependency is shown in Fig. 5.75. Such dependency has also been observed by Rots et al (1985) for reinforced and plain concrete beams and by Darwin (1985) for plain concrete notched beams. However in the practical range of values of ε_{ut} (between say 0.0008 and 0.0018), the difference in the values of the predicted failure load is within the scatter in experimental results for reinforced concrete beams.

5.10.2 Tensile Strength

The tensile strength of concrete significantly influences the predicted failure loads of shear critical beams. For example, the predicted failure load for beam 0A1 was 80 kips (355 kN) for an assumed

tensile strength of 300 psi (2.07 MPa) whereas numerical failure was not obtained even at 97 kips (432 kN) load (i.e, more than 21% increase) when a tensile strength of 757 psi (4.0 MPa) was assumed. However, the ε_{ut} was the same in both cases. This influence of tensile strength on failure load decreases with increasing shear span to depth ratio. For example for beam 0A2, doubling of the tensile strength increased the failure load from 80 kips (355 kN) to 91 kips (405 kN) (approximately 13.8% increase). For beams failing in a ductile manner by longitudinal steel yielding, the effect of the tensile strength on failure load is not significant.

5.10.3 Secondary or Multiple Cracking

The failure load is overestimated when the tensile strength criterion is violated in the analysis after concrete cracking. The influence of secondary or multiple cracking is similar to that of tensile strength. For beam 0A1, for example, the failure load obtained from the analysis was 85 kips (378 kN) (Fig. 5.22c) when secondary cracking was considered whereas failure was not achieved even at 95 kips (423 kN) when secondary cracking was ignored (i.e., when the tensile stress in concrete was allowed to exceed the tensile strength at some Gauss points in directions other than the crack opening direction). The influence of secondary cracking decreases with increasing shear span to depth ratio, similar to the influence of tensile strength. For example, for Beam 0A2, the increase in failure load was only 3.9% when secondary cracking was not considered.

5.10.4 Compressive Stress-Strain Relationship

Considering Fig. 5.73 the reduction in the values of the material moduli at high compressive stresses and the value of the compressive strain softening modulus would be expected to have significant influence on the failure load when failure is governed by curve 'B'. It is also expected that the predicted failure mode is sensitive to those moduli as the difference between the resistance values represented by curves 'A' and 'B' becomes smaller. For Kani's Beam 65, with a/d of 2.5, the predicted failure load is unaffected by the stress-strain relation adopted in regions '-1' and '-2' (Sect. 5.6.2.). For Beam OA1, the value of the compressive strain softening modulus had no effect on the failure load whereas the modulus in region '-1' had only a minor effect (Sect. 5.6.1). For beam OA3, both the compresive strain softening modulus and the modulus in region '-1' greatly influence the predicted failure load (Sect. 5.6.5). For beams with web reinforcement the degree of influence of these moduli is dependent on the shear span to depth ratio, amount of web reinforcement and the amount of longitudinal steel.

In beams with short shear span to depth ratios (less than about 2.0) the influence of the tensile stress in the orthogonal direction on the post-cracking compressive strength also becomes important, as well as the precracking stress strain relationship due to the high compressive stresses parallel to the cracks.

Since the use of a multilinear uniaxial stress-strain relationship in this study has yielded acceptable predictions of beam behavior, greater refinement in modelling the shape of the stress strain curve does not seem to be necessary. However, it is anticipated that, unless attention is paid to all the critical parameters identified herein,

generalized material models will have significant difficulty in properly predicting correct failure modes and loads over the full range of variables as they occur in real structures.

5.10.5 Crack Shear Modulus

The use of a constant crack shear modulus (i.e., a constant shear retention factor) does not adequately represent observed behavior and leads to failure load predictions which are highly dependent on the shear retention factor used. For example, using a constant crack shear modulus of 5 per cent of the uncracked shear modulus leads to close prediction of failure load for beams 0A1, 0A2, and 0A3. But for Kani's beams 65 and 72, the predicted failure loads with this modulus were very low. (For example, the failure load for B72 was 32 per cent lower than the experimental failure load.) When a shear retention factor of 0.4 was used for beam 0A1, failure was not observed even at 100 kips (which is 33 per cent higher than the actual failure load). This dependence of failure load prediction on the shear retention factor is stronger if the tension cut-off criterion is used.

Thus it is essential to account for the reduction in shear modulus with increasing normal crack strain in the finite element analysis of shear critical beams. However, only limited experimental results are available relating the crack shear stress and the crack shear displacement in mixed mode fracture conditions. Also, some simplifying assumptions must be made in deriving an equivalent relationship between crack stress and crack strain. Fortunately, although it is essential that the dependency be accounted for, high accuracy in modelling this relationship does not appear to be necessary in order to obtain reliable

finite element predictions and the bilinear relationship adopted in this study seems adequate.

As mentioned in Chapter 3, a minimum crack shear modulus is required for numerical stability. A value of 1.0 per cent of the uncracked shear modulus is adequate to avoid spurious numerical instability. A value of 5.0 per cent has been used in this study since it matches the test results more closely, leads to faster convergence and does not increase the failure load significantly.

5.10.6 Bond-Slip

The effects of bond slip have been the subject of much speculation both in the context of the physical behavior as well as the numerical analysis procedure. The results of the analysis of several beams with and without bond slip are shown in Table 5.4. It is seen that the effect of bond slip in beams where arch action is not significant (i.e. for $a/d > 2.5$) is to reduce the failure load whereas for $a/d < 2.5$ (where arch action is significant) it increases the failure load.

The reduction in failure load due to bond slip for beams with $a/d > 2.5$ occurs because of the increase in crack strains and the consequent reduction in shear stiffness. For beams with $a/d < 2.5$, the increase in failure load due to bond slip occurs because arch action is enhanced. That arch action increases at the expense of bond slip is evident when the predicted failure load of Kani's Beam 72 assuming perfect bond is compared to that predicted allowing for bond slip (an increase of 10.6 percent). Thus it seems that greater bond stiffening increases beam capacity when beam action controls whereas a reduction of bond stiffness increases beam capacity when arch action controls (although in the

latter case the probability of anchorage failure increases). In either case it is obvious that bond-slip effects have to be considered to obtain better predictions of the beam behavior.

Table 5.1 Summary of Experimental Beams Analysed in This Study

Spec. No.	Concrete f'_c ksi	Concrete f'_t ksi	Beam Dimensions b in.	h in.	d in.	L ft.	Ratio a/d	Reinforcement No. 9[1] bars (or A_s in in.^{2})	p %	No. 4[2] bars	p' %	Spacing No. 2 Stirrups, in.	fy = yield point of main reinf. ksi
Bresler-Scordelis Beams													
OA-1	3.27	.575	12.2	21.9	18.15	12	3.97	4	1.81	0	0	--	80.50
OA-2	3.44	.629	12.0	22.1	18.35	15	4.90	5	2.27	0	0	--	80.50
OA-3	5.45	.600	12.1	21.9	18.17	21	6.94	6	2.74	0	0	--	80.10
A-1	3.49	.559	12.1	22.1	18.35	12	3.92	4	1.80	2	0.180	8 1/4	80.50
A-2	3.52	.540	12.0	22.0	18.27	15	4.93	5	2.28	2	0.182	8 1/4	80.50
A-3	5.08	.629	12.1	22.1	18.35	21	6.91	6	2.73	2	0.182	8 1/4	80.10
Kani's Beams													
B72	3.60	-[4]	6.0	24.0	21.62	10.47	1.96	(3.51)	2.70	0	0	--	55.7
B65	3.91	-[4]	5.89	24.0	21.75	12.25	2.46	(3.61)	2.82	0	0	--	54.2
Burns-Siess Beam													
J-4	4.83	-[4]	8.0	20.0	18.0	13.0	4.33	(1.57)	1.09	-[4]	-[4]	6[5]	44.9

Notes: (1) In two or three layers.
(2) Yield point value f_y = 50.1 ksi for No. 4 bars, compression steel.
(3) Yield point value f_y = 47.2 ksi for No. 2 bars, stirrups. Nominal area of No. 2, based on weight, equals 0.050 sq. in.
(4) Not available.
(5) No. 3 stirrups.
1 ksi = 6.895 MPa; 1 in. = 25.4 mm; 1 in.^{2} = 645 mm^2
Diameter of Bars - No. 2 = 6.4 mm; No.3 = 9.5 mm; No. 4 = 12.7 mm; No. 9 = 28.7 mm

Table 5.2 Input Material Parameters

Case	Beam Mark No.	f'_t (psi)	Ultimate Tensile Strain, ε_{ut}	Elastic Modulus E_o (psi)	Uncracked Shear Modulus	Initial bond Stiffness, psi/in.	Bond Stress Level 1[1], psi	Compression Softening Modulus
1	Bresler-Scordelis 0A1	300	0.0012	3.1×10^6	1.3×10^6	1.21×10^6	484	$-.05E_o$
2	Bresler-Scordelis 0A2	315	0.0008	3.19×10^6	1.33×10^6	1.21×10^6	484	$-.05E_o$
3	Bresler-Scordelis 0A3	300	0.0009	4.21×10^6	1.75×10^5	1.21×10^6	484	$-.05E_o$
4	Burns-Siess J-4	395	.0009	4.0×10^6	1.65×10^6	Perfect bond assumed	-	$-.05E_o$
5	Kani Beam No. 72	325	0.0014	3.28×10^6	1.37×10^6	1.21×10^6	484	$-.05E_o$
6	Kani Beam No. 65	350	0.0009	3.60×10^6	1.50×10^6	1.21×10^6	484	$-.05E_o$
7	Bresler-Scordelis A1	300	.0012	3.1×10^6	1.3×10^6	Perfect bond assumed	-	$-.018E_o$
8	Bresler-Scordelis A2	345	0.0010	3.19×10^6	1.33×10^6	Perfect bond assumed	-	$-.018E_o$
9	Bresler-Scordelis A3	300	0.0009	4.21×10^6	1.75×10^6	1.21×10^6	484	$-.018E_o$

Table 5.3 Comparison of Failure Loads[a]

Beam	Finite Element Prediction	Value from Test	Exp. Failure Load / F.E. Prediction	Value from ACI	ACI Value / F.E. Prediction	Value Per Zsutty (1971)	Zsutty (1971) / F.E. Prediction	Shear Span / Depth
0A1	77.0	75.0	0.97	53.2	0.69	65.4	0.85	3.97
0A2	80.0	80.0	1.00	54.2	0.68	66.5	0.83	4.90
0A3	90.0	85.0	0.94	66.2	0.73	73.4	0.82	6.94
B65	30.0	25.3	0.84	18.9	0.63	26.9	0.89	2.46
B72	37.5	44.3	1.18	19.3	0.51	35.9	0.96	1.96
A1	96.0	105.0	1.09	74.2	0.77	86.4	0.90	3.97
A2	100.0	110.0	1.10	75.2	0.75	87.5	0.88	4.90
A3	115.0	105.0	0.91	87.2	0.76	94.4	0.82	6.94
J4	35.8[b]	34.5	0.96	40.0	Not shear critical	39.1	Not shear critical	4.33
Mean			1.01		0.69		0.87	
Coefficient of Variation			10.44%		12.56%		5.59%	

Notes: a. Loads are in kips; 1 kip = 4.448 kN
b. Yield of main reinforcement

Table 5.4 Influence of Material Parameters

Case	Beam Mark No.	f'_t (psi)	Ultimate Tensile Strain, ε_{ut}	Initial Bond Stiffness, psi/in.	Bond Stress Level 1[1] psi	Compression Softening Modulus	F.E. Prediction / Experimental Failure Load
1	Bresler-Scordelis 0A1	300	0.0012	1.21×10^6	484	$-.05E_o$	1.03
2	Bresler-Scordelis 0A1	300	Tension cut-off	1.21×10^6	484	$-.05E_o$	0.97
3	Bresler-Scordelis 0A1	300	Tension cut-off	Perfect bond assumed	-	$-.05E_o$	1.12
4	Bresler-Scordelis 0A2	315	0.0008	1.21×10^6	484	$-.05E_o$	1.00
5	Bresler-Scordelic 0A2	345	Tension cut-off	1.21×10^6	484	$-.05E_o$	0.95
6	Bresler-Scordelis 0A2	345	Tension cut-off	Perfect bond assumed	-	$-.05E_o$	0.95
7	Bresler-Scordelis 0A3	300	0.0009	1.21×10^6	484	$-.05E_o$	1.06
8	Bresler-Scordęlis 0A3	300	Tension cut-off	1.21×10^6	484	$-.05E_o$	1.02
9	Bresler-Scordelis 0A3	300	Tension cut-off	Perfect bond assumed	-	$-.05E_o$	1.08
10	Burns-Siess J-4	395	.0009	Perfect bond assumed	-	$-.05E_o$	1.04

Table 5.4 Influence of Material Parameters (Continued)

Case	Beam Mark No.	f'_t (psi)	Ultimate Tensile Strain, ε_{ut}	Initial Bond Stiffness, psi/in.	Bond Stress Level 1[1]	Compression Softening Modulus	F.E. Prediction / Experimental Failure Load
11	Burns-Siess J-4	385	Tension cut-off	Perfect bond assumed	-	$-.05E_o$	1.04
12	Kani Beam No. 72	325	0.0018 0.0014	1.21×10^6	484	$-.05E_o$	0.93 0.85
13	Kani Beam No. 72	345	0.0014	Perfect bond assumed	-	$-.05E_o$	0.76
14	Kani Beam No. 72	345	Tension cut-off	1.21×10^6	484	$-.05E_o$	0.68
15	Kani Beam No. 65	350	0.0009	1.21×10^6	484	$-.05E_o$	1.18
16	Kani Beam No. 65	350	0.0014	Perfect bond assumed	-	$-.05E_o$	1.37
17	Kani Beam No. 65	350	0.0014	1.21×10^6	484	$-.05E_o$	1.23
18	Bresler-Scordelis A1	300	.0012	Perfect bond assumed	-	$-.018E_o$	1.05
19	Bresler-Scordelis A1	300	.0014	Perfect bond assumed	-	$-.05E_o$	0.91
20	Bresler-Scordelis A2	345	0.0014	Perfect bond assumed	-	$+.0001E_o$	0.90

Table 5.4 Influence of Material Parameters (Continued)

Case	Beam Mark No.	f'_t (psi)	Ultimate Tensile Strain, ε_{ut}	Initial Bond Stiffness, psi/in.	Bond Stress Level 1[1]	Compression Softening Modulus	F.E. Prediction / Experimental Failure Load
21	Bresler-Scordelis A2	345	.0014	Perfect bond assumed	-	$-.05E_o$	0.84
22	Bresler-Scordelis A3	300	Tension cut-off	Perfect bond assumed	-	$-.05E_o$	0.93
23	Bresler-Scordelis A3	300	0.0009	1.21×10^6	484	$-.05E_o$	1.10

Notes:
1. Effects of bond slips: compare case 2 with case 3; case 5 with case 6; case 8 with case 9; case 12 with case 13 and case 16 with case 17.
2. Tension cut-off versus tension softening: compare case 1 with case 2; case 4 with case 5; case 7 with case 8; case 10 with case 11; case 12 with case 14 and case 22 with case 23.
3. Effect of tension softening modulus: compare two runs in case 12 and case 15 with case 17.
4. Effect of compression strain softening modulus: compare case 18 with case 19 and case 20 with case 21.

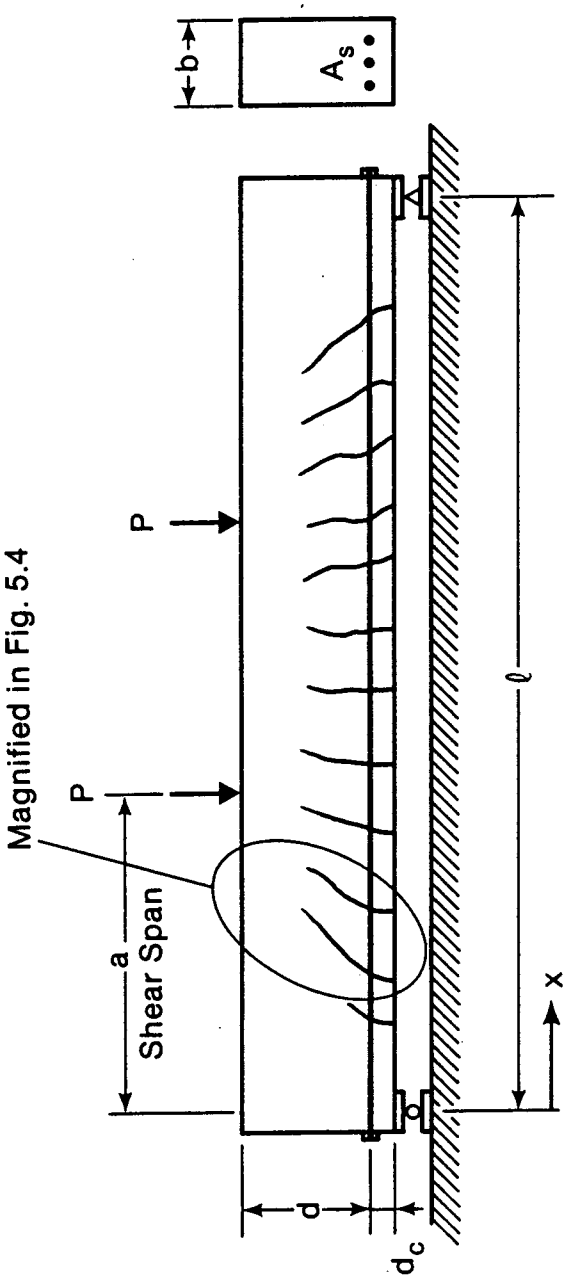

FIG. 5.1. Reinforced Concrete Beam Loaded at Two Points

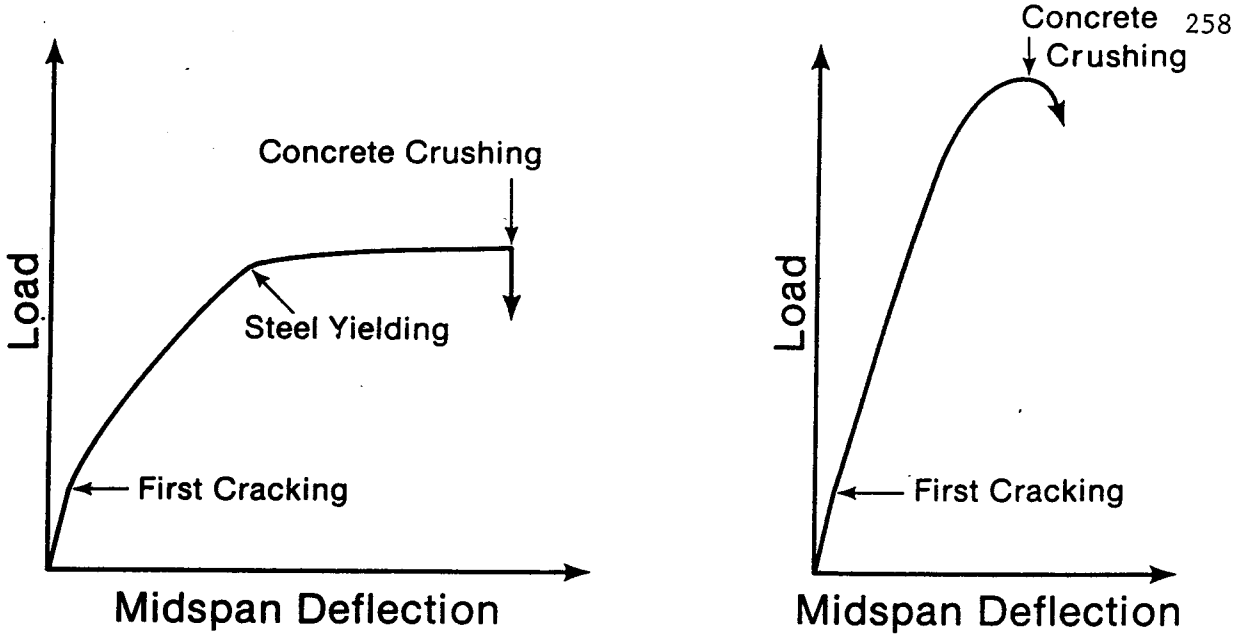

(a) Tension Failure

(b) Compression Failure

(c)

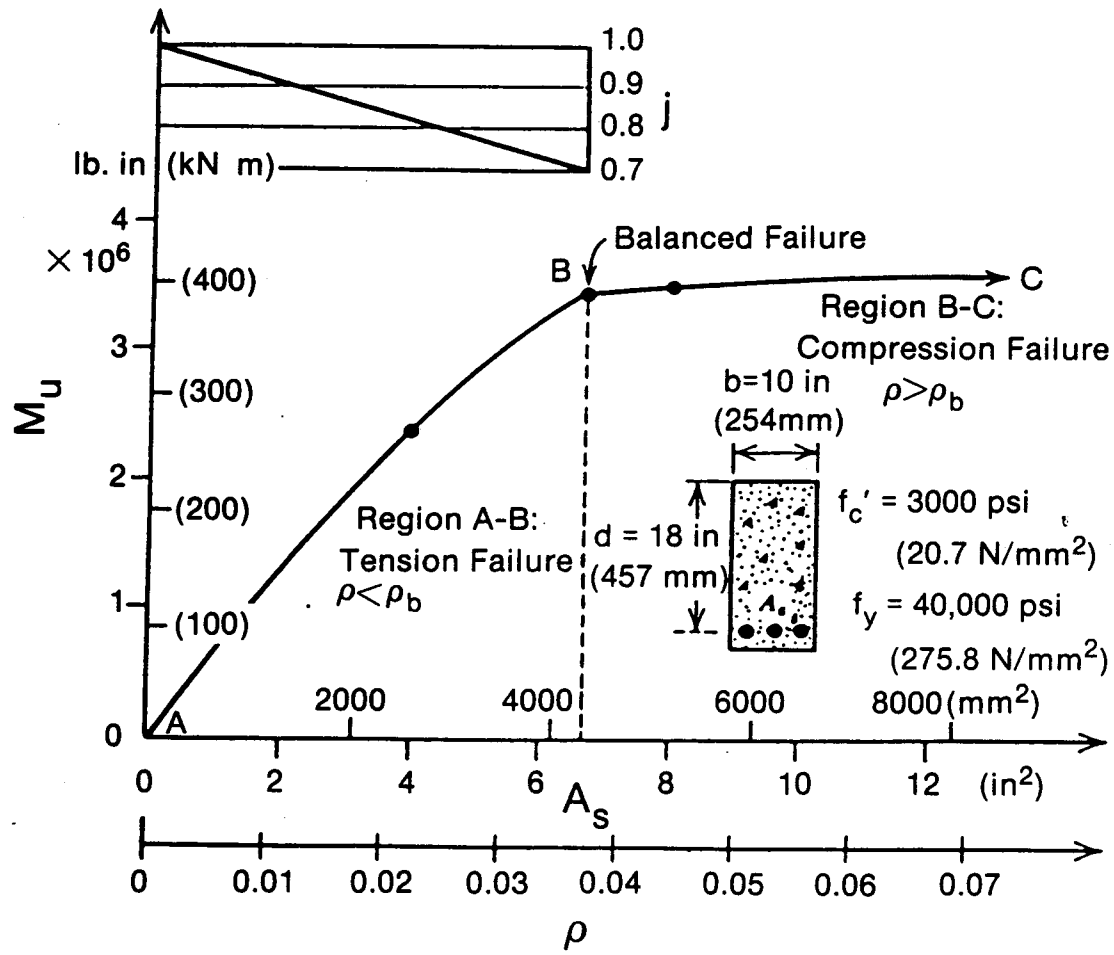

(c) Flexural Strength with Various Steel Contents

FIG. 5.2. Flexural Failure Modes

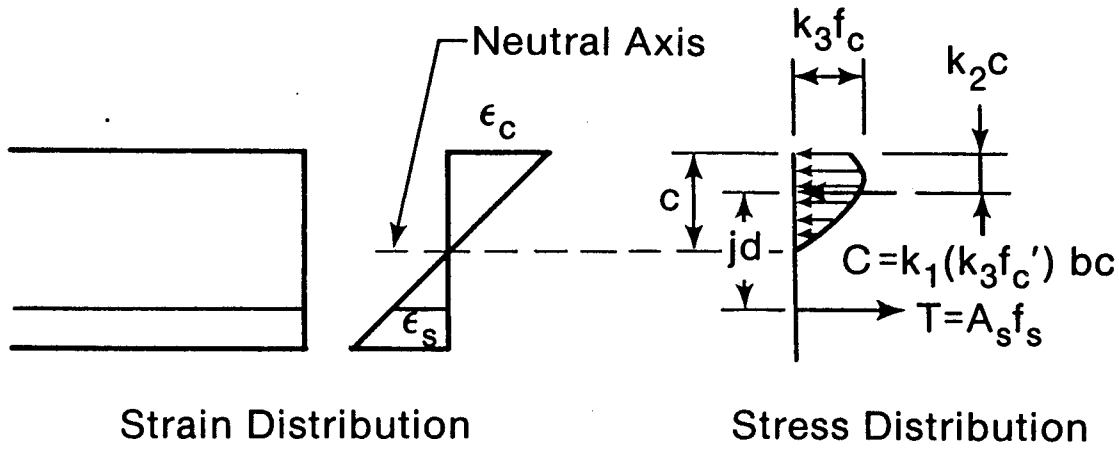

FIG. 5.3. Stress and Strain Distribution at a Section when Flexural Strength is Reached

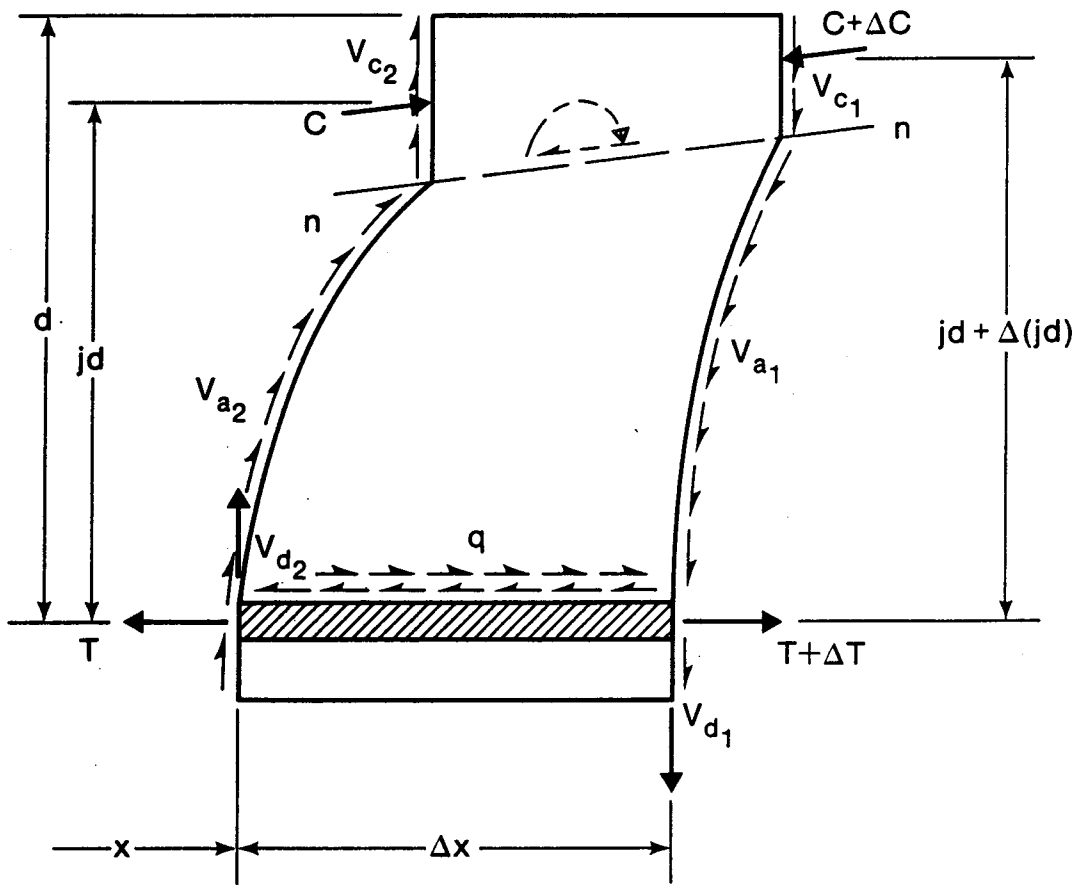

FIG. 5.4. Free Body Diagram of a Concrete Segmenet Between Cracks

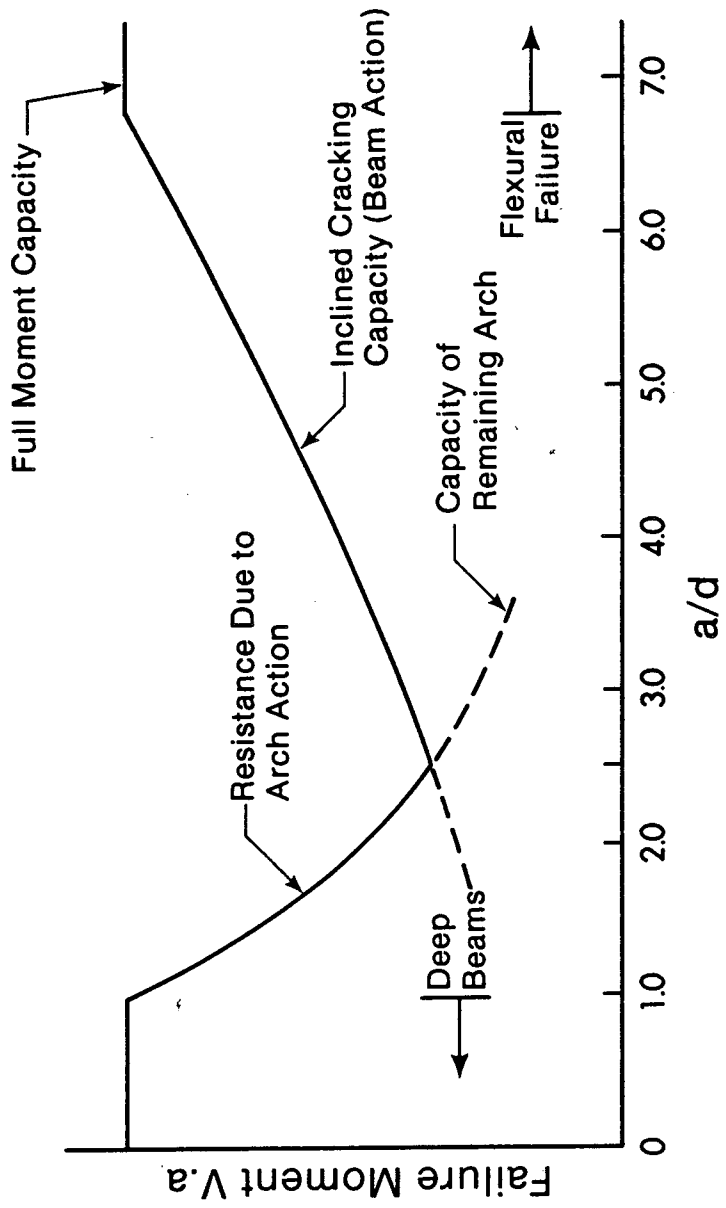

FIG. 5.5. Variation in Shear Capacity with a/d

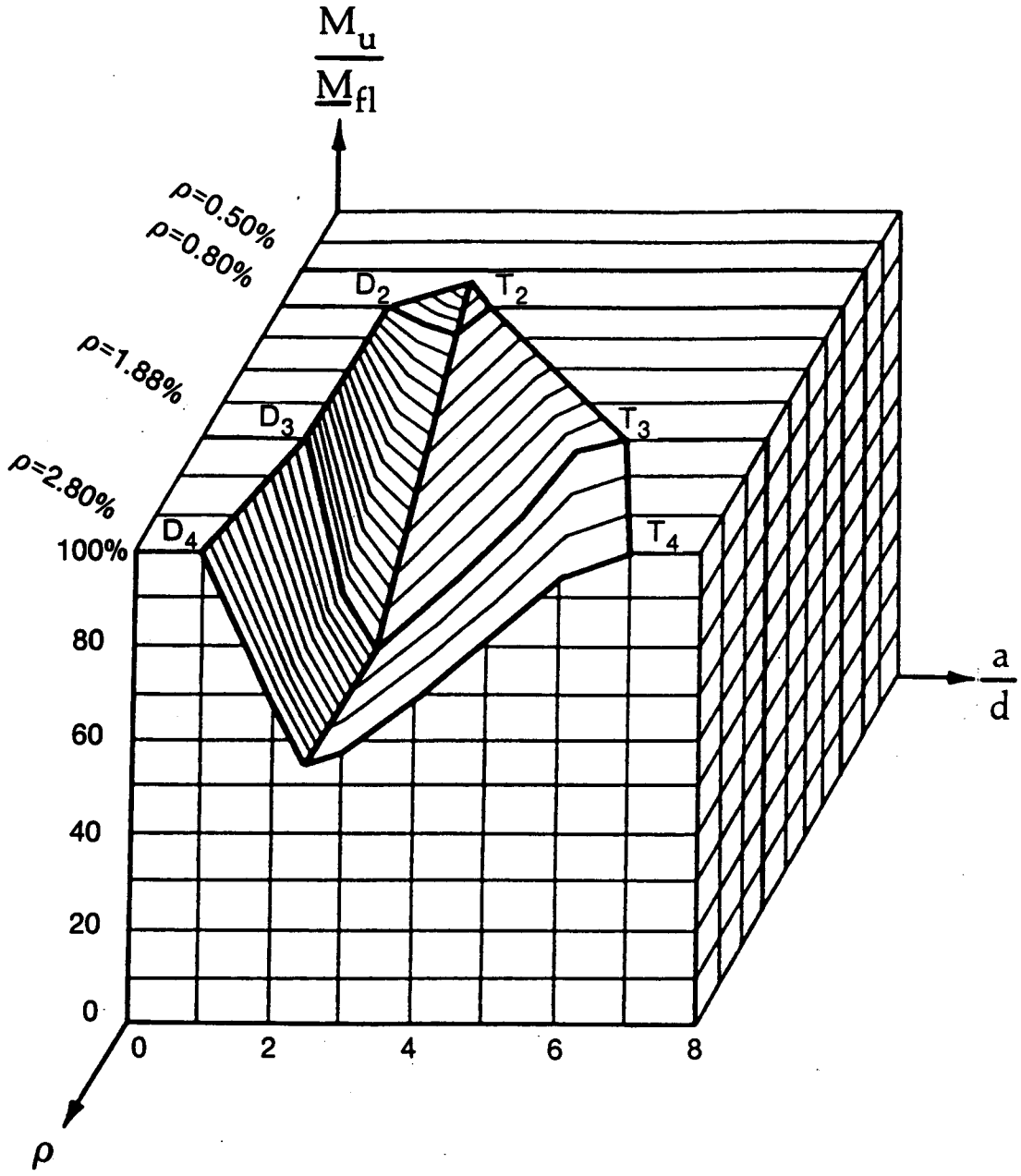

FIG. 5.6. Relative Beam Strength M_u/M_{fl} Versus a/d and ρ (Adapted from Kani, 1979)

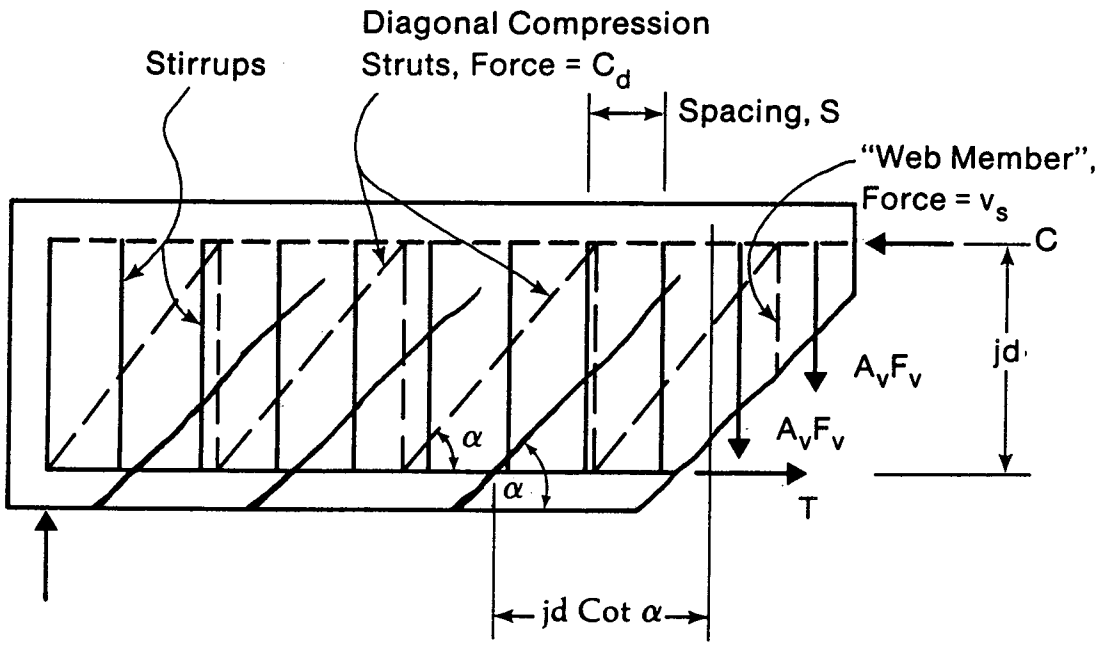

FIG. 5.7. Truss Model

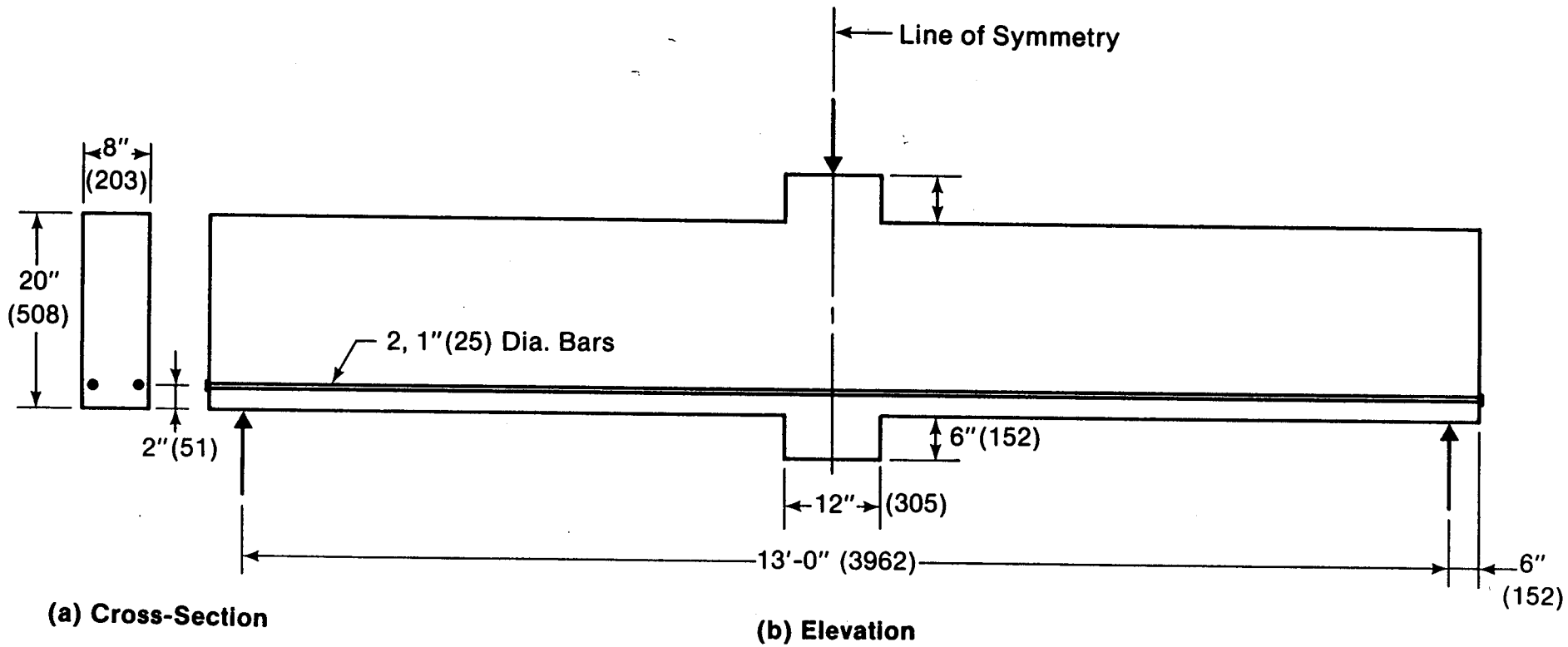

FIG. 5.8. Beam J4 Tested by Burns and Siess (1966)
Note: Dimensions in mm are given in parentheses.

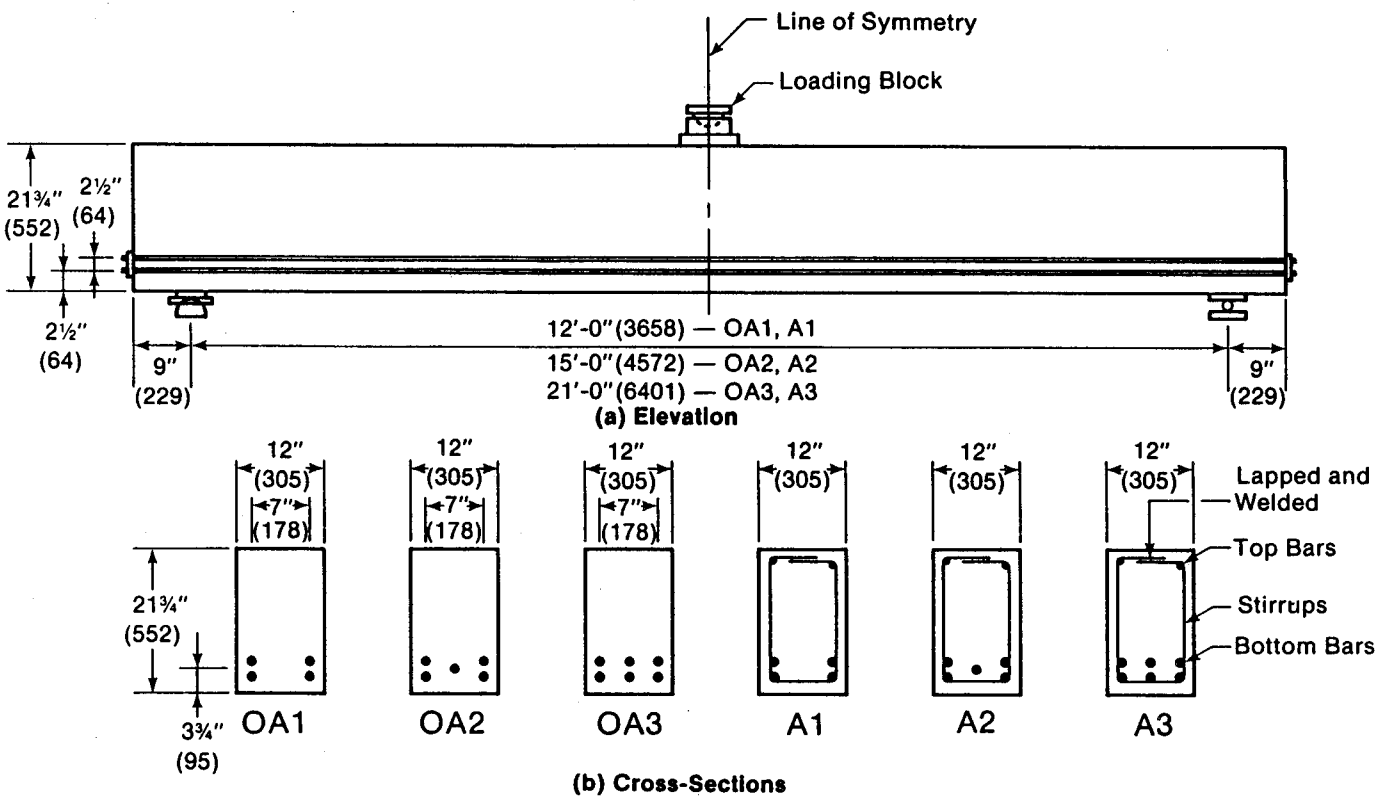

1. All Dimensions Are Nominal; See Table 5.1 for Measured Dimensions
2. All Bottom Bars Are 1.125"(30) Dia., Stirrups Are 0.25"(6) Dia. Spaced at 8.25"(210), Top Bars Are 0.5"(12) Dia.

FIG. 5.9. Beams Tested by Bresler and Scordelis (1961)

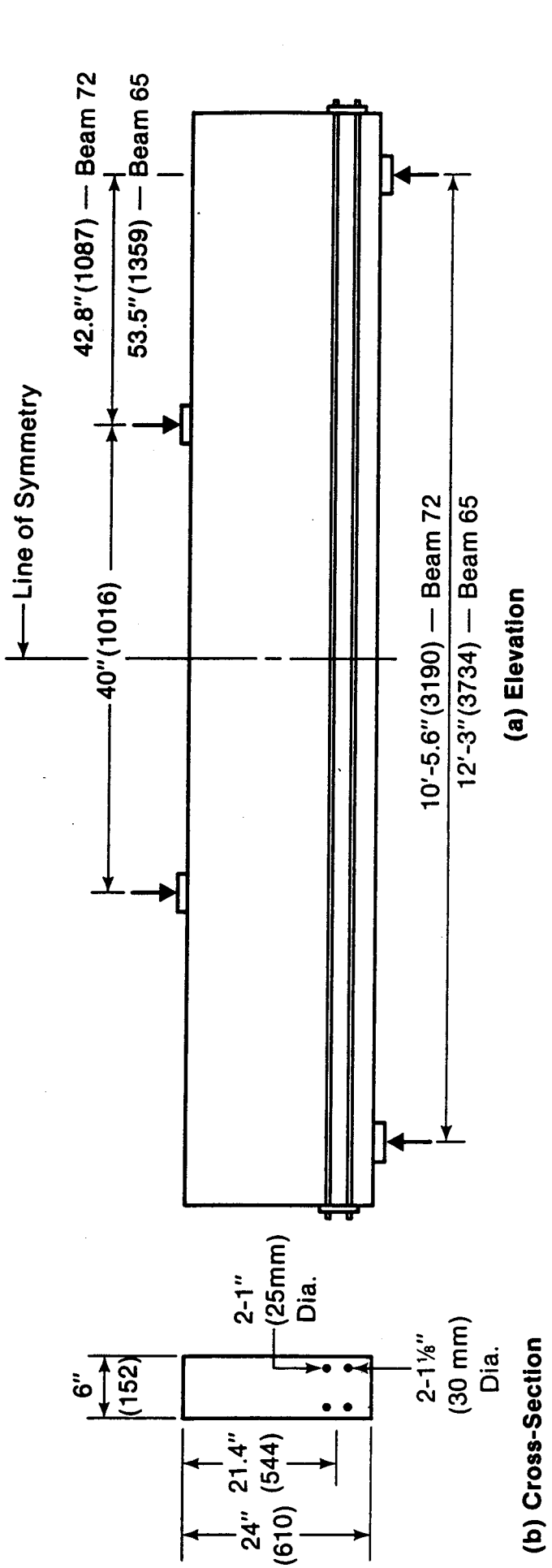

FIG. 5.10. Beams Tested by Kani (1967)

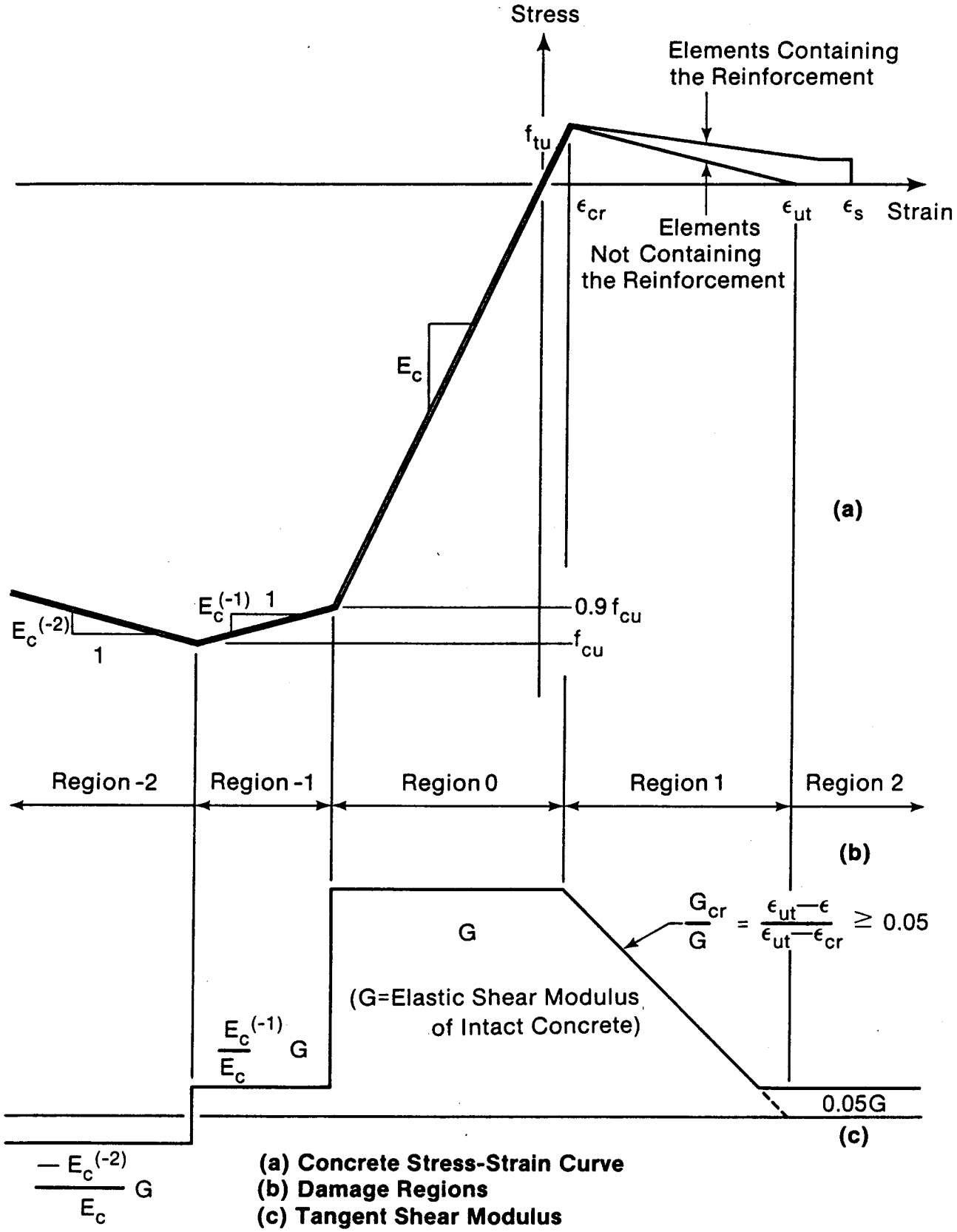

FIG. 5.11. Concrete Moduli used in Stress Computation

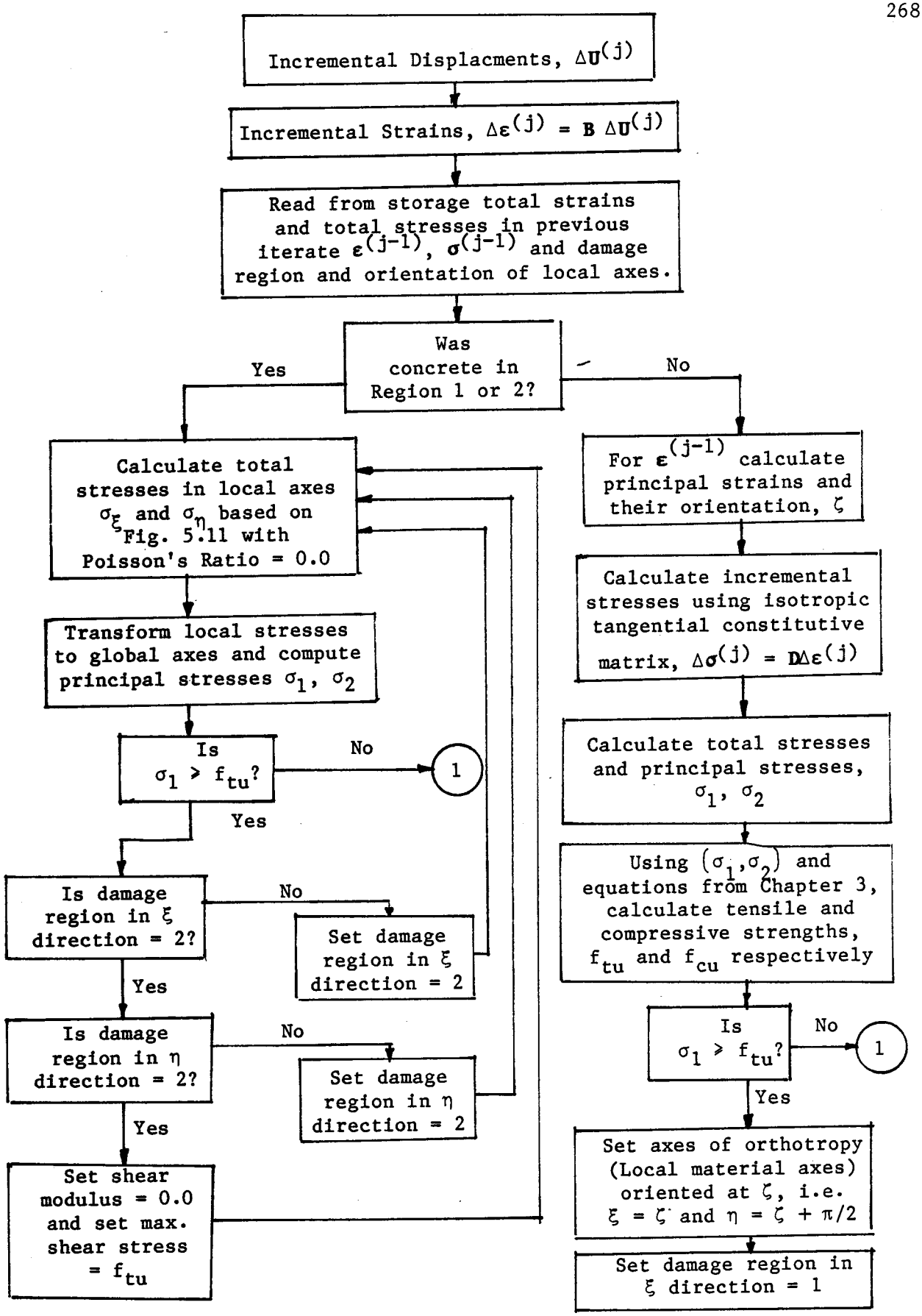
Incremental Displacments, $\Delta U^{(j)}$
Incremental Strains, $\Delta\varepsilon^{(j)} = B\,\Delta U^{(j)}$
Read from storage total strains and total stresses in previous iterate $\varepsilon^{(j-1)}$, $\sigma^{(j-1)}$ and damage region and orientation of local axes.
Was concrete in Region 1 or 2?
Yes
No
Calculate total stresses in local axes σ_ξ and σ_η based on Fig. 5.11 with Poisson's Ratio = 0.0
Transform local stresses to global axes and compute principal stresses σ_1, σ_2
Is $\sigma_1 > f_{tu}$?
No
1
Yes
Is damage region in ξ direction = 2?
No
Set damage region in ξ direction = 2
Yes
Is damage region in η direction = 2?
No
Set damage region in η direction = 2
Yes
Set shear modulus = 0.0 and set max. shear stress = f_{tu}
For $\varepsilon^{(j-1)}$ calculate principal strains and their orientation, ζ
Calculate incremental stresses using isotropic tangential constitutive matrix, $\Delta\sigma^{(j)} = D\Delta\varepsilon^{(j)}$
Calculate total stresses and principal stresses, σ_1, σ_2
Using (σ_1,σ_2) and equations from Chapter 3, calculate tensile and compressive strengths, f_{tu} and f_{cu} respectively
Is $\sigma_1 > f_{tu}$?
No
1
Yes
Set axes of orthotropy (Local material axes) oriented at ζ, i.e. $\xi = \zeta$ and $\eta = \zeta + \pi/2$
Set damage region in ξ direction = 1

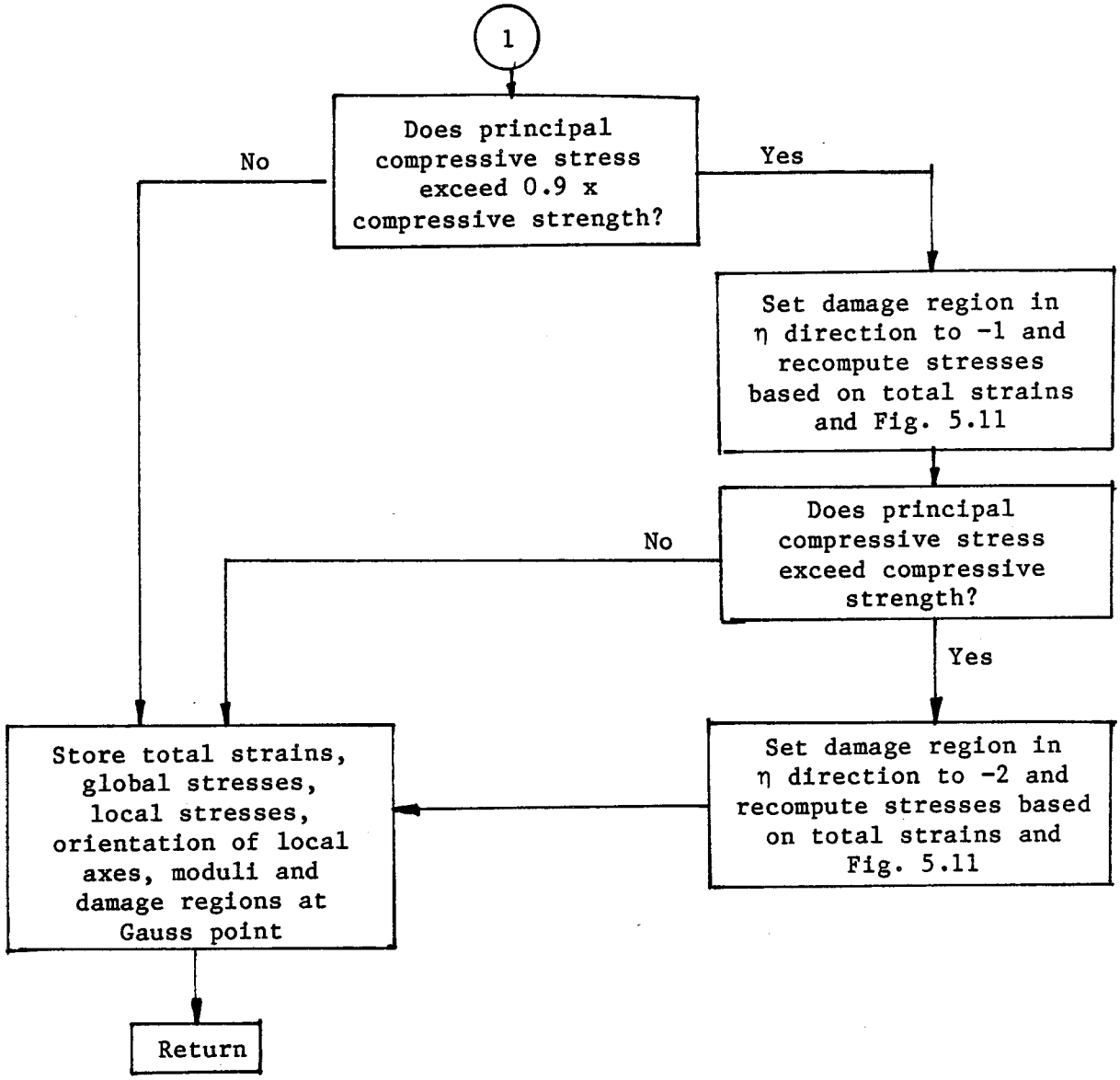

Fig. 5.12 Flow Chart of Stress Computation Subroutine

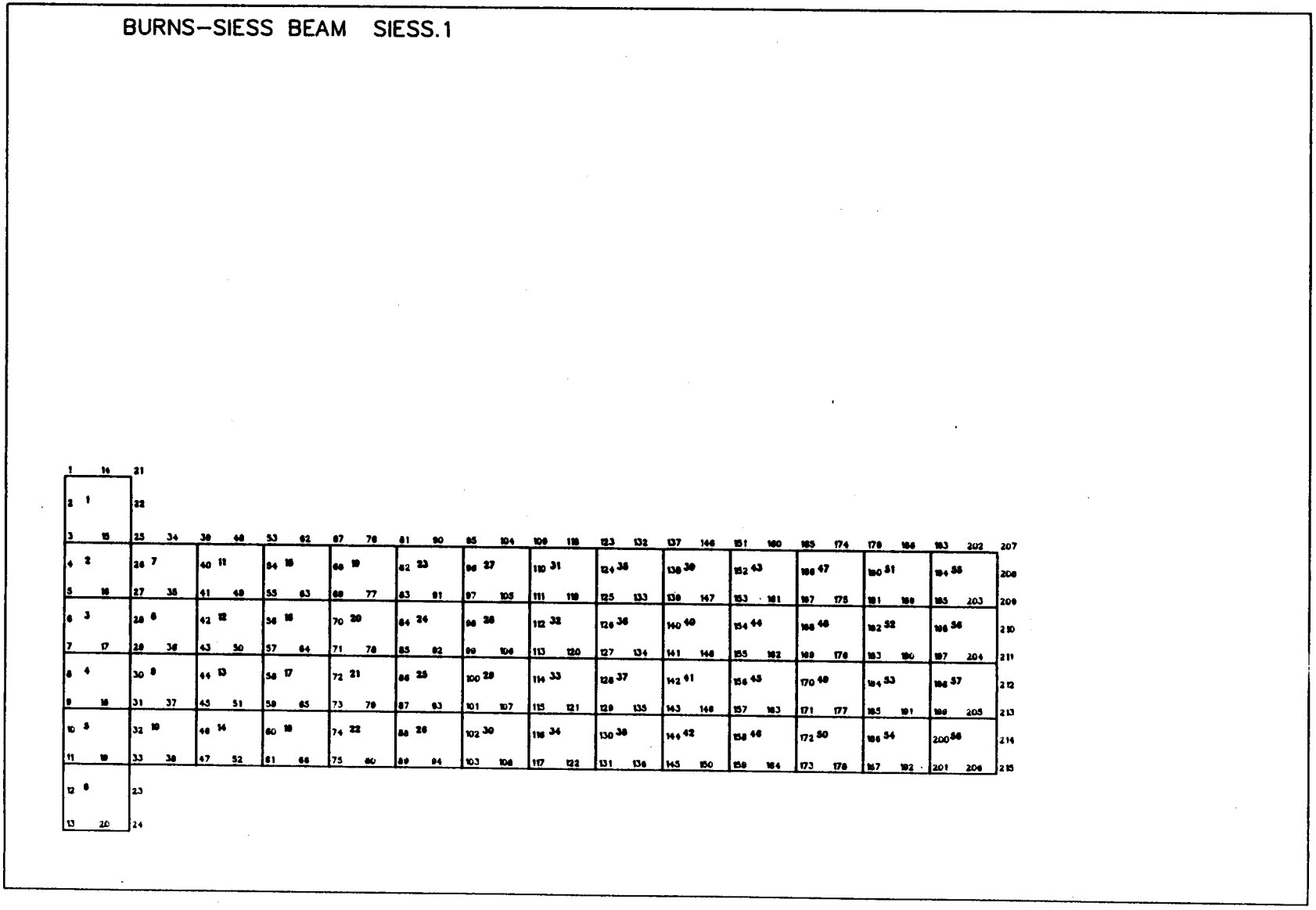

FIG. 5.13. Burns/Siess Beam J4 - Finite Element Mesh Layout

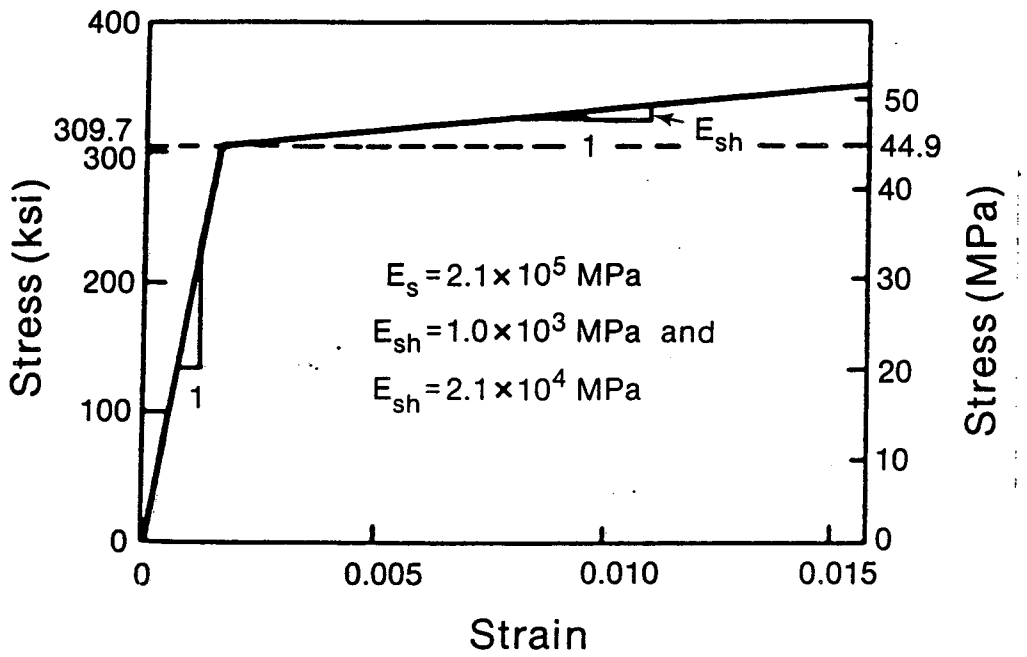

FIG. 5.14. Uniaxial Stress-Strain Curve for Steel - Burns/Siess Beam J4

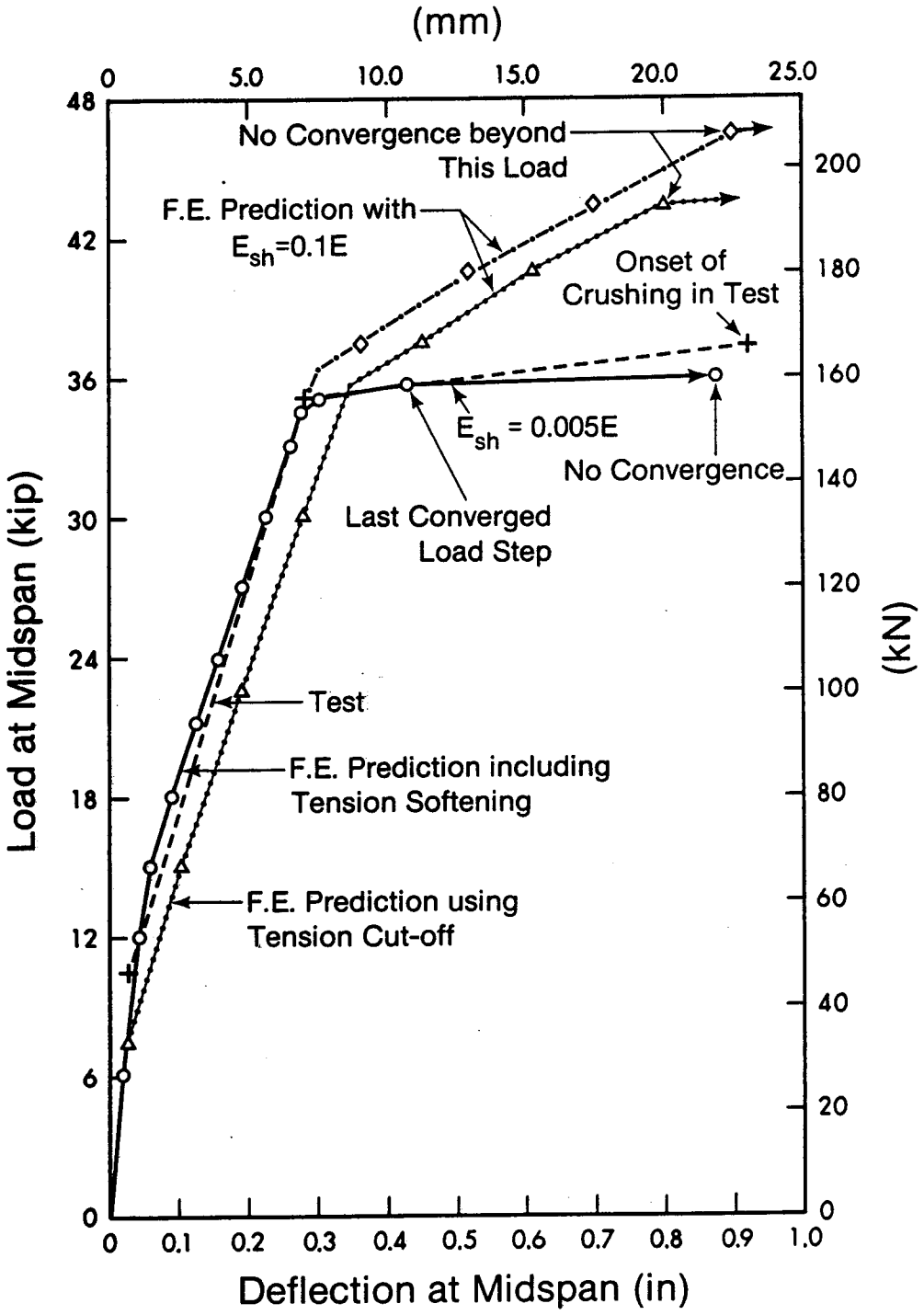

FIG. 5.15. Burns/Siess Beam J4 - Load-Deflection Relationship

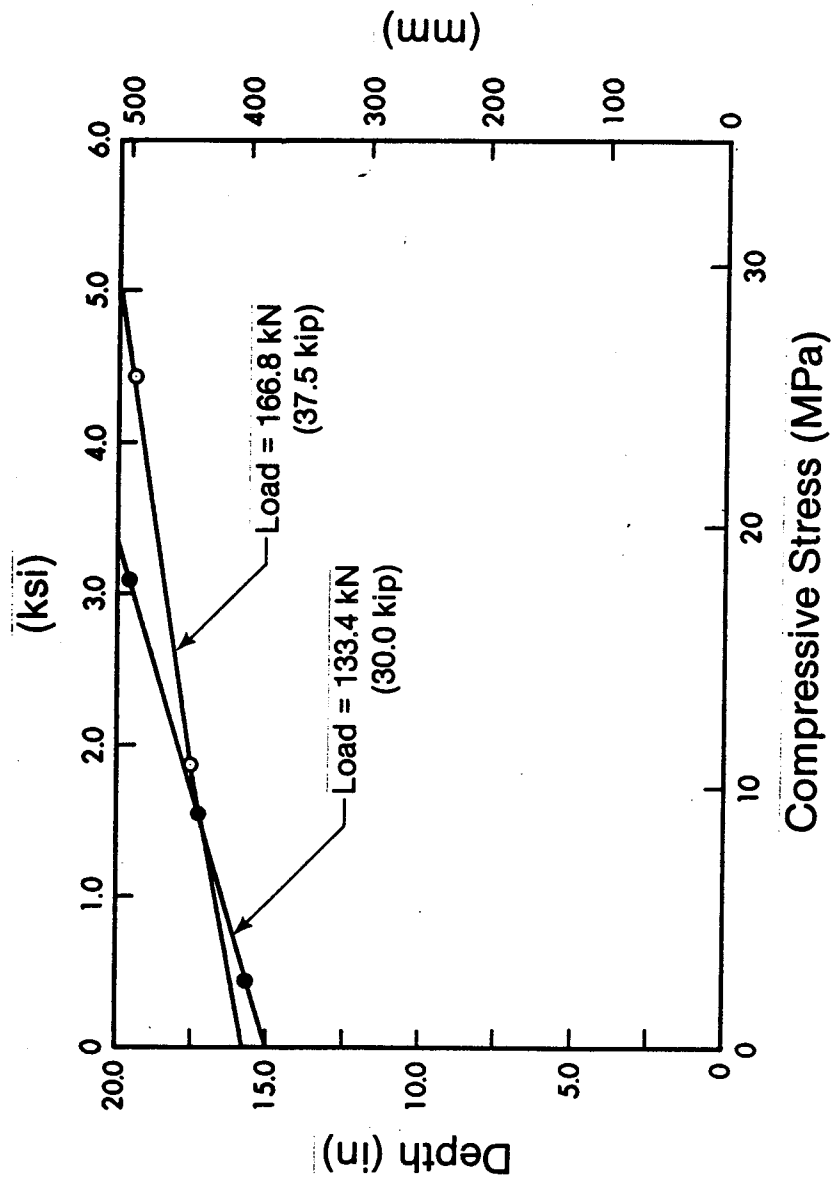

FIG. 5.16. Burns/Siess Beam J4 - Distribution of Normal Stresses

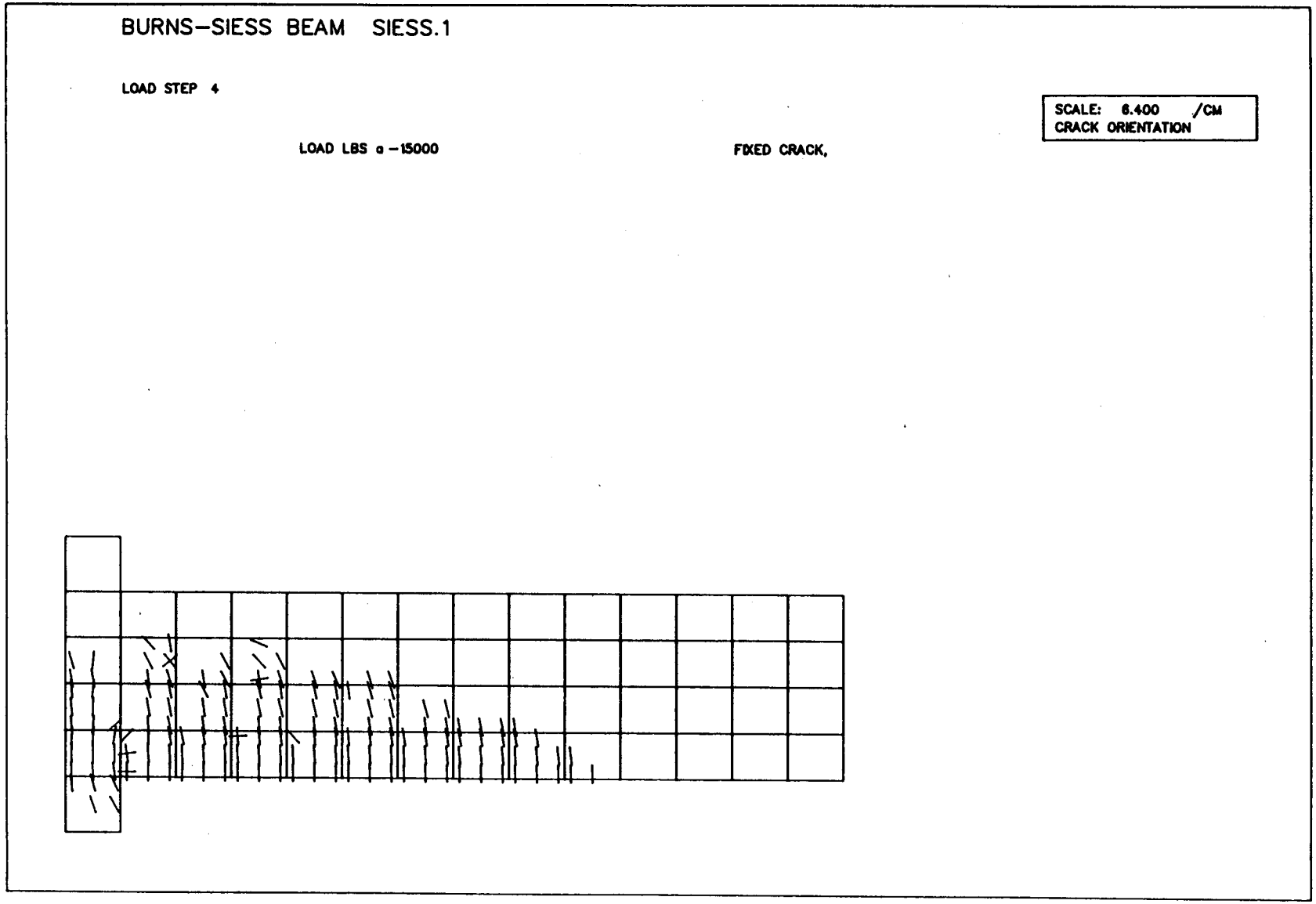

FIG. 5.17. Burns/Siess Beam J4 - Analytical Crack Pattern
(a) Shear = 15 kip (66.7 kN)

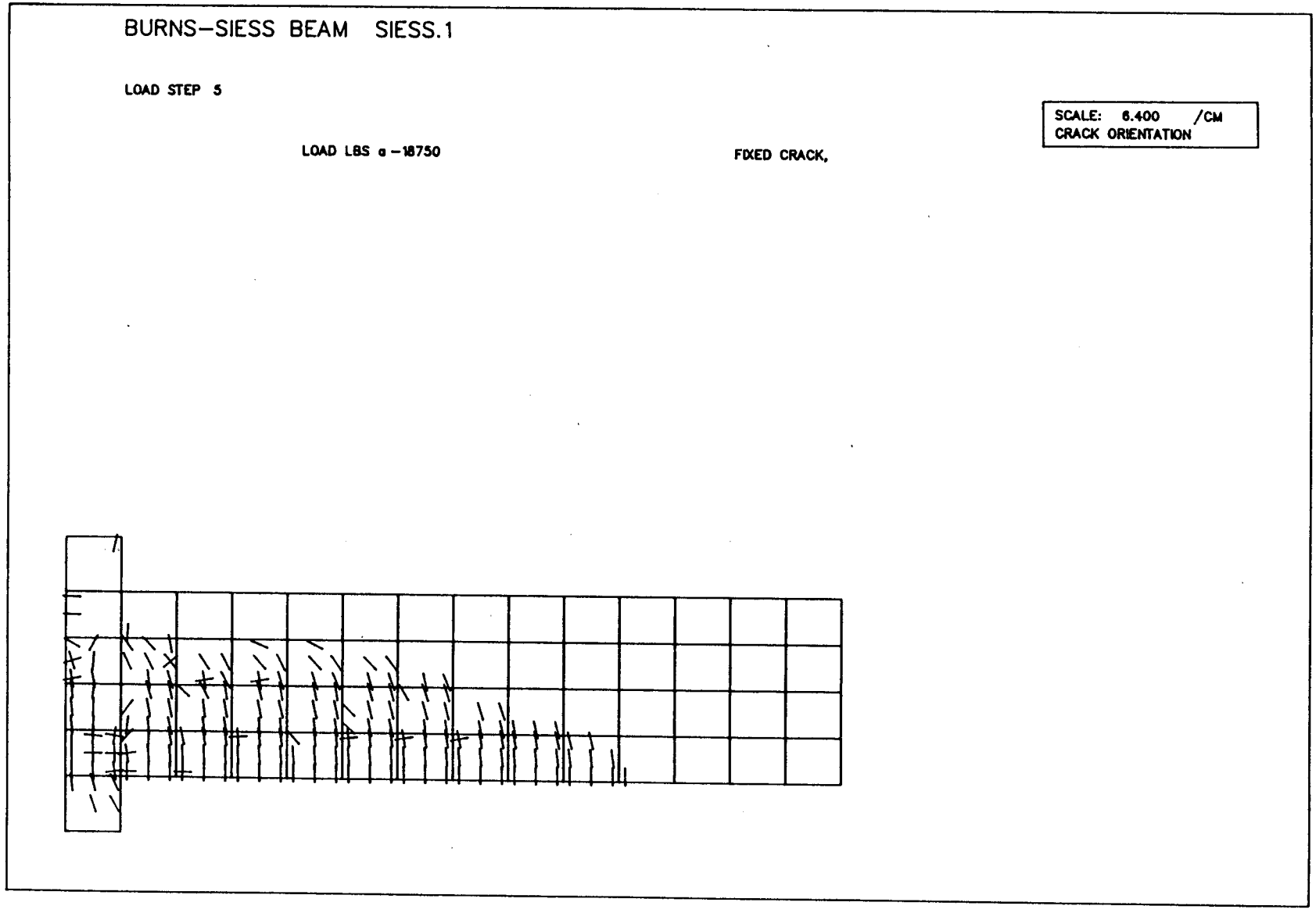

FIG. 5.17. (b) Shear = 18.75 kip (83.4 kN)

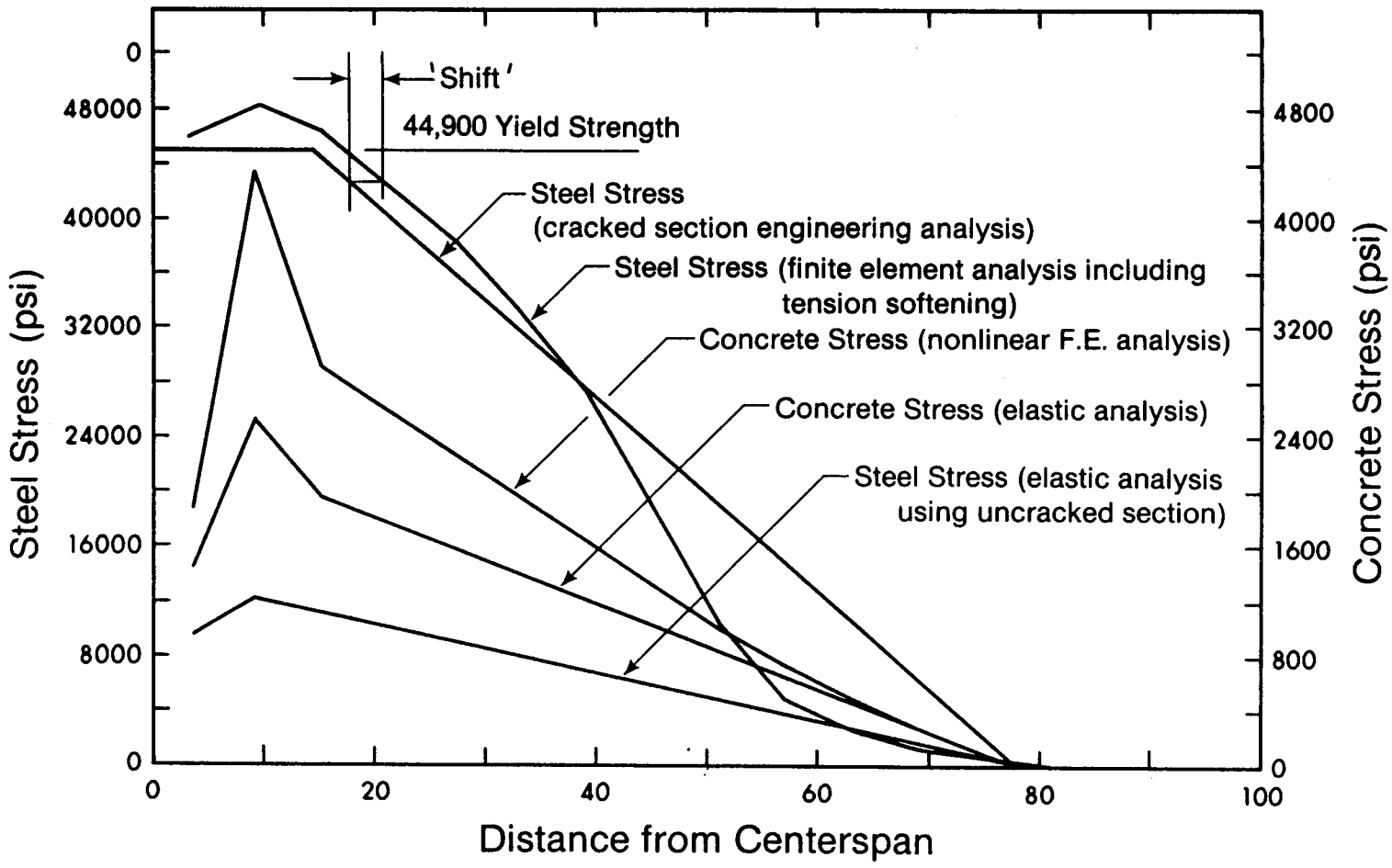

FIG. 5.18. Burns/Siess Beam J4 - Distribution of Steel and Concrete Stresses

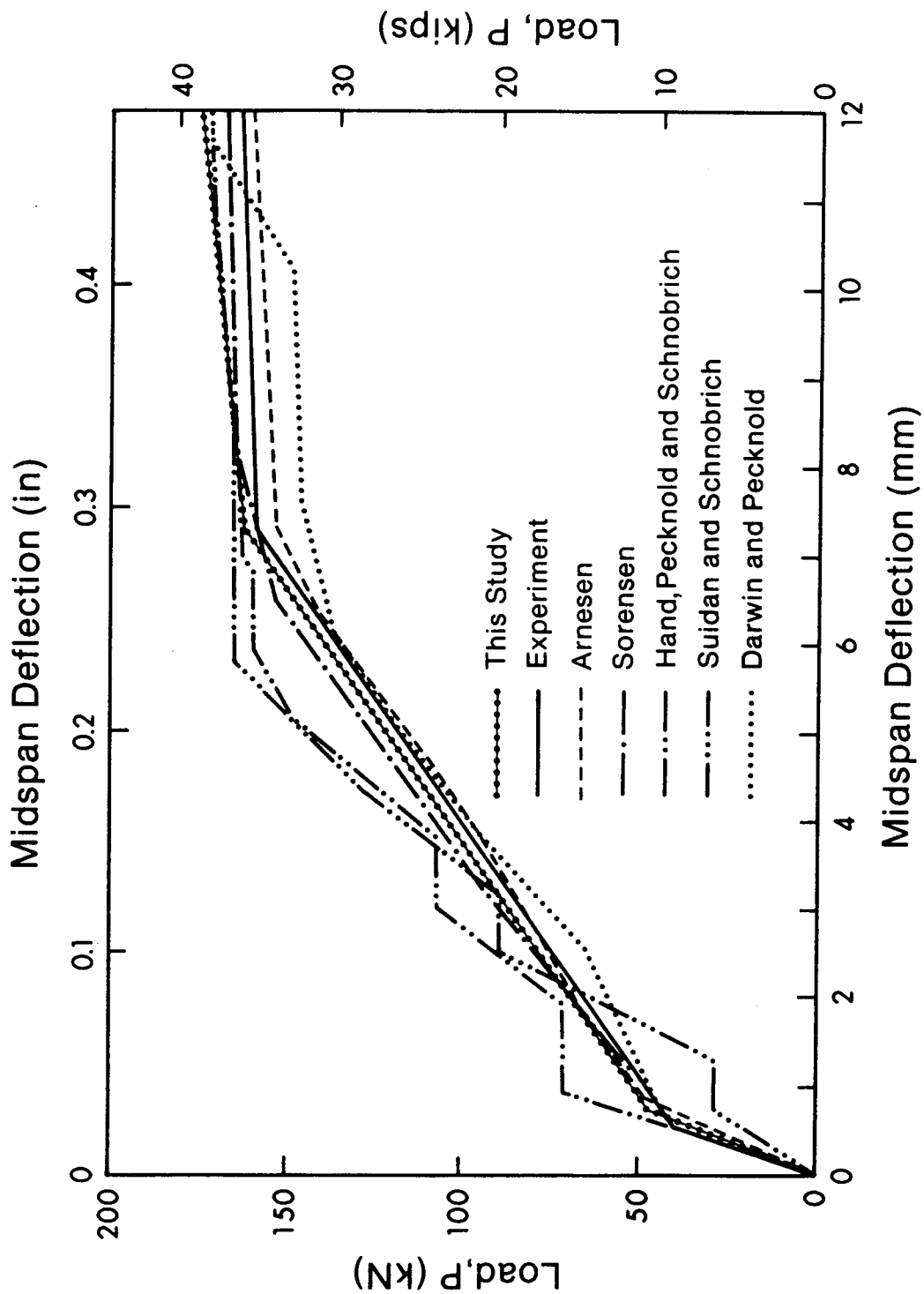

FIG. 5.19. Load-Deflection Curves from Various Investigations Burns/Siess Beam J4

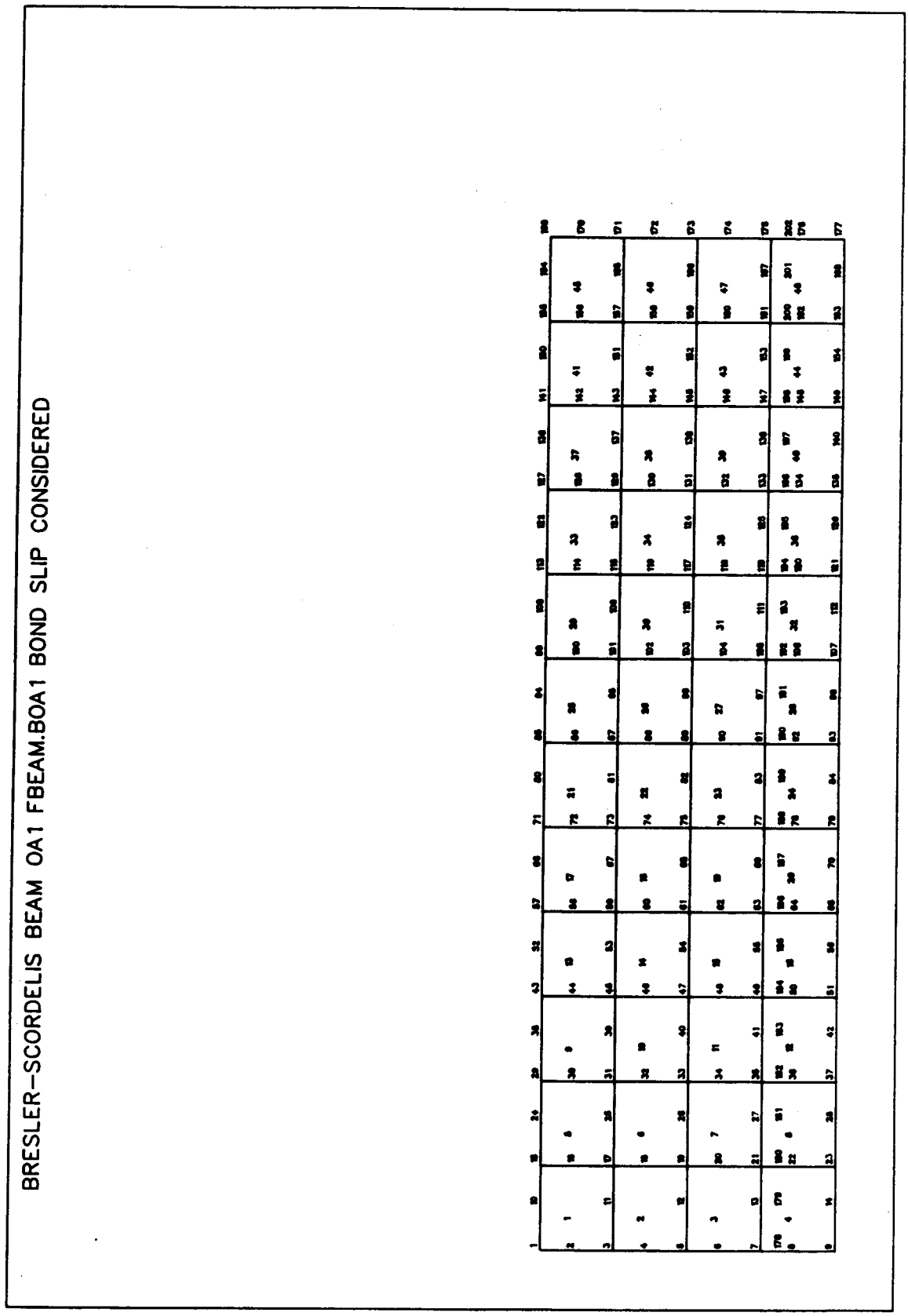

FIG. 5.20. Finite Element Mesh Layout
(a) Bresler/Scordelis Beam OA1

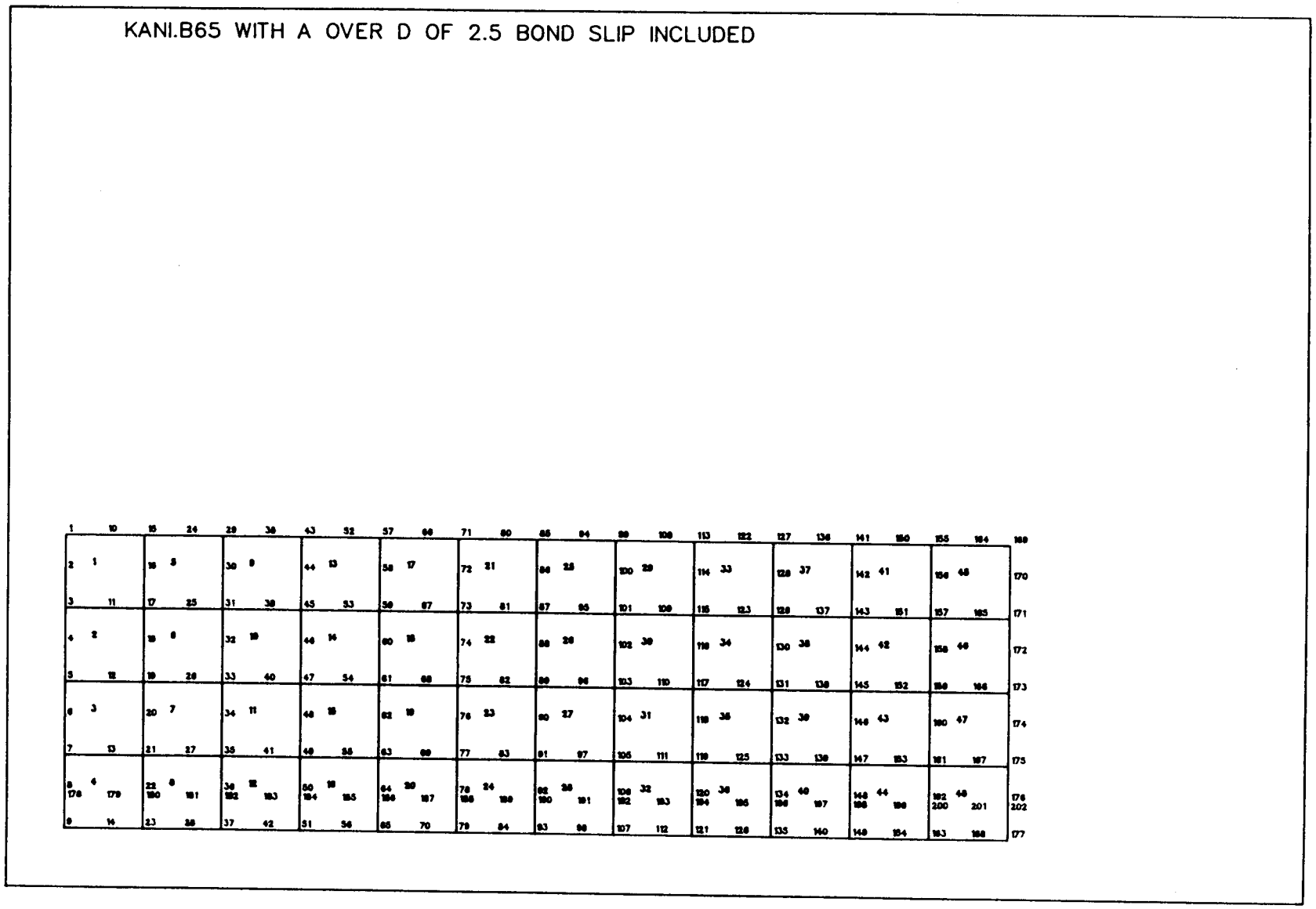

FIG. 5.20. (b) Finite Element Mesh Layout - Kani Beam 65

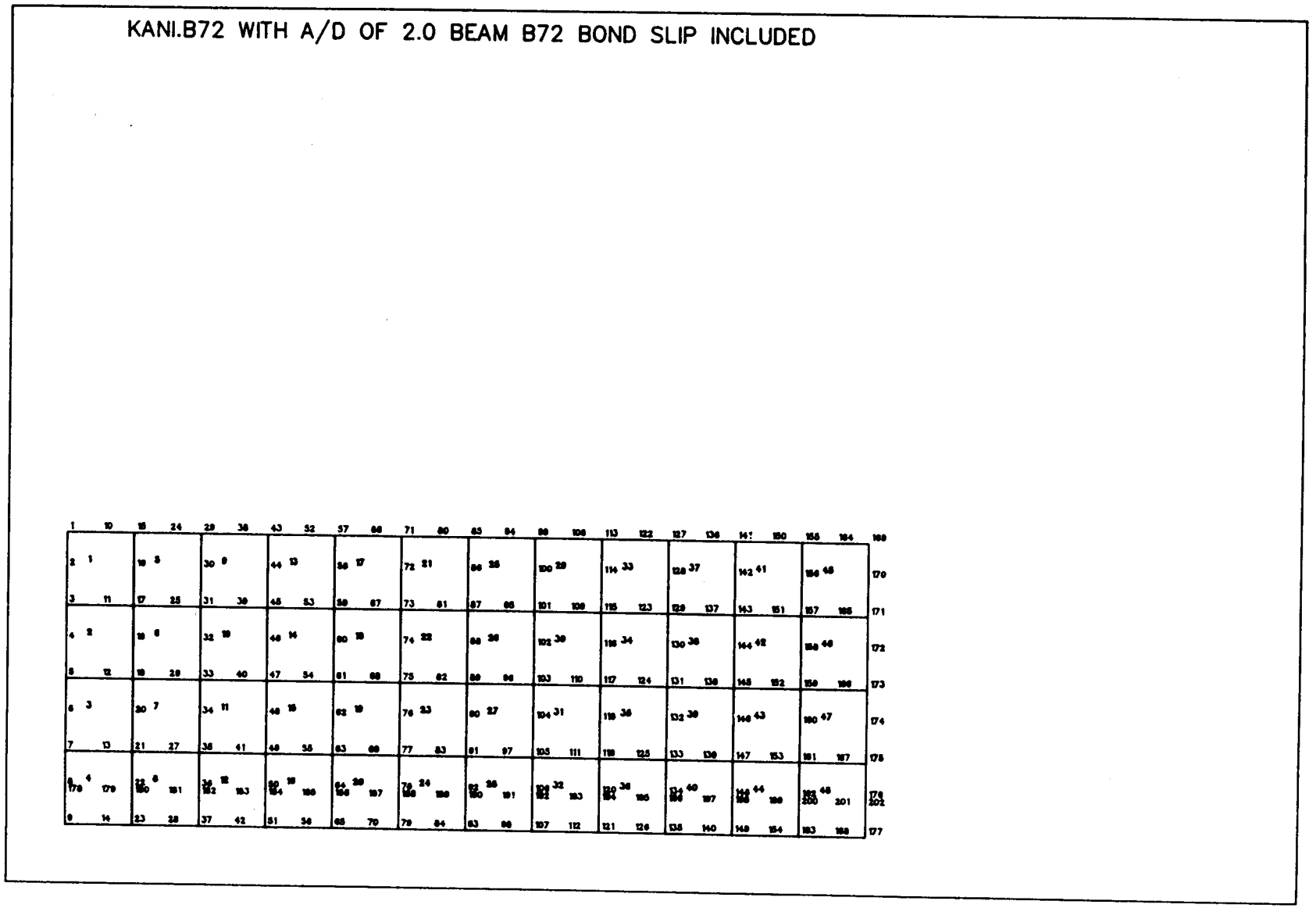

FIG. 5.20. (c) Finite Element Mesh Layout - Kani Beam 72

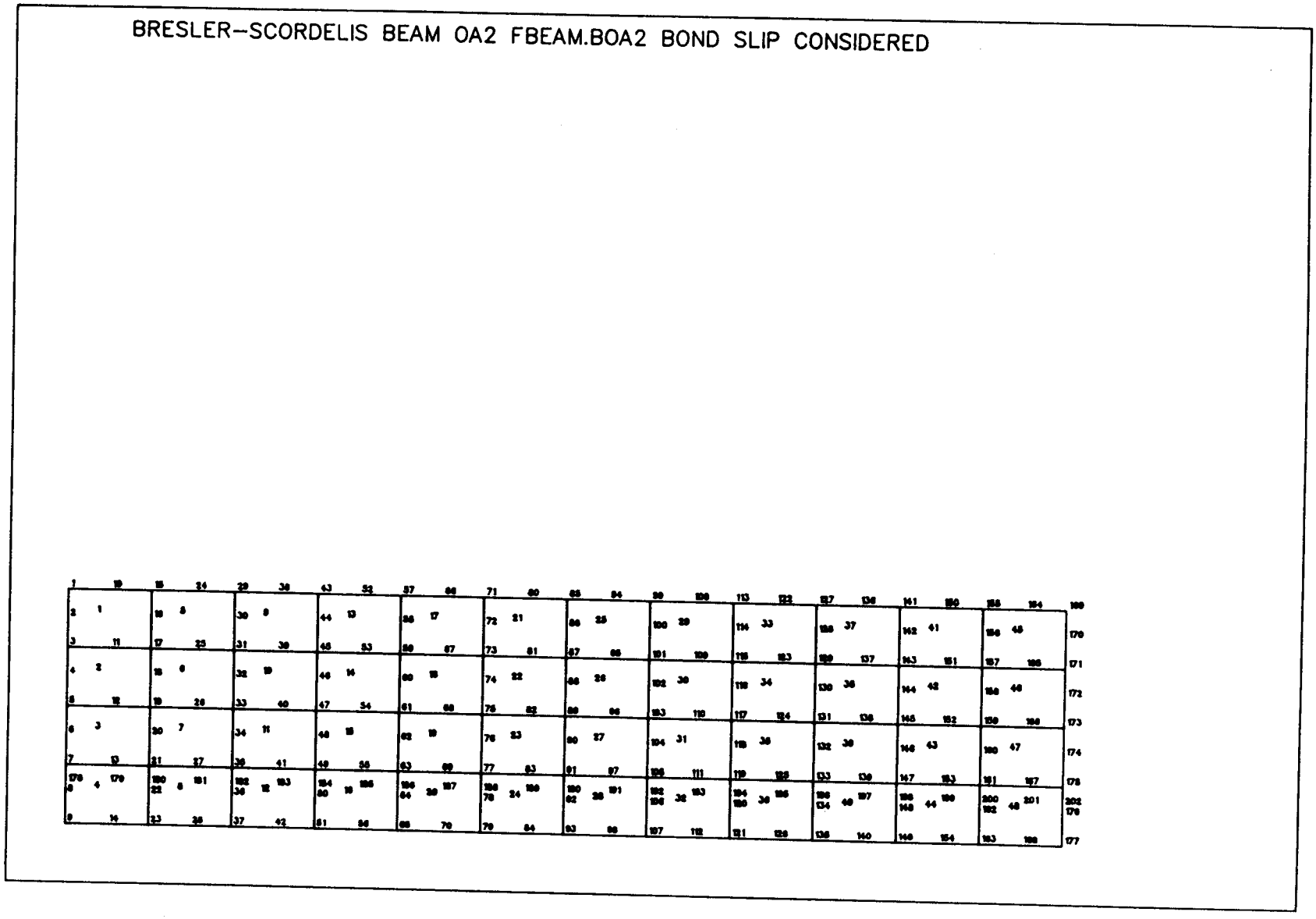

FIG. 5.20. (d) Finite Element Mesh Layout - Bresler/Scordelis Beam OA2

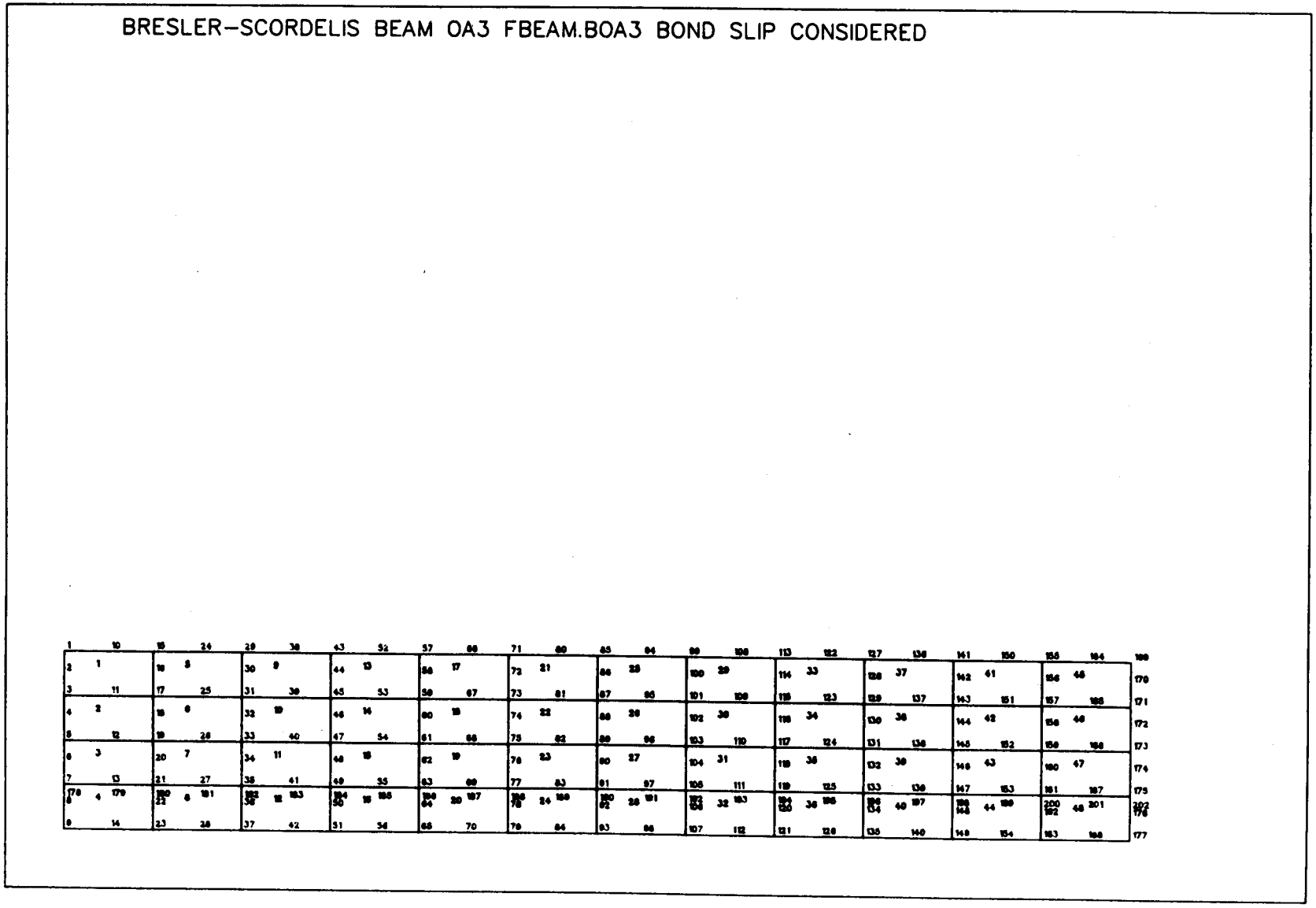

FIG. 5.20. (e) Finite Element Mesh Layout - Bresler/Scordelis Beam OA3

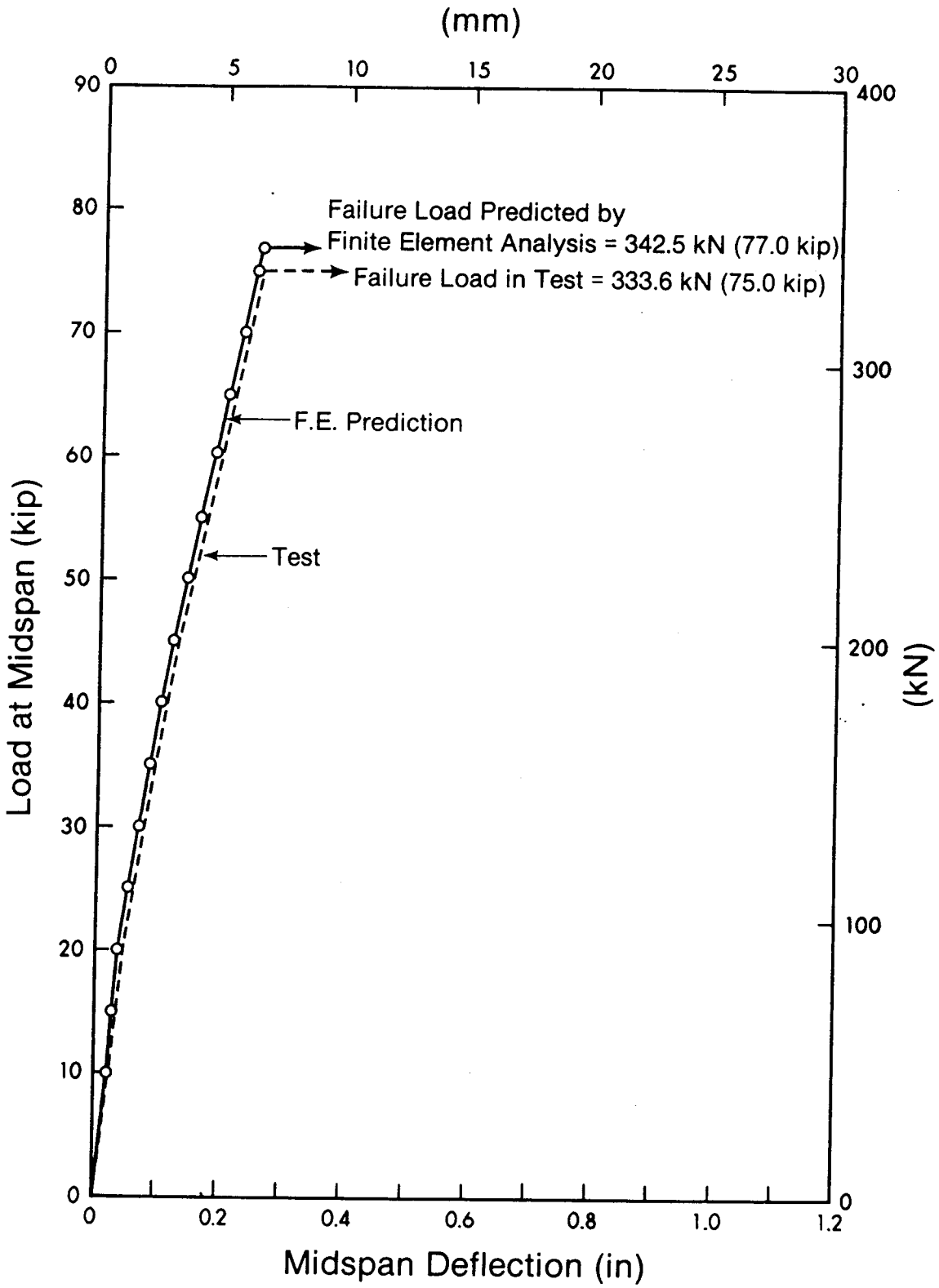

FIG. 5.21. Bresler/Scordelis Beam 0A1 - Load-Deflection Relationship

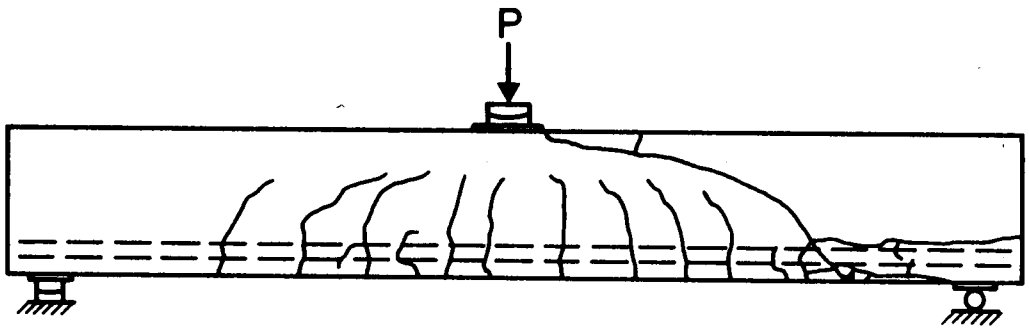

FIG. 5.22. Bresler/Scordelis Beam 0A1 - Crack Patterns
(a) Experimental Crack Pattern - Shear = 37.5 kip (166.8 kN)

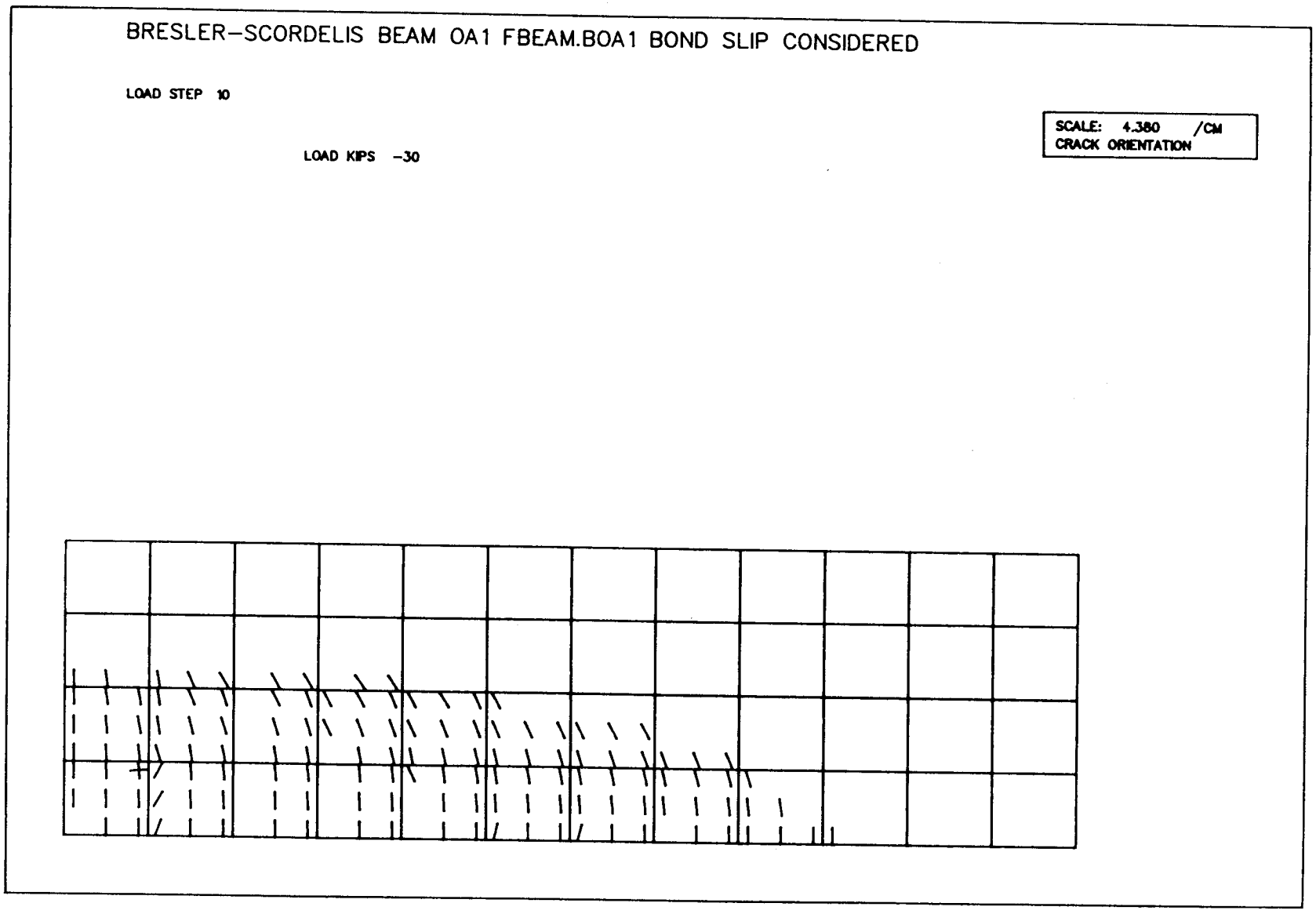

FIG. 5.22. (b) Analytical Crack Pattern - Shear = 30 kip (166.8 kN)

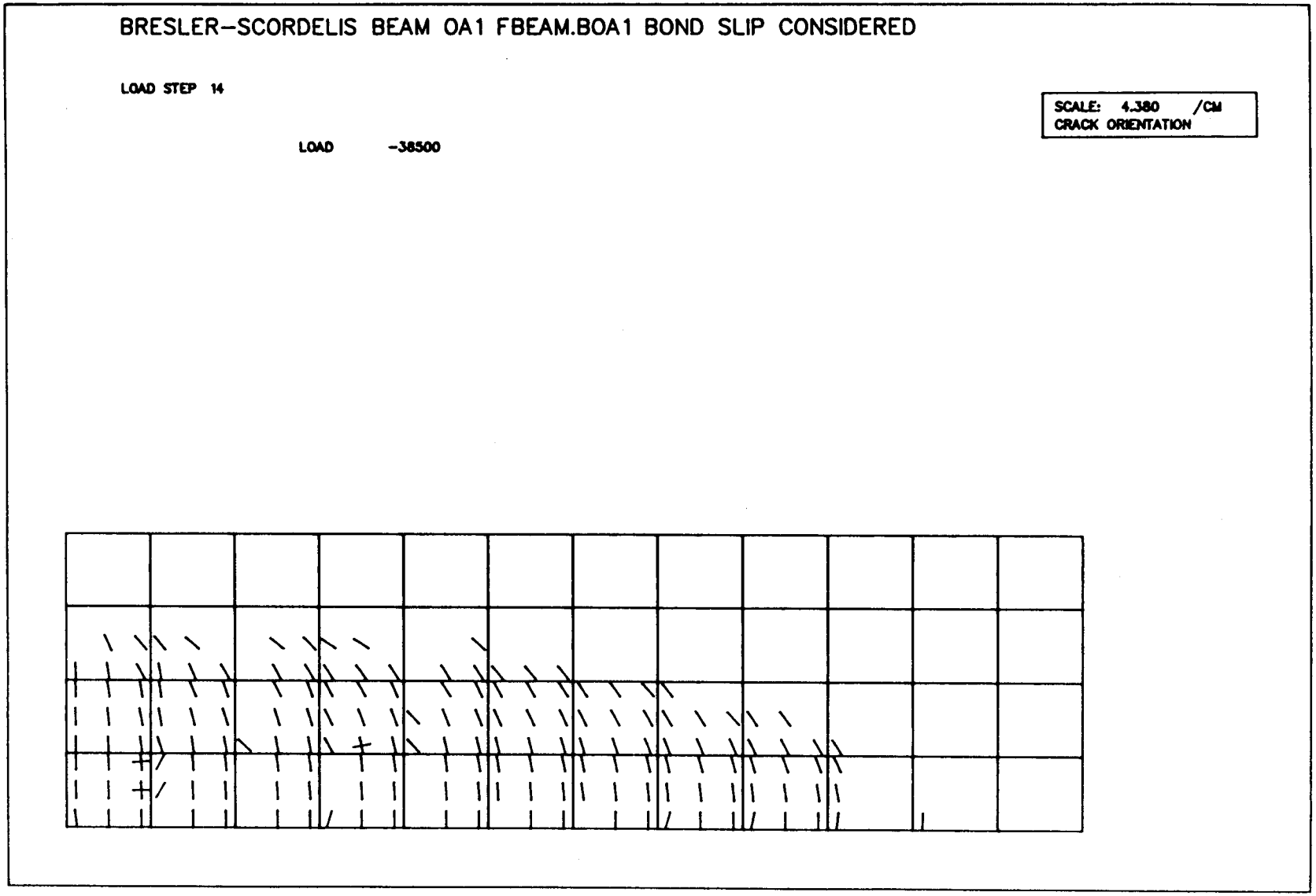

FIG. 5.22. (c) Analytical Crack Pattern - Shear = 38.5 kip (171.3 kN)

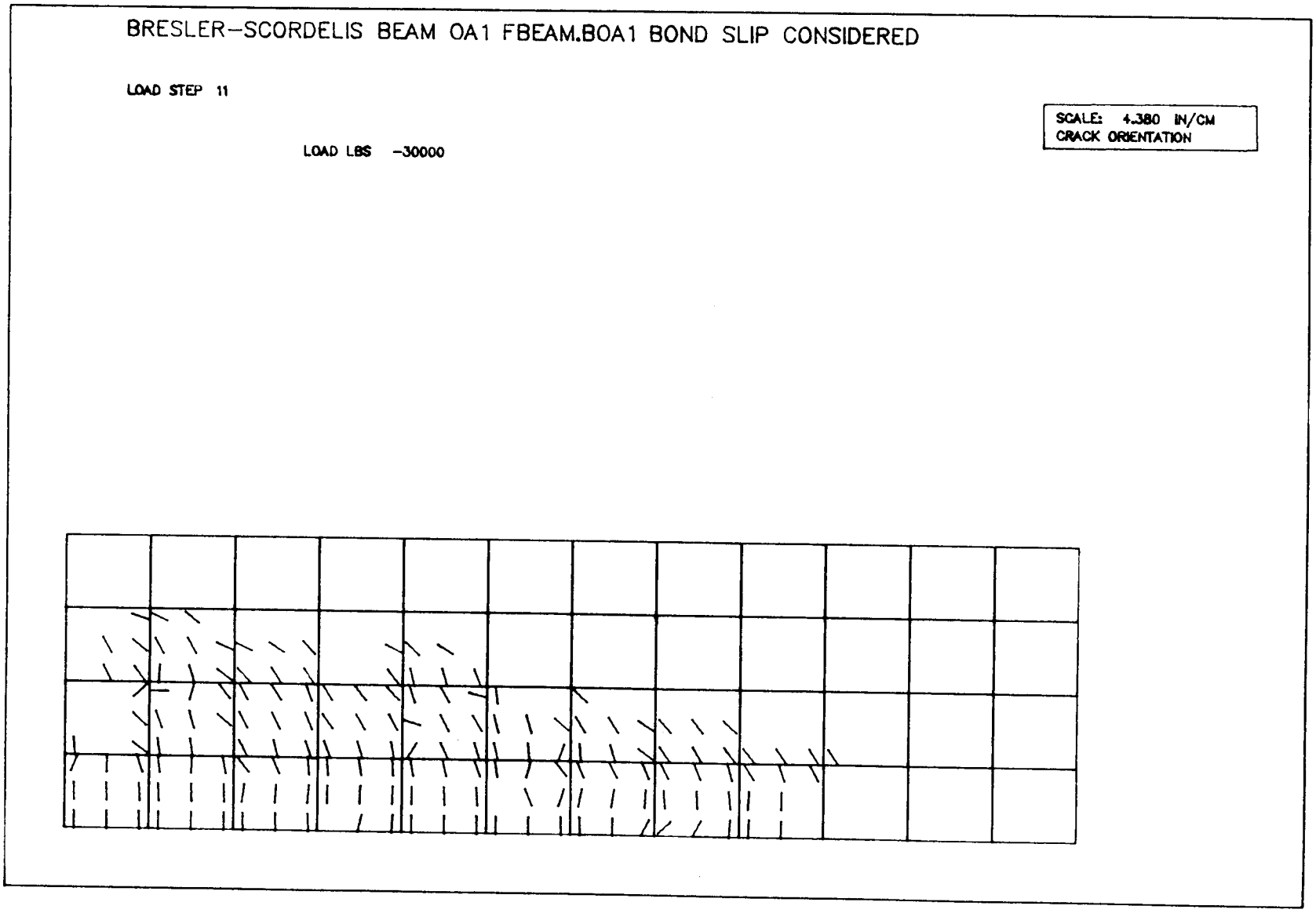

FIG. 5.22. (d) Analytical Crack Pattern Using Tension Cut-Off Criterion
Shear = 30 kip (133.4 kN)

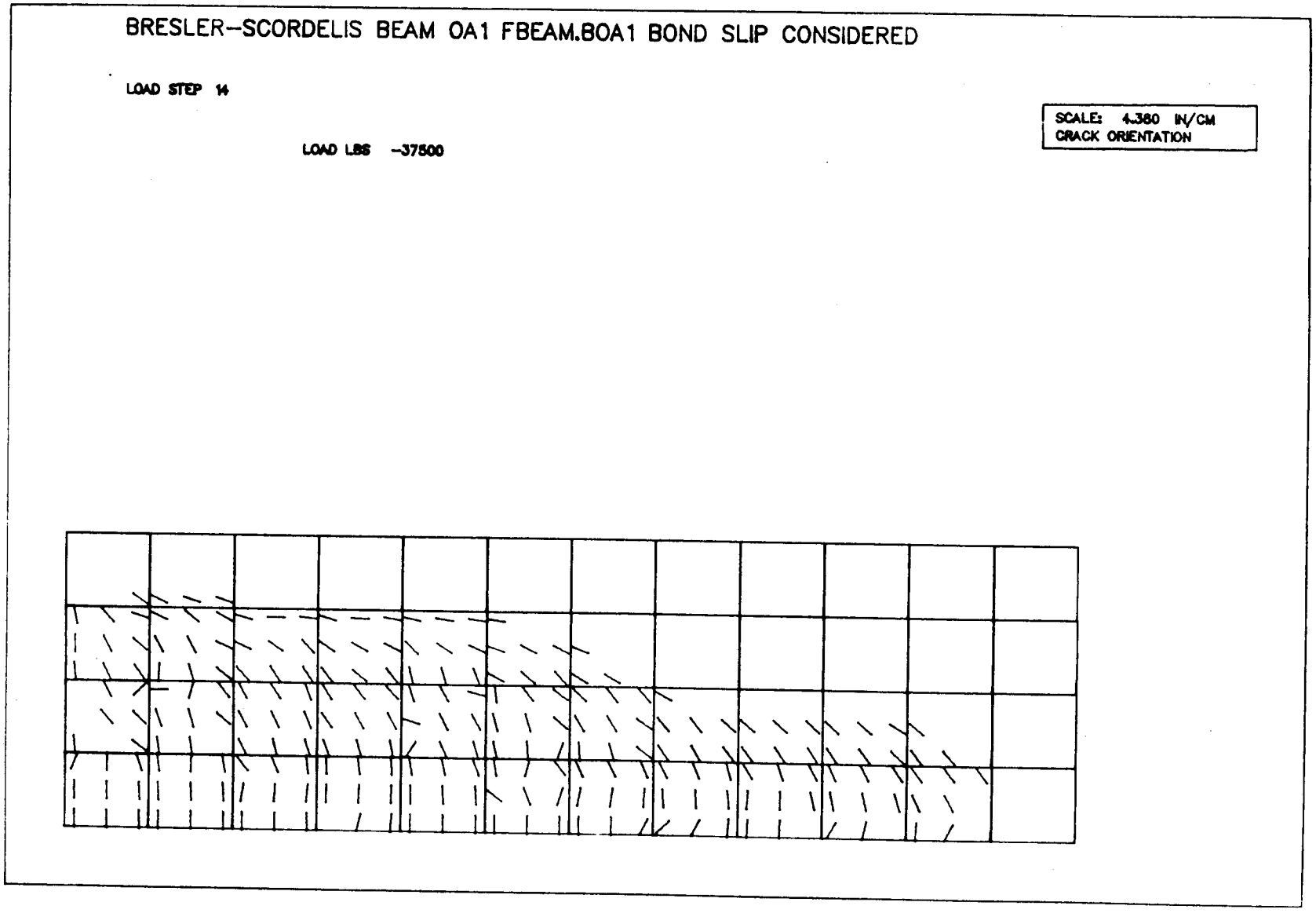

FIG. 5.22. (e) Analytical Crack Pattern Using Tension Cut-Off Criterion
Shear = 37.5 kip (166.8 kN)

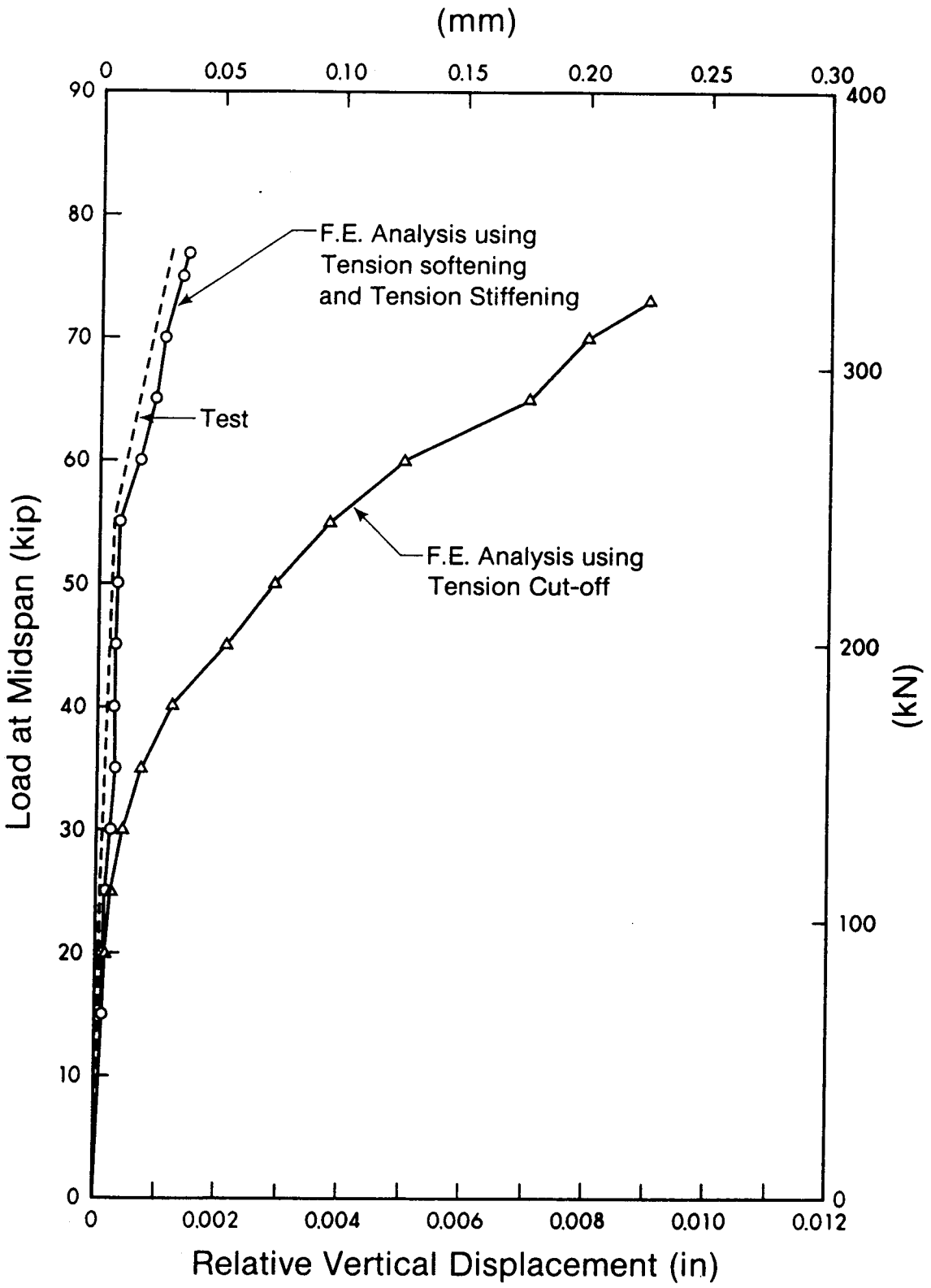

FIG. 5.23. Bresler/Scordelis Beam 0A1 - Relative Vertical Displacement

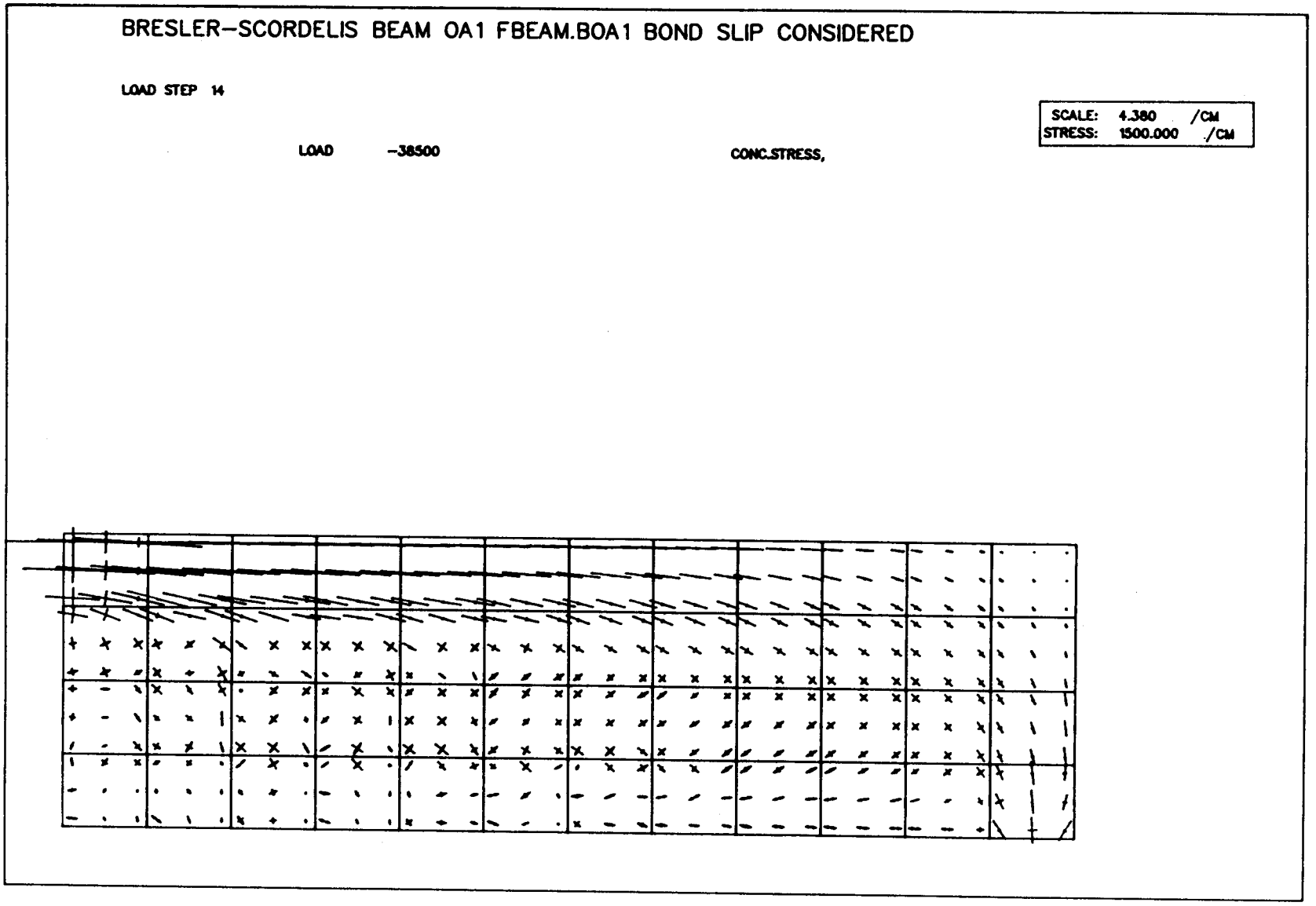

FIG. 5.24. Bresler/Scordelis Beam OA1 - Principal Stress Plot

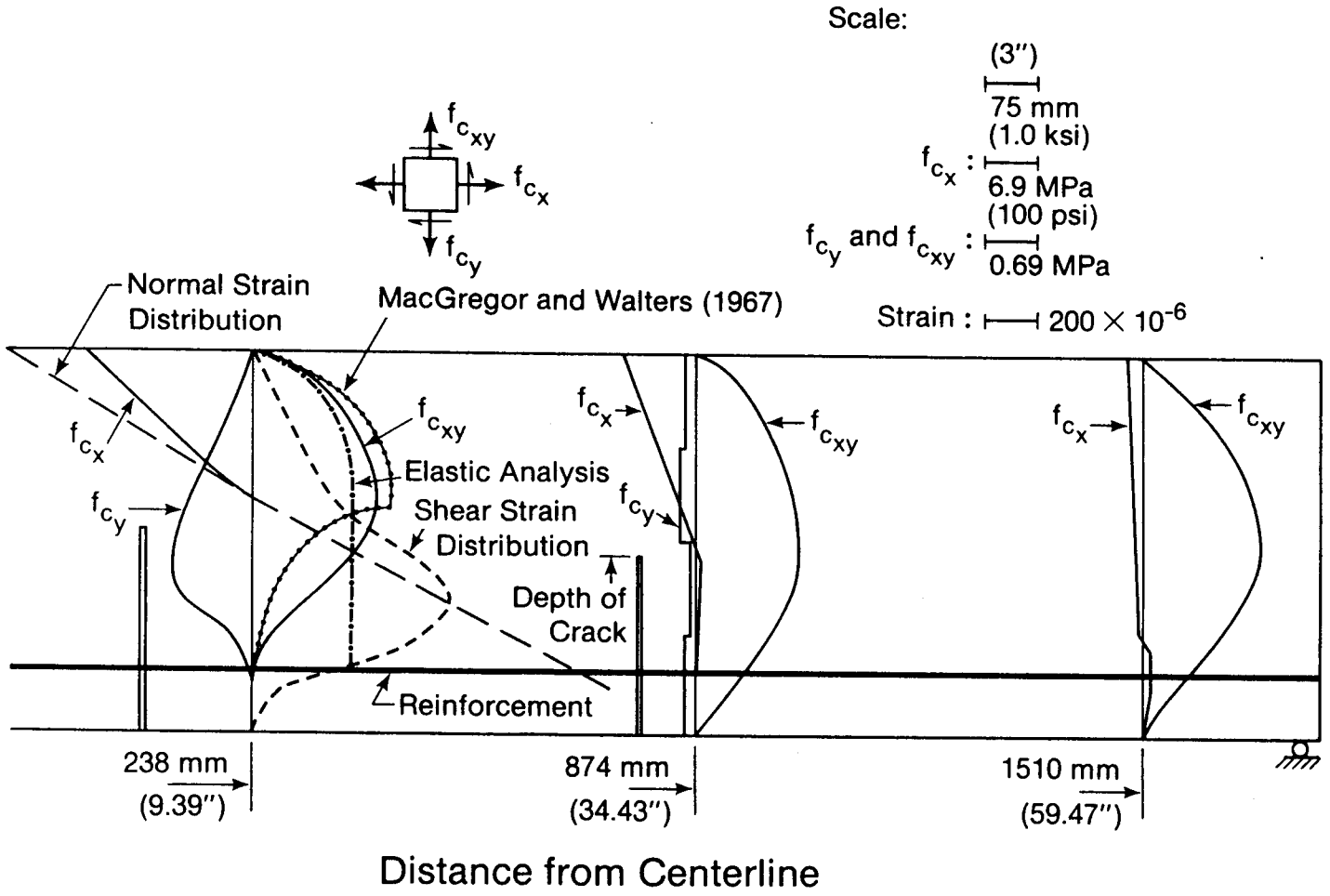

FIG. 5.25. Stress Distribution Across Sections - Bresler/Scordelis Beam 0A1

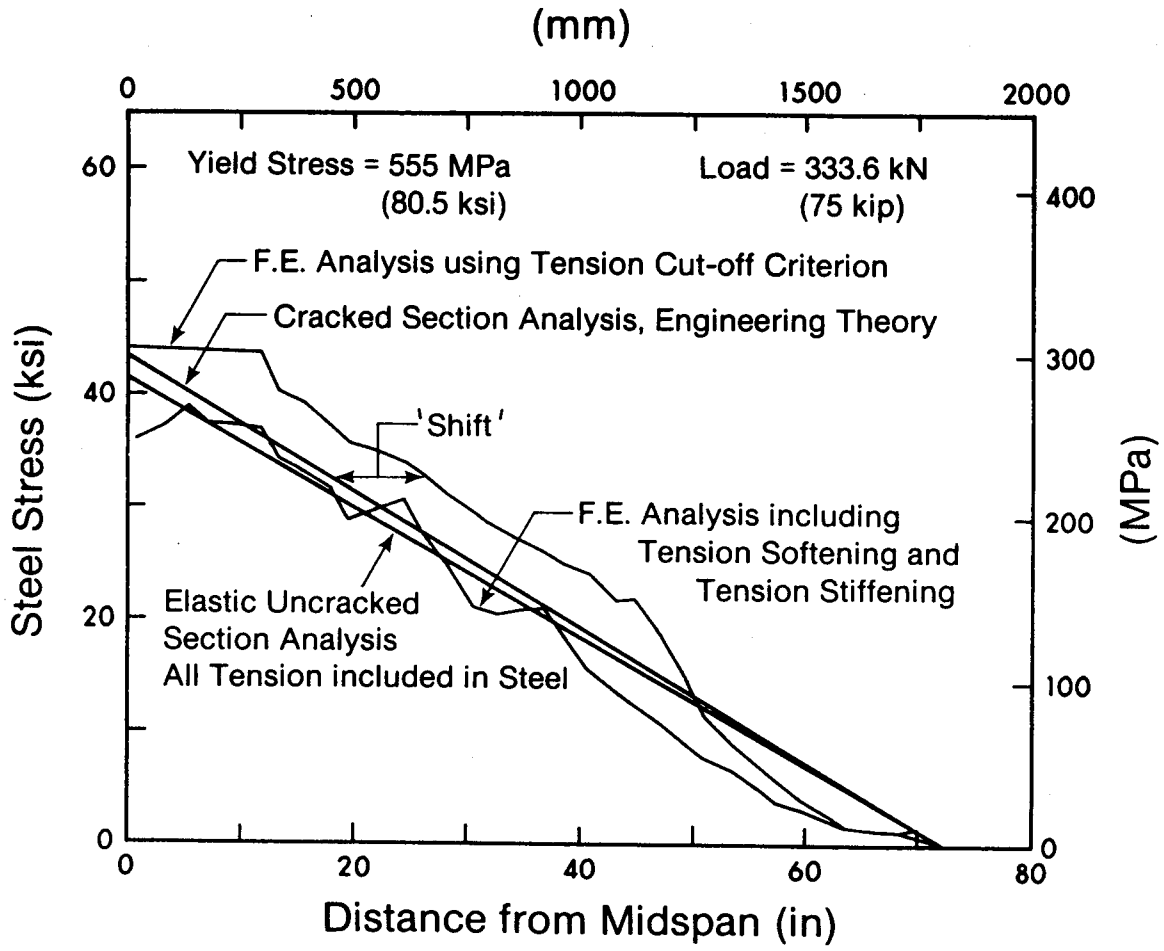

FIG. 5.26. Bresler/Scordelis Beam 0A1 - Distribution of Steel Stresses

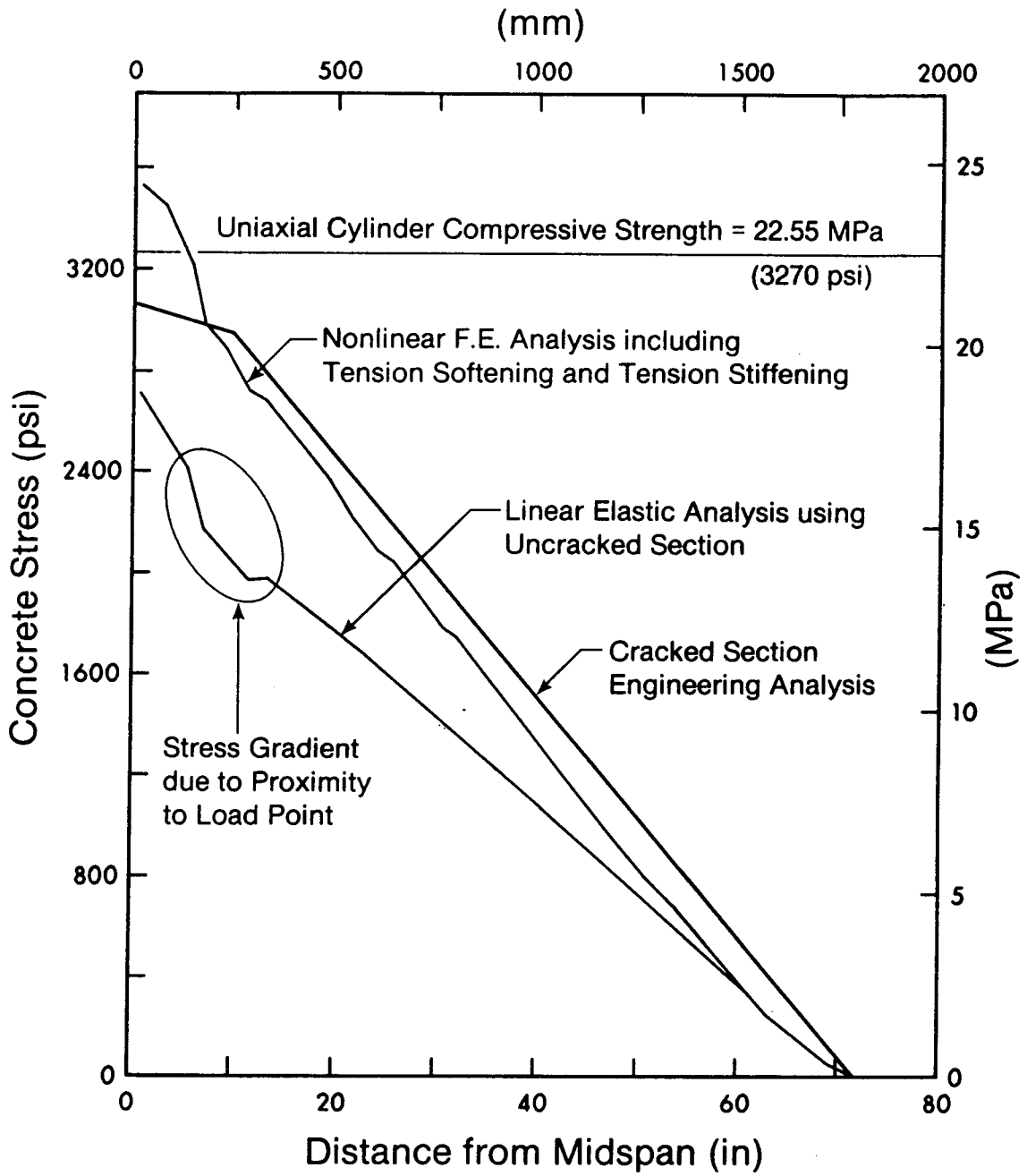

FIG. 5.27. Bresler/Scordelis Beam OA1 - Distribution of Concrete Stresses

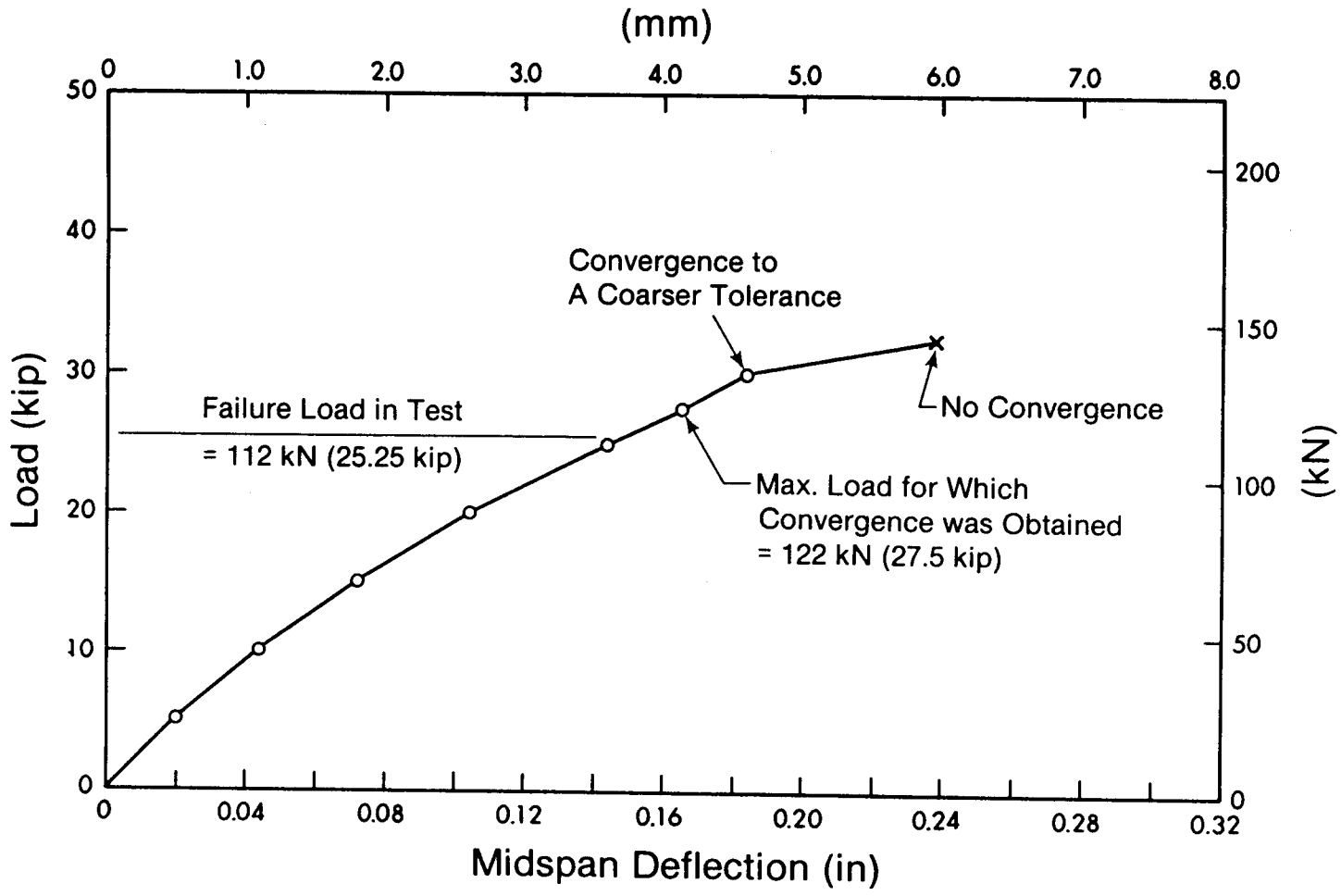

FIG. 5.28. Kani Beam 65 - Load-Deflection Relationship

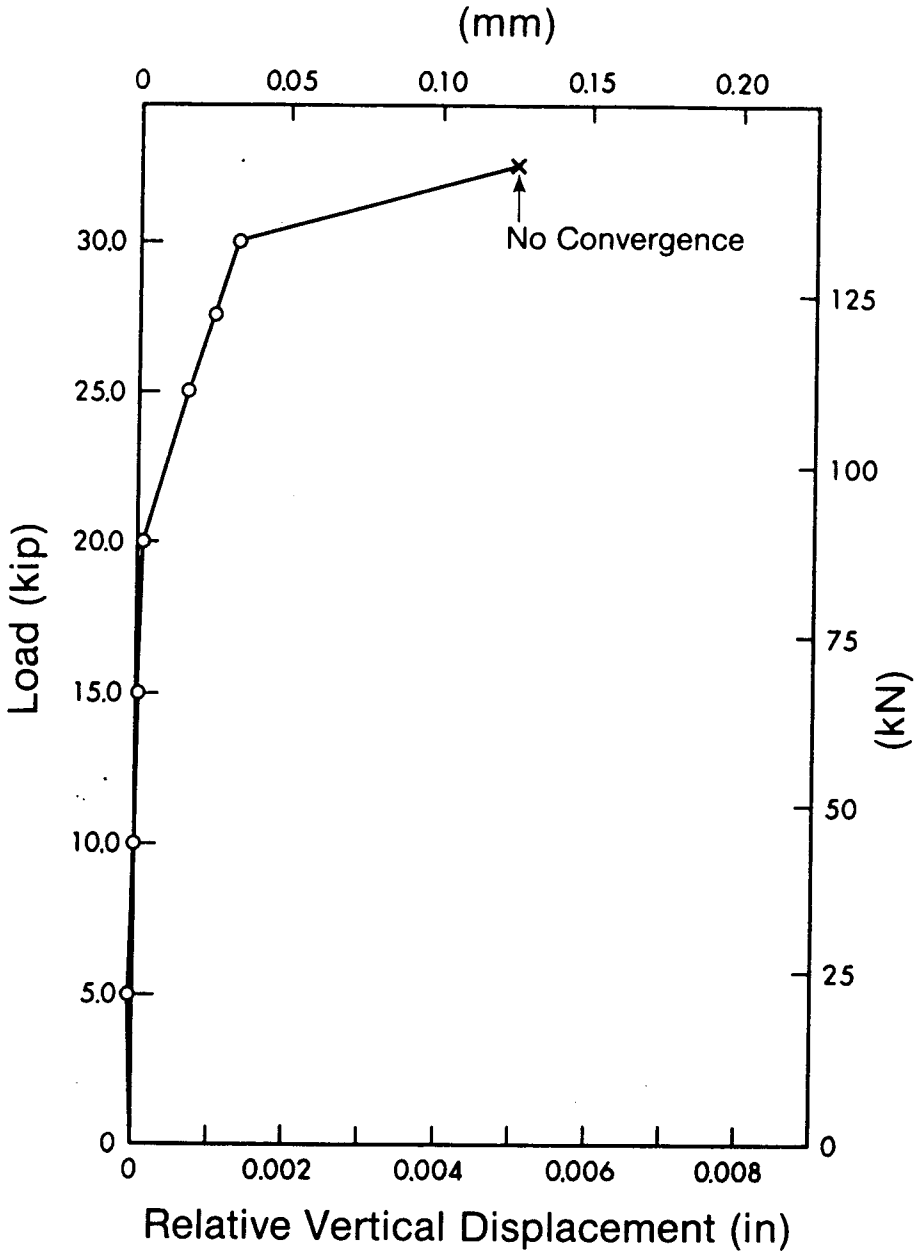

FIG. 5.29. Kani Beam 65 - Relative Vertical Displacement

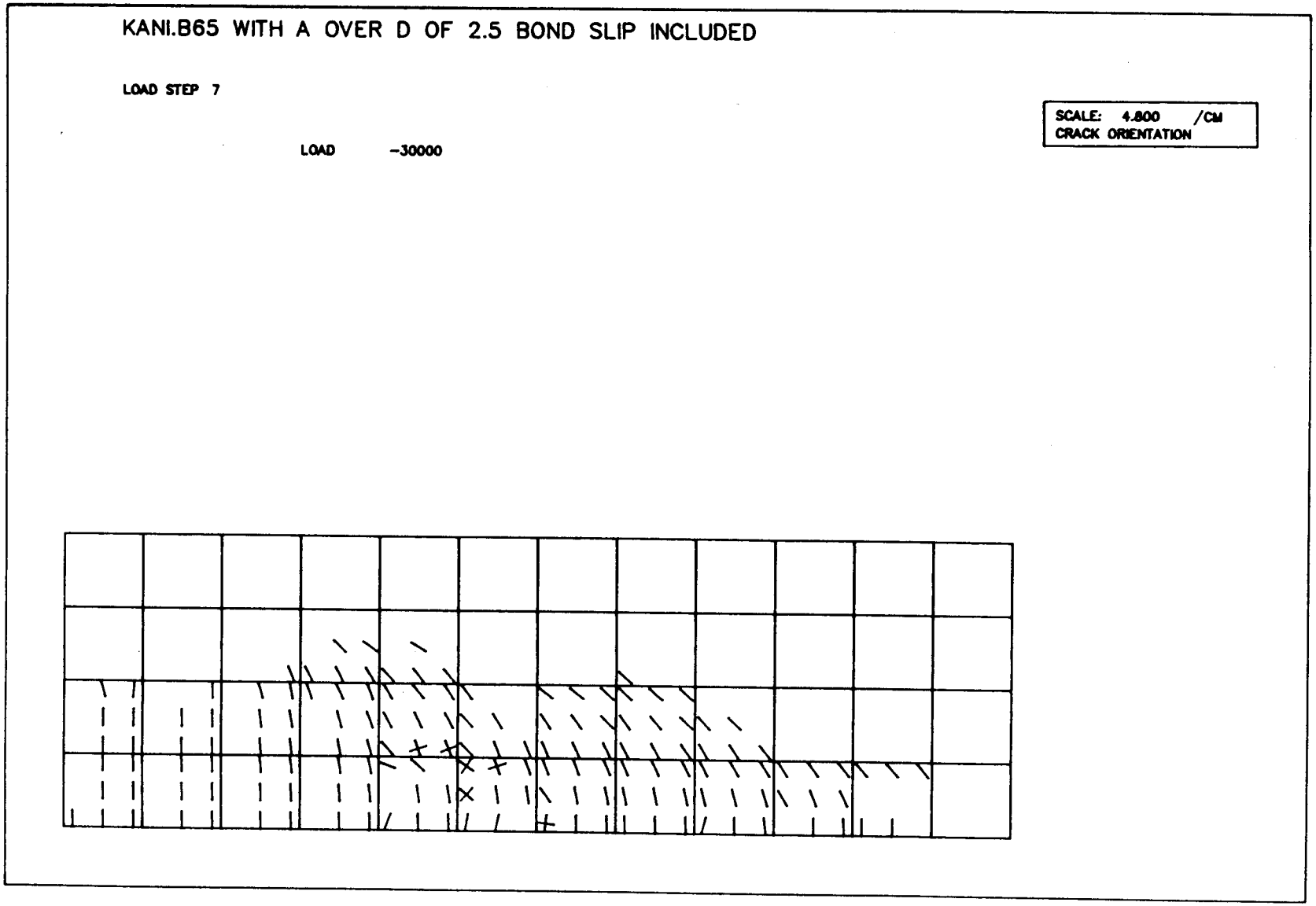

FIG. 5.30. Kani Beam 65 - Analytical Crack Pattern

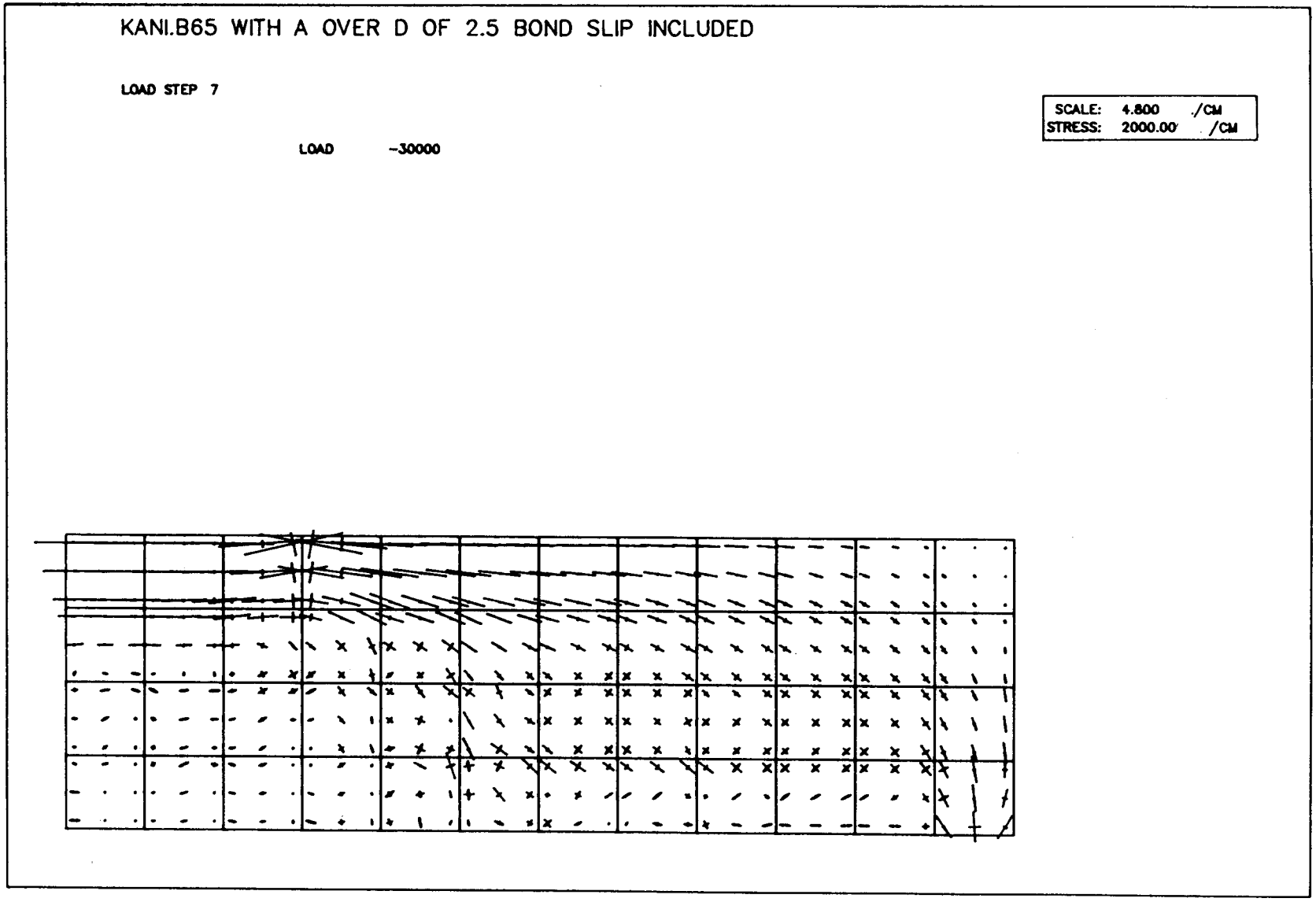

FIG. 5.31. Kani Beam 65 - Principal Stress Plot

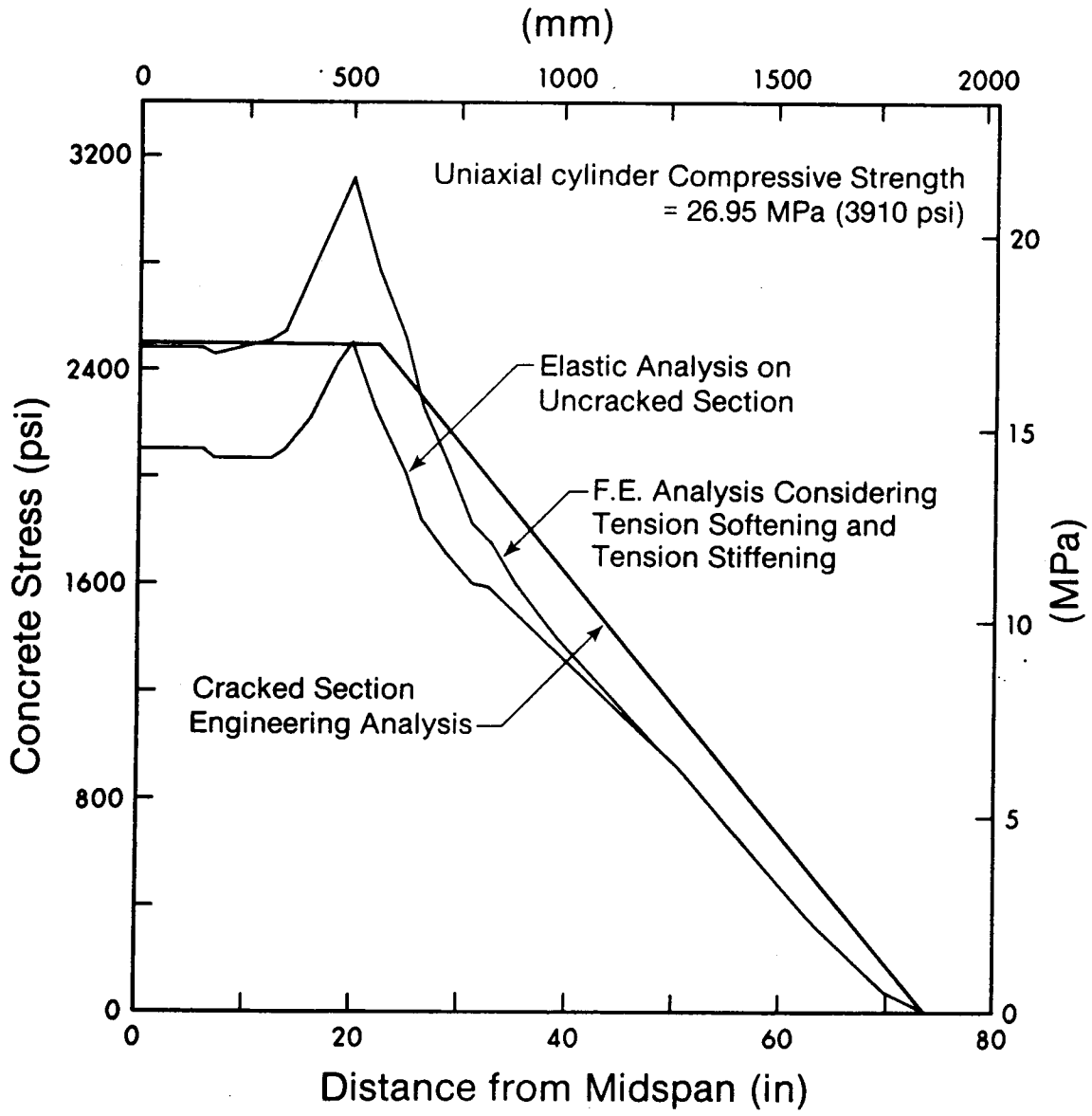

FIG. 5.32. Kani Beam 65 - Distribution of Concrete Stresses

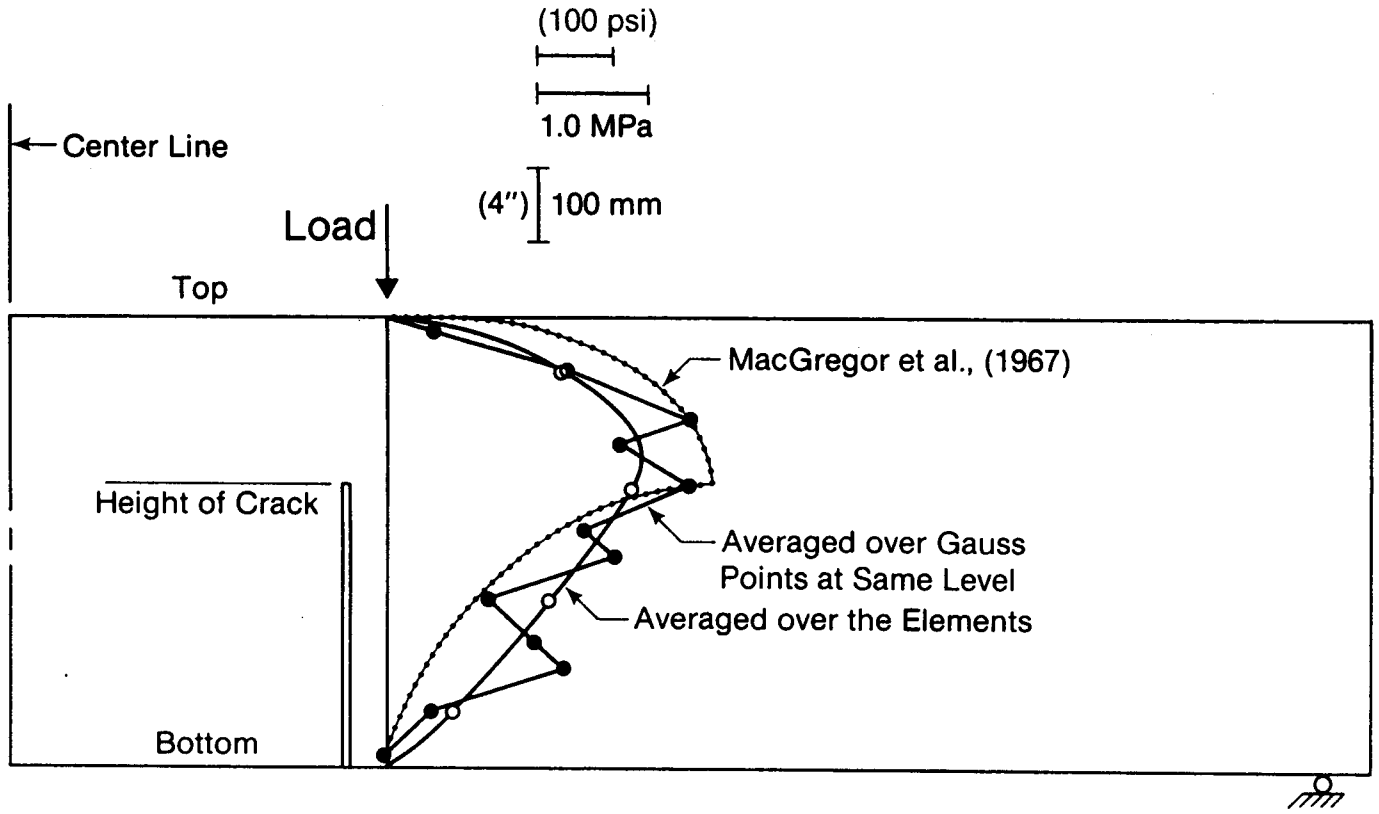

FIG. 5.33. Kani Beam 65 - Shear Stress Distribution at Section Near Load Point

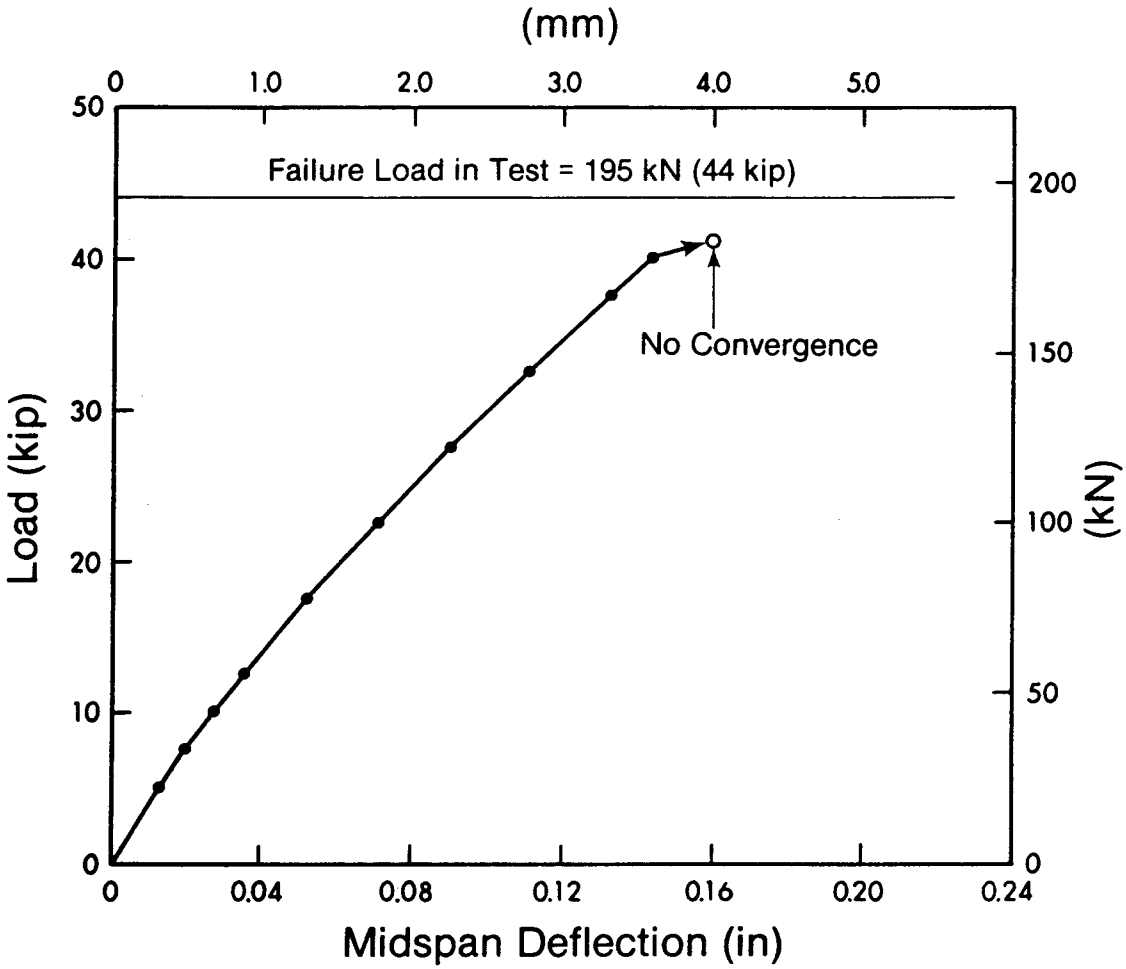

FIG. 5.34. Kani Beam 72 - Load-Deflection Relationship

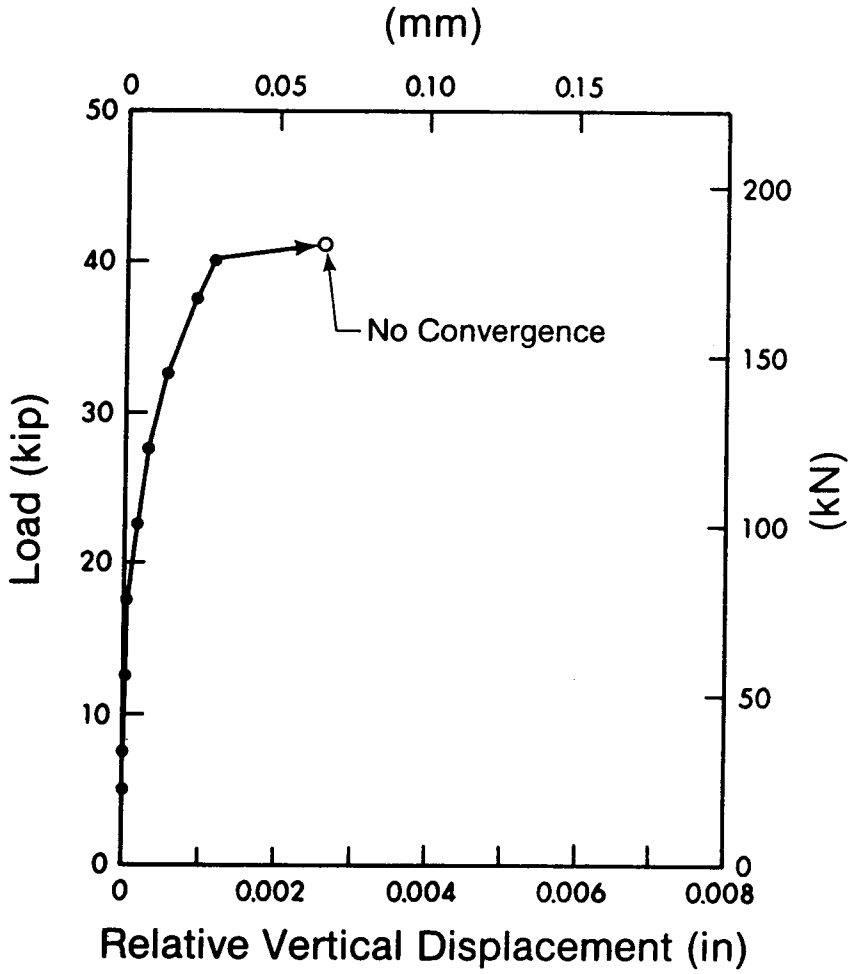

FIG. 5.35. Kani Beam 72 - Relative Vertical Displacement

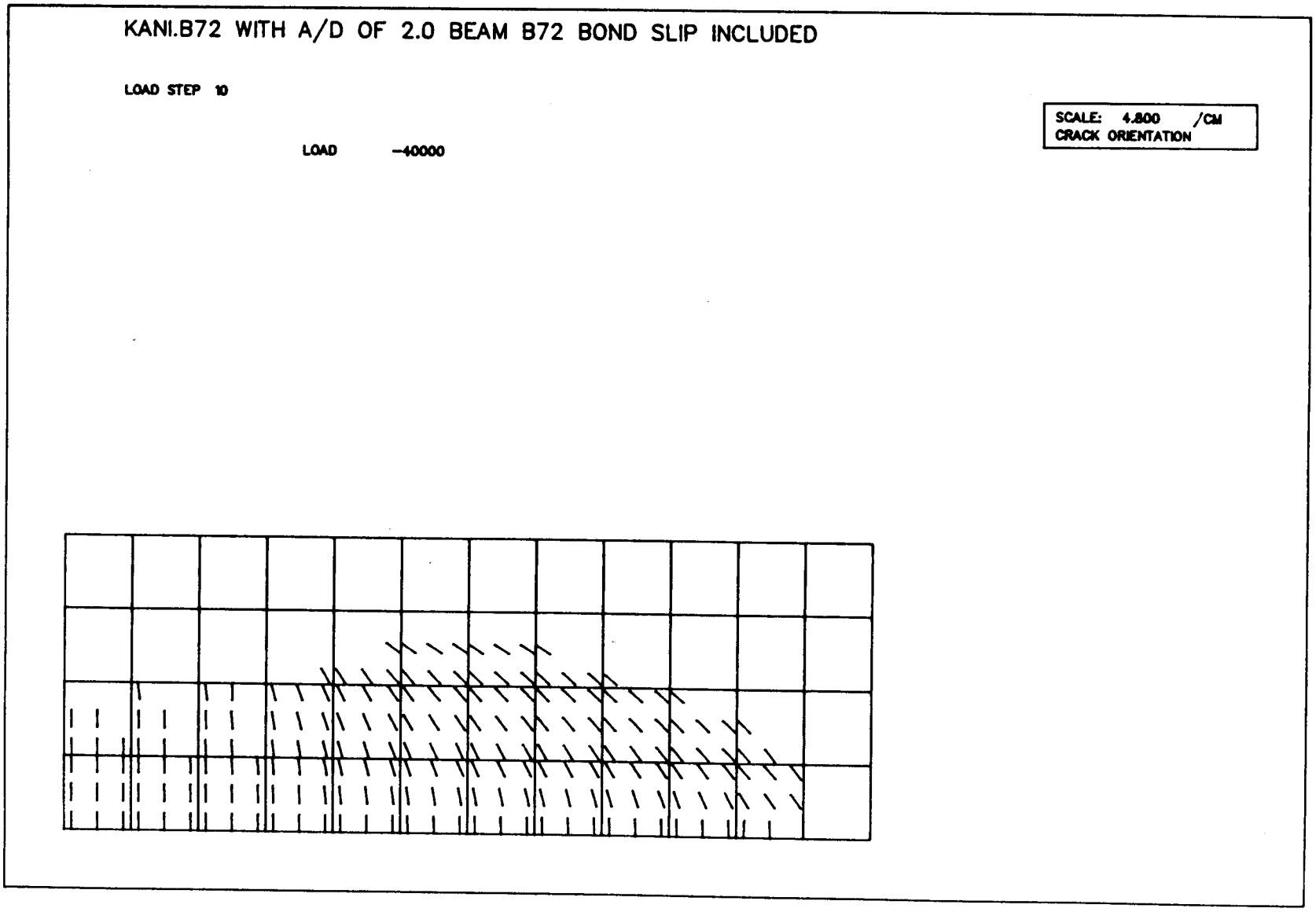

FIG. 5.36. Kani Beam 72 - Analytical Crack Pattern

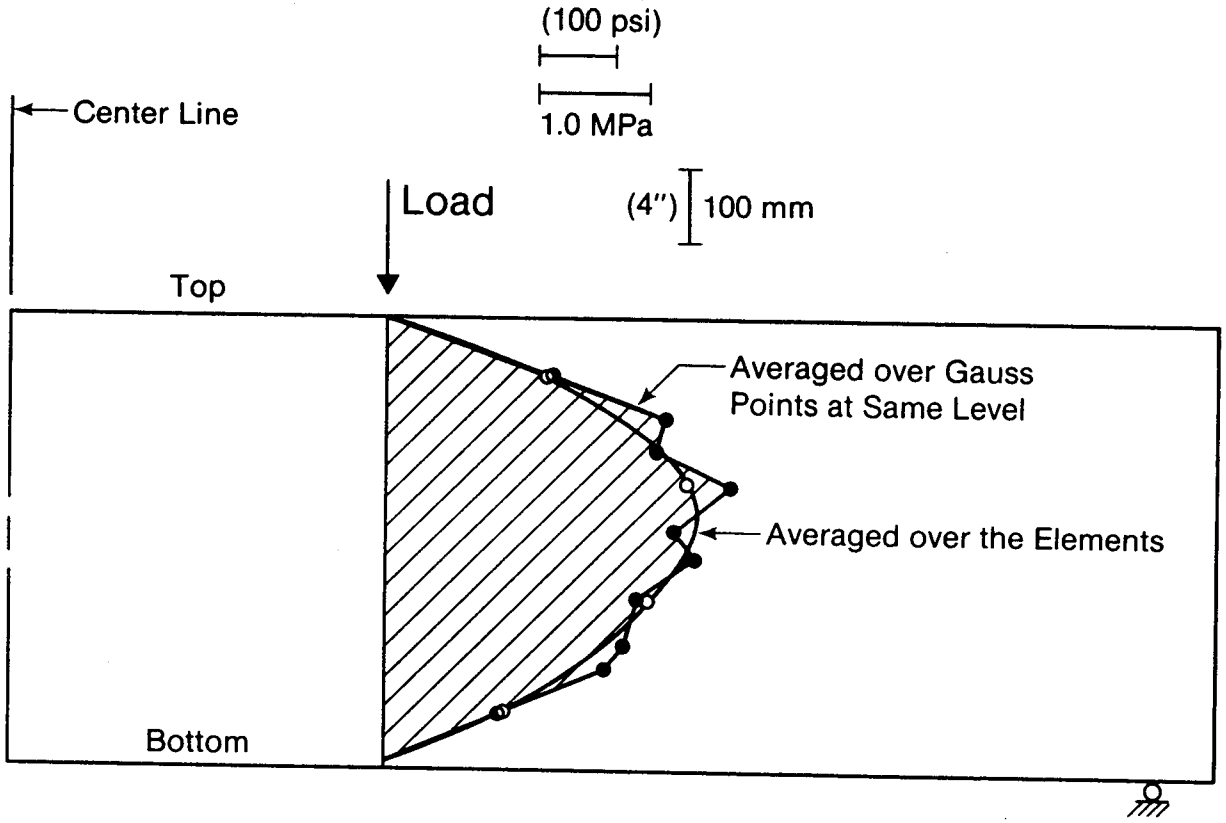

FIG. 5.37. Kani Beam 72 - Shear Stress Distribution at a Section Near Load Point

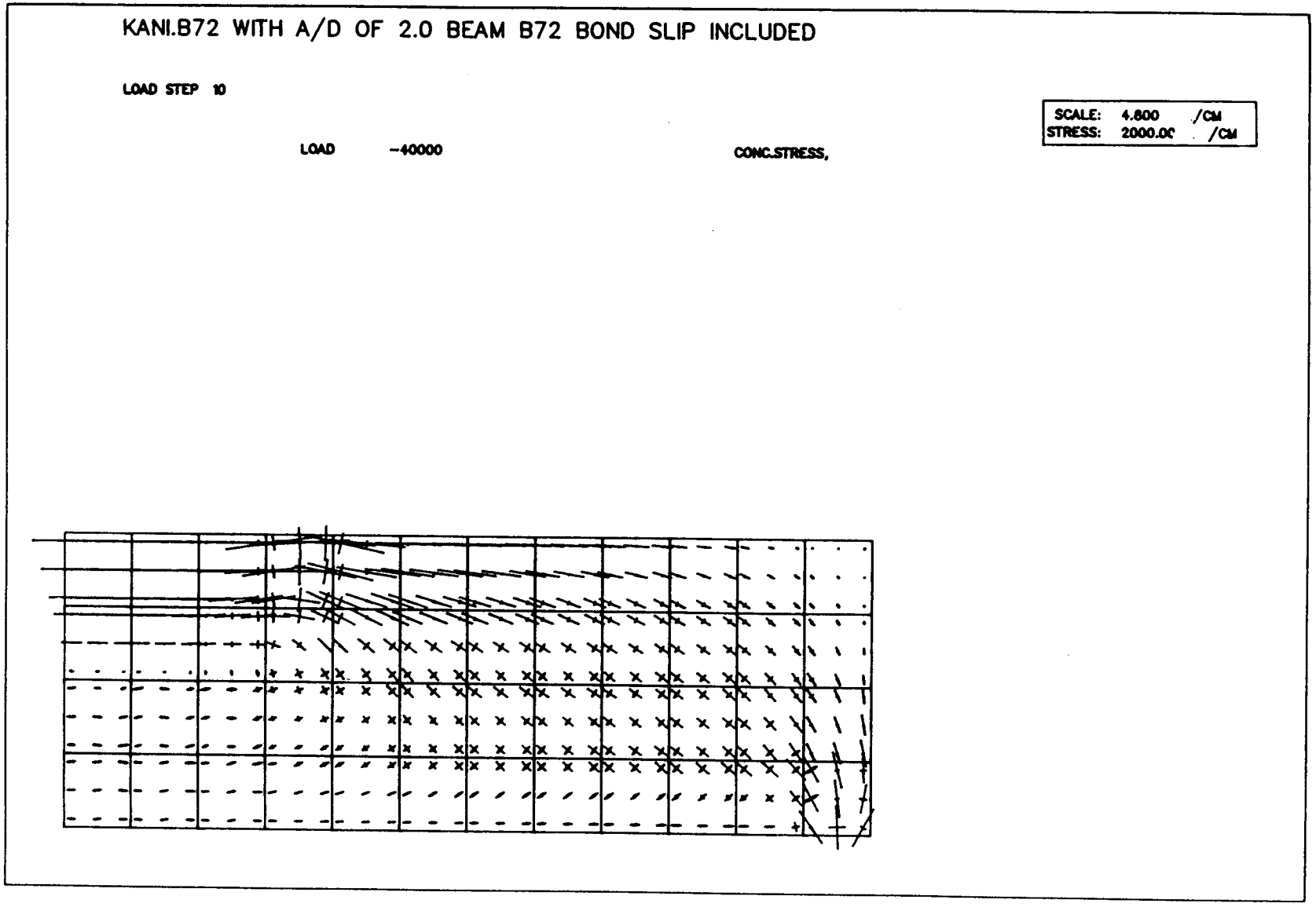

FIG. 5.38. Kani Beam 72 - Principal Stress Plot

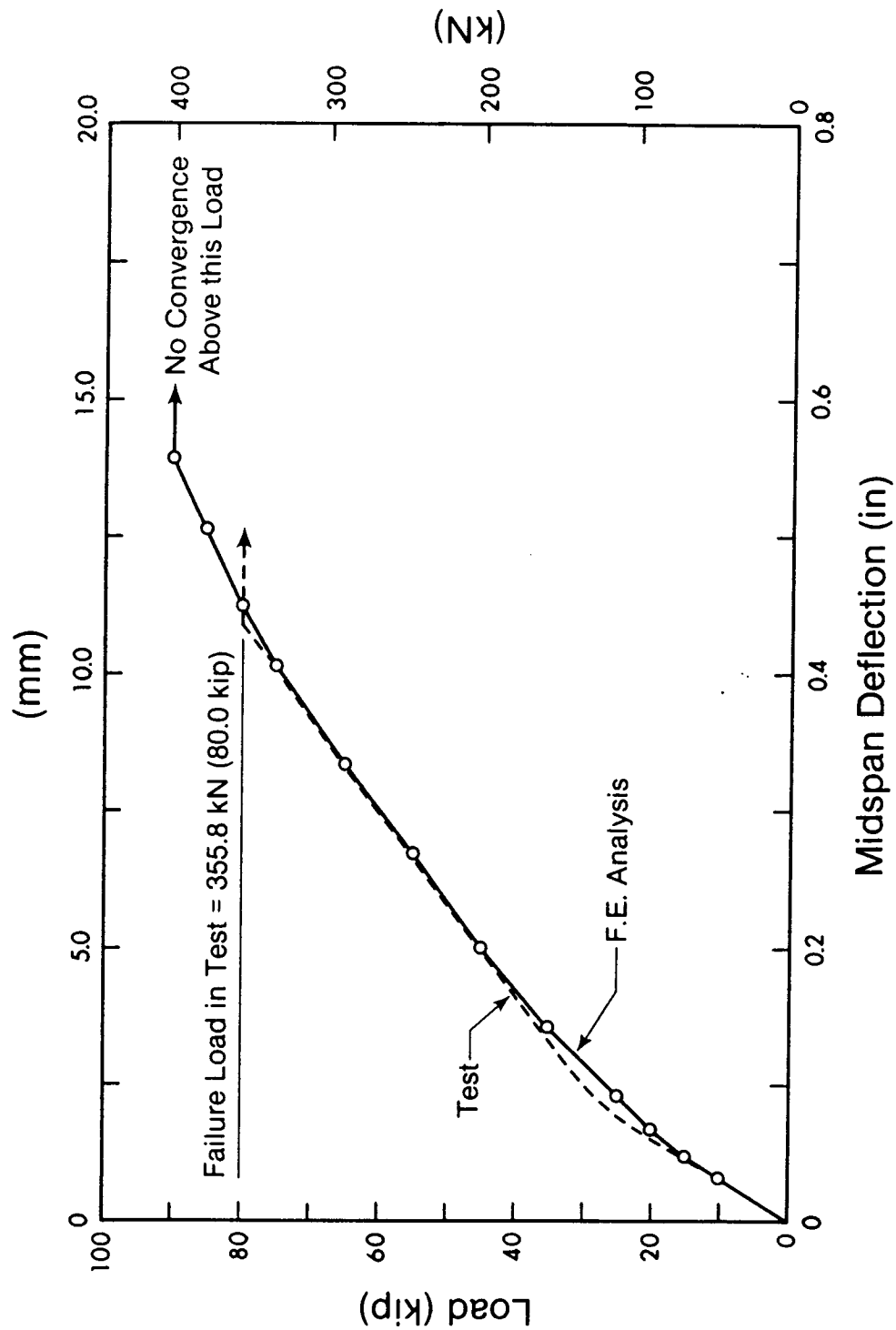

FIG. 5.39. Load-Deflection Relationship - Bresler/Scordelis Beam 0A2

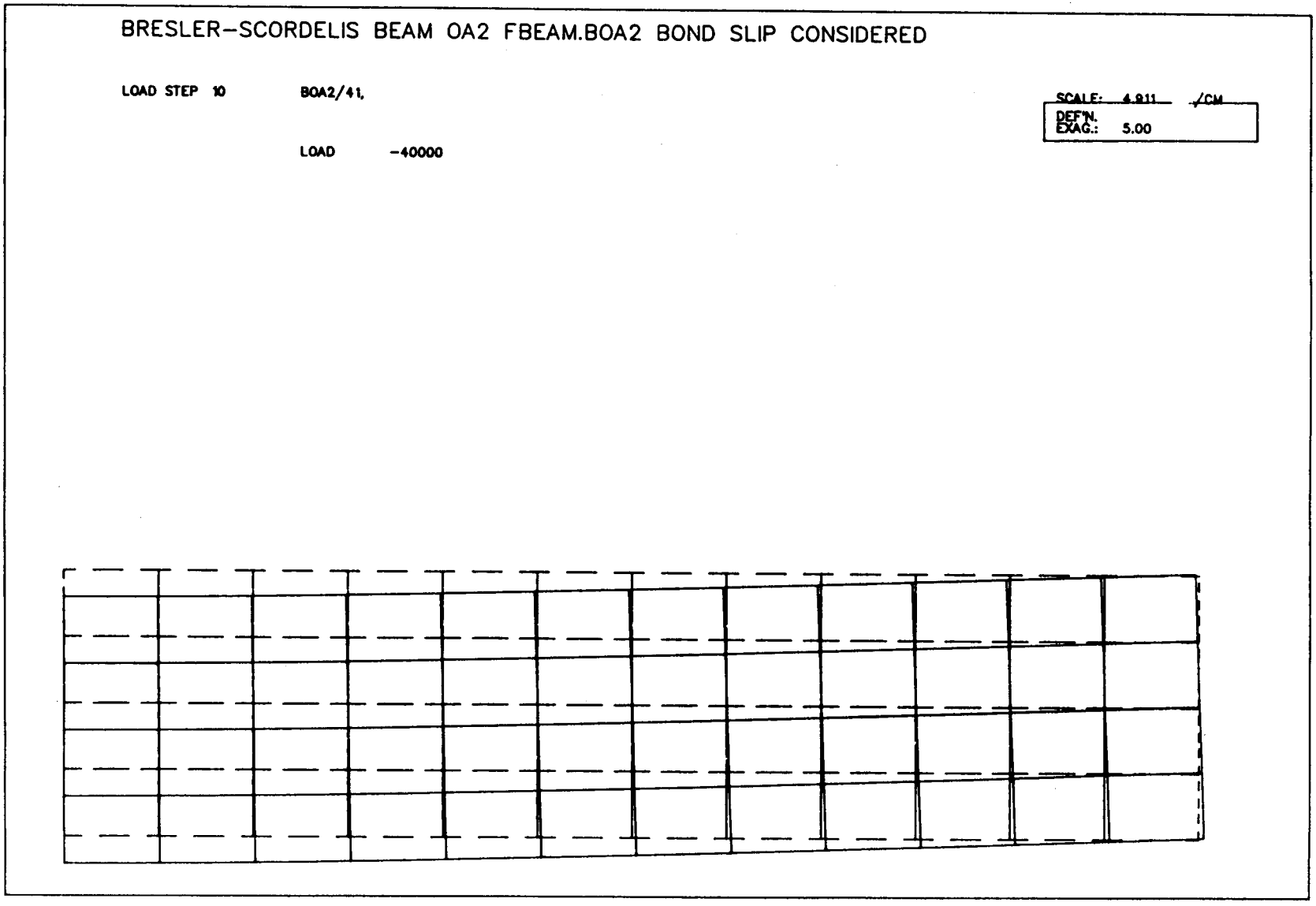

FIG. 5.40. Bresler/Scordelis Beam OA2 - Deflected Shapes
(a) Shear = 40 kip (178 kN)

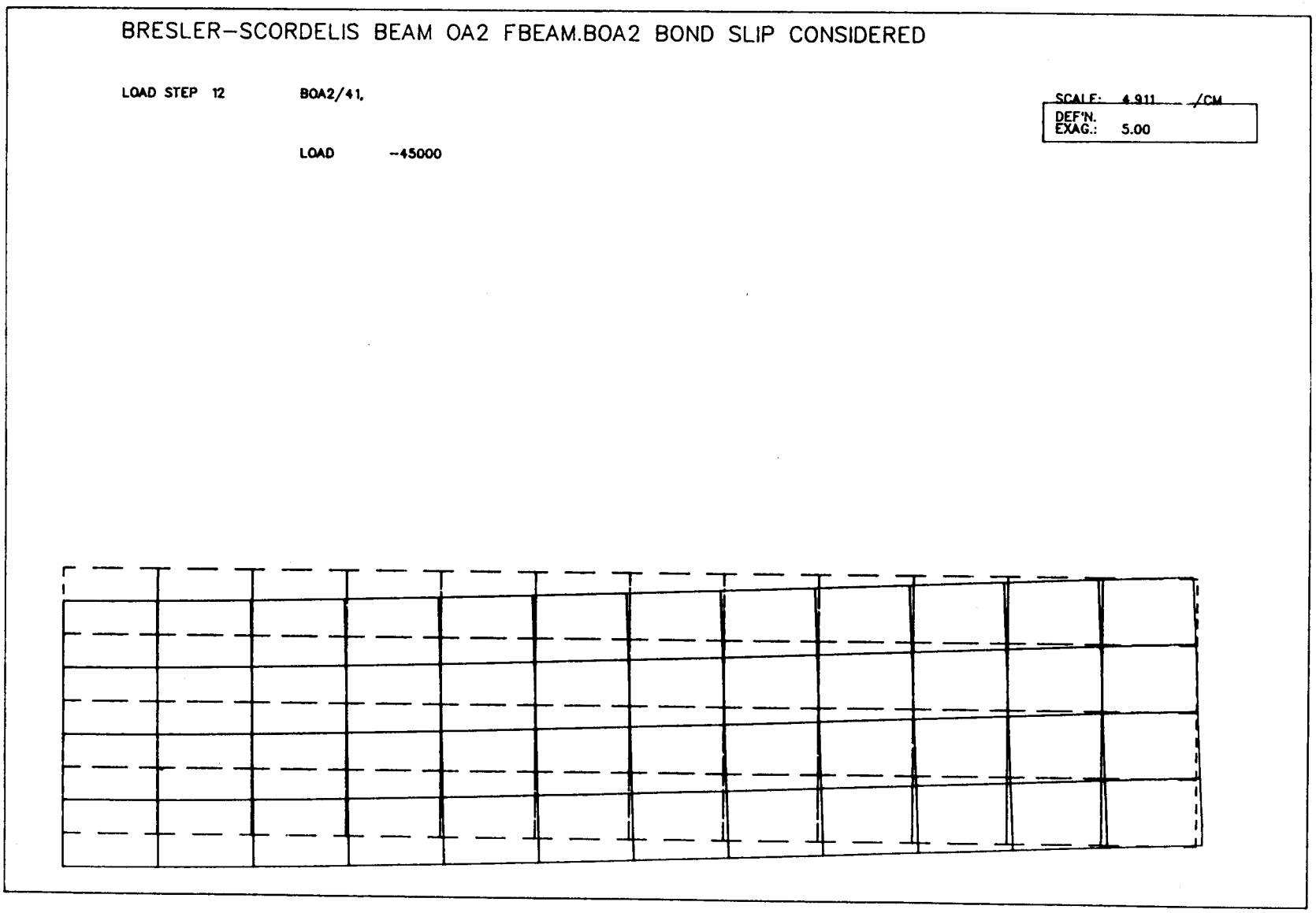

FIG. 5.40. (b) Shear = 45 kip (200 kN)

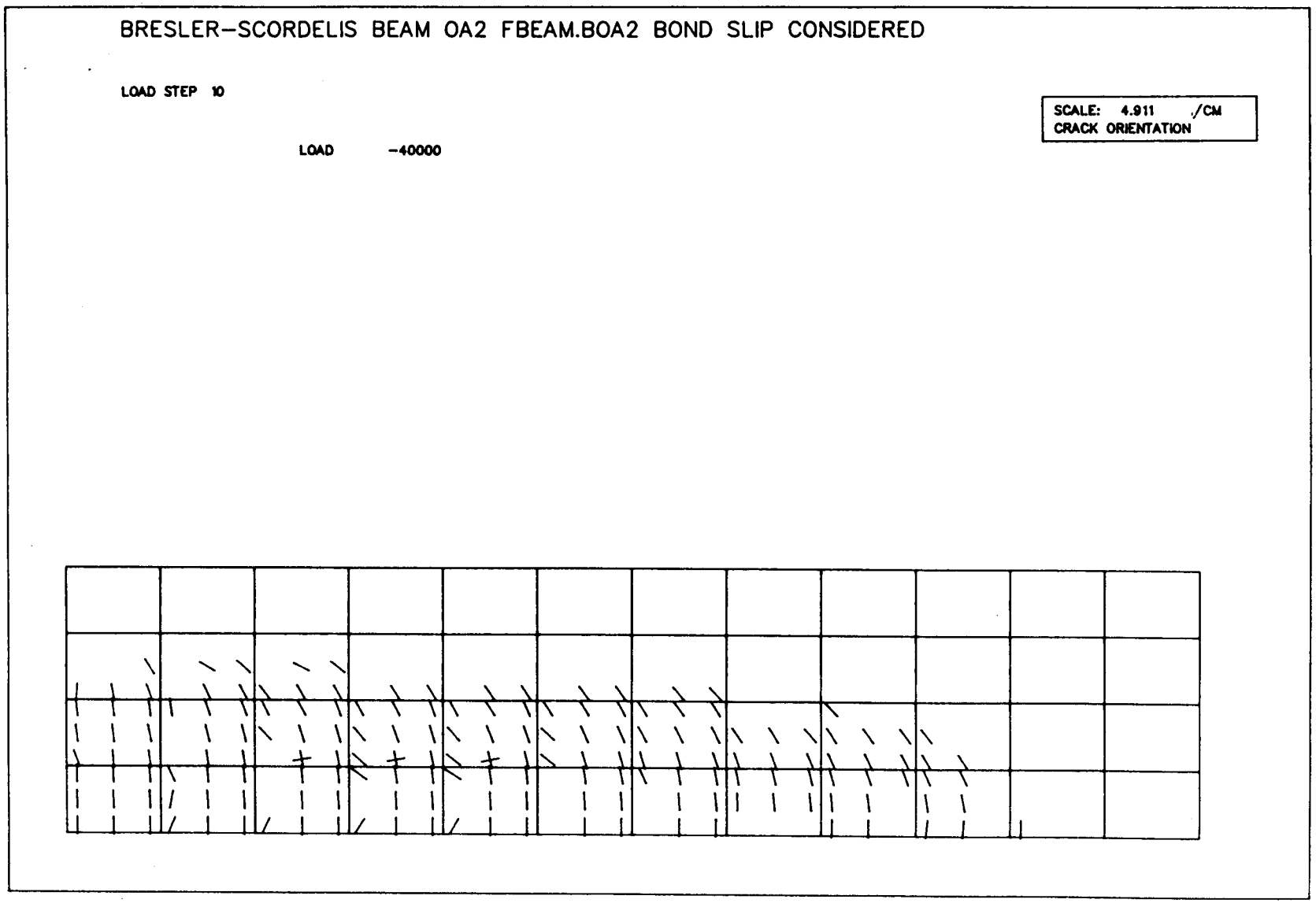

FIG. 5.41. Bresler/Scordelis Beam OA2 - Crack Patterns
(a) Analytical Crack Pattern - Shear = 40 kip (178 kN)

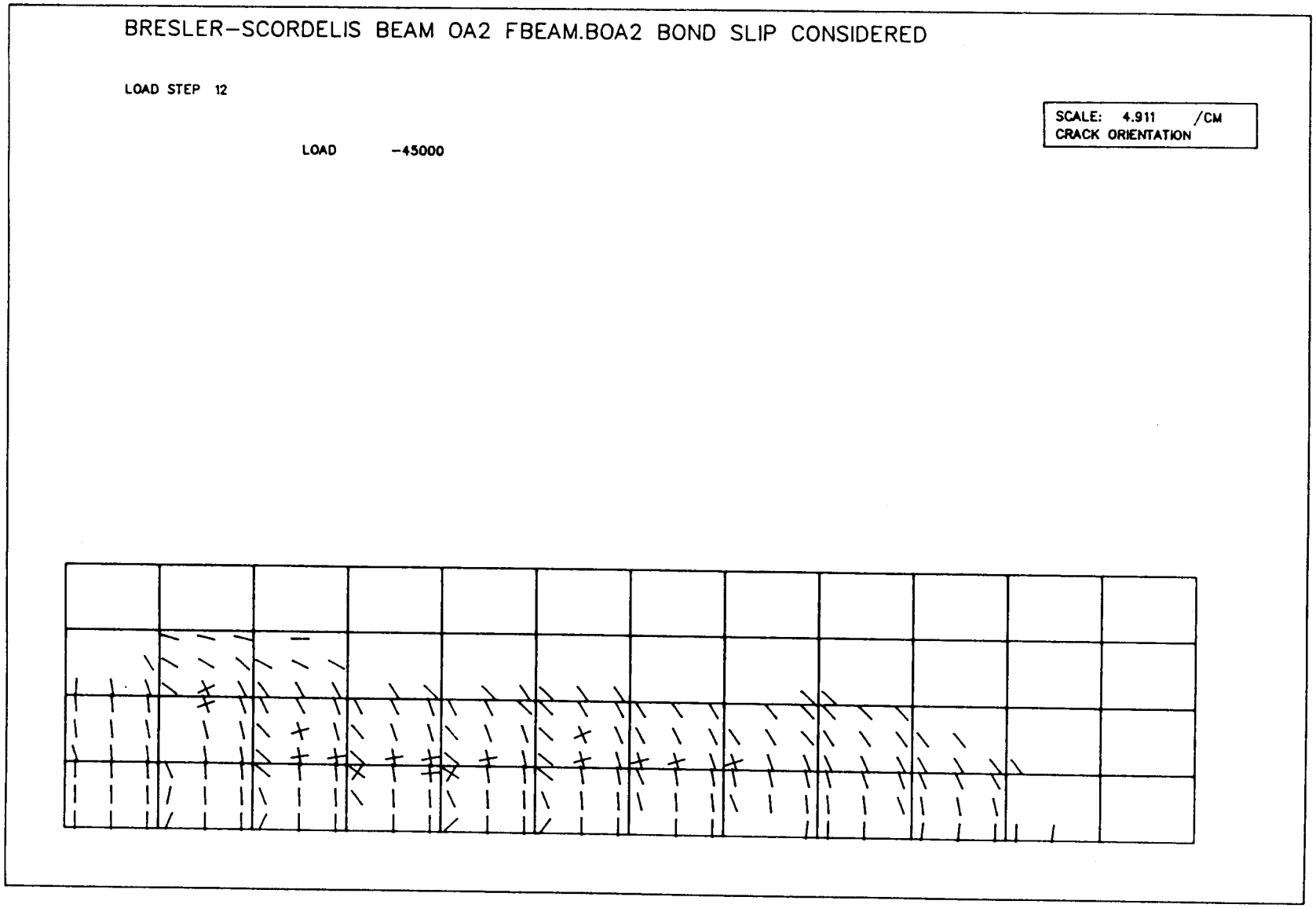

FIG. 5.41. (b) Analytical Crack Pattern - Shear = 45 kip (200 kN)

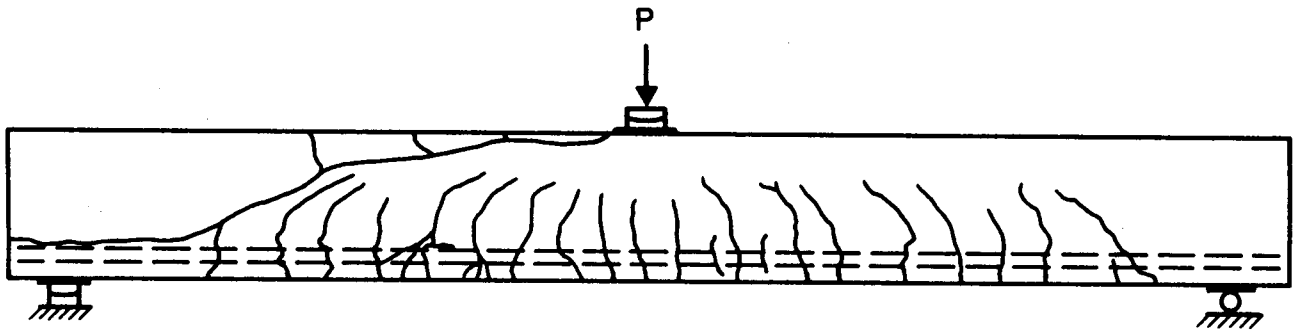

FIG. 5.41. (c) Experimental Crack Pattern - Shear = 40 kip (178 kN)

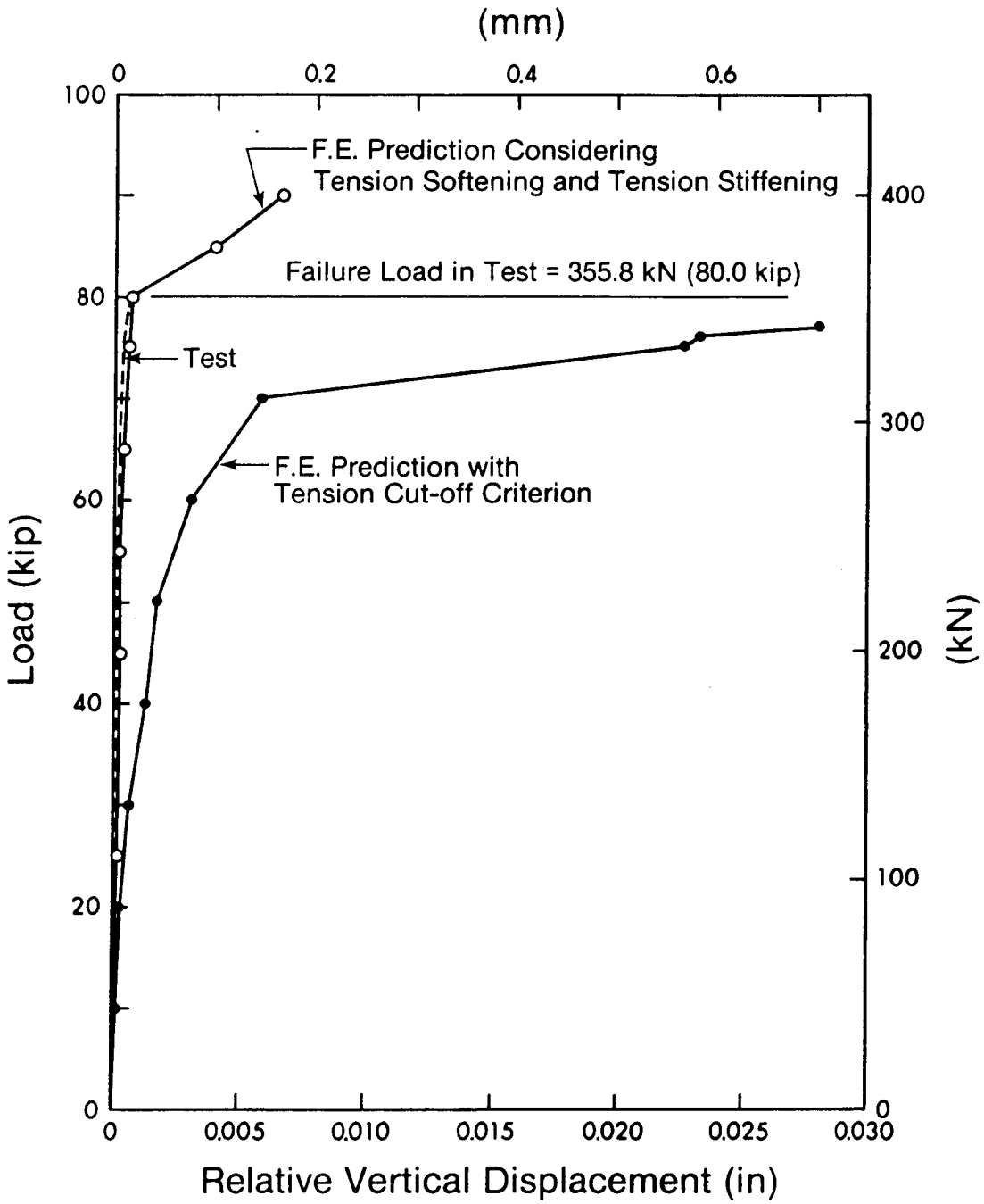

FIG. 5.42. Relative Vertical Displacement - Bresler/Scordelis Beam 0A2

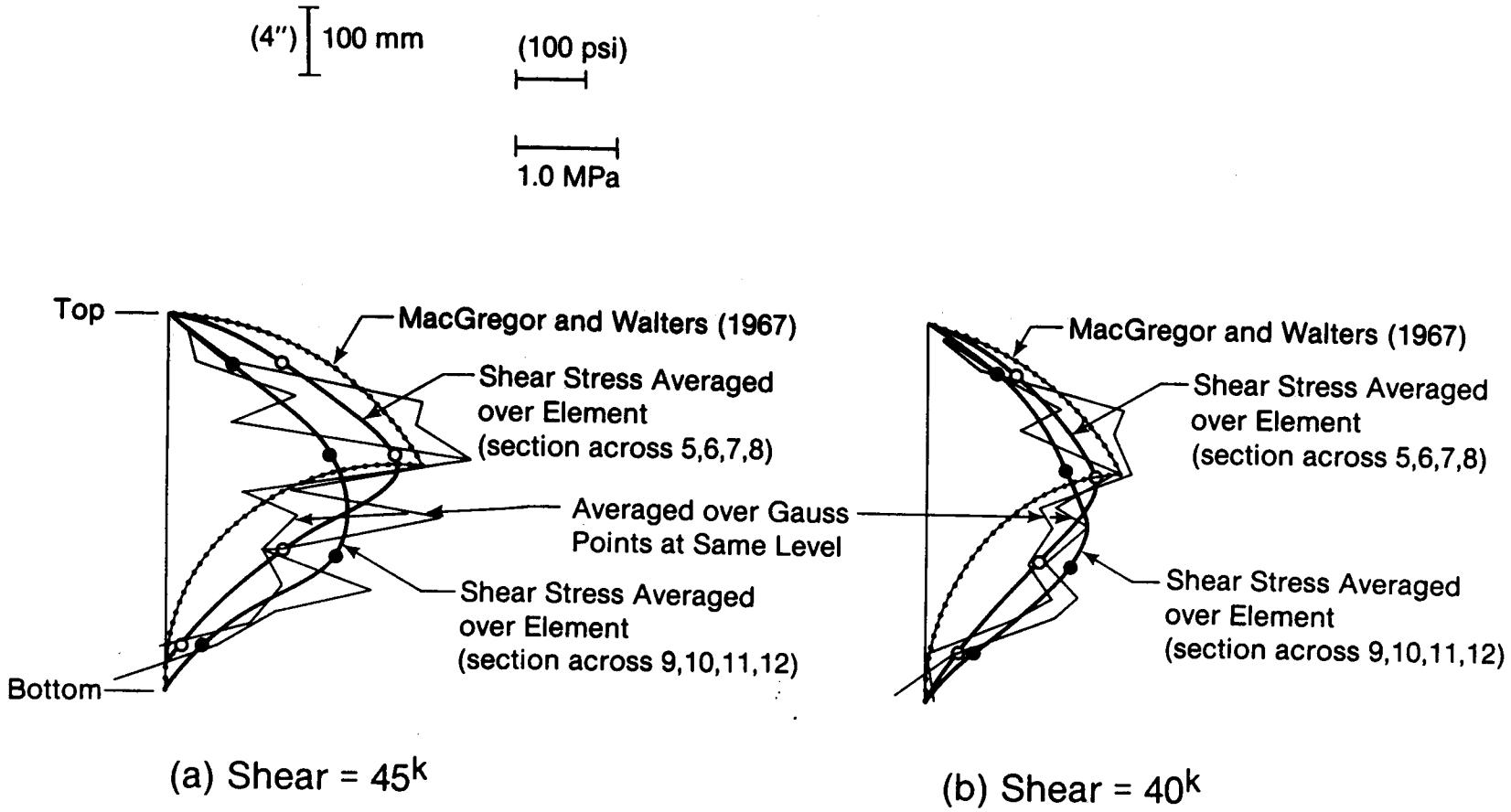

FIG. 5.43. Bresler/Scordelis Beam 0A2 - Distribution of Shear Stresses

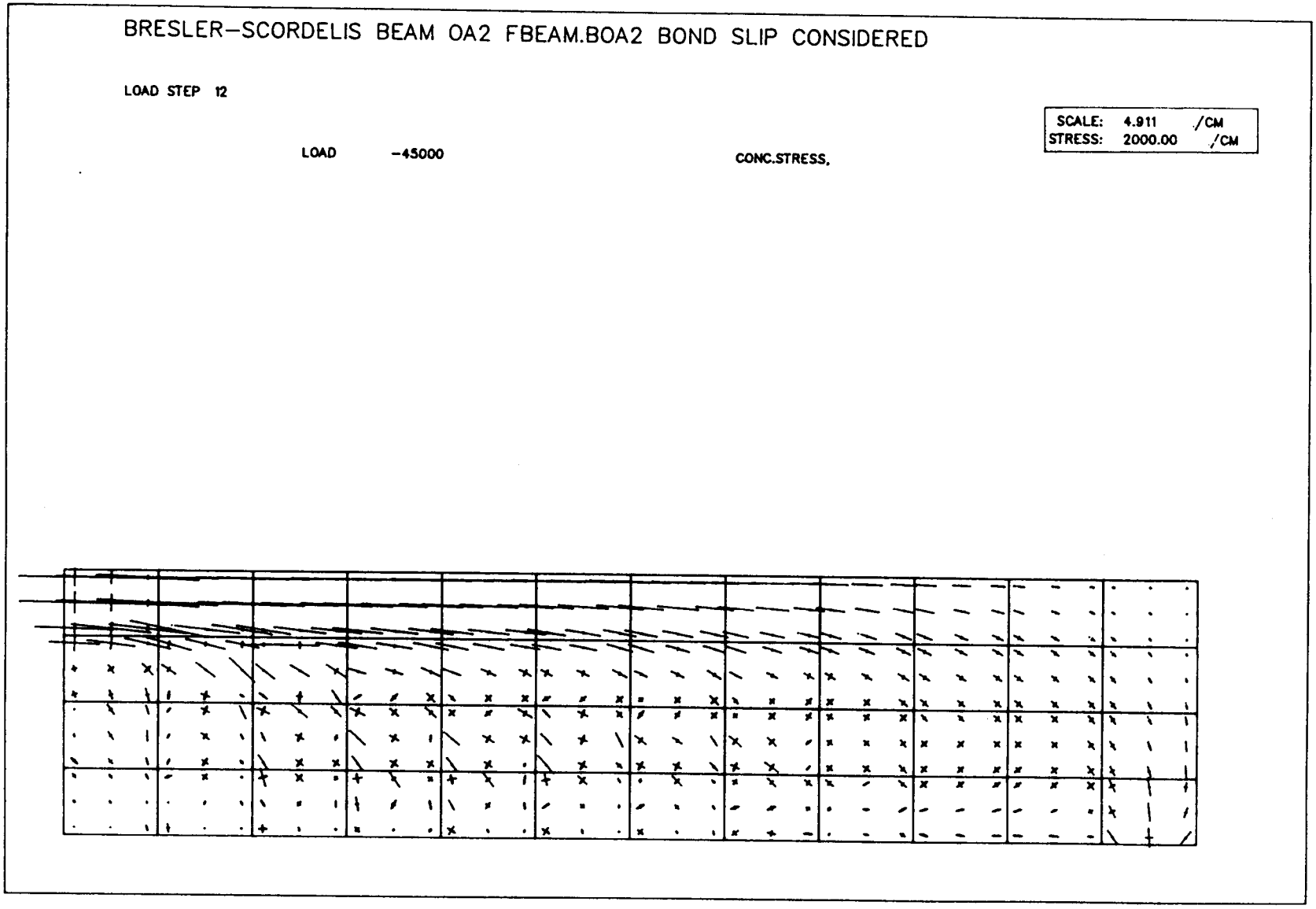

FIG. 5.44. Bresler/Scordelis Beam OA2 - Principal Stress Plot

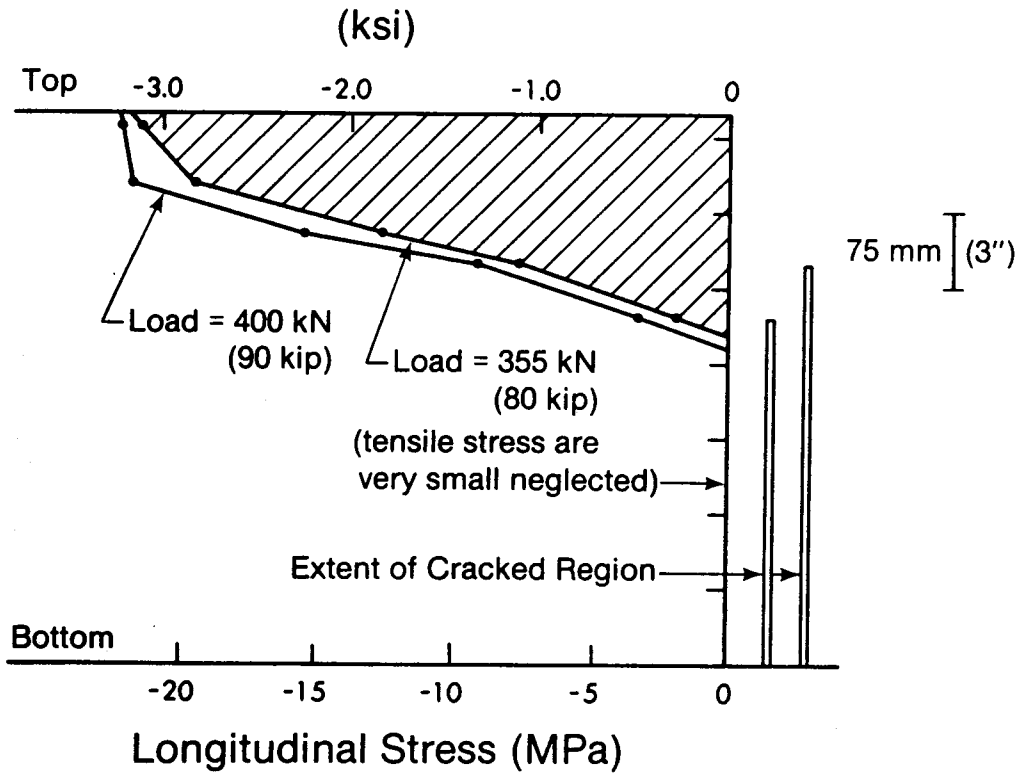

FIG. 5.45. Bresler/Scordelis Beam 0A2 - Distribution of Longitudinal Stress Across Depth

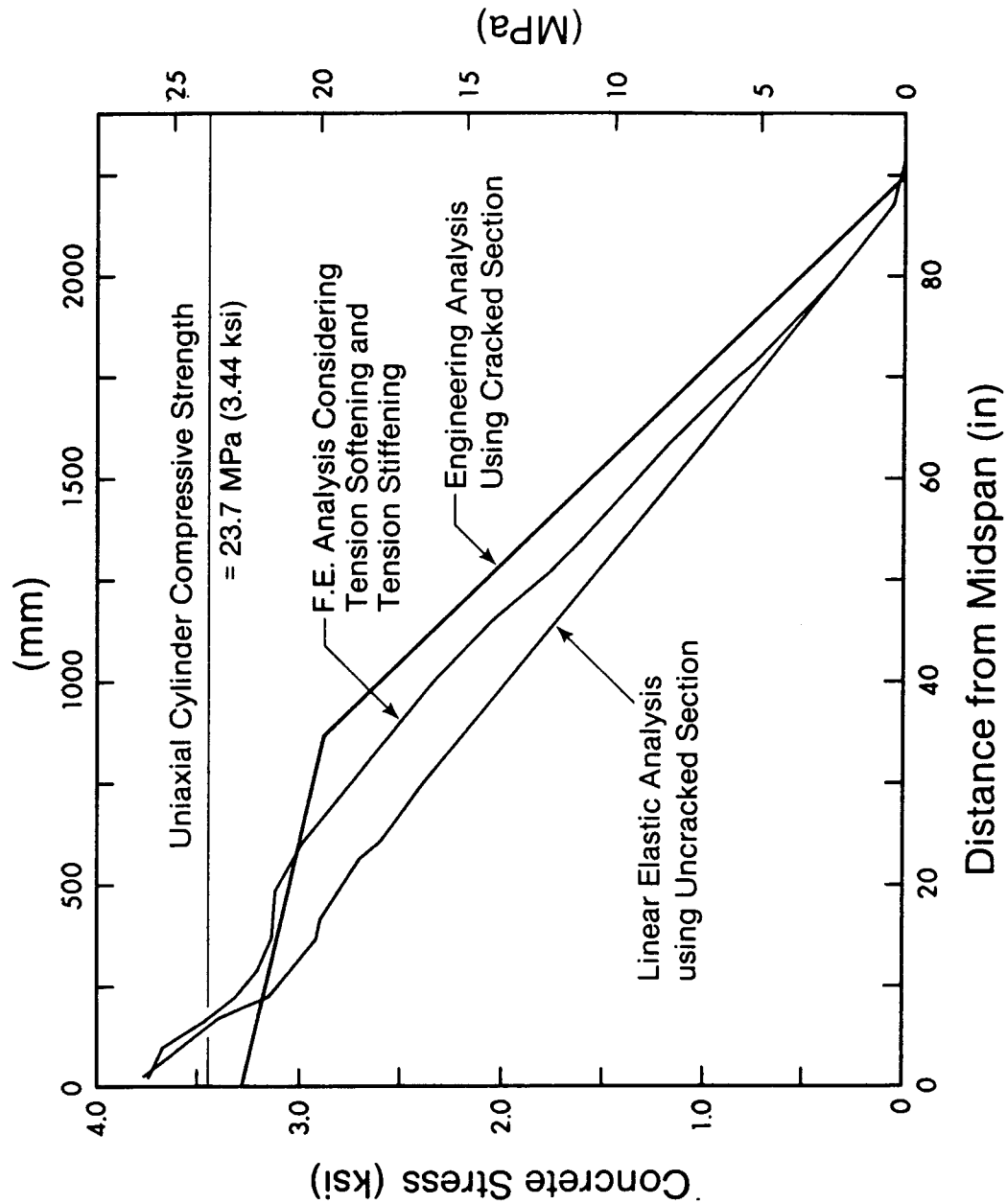

FIG. 5.46. Bresler/Scordelis Beam 0A2 - Distribution of Concrete Stresses

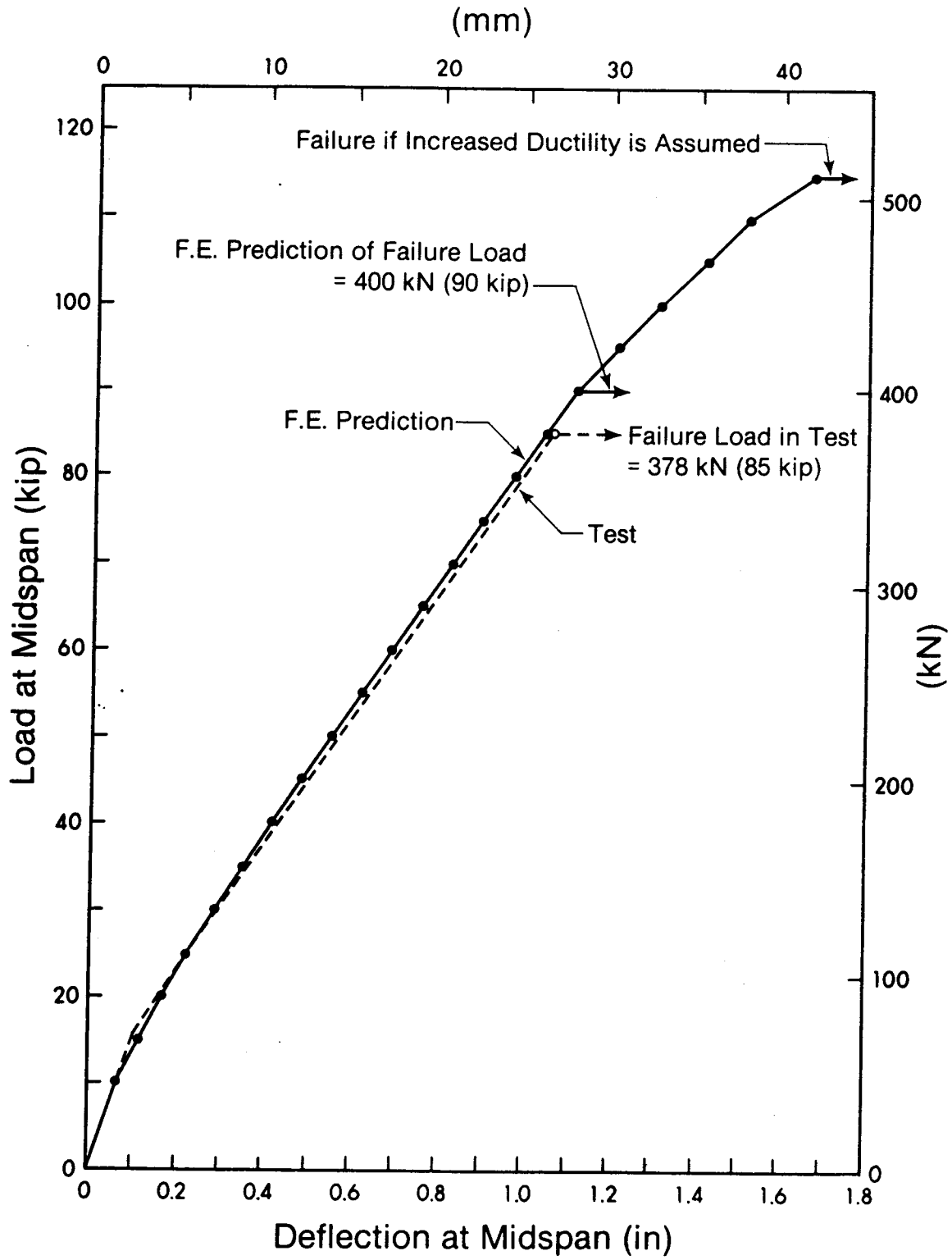

FIG. 5.47. Bresler/Scordelis Beam 0A3 - Load-Deflection Relationship

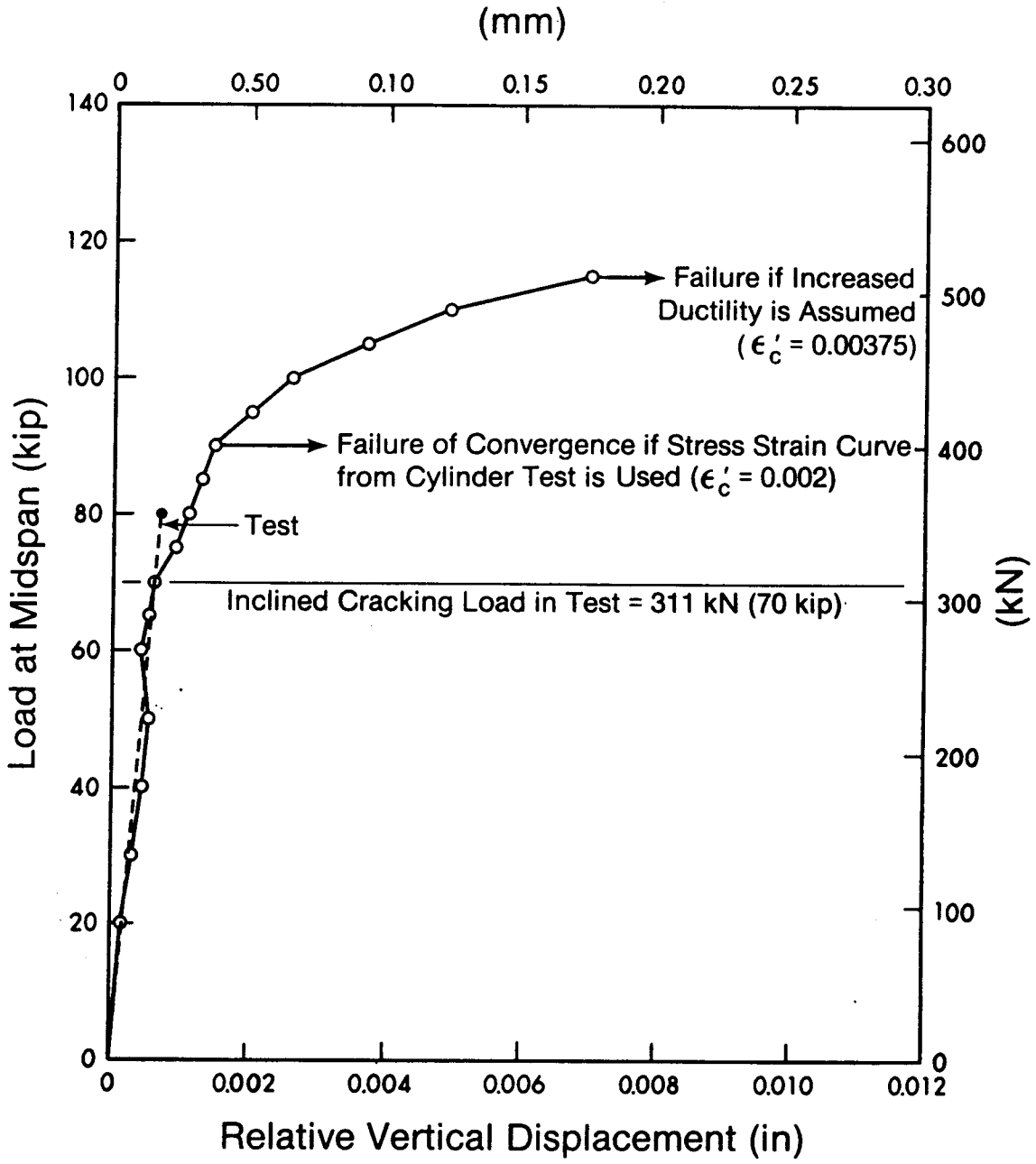

FIG. 5.48. Bresler/Scordelis Beam 0A3 - Relative Vertical Displacement

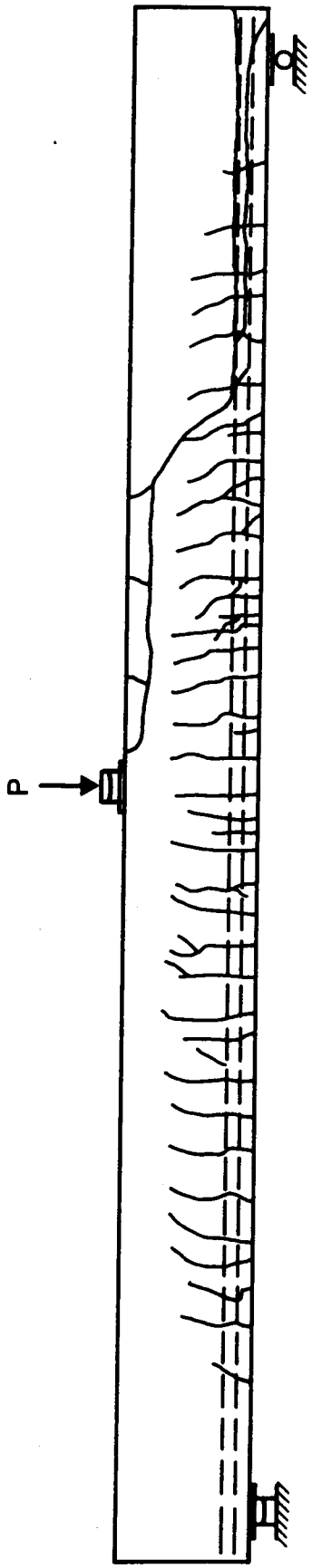

FIG. 5.49. Bresler/Scordelis Beam 0A3 - Crack Patterns
(a) Crack Pattern Observed in Test

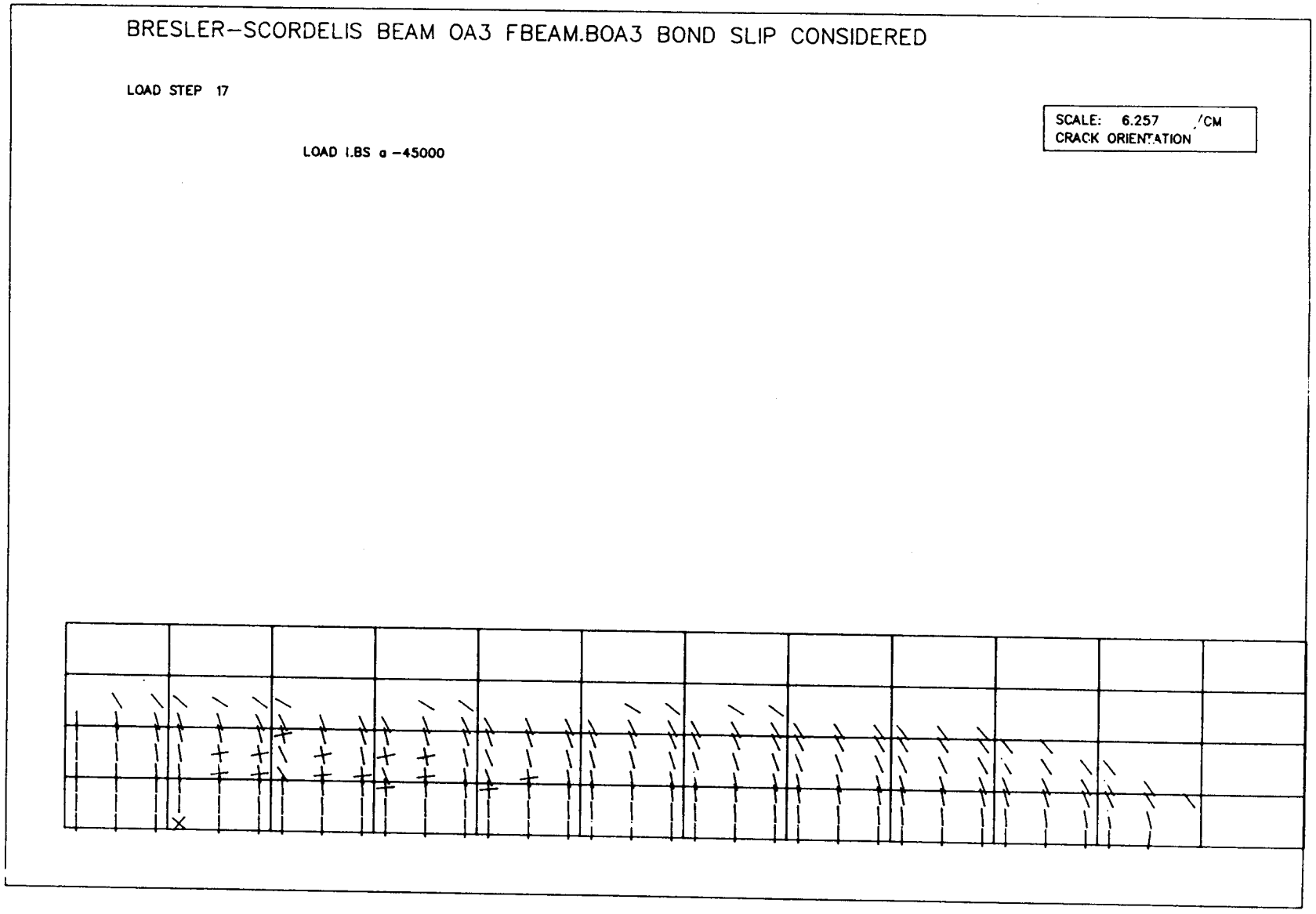

FIG. 5.49. (b) Analytical Crack Pattern

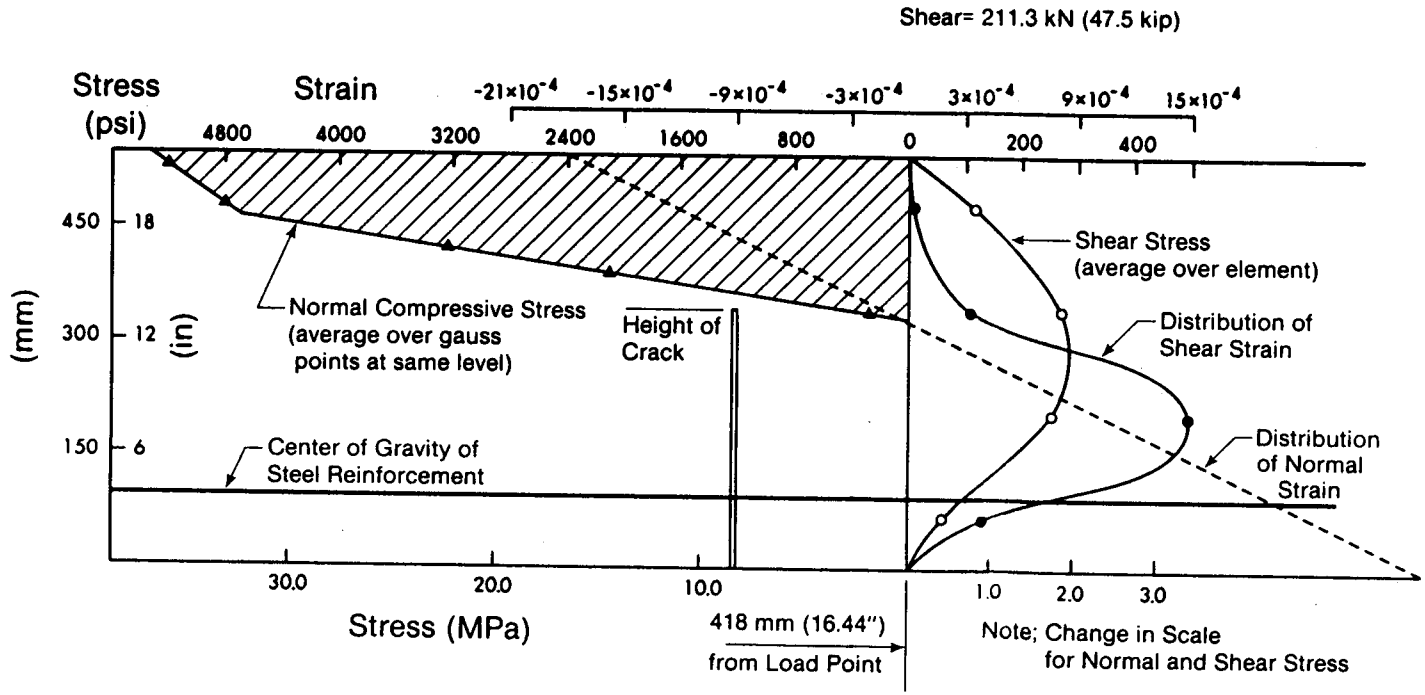

FIG. 5.50. Bresler/Scordelis Beam 0A3 - Stress and Strain Distributions Across Depth

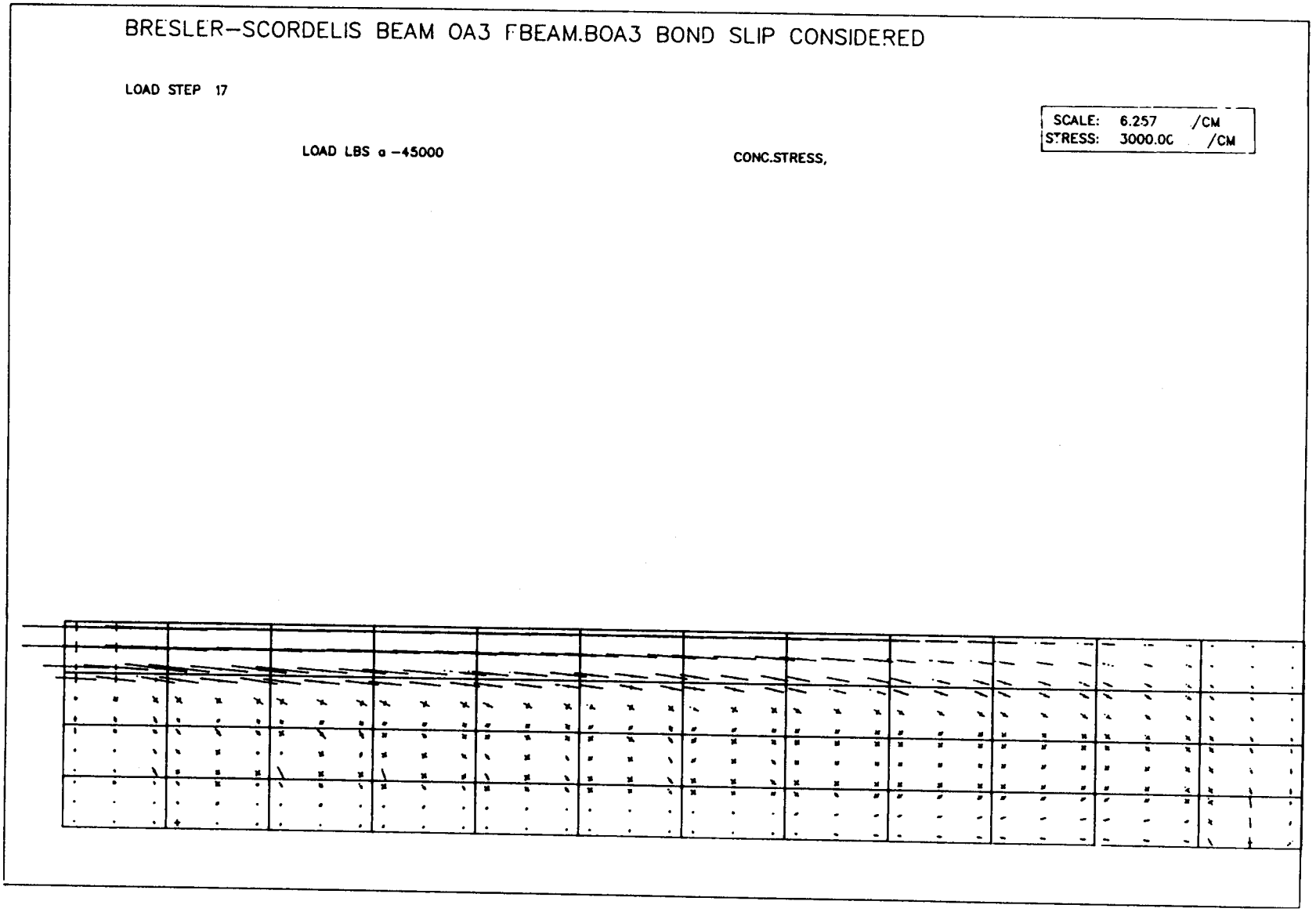

FIG. 5.51. Bresler/Scordelis Beam 0A3 - Principal Stress Plot

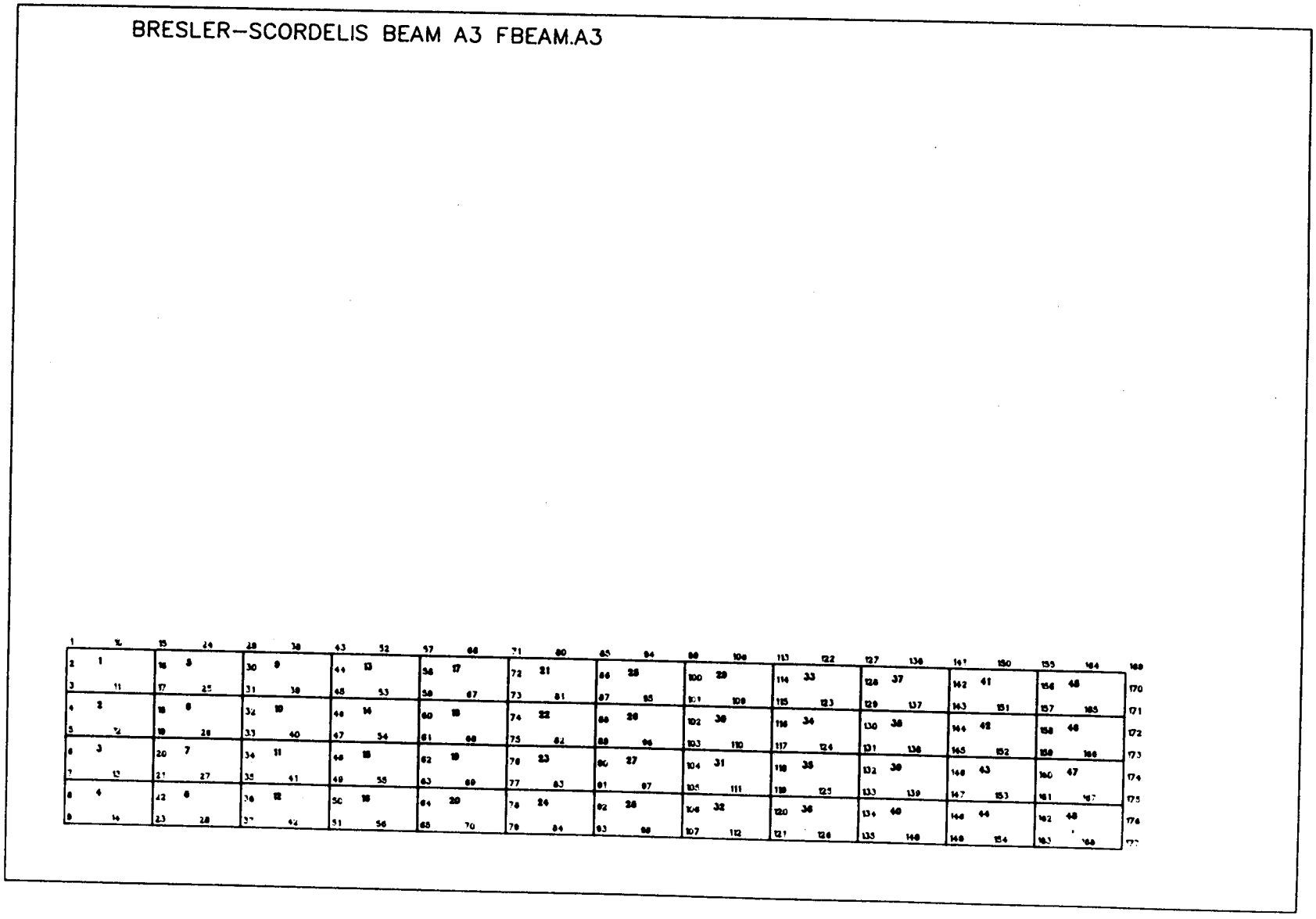

FIG. 5.52. Finite Element Mesh Layout - Beams with Web Reinforcement
(a) Bresler/Scordelis Beam A3

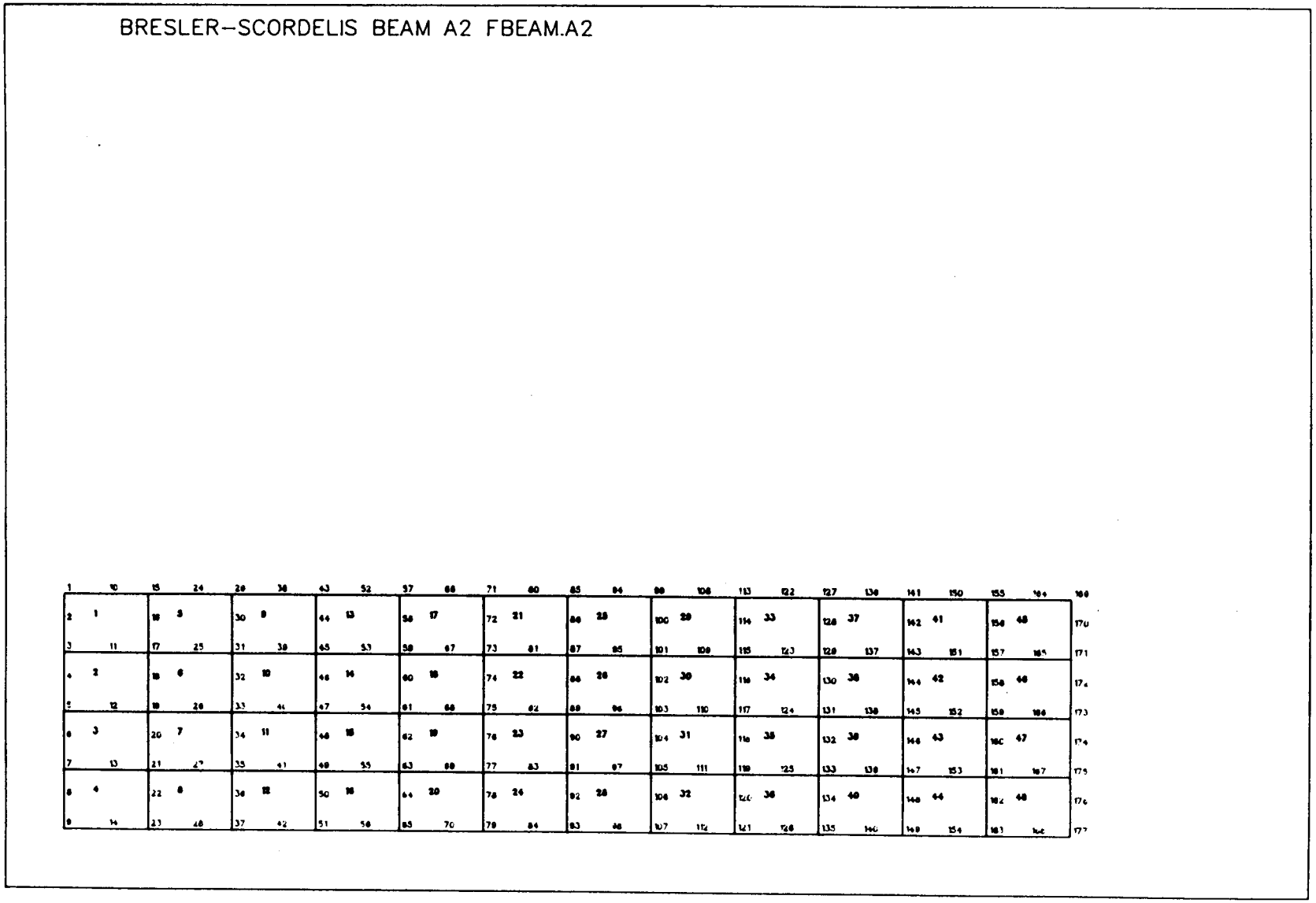

FIG. 5.52. (b) Finite Element Mesh Layout - Bresler/Scordelis Beam A2

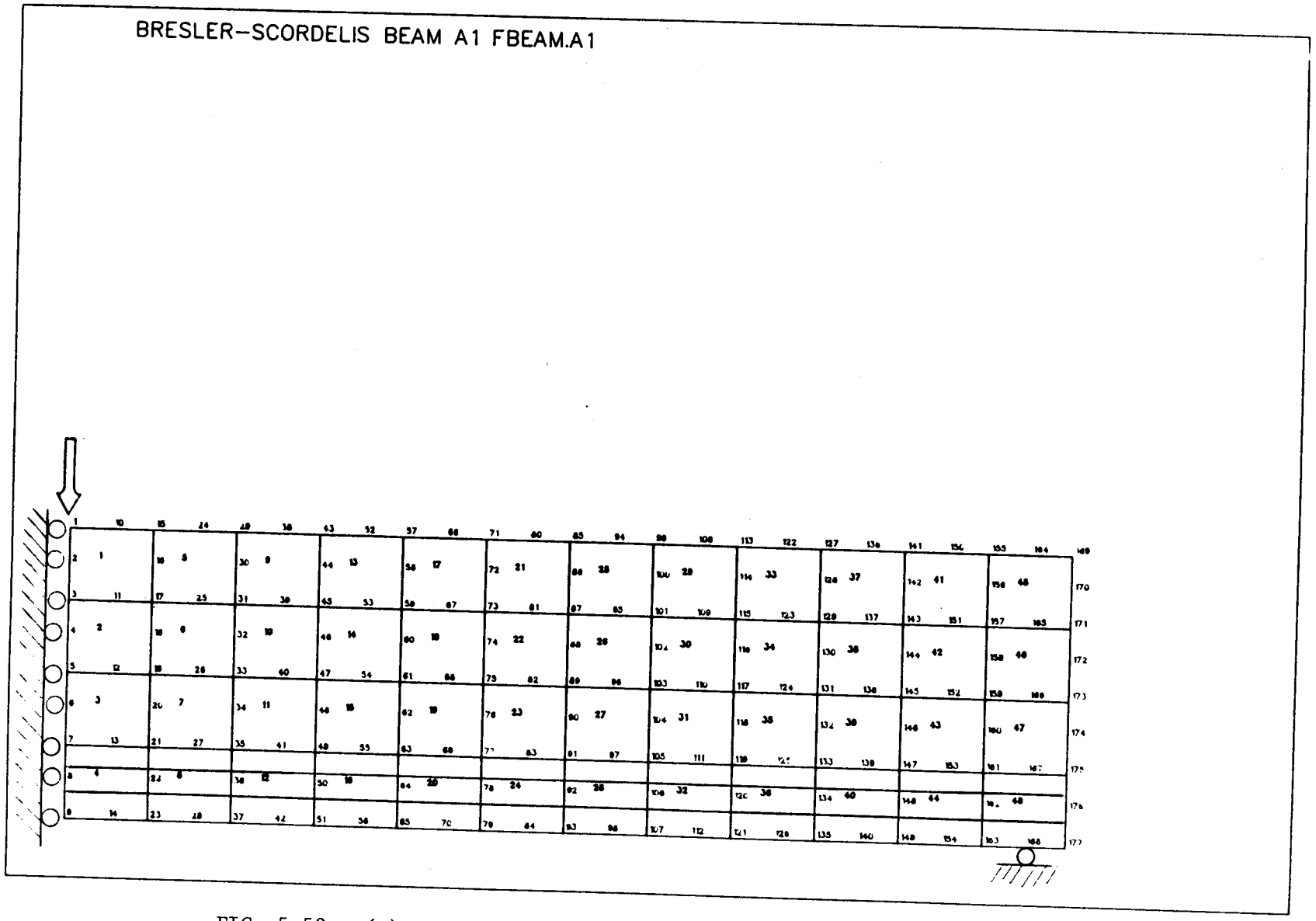

FIG. 5.52. (c) Finite Element Mesh Layout - Bresler/Scordelis Beam A1

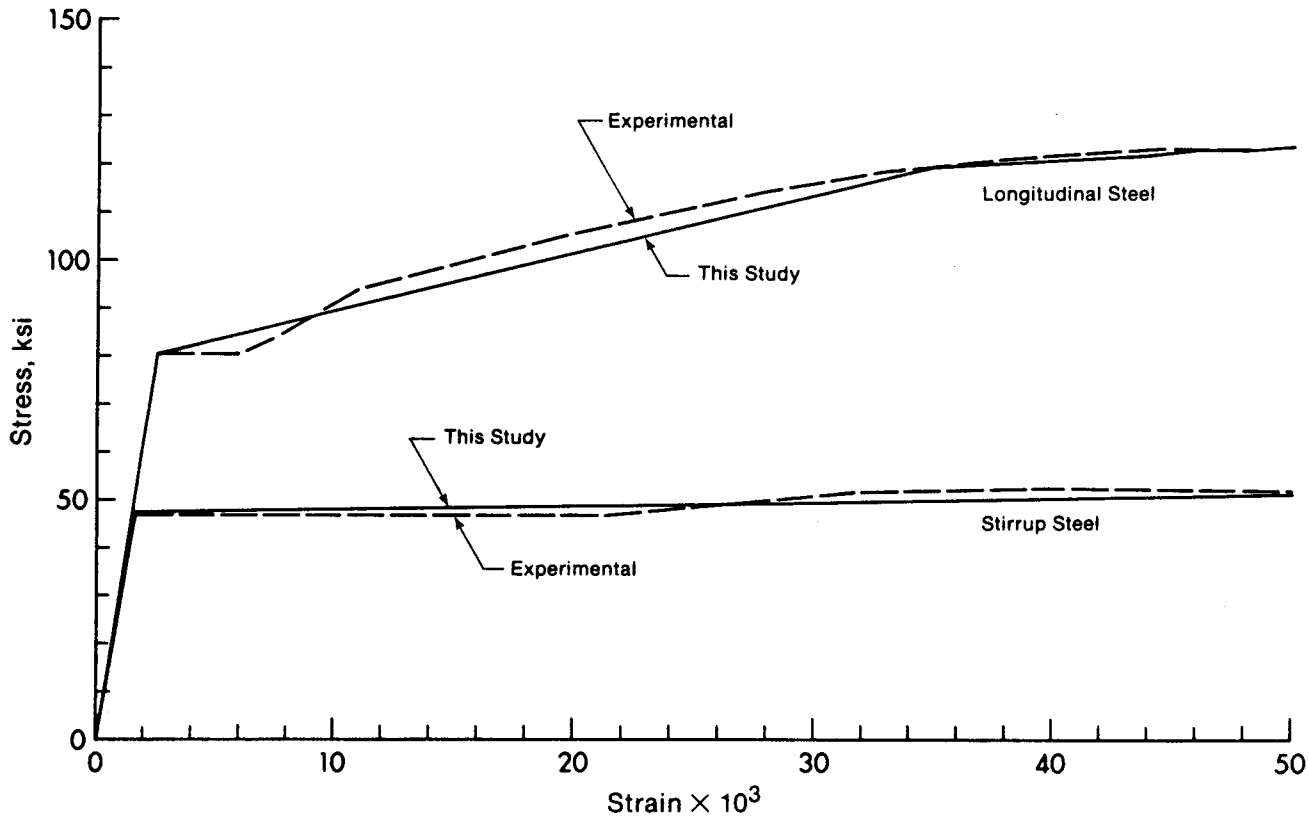

FIG. 5.53. Bresler/Scordelis Beams - Stress-Strain Curves for Steel Reinforcement

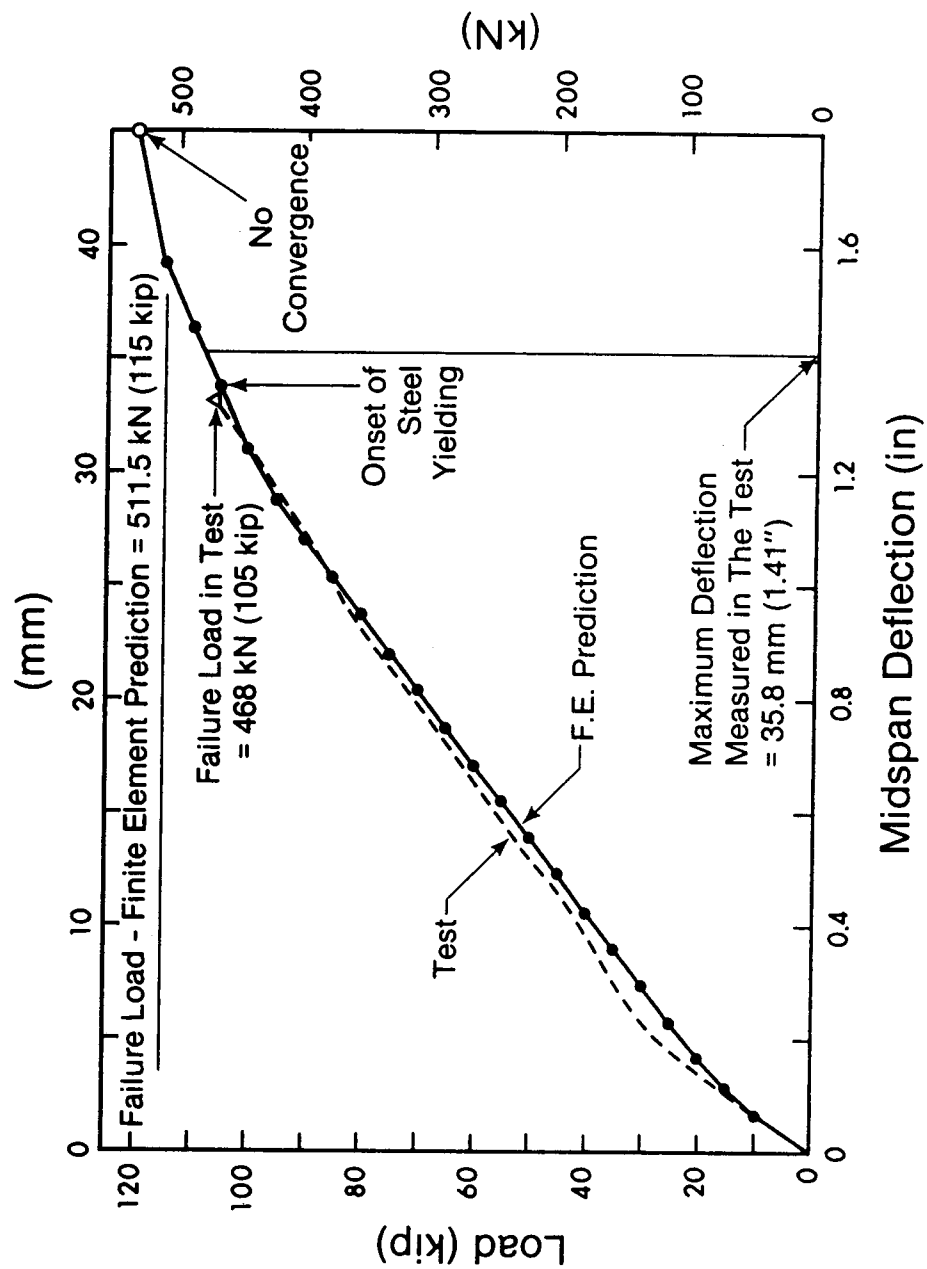

FIG. 5.54. Bresler/Scordelis Beam A3 - Load-Deflection Relationship

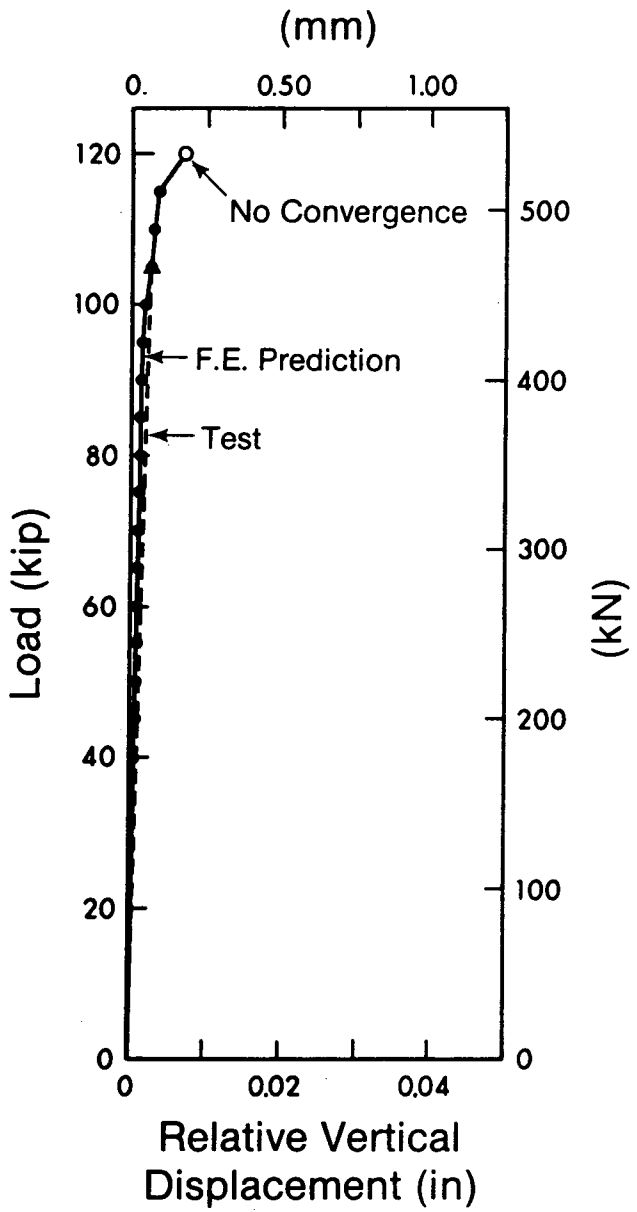

FIG. 5.55. Bresler/Scordelis Beam A3 - Relative Vertical Displacement

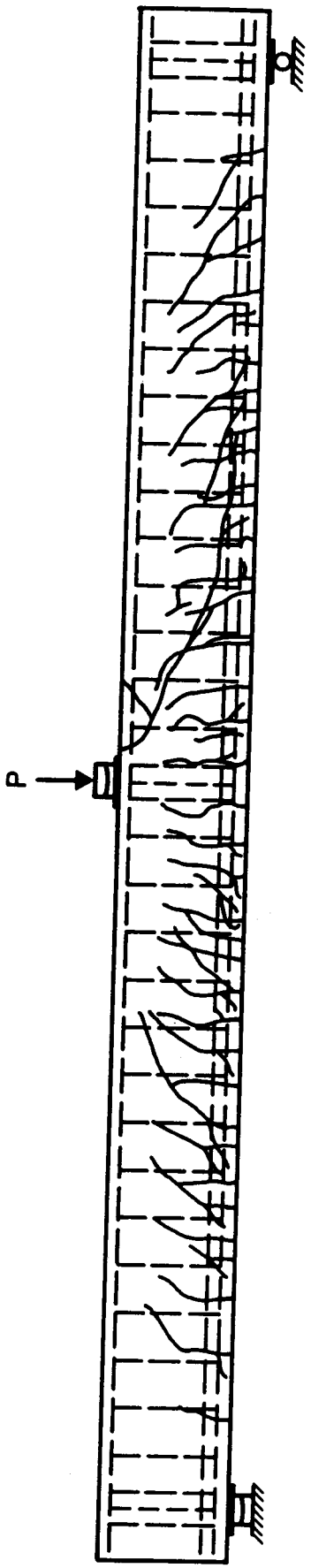

FIG. 5.56. Bresler/Scordelis Beam A3 - Crack Pattern Observed in Test

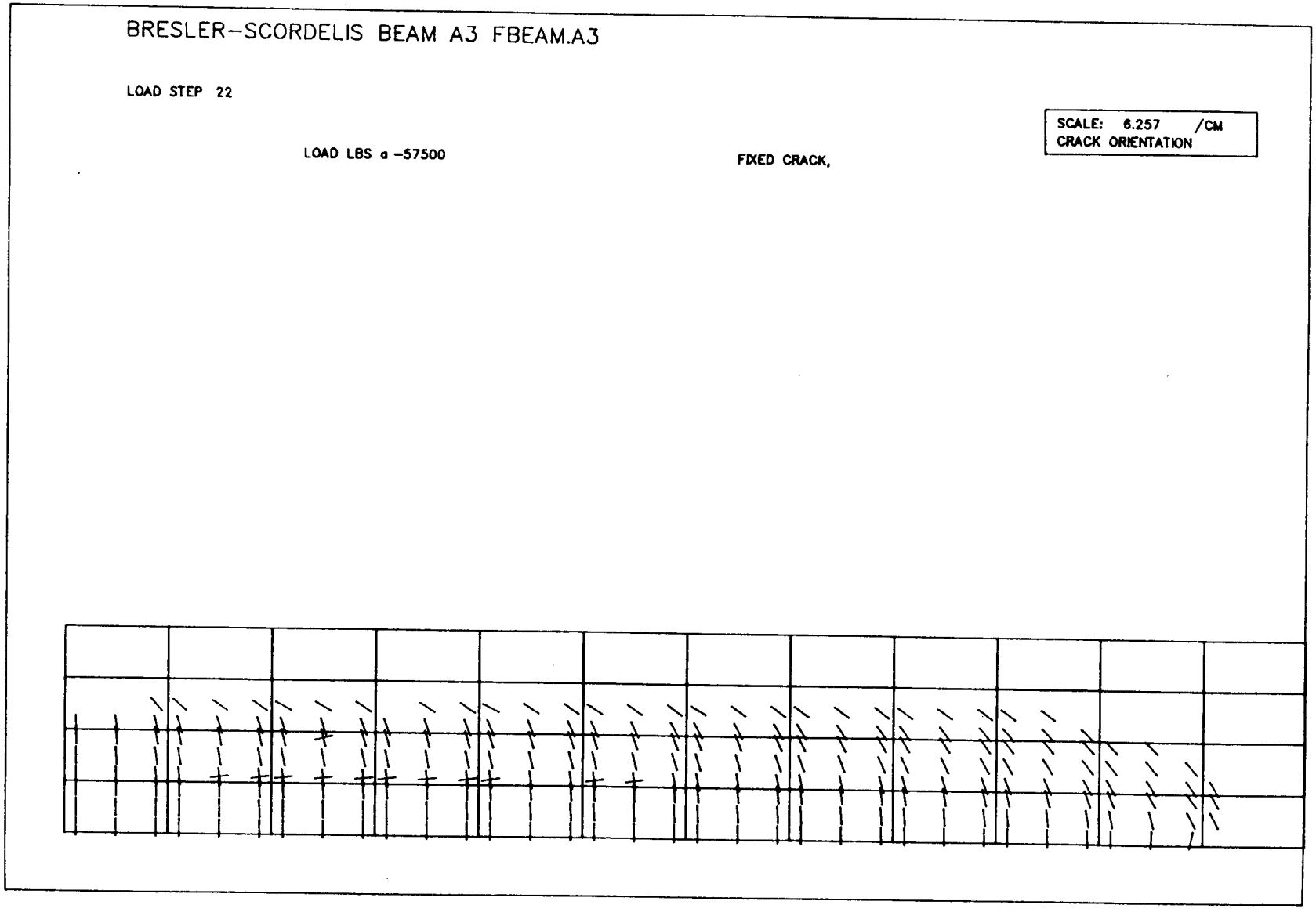

FIG. 5.57. Bresler/Scordelis Beam A3 - Analytical Crack Patterns
(a) Shear = 57.5 kip (255.8 kN)

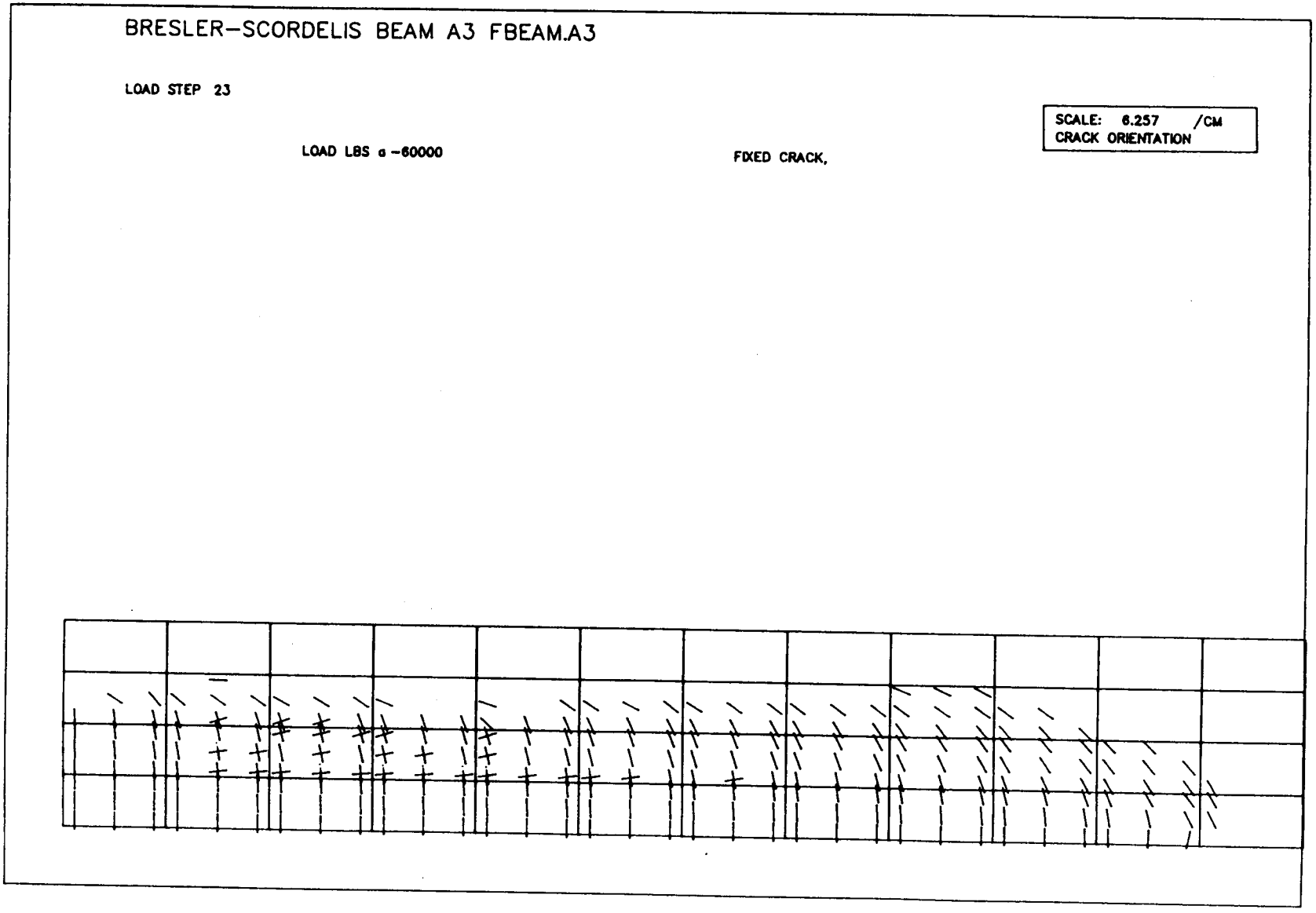

FIG. 5.57. (b) Shear = 60 kip (266.9 kN)

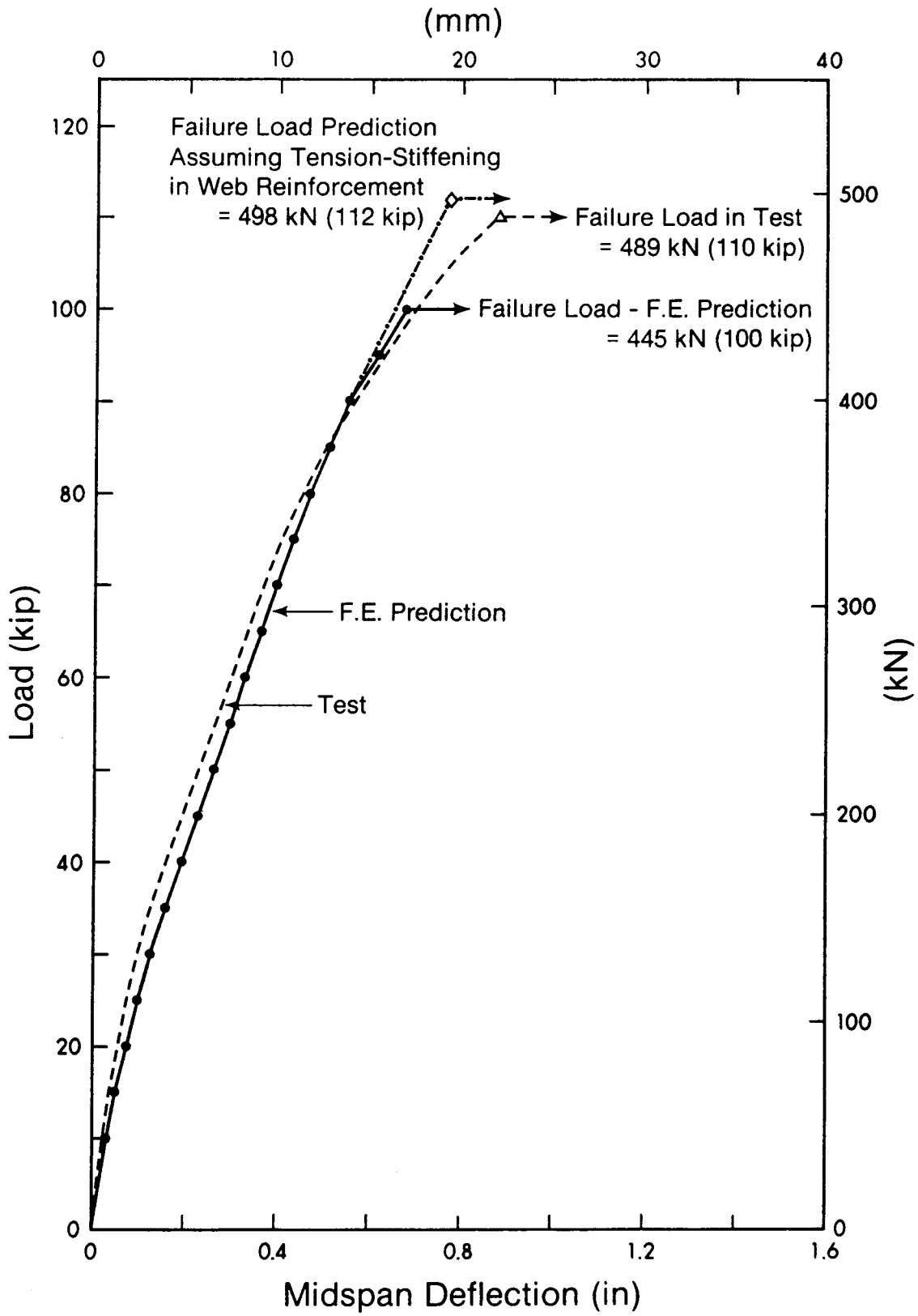

FIG. 5.58. Bresler/Scordelis Beam A2 - Load-Deflection Relationship

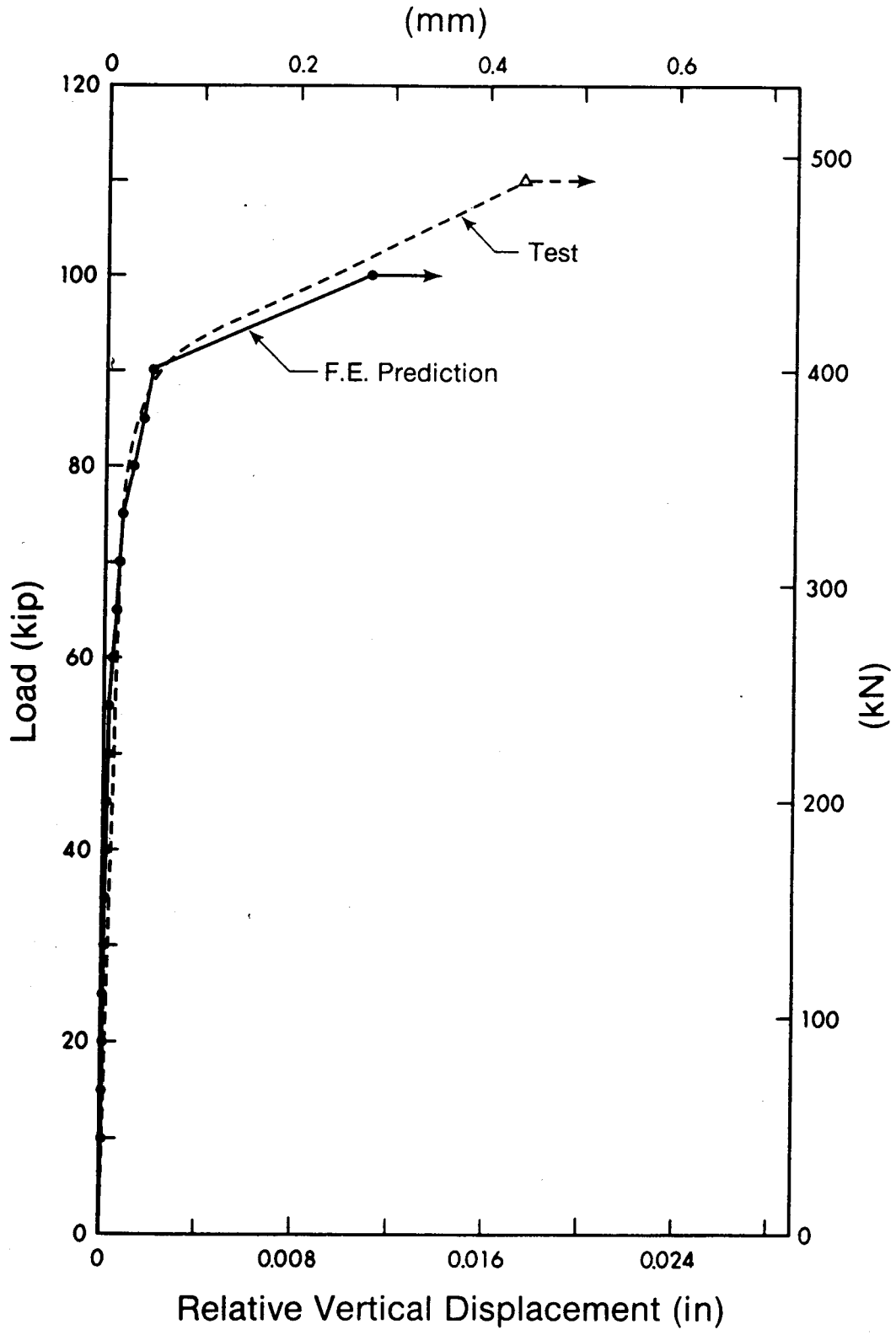

FIG. 5.59. Bresler/Scordelis Beam A2 - Relative Vertical Displacement

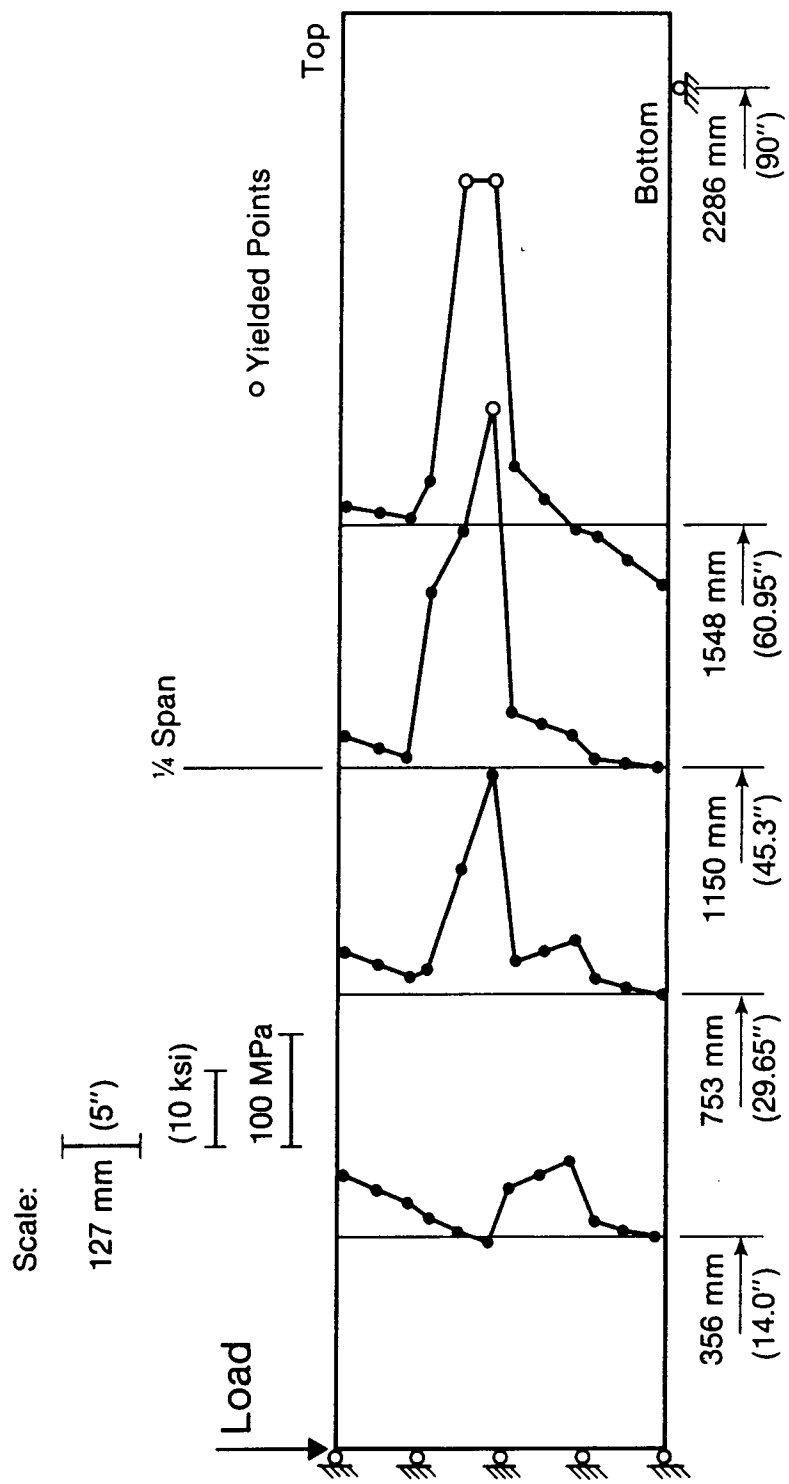

FIG. 5.60. Bresler/Scordelis Beam A2 - Stirrup Stresses at Failure

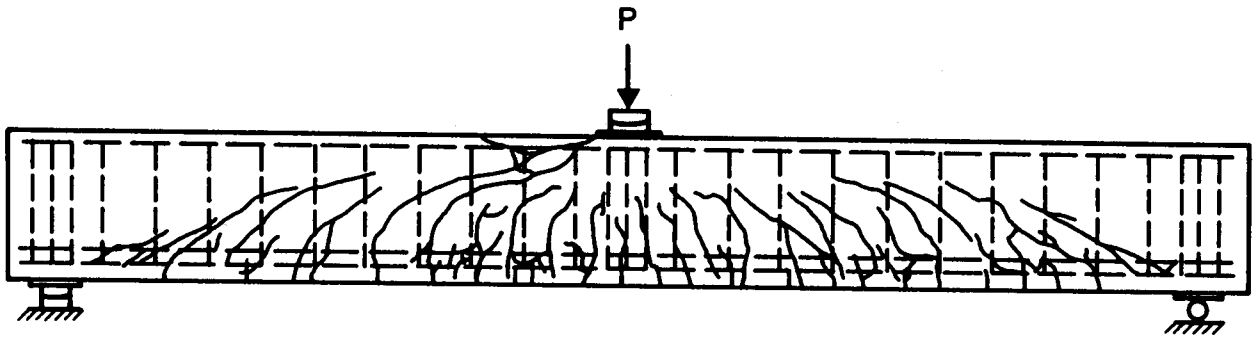

FIG. 5.61. Bresler/Scordelis Beam A2 - Crack Pattern Observed in Test

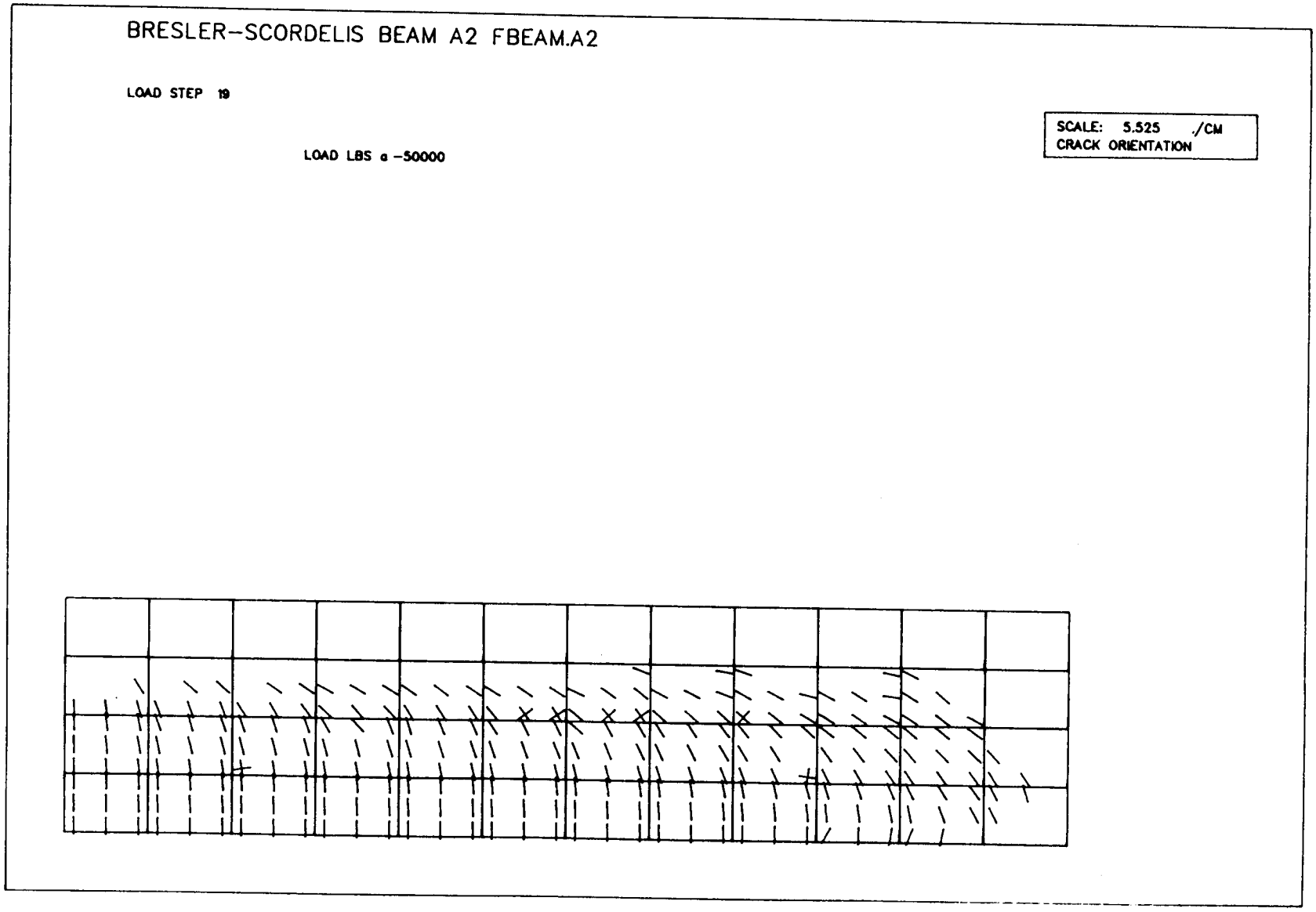

FIG. 5.62. Bresler/Scordelis Beam A2 - Analytical Crack Pattern

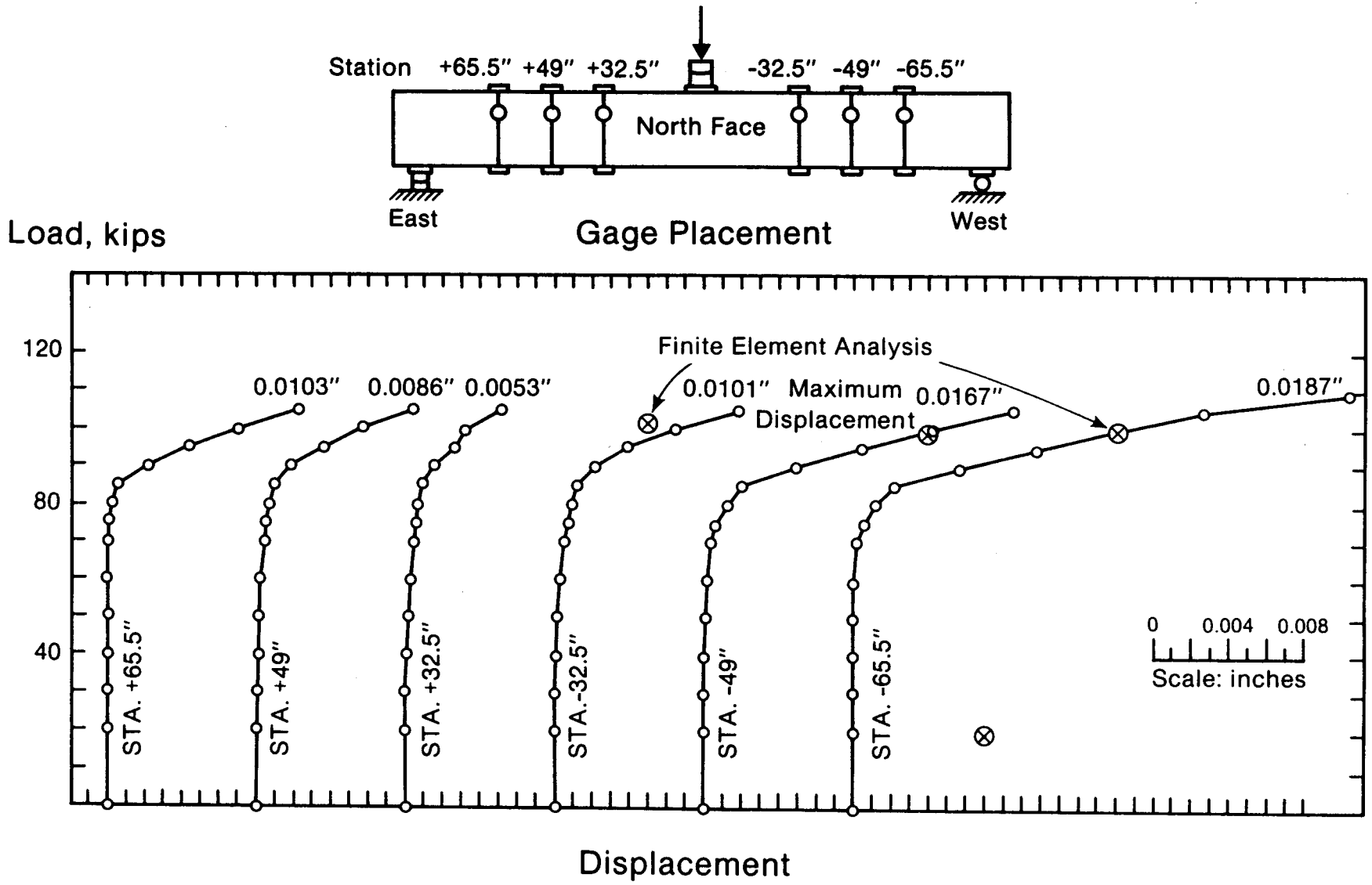

FIG. 5.63. Bresler/Scordelis Beam A2 - Relative Vertical Displacement (Thickening)
(1 in. = 25.4 mm; 1 kip = 4.448 kN)

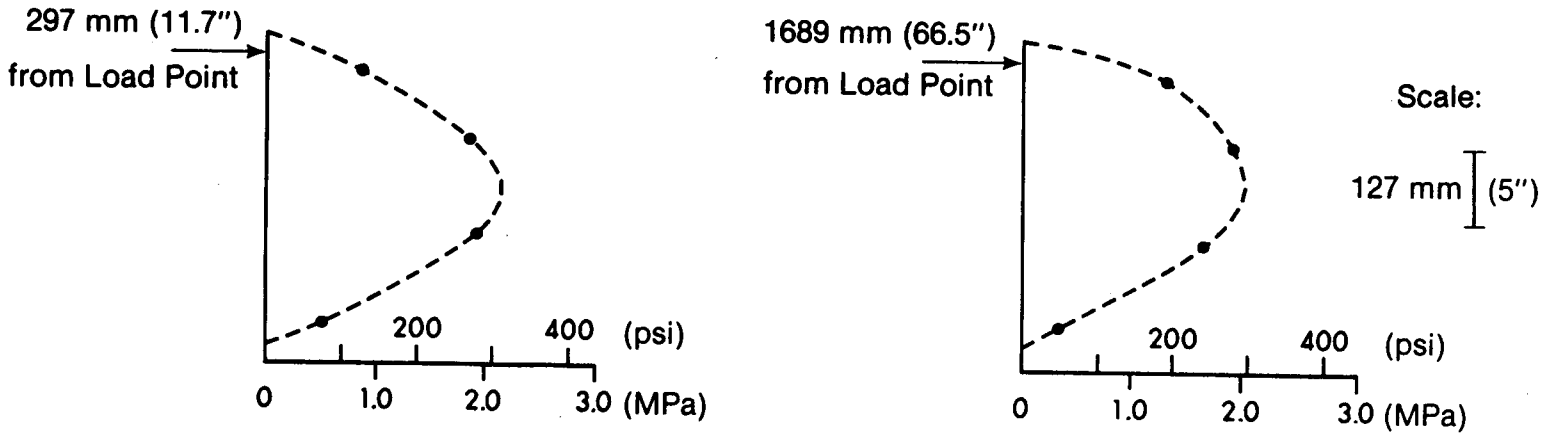

FIG. 5.64. Bresler/Scordelis Beam A2 - Distribution of Shear Stresses

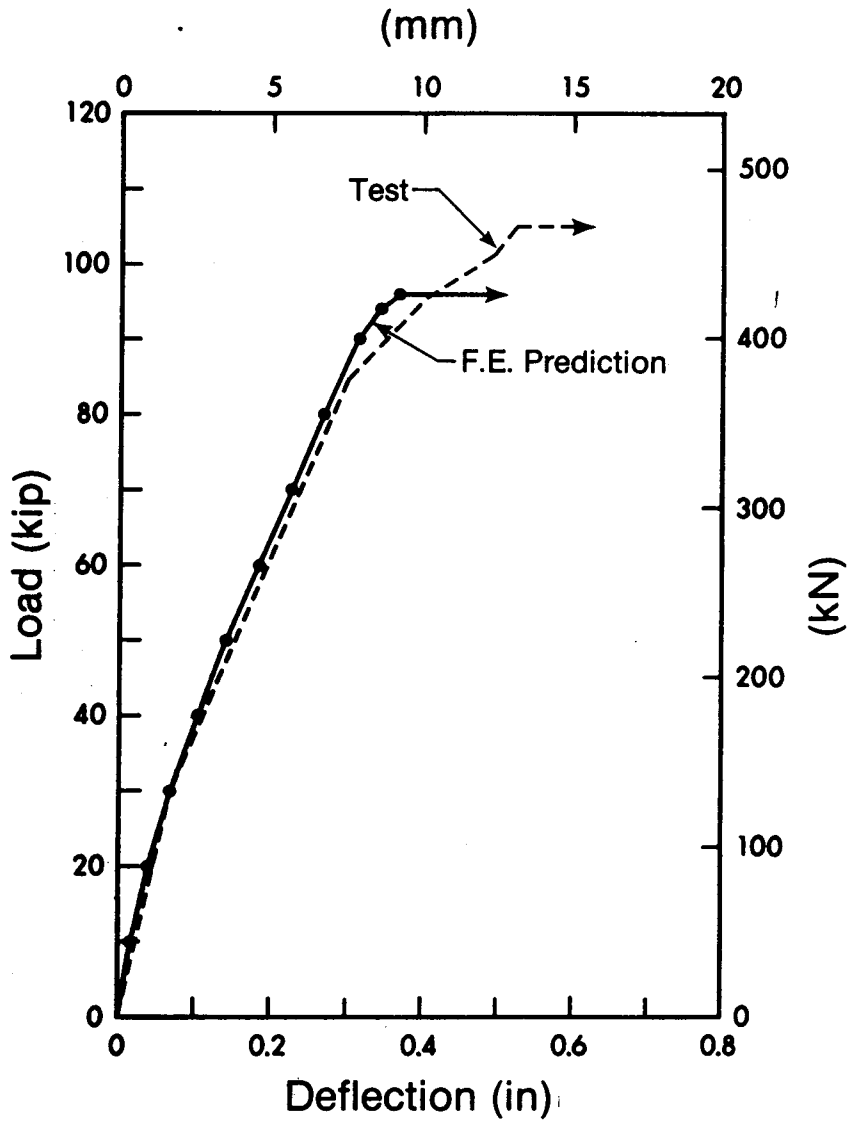

FIG. 5.65. Bresler/Scordelis Beam A1 - Load-Deflection Relationship

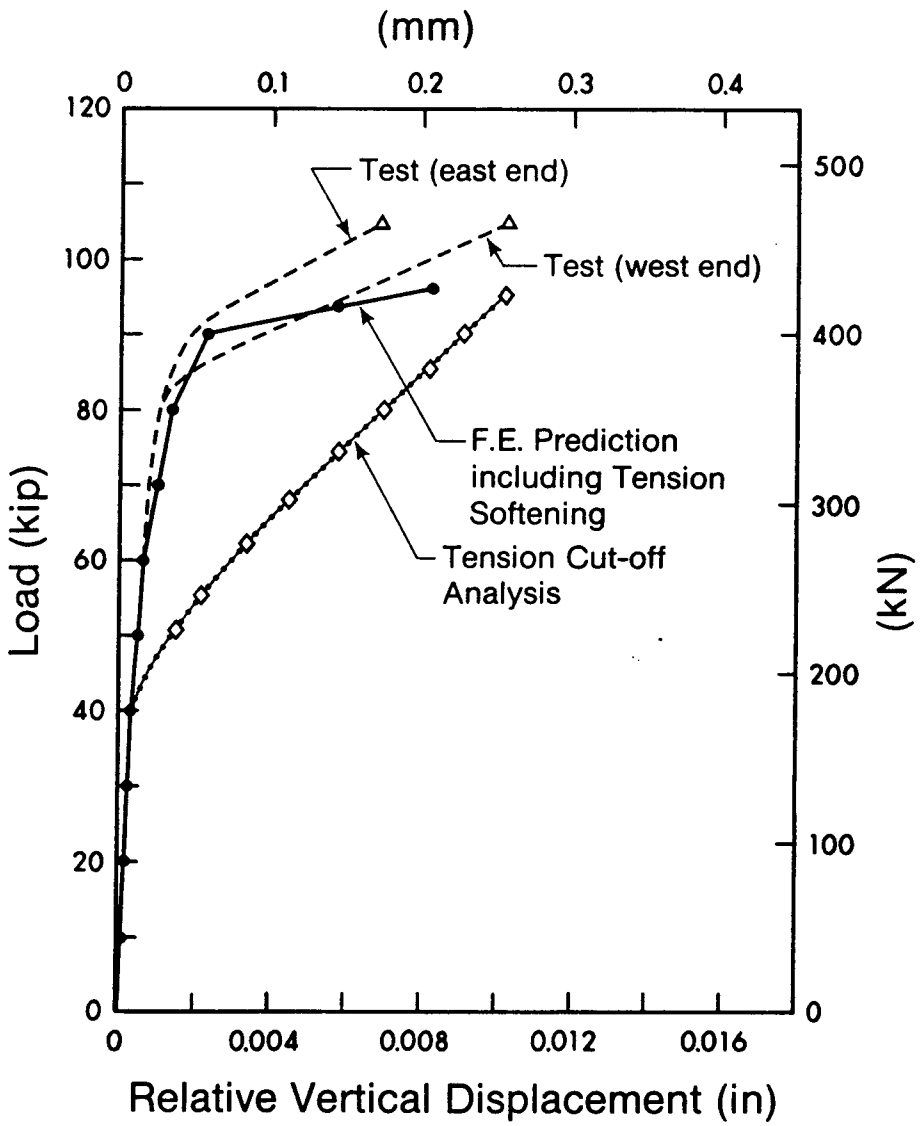

FIG. 5.66. Bresler/Scordelis Beam A1 - Relative Vertical Displacement

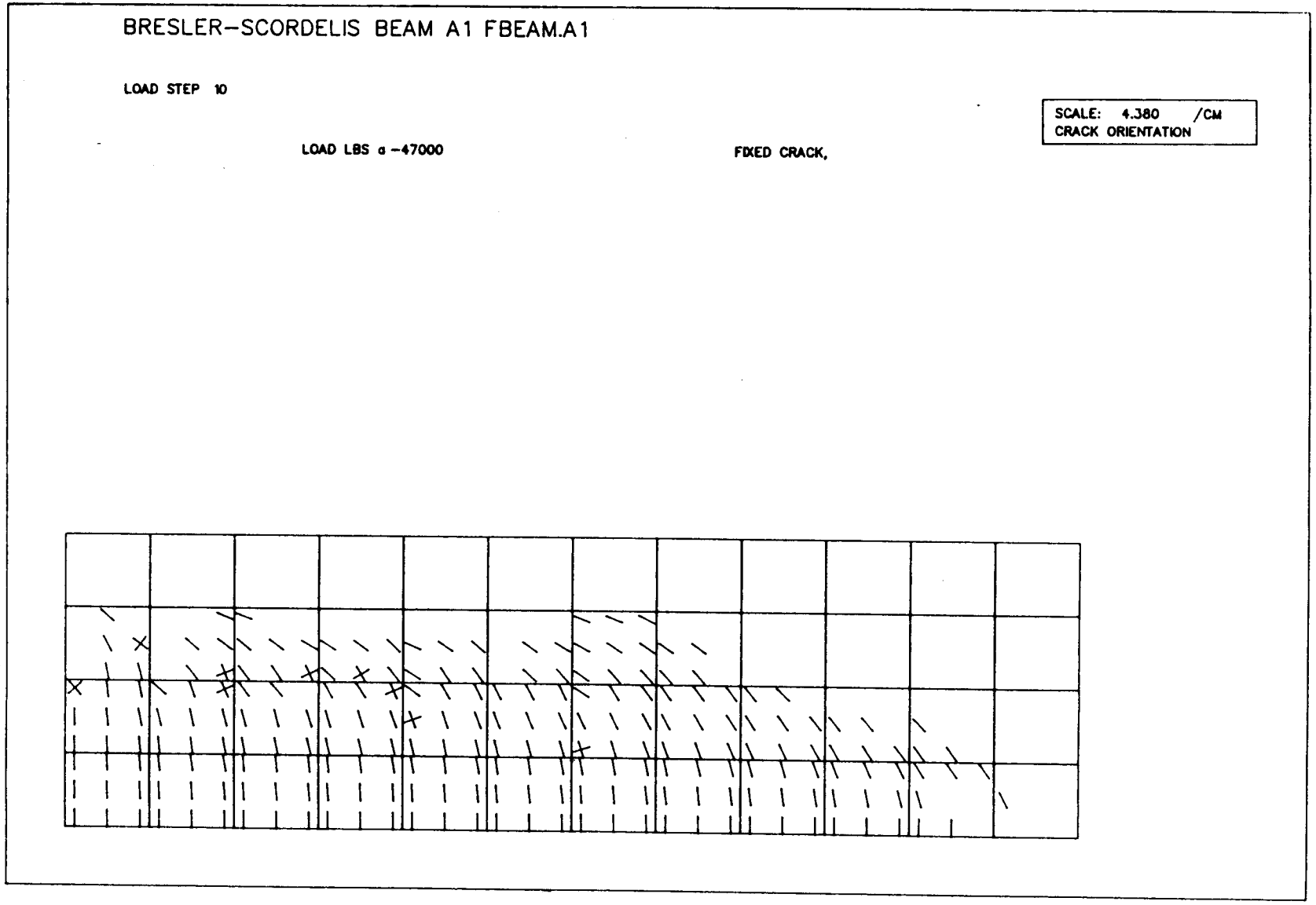

FIG. 5.67. Bresler/Scordelis Beam A1 - Crack Patterns
(a) Analytical Crack Pattern - Load Step Prior to Failure

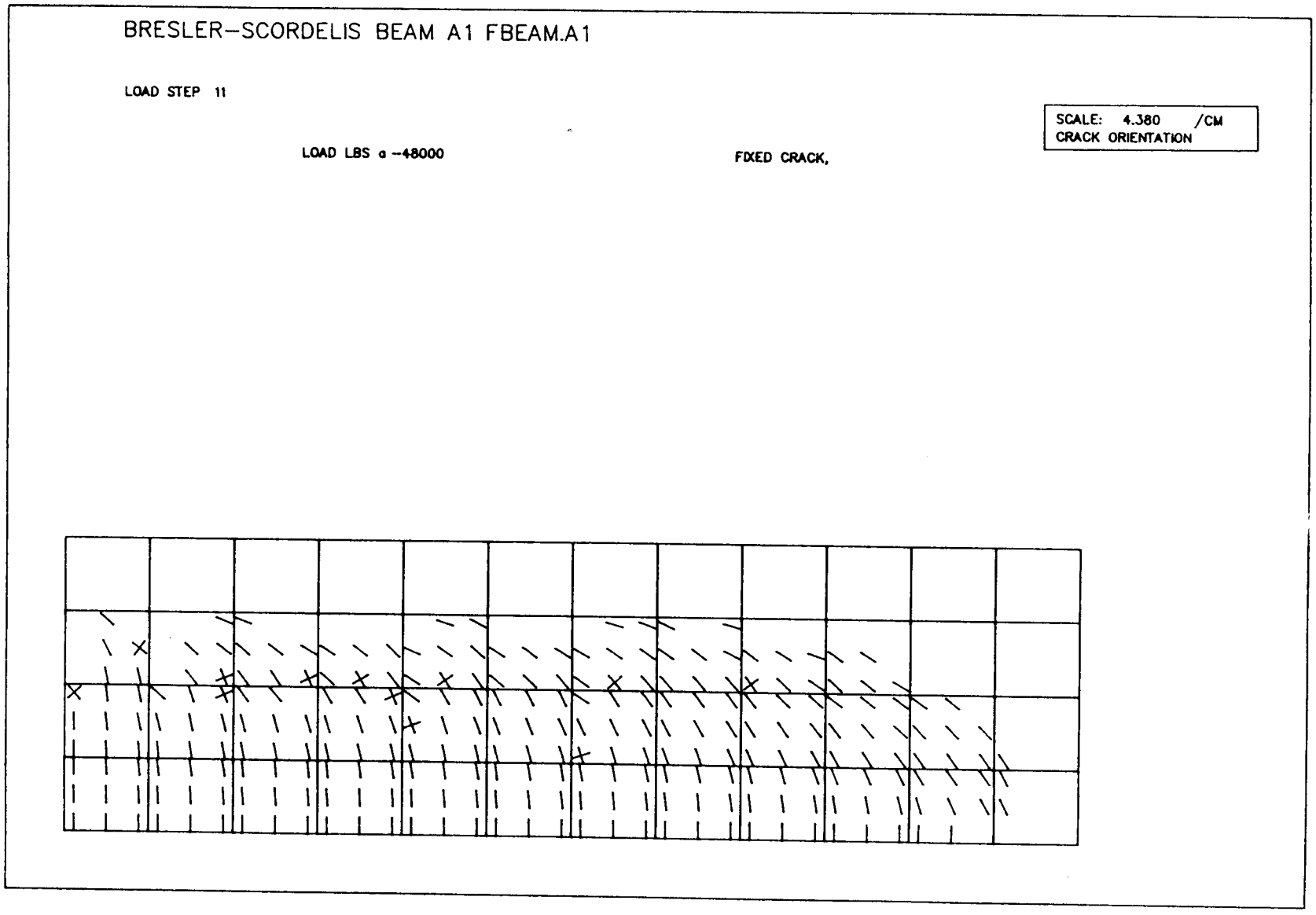

FIG. 5.67. (b) Analytical Crack Pattern - Load Step Corresponding to Failure

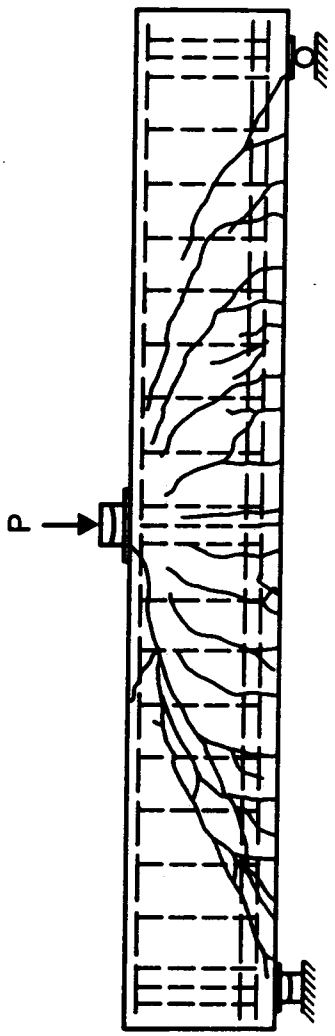

FIG. 5.67. (c) Bresler/Scordelis Beam A1 - Crack Pattern Observed in Test

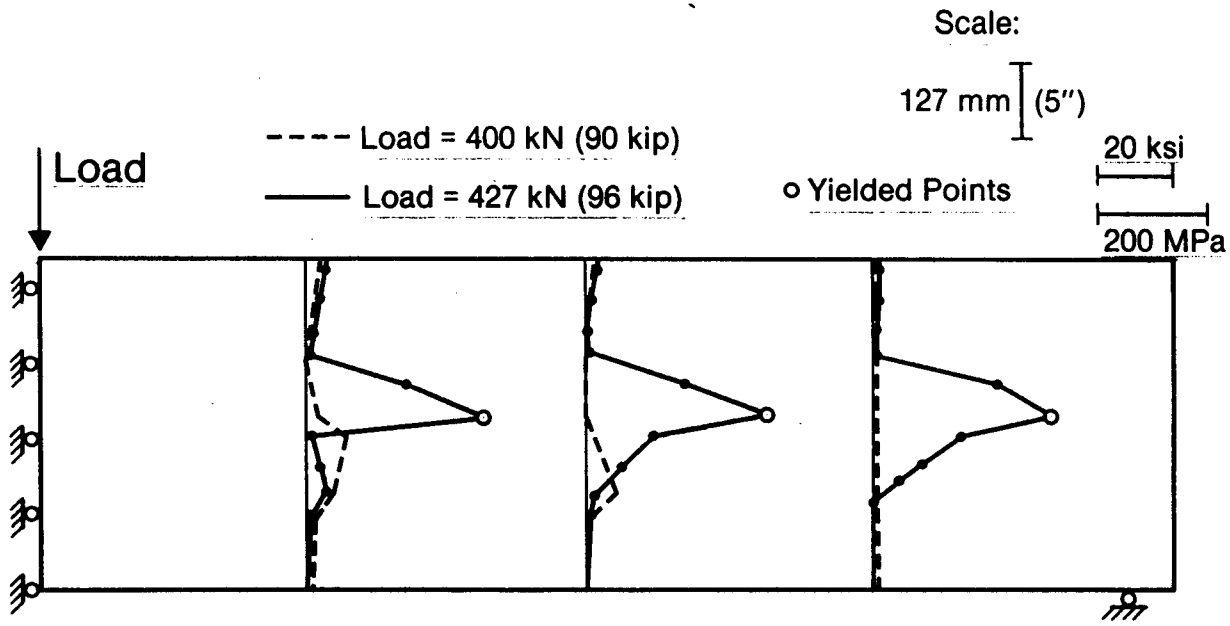

FIG. 5.68. Bresler/Scordelis Beam A1 - Stirrup Stresses at Two Successive Load Steps Near Failure

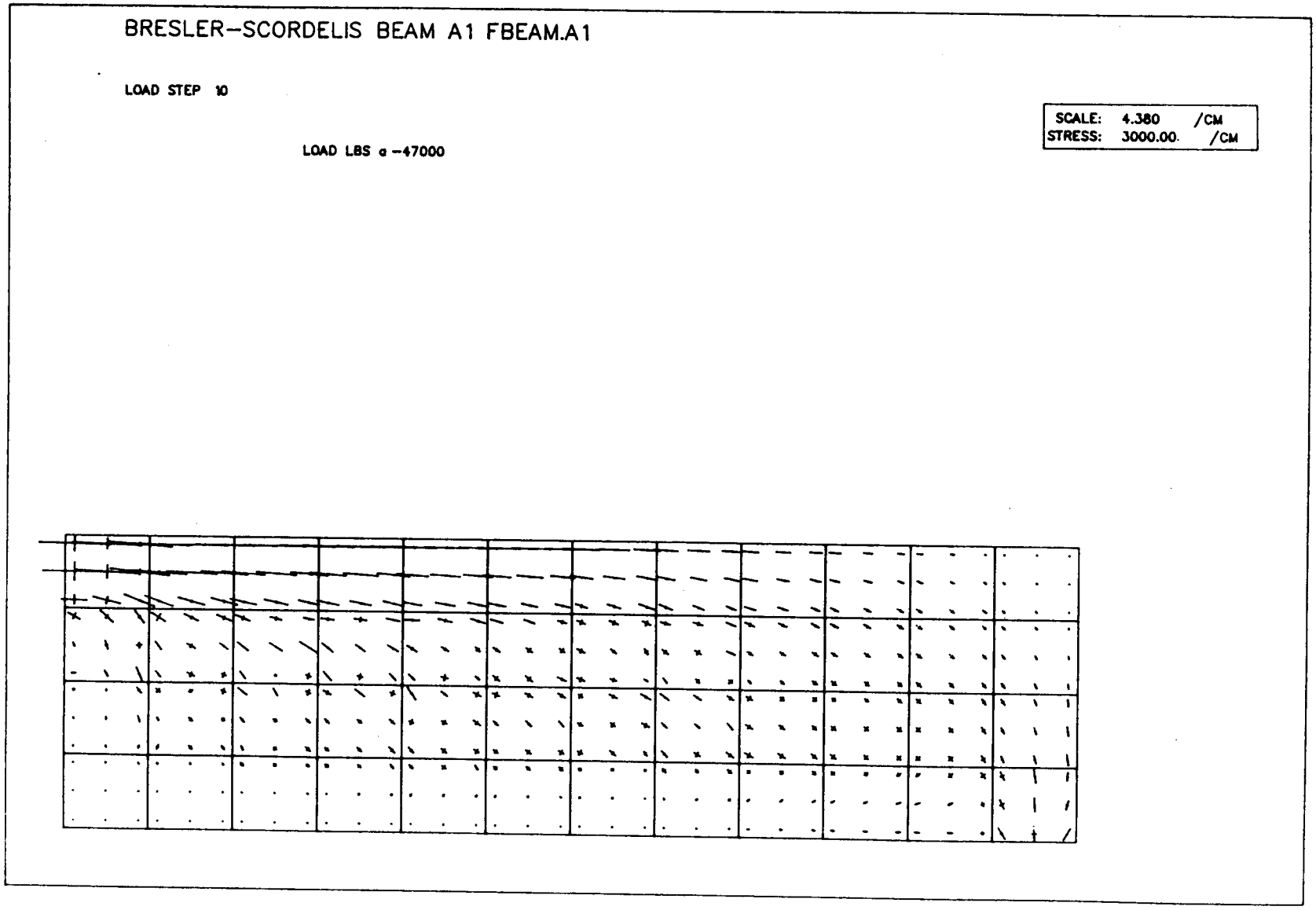

FIG. 5.69. Bresler/Scordelis Beam A1 - Principal Stress Plots
(a) Load Step Prior to Failure

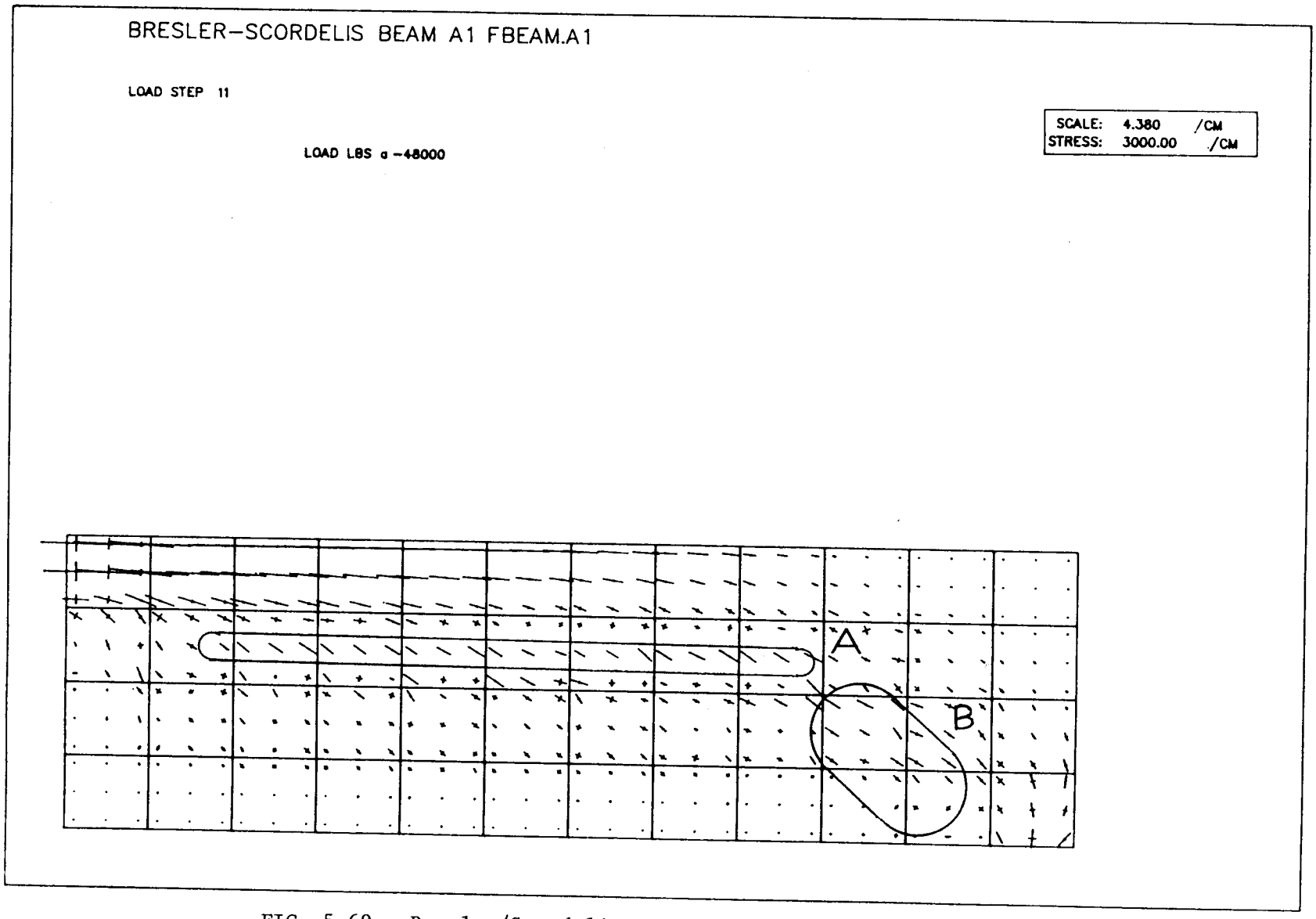

FIG. 5.69. Bresler/Scordelis Beam A1 - Principal Stress Plots
(b) Load Step Corresponding to Failure

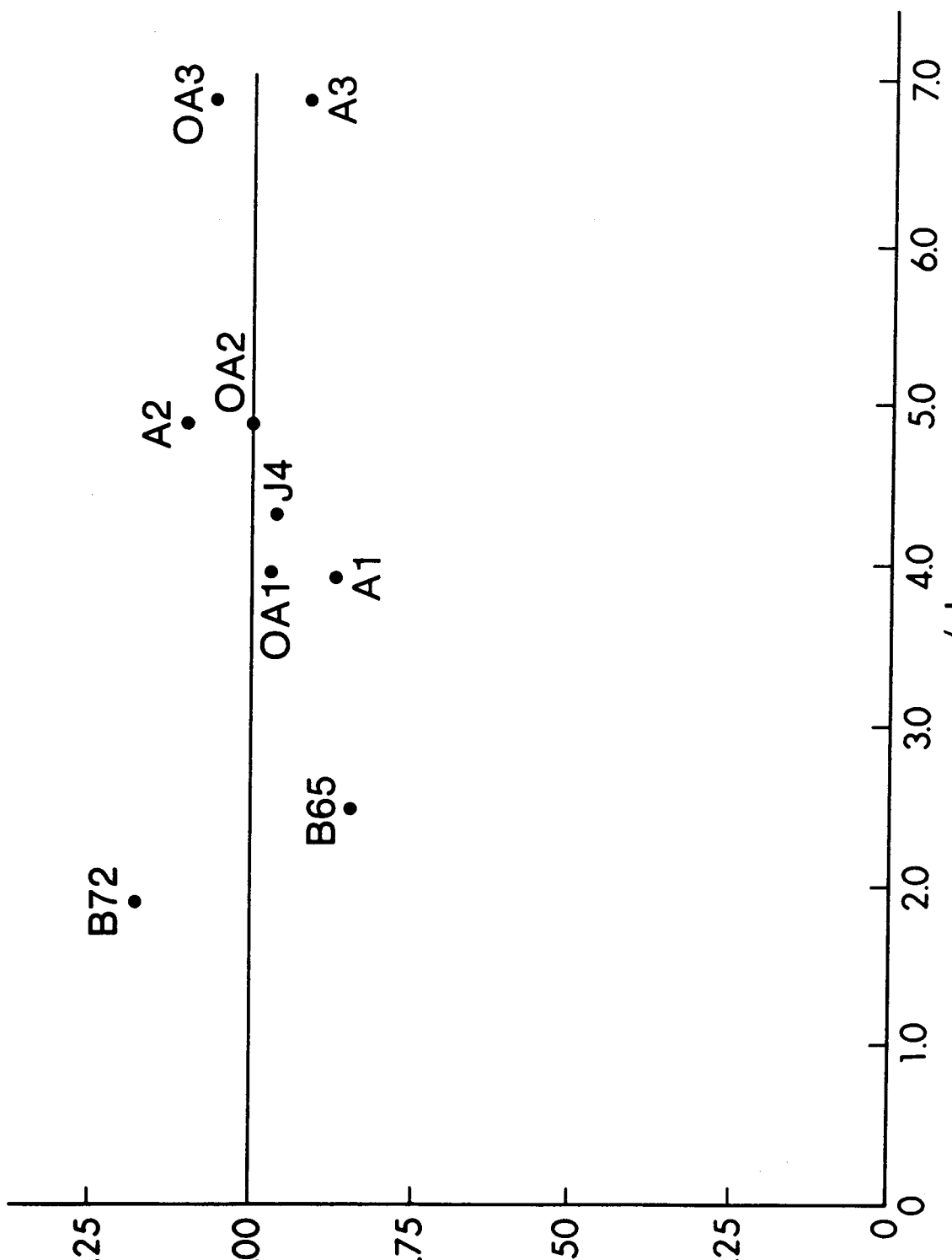

FIG. 5.70. Finite Element Prediction Compared to Test Results

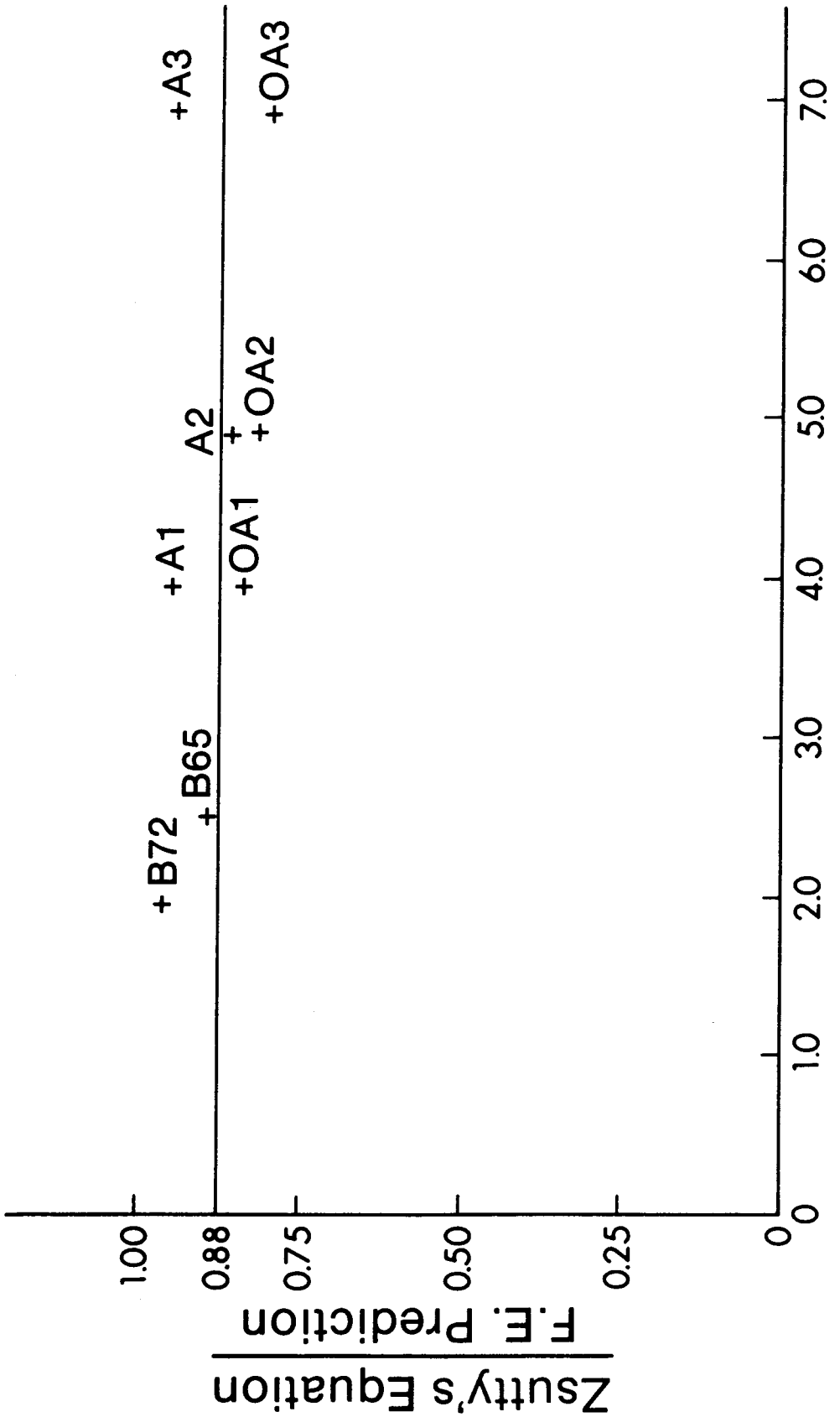

FIG. 5.71. Finite Element Prediction Compared to Zsutty's Equation

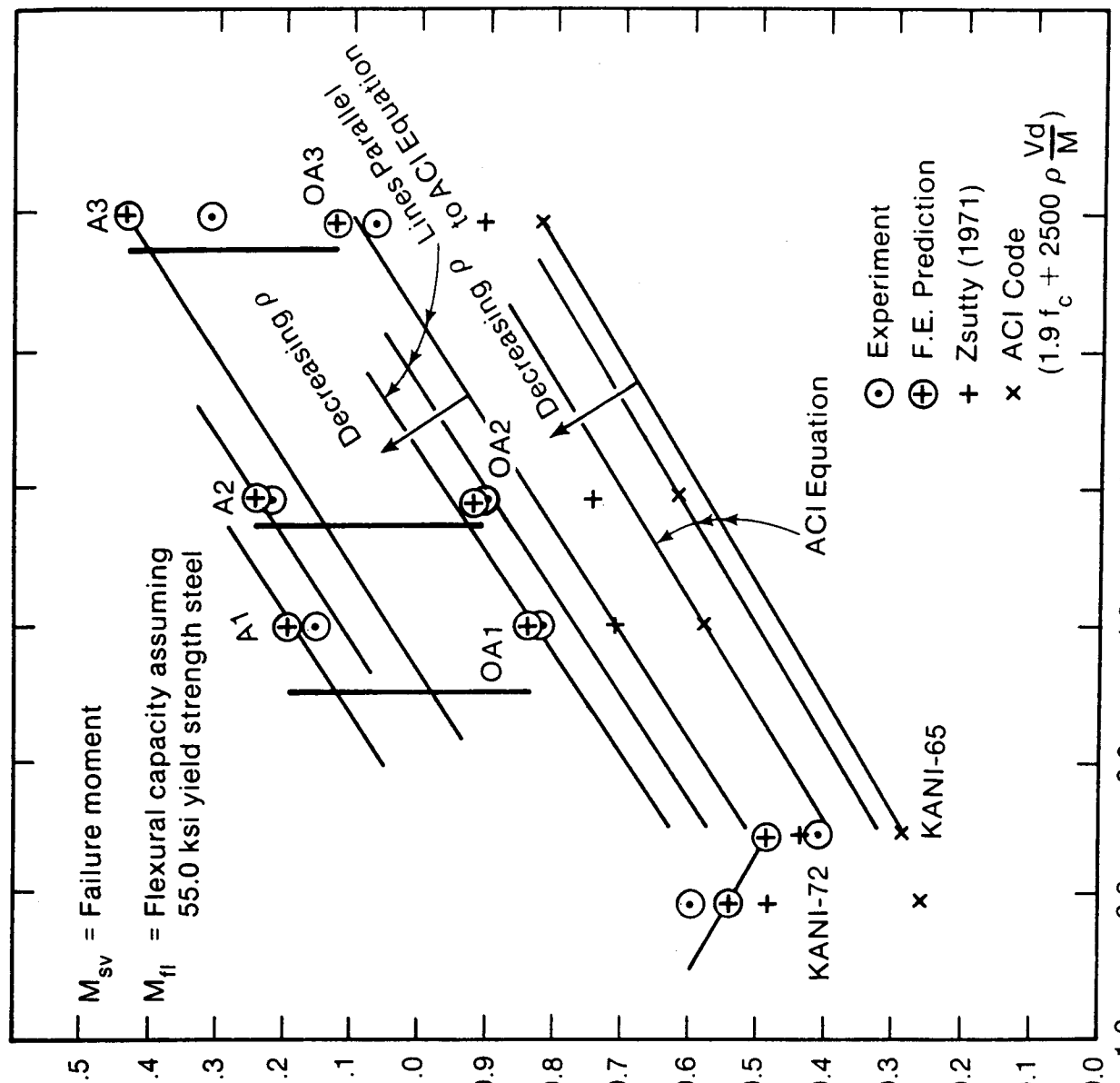

FIG. 5.72. Comparison of Failure Moments

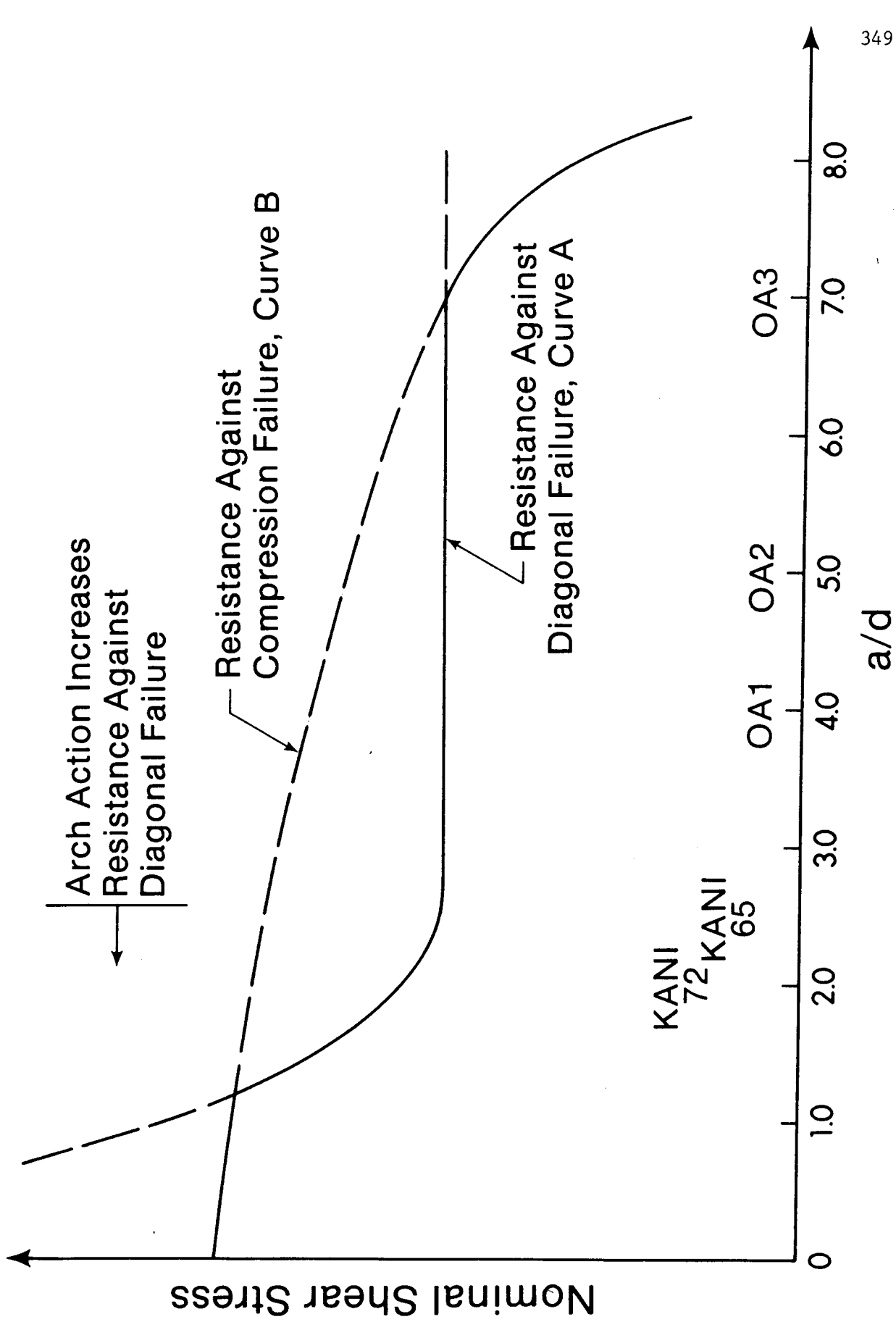

FIG. 5.73. Transition in the Modes of Failure

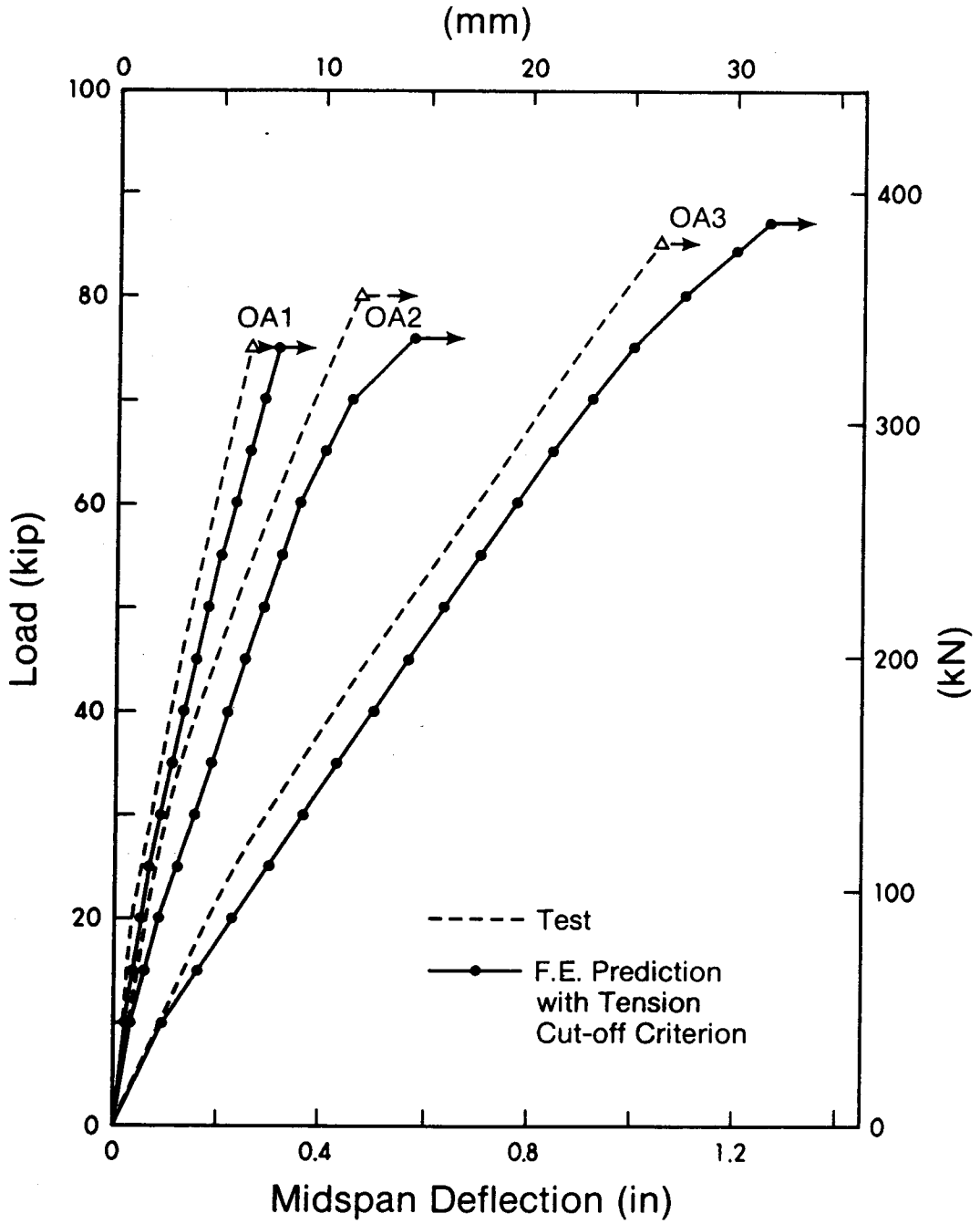

FIG. 5.74. Bresler/Scordelis Beams - Load-Deflection Curves Using Tension Cut-Off Criterion

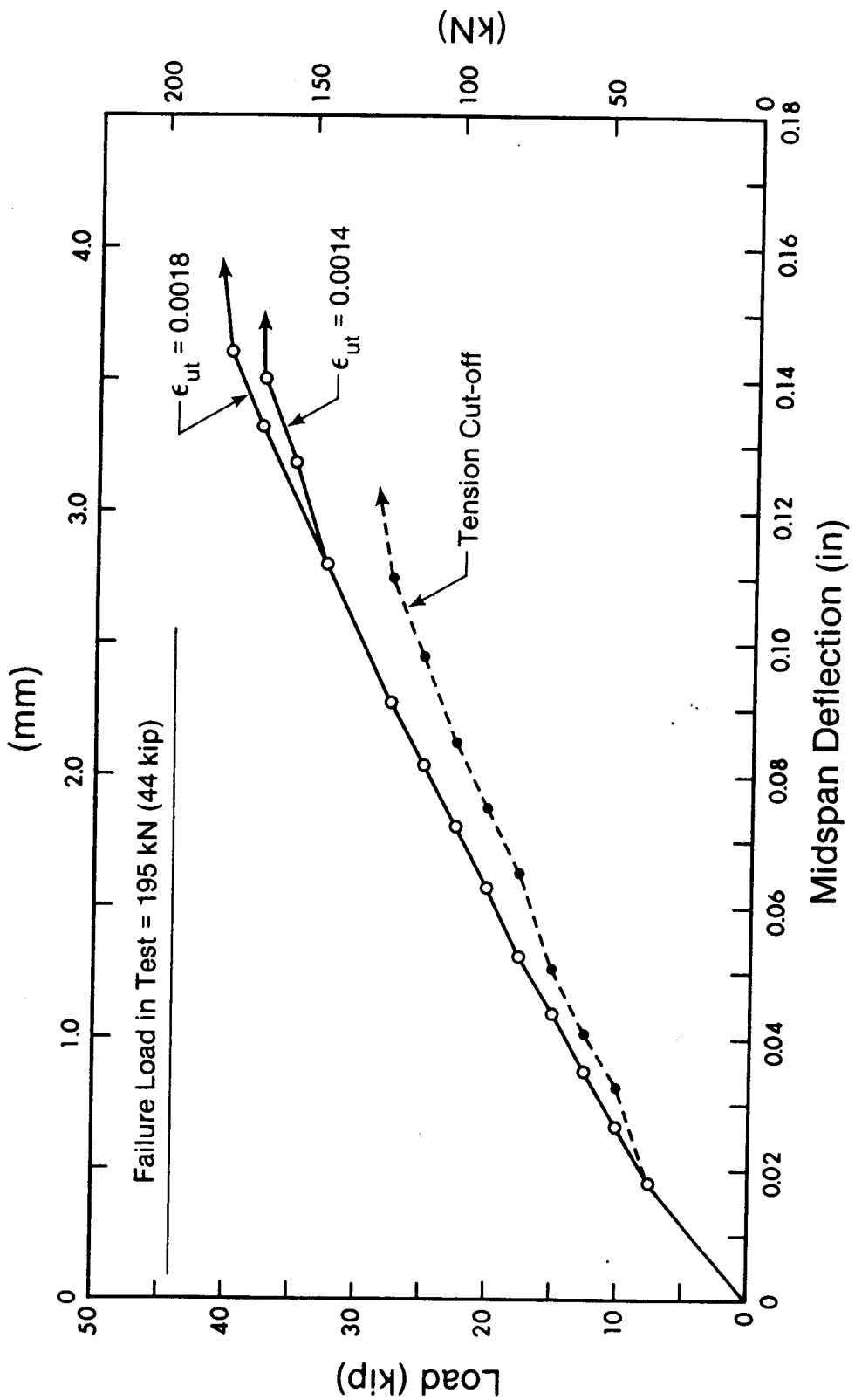

FIG. 5.75. Kani Beam 72 - Influence of Strain-Softening Modulus

CHAPTER 6

SUMMARY AND CONCLUSIONS

6.1 Summary

In this study, simple multilinear constitutive relationships for concrete have been developed which, when incorporated into a nonlinear finite element program, closely predict the behavior of beams and panels exhibiting a wide range of failure modes.

Concrete and reinforcing element formulations have been developed. An embedded formulation for the bond element, wherein the bond slip d.o.f. are added at the reinforcing steel to take into account the bond slip at the concrete/steel interface, has been developed which obviates the need for locating boundary nodes of concrete elements at the reinforcing steel locations.

The fundamentals of concrete behavior and the salient features of various constitutive models that are available in the literature have been discussed. For reliable predictions of the structural behavior of reinforced concrete, the following considerations were included in the nonlinear analysis:

1. Tensile cracking
2. Tension softening and tension stiffening
3. Strain hardening at high compressive stress
4. Strain softening under post-peak compression
5. Post-cracking compressive strength of concrete
6. Variation of shear modulus with the normal crack strain
7. Bond-slip behavior.

The equilibrium and compatibility of net-reinforced concrete

elements have been discussed. The basics of plasticity based methods and the modified compression field theory of Vecchio/Collins (1982) were described. It has been shown that the ultimate strength of net reinforced concrete elements failing by at least one layer of steel yielding can be closely predicted by equilibrium considerations alone when the post-cracking compressive strength criteria developed herein are adopted. The 'rotating crack model', wherein the axes of orthotropy are assumed to coincide with the current principal strain axes, in conjunction with the multilinear material model for concrete adopted in this study, has been found to be adequate to closely predict the behavior of shear panels and net-reinforced deep beams.

The fundamental behavior of reinforced concrete beams has been discussed. Nonlinear finite element analyses have been performed (as described in Chapter 5) on: (1) beams exhibiting ductile flexural failure modes (failure by steel yielding); (2) shear critical beams without web reinforcement and failing by diagonal tension; (3) shear critical beams with web reinforcement and failing by shear compression; (4) deep beams failing in compression, i.e., failure of 'truss' action or 'arch' action (described in Appendix A3); and, (5) deep beams failing by concrete crushing at support locations (described in Chapter 4). The effects on the analysis of various parameters such as tensile strain softening, secondary cracking, shear modulus of cracked concrete, compressive stress-strain relationship and bond slip were investigated. Insights gained during the analysis into the behavior of shear critical beams are discussed.

6.2 Conclusions

1. The major conclusion from this study is that the finite element method can be used to closely predict the behavior of reinforced concrete members subjected to in-plane forces if proper care is taken in modeling the material characteristics. The load deflection behavior, crack pattern, failure load and failure mode can be predicted with an accuracy that is acceptable for engineering purposes.

2. In order to obtain reliable predictions it appears to be necessary to properly include consideration of major sources of nonlinearity in reinforced concrete, namely tensile cracking, tension softening and tension stiffening, strain hardening and strain softening in compression, variation of shear modulus with crack width and bond slip. Great refinements in modeling these phenomena may not be required.

3. The embedded formulation of bond elements developed herein offers the advantage that nodes of solid elements need not be located at reinforcing elements.

4. A hypothesis for estimating the post-cracking compressive strength of concrete based on the biaxial stress conditions prior to cracking has been developed in this study. Ultimate strength predictions using this hypothesis in conjunction with equilibrium considerations alone, have been compared to the test data of Vecchio and Collins (1982) and found to be adequate for panels failing by at least one layer of steel yielding. For panels failing by concrete crushing with no steel yielding, a lower bound on the failure load is obtained.

5. The finite element method, employing the simple multilinear material model, predicts with reasonable accuracy the load deflection

behavior, failure mode and failure load of Vecchio/Collins shear panels failing by steel yielding or concrete crushing including one panel subjected to nonproportional loading.

6. The prediction of ultimate strength of panels failing by concrete crushing is sensitive to the tension-stiffening relation used.

7. The prediction of ultimate strength of panels is insensitive to the shear modulus of cracked concrete used.

8. The finite element method, employing the rotating crack model, and the simple multilinear stress-strain relationship, closely predicts the behavior of a net reinforced deep beam.

9. The finite element analyses lead to the identification of a shear failure criterion for shallow beams as follows. Shear failure occurs when the shear modulus of concrete above or below the neutral axis has decreased sufficiently to produce shear strains of the same order of magnitude as normal strains. The role of the web reinforcement is to increase the load at which the shear stiffness is reduced to a critical value.

10. It is important to model the descending branch of the tensile stress-strain curve of concrete in order to obtain reliable predictions of the behavior of beams.

11. The tensile strength of concrete has a significant effect on the failure load of shear critical beams.

12. Secondary cracking must be considered in order to obtain reliable predictions of the behavior of shear critical beams.

13. For reliable predictions, compressive strain hardening and strain softening must be considered for beams.

14. It is essential that the variation of shear modulus with the

crack width (i.e. normal crack strain in the smeared crack approach) is represented.

15. The effect of bond slip on shear critical beams without web reinforcement is to increase the failure load if shear span to depth ratio (a/d ratio) is less than about 2.5 and to decrease the failure load if a/d > 2.5.

6.3 Recommendations for Future Study

A number of areas remain to be examined for the wider, practical application of the finite element method for the prediction of concrete behavior. Some of these are outlined below.

1. Application to prestressed and partially prestressed concrete members.

2. The effects of bond slip of web reinforcement on the shear capacity of reinforced concrete members.

3. Extension to plane-strain and triaxial stress conditions. Triaxial tests show that even moderate levels of confinement can double the strength and ductility of concrete. The parameters defining the stress-strain curve of concrete may be modified for varying degrees of confinement using failure surfaces similar to the biaxial stress envelope.

4. Large displacement formulations must be developed and tested so as to reliably predict the behavior of reinforced concrete columns.

5. The influence of mesh refinement, aspect ratio and orientation of the elements on the behavior prediction needs to be examined further.

6. Incorporation of a substructuring solution scheme wherein it may be possible to eliminate all degrees of freedom associated with the

linear regions of the structure by static condensation. In this case, computationally more expensive nonlinear analysis will be restricted to only those portions of the structure which are expected to behave nonlinearly under applied loads.

REFERENCES

AKBAR, H and GUPTA, A.K. 1985. Membrane Reinforcement in Concrete Shells - Design Versus Nonlinear Behavior, Research Report, Department of Civil Engineering, North Carolina State University at Rayleigh.

AL-MAHAIDI, R.S. 1979. Nonlinear Finite Element Analysis of Reinforced Concrete Deep Members, Report No. 79-1, Department of Structural Engineering, Cornell University, Ithaca, New York.

ALDSTEDT, E. and BERGRAN, P.G. 1978. Nonlinear Time-Dependent Concrete Frame Analysis, ASCE Journal of the Structural Division, **104** (ST7), pp. 1077-1092.

AMERICAN CONCRETE INSTITUTE COMMITTEE 318. 1983. Building Code Requirements for Reinforced Concrete, ACI, Detroit, MI.

AMERICAN SOCIETY OF CIVIL ENGINEERS. 1982. State of the Art Report on Finite Element Analysis of Reinforced Concrete, Task Committee on Finite Element Analysis of Reinforced Concrete Structures of the Structural Division Committee on Concrete and Masonry Structures, New York.

ARNESEN, A. 1979. Analysis of Reinforced Concrete Shells Considering Material and Geometric Nonlinearities, Report No. 79-1, Division of Structural Mechanics, The Norwegian Institute of Technology,

Trondheim, Norway.

BASE, G.D. 1982. Bond and Control of Cracking in Reinforced Concrete, in Bond in Concrete, Bartos, P. Ed., Applied Science Publishers, London. pp. 446-457.

BATHE, K.J. and MEYER, C. 1982. Nonlinear Analysis of R/C Structures in Practice, ASCE Journal of the Structural Division, **108** (ST7), pp. 1605-1622.

BATHE, K.J. and RAMASWAMY, S. 1979. On Three Dimensional Nonlinear Analysis of Concrete Structures, Nuclear Engineering and Design, Vol. 52, pp. 385-409.

BATHE, K.J. 1982. Finite Element Procedures in Engineering Analysis, Prentice-Hall, Englewood Cliffs, New Jersey.

BAZANT, Z.P. 1985. Mechanics of Fracture and Progressive Cracking in Concrete Structures, in Fracture Mechanics of Concrete: Structural Application and Numerical Calculation, Sih, G.C. and Di Tommaso, A., Eds., Martinus Nighoff Publishers, Dordrecht, The Netherlands.

BAZANT, Z.P. and BHAT, P. 1976. Endochronic Theory of Inelasticity and Failure of Concrete, ASCE Journal of the Engineering Mechanics Division, **102** (EM4) pp. 701-722.

BAZANT, Z.P. and CEDOLIN, L. 1980. Fracture Mechanics of Reinforced Concrete, ASCE Journal of the Engineering Mechanics Division, **106** (EM6), pp. 1287-1306. Also, closure to the discussion, **108** (EM2), 1982, pp. 466-471.

BAZANT, Z.P. and KIM, S.S. 1979. Plastic Fracturing Theory for Concrete, ASCE Journal of the Engineering Mechanics Division, **105** (EM3), pp. 407-428.

BAZANT, Z.P. and OH, B.H. 1983a. Crack Band Theory for Fracture of Concrete, Materials and Structures (RILEM, Paris), Vol. 16, pp. 155-177.

BAZANT, Z.P. and OH, B.H. 1983b. Deformation of Cracked Net-Reinforced Concrete Walls, Journal of Structural Engineering, **109** (No. 1), pp. 93-108.

BAZANT, Z.P. and TSUBAKI, T. 1980. Slip-Dilatancy Model for Cracked Reinforced Concrete, ASCE Journal of the Structural Division, **106** (ST9), pp. 1947-1966.

BEEBY, A.W. 1979. The Prediction of Crack Widths in Hardened Concrete, The Structural Engineer, **57A**, No. 1, pp. 9-17.

BERGAN, P.G. 1984. Some Aspects of Interpolation and Integration in Nonlinear Finite Element Analysis of Reinforced Concrete Structures, Proceedings of the International Conference on

Computer Aided Analysis and Design of Concrete Structures, Split, Yugoslavia, pp. 301-316, Pineridge Press, Swansea, U.K.

BERGAN, P.G. and HOLAND, I. 1978. Nonlinear Finite Element Analysis of Concrete Structures, in Computer Methods in Applied Mechanics and Engineering, **17/18**, pp. 443-467, (Also in FENOMECH '78), North-Holland Publishing Company, Amsterdam.

BRESLER, B. and SCORDELIS, A.C. 1963. Shear Strength of Reinforced Concrete Beams, ACI Journal, **60** (1), pp. 51-73. Also, Report to Reinforced Concrete Research Council, University of California, Berkely, 1961.

BROEK, D. 1982. Elementary Engineering Fracture Mechanics, Martinus Nighoff Publishers, The Hague, The Netherlands.

BUYUKOZTURK, O. 1977. Nonlinear Analysis of Reinforced Concrete Structures, Journal of Computers and Structures, **7**, pp. 149-156.

BURNS, N.H. and SIESS, C.P. 1966. Repeated and Reversed Loading in Reinforced Concrete, ASCE Journal of the Structural Division, **92** (ST5), pp. 65-78.

BUYUKOZTURK, O. and SHAREEF, S.S. 1985. Constitutive Modelling of Concrete in Finite Element Analysis, Computers & Structures, **21** (No. 3), pp. 581-610.

CANADIAN STANDARDS ASSOCIATION. 1984. Design of Concrete Structures for Buildings, National Standard of Canada, CAN3-A23.3-M84, CSA, Rexdale, Ontario, 281 p.

CEB Model Code for Concrete Structures. 1978. International Recommendations, 3rd ed. Cement and Concrete Association, London, England, 348 p.

CEB (Comite Euro-international du Beton), 1982a. Shear, Torsion and Punching - Progress Reprot, Bulletin d'information No. 146, Paris.

CEB (Comitet Euro-international du Beton), 1982b. Bond Action and Bond Behavior of Reinforcement, State of the Art Report, Bulletin d'information No. 151, Paris.

CEDOLIN, L. and DEI POLI, S. 1977. Finite Element Studies of Shear Critical R/C Beams, ASCE Journal of the Engineering Mechanics Division, **103** (EM3), pp. 395-410.

CHEN, W.F. 1982. Plasticity in Reinforced Concrete, McGraw-Hill Book Company, New York.

CHEN, W.F. and YAMAGUCHI, E. 1985. On Constitutive Modelling of Concrete Materials. Seminar on Finite Element Analysis of Reinforced Concrete Structures, Tokyo, Japan Society for the Promotion of Science, Tokyo.

COLLINS, M.P. 1978. Towards Rational Theory for RC Members in Shear, ASCE Journal of the Structural Division, **104** (ST4), pp. 649-666.

COLLINS, M.P. and MITCHELL, D. 1980. Shear and Torsion Design of Prestressed and Non-Prestressed Concrete Beams, Journal of the Prestressed Concrete Institute, **25** (5), Chicago, pp. 32-100.

COLLINS, M.P., VECCHIO, F.J. and MELHORN, G. 1985. An International Competition to Predict the Response of Reinforced Concrete Panels, Canadian Journal of Civil Engineering, **12** (3), pp. 624-644.

COLVILLE, J. and ABBASI, J. 1974. Plane Stress Reinforced Concrete Finite Elements, ASCE Journal of the Structural Division, **100** (ST5), pp. 1067-1084.

COOK, R.D. 1981. Concepts and Applications of Finite Element Analysis, John Wiley & Sons, Inc., New York.

COOK, R.D. 1977. Ways to Improve the Bending Response of Finite Elements, International Journal for Numerical Methods in Engineering, **11**, pp. 1029-1039.

CRISFIELD, M.A. 1984. Difficulties with Current Numerical Models for Reinforced Concrete and Some Tentative Solutions, Proceedings of the International Conference on Computer Aided Analysis and

Design of Concrete Structures, Part I, Split, Yugoslavia, Damjanic et al., Eds., Pineridge Press, Swansea, U.K., pp. 331-357.

DARWIN, D. 1985. Crack Propagation in Concrete - Study of Model Parameters, Seminar on Finite Element Analysis of Reinforced Concrete Structures, Japan Society for the Promotion of Science, Ed., Tokyo.

DARWIN, D. and PECKNOLD, D.A.W. 1974. Inelastic Model for Cyclic Biaxial Loading of Reinforced Concrete, Structural Research Series No. 409, University of Illinois at Urbana-Champaign, Illinois.

DE GROOT, A.K., KUSTERS, G.M.A., and MONNIER, T. 1981. Numerical Modelling of Bond-Slip Behavior, Heron, **26** (No. 1B), Delft University of Technology, The Netherlands.

DODDS, R.H., DARWIN, D., SMITH, J.L. and LEIBENGOOD, L.D. 1982. Grid Size Effects With Smeared Cracking in Finite Element Analysis of Reinforced Concrete, SM Report No. 6, The University of Kansas Center for Research, Inc., Lawrence, Kansas.

DOHERTY, W.P., WILSON, E.L. and TAYLOR, R.L. 1969. Stress Analysis of Axisymmetric Solids Utilizing Higher Order Quadrilateral Finite Elements, Report No. 69-3, Structural Engineering Laboratory, University of California, Berkeley.

DYM, C.L. and SHAMES, I.H. 1973. Solid Mechanics - A Variational Approach, McGraw-Hill Book Company, New York.

ELIGEHAUSEN, R., BERTERO, V.V. and POPOV, E.P. 1983. Local Bond Stress-Slip Relationships for Deformed Bars under Generalized Excitations, Report UCB/EERC 83-23, Earthquake Engineering Research Center, University of California, Berkeley.

ELWI, A.A. and MURRAY, D.W. 1980a. Nonlinear Analysis of Axisymmetric Reinforced Concrete Structures, Structural Engineering Report No. 87, University of Alberta, Edmonton.

ELWI, A.A. and MURRAY, D.W. 1980b. FEPARCS5 - A Finite Element Program for the Analysis of Axisymmetric Reinforced Concrete Structures, Users Manual, Structural Engineering Report No. 93, University of Alberta, Edmonton.

FARDIS, M.N. and BUYUKOZTURK, O. 1980. Shear Stiffness of Concrete by Finite Elements, ASCE Journal of the Structural Division, **106** (ST6), pp. 1311-1327.

FENWICK, R.C. and PAULAY, T. 1968. Mechanisms of Shear Resistance of Concrete Beams, ASCE Journal of the Structural Division, **94** (ST10), pp. 2325-2350.

FILIPPOV, F-C., POPOV, E.P. and BERTERO, V.V. 1983. Modeling of R/C

Joints Under Cyclic Excitations, Journal of Structural Engineering, ASCE, **109** (No. 11), pp. 2666-2684.

FLOEGL, H. and MANG, H.A. 1982. Tension Stiffening Concept Based on Bond Slip, ASCE Journal of the Structural Division, **108** (ST12), pp. 2681-2701.

FRANKLIN, H.A. 1970. Nonlinear Analysis of Reinforced Concrete Frames and Panels, Ph.D. Dissertation, University of California, Berkeley.

GALLAGHER, R.H. 1975. Finite Element Analysis Fundamentals, Prentice-Hall, Inc., Englewood Cliffs, New Jersey.

GAMBAROVA, P. and KARAKOC, C. 1982. Shear Confinement Interaction at the Bar to Concrete Interface, in Bond in Concrete, Bartos, P. Ed., Applied Science Publishers, London, pp. 82-96.

GERSTLE, K.H. 1981. Simple Formulation of Biaxial Concrete Behavior, Journal of the American Concrete Institute, **78** (No. 1), pp. 62-68.

GILBERT, I.G. and WARNER, R.F. 1978. Tension Stiffening in Reinforced Concrete Slabs, ASCE Journal of the Structural Division, **104** (ST12), pp. 1885-1900.

GIURIANI, E. 1981. Experimental Investigation on the Bond-Slip Law of

Deformed Bars in Concrete in Advanced Mechanics of Reinforced Concrete, IABSE Colloquium, Delft University of Technology, The Netherlands.

GIURIANI, E., MIGLIACCI, A. and RIVA, P. 1984. Experimental Investigation on the Local Bond-slip Law in Structural Lightweight Concrete, Corso di Perfezionamento per le Construzioni in Cemento Armato Fratelli Presenti, Studi E Ricerche **6**, Politecnico di Milano, Italia.

GLEMBERG, R. and SAMUELSSON, A. 1984. A General Constitutive Model for Concrete Structures, Proceedings of the International Conference on Computer Aided Analysis and Design of Concrete Structures, Split, Yugoslavia, Damjanic, F. et al., eds., Pineridge Press, Swansea, U.K.

GOPALARATNAM, V.S. and SHAH, S.P. 1984. Softening Response of Plain Concrete in Direct Tension, Technological Institute, Northwestern University, Evanston, Illinois.

GRIFFITH, A.A. 1921. The Phenomena of Rupture and Flow in Solids, Philosophical Transactions, Royal Society of London, **A221**, pp. 163-197.

GUPTA, A.K. and AKBAR, H. 1984. Cracking in Reinforced Concrete Analysis, Journal of Structural Engineering, ASCE, **110** (No. 8), pp. 1735-1746.

HAND, F.R., PECKNOLD, D.A. and SCHNOBRICH, W.C. 1972. A Layered Finite Element Nonlinear Analysis of Reinforced Concrete Plates and Shells, Structural Research Series No. 389, University of Illinois, Urbana.

HILLERBORG, A. 1985. Numerical Methods to Simulate Softening and Fracture of Concrete, in Fracture Mechanics of Concrete: Structural Application and Numerical Calculation, Sih, G.C. and DiTommaso, A. Eds., Martinus Nijhoff Publishers, Dordrcht, The Netherlands.

HOUDE, J. and MIRZA, M.S. 1974. A Finite Element Analysis of Shear Strength of Reinforced Concrete Beams, in Shear in Reinforced Concrete, ACI Publication SP-42, Detroit, pp. 103-128.

HOUDE, J. and MIRZA, M.S. 1972. Investigation of Shear Transfer Across Cracks by Aggregate Interlock, Research Report No. 72-06, Ecole Polytechnique de Montreal, Departement de Genie Civil, Division de Structures, Montreal.

INGRAFFEA, A.R., GERSTLE, W.H., GERGELY, P. and SAOUMA, V. 1984. Fracture Mechanics of Bond in Reinforced Concrete, Journal of Structural Engineering, **110** (No. 4), pp. 871-890.

INGRAFFEA, A.R. and SAOUMA, V. 1985. Numerical Modeling of Discrete Crack Propagation in Reinforced and Plain Concrete, in Fracture

Mechanics of Concrete, Sih, G.C. and Di Tommaso, A., Eds., Martinus Nijhoff Publishers, Dordrecht, The Netherlands.

JIANG, D.H., SHAH, S.P. and ANDONIAN, A-T. 1984. Study of the Transfer of Tensile Forces by Bond, ACI Journal, **81**, No. 3, Detroit, pp. 251-259.

JIMINEZ, R., GERGELY, P. and WHITE, R.N. 1978. Shear Transfer Across Cracks in Reinforced Concrete, Report 78-4, Department of Structural Engineering, Cornell University, 357 pp.

KANI, M.W., HUGGINS, M.W. and WITTKOPP, R.R. 1979. Kani on Shear in Reinforced Concrete, Department of Civil Engineering, University of Toronto Press, Canada.

KRAUTHAMMAR, T. and HALL, W.J. 1982. Modified Analysis of Reinforced Concrete Beams, ASCE Journal of the Structural Division, **108** (ST2), pp. 457-475.

KUPFER, H., HILSDORF, H-K. and RUSCH, H. 1969. Behavior of Concrete Under Biaxial Stresses, ACI Journal, **66** (No. 8), pp. 656-666.

KUPFER, H. and GERSTLE, K. 1973. Behavior of Concrete Under Biaxial Stresses, ASCE Journal of the Engineering Mechanics Division, **99** (EM4), pp.

LEONHARDT, F. and WALTHER, R. 1966. Wandertige Trager, Report,

Deutscher Ausschuß für Stahlbeton, Heft 178, Berlin. (in German)

LIU, T-C.Y., NILSON, A.H. and SLATE, F.O. 1972. Biaxial Stress-Strain Relations for Concrete, ASCE Journal of the Structural Division, **98** (ST5), pp. 1025-1034.

MACGREGOR, J.G., Chmn. 1978. The Shear Strength of Reinforced Concrete Members, Task Committee on Masonry and Reinforced Concrete of the Structural Division, ASCE Journal of the Structural Division, **99** (ST6), pp. 1091-1187.

MACGREGOR, J.G. and WALTERS, J.R.V. 1967. Analysis of Inclined Cracking Shear in Slender Reinforced Concrete Beams, ACI Journal, **64** (10), pp. 644-653.

MARTI, P. 1985. Basic Tools of Reinforced Concrete Beam Design, ACI Journal, **82** (1), pp. 46-56.

MILFORD, R.V. 1984. Nonlinear Behavior of Reinforced Concrete Cooling Towers, Ph.D. Thesis, University of Illinois at Urbana-Champaign, Illinois.

MILFORD, R.V. and SCHNOBRICH, W.C. 1984. Numerical Model for Cracked Reinforced Concrete, presented at the International Conference on Computer Aided Analysis and Design of Concrete Structures, Split, Yugoslavia, Damjanic, F. et al., Eds., Pineridge Press, Swansea, U.K.

MINDESS, S. and YOUNG, F. 1981. Concrete. Prentice-Hall, Inc., Englewood Cliffs, N.J.

MIRZA, S.M. and HOUDE, J. 1979. Study of Bond Stress-Slip Relationships in Reinforced Concrete, ACI Journal, **76** (No. 1), pp. 19-46.

MURRAY, D.W., CHITNUYANONDH, L., WONG, C. and RIJUB-AGHA, K.Y. 1978. Inelastic Analysis of Prestressed Concrete Secondary Containments, Structural Engineering Report No. 67, University of Alberta, Edmonton.

MURRAY, D.W., CHITNUYANONDH, L. and WONG, C. 1980. Implementation of Elastic-Plastic Concrete Relationship, Computer Methods in Applied Mechanics and Engineering, **23**, pp. 35-57.

NAM, C.H. and SALMON, C.G. 1974. Finite Element Analysis of Concrete Beams, ASCE Journal of the Structural Division, **100** (ST12), pp. 2419-2432.

NIELSEN, M.P. 1984. Limit Analysis and Concrete Plasticity, Prentice Hall, Inc., New Jersey.

NILSON, A.H. 1968. Nonlinear Analysis of Reinforced Concrete by the Finite Element Method, ACI Journal, **65** (No. 9)

NILSON, A.H. 1972. Internal Measurements of Bond Slip, ACI Journal, **69**

No. 7, pp. 439-441.

NGO, D. 1975. A Network-Topological Approach to the Finite Element Analysis of Progressive Crack Growth in Concrete Members, Ph.D. Thesis, University of California, Berkeley, California.

NGO, D. and SCORDELIS, A.C. 1967. Finite Element Analysis of Reinforced Concrete Beams, ACI Journal, **64** (No. 3).

OTTOSEN, N.S. 1982. 2-D Finite Element Analysis of Massive RC Structures, ASCE Journal of the Structural Division, **108** (ST8), pp. 1874-1893.

PARK, R. and PAULAY, T. 1975. Reinforced Concrete Structures, John Wiley & Sons, Inc., New York.

PAULAY, T., and LOEBER, P.S. 1974. Shear Transfer by Aggregate Interlock, in Shear in Reinforced Concrete, Vol. I, SP-42, American Concrete Institute, Detroit, Michigan.

PERDIKARIS, P.C., HILMY, S. and WHITE, R.N. 1985. Extensional Stiffness of Precracked R/C Panels, Journal of Structural Engineering, ASCE, **111** (No. 3), pp. 487-504.

PERDIKARIS, P.C. and WHITE, R.N. 1985. Shear Modulus of Precracked R/C Panels, Journal of Structural Engineering, ASCE, **111** (No. 2), pp. 270-289.

RAPHAEL, J.M. 1984. Tensile Strength of Concrete, Journal of the American Concrete Institute, **81** (2), pp. 158-165.

REINHARDT, H.W. and WALRAVEN, J.C. 1982. Cracks in Concrete Subject to Shear, ASCE Journal of the Structural Division, **108** (ST1), pp. 207-224.

RIGGS, H.R. 1981. A Crack Model for Finite Element Analysis of Concrete, Ph.D. Thesis, University of California, Berkely.

ROGOWSKY, D.M. and MACGREGOR, J.G. 1983. Tests of Reinforced Concrete Deep Beams, Structural Engineering Report No. 109, University of Alberta, Edmonton.

ROGOWSKY, D.M. and MACGREGOR, J.G. 1983. Shear Strength of Deep Reinforced Concrete Continuous Beams, Structural Engineering Report No. 110, University of Alberta, Edmonton.

ROMSTAD, K.M., TAYLOR, M.A. and HERMANN, L.R. 1974. Numerical Biaxial Characterization for Concrete, ASCE Journal of the Engineering Mechanics Division, **100** (EM5), pp. 935-948.

ROTS, J.G., NAUTA, P., KUSTERS, G.M.A. and BLAAUWENDRAAD. 1985. Smeared Crack Approach and Fracture Localization in Concrete, Heron, **30** (No. 1), Delft University of Technology, The Netherlands.

SCANLON, A. and MURRAY, D.W. 1972. An Analysis to Determine the Effects of Cracking in Reinforced Concrete Slabs, Proceedings of the Specialty Conference on Finite Element Method in Civil Engineering, McGill University, Montreal, pp. 841-868.

SCORDELIS, A.C., NGO, N.G. and FRANKLIN, H.A. 1974. Finite Element Study of Reinforced Concrete Beams with Diagonal Tension Cracks, in ACI Publication SP-42, Detroit, pp. 79-102.

SCORDELIS, A.C. 1978. Finite Element Modeling of Reinforced Concrete Structures. Analisi Delle Strutture in Cemento Arnato Mediante Il Metodo Degli Elementi Finiti (in English), Seminar, Politcnico Di Milano, pp. 63-113.

SCORDELIS, A.C. 1985. Past, Present and Future Developments, Seminar on Finite Element Analysis of Reinforced Concrete Structures, Japan Society for the Promotion of Science, Volume I, Tokyo, pp. 203-212.

SOMAYAJI, S. and SHAH, S.P. 1981. Bond Stress Versus Slip Relationship and Cracking Response of Tension Members, ACI Journal, Title No. 78-20, pp. 217-225.

SUIDAN, M. and SCHNOBRICH, W.C. 1973. Finite Element Analysis of Reinforced Concrete, ASCE Journal of the Structural Division, 99 (ST10)

TANIGUCHI, H. 1984. Nonlinear Analysis of Reinforced Concrete Structures by the Finite Element Method, Ph.D. Dissertation, University of Akron, Ohio.

TAYLOR, H.P.J. 1974. The Fundamental Behavior of Reinforced Concrete Beams in Bending and Shear, in Shear in Reinforced Concrete, Vol. 1, SP-42, American Concrete Institute, Detroit, pp. 43-78.

TEPFERS, R. 1979. Cracking of Concrete Cover Along Anchored Deformed Reinforcing Bars, Magazine of Concrete Research, **31** (106), London, pp. 3-12.

VALLENAS, J., BERTERO, V.V. and POPOV, E.P. 1977. Concrete Confined by Rectangular Hoops and Subjected to Axial Loads, Report No. UCB/EERC-77/13, University of California, Berkeley.

VALLIPPAN, S. and DOOLAN, T.F. 1972. Nonlinear Stress Analysis of Reinforced Concrete, ASCE Journal of the Structural Division, **98** (ST4), pp. 885-898.

VECCHIO, F. and COLLINS, M.P. 1982. The Response of Reinforced Concrete to In-Plane Shear and Normal Stresses, Publication No. 82-03, Department of Civil Engineering, University of Toronto.

WALRAVEN, J.C. 1981. Fundamental Analysis of Aggregate Interlock, ASCE Journal of the Structural Division, **107** (ST11), pp. 2245-2270.

WILLAM, K.J. 1984. Experimental and Computational Aspects of Concrete Fracture, Proceedings of the International Conference on Computer-Aided Analysis and Design of Concrete Structures, Part I, Split, Yugoslavia, Damjanic et al., Eds., Pineridge Press, Swansea, U.K., pp. 33-69.

WILLAM, K.J. HURLBUT, B. and STURE, S. 1985. Experimental, Constitutive and Computational Aspects of Concrete Failure, Seminar on Finite Element Analysis of Reinforced Concrete Strutures, Japan Society for the Promotion of Science, Tokyo, pp. 149-171.

WIUM, D.J.W., BUYUKOZTURK, O. and LI, V.C. 1984. Hybrid Model for Discrete Cracks in Concrete, Journal of Engineering Mechanics, ASCE, **110** (No. 8), pp. 1211-1229.

YANKELEVSKY, D.Z. 1985. New Finite Element for Bond-Slip Analysis, Journal of Structural Engineering, ASCE, **111** (No. 7), pp. 1533-1542.

ZIENKIEWICZ, O.C. 1977. The Finite Element Method, McGraw-Hill Book Company (UK) Ltd., London.

ZSUTTY, T. 1971. Shear Strength Prediction for Separate Categories of Simple Beam Tests, ACI Journal, Title No. 68-15, February, pp. 138-143.

APPENDIX A1

ISOPARAMETRIC ELEMENT FORMULATION WITH VARIABLE NUMBER OF NODES

A1.1 Formulation

The basic procedure in the isoparametric finite element formulation is to express the element coordinates and element displacements in the form of interpolations using the natural coordinate system of the element. Consider, for example, a two dimensional bicubic plane-stress isoparametric serendipity element, for which the global and natural coordinates are shown in Fig. A1.1. The coordinate interpolations are

$$x = \sum_{i=1}^{q} N_i x_i \qquad \text{(A1.1a)}$$

$$y = \sum_{i=1}^{q} N_i y_i \qquad \text{(A1.1b)}$$

where x and y are the coordinates at any point of the element, and x_i, y_i, i = 1, 2 ... q, are the coordinates of the q element nodes. (In Fig. A1.1 q = 12.) The interpolation functions N_i are defined in the natural coordinate system of the element, which has variables ξ and η that each vary from -1 to +1. The fundamental property of the interpolation function N_i is that its value in the natural coordinate system is unity at node i and zero at all other nodes. That is $N_i(\xi_j, n_j) = \delta_{ij}$ in which δ_{ij} is the Kronecker delta. Using this condition, the functions N_i corresponding to a specific nodal point layout could be solved in a systematic manner. However, it is convenient to construct them by inspection (Bathe, 1982). The formulation is achieved by first constructing the interpolations

corresponding to a basic bilinear element, given by

$$N_i = \frac{1}{4}(1 + \xi\xi_i)(1 + \eta\eta_i) \quad , \quad i = 1, 2, 3, 4 \tag{A1.2}$$

The addition of another node then results in an additional interpolation function and a corresponding correction to be applied to the already existing interpolation functions. Table A1.1 shows the interpolation functions of four to twelve variable-number-node two dimensional elements, of which the bicubic element shown in Fig. A1.1 has the greatest number of nodes.

The application of the above technique can be illustrated for a seven node element shown in Fig. A1.2. For this element,

$$N_\ell = N_6 = \frac{1}{2}(1 - \eta^2)(1 + \xi) \tag{A1.3a}$$

$$N_n = N_7 = \frac{1}{32}(9 + 27\xi - 9\xi^2 - 27\xi^3)(1 + \eta) \tag{A1.3b}$$

$$N_o = N_{11} = \frac{1}{32}(9 - 27\xi - 9\xi^2 + 27\xi^3)(1 + \eta) \tag{A1.3c}$$

$$N_j = N_1 = \frac{1}{4}(1 - \xi)(1 - \eta) \tag{A1.3d}$$

$$N_k = N_2 - \frac{1}{2}N_6 = \frac{1}{4}(1 + \xi)(1 - \eta) - \frac{1}{2}N_\ell \tag{A1.3e}$$

$$N_m = N_3 - \frac{1}{2}N_6 - \frac{2}{3}N_7 - \frac{1}{3}N_o \tag{A1.3f}$$

$$= \frac{1}{4}(1 + \xi)(1 + \eta) - \frac{1}{2}N_\ell - \frac{2}{3}N_n - \frac{1}{3}N_o \tag{A1.3g}$$

$$N_p = N_4 - \frac{2}{3} N_{11} - \frac{1}{3} N_7 \qquad \text{(A1.3h)}$$

$$= \frac{1}{4} (1 - \xi)(1 + \eta) - \frac{2}{3} N_o - \frac{1}{3} N_n \qquad \text{(A1.3k)}$$

This technique has been extended to the formulation of Lagrangian elements as well. For a biquadratic Lagrangian element (which has one intermediate node on each of the four sides and one internal node) the shape function, N_c, corresponding to the internal node is given by

$$N_c = (1 - \xi^2)\ (1 - \eta^2) \qquad \text{(A1.4)}$$

and corrections are made to the side nodes and corner nodes as

$$N_i\Big|_{\text{Lagrangian}} = N_i\Big|_{\text{serendipity}} - \frac{1}{2} N_c \text{ for midside nodes} \qquad \text{(A1.5a)}$$

and $$N_i\Big|_{\text{Lagrangian}} = N_i\Big|_{\text{serendipity}} - \frac{1}{4} N_c \text{ for corner nodes} \qquad \text{(A1.5b)}$$

where $N_i\Big|_{\text{serendipity}}$ is the function obtained from Table A1.1.

Similarly, the 16 noded cubic Lagrangian element can also be constructed.

The version of FEPARCS used for this study had the capability of treating variable node isoparametric Lagrangian or serendipity elements up to bicubic order.

TABLE A1.1 - Variable-Number-Node Shape Functions

Basic Shape Function	Include only if one intermediate node present				Include if two intermediate nodes are present							
	5	6	7	8	5	6	7	8	9	10	11	12
$N_1 = \frac{1}{4}(1-\xi)(1-\eta)$	$-\frac{1}{2}N_5$			$-\frac{1}{2}N_8$	$-\frac{2}{3}N_5$			$-\frac{1}{3}N_8$	$-\frac{1}{3}N_9$			$-\frac{2}{3}N_{12}$
$N_2 = \frac{1}{4}(1+\xi)(1-\eta)$	$-\frac{1}{2}N_5$	$-\frac{1}{2}N_6$			$-\frac{1}{3}N_5$	$-\frac{2}{3}N_6$			$-\frac{2}{3}N_9$	$-\frac{1}{3}N_{10}$		
$N_3 = \frac{1}{4}(1+\xi)(1+\eta)$		$-\frac{1}{2}N_6$	$-\frac{1}{2}N_7$			$-\frac{1}{3}N_6$	$-\frac{2}{3}N_7$			$-\frac{2}{3}N_{10}$	$-\frac{1}{3}N_{11}$	
$N_4 = \frac{1}{4}(1-\xi)(1+\eta)$			$-\frac{1}{2}N_7$	$-\frac{1}{2}N_8$			$-\frac{1}{3}N_7$	$-\frac{2}{3}N_8$			$-\frac{2}{3}N_{11}$	$-\frac{1}{3}N_{12}$
$N_5 = \frac{1}{2}(1-\xi^2)(1-\eta)$												
$N_6 = \frac{1}{2}(1-\eta^2)(1+\xi)$												
$N_7 = \frac{1}{2}(1-\xi^2)(1+\eta)$ ← Use if only one intermediate node is present												
$N_8 = \frac{1}{2}(1-\eta^2)(1-\xi)$												
$N_5 = \frac{1}{32}(9-27\xi-9\xi^2+27\xi^3)(1-\eta)$												
$N_9 = \frac{1}{32}(9+27\xi-9\xi^2-27\xi^3)(1-\eta)$												
$N_6 = \frac{1}{32}(9-27\eta-9\eta^2+27\eta^3)(1+\xi)$												
$N_{10} = \frac{1}{32}(9+27\eta-9\eta^2-27\eta^3)(1+\xi)$ ← Use if two intermediate nodes are present.												
$N_7 = \frac{1}{32}(9+27\xi-9\xi^2-27\xi^3)(1+\eta)$												
$N_{11} = \frac{1}{32}(9-27\xi-9\xi^2+27\xi^3)(1+\eta)$												
$N_8 = \frac{1}{32}(9+27\eta-9\eta^2-27\eta^3)(1-\xi)$												
$N_{12} = \frac{1}{32}(9-27\eta-9\eta^2+27\eta^3)(1-\xi)$												

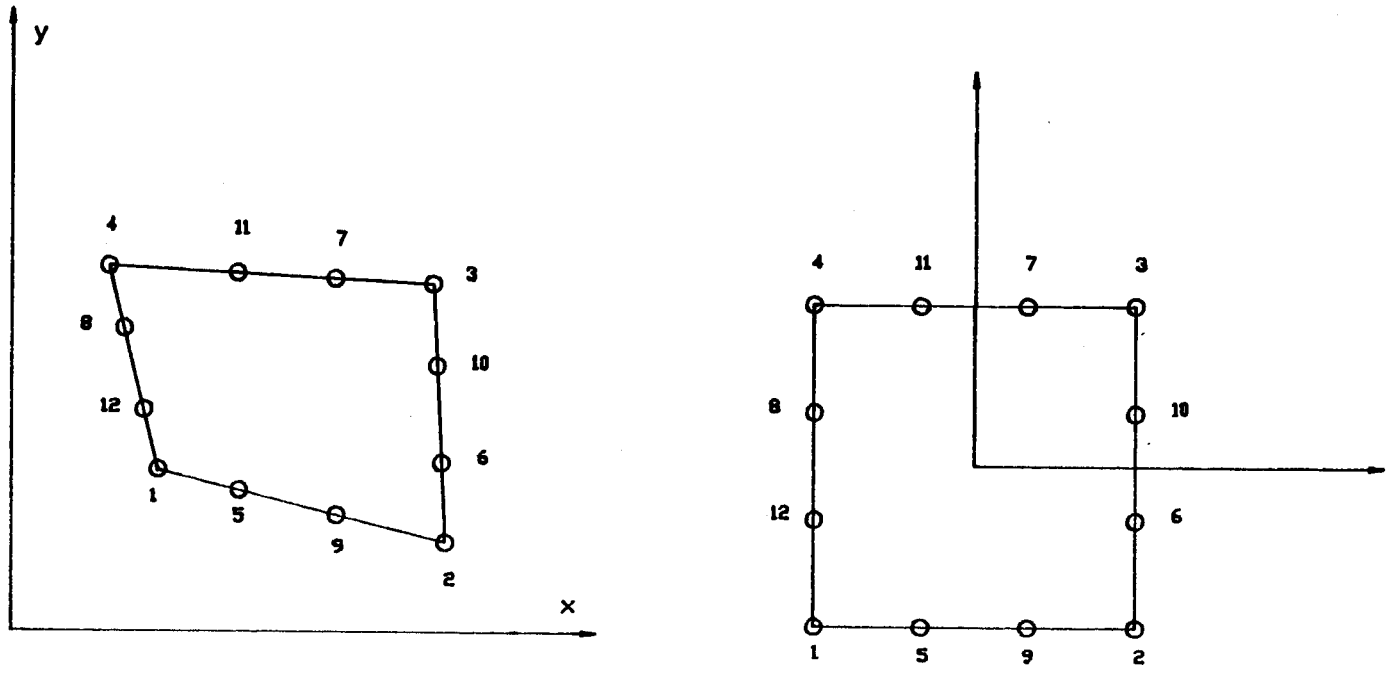

(a) Element in Global Coordinates

(b) Element in Natural Coordinates
'Parent Element'

Fig. A1.1 Isoparametric Variable-Number-Node Element

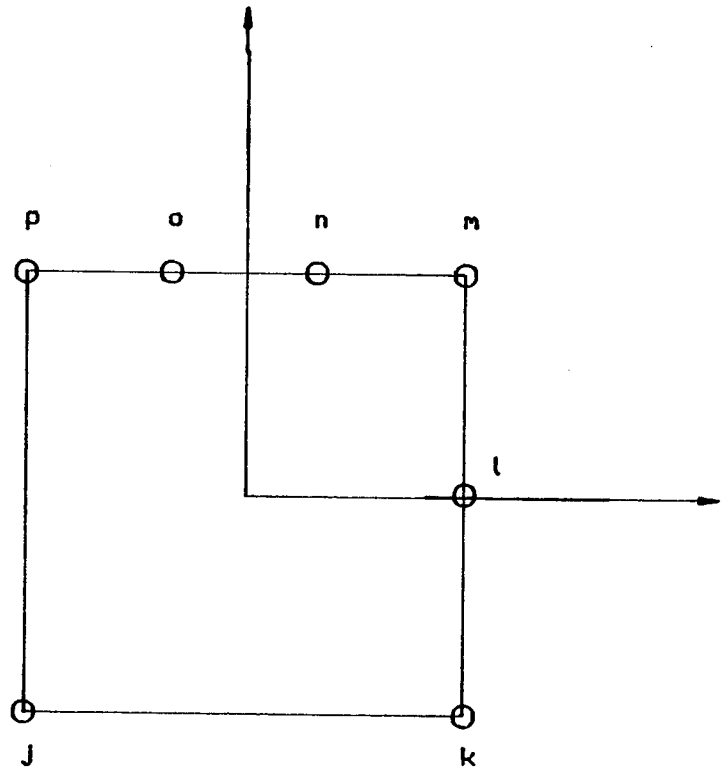

Fig. A1.2 Seven-node Isoparametric Element

APPENDIX A2

STRAIN TRANSFORMATIONS

Referring to Figs. A2.1a and A.2.1b,

BOA = $2\theta'$

since BO = AO (Both radii)

OBA = $90 - \theta'$

which leads to, in ΔBCA, BAC = θ'

$$\tan \theta' = \frac{BC}{CA} = \frac{-\varepsilon_2 + \varepsilon_x}{\left(\frac{\gamma_{xy}}{2}\right)} \qquad (A2.1)$$

Since ΔBAC and ΔDEF are similar, FED = θ'

$$\tan \theta' = \frac{FD}{FE} = \frac{\varepsilon_1 - \varepsilon_y}{\left(\frac{\gamma_{xy}}{2}\right)} \qquad (A2.2)$$

Since ADE = 90°, and FDE = $90 - \theta'$, CDA = θ'

In ΔCDA,

$$\tan \theta' = \frac{\left(\frac{\gamma_{xy}}{2}\right)}{\varepsilon_1 - \varepsilon_x} \qquad (A2.3)$$

Substituting for $\left(\frac{\gamma_{xy}}{2}\right)$ from Eq. (A2.2) into Eq. (A2.3) yields

$$\tan^2 \theta' = \frac{\varepsilon_1 - \varepsilon_y}{\varepsilon_1 - \varepsilon_x} \qquad (A2.4)$$

Substituting for $\left(\frac{\gamma_{xy}}{2}\right)$ from Eq. (A2.1) into Eq. (A2.3) yields

$$\tan^2 \theta' = \frac{-\varepsilon_2 + \varepsilon_x}{\varepsilon_1 - \varepsilon_x} \qquad \text{(A2.5)}$$

Substituting for $\left(\frac{\gamma_{xy}}{2}\right)$ from Eq. (A2.1) into Eq. (A2.2) yields

$$\varepsilon_1 + \varepsilon_2 = \varepsilon_x + \varepsilon_y \qquad \text{(A2.6)}$$

Equations A2.1, A2.4 and A2.6 are Eqs. 4.18 of Sect. 4.2.4.

Appendix A2 - Strain Transformations

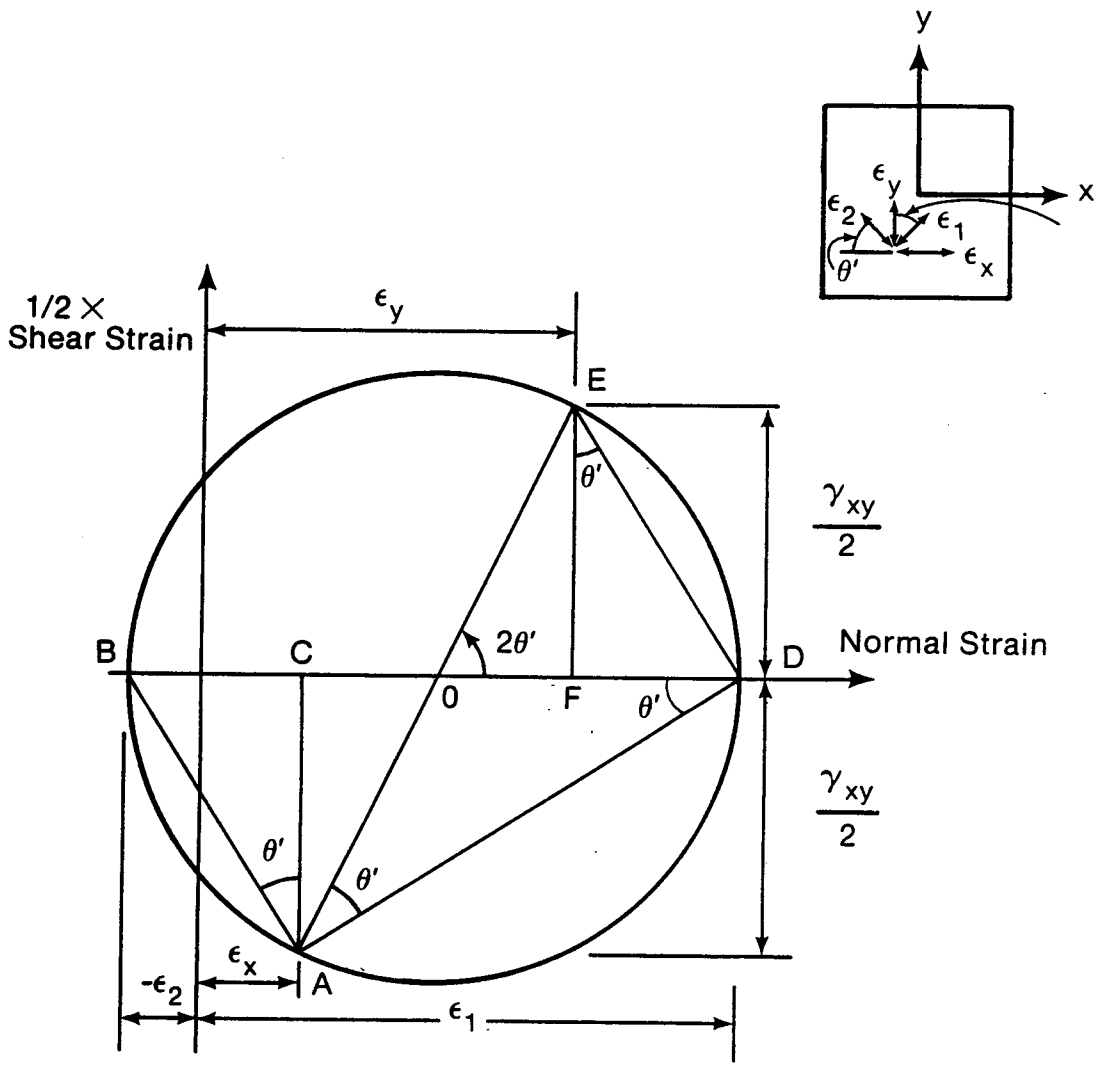

FIG. A2.1. Mohr's Circles of Strain

APPENDIX A3

STUDY OF MODELING PARAMETERS FOR NONLINEAR FINITE ELEMENT ANALYSIS

A3.1 Introduction

The interaction between material modeling, spatial discretization and solution procedures directly influences the behavior predictions that are made using the finite element analysis. The degree of accuracy of the material model should be viewed in light of the errors due to spatial discretization and solution algorithms.

In this Appendix, some 'patch tests' made on the solid, reinforcing and bond element formulations described in Chapter 2 are discussed. The influence of various modeling parameters, such as, order of the element, order of numerical integration, mesh size and layout, is briefly described.

A3.2 Studies on Bond Element Formulation

The embedded formulation of the bond element described in Chapter 2, Sect. 2.4.2, was verified by its application to the analysis of a tension-pull specimen tested by Broms (ASCE, 1982). This specimen was also analysed using the FEM by Nilson, Houde and Khouzam (ASCE, 1982). Since this part of the study is concerned with the verification of the embedded formulation of the bond element, the results of this analysis will be compared to those by Khouzam (ASCE, 1982) who modeled the bond zone using cracked concrete elements.

The specimen and the finite element mesh layout are shown in Fig. A3.1. Since the specimen is symmetrical about two axes, only one quarter of the specimen is modelled, with the appropriate boundary

conditions. (Note that it is not necessary to place the steel at the boundary of the solid elements, but this configuration gives the best model for the problem under consideration.)

With the embedded formulation for reinforcement, external load cannot be applied directly to reinforcement. Load is applied to concrete and to the slip d.o.f. to result in load being applied to the reinforcing bar, as shown in Fig. A3.1. In this figure, tension R is applied to the reinforcing bar by applying R to concrete node (number 8) and R to the slip degree of freedom (number 22). When the location of reinforcement does not coincide with boundary nodes, work equivalent loads are applied to the concrete nodes, i.e., the load R is apportioned to the nodes such that

$$R_i = \phi_i(\xi_s) \quad \text{and} \quad \Sigma R_i = R$$

where $\phi_i(\xi_s)$ is the shape function corresponding to node i evaluated at the natural coordinate location of the reinforcement, ξ_s, and R_i is the lod apportioned to node i.

Concrete is assumed linear elastic and bond stiffness is held constant at 2000 ksi/in (543 MPa/mm). The stress distribution in steel and the bond stress distribution are shown in Fig. A3.2a and b for load P of 4 kips (17.8 kN), 8 kips (35.6 kN) and 12 kips (53.4 kN). It is seen that bond stress is negligibly small in the middle half-length of the specimen while the maximum bond stress at the end of the specimen increases with the load. The stress in the steel also increases with load, but at the center is less than half the applied load. If the specimen is considered analagous to a segment of concrete between two

adjacent cracks in the tension zone of a beam, it can be deduced, from the proportionality of stress distribution to applied load, that the stiffness of this segment remains constant if the crack pattern is stabilized and if the bond stiffness remains constant.

The stress distribution in concrete along the length of the specimen is shown in Fig. A3.3 for a load of P = 14 kips (62.3 kN). It is seen that the stress is approximately constant in the mid half-length of the specimen (which is to be expected since the bond stress is negligible in this length). Over this middle segment a plane sections remain plane condition has essentially been achieved. Towards the end of the specimen considerable distortion of the cross-section occurs. Although there are some points of high local tensile stress at the loaded end of the specimen, the average stress in concrete is greater in the mid half-length. Thus, one or more cracks may form through the entire depth of the specimen anywhere in the midlength.

In order to investigate the effect of crack formation on the bond stress distribution, three cracks were introduced in the model, one at a time, as shown in Fig. A3.4. The first crack was introduced at the midlength of the specimen. The second and third cracks were introduced at equal distances from the previous crack, as shown in Fig. A3.4. The cracks were modeled by the physical separation of the adjacent nodes and the reinforcing bar crossing the crack was modeled as a truss element. The displacement interpolation matrix for this truss element is given by

$$u_s = \left\langle 1 - \frac{x}{L} , \frac{x}{L} , 1 - \frac{x}{L} , \frac{x}{L} \right\rangle \begin{Bmatrix} U_{ci} \\ U_{cj} \\ U_{bi} \\ U_{bj} \end{Bmatrix}$$

where U_{ci} and U_{cj} are the displacements at the concrete nodes, U_{bi} and U_{bj} are the displacements at the slip degrees of freedom, u_s is the displacement of the truss element (steel reinforcement) at coordinate x and L is the length of the truss element (i.e. width of crack). The strain-displacement matrix and the stiffness matrix are obtained from the displacement interpolation matrix as described in Chapter 2.

The resulting distributions of bond and steel stresses are shown in Fig. A3.5a and A3.5b respectively for a load level of P = 14 kips (62.3 kN). It is seen that: (1) tension stiffening decreases with decrease in crack spacing, because the average stress and strain in the steel increase; and, (2) the maximum local bond stress decreases, although only by a small amount, with decrease in crack spacing.

The bond stress, steel stress and concrete stress distributions may be compared to those obtained by Khouzam (ASCE, 1982) shown in Fig. A3.6a, b, c and d. It is seen that the distributions are similar, equilibrium is satisfied and hence the bond element formulation is verified.

A3.3 Studies on Solid Element Formulation

A3.3.1 Stiffness Characteristics

A3.3.1.1 Introduction

Stiffness characteristics of solid elements for use in a linear elastic analysis have been now well established (see for example, Zienkiewicz, 1977) for reduced as well as full integration. However, the numerical behavior of cracked concrete elements has not been studied as extensively.

Dodds et al. (1982) studied the stiffness characteristics of unreinforced cracked elements with varying crack orientations using eigenanalyses on the element stiffness matrices. Eigenvalues of a stiffness matrix are proportional to the strain energy generated when an element is deformed in the shape of the corresponding eigenvector. Rigid body motion generates no strain energy and thus is associated with a zero eigenvalue.

A3.3.1.2 Eigenvalue Analysis of Cracked Concrete Elements

The results of eigenanalysis by Dodds et al. are summarized in Table A3.1 for elements of the type illustrated in Figs. A3.7a and b. Three of the zero eigenvalues in the table correspond to the three rigid body motions (two translations and one rotation). As seen from the table, the linear serendipity element with a system of parallel cracks has one additional zero eigenvalue whereas the fully integrated quadratic element has three additional zero eigenvalues. However, in most practical problems, cracks form with varying orientations at different Gauss points inside an element. Both the linear and fully integrated quadratic elements with randomly oriented cracks (Fig. A3.7b) have no zero energy deformation modes in excess of the three required for rigid body motion. For the linear element, altering the orientation of just one of four initially parallel cracks eliminates the single excess zero energy mode. In a fully integrated quadratic element, the three excess zero energy modes are eliminated by varying the orientation of just three (of nine) initially parallel cracks. The quadratic element with reduced integration, however, has eight zero energy modes irrespective of the crack orientations. Moreover, the formation of each

crack at any Gauss point in this element introduces a zero energy deformation mode, i.e., an element with one cracked Gauss point has a total of five zero energy modes of deformation.

A3.3.1.3 Eigenvalue Analysis of Cracked, Reinforced Concrete Elements

In this study, the effect of embedding the reinforcement on the stiffness characteristics of the solid element was investigated. The results are summarized in Table A3.2 for the elements shown in Fig. A3.7d and e. The provision of reinforcement, as shown (in two directions), eliminates all the excess zero energy modes even when reduced integration is used. Thus reduced integration may be used for net reinforced elements. Even for elements reinforced in one direction only and for unreinforced elements reduced integration may be used if the element, when assembled in the structure, is restrained such that spurious zero energy modes are not activated. In shear critical beams, where the cracked elements must resist shear and compression, the behavior prediction becomes unreliable if the cracked elements have spurious zero energy modes.

A3.3.2 Linear Versus Quadratic Elements

A3.3.2.1 Introduction

Bilinear serendipity elements are too stiff in bending because of the shear distortion that must accompany the flexural deformation. This is illustrated in Fig. A3.8 (Doherty et al., 1969). The inaccuracy of results with this element increases with the L/H ratio. A number of methods have been proposed to reduce or eliminate the spurious shear energy such as selective integration and addition of incompatible modes

(Cook, 1981). Selective integration involves sampling the shear strain at the center of the element while the normal strains are sampled at the Gauss points. An explanation of how selective integration alleviates this problem follows.

The displacement interpolation functions for the bilinear element are given by

$$u = a_o + a_1\xi + a_2\eta + a_3\xi\eta \tag{A3.1a}$$

$$v = b_o + b_1\xi + b_2\eta + b_3\xi\eta \tag{A3.1b}$$

where ξ and η are the natural coordinates and a_o, b_o etc. are constants.

The shear strain is given by

$$\gamma_{\xi\eta} = \frac{\partial u}{\partial \eta} + \frac{\partial v}{\partial \xi} \tag{A3.2}$$

$$= a_2 + a_3\xi + b_1 + b_3\eta \tag{A3.3}$$

The constant shear strain modes and the spurious shear strain modes associated with bending deformation are indicated in Fig. A3.9a and b, respectively. The $a_3\xi$ and $b_3\eta$ terms in Eq. A3.3 arise from the $\xi\eta$ term in Eqs. A3.1, and produce the spurious shear strains indicated in Fig. A3.9b. If the shear strains are evaluated only at $\xi = 0 = \eta$, the spurious strain corresponding to the $\xi\eta$ term will disappear whereas the terms corresponding to the constant shear strain will remain.

A3.3.2.2 Analyses by Dodds et al. (1982)

Dodds et al. (1982) made the following observations from their analyses on shallow and deep beams. No attempt was made in their analyses using linear elements to avoid spurious shear strains.

1. Linear elements, because of the spurious shear strains associated with them, exhibit erratic crack pattern with coarse mesh layout. For example, at least 5 elements through the depth were required for R/C beam analyses in order to obtain a reliable crack pattern.

   In a quadratic element, all the Gauss points may not have cracked even after the crack pattern has been stabilized, whereas in a linear element all the Gauss points are cracked or none at all.

2. For beams in which the load carrying mechanism remains the same throughout the entire load range, the load deflection curves and failure loads predicted using the linear elements are essentially the same as those using fully integrated quadratic elements, for a fine mesh layout. Whereas, in beams where a change in the load carrying mechanism occurs (as in a deep beam where the change from beam behavior to tied arch behavior occurs) the load deflection behavior predicted using linear elements is stiffer than that using quadratic elements for the same total number of degrees of freedom. Also the predictive load at which the transition from a beam to tied arch mechanism occurs depends on the element type. However the predictive failure load is the same using linear and quadratic elements.

3. Both linear elements and fully integrated quadratic elements

exhibit monotonic convergence with grid refinement.

In their analyses, Dodds et al. investigated beams which invariably achieved stable equilibrium configurations following extensive crack formation, when load had been transferred to the reinforcement, and all the beams failed in a ductile manner by steel yielding. They used a tension cut-off criterion. Also, they did not analyse any test beams in order to make comparisons to experimental data.

A3.3.2.3 Analysis of a Shear-Critical Shallow Beam

In this study, a shear critical beam tested by Bresler and Scordelis, Beam XOB-1, was analysed by modeling it in turn with linear elements and quadratic elements with approximately the same total number of nodes. This beam, with a shear span to depth ratio of approximately 4.0, failed in the test in diagonal tension (the reinforcement did not yield at failure). Tension softening and tension stiffening were combined and represented by the descending branch of the average tensile stress-strain curve for concrete as described in Sect. 3.5. A constant shear retention factor of 0.4 was used. The mesh layouts for linear and quadratic elements are shown in Fig. A3.10a and b respectively. The input material parameters are indicated in Table A3.3.

The load deflection behavior predicted from the analysis is shown in Fig. A3.11. It is seen that the predicted behavior is essentially identical with linear and quadratic elements and shows reasonable agreement with the behavior observed in the test. The predicted crack patterns are shown in Figs. A3.12a and b and can be compared to that observed in the test which is shown in Fig. A3.12c. It is seen that there is no significant difference between the crack patterns predicted

using linear elements and quadratic elements.

Thus it can be concluded that linear and quadratic elements, for the same total number of d.o.f., lead to essentially the same predictions of the behavior of shallow beams wherein the load carrying mechanism does not change.

A3.3.2.4 Analysis of a Deep Beam

In their analyses which assumed a constant shear retention factor of 0.4, Dodds et al. (1982) observed signficant difference in the predicted load deflection behavior of deep beams (wherein the load carrying mechanism changed from beam action to arch action) when linear elements and quadratic elements were compared, although the predicted failure load was approximately the same. (Since the predicted failure mode was by steel yielding, it would be expected that the same failure load is predicted.) They also found that the load corresponding to a change in the load carrying mechanism (from beam to truss action) depends on the type of the element.

In this study, the effect of the element type on the predicted behavior of deep beams has been investigated by analysing a deep beam which failed by concrete crushing. This beam, with a shear span to depth ratio (a/d ratio) of 1.0, was tested by Rogowsky and MacGregor (1983). The beam details are shown in Fig. A3.13. Stirrups were provided at only one end of the beam. The beam was loaded and supported through column stubs cast integrally with the beam.

In the test, major inclined cracks developed 'almost instantaneously' at a jack load of about 350 kN. The observed crack pattern is shown in Fig. A3.14. After inclined cracking, the behavior

was essentially that of a truss or tied-arch. The stirrups crossing the major inclined crack in the North shear span were at or near yield at failure. Some of these stirrups reached yield at 50 to 60 percent of the failure load. Failure occurred in the North end (which contained stirrups) by concrete crushing at a load of 1204 kN. The beam was then externally reinforced and retested until compression failure occurred in the South end of the beam as well at a load of 1397 kN.

The finite element mesh layout using quadratic elements is shown in Fig. A3.15 and that using bilinear elements is shown in Fig. A3.16. Since the beam is symmetrical except for the presence of web reinforcement in one half span, only half the span is modelled excluding the web reinforcement. (Since a number of stirrups in the test yielded shortly after cracking, their presence is not considered to alter significantly the behavioral symmetry.) The input material parameters derived from specimen tests and reported by Rogowsky and MacGregor are shown in Table A3.4.

In the finite element analysis, approximately 10 load steps were used. (This compares with 7 load steps used in the test.) The first load step in numerical analysis was 400 kN and subsequent load steps were 100 kN. A convergence tolerance of 0.1% on the incremental displacement norm and 1.0% on the unbalanced force vector norm were used. The standard Newton-Raphson iterative scheme with structure stiffness matrix updated every iterate was used.

Failure in numerical analysis occurred when a negative element appeared in the main diagonal of the tangential structure stiffness matrix. For the quadratic elements, this occurred at a total load of 1100 kN. The size of the load step was subsequently reduced to 40 kN

and the iterative procedure converged up to a total load of 1180 kN. For the linear elements, the failure in convergence, again as manifested by a negative element on a main diagonal, occurred at a total load of 1200 kN. Any reduction in the size of the load step beyond this level did not produce convergence. Thus the failure load using bilinear elements is taken as 1200 kN while that using quadratic elements is taken as 1180 kN. This compares with the test values of 1204 kN and 1397 kN.

The load deflection curves using quadratic elements and linear elements are shown in Fig. A3.17. The load-deflection curve, labelled 'test', has been adjusted for support settlement, as described in the report by Rogowsky and MacGregor (1983). It is seen that quadratic elements, for approximately the same total d.o.f., predict a softer load deflection response at higher load levels than bilinear elements. The increased stiffness of the bilinear elements might be attributed to the spurious shear energy associated with these elements. This becomes significant after cracking, when the deflection due to shear is considerably more important.

The predicted load range corresponding to a change in the load carrying mechanism (from beam action to truss or arch action) is the same with bilinear elements and quadratic elements. This is seen by comparing the crack pattern for four load steps, shown in Figs. A3.18 to A3.21 (the crack pattern is essentially stabilized at a load of 400 kN) and the load-deflection response shown in Fig. A3.17. This behavior is in contrast to the findings of Dodds et al., whose finite element analysis on deep beams showed that the transition load predicted using linear elements to be significantly higher than that using quadratic

elements. This difference might be attributed to the tension cut-off criterion they have used whereas the analysis herein used a descending branch in the tensile stress-strain relation with $\varepsilon_{ut} = 0.0009$, as indicated in Table A3.4.

The failure mode has been correctly predicted using bilinear elements as well as quadratic elements. Figures A3.22 and A3.23 show the compression strain hardening or strain softening regions. (These are shown by lines at Gauss points with arrowheads at both ends. A cross with arrowheads on both lines indicates that the Gauss point has entered the compression hardening region, (-1), or softening region, (-2), and had cracked in tension at a previous load step.) Although bilinear elements have more Gauss points in the hardening/softening region, the crushing of the compression 'strut' is apparent in both element types. The compression 'strut' may be more easily identified in the principal stress plot shown in Figs. A3.24 and A3.25.

The distributions of steel strains predicted using linear elements and quadratic elements are compared to the strain gage measurements in Fig. A3.26. Both the linear elements and quadratic elements predict closely the distribution of steel strains. The linear elements, being stiffer, predict lower steel strains.

Thus it can be concluded that linear and quadratic elements give comparable results for load deflection response, cracking patterns, failure loads, failure modes and distribution of stresses.

A3.3.3 Effect of Mesh Refinement

A3.3.3.1 Introduction

As for all linear finite element analyses, mesh refinement also has

some effect on the computed results in the nonlinear material analysis. However, Bazant and Cedolin (1980), based on their studies on a reinforced concrete panel containing a single crack, found that the crack propagation (i.e., extension) depends on the size of the element if a tensile strength criterion only is used to determine cracking. (Increasing the finite element size by four times, the load that would cause crack propagation in an example problem they selected, was obtained about 3.5 times larger.) Thus they concluded that the use of a tensile strength criterion alone to determine crack propagation does not satisfy the condition of objectivity which requires that the solutions for meshes of different finite element size be the same, except for a negligible numerical error. They proposed that an objective as well as a physically realistic criterion for crack band extension is the value of the fracture energy dissipated during a unit extension of the crack band and that this energy criterion is important for reinforced as well as plain concrete.

There is now general agreement on the need for a fracture mechanics based approach when the propagation of individual cracks in massive structures (such as dams and large bridge girders) is of interest. However, in the analysis of common reinforced concrete structures such as beams and panels that develop numerous cracks, the need for an energy criterion has been disputed (Dodds et al., 1982).

In order to investigate the effect of mesh refinement on the computed response of reinforced concrete structures, Dodds et al. (1982), investigated shallow and deep beams with varying element sizes. A partial summary of results from their numerical analysis has been given in Sect. A3.3.2. All the beams they investigated invariably

achieved stable equilibrium configurations following extensive crack formation when load had been transferred to the reinforcement and failed in a ductile manner by steel yielding. They used the tension cut-off criterion alone (i.e. stress based approach). Based on their analyses, they concluded that a stress-based approach (ignoring fracture energy considerations) is adequate to determine the overall response of these beams. The load deflection response converged to the same solution with grid refinement. The failure loads predicted by the coarse mesh and fine mesh were essentially the same.

Included in the study by Dodds et al. (1982) on the effect of mesh refinement was a deep beam (with shear-span to depth ratio of 1.0) that they identified as being 'shear critical'. (In fact this beam is not 'shear critical' since the failure mode is ductile flexure, i.e. the full flexural capacity has been attained at failure.) Their analysis of this beam indicated that the transition load at which a change in the load carrying mechanism occurs (from beam action to truss action) is sensitive to the element size but the failure load is not.

The same deep beam was also analysed by Bazant and Cedolin in the 1982 closure to the discussion of Bazant and Cedolin (1980), who investigated the effects of ignoring the fracture energy criterion. Bazant and Cedolin used very small load steps and varying grid layouts. They found that the load required to extend cracking at midspan to a specific height depended on the element size used if the fracture energy criterion is ignored. Whereas if an equivalent strength, based on fracture energy considerations, is adopted this load was relatively independent of the mesh size.

A3.3.3.2 Mesh Refinement Study of a Deep Beam

In this study, the effects of mesh refinement are investigated by analysing the deep beam (shear span to depth ratio of ≃ 1.0) tested by Rogowsky and MacGregor (1983) which was analyzed in Sect. A3.3.2. The coarse mesh layout for this beam is shown in Fig. A3.27. The results of the analysis using this mesh of linear elements can be compared to those obtained using the finer mesh shown in Fig. A3.16. The input material properties are shown in Table A3.4. Two analyses were made with the coarse mesh layout; one with $\varepsilon_{ut} = 0.0009$ which is the same as that used for the fine mesh layout and another with $\varepsilon_{ut} = 0.00045$ (i.e., using the same fracture energy release rate as for the fine mesh).

The load versus midspan deflection relationships obtained from the analyses are shown in Fig. A3.28. The analysis using the fine mesh layout correctly predicts the failure mode as being brittle (i.e concrete crushing with no steel yielding), whereas those using the coarse mesh layout predict ductile failure mode (steel yielding before concrete crushing). Of particular interest is the difference in the behavior predictions using the same fracture energy release rate for both fine and coarse mesh layouts. The coarse mesh layout with ε_{ut} of 0.00045, although less stiff than with $\varepsilon_{ut} = 0.0009$, fails to predict the correct failure mode and load. This may be explained as follows.

Stresses and 'damage regions' are calculated only at Gauss points. However, the 'failure' of the structural system (i.e., beam or panel in this study) is assumed to have been reached only if one or more nodes become unsupported in one or more d.o.f. Such local failure at a node occurs only if all the elements connected to this node fail. An element can fail only if the combined contribution to the load capacity

of all the integration points within that element decreases with increase in load. Thus, when significant strain gradient is present, larger elements (i.e. elements significantly larger than the strain-softening region) 'contain' the local damaged zones whereas smaller elements 'are contained' in the damaged zones.

This is evident when the compression strain softening region for the Rogowsky-MacGregor Beam at a load of 1200 kN for the coarse mesh layout (with ε_{ut} = 0.00045), shown in Fig. A3.29, is compared to that for fine mesh layout (with the same fracture energy release rate) shown in Fig. A3.23. Although the extent of the compression softening region (as indicated by lines/crosses with arrowheads) is essentially the same in both cases, the fine mesh layout predicted failure at this load whereas the coarse mesh layout did not. The coarse mesh layout predicts compression failure only when the softening has progressed through a number of adjacent elements, as shown in Fig. A3.30.

Thus, it can be concluded that for this deep beam the spatial discretization has a significant effect on the failure load prediction and this effect has not been eliminated using fracture energy considerations.

The objectivity with respect to crack extension (propagation) may be deduced by comparing the crack patterns at 800 kN load level for the coarse mesh layout with ε_{ut} = 0.00045 (Fig. A3.31) and ε_{ut} = 0.0009 (Fig. A3.32) and for the fine mesh layout (Fig. A3.21b). It is seen that with ε_{ut} adjusted, based on mesh size to obtain the same fracture energy release rate, the crack pattern and the extent of crack propagation are essentially the same for both fine and coarse mesh layouts (Figs. A3.21b and A3.31) whereas the coarse mesh layout with no

adjustment of ε_{ut} for mesh size has resulted in reduced crack height and a fewer number of cracked elements. However, the predicted failure load is not significantly different for the two coarse mesh layouts (1440 kN vs. 1480 kN).

A3.3.3.3 Mesh Refinement Study of a Shallow Beam

Because the failure of the Rogowsky/MacGregor deep beam was by compressive failure of the concrete 'strut', a more appropriate example for illustrating the need for fracture energy considerations in cracking problems might be a reinforced concrete beam failing in the diagonal tension mode. In this study, the Bresler-Scordelis beam X0B-1, with a shear span to depth ratio of 4.0 was also investigated with different mesh layouts. The coarse mesh layout of quadratic elements is shown in Fig. A3.33. The results using this layout may be compared to those using the finer mesh layout shown in Fig. A3.10b.

Two analyses were performed with coarse mesh layout, one with ε_{ut} = 0.0014 (same as fine mesh) and the other with ε_{ut} = 0.0005 (to give approximately the same fracture energy release rate as fine mesh). The crack shear modulus was taken as

$$G_{cr} = \left(\frac{0.0014 - \varepsilon}{0.0014 - \varepsilon_{cr}}\right) G \qquad \text{(A3.4)}$$

in all three cases. Convergence tolerances of 0.1% on the incremental displacement vector norm and 1.0% on the unbalanced force vector norm were used. A load step size of approximately 10 per cent of maximum load was used. The standard Newton Raphson iterative procedure with the stiffness matrix of structure updated every iterate was adopted.

The load versus midspan deflection curves are shown in Fig. A3.34. It is seen that the coarse mesh layout with ε_{ut} = 0.0014 and the fine mesh layout, also with ε_{ut} =0.0014, exhibit essentially the same load deflection behavior except that failure of convergence occurs at a lower load for the fine mesh layout (37 kips (165 kN) compared to 44 kips (195 kN)) for coarse mesh layout). The coarse mesh layout with ε_{ut} = 0.0005 shows a significantly more flexible load deflection response, especially at higher load levels.

The analytical crack pattern for three different load levels are shown in Figs. A3.35a through A3.37c for each of the three cases. It is seen that the crack pattern using the coarse mesh layout with ε_{ut} = 0.0014 is essentially the same as for the fine mesh layout (also with ε_{ut} = 0.0014) at loads 22 kips (98 kN) (Figs. A3.35) and 32 kips (142 kN) (Figs. A3.36), whereas some 'crack localization' and greater crack height are seen with the fine mesh layout at a load level of 37 kips (165 kN) (Figs. A3.37). The crack patern for the coarse mesh layout with ε_{ut} = 0.0005 shows greater height and extent of cracks at higher load levels.

Thus, for this beam, adjustment of ε_{ut} (i.e. the descending branch of the tensile stress strain curve of concrete) based on the mesh size leads to different crack patterns whereas the crack pattern remains essentially constant for different mesh sizes if ε_{ut} is held constant. This is in direct contrast to the case of the propagation of a single crack in a notched member wherein objectivity with respect to mesh refinement is obtained only if ε_{ut} is adjusted based on the element size at the crack tip. The difference in the predicted failure loads using the fine and coarse mesh layouts with the same ε_{ut} is attributable to

the strain gradient along the span length and is related to the load at which elements connected to a node start to decrease in stiffness, as explained for the Rogowsky-MacGregor deep beam. However, in this shallow beam the reduction in stiffness is associated with the cracking in the tension zone which reduces the shear stiffness.

It must be emphasized that the difference in the mesh layouts selected for comparisons were somewhat high. This was done in order to readily identify the effects of element size and layout. Some guidelines may be established for selecting the mesh size from the foregoing.

A3.3.3.4 Selection of Mesh Size

A number of investigators (for instance, Rots et al., 1985; Glemberg and Samuelsson, 1984; and, Crisfield, 1984) have used the following Eq. A3.5 to determine ε_{ut} when analysing shear critical beams with h as the length tributary to a Gauss point. That is,

$$\varepsilon_{ut} = \frac{2G_F}{f'_t h} \qquad \text{(A3.5)}$$

However, as discussed in Chapter 3, Sect. 3.7.2, Eq. A3.5 relates to the propagation of a single crack. In R/C beams a number of cracks develop at different spacings in the tension zone, based on such parameters as the depth of the tension zone, reinforcement ratio and bond characteristics of reinforcement. In order to obtain objective results with respect to mesh refinement for these beams (i.e., to obtain the same load displacement response in the tension zone independent of the mesh size) it is appropriate to use in Eq. A3.5 the value of h as

the expected crack spacing.

For example, the total elongation of a tension pull specimen of length L, containing cracks at a spacing of h is given by $\frac{L}{h} w_{max}$ where w_{max} is the opening displacement of a single crack when the stress has reduced to zero. In order to obtain this elongation with the smeared crack approach,

$$\varepsilon_{ut} L = \frac{L}{h} w_{max} \tag{A3.6}$$

Since the fracture energy release rate of a single crack is given by the area under the stress-displacement curve of that crack (Eq. 3.1)

$$G_F = \frac{1}{2} f_{tu} w_{max} \tag{A3.7}$$

Substituting for w_{max} from Eq. A3.6 into Eq. A3.7,

$$\varepsilon_{ut} = \frac{2G_F}{f_{tu} h} \tag{A3.8}$$

These two aspects (i.e., crack propagation and correct fracture energy representation) may be reconciled by selecting the mesh size such that the length tributary to a Gauss point is approximately the same as the expected crack spacing. This does not imply a serious limitation on the selection of the mesh size since, as discussed in Sect. 5.10.1, in the practical range of values of ε_{ut} (between say 0.008 and 0.0018) the difference in the predicted failure loads is well within the scatter in experimental results.

In beams where compressive failure of concrete may occur, the mesh

size selected should be such that the local failure of a node does in fact indicate the failure of the structure, unless solution strategies which are able to trace the descending branch of the load-deformation response of the entire structure, are adopted.

A3.4 Conclusions

The following conclusions may be drawn from this study on modeling parameters:

1. The embedded bond element formulation gives results comparable to discrete formulations and offers the advantage that reinforcing elements need not be located at the boundaries of solid elements.
2. Reduced integration may be used if the elements are reinforced in two orthogonal directions. For cracked concrete elements, either unreinforced or reinforced in one direction only, reduced integration may not be used because of the spurious zero energy modes exhibited by reduce integration.
3. There is no significant difference in the behavior predictions of beams using linear and quadratic elements for the same total number of degrees of freedom. For deep beams, models with quadratic elements have an advantage in that such models are somewhat more flexible than those using linear elements.
4. Mesh size and layout has a significant effect on the behavior predictions of beams and this effect cannot be eliminated by simply adjusting the descending branch of the tensile stress-strain curve of concrete (based on the mesh size to obtain the same fracture energy release rate). Some guidelines for the

selection of mesh size have been given in Sect. A3.3.

5. When failure of one or more nodes (as manifested by a zero or negative element on the main diagonal of the tangent structure stiffness matrix) is assumed to indicate the failure of the structure, as is done in this study, the mesh size selected must be such that this local failure does, in fact, relate to the failure of the structure. Failure of a node occurs only when all elements connected to the node fail.
6. With the smeared crack approach, fracture energy considerations can be included in the analysis of a structure with a number of cracks by using the expected crack spacing in place of the width of the crack band in the expression for fracture energy release rate.

Table A3.1

Unreinforced Element Eigenvalue Analysis
(Dodds et al., 1982)

Element Type	Order of Integration	Total D.O.F.	Number of Zero Eigenvalues		
			Uncracked	Parallel Cracks	Random Cracks
Linear	2 x 2	8	3	4	3
Quadratic	3 x 3	16	3	6	3
Quadratic	2 x 2	16	4	8	8

Table A3.2

Reinforced Element Eigenvalue Analysis

Element Type	Order of Integration	Number of Zero Eigenvalues	
		Unconstrained	Constrained
Quadratic, uncracked	3 x 3	3	0
Quadratic, uncracked	2 x 2	3	0
Quadratic, $E_x = 0$	2 x 2	3	0
Quadratic, $E_x = 0$	3 x 3	3	0
Quadratic, $E_{45°} = 0$	2 x 2		0
Quadratic, $E_y = 0$	2 x 2		0

Table A3.3

Input Parameter for Bresler Scordelis Beam XOB-1

Concrete	
E_c, ksi (MPa)	3100 (21375)
G, ksi (MPa)	1300 (8964)
ν, (Poisson's ratio)	0.2
f'_c, ksi (MPa)	3.66 (25.2)
f'_t, ksi (MPa)	0.312 (2.15)
ε_{ut}	0.0014
Steel	
A_s, $in.^2$ (mm^2)	4.0 (2586)
f_y, ksi (MPa)	96.5 (665)
E_s, ksi (MPa)	29000 (199955)
ρ	0.0244
Geometry	
Span, ft (m)	12.0 (3.66)
h, overall depth, in. (mm)	21.8 (554)
b, thickness, in. (mm)	9.1 (231)
d, effective depth, in. (mm)	18.03 (458)
a/d	3.99

Table A3.4

Input Parameters for Rogowsky-MacGregor Beam 1/1.0

Concrete	
E_c (MPa)	20000.0
G (MPa)	8333.0
ν (Poisson's ratio)	0.2
f'_c (MPa)	26.1
f'_t (MPa)	2.28
ε_{ut}	0.0009
G_{cr}	$\left(\frac{0.01 - \varepsilon}{0.01 - \varepsilon_{cr}}\right)$ G
Steel	
E_s (MPa)	200000.0
f_y (MPa)	380.0
E_{sh} (MPa)	10000.0
A_s (mm^2)	1800.0
ρ	0.0095

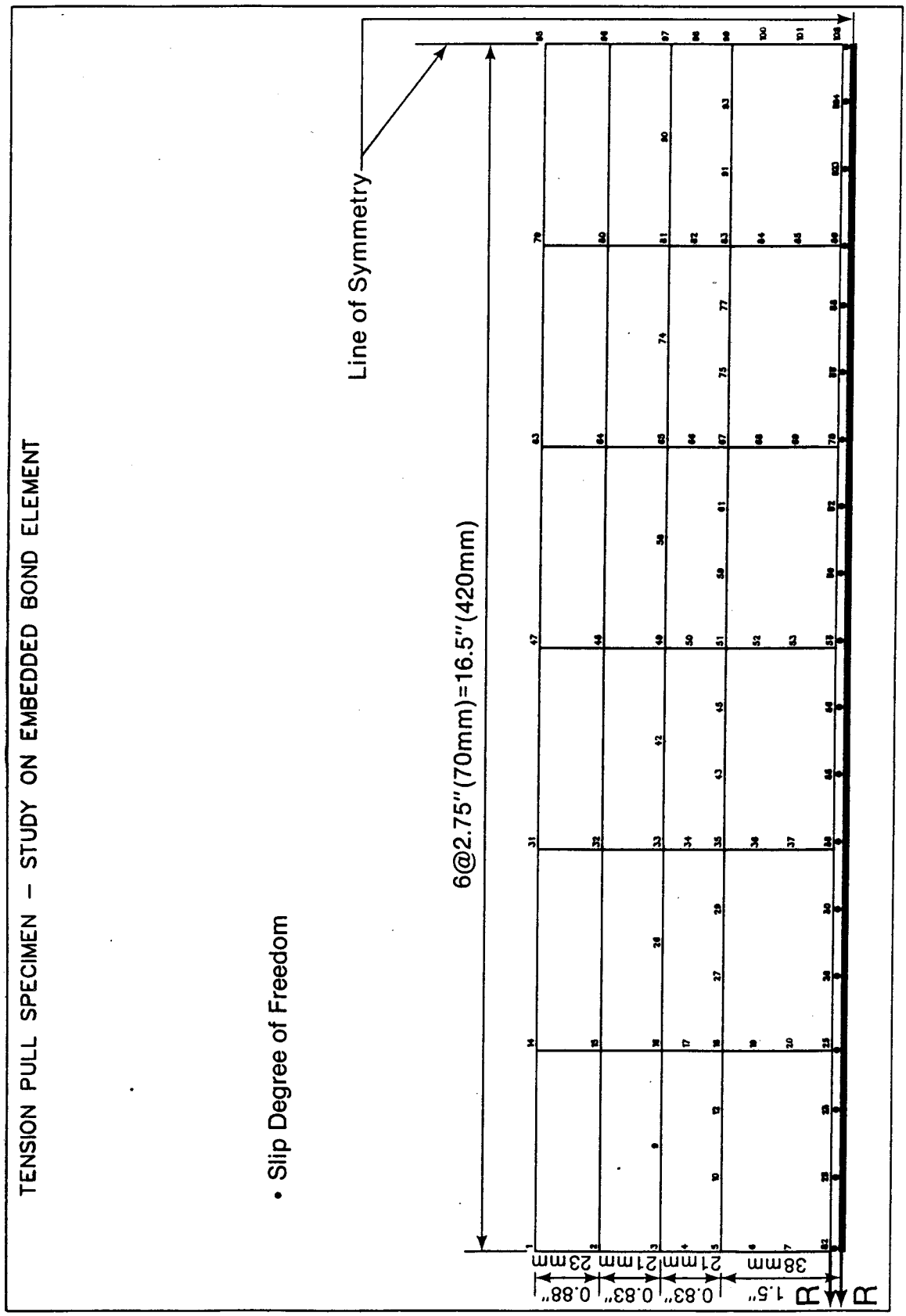

FIG. A3.1. Tension Pull Specimen - Mesh Layout

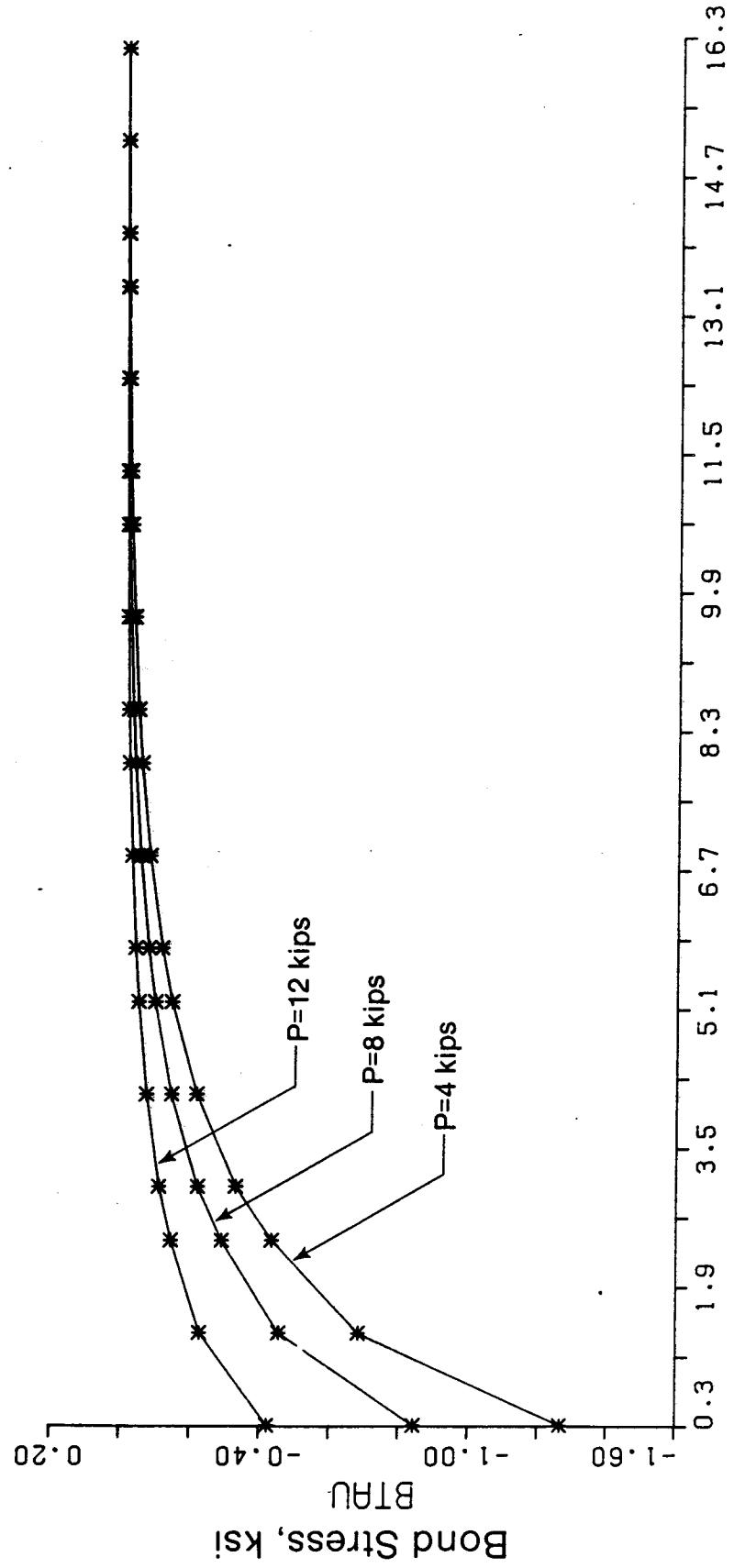

FIG. A3.2. Uncracked Tension Pull Specimen
(a) Bond Stress Distribution (1 ksi = 6.895 MPa; 1 in. = 25.4 mm)

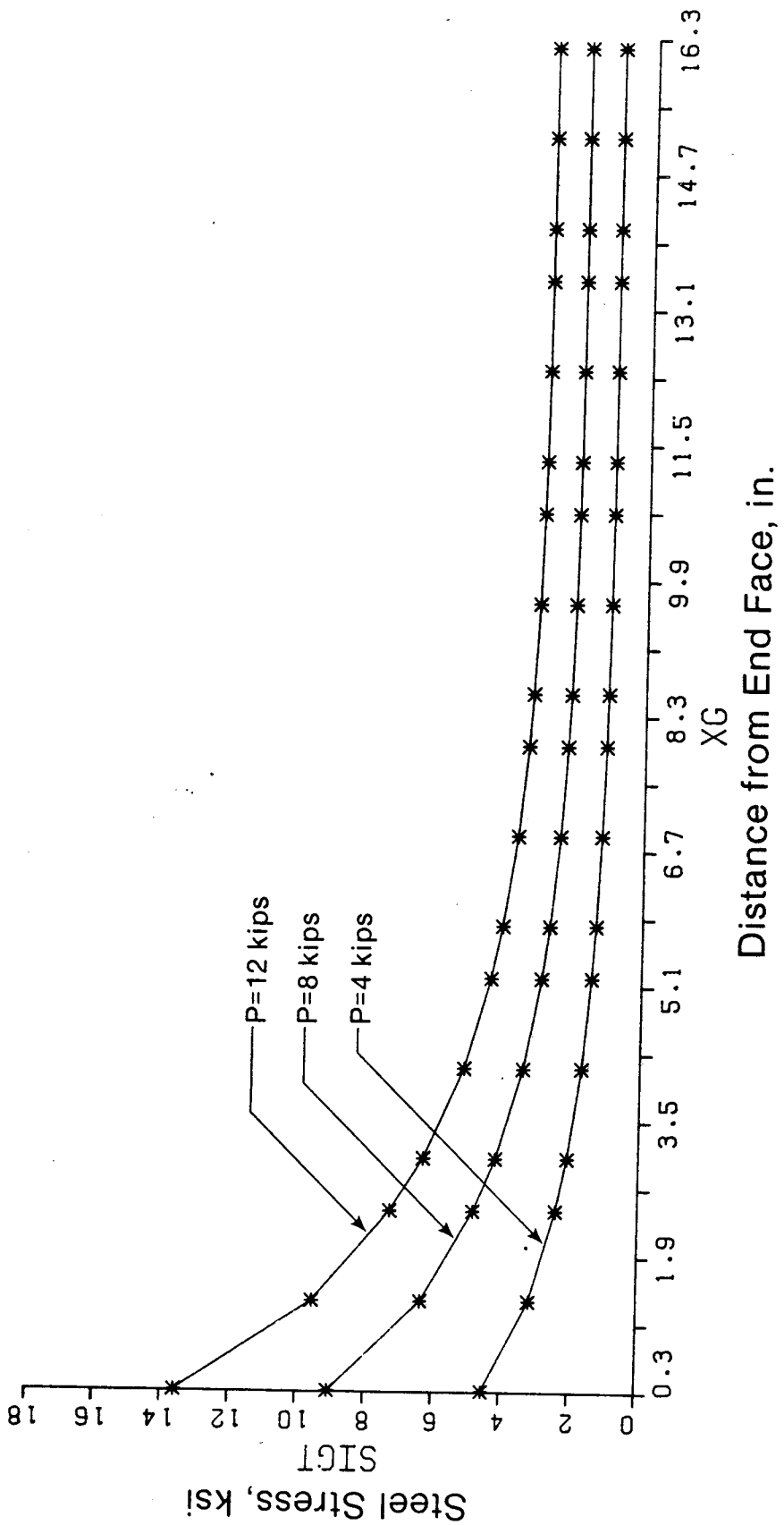

FIG. A3.2. Uncracked Tension Pull Specimen (Continued)
(b) Steel Stress Distribution (1 ksi = 6.895 MPa; 1 in. = 25.4 mm)

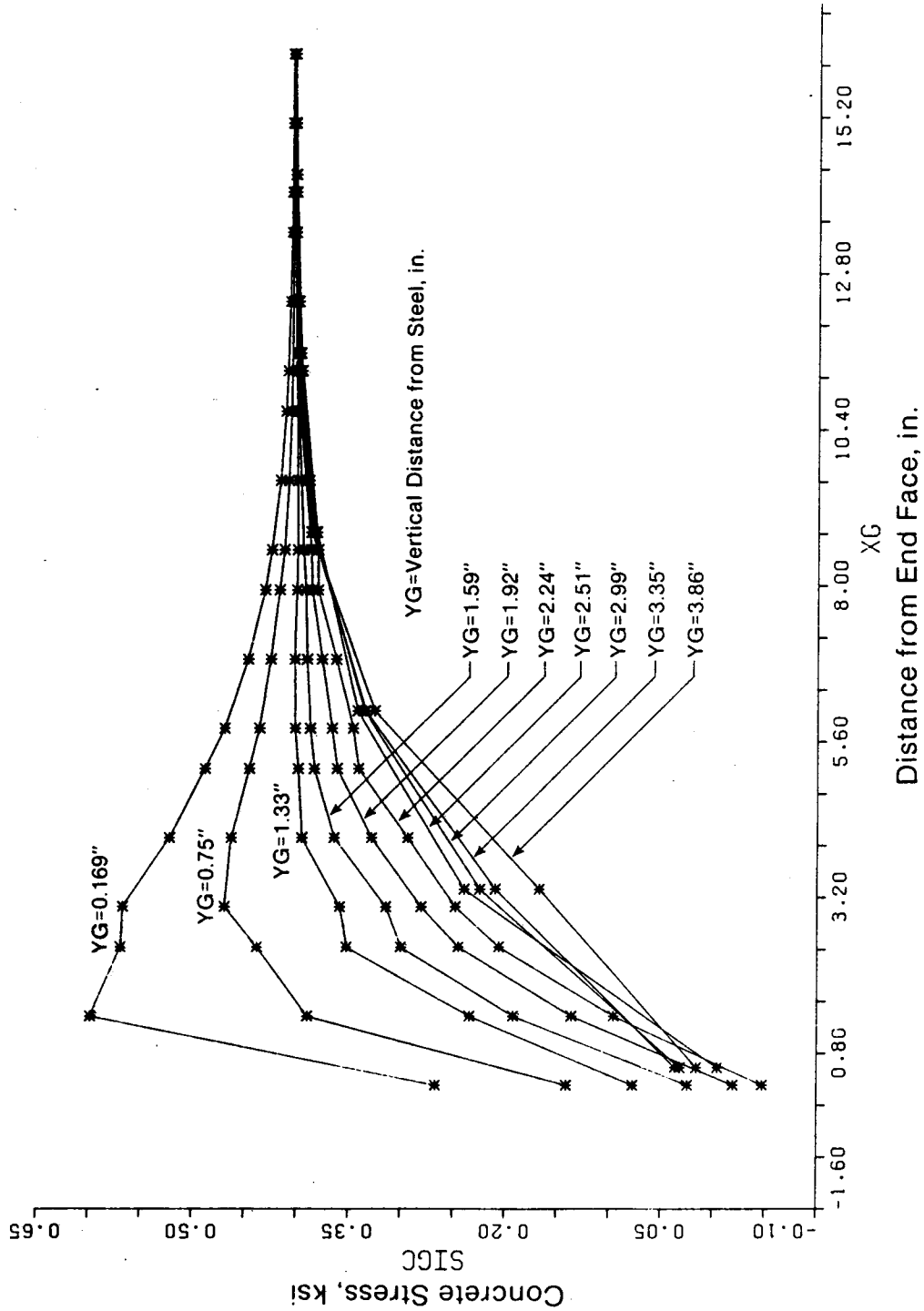

FIG. A3.3. Concrete Stress Distribution - Uncracked Tension Pull Specimen

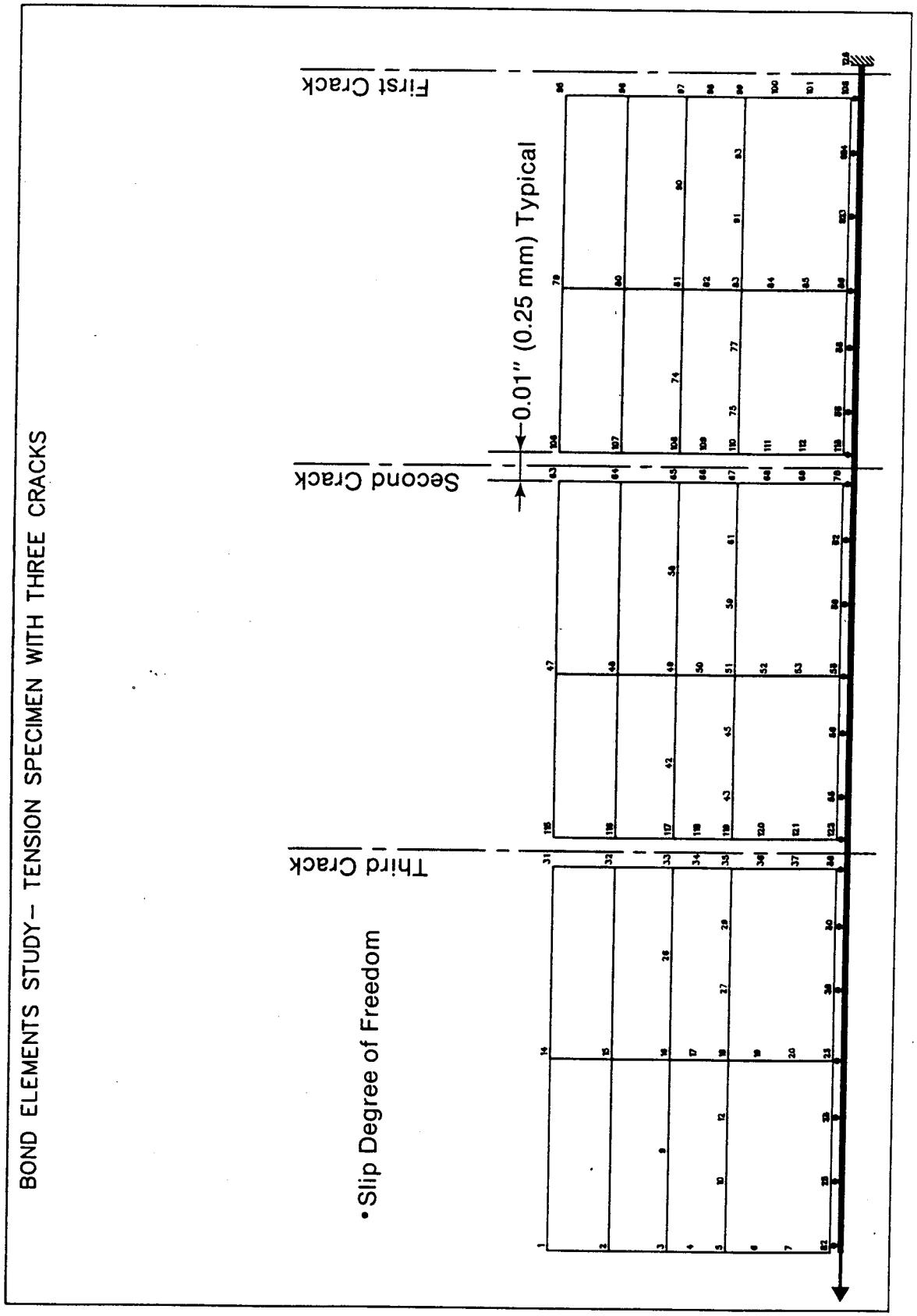

FIG. A3.4. Finite Element Mesh Layout - Tension Pull Specimen with Three Cracks

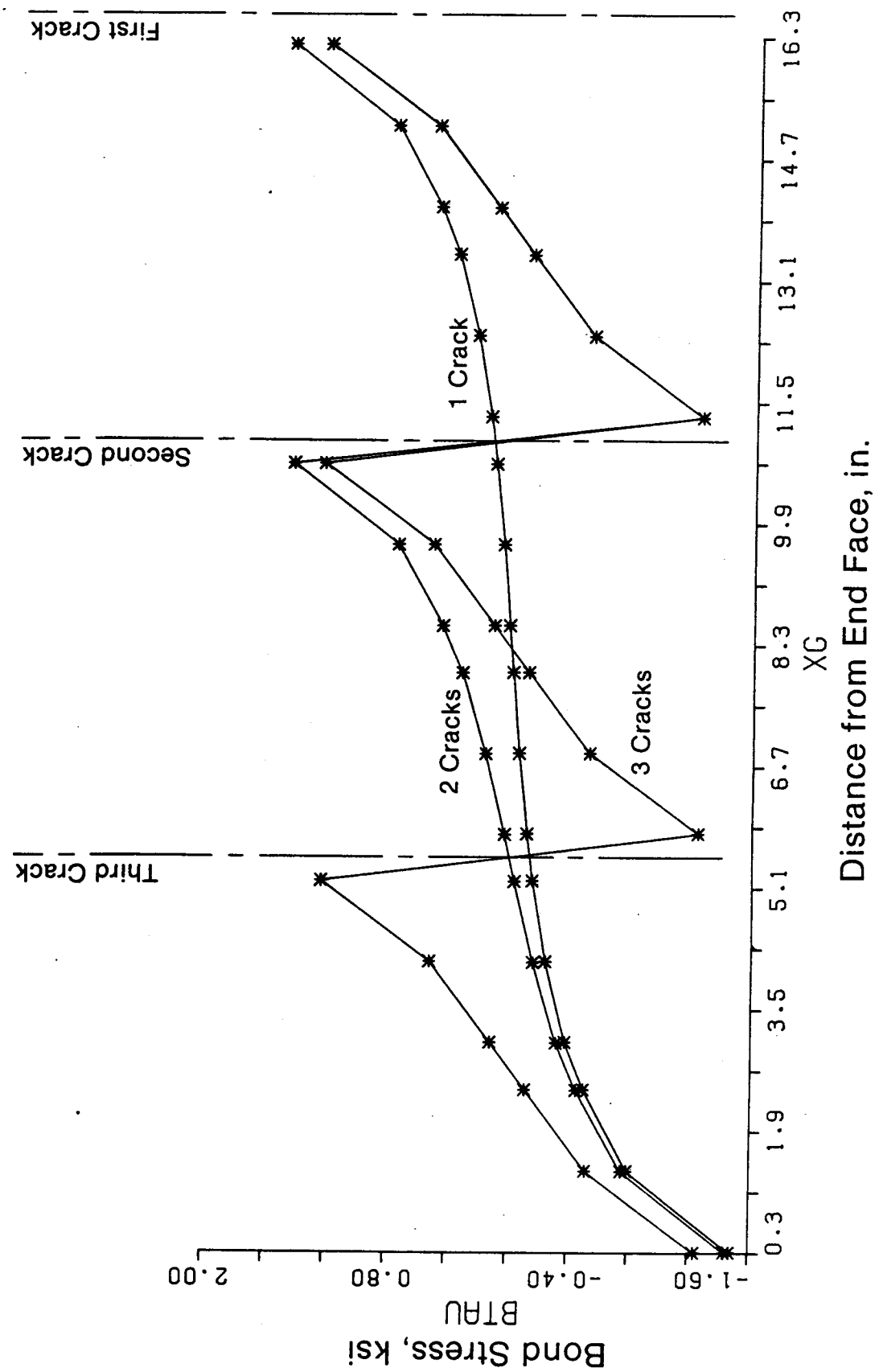

FIG. A3.5. Cracked Tension Pull Specimen
(a) Bond Stress Distribution (1 ksi = 6.895 MPa; 1 in. = 25.4 mm)

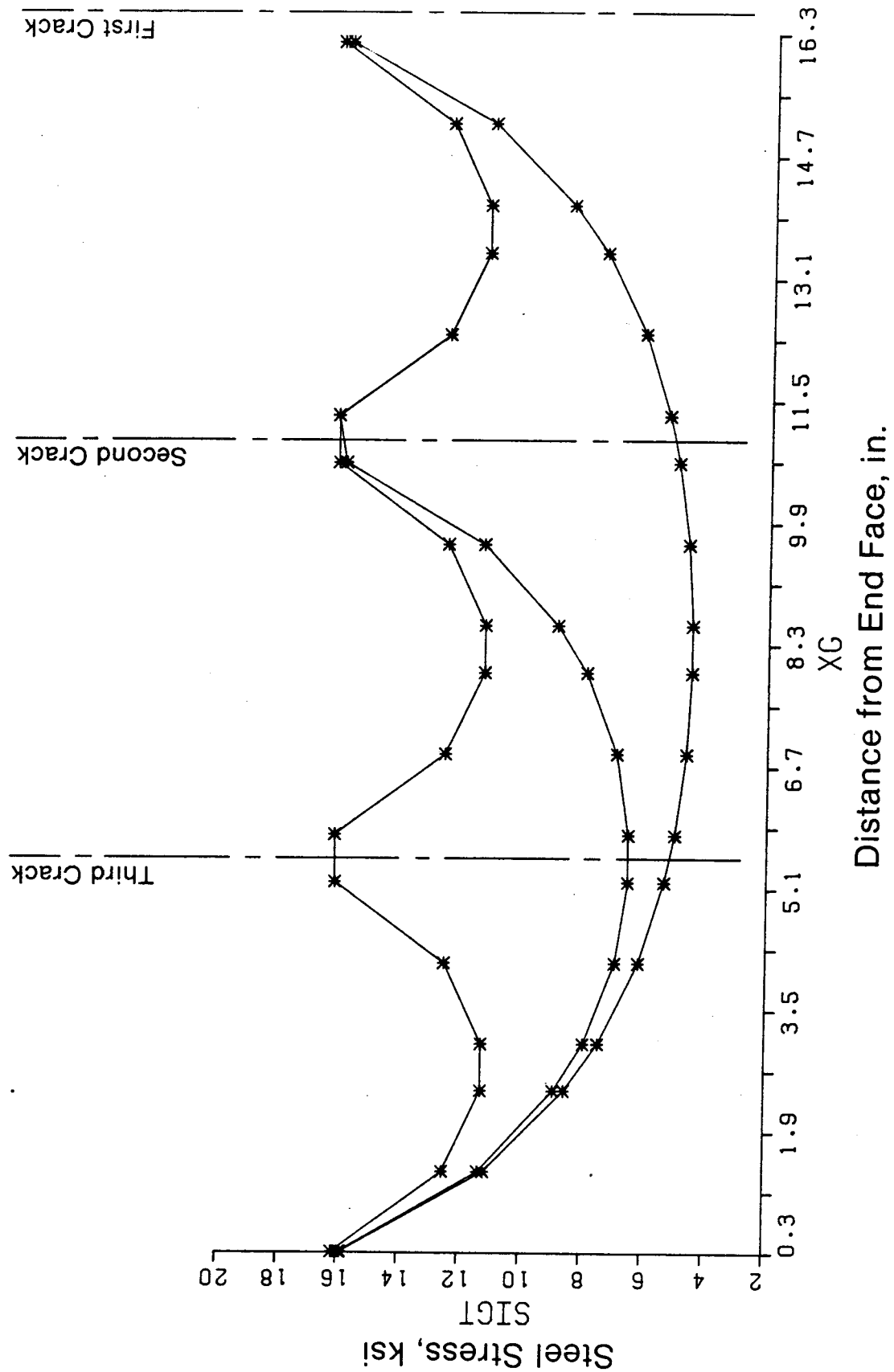

FIG. A3.5. Cracked Tension Pull Specimen (Continued)
(b) Steel Stress Distribution (1 ksi = 6.895 MPa; 1 in. = 25.4 mm)

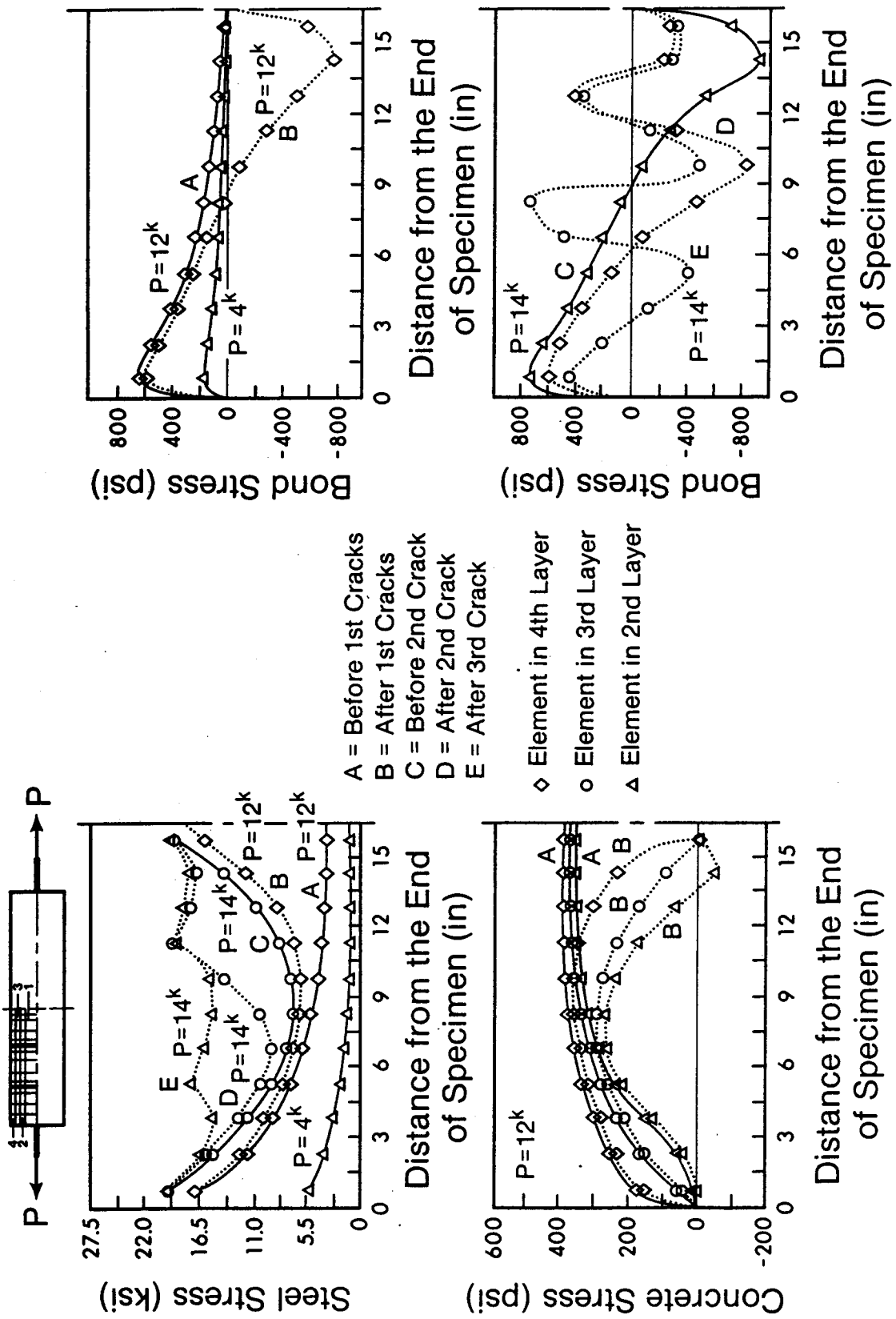

FIG. A3.6. Analysis of Tension Pull Specimen by Khouzam (Adapted from Source, 1982)

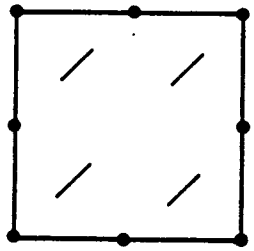

(a) Parallel Cracks

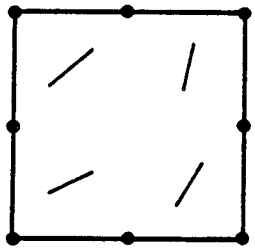

(b) Random Cracks

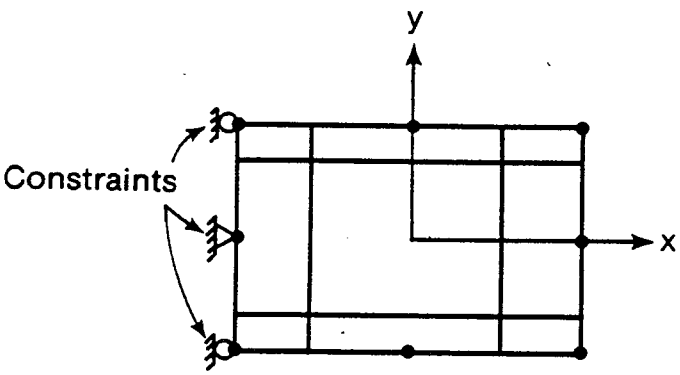

(c) Uncracked Element

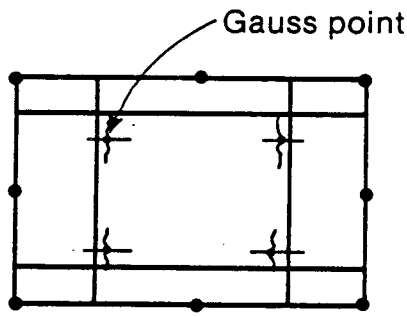

(d) Cracked in y Direction

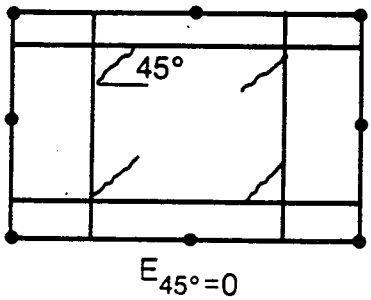

(e) Cracked at 45°

FIG. A3.7. Cracked Elements

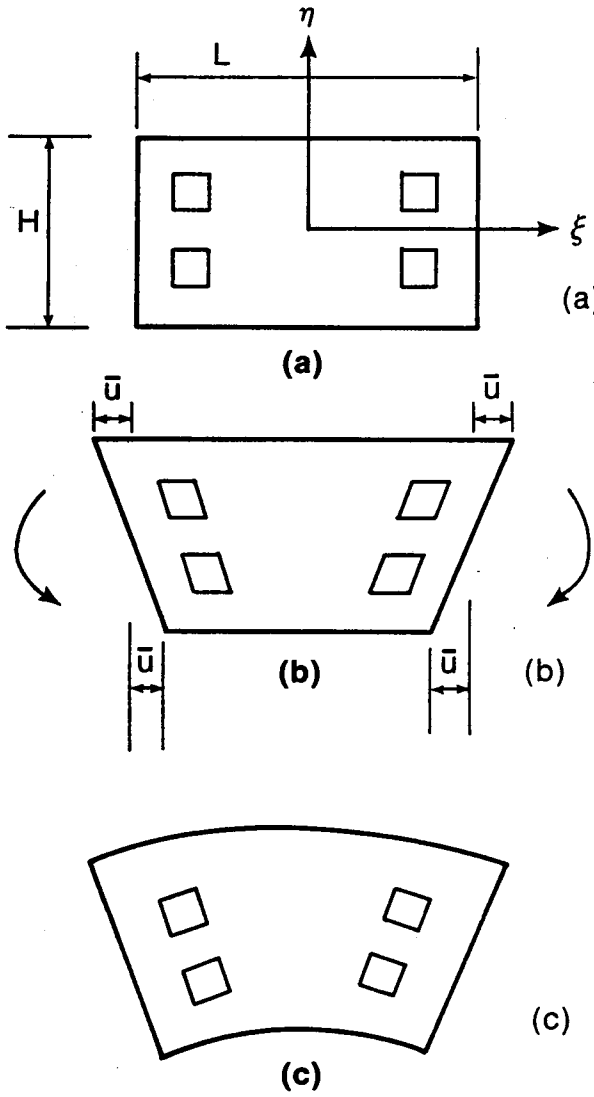

(a) Undeformed shape

(b) Response of a bilinear element under pure bending

(c) The correct shape of a beam segment in pure bending

FIG. A3.8. Deformation of a Bilinear Element in Pure Bending

(a) Constant Shear Strain Modes

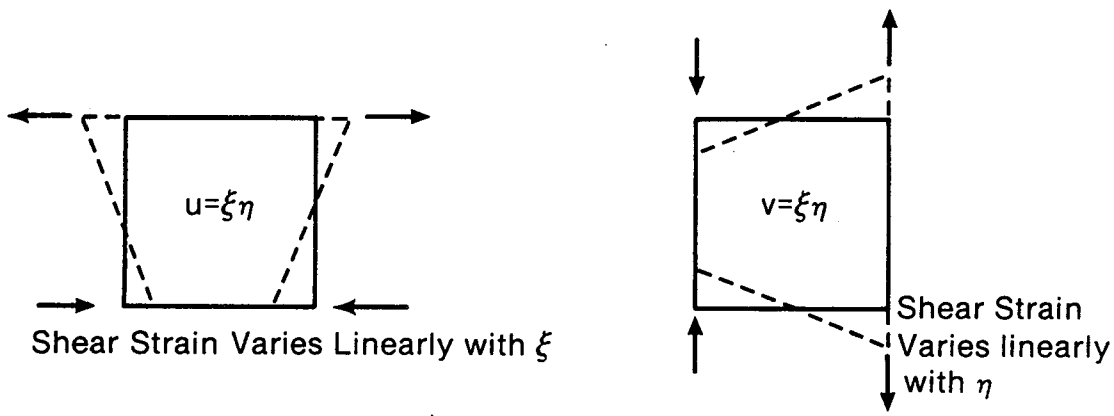

(b) Linear Strain Modes Associated with Bending

FIG. A3.9. Displacement Modes of Bilinear Element

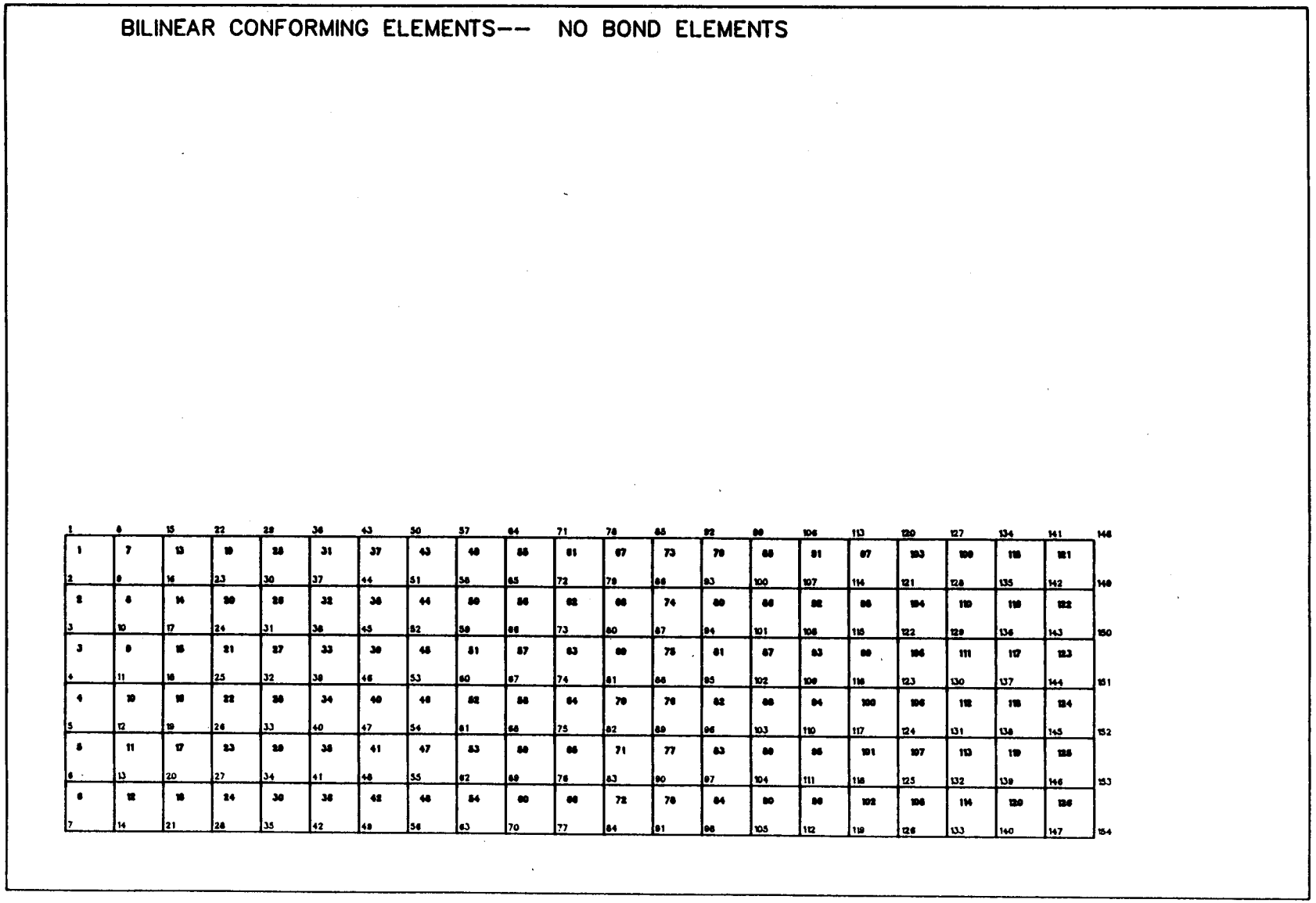

FIG. A3.10. Finite Element Mesh Layout - Bresler/Scordelis Beam XOB1
(a) Bilinear Elements

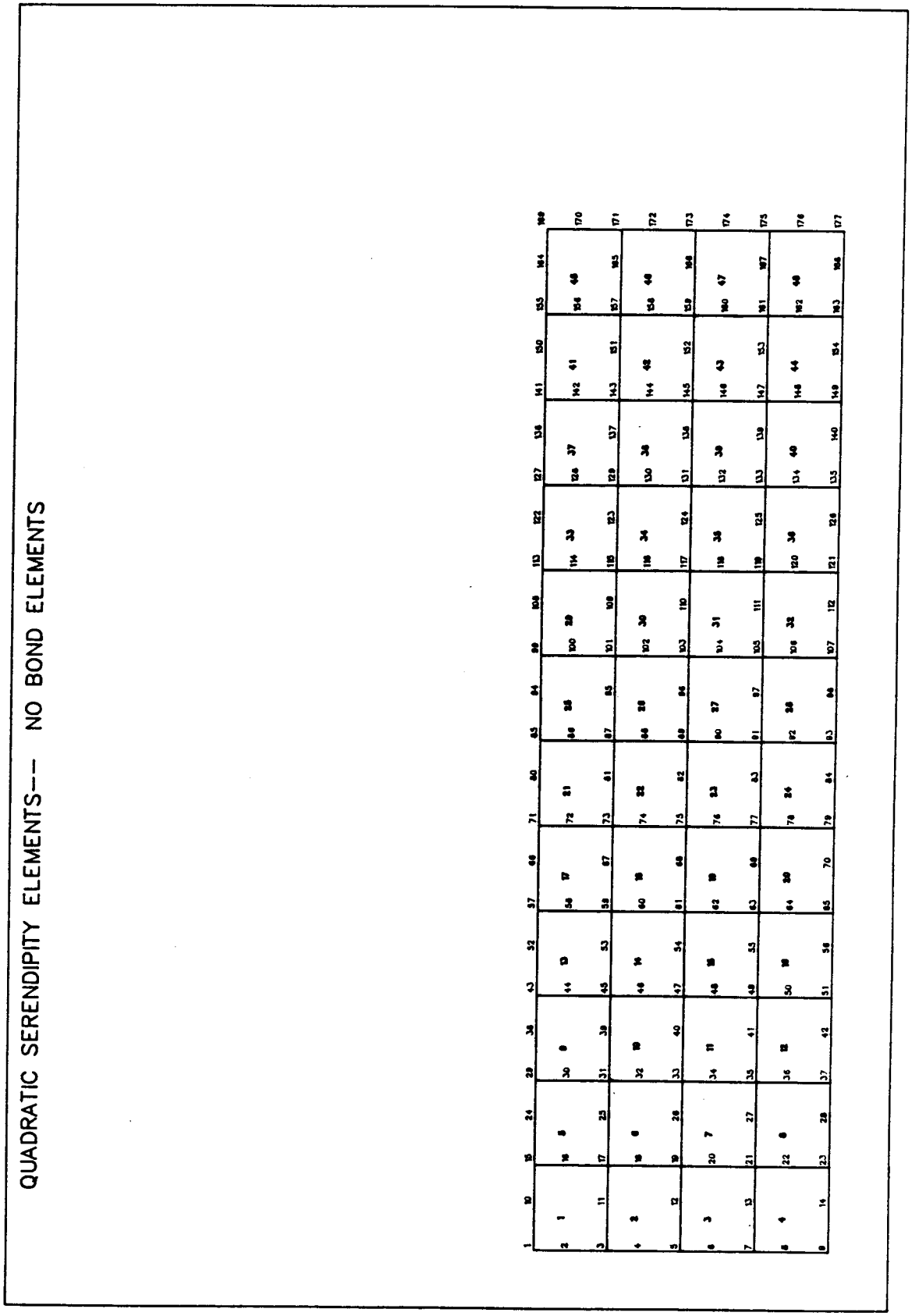

FIG. A3.10. (b) Quadratic Elements

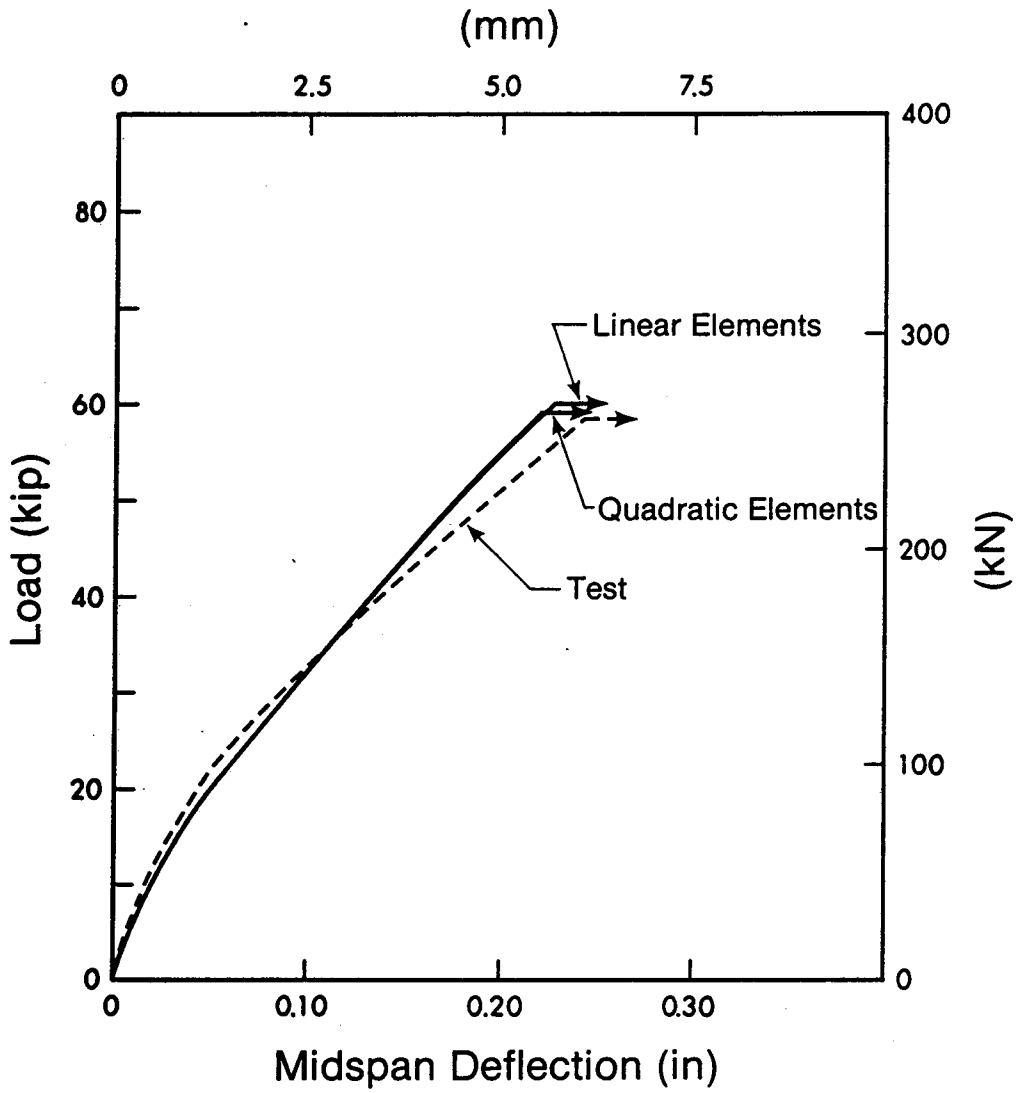

FIG. A3.11. Load-Deflection Curves for Beam XOB-1 - Linear vs Quadratic Elements

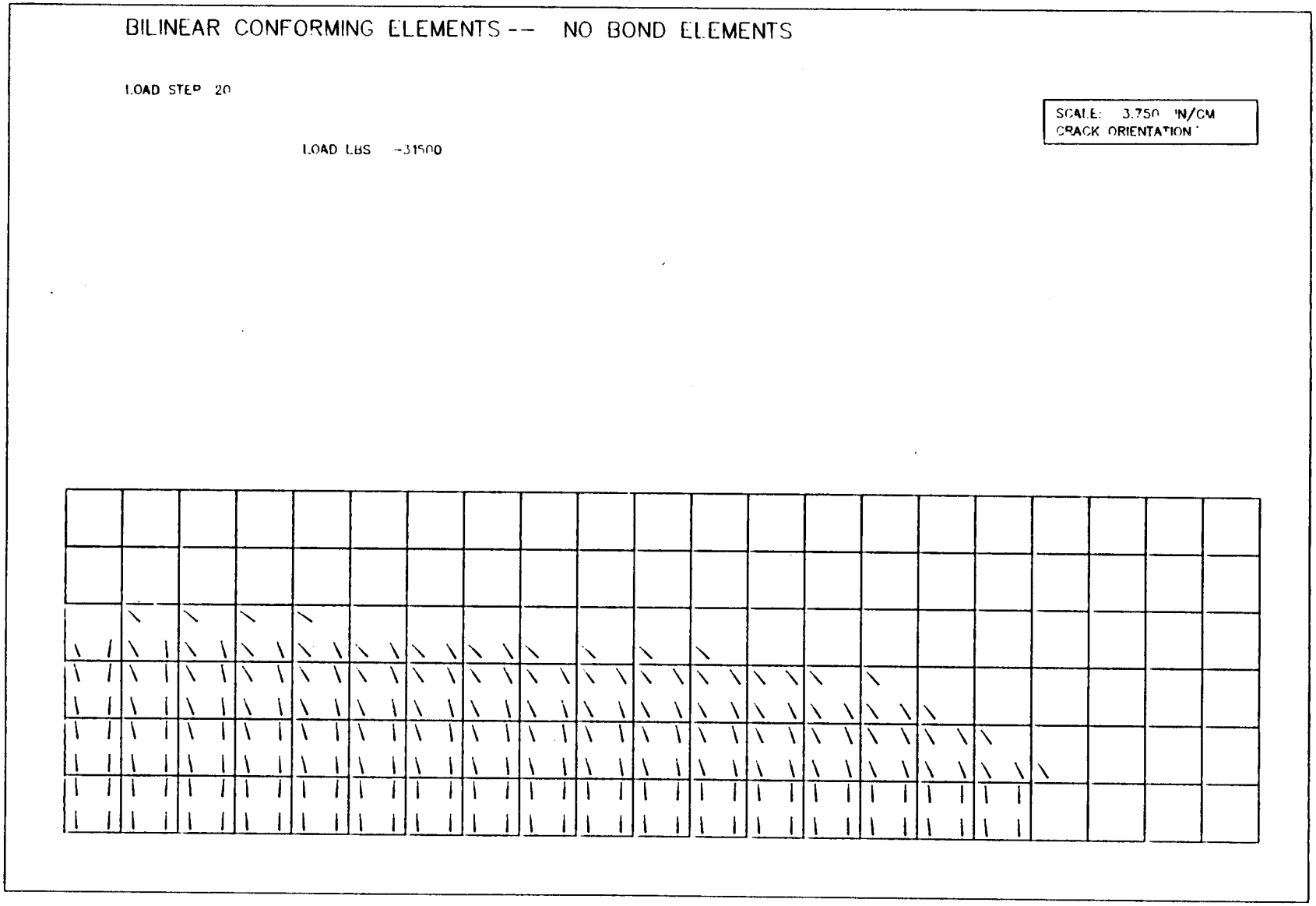

FIG. A3.12. Bresler/Scordelis Beam XOB1 - Analytical Crack Pattern
(a) Bilinear Elements

BAL

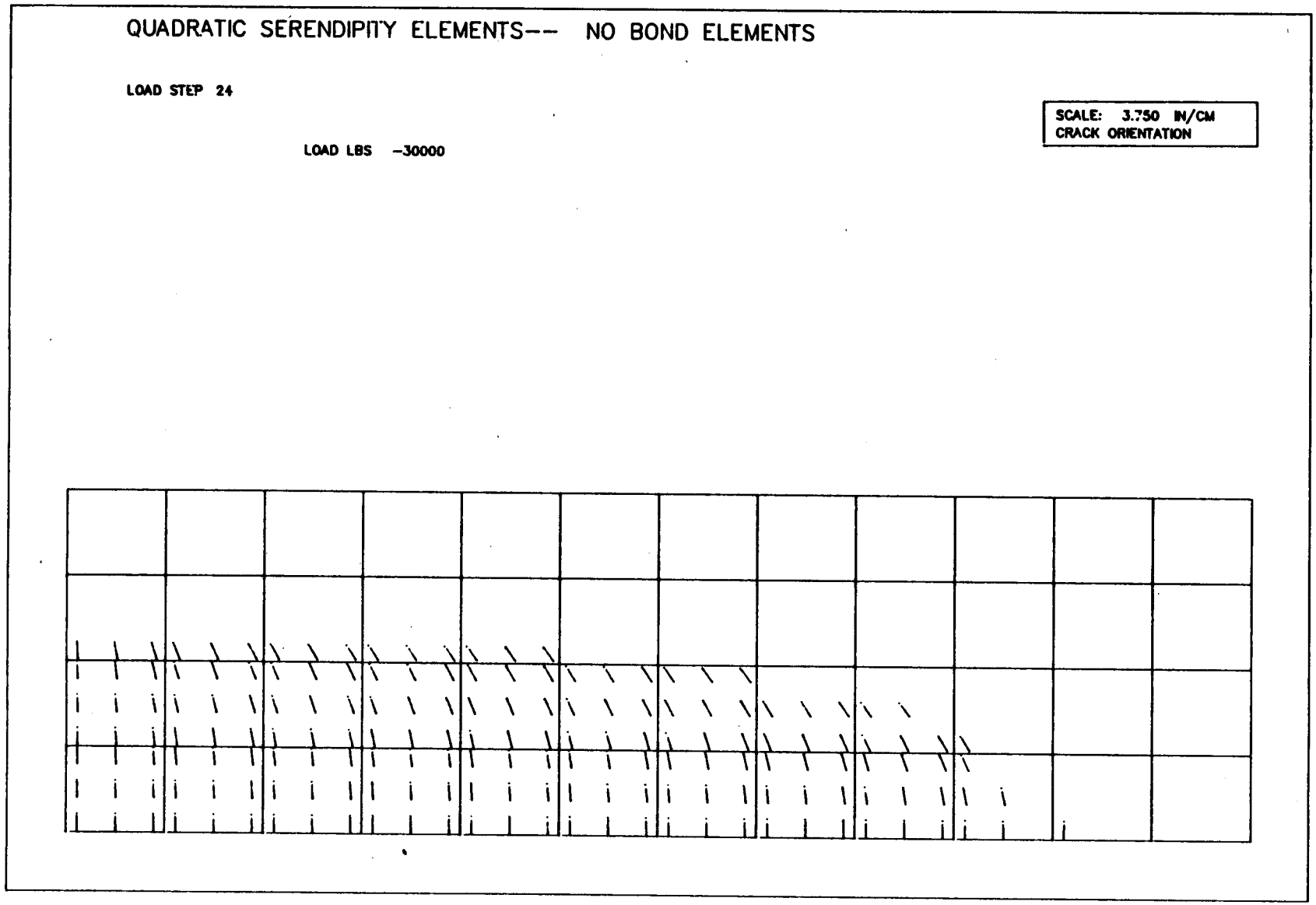

FIG. A3.12. (b) Quadratic Elements

BAL

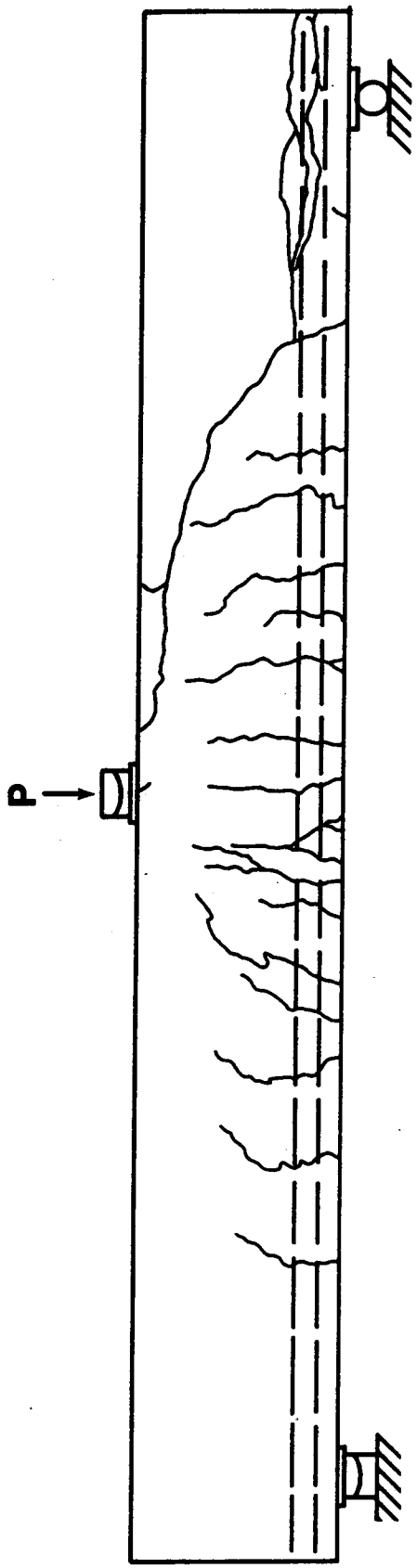

FIG. A3.12. (c) Crack Pattern Observed in Test

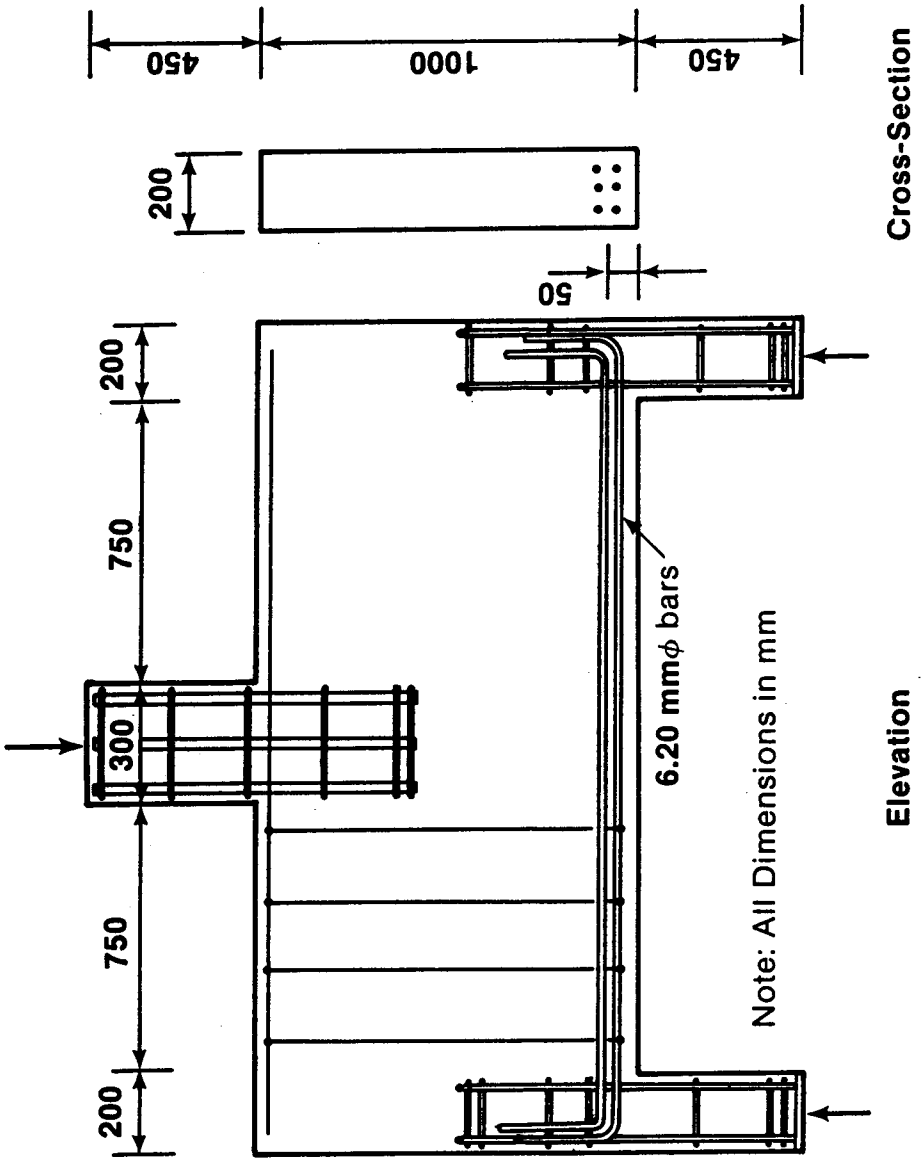

FIG. A3.13. Rogowsky/MacGregor Deep Beam 1/1.0

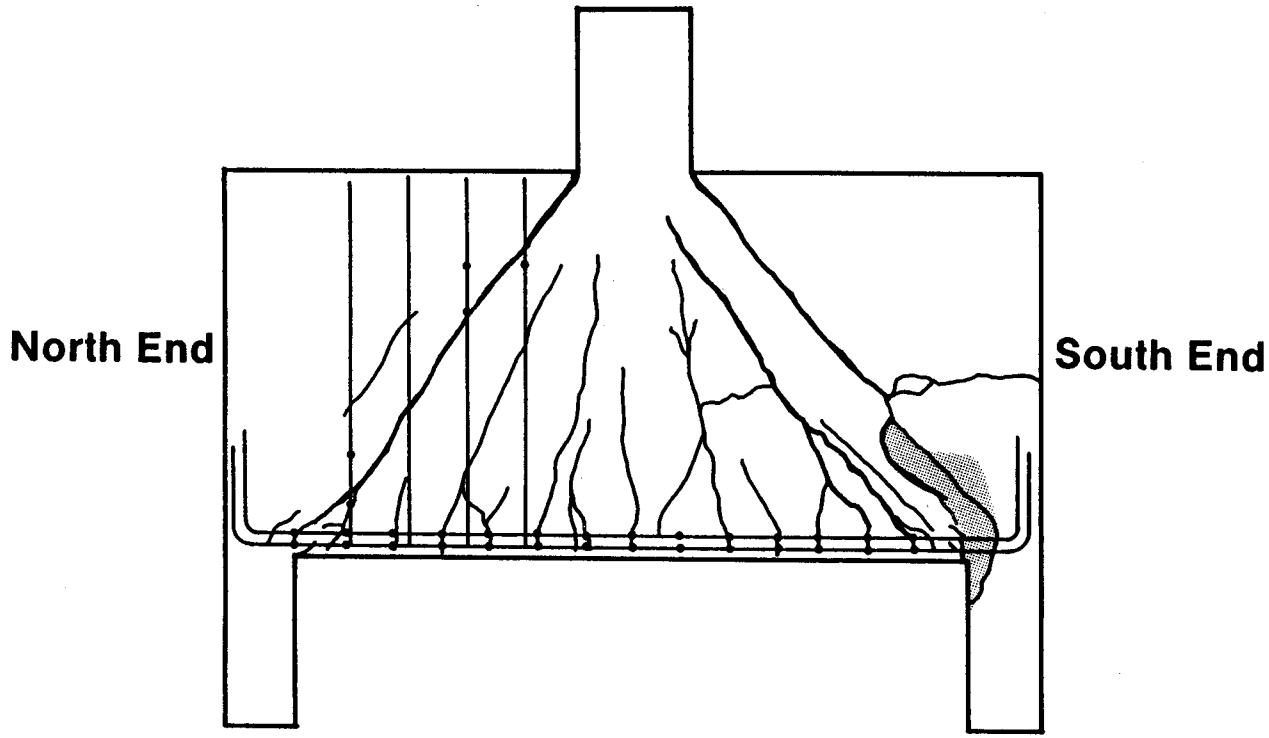

FIG. A3.14. Rogowsky/MacGregor Deep Beam 1/1.0 - Crack Pattern Observed in Test

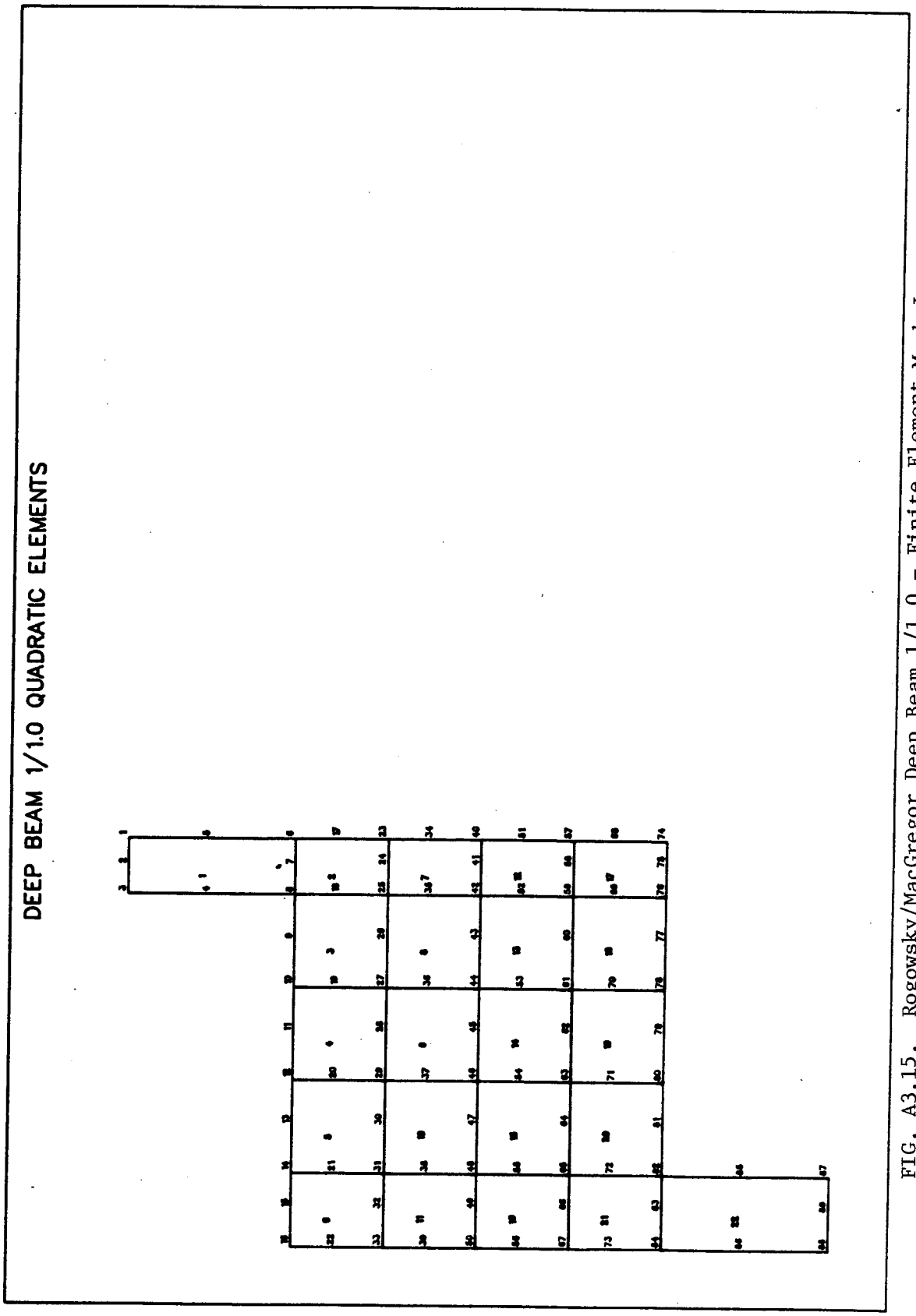

FIG. A3.15. Rogowsky/MacGregor Deep Beam 1/1.0 - Finite Element Mesh Layout
Quadratic Elements

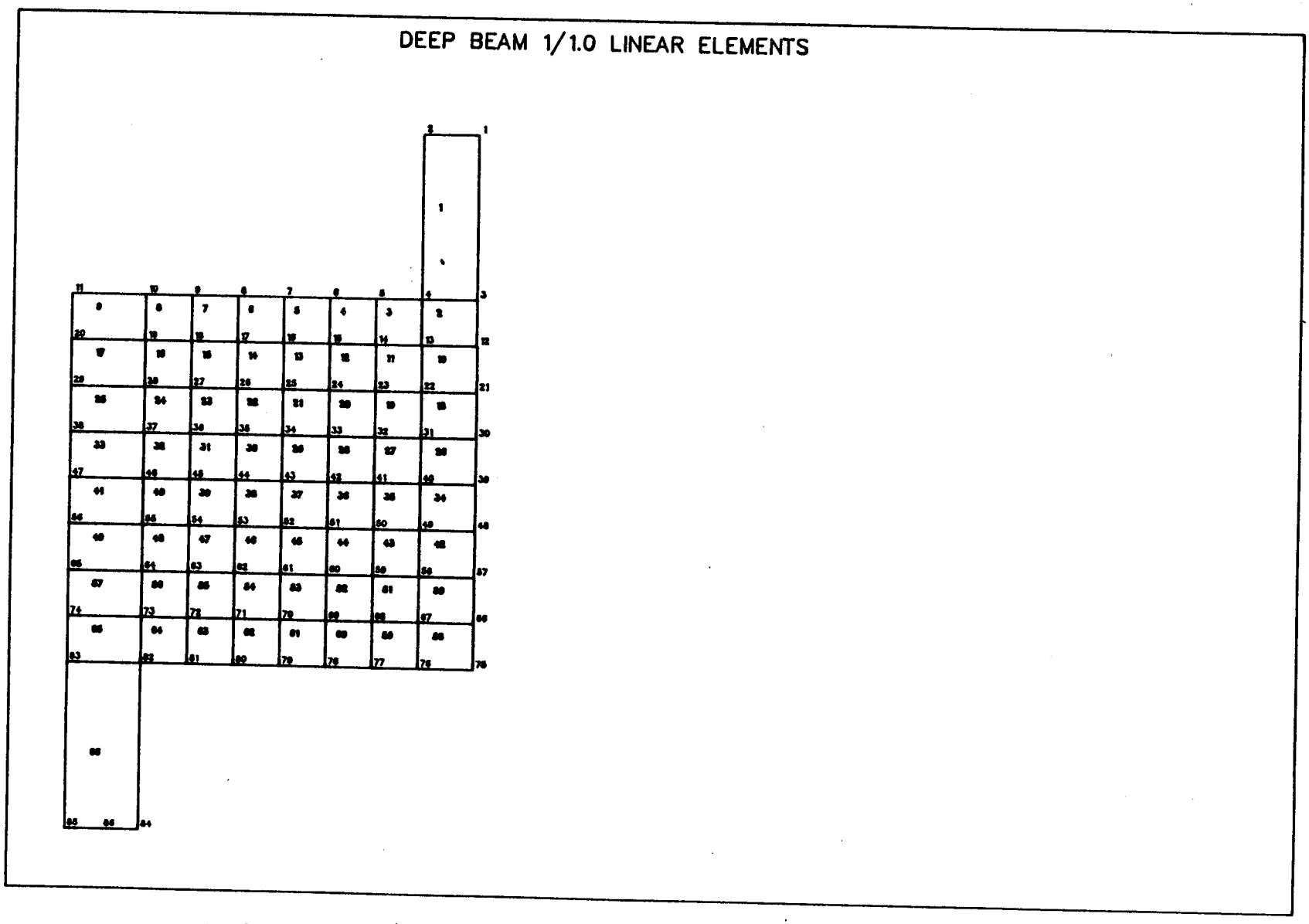

FIG. A3.16. Rogowsky/MacGregor Deep Beam 1/1.0 - Finite Element Mesh Layout
Bilinear Elements

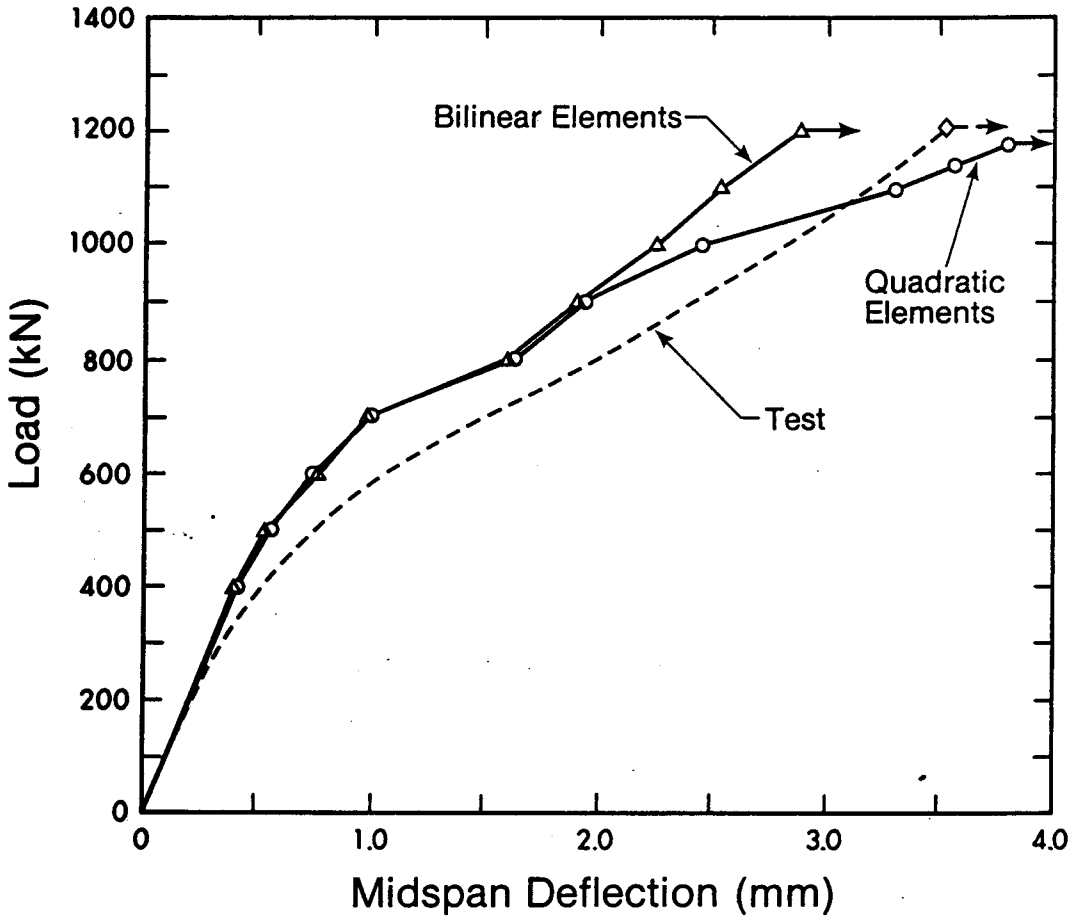

FIG. A3.17. Rogowsky/MacGregor Deep Beam - Load-Deflection Relationship Linear vs Quadratic Elements

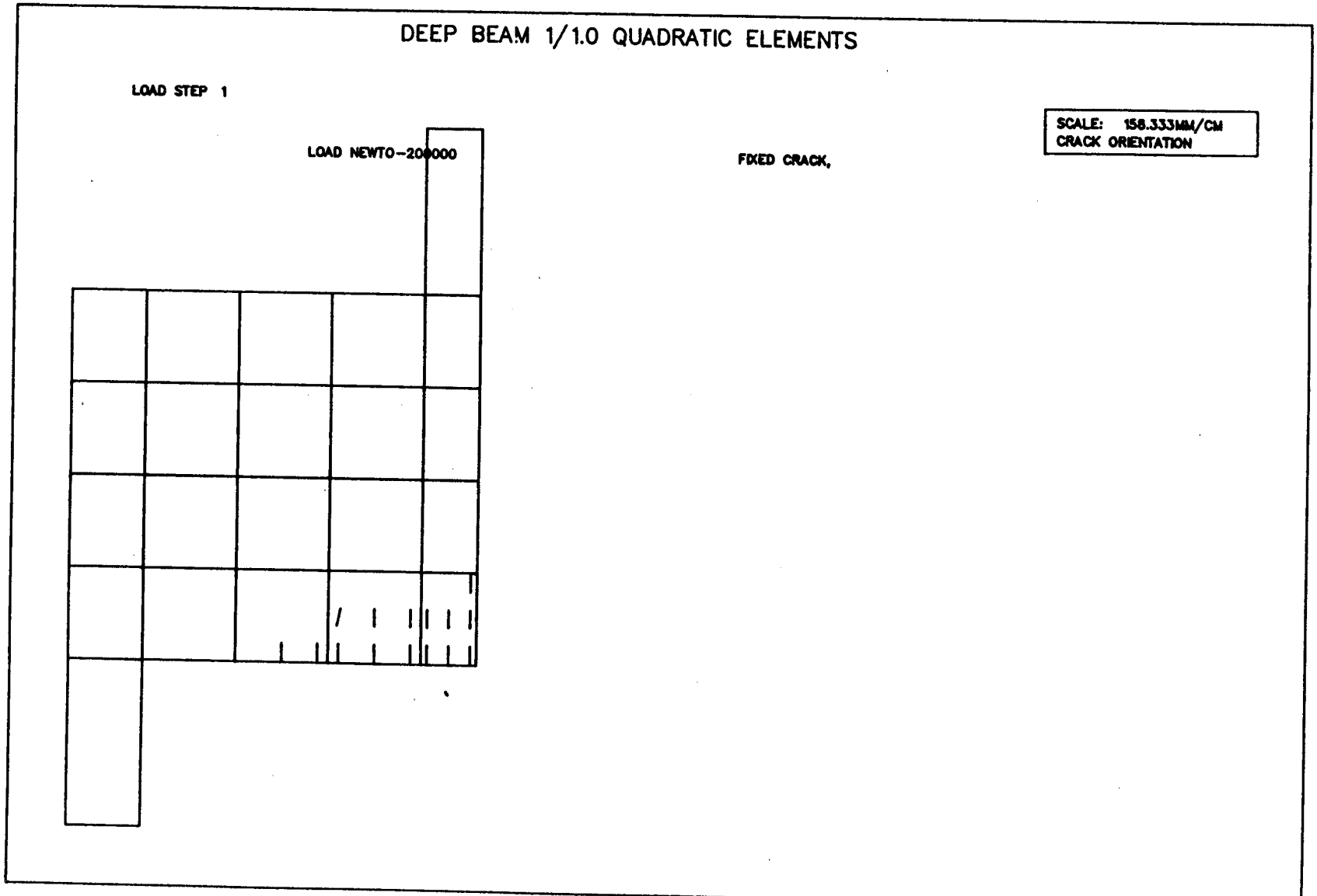

FIG. A3.18. Rogowsky/MacGregor Deep Beam 1/1.0 - Analytical Crack Pattern - Shear = 200 kN
(a) Quadratic Elements

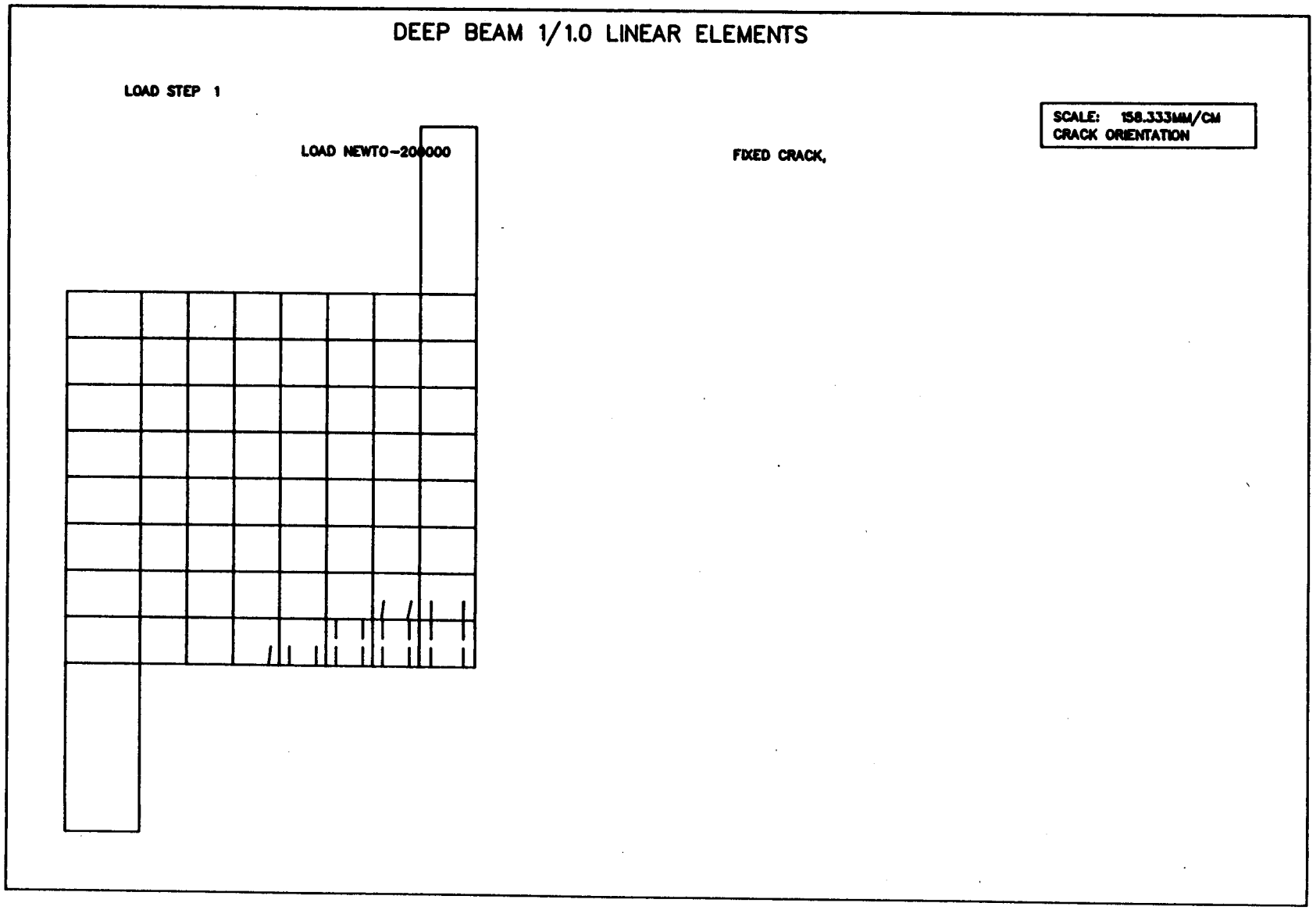

FIG. A3.18. (b) Bilinear Elements

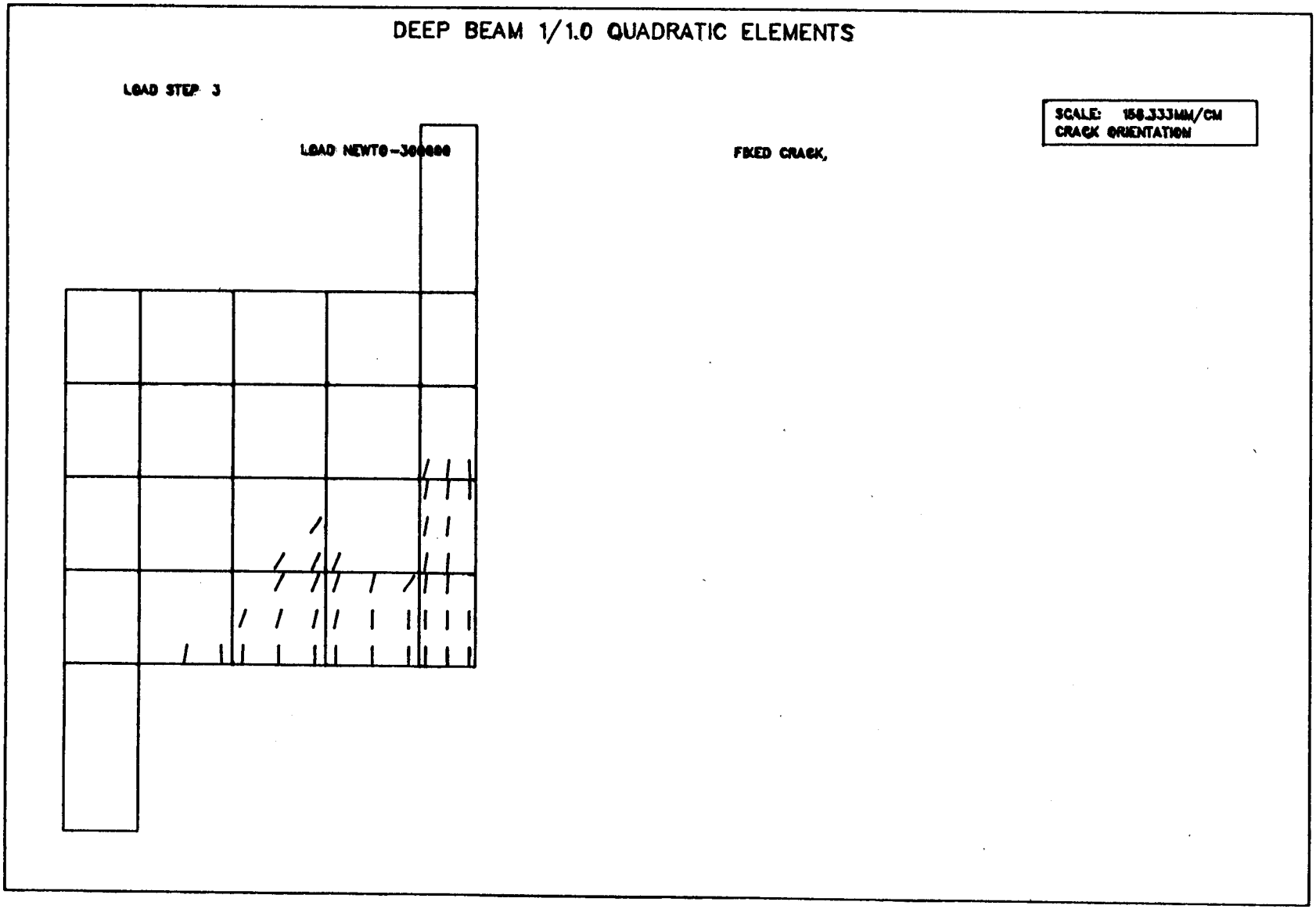

FIG. A3.19. Rogowsky/MacGregor Deep Beam 1/1.0 - Analytical Crack Pattern - Shear = 300 kN
(a) Quadratic Elements

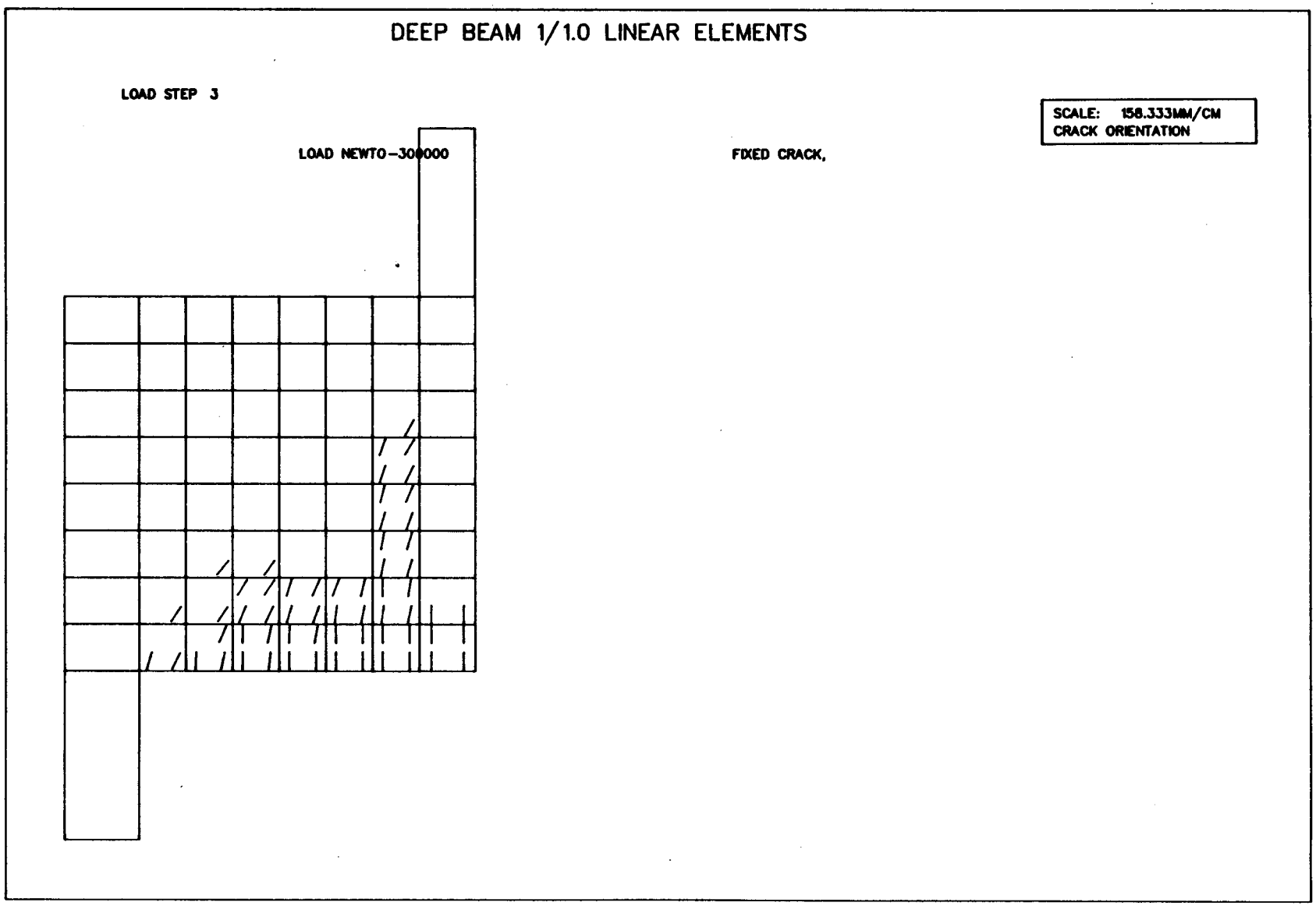

FIG. A3.19. (b) Bilinear Elements

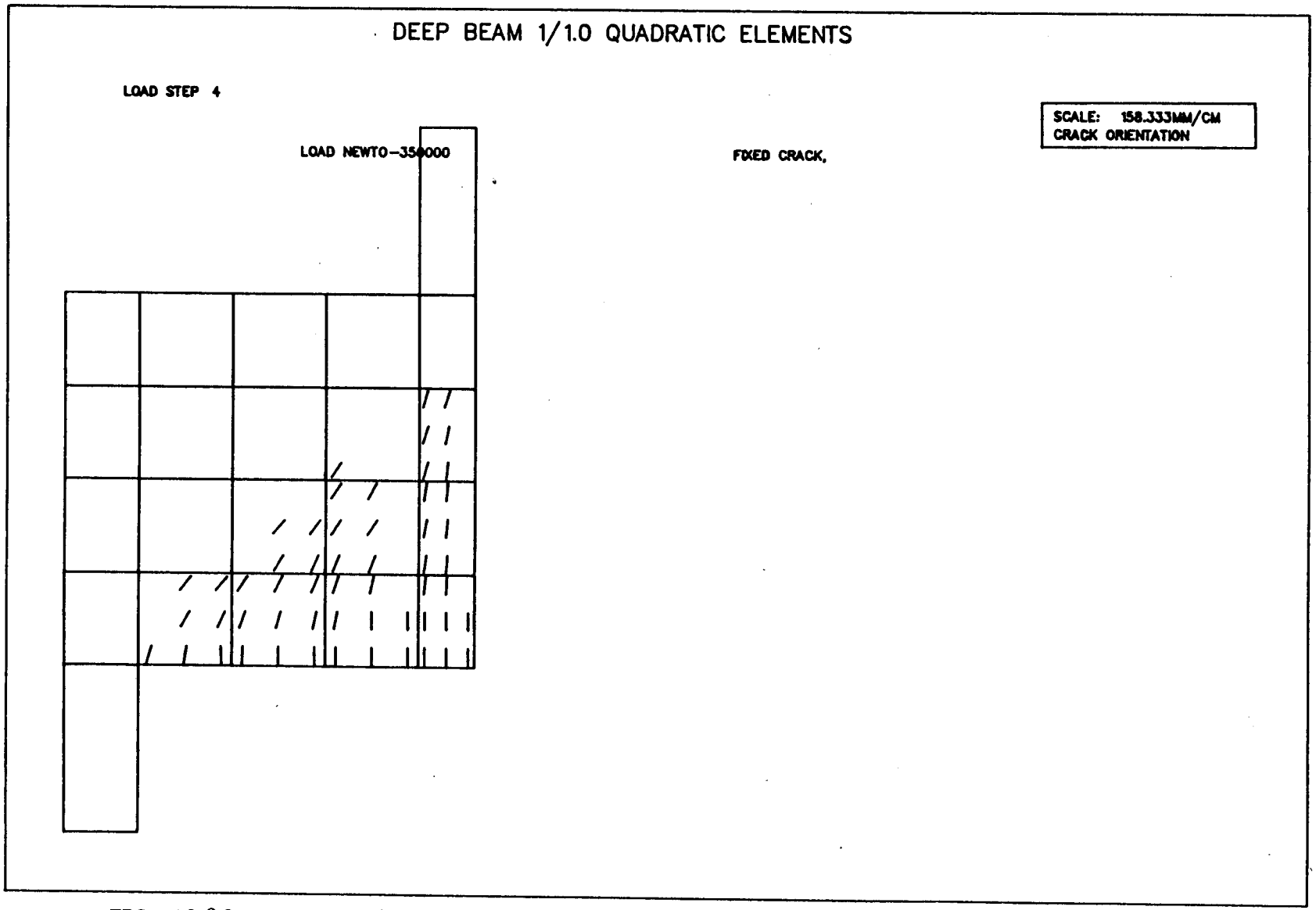

FIG. A3.20. Rogowsky/MacGregor Deep Beam 1/1.0 - Analytical Crack Pattern - Shear = 350 kN
(a) Quadratic Elements

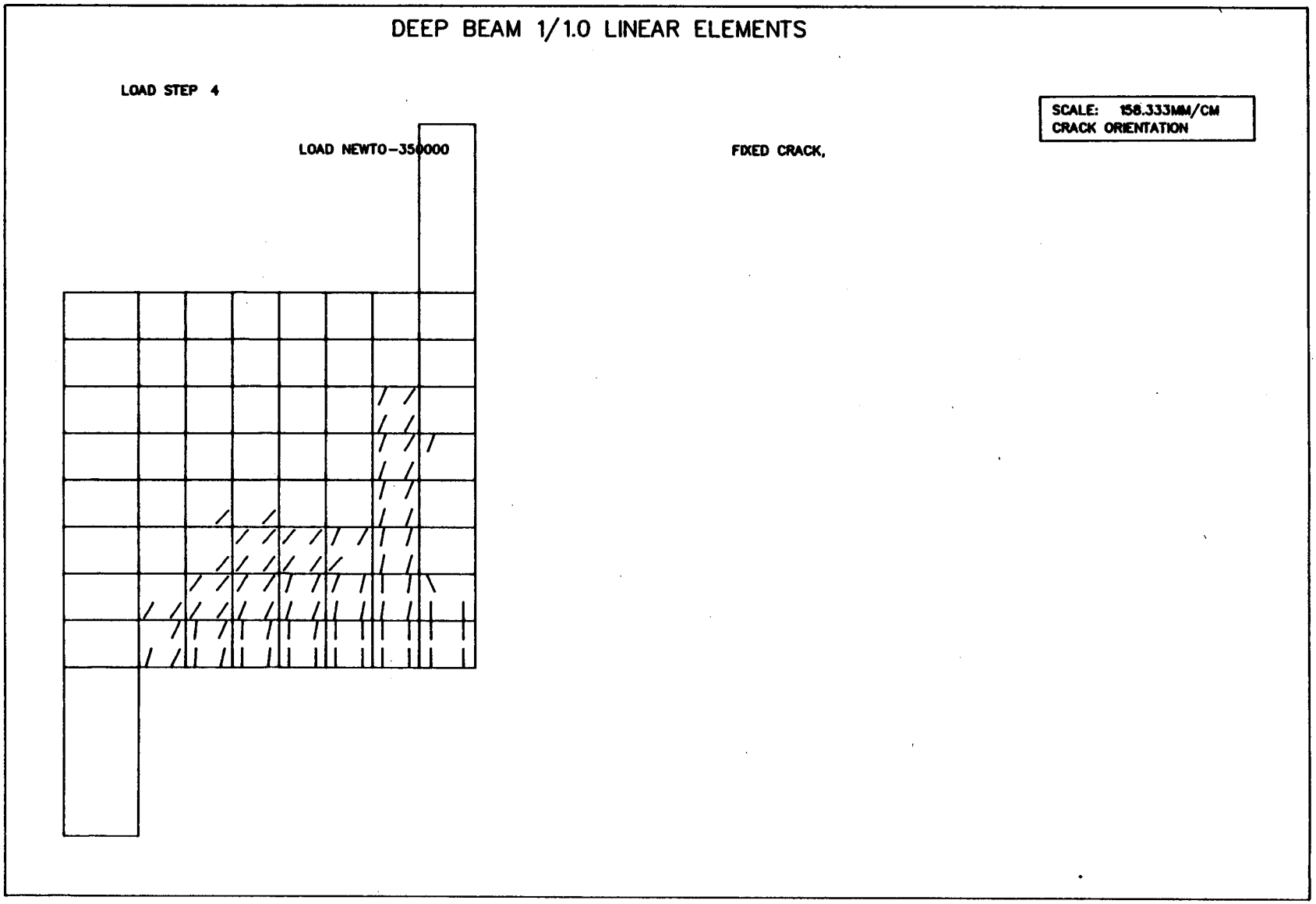

FIG. A3.20. (b) Bilinear Elements

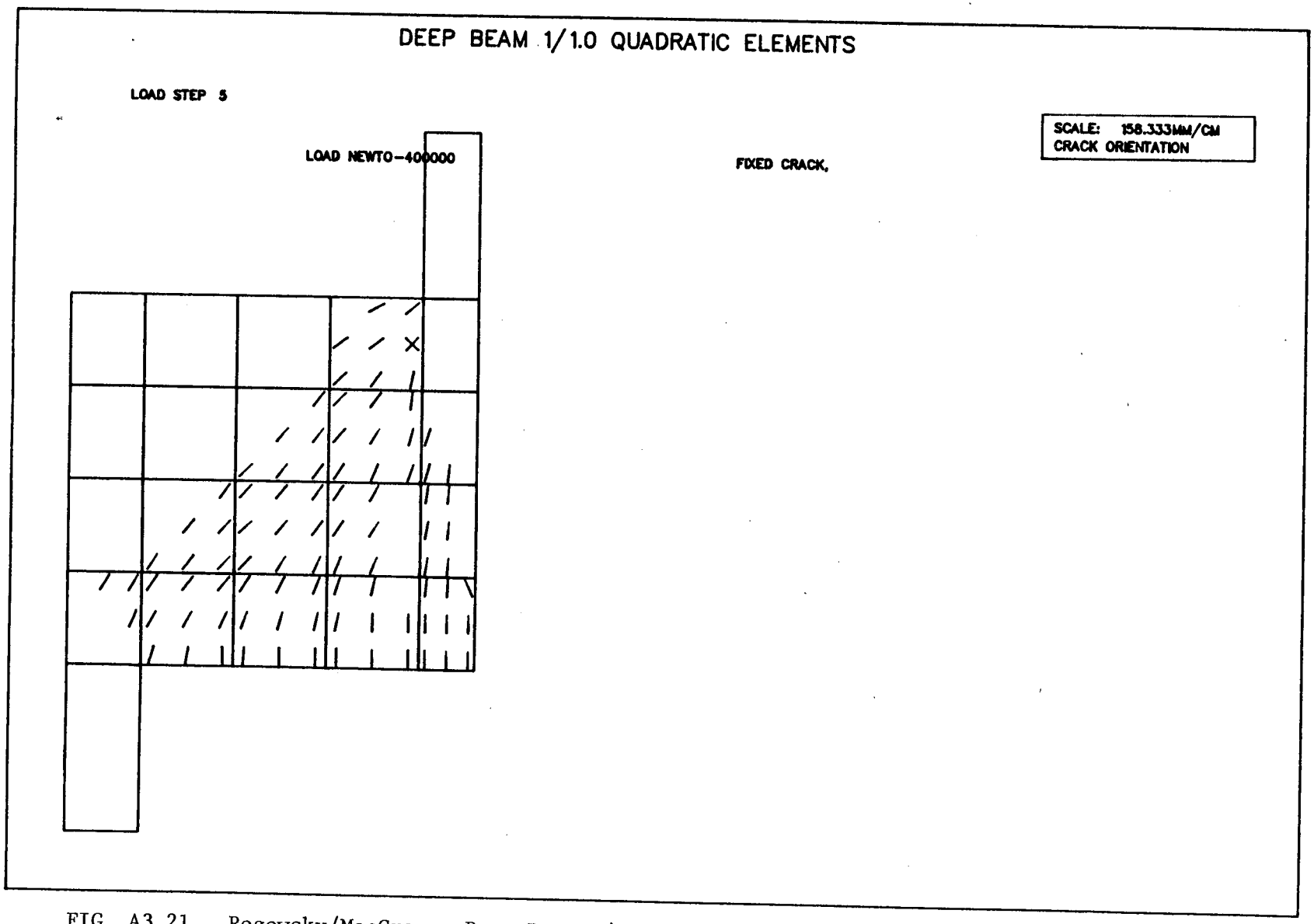

FIG. A3.21. Rogowsky/MacGregor Deep Beam 1/1.0 - Analytical Crack Pattern - Shear = 400 kN
(a) Quadratic Elements

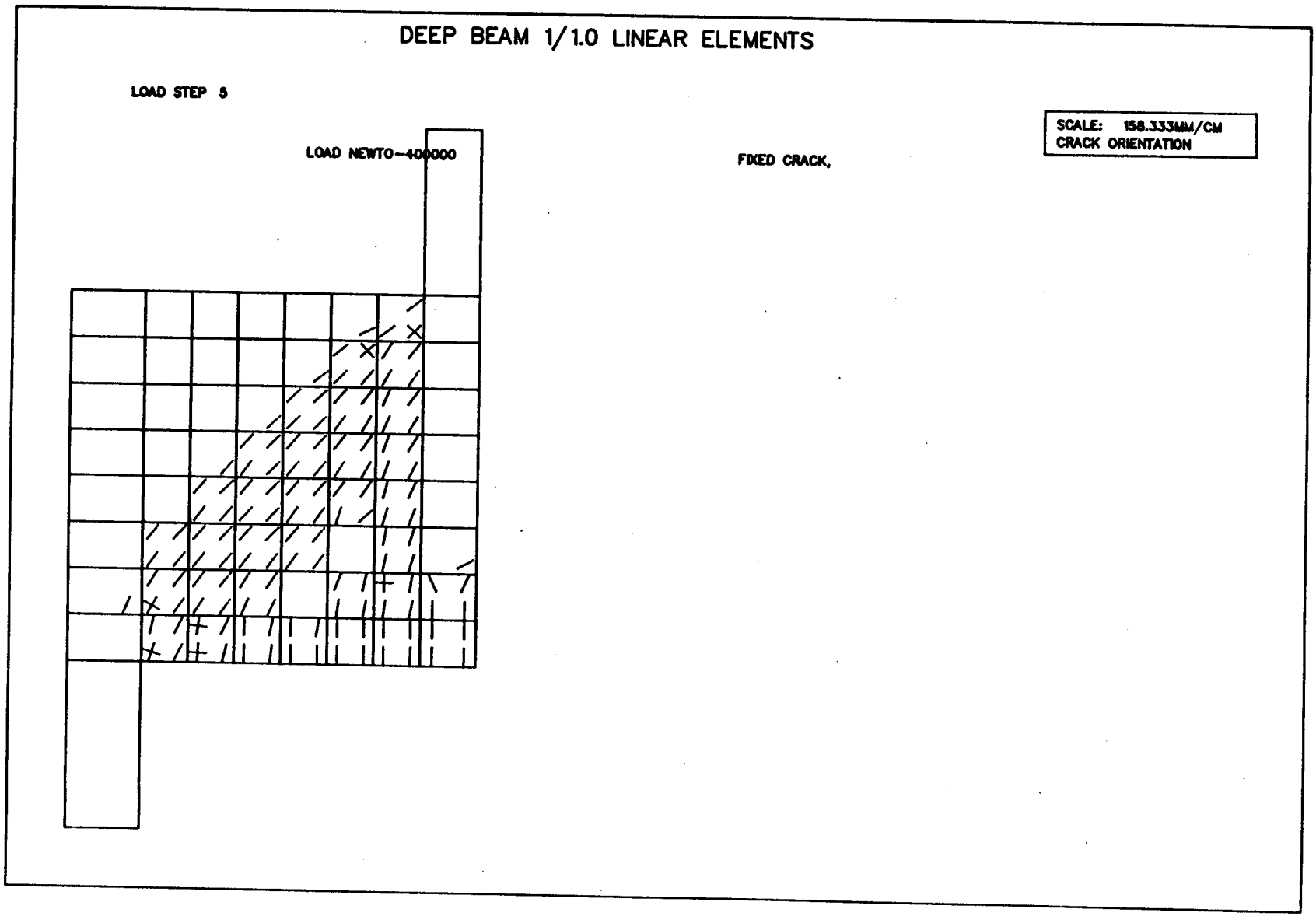

FIG. A3.21. (b) Bilinear Elements

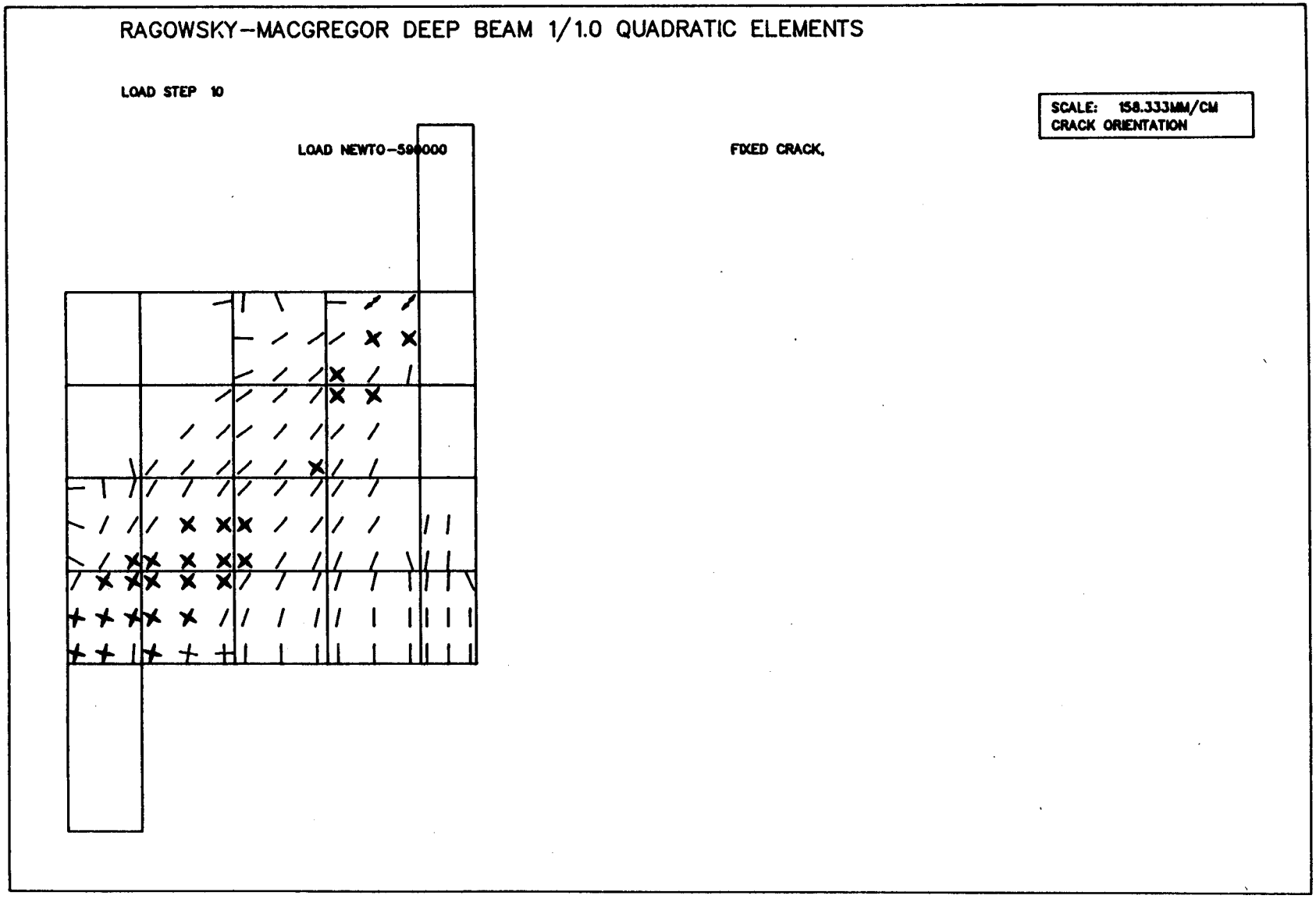

FIG. A3.22. Rogowsky/MacGregor Deep Beam 1/1.0 - Compression Strain Hardening/Softening Regions - Quadratic Elements

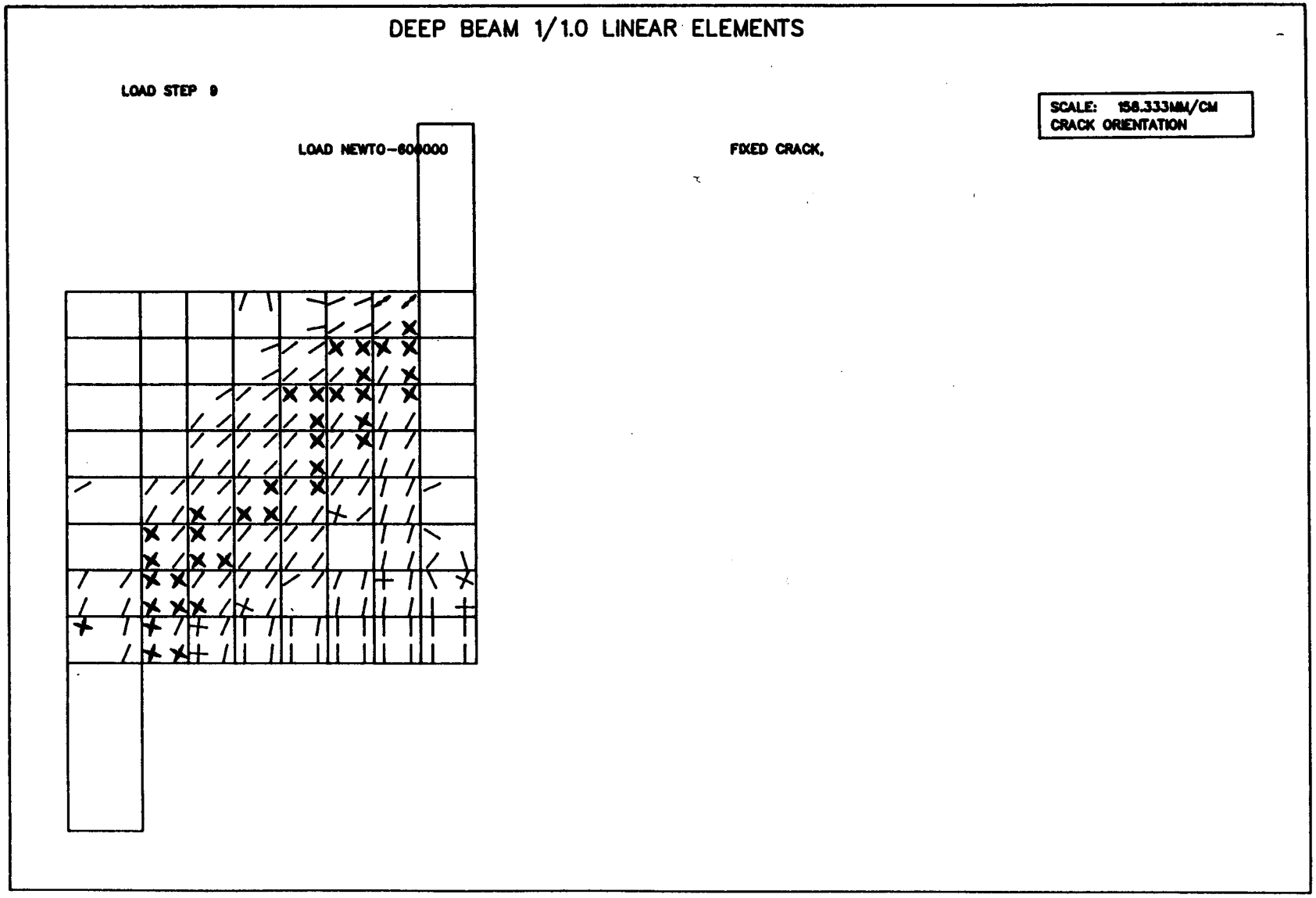

FIG. A3.23. Compression Strain Hardening/Softening Regions - Bilinear Elements

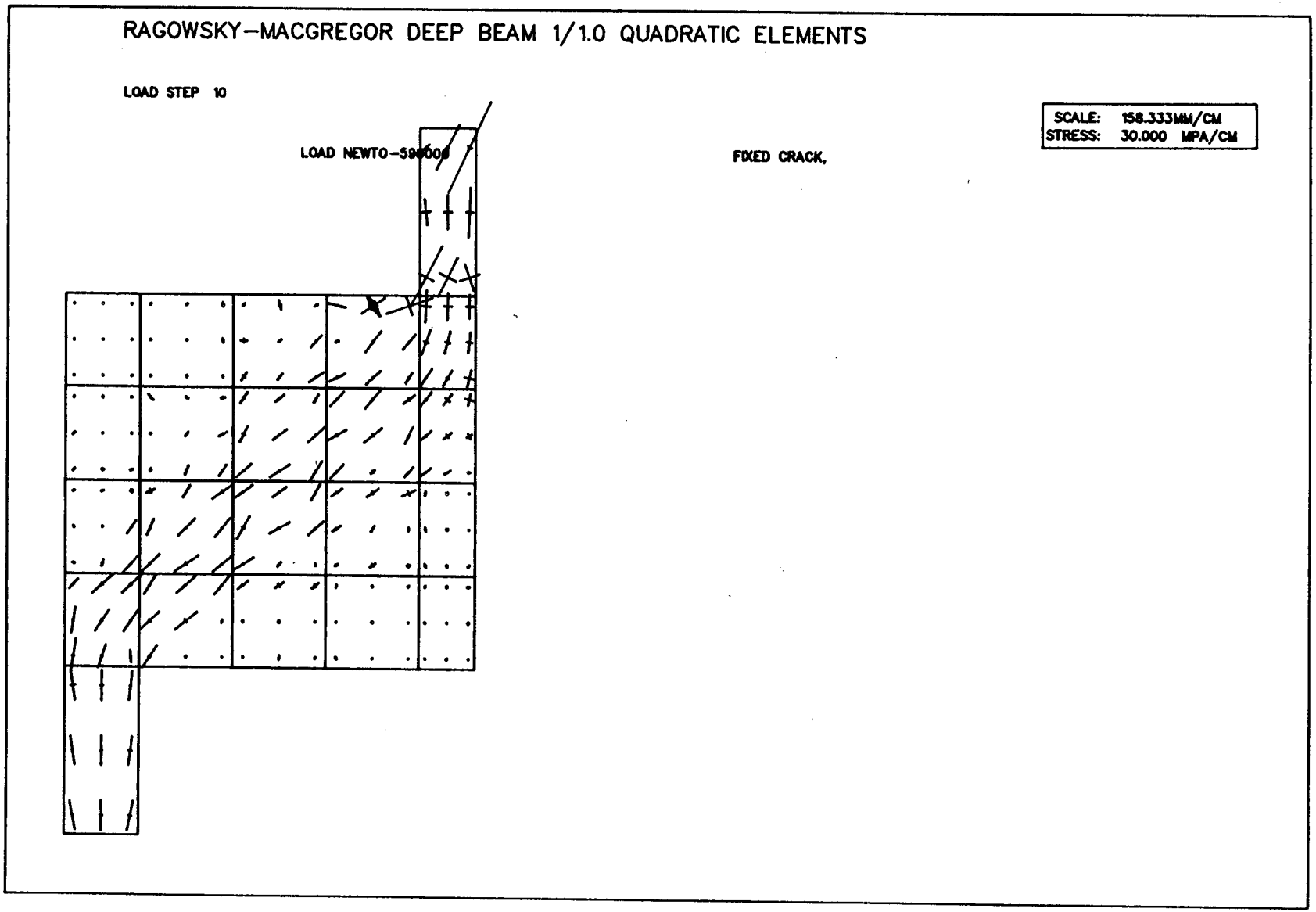

FIG. A3.24. Rogowsky/MacGregor Deep Beam 1/1.0 - Principal Stress Plot - Quadratic Elements

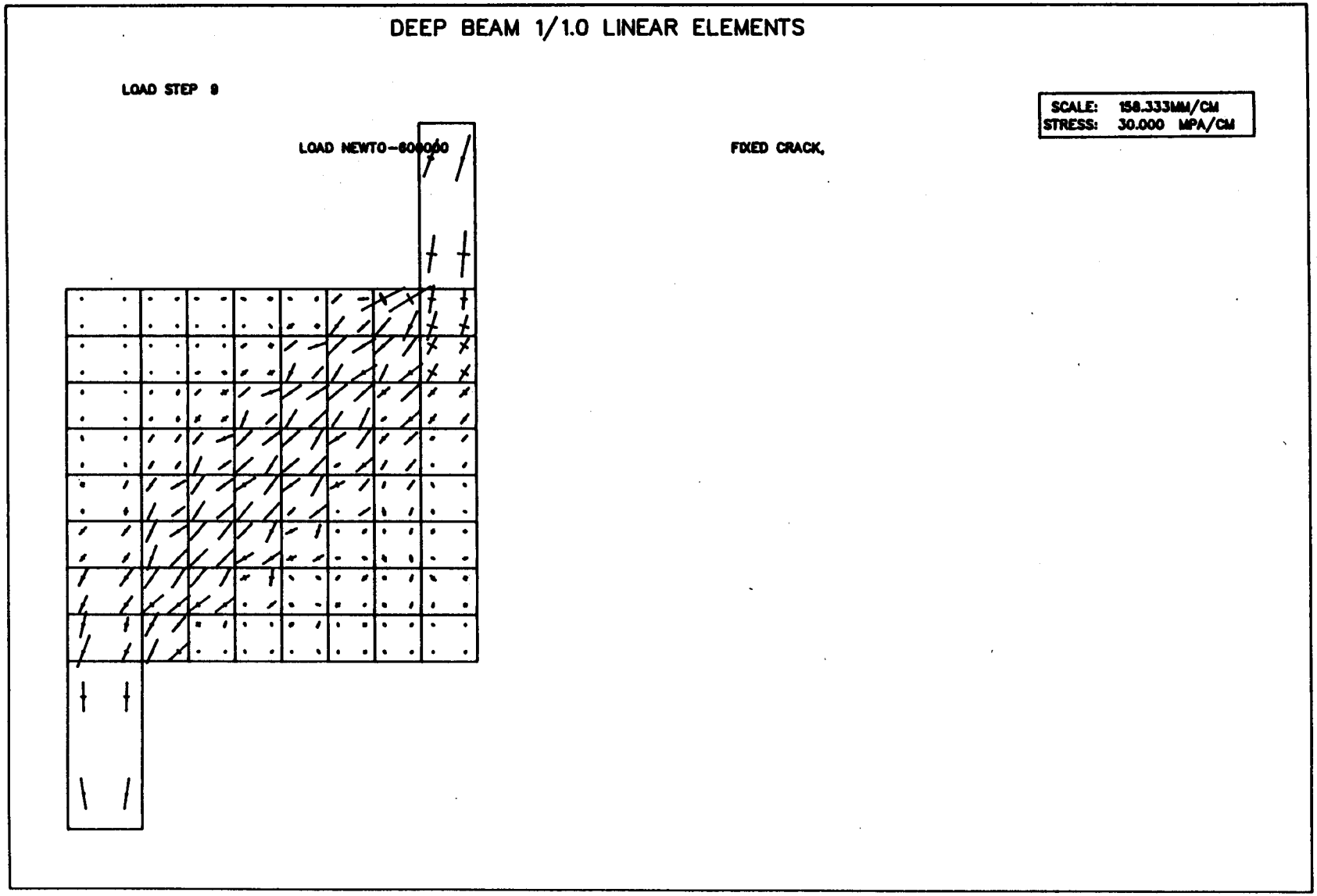

FIG. A3.25. Rogowsky/MacGregor Deep Beam 1/1.0 - Principal Stress Plot - Bilinear Elements

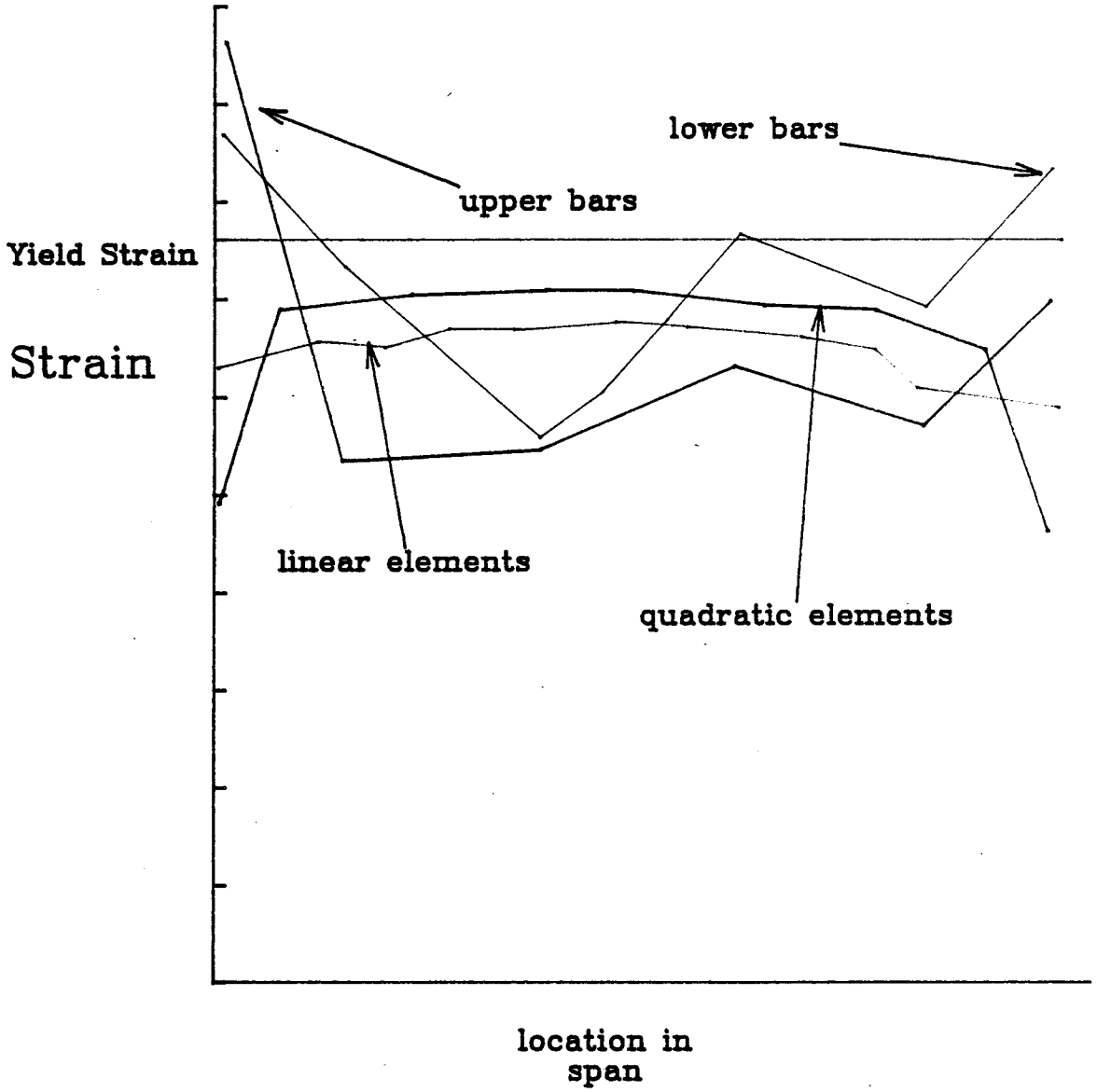

Fig. A3.26 Steel Strains

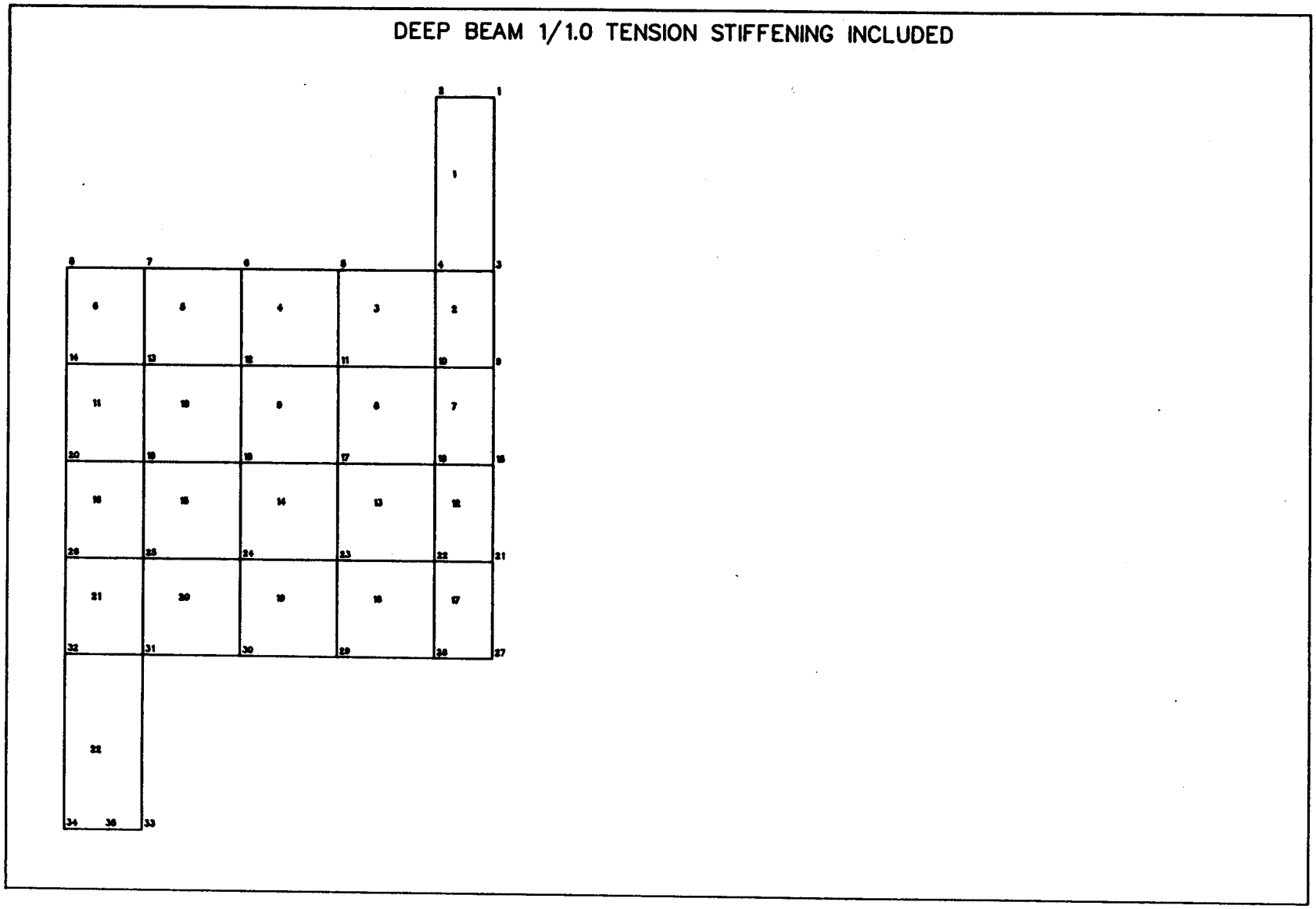

FIG. A3.27. Rogowsky/MacGregor Deep Beam 1/1.0 - Coarse Mesh Layout

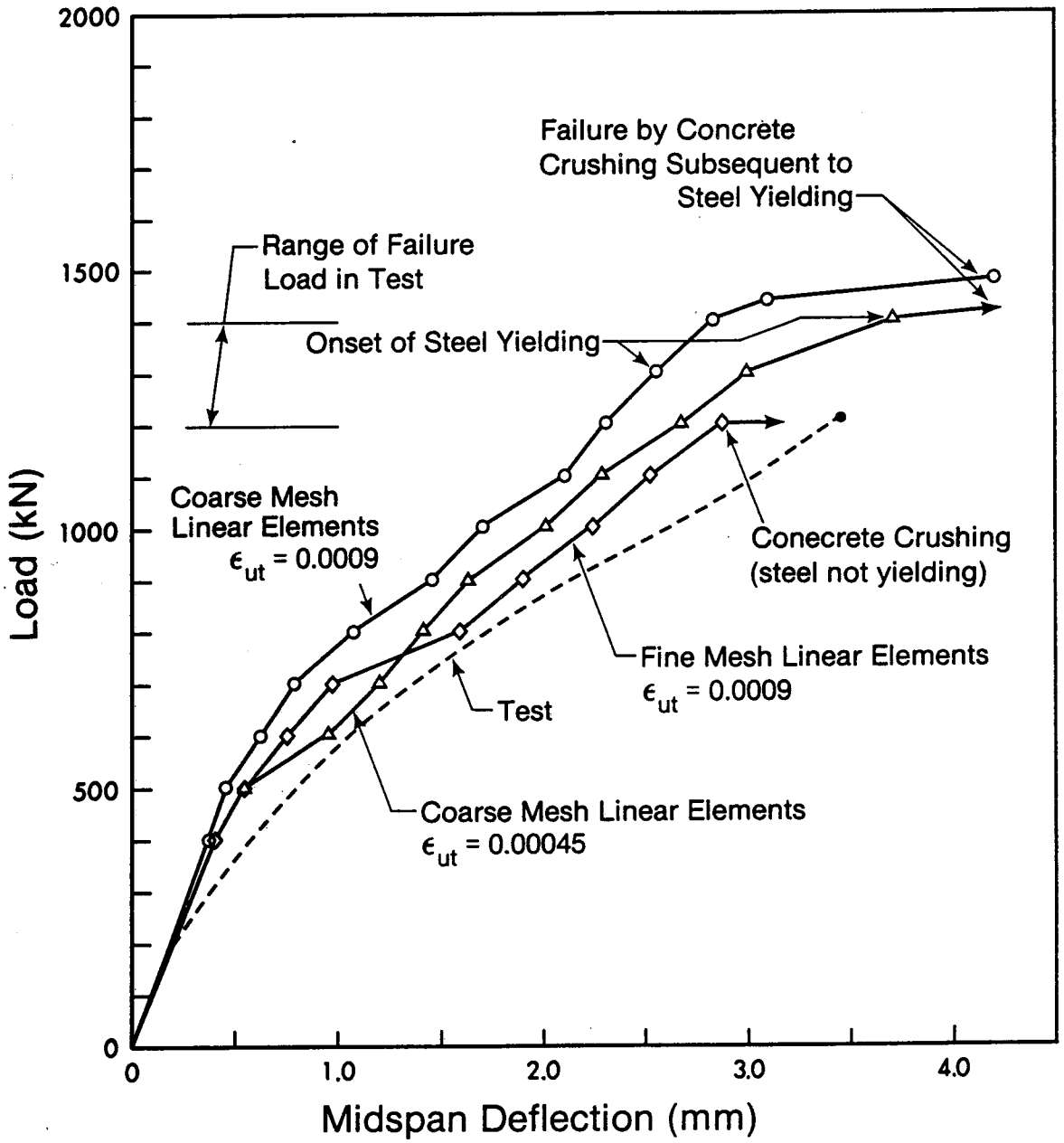

FIG. A3.28. Load-Deflection Relationship for Rogowsky/MacGregor Deep Beam - Effect of Mesh Reinforcement

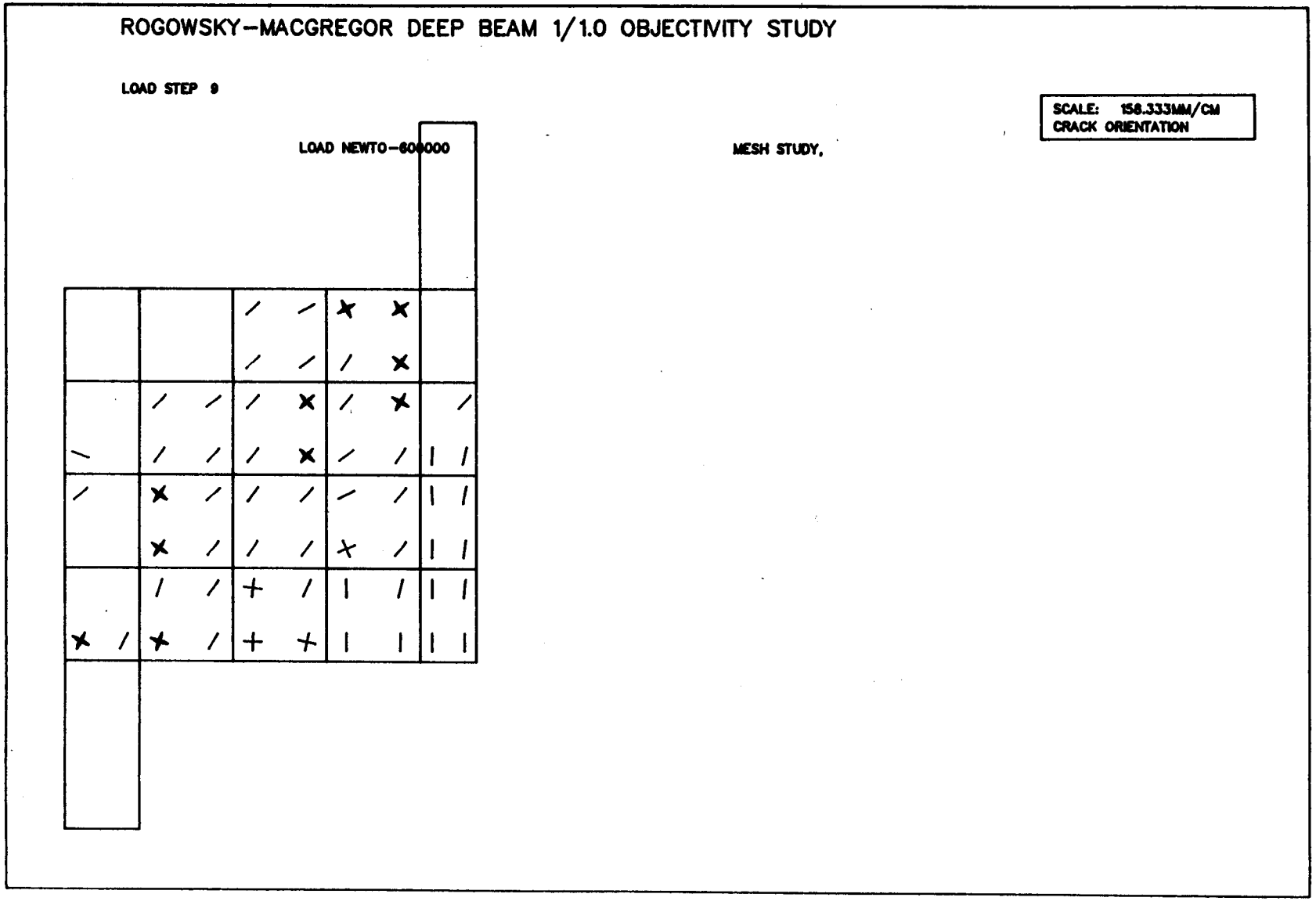

FIG. A3.29. Compression Strain Hardening/Softening Regions - Coarse Mesh Layout

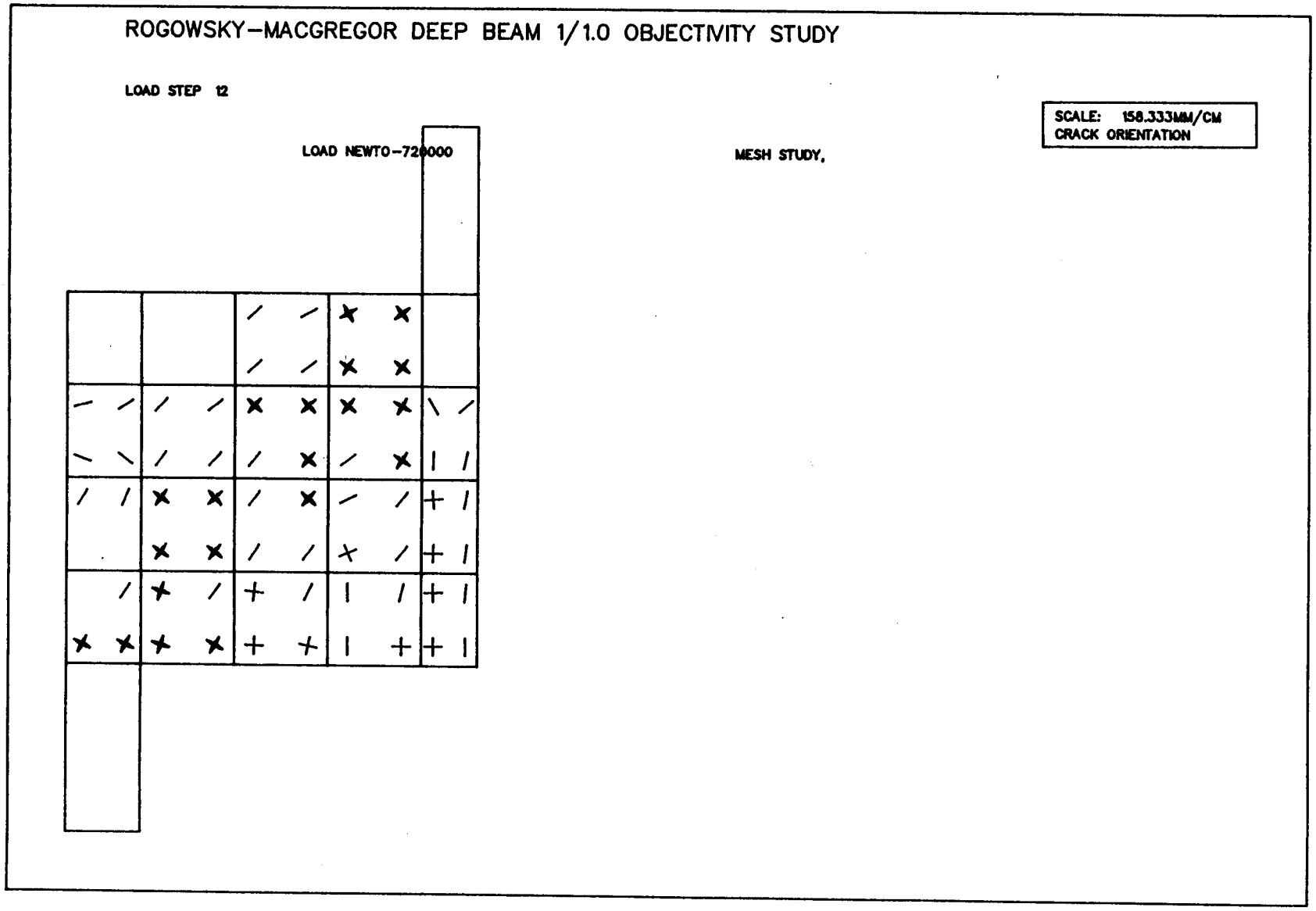

FIG. A3.30. Spreading of Compression Strain Hardening/Softening Regions - Coarse Mesh Layout

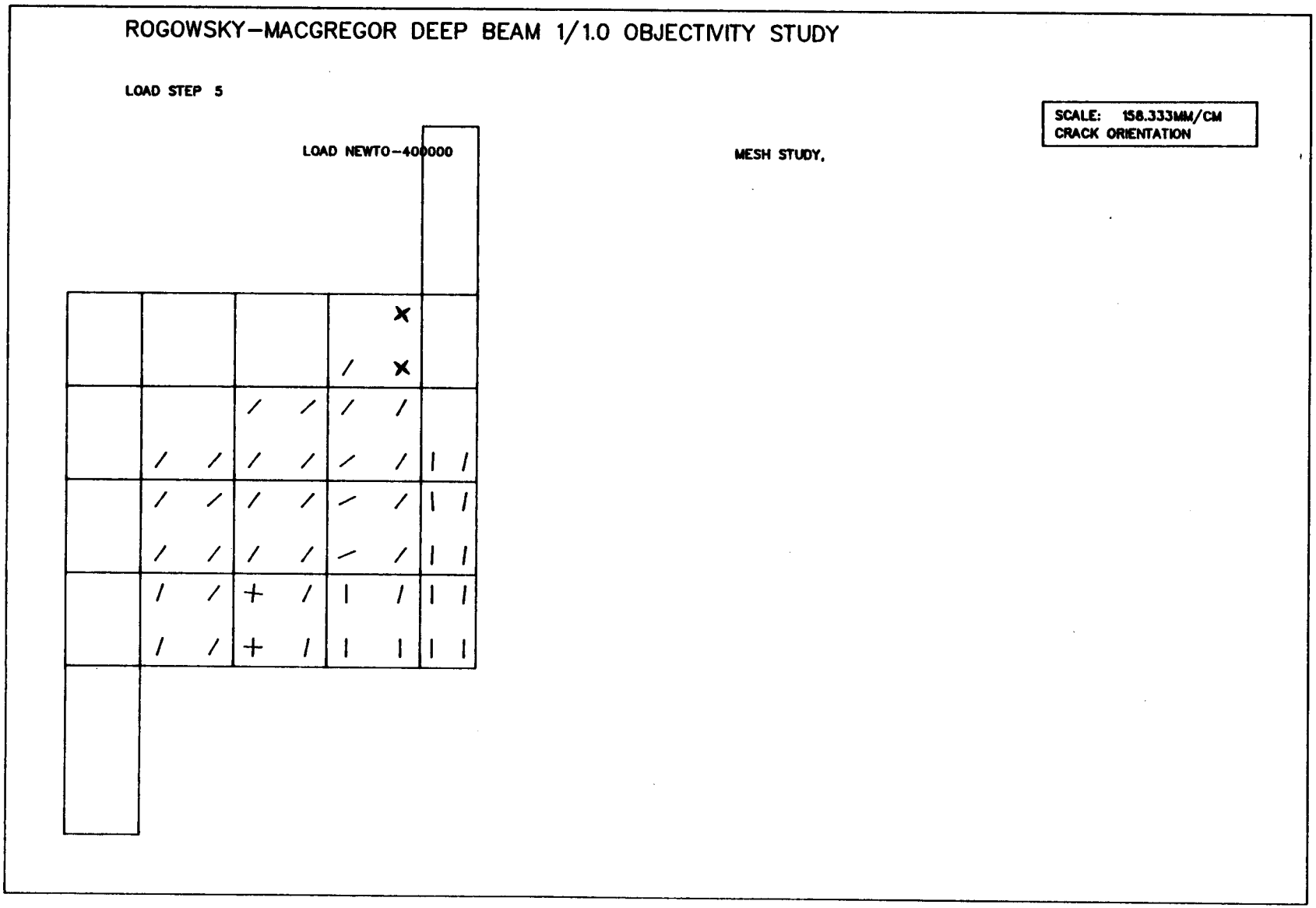

FIG. A3.31. Analytical Crack Pattern at Shear = 400 kN with ε_{ut} = 0.00045 - Coarse Mesh Layout

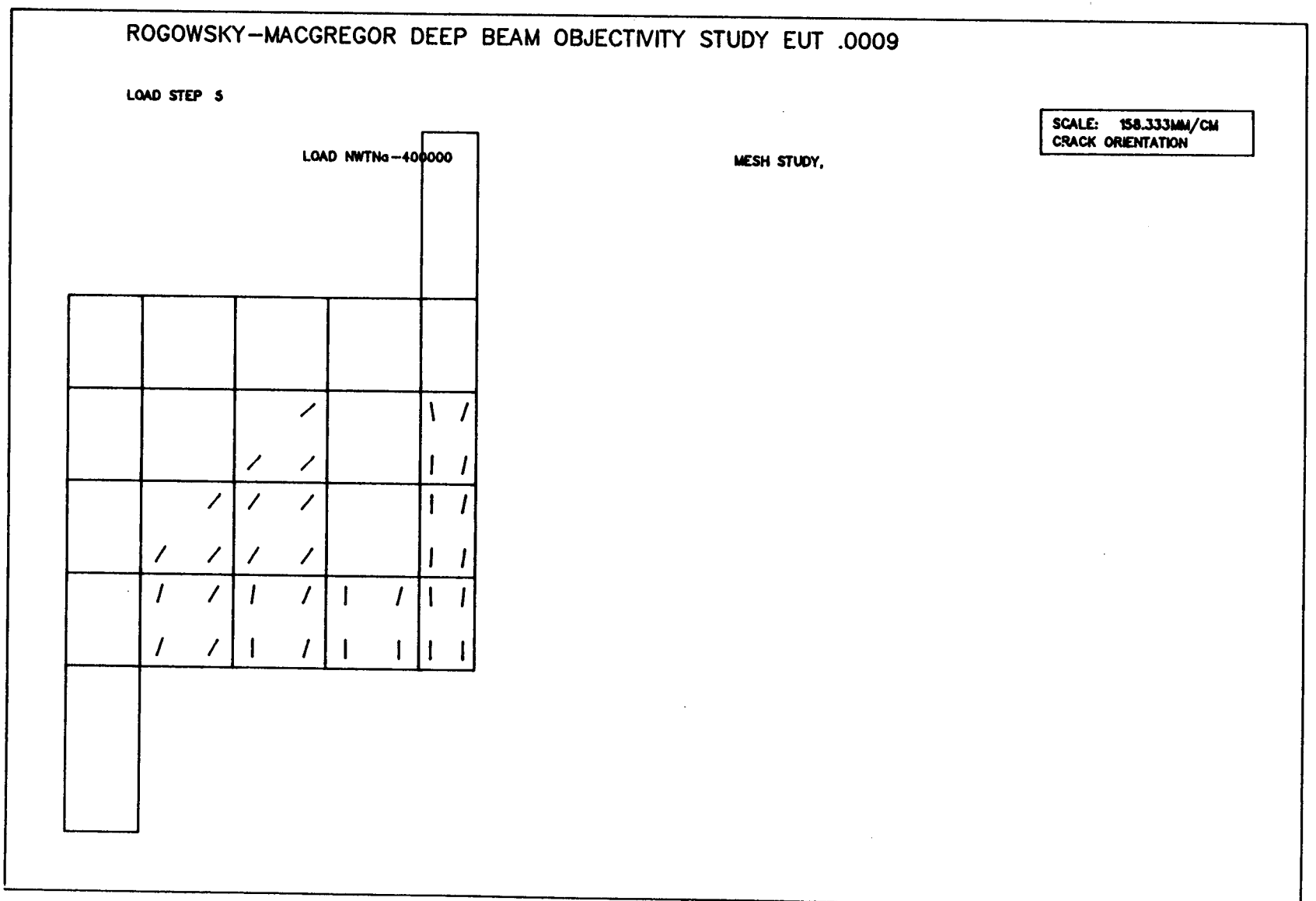

FIG. A3.32. Analytical Crack Pattern at Shear = 400 kN with ε_{ut} = 0.0009 - Coarse Mesh Layout

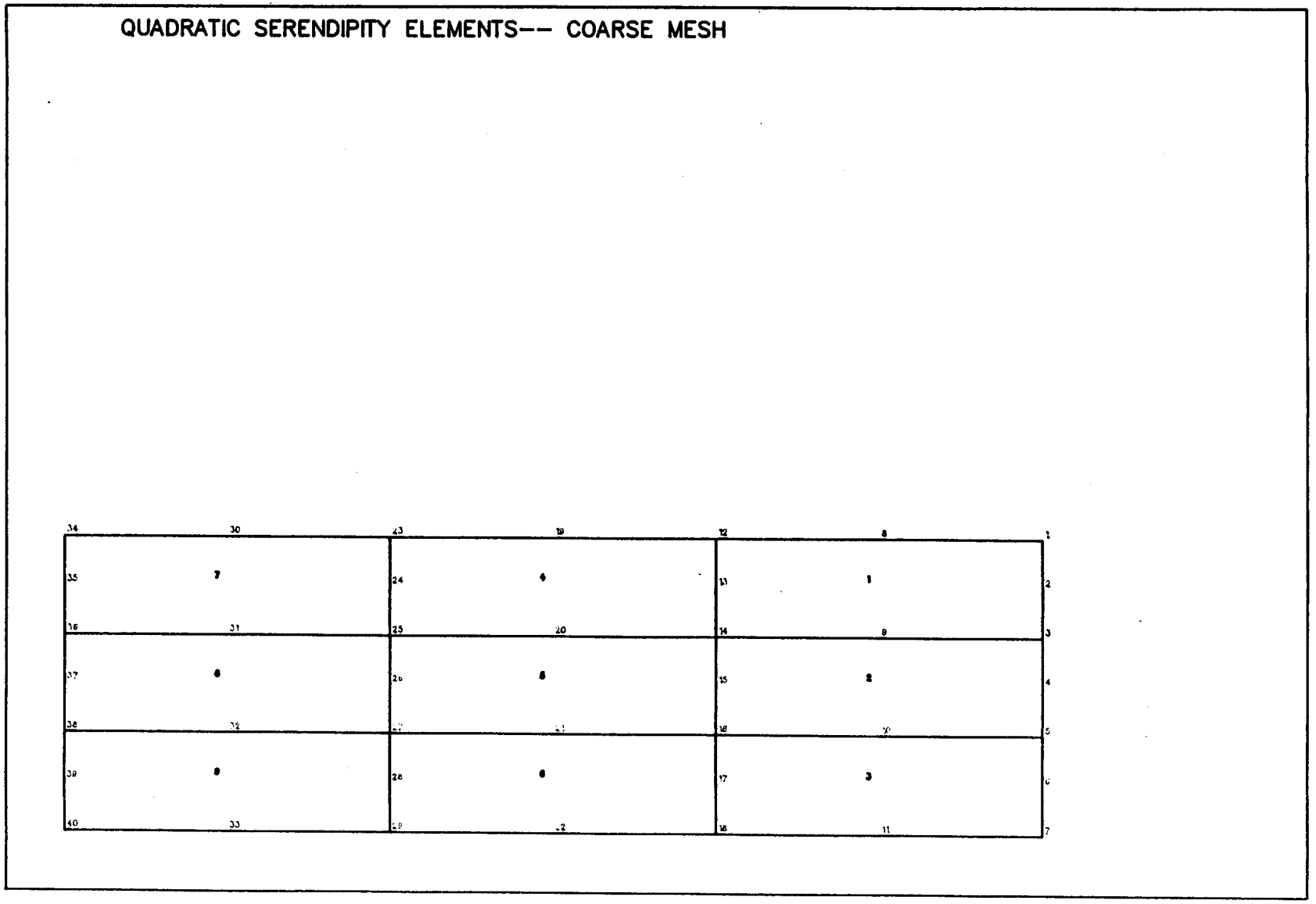

FIG. A3.33. Bresler/Scordelis Beam XOB1 - Coarse Mesh Layout

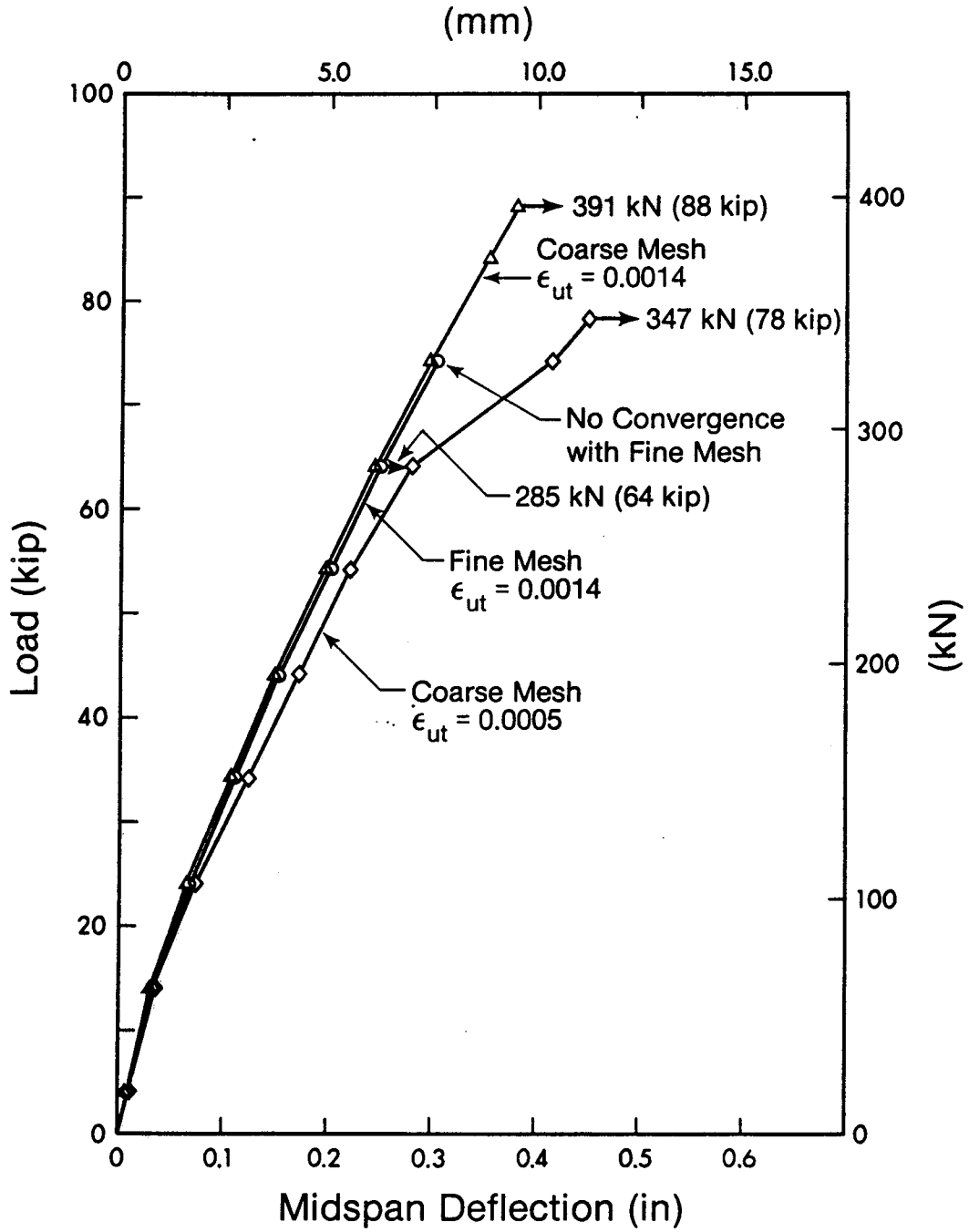

FIG. A3.34. Load-Deflection Relationships for Beam XOB-1
Effect of Mesh Refinement

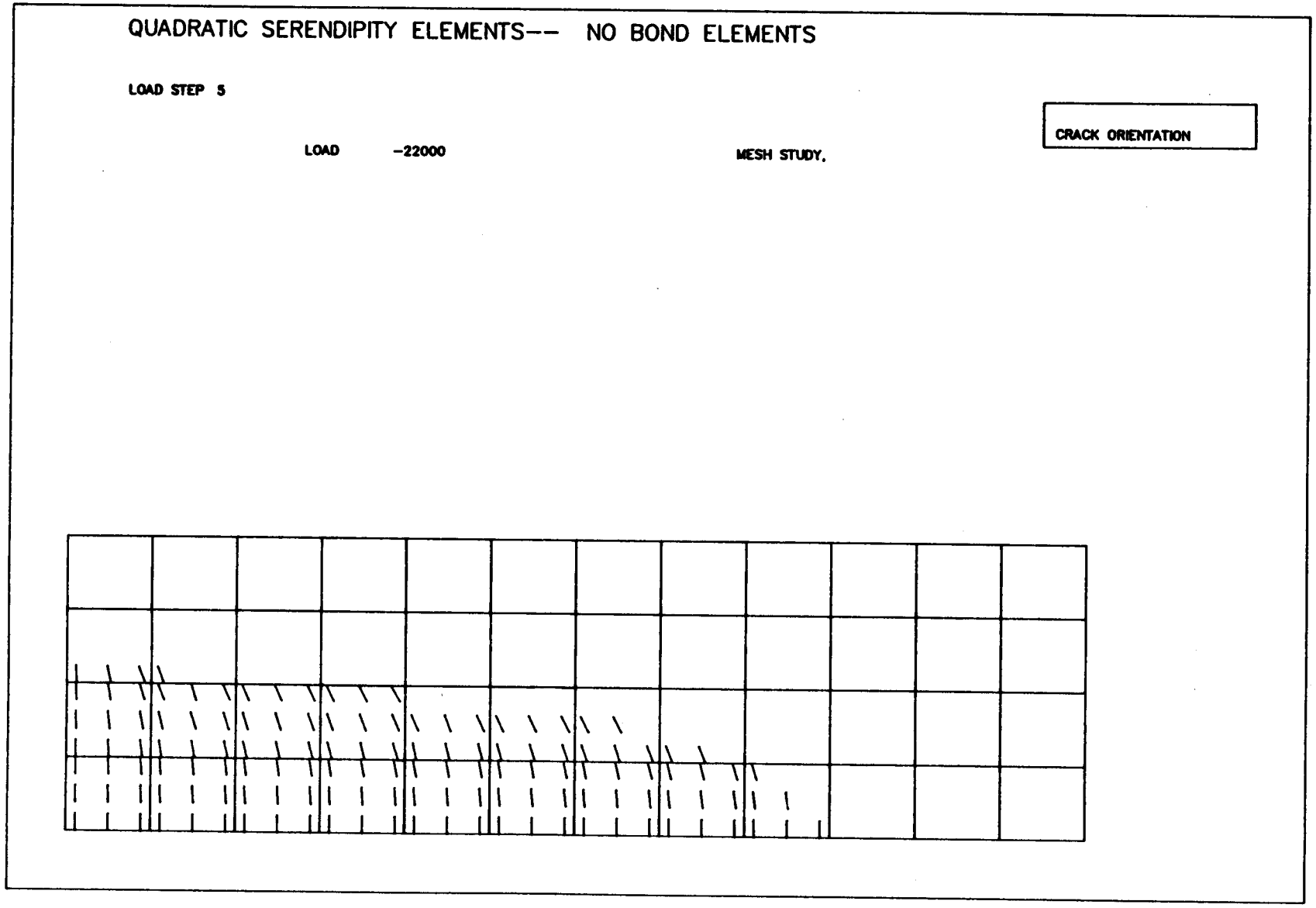

FIG. A3.35. Analytical Crack Pattern - Bresler/Scordelis Beam XOB1 - Shear = 22 kip (97.9 kN)
(a) Fine Mesh Layout - ε_{ut} = 0.0014

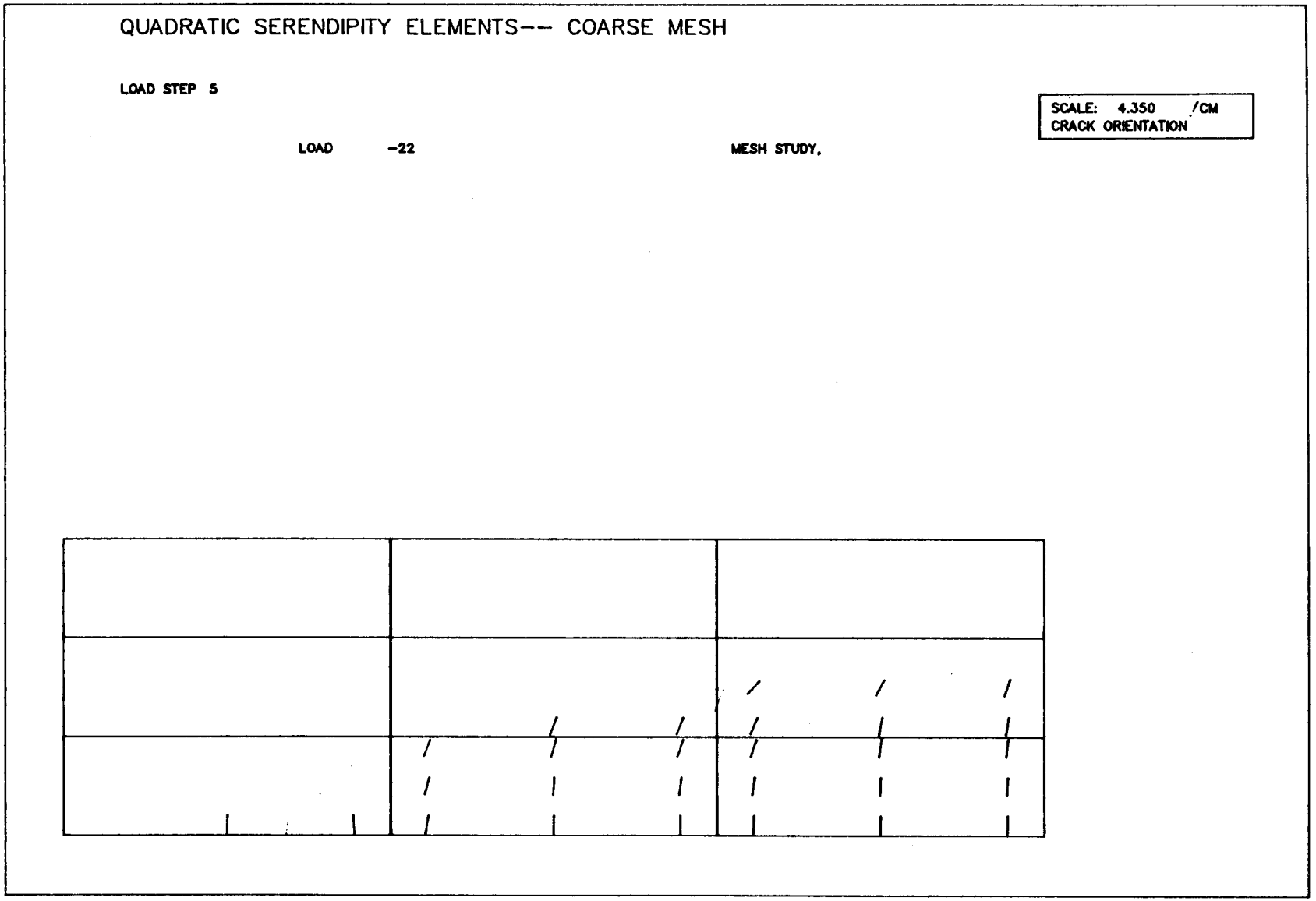

FIG. A3.35. (b) Coarse Mesh Layout, $\varepsilon_{ut} = 0.0014$

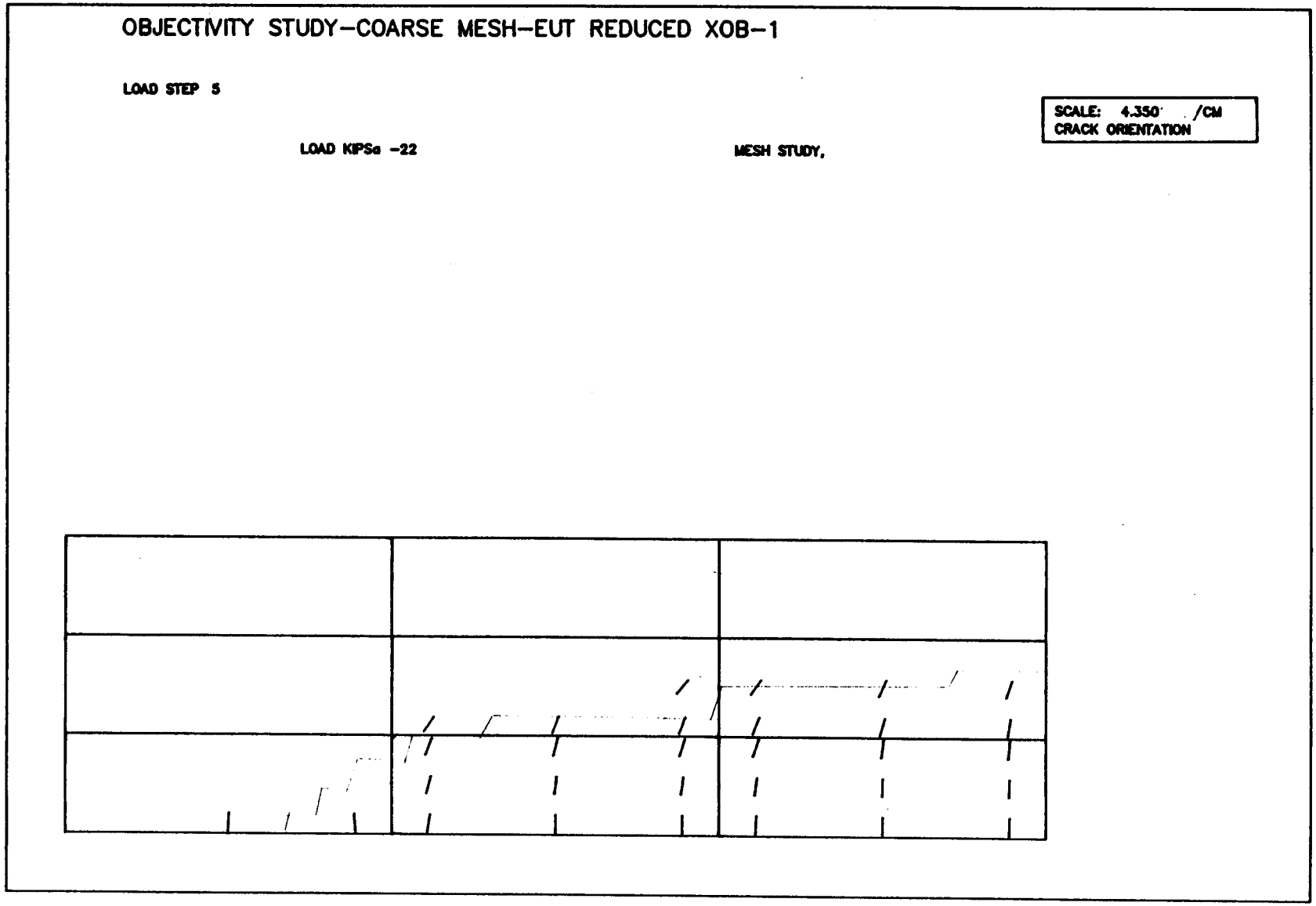

FIG. A3.35. (c) Coarse Mesh Layout, $\varepsilon_{ut} = 0.0005$

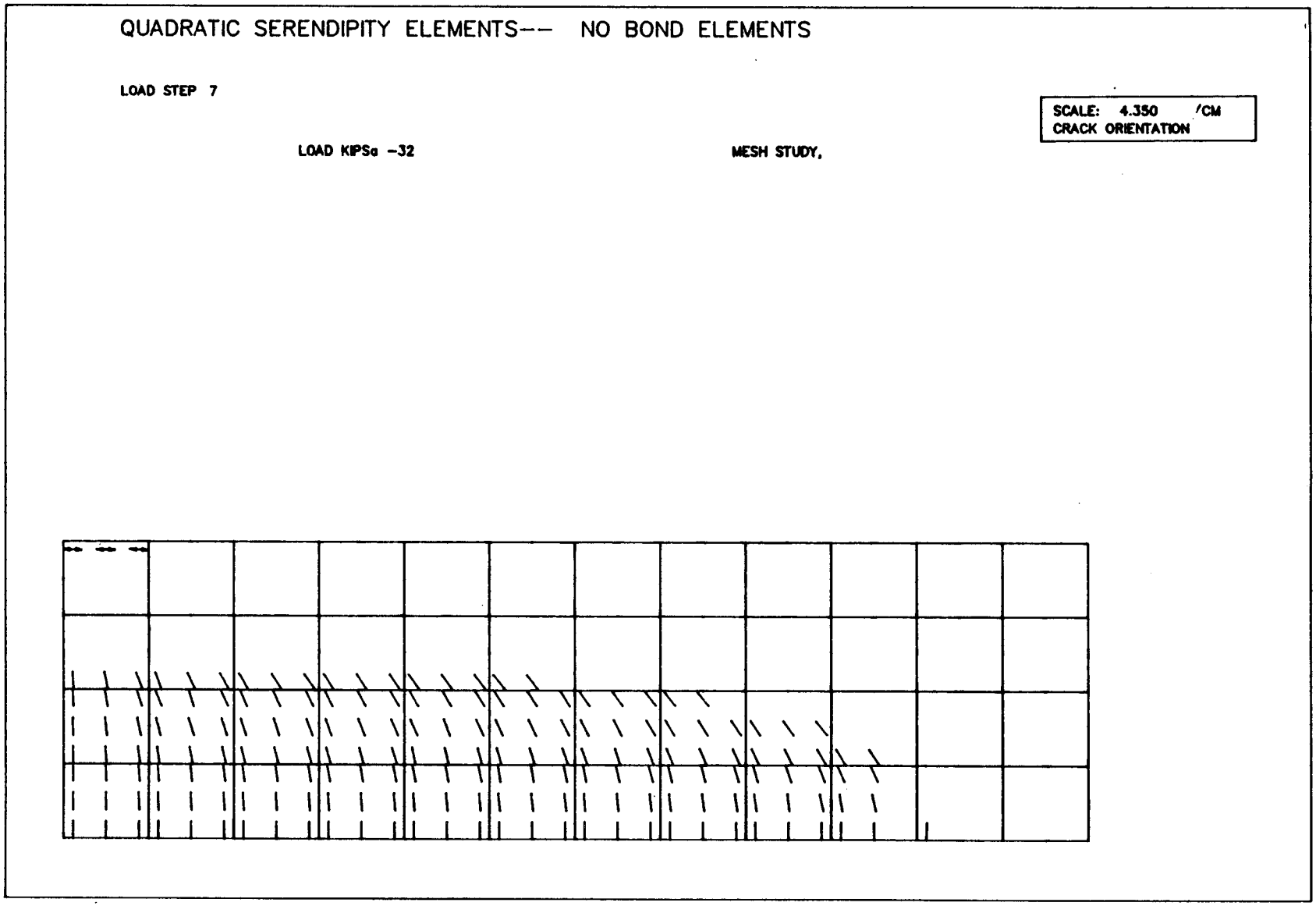

FIG. A3.36. Analytical Crack Pattern - Bresler/Scordelis Beam XOB1 - Shear = 32 kip (142.3 kN)
(a) Fine Mesh Layout, ε_{ut} = 0.0014

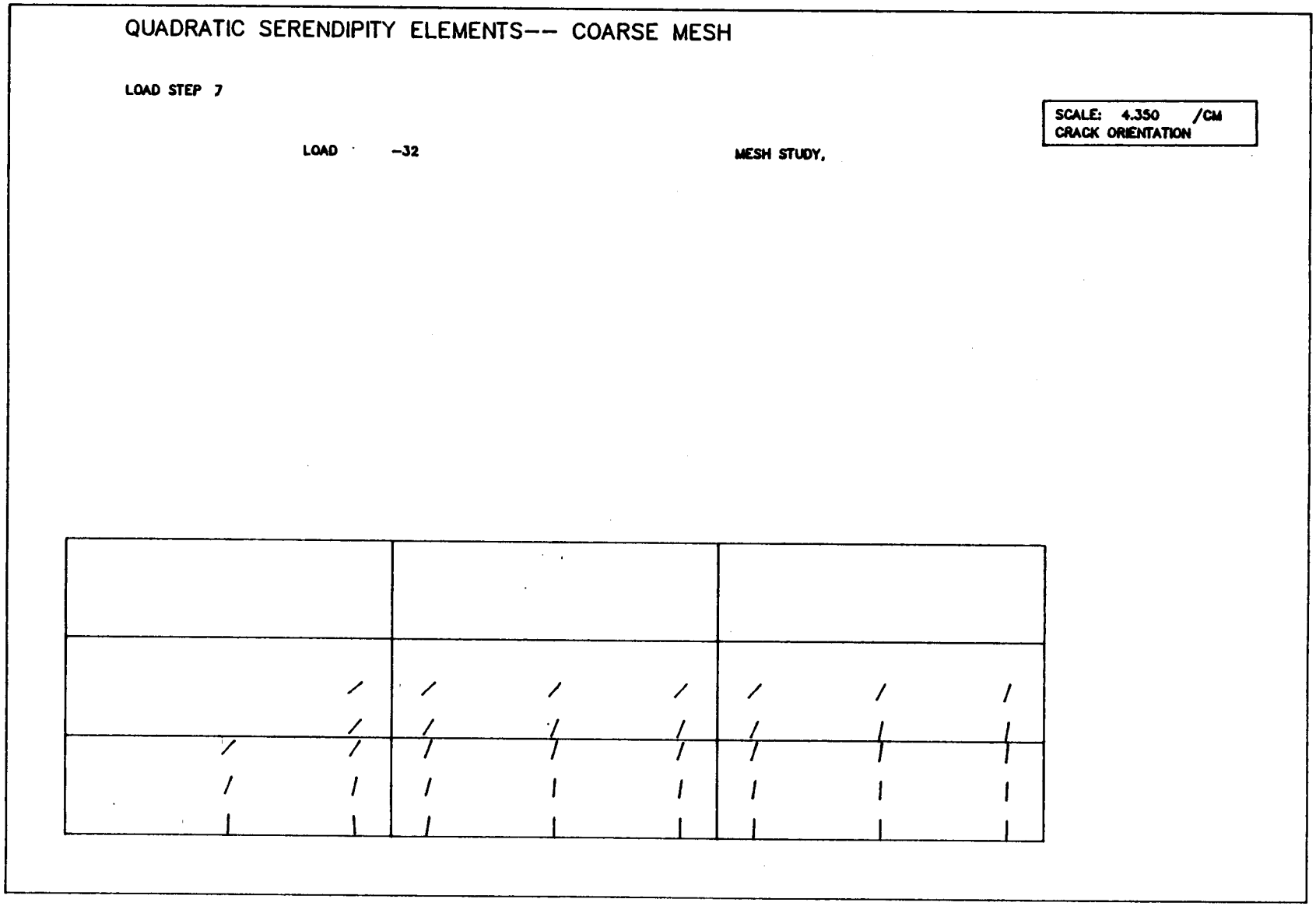

FIG. A3.36. (b) Coarse Mesh Layout, $\varepsilon_{ut} = 0.0014$

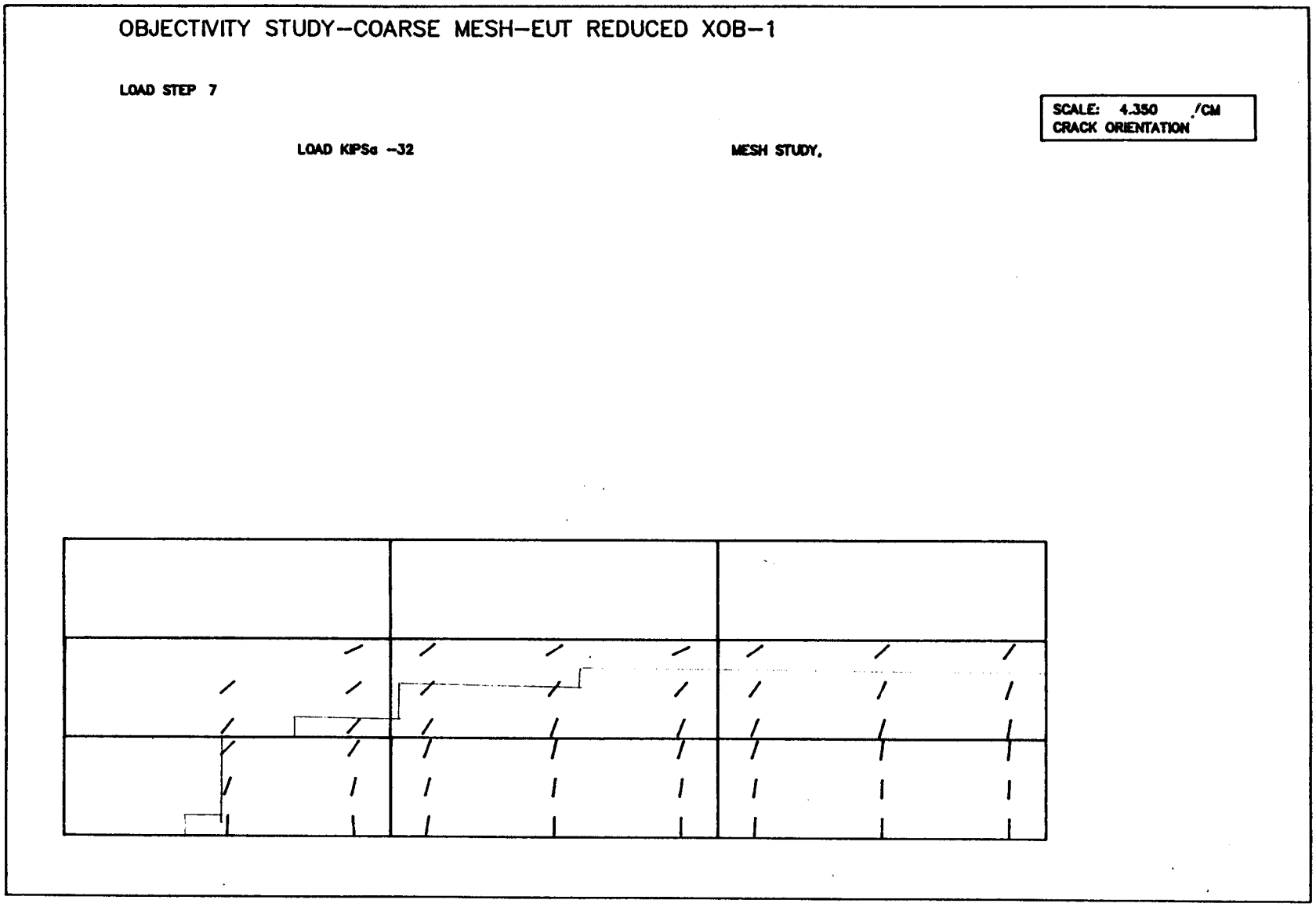

FIG. A3.36. (c) Coarse Mesh Layout, $\varepsilon_{ut} = 0.0005$

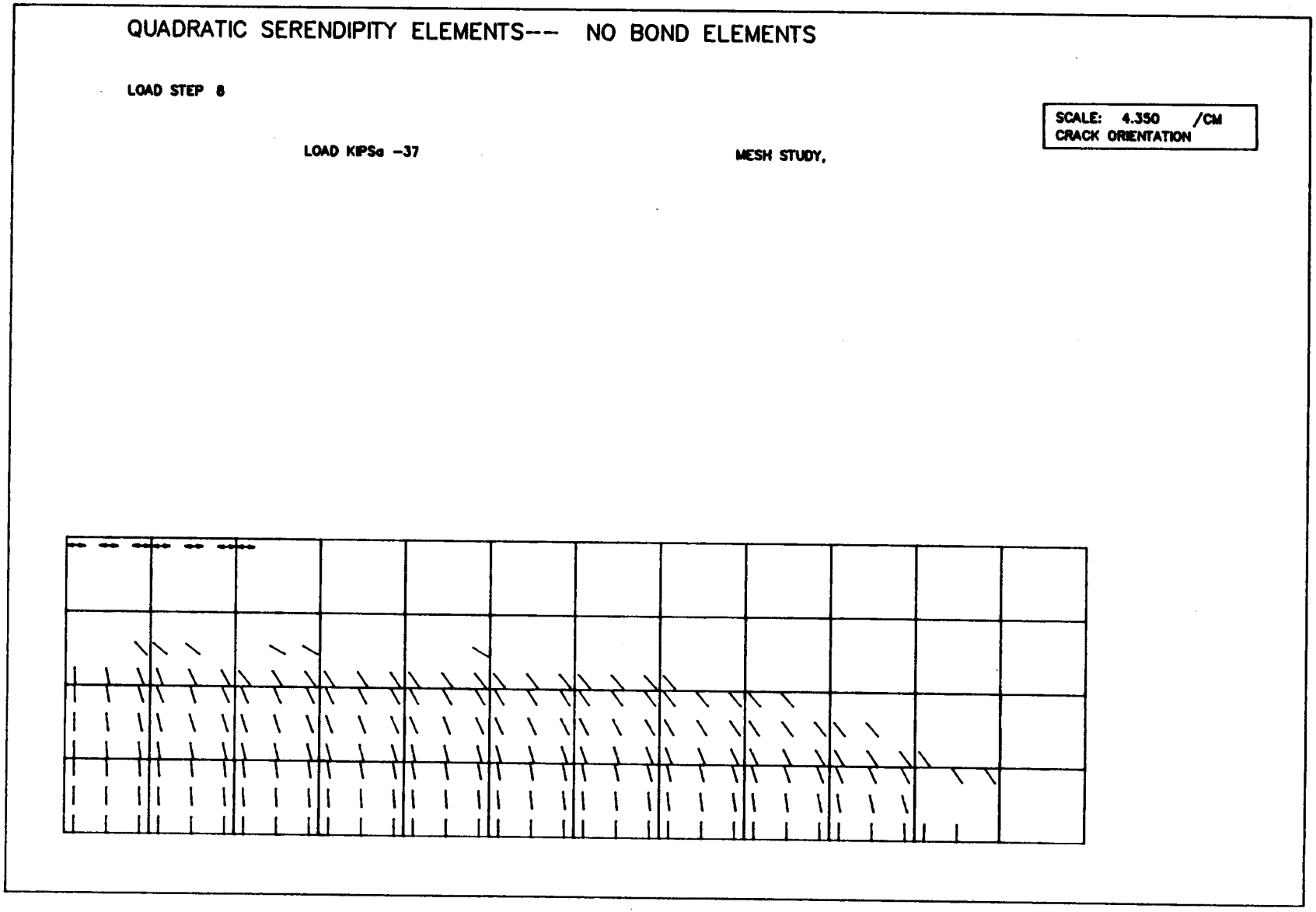

FIG. A3.37. Analytical Crack Pattern - Bresler/Scordelis Beam X0B1 - Shear = 37 kip (164.6 kN)
(a) Fine Mesh Layout, ε_{ut} = 0.0014

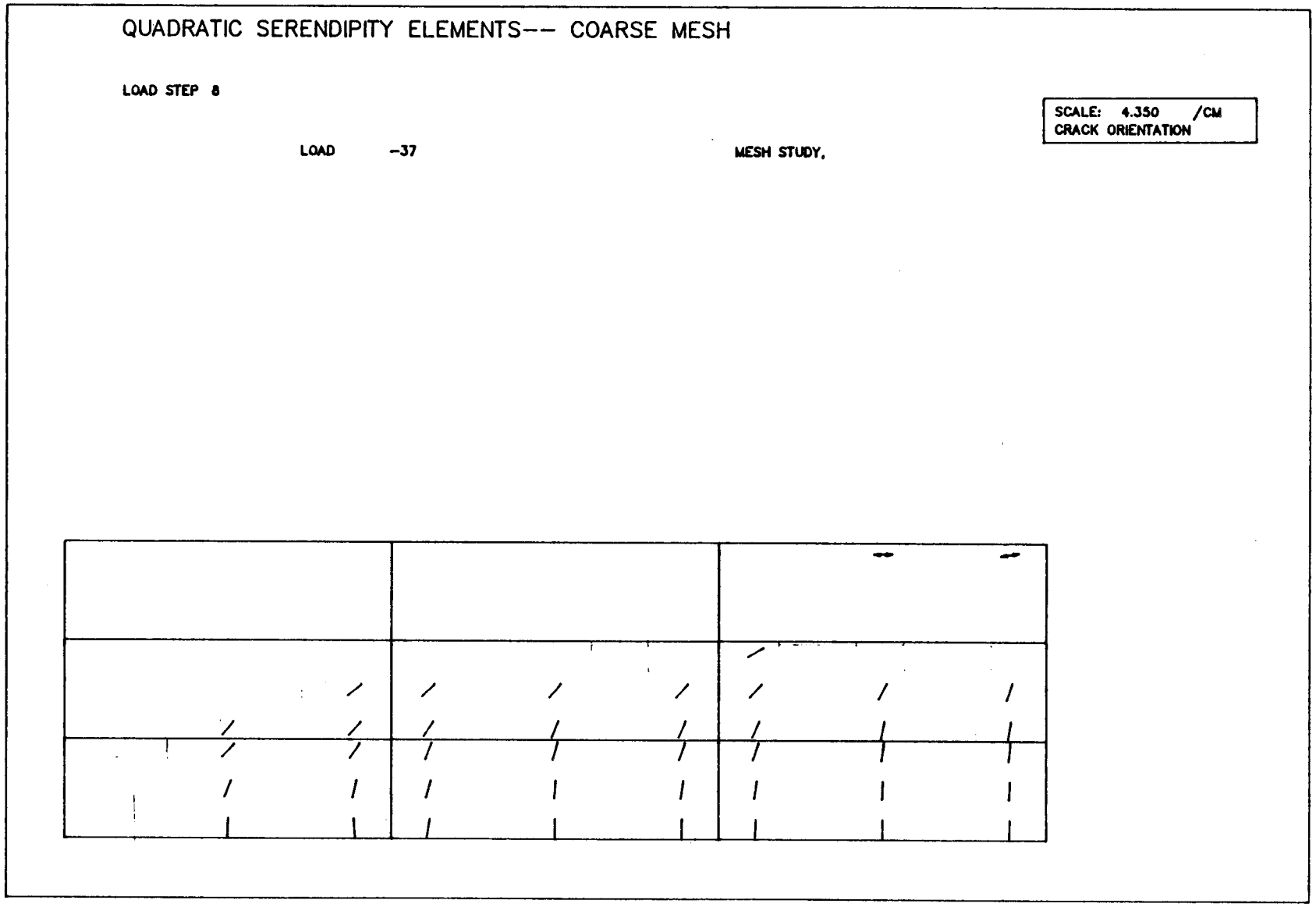

FIG. A3.37. (b) Coarse Mesh Layout, $\varepsilon_{ut} = 0.0014$

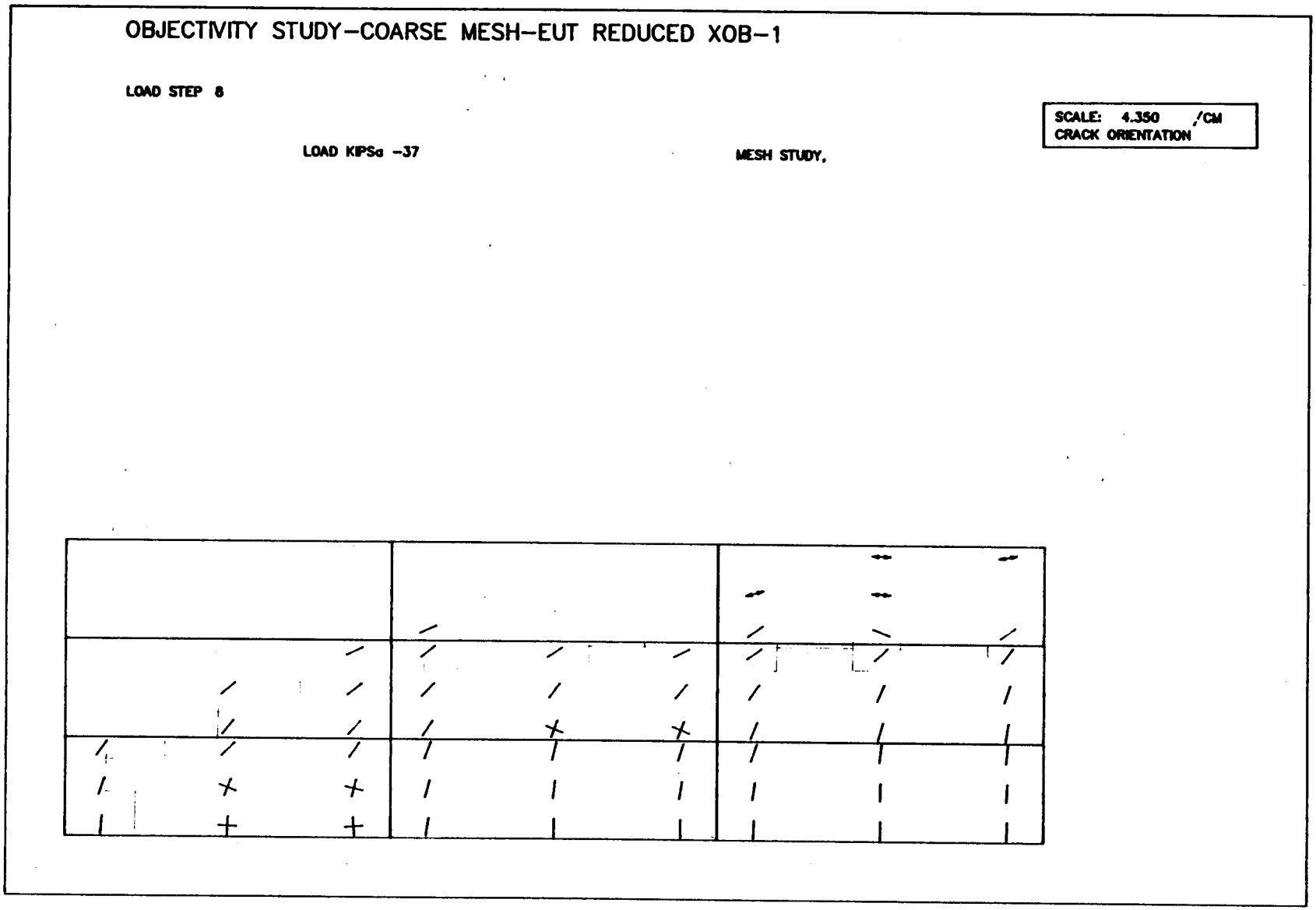

FIG. A3.37. (c) Coarse Mesh Layout, $\varepsilon_{ut} = 0.0005$

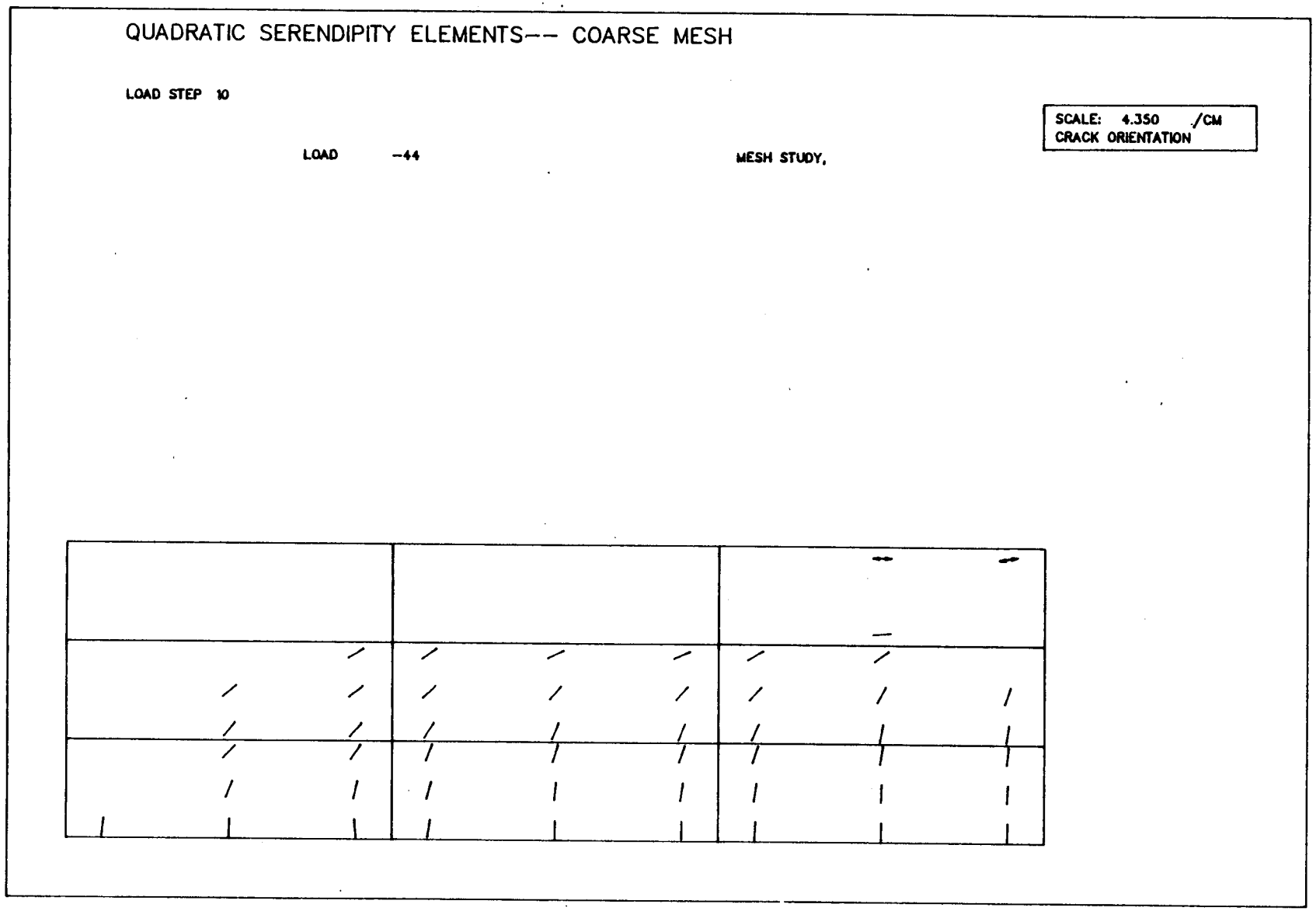

FIG. A3.38. Analytical Crack Pattern - Bresler/Scordelis Beam XOB1 - Shear = 44 kip (195.7 kN) ε_{ut} = 0.0014 - Coarse Mesh Layout

APPENDIX A4

DETERMINATION OF CONCRETE MATERIAL PROPERTIES FOR FINITE ELEMENT ANALYSIS

A4.1 Elastic Moduli

As described in Chapter 3, the stress-strain relationship of concrete in uniaxial compression is idealized using the multilinear curve shown in Fig. A4.1. The initial elastic modulus of concrete is assumed to be given by Eq. A4.1 for normal weight concrete.

$$E_c^{(o)} = 57000 \sqrt{0.9f'_c} \quad \text{in Imperial units}$$

$$E_c^{(o)} = 5000 \sqrt{0.9f'_c} \quad \text{in SI units} \qquad \text{(A4.1)}$$

where $E_c^{(o)}$ is the elastic modulus in psi (MPa) and f'_c is the cylinder compressive strength in psi (MPa).

This compares with the ACI formula for secant modulus at $0.5f'_c$, given by Eq. A4.2

$$E_{c_{(ACI)}}^{(o)} = 57000 \sqrt{f'_c} \quad \text{in Imperial units}$$

$$E_{c_{(ACI)}}^{(o)} = 5000 \sqrt{f'_c} \quad \text{in SI units} \qquad \text{(A4.2)}$$

The modulus in region -1, $E_c^{(-1)}$, called the compressive strain hardening modulus, is taken as shown in Fig. A4.1. (In the absence of test results, $E_c^{(-1)}$ is taken as $E_c^{(o)}/9$ for unconfined concrete and $0.05E_c^{(o)}$ for concrete confined by stirrups.)

The compressive strain softening modulus, $E_c^{(-2)}$, depends on: (1) the concrete strength (the higher the peak stress, the greater the stress decrement for a given strain increment, as shown in Fig. A4.2); (2) the specimen size (since strain softening is not a material property, as discussed in Chapter 3); (3) the confinement provided by steel stirrups; and, (4) multiaxial stress conditions.

The dependence of the strain softening modulus on the specimen size (and thus on the finite element mesh size) is shown in Fig. A4.3. This dependency is due to strain localization, as discussed in Chapter 3. However, it is difficult to incorporate this dependency in a finite element model unless the location of the strain localization band can be determined a priori. Thus, for the present, a strain softening modulus of $-0.05E_c$ has been adopted for unconfined concrete.

The effects of confinement on the strain-softening modulus have been investigated by a number of researchers who arrived at varying (and some contradictory) results as shown in Fig. A4.4a to g. In this study, the expression proposed by Vallenas, Bertero and Popov (1977) and modified by Krauthammer and Hall (1982) has been further modified as given by Eqs. A4.4a to e. The relationship is illustrated in Fig. A4.4(g).

$$f_c = f'_c \, k \left[1 - 0.8Z \, \varepsilon_o \left(\frac{\varepsilon}{\varepsilon_o} - 1\right)\right] \qquad \text{(A4.4a)}$$

where

$$k = 1 + 0.0091 \left(1 - 0.245 \frac{S}{h''}\right) \frac{\rho'' f_y''}{\sqrt{f'_c}} \qquad \text{(A4.4b)}$$

$$Z = \frac{0.5}{\frac{3}{4}\rho''\left(\frac{h''}{S}\right)^{1/2} + \frac{3 + 0.002f'_c}{f'_c - 1000} - 0.002} \qquad \text{(A4.4c)}$$

$$\varepsilon_o = 0.0024 + 0.005\left(1 - 0.734\,\frac{S}{h''}\right)\rho''\,\frac{fy''}{\sqrt{f'_c}} \qquad \text{(A4.4d)}$$

$h'' = 0.5\left(h''_1 + h''_2\right)$, in which h''_1 and h''_2 are the dimensions of the two sides that describe the rectangular compressive zone in a beam, as shown in Fig. A4.4h, in inches.

ρ'' = the ratio of the total volume of the confining transverse reinforcement to the volume of the confined concrete in the compressive zone; S = the spacing of the transverse reinforcement, in.; f''_y = yield strength of the transverse reinforcement, psi; and f'_c = the unconfined compressive strength of concrete, psi.

The factor k accounts for the increase in strength resulting from confinement while Z accounts for the increase in post peak stiffness.

Equations A4.4b, A4.4c and A4.4d are modified to account for the cover concrete, which is unconfined, as follows.

$$E_c^{(-2)} = \frac{A_o E_o + A_1 E_1}{A_o + A_1} \qquad \text{(A4.4f)}$$

where A_o is the area of the unconfined concrete in the compressive zone of the beam; E_o is the strain softening modulus ignoring the confining effect of hoops; A_1 is the area of concrete used in the calculation of ρ''; and, E_1 is the strain softening modulus as obtained using Eqs. A4.4a to e.

The dependence of the strain softening modulus on the multiaxial

stress conditions is shown in Fig. A4.5 for the case of biaxial compression. However, test results are lacking for concrete under combined tension and compression. This dependence has not been included in this study.

A.4.2 Poisson's Ratio

Poisson's ratio of concrete apparently depends on the stress level. Kupfer et al. (1969) found the value of Poisson's ratio to be in the range of 0.18 to 0.20 at lower stress levels when concrete can be considered to be elastic. Vecchio and Collins (1982), based on a test of a R/C shear panel, reported the value of Poisson's ratio to range from 0.10 at intermediate stress levels to 0.25 near ultimate stress level. At high compressive stress levels concrete exhibits volume dilation (Kupfer et al., 1969) and hence an increase in the apparent Poisson's ratio. However, considering the localized nature of concrete failure (Chapter 3) it would appear that the volume dilation is due to the onset of a splitting mode of failure. Therefore, in this study Poisson's ratio is assumed constant. The recommended values of Poisson's ratios are 0.125 (Vecchio and Collins, 1982) for elements containing reinforcement and 0.2 (Kupfer et al., 1969) otherwise.

A4.3 Tensile Strength

Since a strain-softening branch is used to describe the stress-strain behavior of concrete in tension, the tensile strength to be input is ideally obtained from direct tension tests. However direct tension tests to obtain reliable results are difficult to perform and hence the split tension test or flexural test are used to determine tensile

strength. Values obtained from the split tension tests could be used directly as f_t' for this study. However, modulus of rupture values derived from flexural tests assume elastic conditions at failure and hence have to be modified to obtain direct tensile strengths, as described in the following paragraphs.

As discussed in Chapter 3, a fracture process zone of finite dimension exists ahead of a crack tip in concrete. Modulus of rupture tests are usually performed on specimens (6 in. x 6 in.) 150 mm x 150 mm in cross section. For such small beams, a full fracture process zone does not develop (Hillerborg, 1985) when maximum load carrying capacity is obtained. The theoretical development of the fracture zone, and the corresponding stress distribution, load and deflection for a notched beam in bending are shown in Fig. A4.6 (Hillerborg, 1985). At maximum load the length of the fracture zone is about 50 mm (2 in.) for the specimen of Fig. A4.6. The stress distributions at maximum load for beams of different depths are shown in Fig. A4.7. It is evident that the stress distributions at maximum load are highly dependent on the beam depth. For small beams the distribution approaches that given by the theory of plasticity whereas for deep beams it approaches that given by the theory of elasticity. The variation in the length of the fracture zone at maximum load with the beam depth is shown in Fig. A4.8. It can be seen from this figure that for the modulus of rupture specimen the length of the fracture process zone is approximately 50 mm (2 in.). Figure A4.9 shows the stress distribution at failure of the modulus of rupture specimen assumed herein to determine the tensile strength as follows.

The failure moment obtained using linear elastic theory and a

tension cut-off is

$$M = \frac{1}{6} f_r b d^2 \qquad \text{(A4.5)}$$

where f_r = modulus of rupture.

For equilibrium, the sum of the horizontal forces should vanish.

$$\frac{1}{2} f_c \, c = \Delta a \, f'_t + \frac{1}{2} (d - c - \Delta a) \, f'_t \qquad \text{(A4.6)}$$

Also, for the stress distribution assumed,

$$\frac{f'_t}{d - c - \Delta a} = \frac{f_c}{c} \qquad \text{(A4.7)}$$

Substituting for f_c, from Eq. A4.7 into Eq. A4.6, the following expression for c is obtained.

$$\frac{1}{2} c^2 - (d - c - \Delta a) \, \Delta a - \frac{1}{2} (d - c - \Delta a)^2 = 0 \qquad \text{(A4.8)}$$

With d = 6" (152 mm) and Δa = 2" (50 mm), Eq. A4.8 yields c = 2.67" (68 mm). Substituting c = 2.67" (68 mm) in Eq. A4.7 yields

$$f_c = 2 f'_t \qquad \text{(A4.9)}$$

The failure moment for the stress distribution assumed in Fig. A4.9b is, therefore, (using Imperial units)

$$M = \left(\frac{1}{2} (2f'_t)(2.67)^2(.667) + \frac{1}{2} f'_t \, (1.33)^2(.667)\right.$$

$$+ (2)\ f'_t\ (2.33))\ b \qquad \text{(A4.10)}$$

$$= 60.0\ f'_t$$

Substituting for b and d in Eq. A4.5,

$$M = 36\ f_r \qquad \text{(A4.11)}$$

Substituting for M from Eq. A4.11 into Eq. A4.10 and solving for f'_t, we obtain

$$f'_t = 0.6 f_r \qquad \text{(A4.12)}$$

In the absence of test results on direct tensile strength an expression for f_r obtained from experimental results by Rapheal (1984) as

$$f_r = 2.3\ (f'_c)^{2/3} \quad \text{in Imperial units} \qquad \text{(A4.13)}$$

may be used to determine this input value. Substituting for f_r from Eq. A4.13 into Eq. A4.12,

$$f'_t = 1.38\ (f'_c)^{2/3} \quad \text{in Imperial units} \qquad \text{(A4.14)}$$

f'_c abd f'_t in psi

$$f'_t = 0.263\ (f'_c)^{2/3} \quad \text{in SI units} \qquad \text{(A4.14b)}$$

f'_c and f'_t in MPa

A4.4 Tension Softening and Tension Stiffening

The ultimate tensile strain, ε_{ut}, is related to the fracture energy release rate, G_F, by Eq. A4.15, as described in Chapter 3, Sect. 3.2.

$$\varepsilon_{ut} = \frac{2G_F}{f'_t h} \qquad \text{(A4.15)}$$

where h is the width of the crack band.

Only a very limited number of tests have been performed to determine G_F and there does not appear to be any relationship yet derived from tests relating G_F to other material properties such as f'_t. Also, most of the fracture tests were performed on small scale specimens wherein the fracture zone could not be fully developed. Tests by Gopalaratnam and Shah (1984) and Peterson (as used by Rots et al., 1985) indicate G_F to range from 50 N/m to 150 N/m (0.286 lb/in. to 0.856 lb/in.). In the study a value of 100 N/m (0.571 lb/in.) has been adopted.

Equation A4.15 was derived in Chapter 3 in order to obtain a mesh independent response for the propagation of a single crack. Indeed most of the work in the application of the fracture energy release rate concept in the literature has related to such an individual crack, often predetermined as in notched specimens. In R/C beams, however, cracks form at different spacings in the tension zone based on a number of parameters such as the depth of the tension zone, bond characteristics of the reinforcement, area of bars and the statistical scatter in the tensile strength of concrete. Since G_F is the fracture energy consumed

in the formation of a single crack, it is appropriate to assume in Eq. A4.15 that h is the average crack spacing. The average crack spacing may be calculated using Eq. 3.9, reproduced herein as Eq. A4.16.

$$S_m = K_1 C + K_2 \frac{\phi}{\rho_{eff}} \qquad \text{(A4.16)}$$

where S_m is the mean crack spacing, ϕ is the diameter of reinforcement and ρ_{eff} is the effective steel ratio based on the effective concrete area, as determined from Fig. 3.7b; K_1 and K_2 are constants obtained from Table 3.1.

The effect of tension stiffening is included in the average tensile stress-strain curve for concrete. As discussed in Chapter 3, Sect. 3.3, the tension stiffening effect decreases with decrease in proximity to the reinforcement. Thus, Eq. 3.20 and Eq. 3.21 are used for the element containing the reinforcement and progressively decreasing tension stiffening is used for the elements at increasing distance from the reinforcement. The beams analysed in this study were modelled with 4 elements along the height. The tension stiffening adopted for different elements is shown in Fig. A4.10. The influence of the descending branch of the tensile stress strain curve on the top row of elements is not significant because they are mostly uncracked. The bottom element has the most tension-stiffening effect and the elements immediately above the bottom element have less but significant tension stiffening effect. The value of ε_{xt} has been taken as $1.33\varepsilon_{ut}$ for these elements. The values of ε_{xt} have been denoted as ε_{ut} in Table 5.2 and Table 5.4.

A4.5 Required Accuracy of Input Parameters

All input material parameters for the analysis of R/C beams can thus be determined as described in this Appendix. The statistical scatter in the specimen test results must be taken into account in interpretting the analytical results. The influence of various input parameters on the analytical behavior prediction is described in Chapter 5 and Appendix A3.

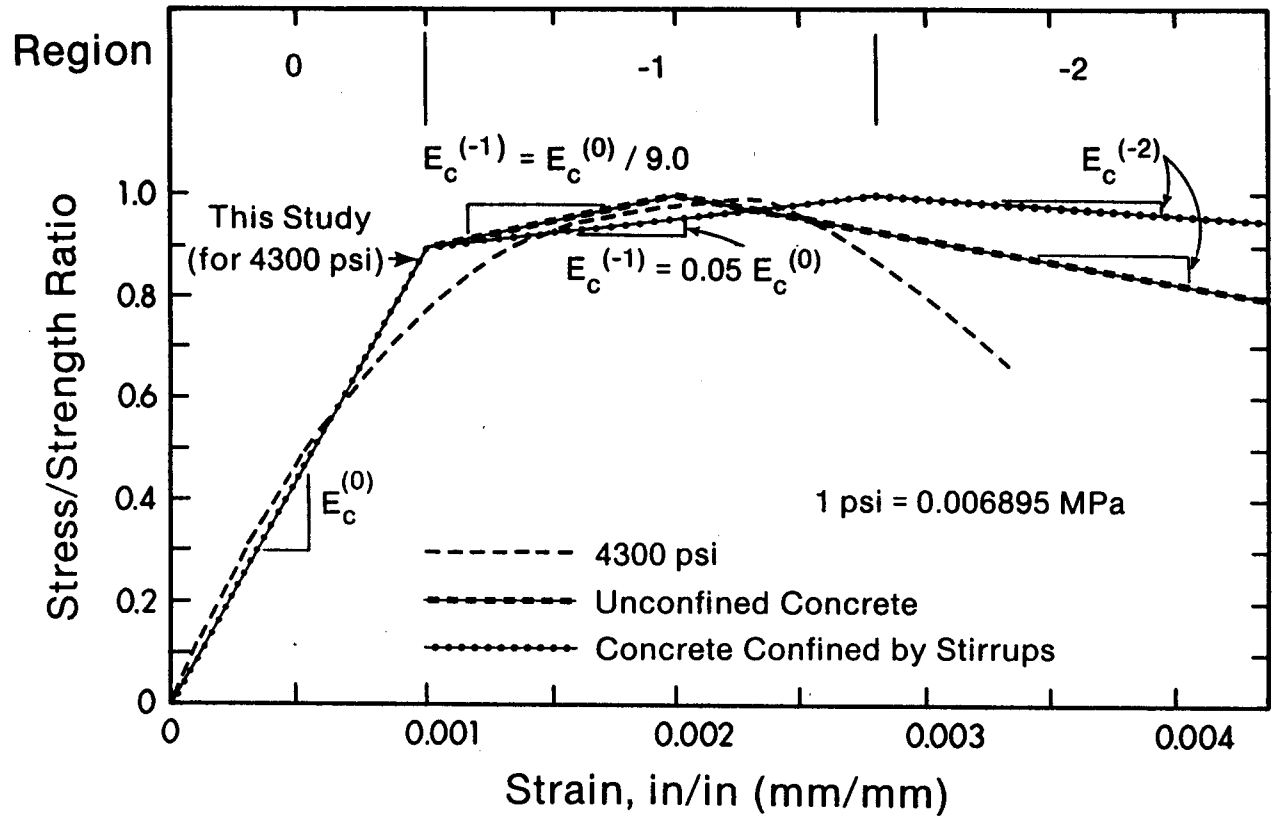

FIG. A4.1. Uniaxial Compressive Stress-Strain Relationship for Concrete

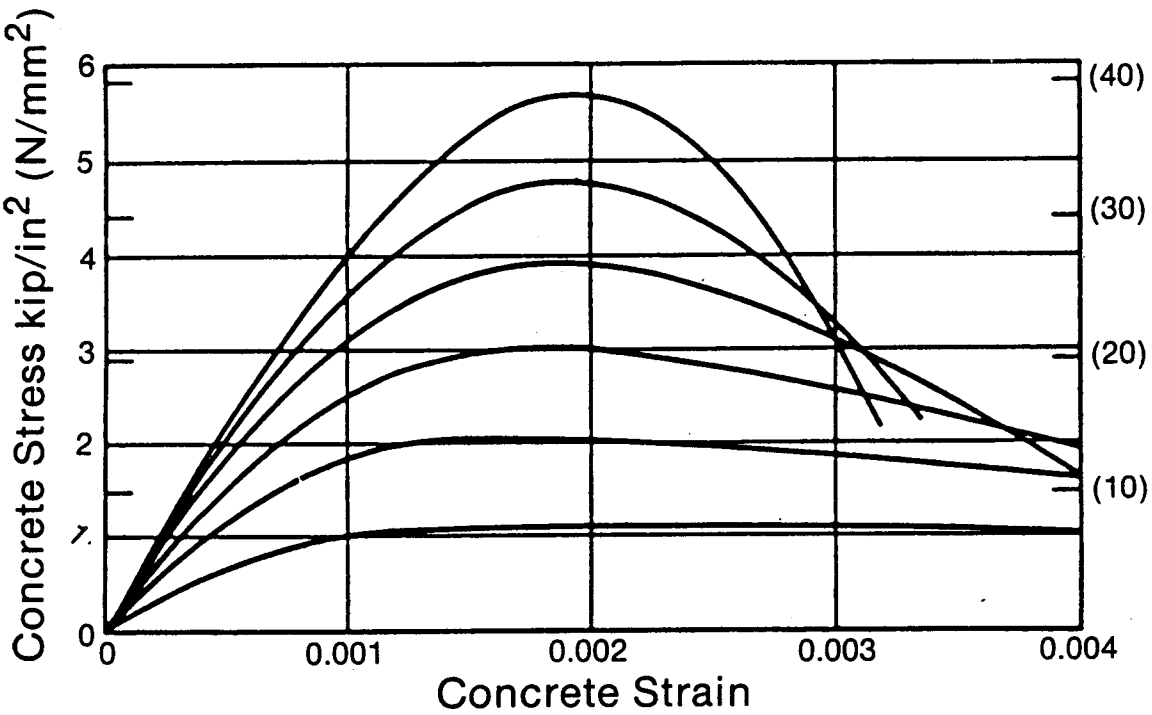

FIG. A4.2. Stress-Strain Curves for Concrete Cylinders Loaded in Uniaxial Compression

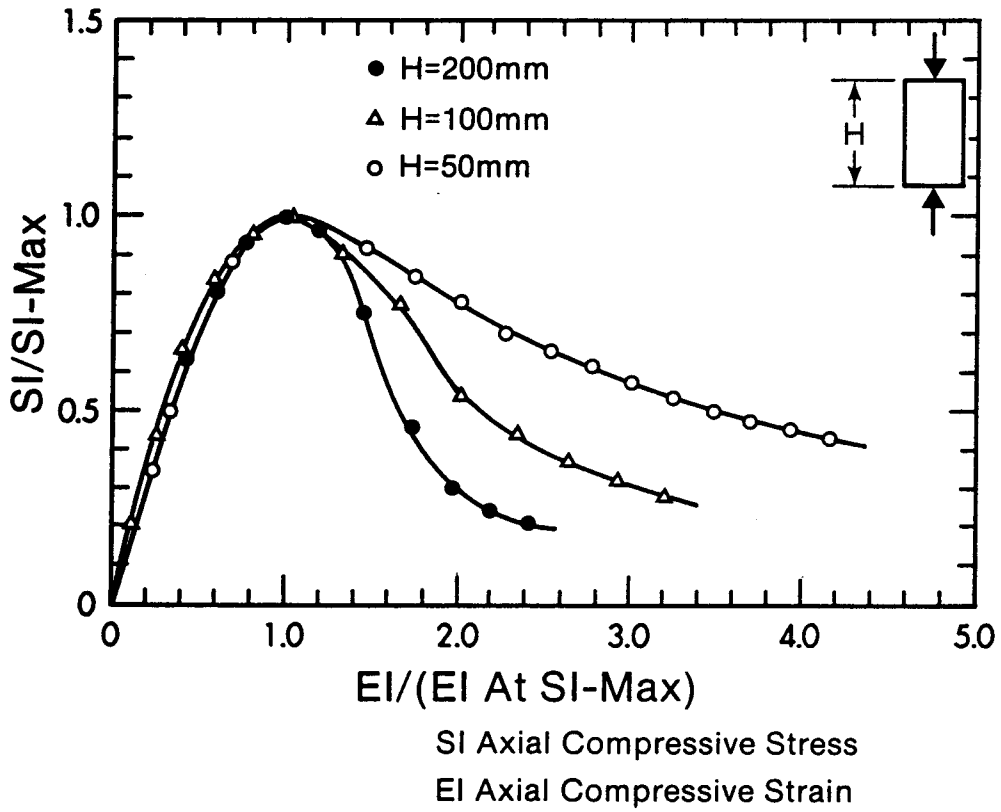

FIG. A4.3. Influence of Specimen Height on Uniaxial Stress-Strain Curve (Adapted from Chen, 1985)

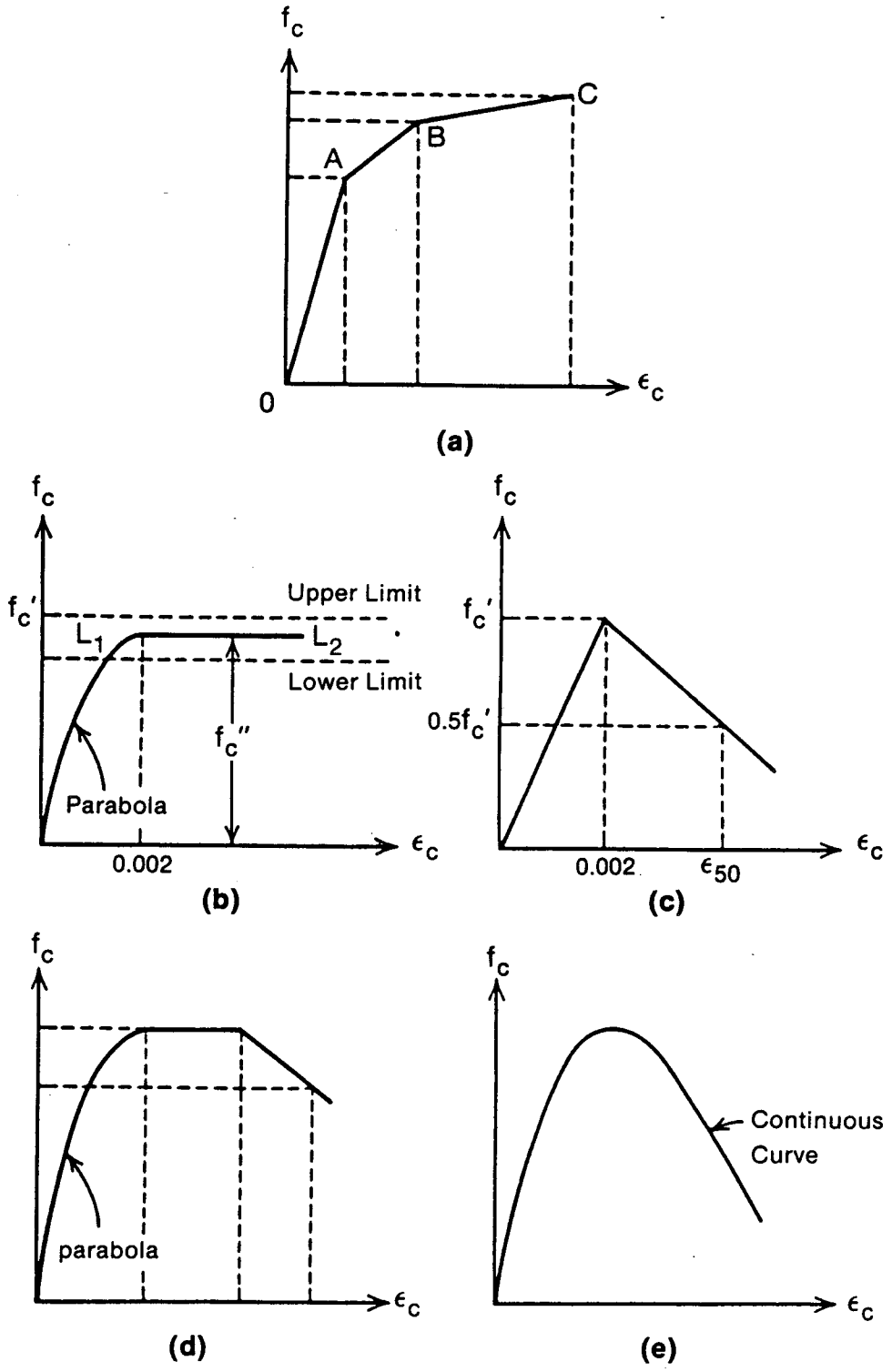

FIG. A.4.4. Some Proposed Stress-Strain Curves for Concrete Confined by Rectangular Hoops (Adapted from Park and Paulay, 1975)

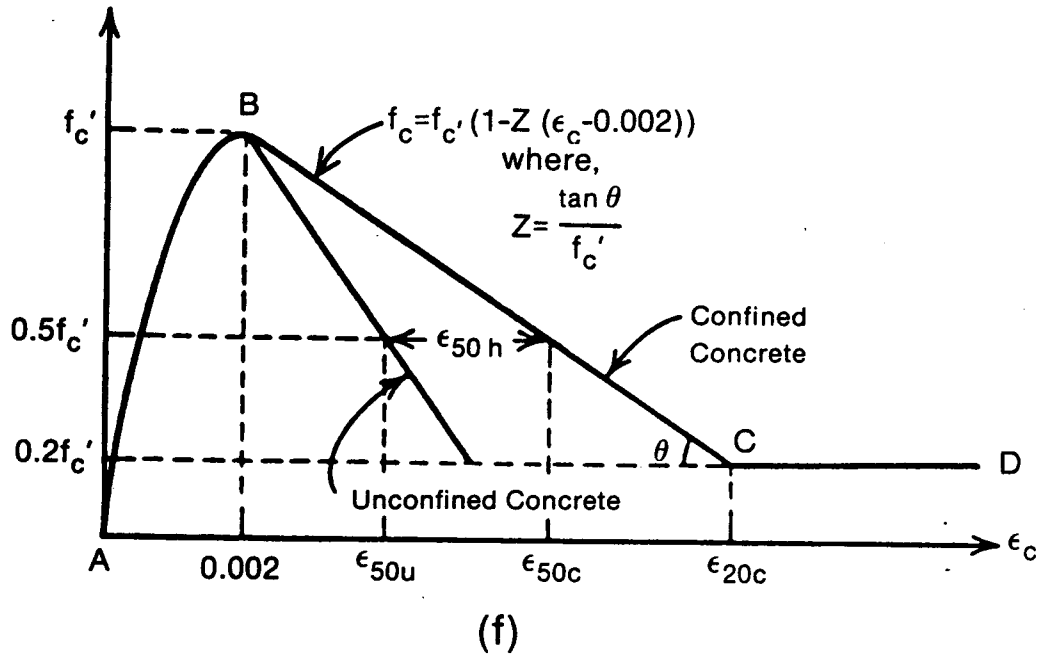

FIG. A4.4. (Continued)

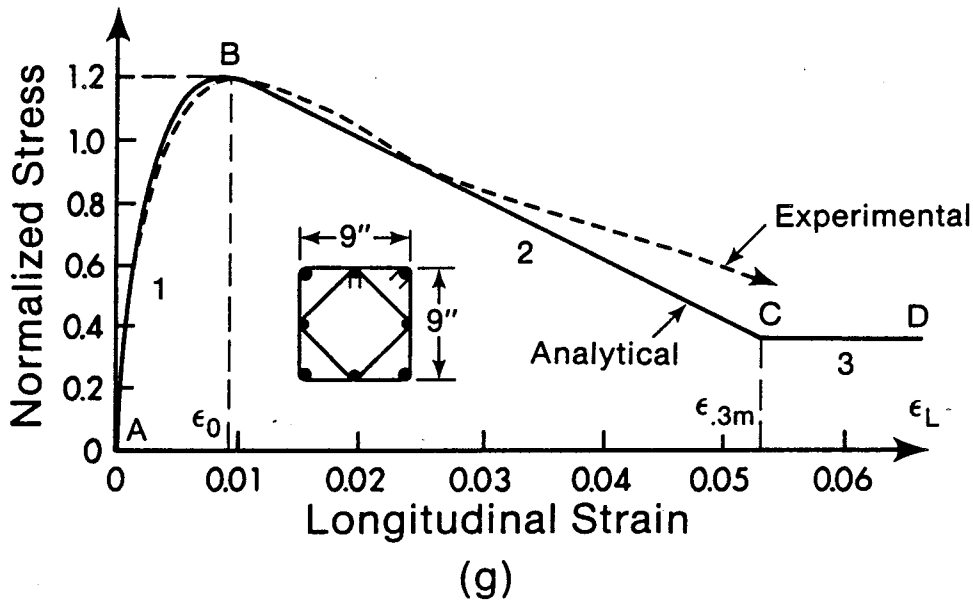

FIG. A4.4. (Continued)

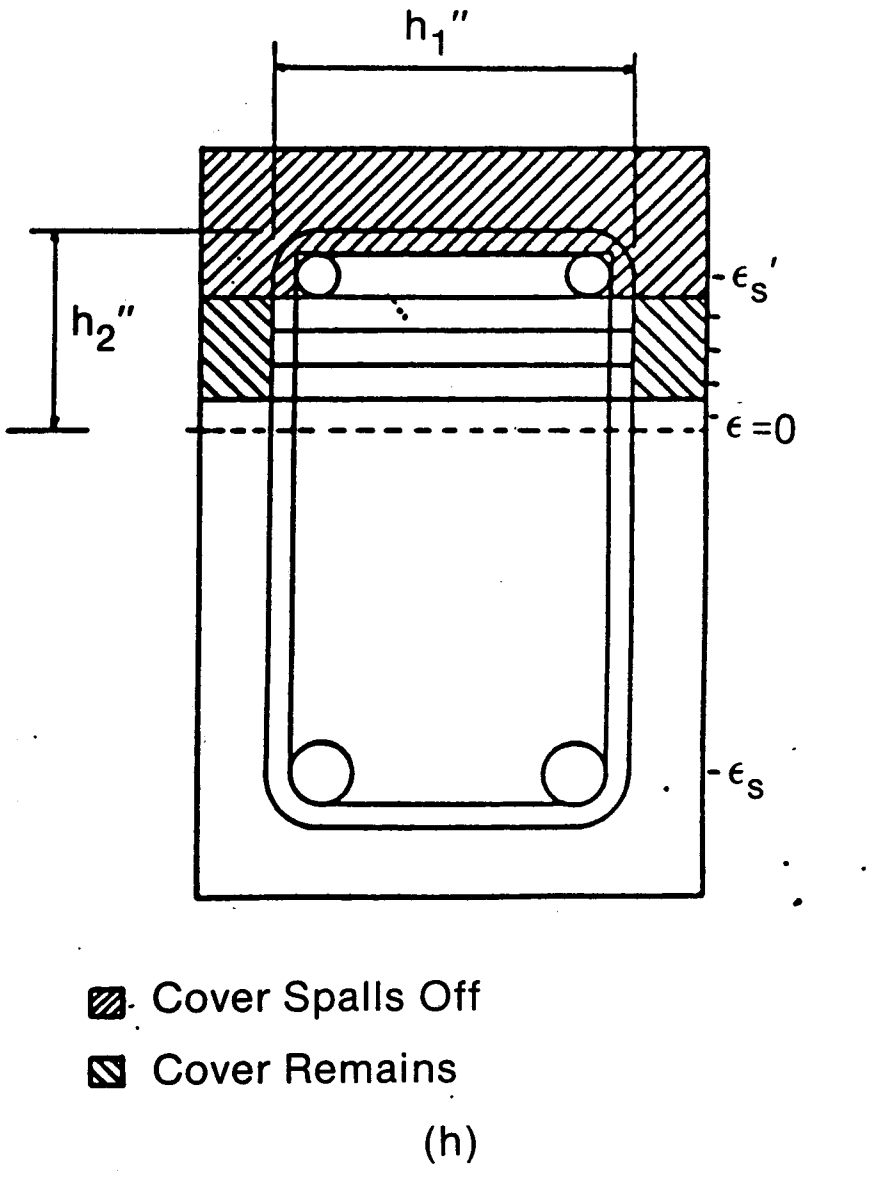

FIG. A4.4. (h) Sketch Explainaing the h" Term in Eqs. A4.4b and A4.4d (Adapted from Krauthammar and Hall, 1982)

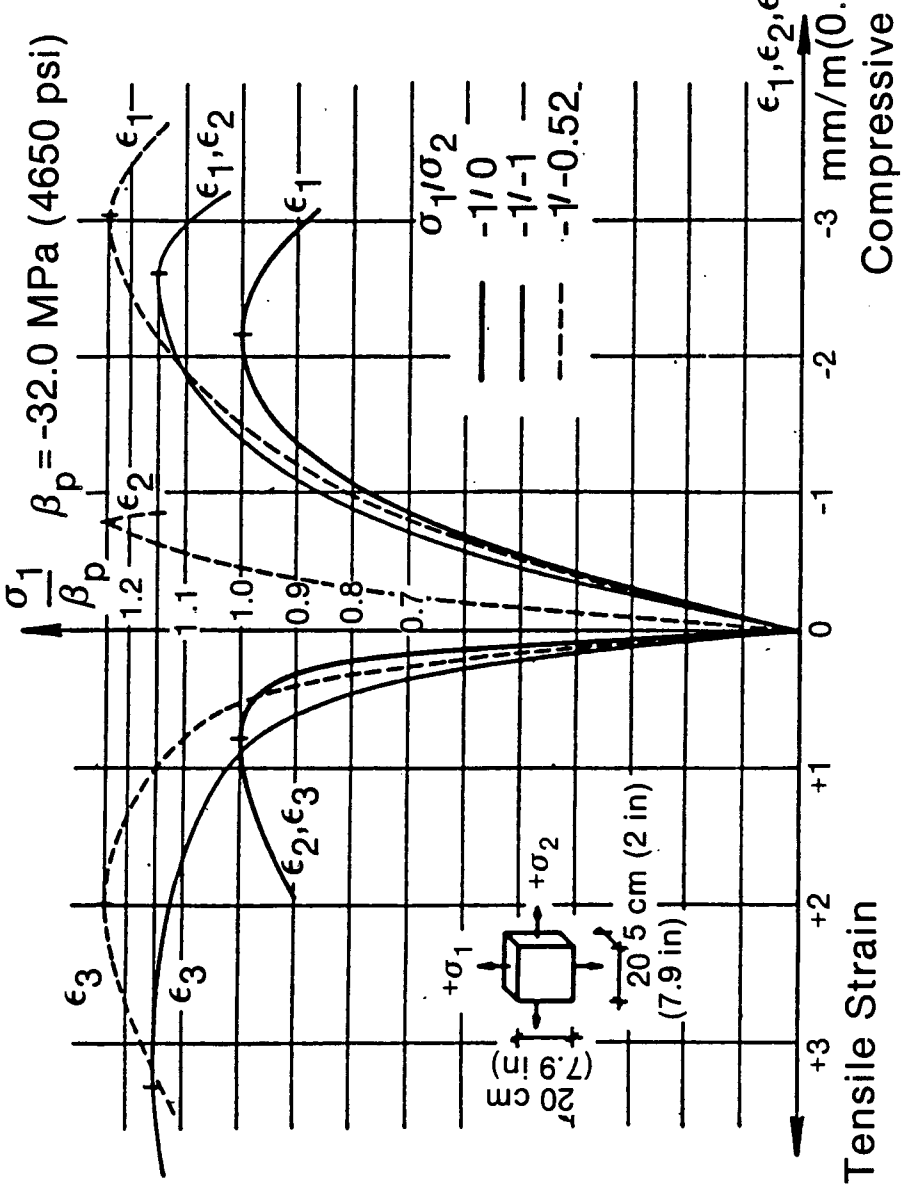

FIG. A4.5. Stress-Strain Relationships of Concrete Under Biaxial Compression (Adapted from Kupfer et al., 1969) β_p = cube compressive strength

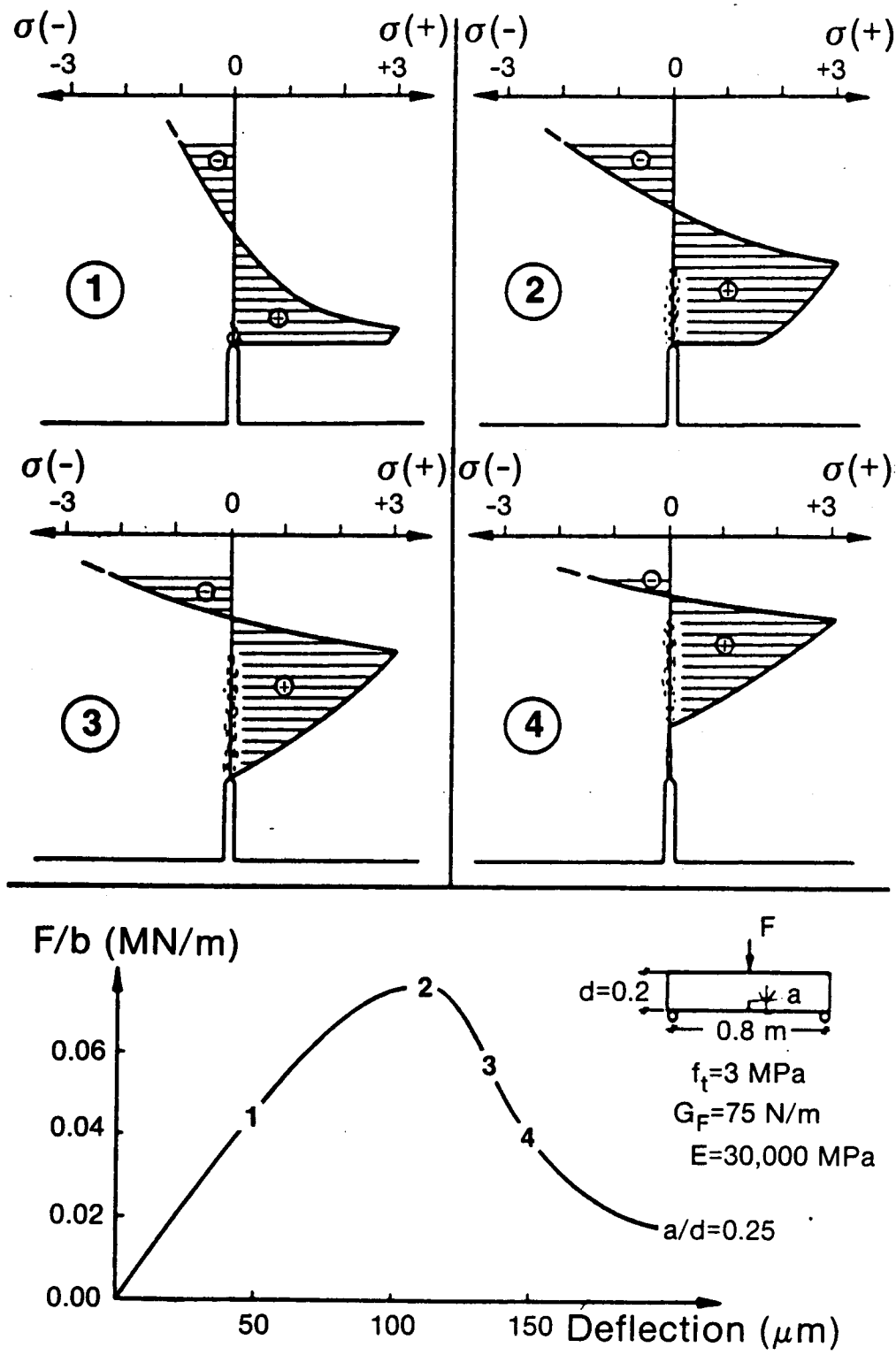

FIG. A4.6. The Theoretical Development of the Fracture Zone, the Corresponding Stress Distribution, and Load-Deflection Curve (Adapted from Hillerborg, 1985)

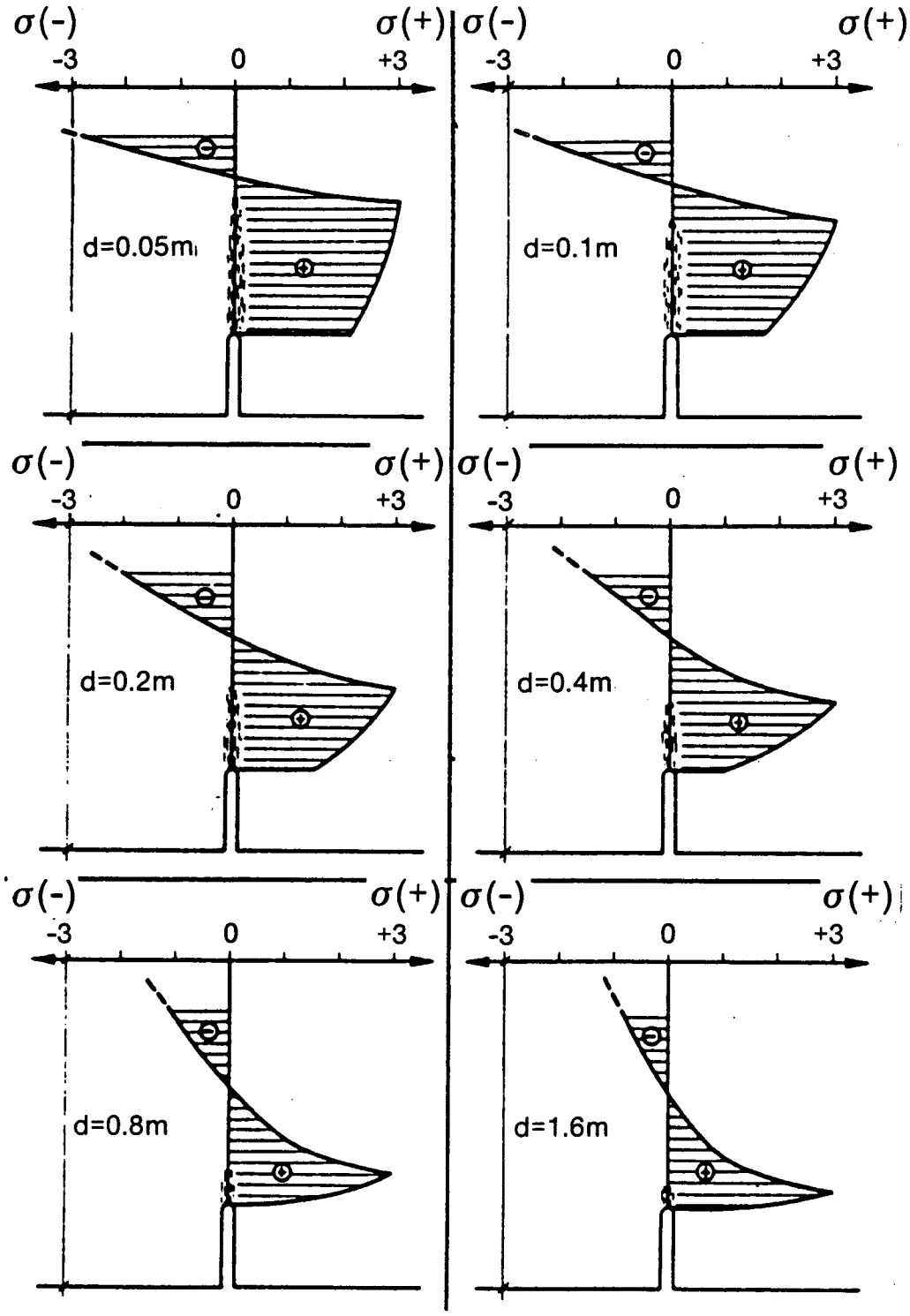

FIG. A4.7. Stress Distribution in Front of the Notch Tip at Maximum Load for Different Beam Depths d. Properties as per Fig. A4.6. Beam Length= 4d (Adapted from Hillerborg, 1985)

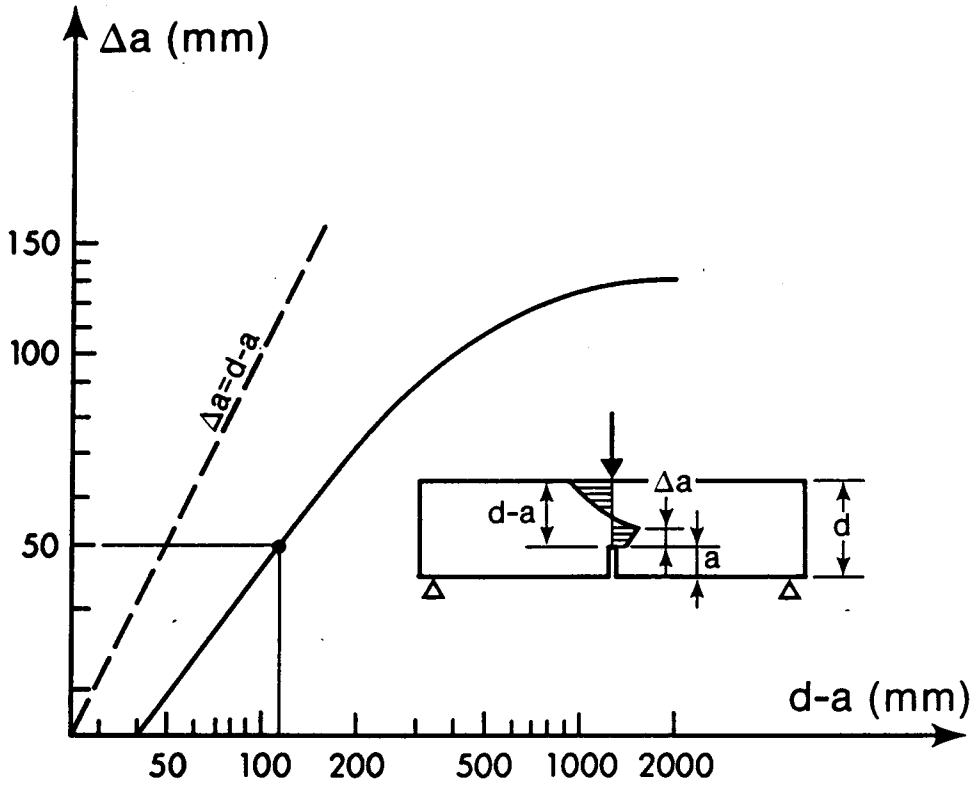

FIG. A4.8. Variation of Fracture Zone Length Δa at Maximum Load with Ligament Depth d-a. (Adapted from Hillerborg, 1985)

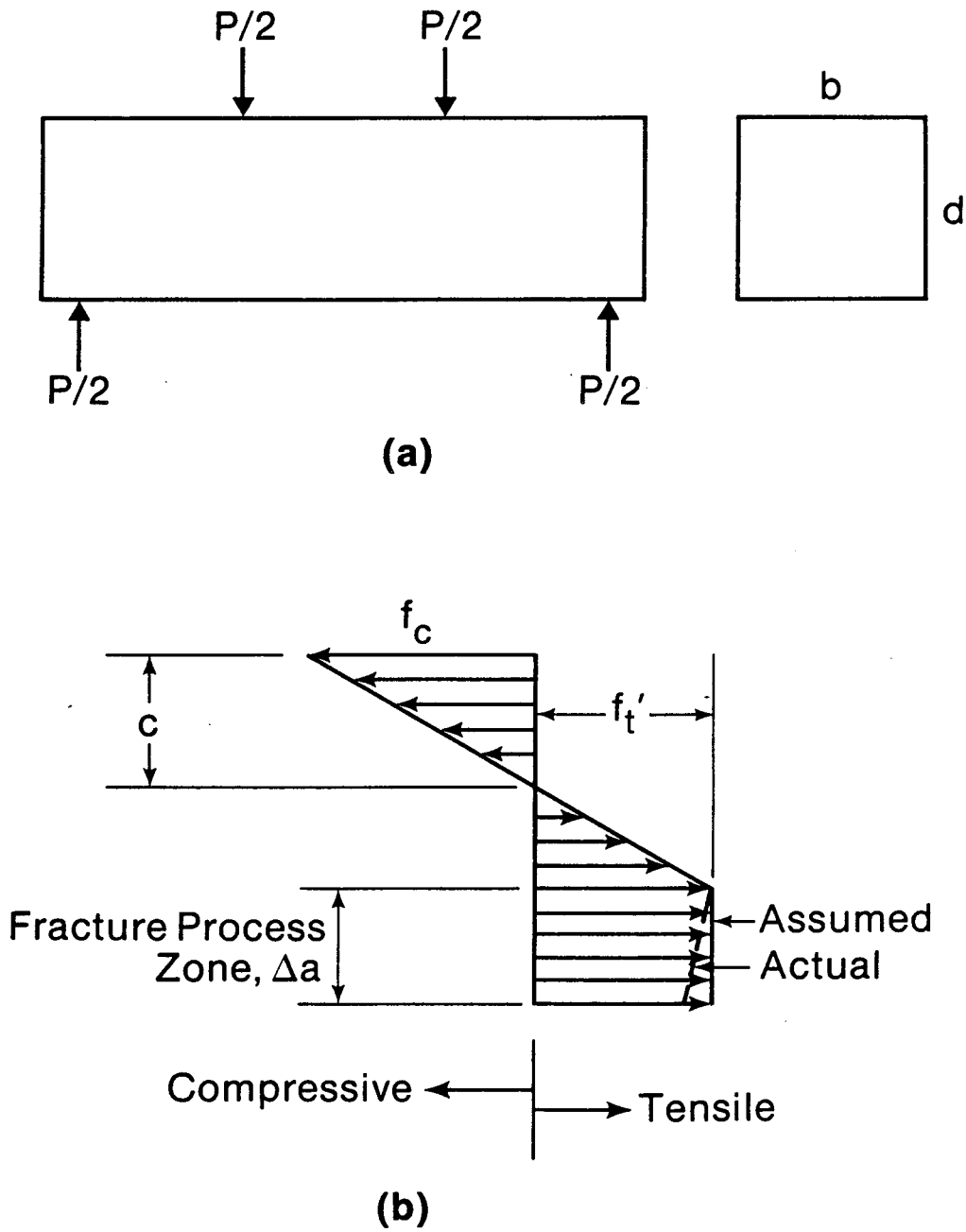

FIG. A4.9. Modulus of Rupture Test (a) Loading Arrangement and Specimen (b) Stress Distribution Across the Section at Midspan

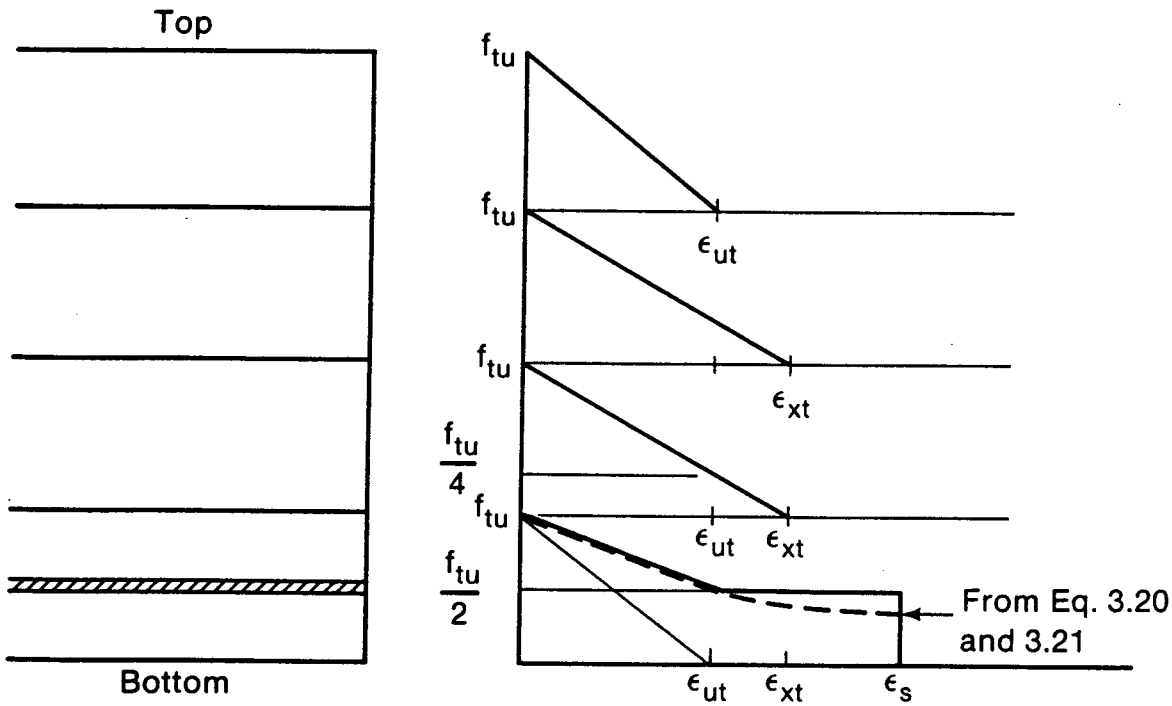

FIG. A4.10. Tensile Stress-Strain Curves for Elements Depending on Proximity to Reinforcement